Estimation of Rain Attenuation at C, Ka, Ku and V Bands for Satellite Links in South Africa

S. J. Malinga[1], **P. A. Owolawi**[1], **and T. J. O. Afullo**[2]

[1]Department of Electrical Engineering, Mangosuthu University of Technology
Umlazi, KwaZulu-Natal, South Africa
[2]Department of Electrical, Computer and Electronics Engineering
University of KwaZulu-Natal, Durban, South Africa

Abstract— Despite the fact that over 20 fibre optic cable networks have been rolled out in Africa, satellite infrastructures continue to fulfil an important role in providing communication access to rural, remote and inland areas across the globe. The fast growth in telecommunications, increased demand for bandwidth, congestion in lower frequency bands and miniaturization of communication equipment have forced the designers to employ higher frequency bands such as the C (4 to 8 GHz), Ka (26.5 to 40 GHz), Ku (12 to 18 GHz) and V (40 to 75 GHz) bands. Rain is the most deleterious to signal propagation in these bands. The contribution of rain attenuation to the quality of signal in these bands, especially in the tropical and subtropical bands in which South Africa is located, needs to be studied. The aims of this paper are to estimate the magnitude of rain attenuation using the ITU-R model, carry out link performance analysis, and then propose reasonable, adequate fade margins that need to be applied for all provinces in South Africa.

1. INTRODUCTION

Consumer diversity, demands for bandwidth, and service convergence have led to a tremendous growth in communication systems. These have resulted in congestion at lower frequency bands, and consequently increased the need for higher frequency band usage. At these frequencies, however, the presence of rain causes degradation of signals, especially above 10 GHz [1]. The many advantages of telecommunications systems operating at higher frequencies include: large bandwidth, increased frequency reuse, small device size and wide range of spectrum availability. The major obstacle to these frequency ranges is rain. In South Africa, extensive studies done by Owolawi [2] have revealed different climatic zones in the country. In recent years, the roll-out of fibre optic networks has not diminished the importance of satellite communication systems, especially for rural, remote and inland cities across the globe. The earlier satellite networks operate at L, S, C, and X bands, while the recent ones start operating at Ku, K, Ka, Q and V bands.

Demand for broadband service is exhausting the available capacity of existing C- and Ku-band satellite networks. The recent motivation by Hughes to support Vodacom South Africa in their latest coverage expansion, by providing the first Ka-band satellite that will provide broadband internet access to South Africa and other African countries, is the key reason behind this work. The impacts of rain rate along the satellite path in Southern Africa, where mixed climate conditions (tropical, sub-tropical and temperate) are common, demand special attention with respect to rain attenuation modeling [3]. Electromagnetic waves passing through raindrops at any of these bands will be absorbed, scattered, or passed through the medium. This scattering and absorption processes are termed rain attenuation. The attenuation caused by the rain depends on parameters such as the size of raindrops, rain temperature, drop velocity, polarization, rain rate, drop orientation and transmitting frequency. Since rain attenuation is the primary obstacle to good quality and availability of signal at these bands, the development of rain attenuation models has been the focus of many researchers, and several measurement campaigns, theoretical and analytical models have been established. Many rain attenuation models, both of terrestrial and satellite paths, are semi-empirical in nature due to the incomplete understanding of the physics of rain and lack of accurate characterization of the various sources that produce the impairments. Rain attenuation is estimated by integrating the specific attenuation along the earth-space path. The specific rain attenuation is mathematically calculated by using empirical parameters such as the cumulative distribution of one-minute rain rate at a given probability of exceedence. In this present work, estimated specific rain attenuation at various satellite frequency bands is proposed, based on the ITU-R recommendations [4, 5], using a database of rainfall over ten years in all the provinces in South Africa. Specific attention is given to Ku and Ka bands in terms of application, which may be of interest to systems designers and telecommunications operators in South Africa.

Table 1: Average rain rate at 0.01% for all provinces in South Africa.

South Africa Province/Site	**Rain Rate at 0.01% (mm/hr)**	**Lat/Long**
Eastern Cape (Fort Beaufort)	53 mm/hr	−32.7/26.6
Gauteng (Pretoria)	61 mm/hr	−25.7/28.1
KwaZulu-Natal (Durban)	73 mm/hr	−29.9/30.9
Mpumalaga (Ermelo)	76 mm/hr	−26.4/29.9
Northern Cape (Kimberley)	59 mm/hr	−28.7/24.7
Free-State (Bethlehem)	60 mm/hr	−33.9/18.9
Limpopo (Tshipise)	50 mm/hr	−22.6/30.1
North West (Klerksdorp)	67 mm/hr	−26.8/26.6
Western Cape (Cape Town)	25 mm/hr	−33.9/18.6

2. RAIN RATE DISTRIBUTION IN SOUTH AFRICA

The probability distributions of rain rate for the nine provinces in South Africa is presented in Table 1. The details of data collection, and processes and procedure for the conversion of the available rain data from 5-minute integration time to 1-minute equivalent are recorded by Owolawi [2]. The rain rate for one site in each province is considered and presented as a provincial rain rate in Table 1. It is important to mention that the rain rate presented is at 0.01% percentage of exceedance and at 1-minute integration time, as recommended by ITU-R for the estimation of specific rain attenuation.

It is also notable that the highest rain rate is observed in Mpumalaga with KwaZulu-Natal coming a close second. The lowest rain rate distribution at 0.01% is observed in the Western Cape.

3. RAIN HEIGHT AND NOISE TEMPERATURE

Estimation of rain attenuation along the slant-path of a satellite link requires an understanding of rain height. The method, adopted by ITU-R, assumes the rain structure to be uniform from the ground level to the 0°C isotherm height, h_R, simply termed the effective rain height. Often the empirical formula is used to estimate the value of h_R due to a scarcity of measured data. Most of the referenced rain height experiments were done in Europe and Asia, and very little data is available in Africa except in West Africa [6–10]. As a result, the current work uses the latest ITU Recommendation P.839-3 [6]. Though the model is less accurate, it is widely employed to calculate the average rain height. The mean rain height above mean sea level is expressed as:

$$h_R = h_0 + 0.36\,\text{km} \tag{1}$$

where h_0 is the average annual 0°C isotherm height. If the h_0 is not available from local data, a global contour map is used, as presented in reference [6], and bilinear interpolation is used to determine any unavailable grid line on the map.

4. SLANT PATH RAIN ATTENUATION MODELS

In this section, a rain attenuation model is presented that has performed well for many regions and different rain types. This rain attenuation model is the ITU-R model, which is the most widely accepted international method and benchmark for comparative studies. This model is semi-empirical and often employs the local climatic parameters at a desired probability of exceedance.

4.1. ITU-R Rain Attenuation Model

The ITU-R 618-10 [4] gives summarized procedures for the computation of a satellite path rain attenuation. In order to compute the slant-path rain attenuation using point rainfall rate, the following parameters are required:

f: the frequency of operation in GHz,
θ: the elevation angle to the satellite, in degrees,
ϕ: the latitude of the ground station, in degrees N and S,
h_s: the height of the ground station above sea level, in km,

R_e: effective radius of the Earth (8 500 km),
$R_{0.01}$: point rainfall rate for the location of interest for 0.01% of an average year (mm/hr).

Step-by-step procedures for the computation of the rain attenuation along the slant-path of a satellite system are summarized as follows:

***Step 1*:** Determine the rain height, h_R, as given in (1) and contour map in Recommendation ITU-R P.839.

***Step 2*:** Determine the slant-path length and the horizontal projection.

The slant-path length L_s, expressed in km, is calculated from:

$$L_s = \left\{ \begin{array}{ll} \frac{(h_r - h_s)}{\sin\theta} & \text{for } \theta \geq 5^\circ \\ \frac{2(h_r - h_s)}{\left(\sin^2\theta + \frac{2(h_r - h_s)}{R_e}\right)^{1/2} + \sin\theta} & \text{for } \theta < 5^\circ \end{array} \right\} \text{ (km)} \tag{2}$$

The horizontal projection is then expressed as:

$$L_G = L_s \cos(\theta) \tag{3}$$

where L_G and L_s are in km.

***Step 3*:** Determine the rain rate at 0.01% for the location of interest over an average year. In this work, Table 1 is used, which is a derived rain rate at one-minute integration time at 0.01% of exceedance from long-term local data.

***Step 4*:** Calculate the specific attenuation, a function of desired frequency, polarization and rain rate. The relationship between rain rate, R (mm/h), and specific attenuation, γ (dB/km), is given as:

$$\gamma = aR^b \text{ (dB/km)} \tag{4}$$

a and b are regression coefficients which depend on the drop shape of the falling rain, raindrop density, polarization and frequency. The regression coefficients in Equation (1) are computed by using ITU-R P.838-3 [4]:

$$a = \left[a_H + a_V + (a_H - a_V)\cos^2\theta\cos 2\tau\right]/2 \tag{5}$$

$$b = \left[a_H b_H + a_V b_V + (a_H b_H - a_V b_V)\cos^2\theta\cos 2\tau\right]/2a \tag{6}$$

where τ is the polarization tilt angle relative to the horizontal and θ is the path elevation angle. The polarization tilt angle $\tau = 90^\circ$ for vertical polarization and $\tau = 0^\circ$ for horizontal polarization while circular polarization is given as $\tau = 45^\circ$. The frequency dependent coefficients a_H, a_V, b_H and b_V are presented in Table 2 for both horizontal and vertical polarization over frequencies of 1–400 GHz.

***Step 5*:** Calculate the horizontal reduction factor, $r_{0.01}$ at 0.01% probability and expressed as:

$$r_{0.01} = \frac{1}{1 + 0.78\sqrt{\frac{L_G \gamma_R}{f}} - 0.38(1 - e^{-2L_G})} \tag{7}$$

Note: L_G is the horizontal projection as determined in Step 2 and f is the operating frequency measured in GHz.

***Step 6*:** Calculate the vertical adjustment factor, $v_{0.01}$, for 0.01% of the time.

$$v_{0.01} = \frac{1}{1 + \sqrt{\sin(\theta)}\left[31\left(1 - e^{-(\theta/1+x)}\right)\frac{\sqrt{L_R\gamma_R}}{f^2} - 0.45\right]} \tag{8}$$

$$L_R = \left\{ \begin{array}{ll} \frac{L_G r_{0.01}}{\cos\theta} \text{ km} & \text{for } \xi > \theta \\ \frac{(h_R - h_s)}{\sin\theta} \text{ km} & \text{for } \xi \leq \theta \end{array} \right\} \tag{9}$$

and

$$\xi = \tan^{-1}\left(\frac{h_R - h_s}{L_G r_{0.01}}\right) \text{ degrees} \tag{10}$$

$$x = \left\{ \begin{array}{ll} 36 - |\phi| \text{ degrees} & \text{for } |\phi| < 36 \\ 0 & \text{for } |\phi| \geq 36 \end{array} \right\} \tag{11}$$

Table 2: The specific attenuation parameters.

Frequency GHz	a_H	a_V	b_H	b_V
1	0.000387	0.00000352	0.912	0.880
2	0.00154	0.000138	0.963	0.923
4	0.000650	0.000591	1.121	1.075
6	0.00175	0.0155	1.308	1.265
7	0.00301	0.00265	1.332	1.312
8	0.00454	0.00395	1.327	1.310
10	0.0101	0.00887	1.276	1.264
12	0.0188	0.0168	1.217	1.200
15	0.0367	0.0335	1.154	1.128
20	0.0751	0.0691	1.099	1.065
25	0.124	0.113	1.061	1.030
30	0.187	0.167	1.021	1.000
35	0.263	0.233	0.979	0.963
40	0.350	0.310	0.939	0.929
45	0.442	0.393	0.903	0.897
50	0.536	0.479	0.873	0.868
60	0.707	0.642	0.826	0.824
70	0.851	0.784	0.793	0.793
80	0.975	0.906	0.769	0.769
90	1.06	0.999	0.753	0.754
100	1.12	1.06	0.743	0.744
120	1.18	1.13	0.731	0.732
150	1.31	1.27	0.710	0.711
200	1.45	1.42	0.689	0.690
300	1.36	1.35	0.688	0.689
400	1.32	1.31	0.683	0.684

***Step 7*:** The effective path length is then computed from:

$$L_E = L_R v_{0.01}\,\mathrm{km} \tag{12}$$

***Step 8*:** Calculate the attenuation exceeded for 0.01% of an average year.

$$A_{0.01} = \gamma_R L_E\,\mathrm{dB} \tag{13}$$

The attenuation value for other percentages of exceedance is determined by using the expression below:

$$A_p = A_{0.01}\left(\frac{p}{0.01}\right)^{-[0.655+0.033\ln(p)-0.045\ln(A_{0.01})-\beta(1-p)\sin(\theta)]}\,\mathrm{dB} \tag{14}$$

where

$$\beta = \left\{\begin{array}{ll} 0 & \text{if } p \geq 1\% \text{ or } |\phi| \geq 36^\circ \\ -0.005(|\phi|-36) & \text{if } p < 1\% \text{ and } |\phi| < 36^\circ \text{ and } \theta \geq 25^\circ \\ -0.005(|\phi|-36)+1.8-4.25\sin\theta & \text{otherwise} \end{array}\right\} \tag{15}$$

5. SATELLITE SERVICES

There is a vast variety of satellites orbiting the earth and offering different services to different parts of the world. Most satellite services are offered at C and Ku-band frequencies, with a lot of interest emerging in deploying Ka-band based satellites as well. The advantages offered by satellite-based services include terrain independence and large coverage area. The congestion at lower bands due to increased demand for diverse services and increased bandwidth demand calls for exploration of the advantages offered by higher frequency bands. The major drawback to operating at such frequencies (Ka-band and above) is signal distortion due to factors such as free space and rainfall. The most prominent, however, is the presence of rainfall along the signal path. This paper thus focuses on the signal fading due to rainfall at frequencies up to V-band.

5.1. Geostationary Satellites

Satellites whose orbit appears to be stationary relative to the earth exhibit circular orbits. These satellites are thus refered to as having a geostationery earth orbit (GEO) and hence the term geostationary satellite. Geostationery satellites rotate at a constant speed equal to that of the earth with an inclination of zero, i.e., the satellite's orbit lies in the equatorial plane of the earth. Their large distance from the earth gives them a large coverage area as opposed to low earth orbit (LEO) satellites. A GEO satellite offers a 24 hour view of a particular area, which leads to its wide use as a provider for broadcast satellite services (BSS) and multipoint applications. However, the GEO's distance from the earth leads to a comparatively weak signal strength and a time delay in the received signal. This is a challenge that system designers are faced with and hence compensation techniques are employed to curb this situation.

The results obtained in this paper make use of the Intesat 17 (IS-17) satellite located at 66°E as its service footprint covers the area of study adequately. The geo-characteristic parameters for each location are shown in Table 3. In this table the attenuations (in dB) that are expected for 0.01% of the time and the effective path lengths (in km) for frequencies ranging from C-band up to V-band for circular, horizontal, and vertical polarizations are shown.

The elevation angle for each region is also shown (in degrees). The elevation angle is the angle between the horizontal along the earth's surface and the center line of the satellite's transmission beam as shown in Figure 1. This angle translates into the visibility (coverage) of the horizon to the satellite's beam, with an angle of zero degrees, ensuring visibility from all directions (ideal case). Rainfall attenuation, however, is strongly dependent on two factors: the operating frequency and the local rain rate. The results in Table 3 show that the area with the lowest rain rate at 0.01% exceedance (Cape Town with a value of 25 mm/h) will experience the least attenuation for the same percentage of exceedance at a given frequency. Conversely, it is true that the area with the highest rain rate at 0.01% exceedance (Ermelo with a value of 76 mm/h) experiences the highest signal degradation for the same percentage of exceedance at a given frequency.

The results of Table 3 are also diplayed graphically in Figure 2 and Figure 3. Figure 2 shows the variation of the attenuation at 0.01% of exceedance with frequency, for all the areas under study. The effects of polarization are also shown as this is a consideration for antenna polarity needed by system designers.

The effective path length for each region is determined and its dependency on frequency and elevation angle is evident. This length is used instead of the actual geometric length due to the non-uniformity of rain density as the signal travels through a rainy medium. The location with

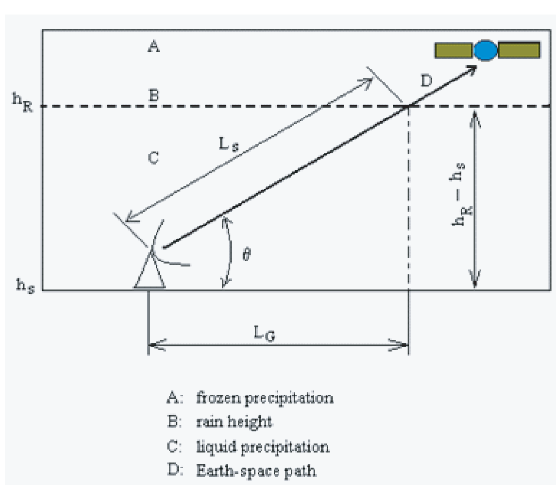

Figure 1: Slant path through rain.

Table 3: Characteristics for locations in South Africa at 0.01% time of exceedance.

			Attenuation for 0.01% of time and Effective path length					
Location	Frequency (GHz)	Elevation Angle (°)	Circular		Horizontal		Vertical	
			$A_{0.01}$ (dB)	L_E (km)	$A_{0.01}$ (dB)	L_E (km)	$A_{0.01}$ (dB)	L_E (km)
Bethlehem	4	26.7°	0.4609	10.1799	0.7474	9.9343	0.4163	10.2298
	8		7.3072	6.6407	7.8191	6.4013	6.7780	6.9178
	12		16.2329	6.0082	17.4814	5.7842	15.1020	6.2317
	18		30.1983	5.7685	32.8390	5.5319	27.9804	5.9885
	26.5		50.9177	5.6110	54.7199	5.4154	47.2461	5.8180
	40		80.8603	5.6080	84.6843	5.4842	77.0819	5.7377
	48		95.0743	5.7014	98.7186	5.6002	91.4850	5.8060
	75		127.9248	6.1725	130.1286	6.1247	125.7473	6.2207
Cape Town	4	26.4°	0.1487	10.7497	0.1972	10.6436	0.1468	10.7542
	8		3.7325	11.4095	4.2487	11.7503	3.4142	11.6610
	12		8.3613	8.4816	8.8294	8.2262	7.9403	8.7469
	18		16.3508	7.7663	17.3737	7.5455	15.4870	7.9725
	26.5		28.7665	7.3542	30.5685	7.1546	27.0192	7.5667
	40		48.5640	7.1193	50.5434	6.9941	46.6038	7.2507
	48		58.6595	7.1351	60.5617	7.0352	56.7809	7.2384
	75		83.0914	7.5077	84.2548	7.4621	81.9398	7.5538
Durban	4	38.4°	0.4816	8.1551	0.8218	7.9794	0.4259	8.1937
	8		8.1321	5.6319	8.7098	5.4286	7.5383	5.8699
	12		17.3709	5.1296	18.8020	4.9335	16.0839	5.3265
	18		31.6598	4.9314	34.6613	4.7227	29.1568	5.1265
	26.5		52.6433	4.8044	56.8030	4.6357	48.6474	4.9835
	40		82.1961	4.8207	86.2863	4.7139	78.1667	4.9327
	48		95.9097	4.9088	99.7862	4.8211	92.1017	4.9996
	75		127.0373	5.3261	129.3459	5.2840	124.7595	5.3686
Ermelo	4	39.7°	0.5138	8.2385	0.8933	8.1325	0.4516	8.2636
	8		8.6734	5.6807	9.3008	5.4813	8.0292	5.9142
	12		18.2123	5.1343	19.7456	4.9401	16.8361	5.3293
	18		32.8177	4.9020	35.9913	4.6949	30.1757	5.0957
	26.5		54.1693	4.7560	58.5035	4.5891	50.0101	4.9330
	40		84.0374	4.7618	88.2608	4.6563	79.8791	4.8727
	48		97.8242	4.8466	101.8174	4.7596	93.9033	4.9365
	75		129.0140	5.2551	131.3815	5.2133	126.6785	5.2973
Fort Beaufort	4	33.3°	0.3368	8.7993	0.5302	8.5952	0.3080	8.8367
	8		6.1075	6.5913	6.5193	6.3420	5.6892	6.8905
	12		13.7248	5.8600	14.7515	5.6521	12.7973	6.0690
	18		25.7554	5.5977	27.9455	5.3837	23.9189	5.7971
	26.5		43.7342	5.4298	46.9708	5.2515	40.6136	5.6188
	40		70.0710	5.4034	73.3646	5.2908	66.8201	5.5215
	48		82.6717	5.4802	85.8119	5.3884	79.5812	5.5752
	75		111.8571	5.8989	113.7500	5.8556	109.9874	5.9428
Kimberley	4	34.1°	0.4044	9.1377	0.6622	9.0411	0.3649	9.1579
	8		7.0987	6.6031	7.6019	6.3706	6.5850	6.8785
	12		15.4464	5.8288	16.6621	5.6238	14.3513	6.0346
	18		28.3315	5.5074	30.8583	5.2936	26.2182	5.7067
	26.5		47.3760	5.3057	50.9807	5.1294	43.9060	5.4926
	40		74.8319	5.2650	78.4266	4.1535	71.2862	5.3819
	48		87.8138	5.3380	91.2260	5.2468	84.4577	5.4323
	75		117.6630	5.7461	119.7047	5.7029	115.6469	5.7898
Klerksdorp	4	36.7°	0.4595	8.7393	0.7769	8.6536	0.4091	8.7591
	8		7.8934	6.1563	8.4615	5.9418	7.3117	6.4086
	12		16.8355	5.4876	18.2102	5.2882	15.5996	5.6877
	18		30.5508	5.2029	33.3944	4.9925	28.1783	5.3992
	26.5		50.6980	5.0245	54.6579	4.8531	46.8923	5.2063
	40		79.3005	5.0047	83.1990	4.8962	75.4586	5.1184
	48		92.6614	5.0828	96.3537	4.9938	89.0329	5.1748
	75		123.1336	5.4896	125.3321	5.4472	120.9639	5.5325
Pretoria	4	38.6°	0.3939	8.5060	0.6509	8.4249	0.3541	8.5232
	8		7.2004	6.3954	7.7052	6.1648	6.6892	6.6732
	12		15.5001	5.6288	16.7346	5.4299	14.3913	5.8294
	18		28.2984	5.3134	30.8635	5.1070	26.1584	5.5065
	26.5		47.1866	5.1179	50.8224	4.9486	43.6930	5.2976
	40		74.2932	5.0802	77.9035	4.9732	70.7361	5.1925
	48		87.0530	5.1512	90.4749	5.0635	83.6904	5.2418
	75		116.2884	5.5450	118.3257	5.5031	114.2777	5.5873
Tshipise	4	42.0°	0.2892	8.1758	0.4560	8.1145	0.2654	8.1871
	8		6.1332	7.1756	6.4849	6.8410	5.8419	7.6677
	12		13.1683	6.0126	14.1444	5.8061	12.2962	6.2252
	18		24.2786	5.6065	26.3346	5.4034	22.5650	5.7980
	26.5		40.8491	5.3637	43.8846	5.1957	37.9347	5.5431
	40		65.1933	5.2841	68.2654	5.1782	62.1679	5.3955
	48		76.8522	5.3400	79.7687	5.2536	73.9868	5.4295
	75		103.8973	5.7128	105.6321	5.6713	102.1854	5.7548

the lowest elevation angle exhibits the longest effective path length (Cape Town with an elevation angle of 26.4 degrees). The opposite is expected to be true. However, the results in Table 3 suggest that the variability of local rain rate has an influence on the effective path length. Notwithstanding this observation, the general conclusion can still be drawn that areas of high elevation exhibit short effective path lengths given the small contribution due to varying local rain rates. Unlike attenuation, the effective path length depends strongly on elevation angle and frequency of operation. These results are displayed graphically in Figure 3 to show the variability of the effective path length with frequency for each location.

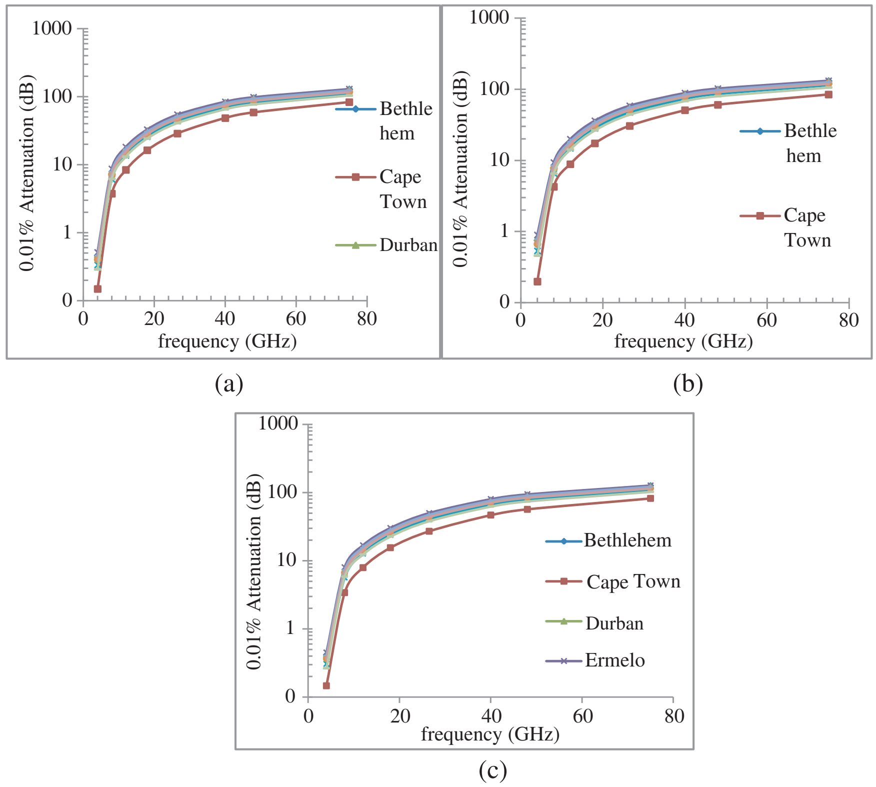

Figure 2: Attenuation at 0.01% exceedence for all regions for (a) circular polarization, (b) horizontal polarization, and (c) vertical polarization.

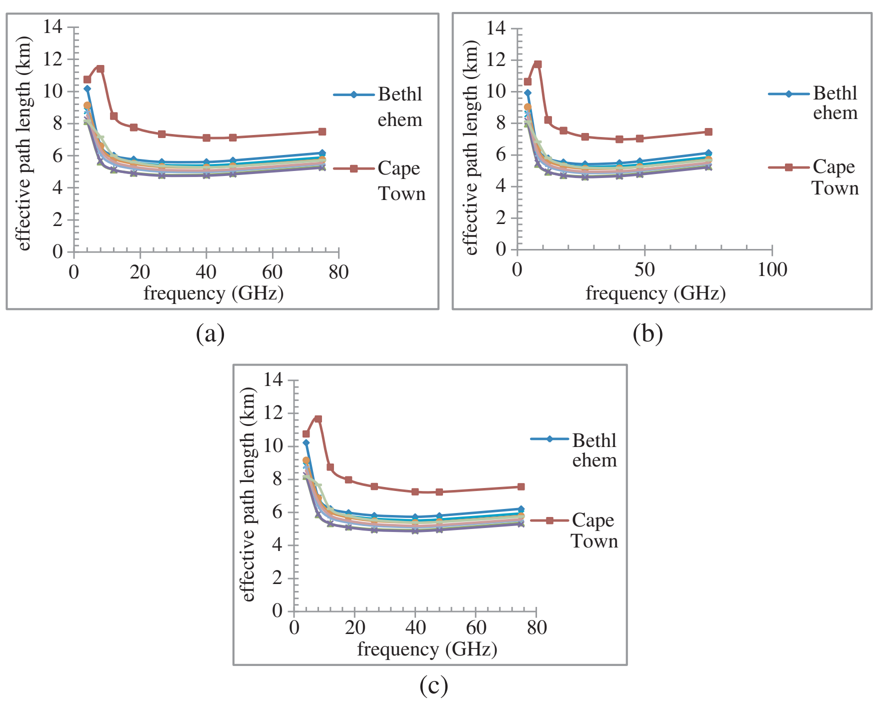

Figure 3: Effective path length for all regions for (a) circular polarization, (b) horizontal polarization, and (c) vertical polarization.

The elevation angles give designers an idea as to the positioning of ground station antennas for maximum energy transfer with little to no tracking required (considering GEO satellites). All the areas under study have an elevation angle above 25 degrees, which permits the use of the approximation given in the first condition of Equation (2).

Figures 2(a)–(c) show the attenuation expected to be exceeded for 0.01% of the time in an average year. The fade margins are higher for horizontally polarized signals as expected while the vertical polarity gives the minimum fade margins. Circularly polarized electromagnetic waves (EM) experience a mid-average fade margin with respect to both horizontally and vertically polarized signals. Different polarizations are chosen by service providers for different reasons such as cross-polarization discrimination and frequency reuse.

Figures 3(a)–(c) show how the effective path length changes as the frequency of operation changes. At lower frequencies, e.g., C-band, the effective path length is quite long but reduces almost exponentially at around Ku-band frequencies. As frequency increases into the Ka-band frequencies, the effective path length maintains a uniform value. It also appears that at V-bands, the effective path length begins to increase consistently with increasing frequency. The increase is, however, steady but could be rapid at millimetre bands.

6. EARTH-SPACE RAIN ATTENUATION

Earlier satellites have been offering services at C-band frequencies but the demand for increased bandwidth has seen this band exhausted and inadequate in supporting the fast data rates associated with modern applications. The advantages at these bands are quite evident from Figure 4 citing low attenuation levels even at high availability requirements. In this paper, maximum fade depths were determined for probabilities ranging from 0.001% to 5%. Evidently, as the availability increases, so does the required rain fade margin. The variability of rainfall attenuation with availability is location dependent as well as frequency dependent. For the two frequencies considered in Figure 4 (lower and upper bounds for C-band), as discussed in Section 5, Cape Town has the least attenuation for all the percentage availabilities considered. It also follows, given the local rain rates, that Ermelo experiences the highest rainfall attenuation within the range of the probabilities considered. The results are consistent with the notion that higher rain rates require high fade margins. This may be true for terrestrial radio links where the elevation angle is considered to be uniform (zero) for all locations. However, the effect of elevation angle on attenuation (Equations (9) through (14)), is such that locations of higher rain rate may have lower attenuation as compared to those with lower rain rates for 0.01% of the time. This means that areas having the same rain rate do not necessarily have to have equal fade margins. The dependency of rainfall attenuation on geographical location plays an important role in this anlysis.

The effect of effective path length on rain attenuation is observed in Figure 4(a). For probabilities of outage above 2% of the time (availability of 98% or less), there is a noticeable overlapping behaviour amongst the graphs. The graph for Tshipise prominently displays this scenario. This is a result of different effective path lengths for different locations. The same scenario is less prominent in Figure 4(b), which is probably nullified by the higher frequency of 8 GHz. It is even clearer at Ku-, Ka-, and V-band frequencies as shown in Figures 5, 6, and 7 respectively.

The Intelsat 17 (IS-17) provides good coverage in South Africa, transmitting at Ku-band frequencies with a beam peak of up to 53.3 dBW. The uplink frequencies range from 13.75–4.50 GHz with the downlink range of 10.95–11.70 GHz [IS-17 factsheet]. The increased demand for bandwidth for greater data flow and the over-crowding of the electromagnetic spectrum may see this provision inadequate for the numerous applications of satellite systems. The trend recently has been to utilize Ka-band frequencies for satellite communications, with uplink frequencies of 30 GHz and downlink frequencies of 20.2 GHz [11].

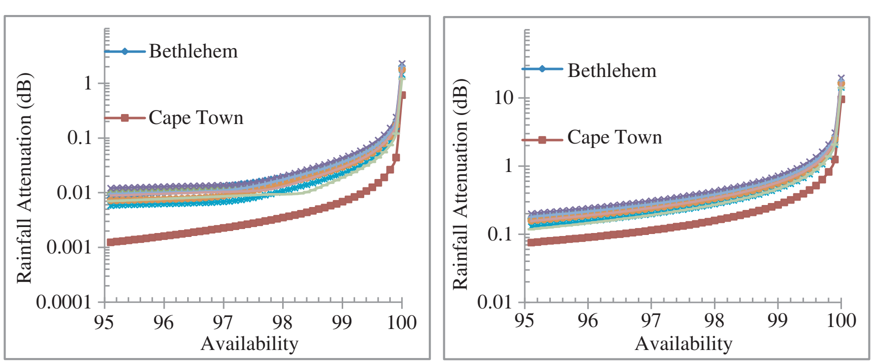

(a) (b)

Figure 4: Attenuation at C-band for horizontal polarization for all locations at (a) 4 GHz and (b) 8 GHz.

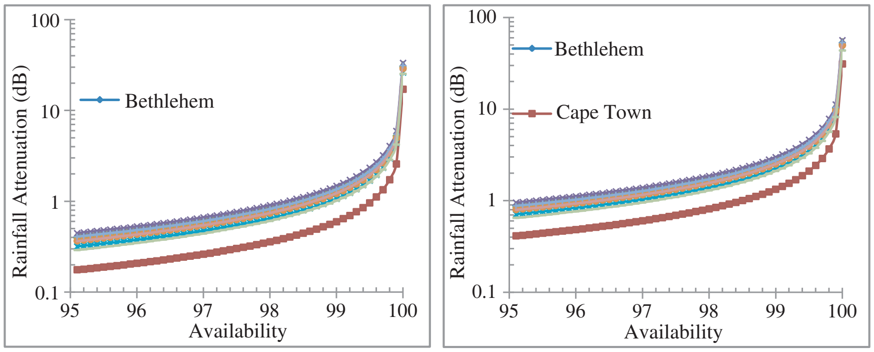

(a) (b)

Figure 5: Attenuation at Ku-band for vertical polarization for all locations at (a) 12 GHz and (b) 18 GHz.

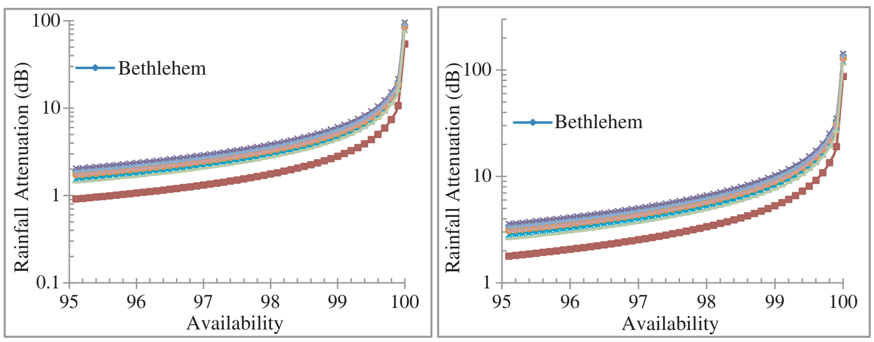

(a) (b)

Figure 6: Ka-band circular polarization for all provinces at (a) 26.5 GHz and (b) 40 GHz.

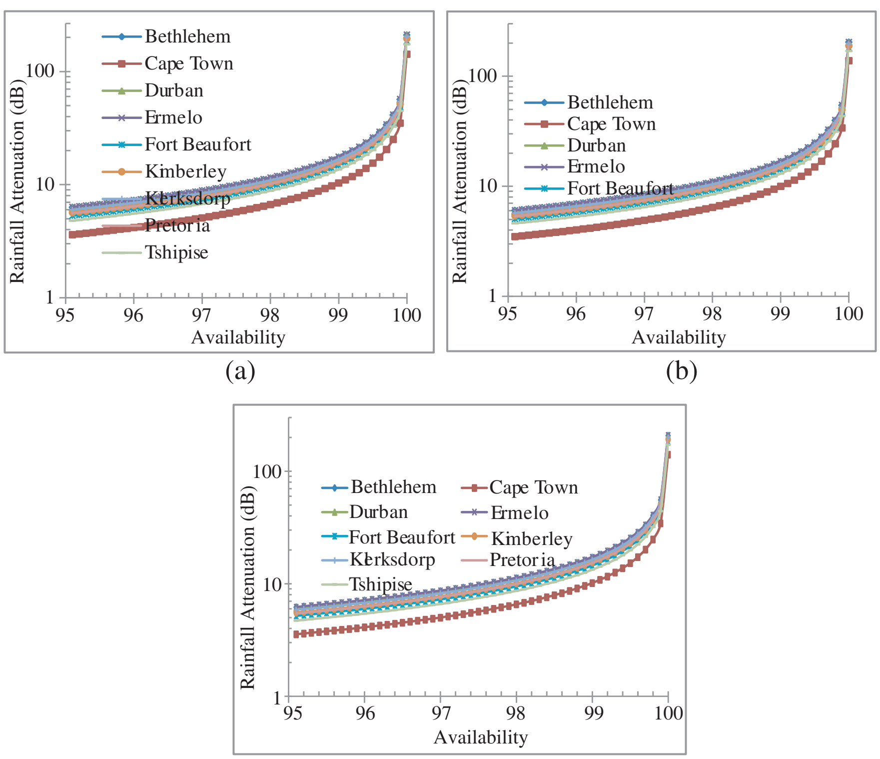

(c)

Figure 7: V-band at 75 GHz for all provinces for (a) horizontal polarization, (b) vertical polarization, and (c) circular polarization.

Despite the obvious merits that include less propagation losses (due to hydrometeours), less free space loss and the ability to penetrate foliage, lower frequencies do not provide for restrictions in power requirements, easy transmit-to-receive isolation, and antenna aperture size. Utilization of Ka-band frequencies and even higher can provide spectral relief for satellite applications with reasonably sized antennas and reduced power requirements. Figures 6 and 7 show that operating at Ka- and V-bands requires a considerable amount of fade margin as compared to operating at lower bands.

The difference in fade margin requirements due to polarization is minimal. The worst case difference, as expected, is between the vertical and horizontal polarizations, with a value of 4.7 dB at 75 GHz for Ermelo. Considering the band in question, this is a relatively small difference. For lower frequency bands the difference is very little, making it a non-viable factor to consider for choice of polarization. However, for linear polarization, precision alignment is required for the earth station antenna to maximize reception from the satellite. Given the height of the satellite above the earth, transmission latencies are imminent. Since the satellite is of geostationary type, it has a fixed radius of orbit of about 42 242 km. Its height above the earth surface is therefore given by:

$$h_{GEO} = (42242 - 6378) = 35864\,\text{km} \tag{16}$$

The following expression is used to estimate the time delay experienced by an electromagnetic wave travelling from an earth station to the satellite and back:

$$t_{delay} = \frac{2 * 35864\,\text{km}}{3 * 10^8 * 10^{-3}\,\text{km/s}} = 0.239\,\text{s} \tag{17}$$

The transmission delay is in the order of about 240 ms for a one-way trip.

The rate of advancement in satellite communications will ultimately lead to satellite usage across all communication fields including access to telephone networks from anywhere around the globe. Unlike C- and Ku-bands, Ka-band employs multiple spot beams which makes it attractive in terms of focus and frequency reuse. Over a wide geographical area, the same frequency range can be reused many times provided adjacent spot beams use a different frequency.

7. CONCLUSION

The results obtained in this paper are based on the Intelsat 17 (IS-17) satellite characteristics which operate at C- and Ku-band and projections are made into higher frequency bands. Across all the frequency bands from C-band up to V-band, rainfall attenuation, elevation angle, and effective path length have been determined for satellite link applications in South Africa. A consideration has been made for link availabilities from 95% up to 99.999% of the time. It is noted that the severity of the degradation of the propagating signal increases with increasing availability. However, for a given percentage availability, the signal degradation increases with an increase in operating frequency of the satellite link. It is observed for example in Figure 6(a) and more clearly from Table 3, that a fade margin in excess of 50.7 dB is required for 99.99% availability in Klerksdorp considering circular polarization at 26.5 GHz. For the same location, availability, and polarization, a fade margin of 79.3 dB is required for the operating frequency of 40 GHz.

Results displayed in Table 3 show that areas of lower elevation angles have longer effective path lengths. These areas are expected to suffer higher loss in dB during operation since signals traverse a longer atmosphere and the overall slant path is increased. For a given location, the effective path length varies inversely proportional to the frequency of operation up to at least 40 GHz. Beyond this frequency a direct proportionality relationship is observed consistently up to 75 GHz. It can thus be inferred that this relationship is valid for even higher frequencies not under consideration in this paper. It is seen through Equation (13) that the effective path length is directly proportional to the rainfall attenuation. However, for the satellite under consideration and the region of study, the contribution to the overall attenuation due to the effective path length (elevation angle) is of little effect due to other dominant factors such as frequency and local rain rate. This is to say that these results are exclusive to this study and hence the conclusion reached herein.

Considering all the locations under study for South Africa, Cape Town requires significantly the lowest fade margin at all frequencies and percentage availabilities. Conversly, Ermelo requires the highest fade margin at all frequencies and percentage availabilities. A number of other locations also experience almost the same level of degradation as Ermelo. The two notable ones are Bethlehem and Durban. In comparison with Ermelo, at 75 GHz, Bethlehem is 1.25 dB off while Durban is 2.04 dB off considering horizontal polarization. For circular polarization Bethlehem and Durban are off by 1.09 dB and 1.97 dB, respectively, while for vertical polarization they are 0.93 dB and 1.92 dB off, respectively. It should be noted that all these comparisons are made for 99.99% availability. Despite having the smallest elevation angle of 26.4 degrees, Cape Town maintains a low fade margin requirement and this can only be attributed to its significantly low local rain rate of 25 mm/h. Tshipise has the highest elevation angle of 42 degrees and local rain rate of 50 mm/h (twice that of Cape Town). It remains in need of higher fade margins as compared to Cape Town though less prone to degradation as compared to the other locations in the country.

At the lower bound of the Ka-band, 26.5 GHz, it is observed that the lowest rain attenuation of about 27 dB (for Cape Town) is obtained with the highest value of 50 dB obtained for Ermelo for 0.01% of the time. For the same demand at 40 GHz, the minimum and maximum fade margins required are 46.6 dB and 79.9 dB respectively. So 27 dB and 80 dB can be considered the minimum and the maximum attenuation levels at Ka-bands for 99.99% availability for satellite communications links in South Africa.

REFERENCES

1. Moupfouma, F., "Improvement of a rain attenuation prediction method for terrestrial microwave links," *IEEE Transaction on Antennas and Propagation*, Vol. 32, No. 12, 1368–1372, 1984.
2. Owolawi, P. A., "Rainfall rate probability density evaluation and mapping for the estimation of rain attenuation in South Africa and surrounding islands," *Progress In Electromagnetics Research*, Vol. 112, 155–181, 2011.
3. "Propagation data and prediction methods required for the design of Earth-space telecommunications systems," Recommendation ITU-R P.618-10, ITU-R P Sers., October 2009.
4. "Propagation data and prediction methods required for the design of terrestrial line-of-sight systems," Recommendation ITU-R P.530-12, ITU-R P Sers., February 2007.
5. "Propagation data and prediction methods required for the design of Earth-space telecommunication systems," ITU-R P.618-8, ITU, Geneva, Switzerland, 2003.
6. "Rain height model for prediction methods," Recommendation ITU-R P.839-3, ITU-R P Sers., Geneva, International Telecommunications Union, 2001.
7. Mondal, N. C. and S.K. Sarkar, "Rain height in relation to 0–1°C isotherm height for satellite communication over the Indian Subcontinent," *Theoretical and Applied Climatology*, Vol. 76, 89–104, 2003.
8. Ong, J. T., K. I. Timothy, F. B. L. Choo, and W. L. Carron, "Effective rain height statistics for slant path attenuation prediction in Singapore," *Electronic Letters*, Vol. 36, No. 7, 661–663, 2000.
9. Parshoatam, S., I. S. Hudiara, and M. L. Singh, "Estimation of effective rain height at 29 GHz at Amritsar (tropical region)," *IEEE Transaction on Antennas and Propagation*, Vol. 55, No. 5, 1463–1465, 2007.
10. Ajayi, G. O. and F. Barbaliscia, "Prediction of attenuation due to rain: Characteristics of the 0°C isotherm in temperate and tropical climates," *International Journal of Satellite Communication*, Vol. 8, 187–196, 1990.
11. Seybold, J. S., *Introduction to RF Propagation*, 255–270, John Wiley & Sons, Hoboken, NJ, 2005.

Computation of Rain Attenuation through Scattering at Microwave and Millimeter Bands in South Africa

S. J. Malinga[1], P. A. Owolawi[1], and T. J. O. Afullo[2]

[1]Department of Electrical Engineering, Mangosuthu University of Technology
Umlazi, KwaZulu-Natal, South Africa
[2]Department of Electrical, Computer, and Electronics Engineering
University of KwaZulu-Natal, Durban, South Africa

Abstract— Attenuation due to rain at frequencies above 10 GHz in temperate climates and above 7 GHz in tropical, sub-tropical and equatorial climates is a critical factor for both terrestrial and satellite link system designers. This paper presents results of computed and measured attenuation due to rain, using the spherical method (Mie Scattering technique) and non-spherical method (Pruppacher and Pitter technique). The derived scattering amplitude coefficients are incorporated with available measured rain rate and droplet size distribution data to estimate specific and total attenuation for the region of South Africa. The results are then compared with the few existing rain attenuation models and the one-year attenuation measurement campaign in Durban, South Africa. The results are further applied to the terrestrial radio links and satellite links at a chosen rain rate and specified frequencies.

1. INTRODUCTION

The growing demand for additional communication capacity has forced researchers to exploit the advantages inherent in the higher frequency spectrum. These advantages include: robust bandwidth, frequency-reuse, equipment miniaturization and the short time of deployment [1].

At these spectra the increased attenuation due to rain becomes one of the key limiting factors for the optimum performance of radio links via terrestrial and satellite paths. In temperate regions propagation of radio signals at frequencies above 10 GHz is susceptible to the adverse effects of rain while at lower frequencies around 7 GHz these effects become of greater concern in tropical, sub-tropical and equatorial regions of the world [2]. Generally, there are two ways of estimating rain attenuation as described in [3] by Olsen and Roger. One is by using theoretical methods, where the main concern centers on the computational method such as the approximation method, while the other approach uses the empirical method [4]. The latter is the more popular method employed by many researchers because it yields the most precise results. Some limitations exist for the empirical method, however, namely the availability of funds to support many years of experimental campaigns across a multiplicity of experimental sites. The combination of methods is the focus of this paper. The available rain rate data and its drop size data together with computational theory will be used to estimate the specific attenuation and total attenuation due to rain for the region of South Africa.

The sections presented in this paper are: regional cumulative distribution of rain, rain drop size distributions and its model, the raindrop as a spherical and non-spherical object, modelling of scattering amplitude, specific and total rain attenuation calculations, comparative studies between derived coefficients and established models, and the application of the proposed model.

2. REGIONAL CUMULATIVE DISTRIBUTION OF RAIN

In order to calculate the specific rain attenuation, three parameters are of importance: the cumulative distribution of rain, raindrop size distribution and the chosen frequency. The first two parameters depend on the geographical or regional boundary while the the third one does not. According to the International Telecommunication Union (ITU), estimation of rain attenuation needs to be carried out at a lower rain rate integration time, i.e., less than or equal to 1-minute. In the work done by Owolawi [5], a simple hybrid method was developed to convert the available five-minute data into its one-minute equivalent in all the provinces in the Republic of South Africa. The rain rate data acquisition systems employed in this work are the same as the ones employed in [1]. The derived one-minute rain rate equivalent was used to obtain the modelled rain rate cumulative distribution for the region as presented by Owolawi [1]. The method of maximum likelihood estimator (MLE) has been employed to model the distributions and to develop the regional contour

Table 1: Rain rate at 0.01% of Exceedence for all the provinces of South Africa.

South African Province/Site	Eastern Cape • Fort Beaufort: 53mm/hr • Bisho: 57mm/hr • Umtata: 70mm/hr • Port-Alfred: 58mm/hr	Gauteng • Pretoria: 61mm/hr • Springs: 75mm/hr	KwaZulu-Natal • Durban: 73mm/hr • Ladysmith: 75mm/hr • Pietermaritzburg: 79mm/hr
South African Province/Site	Northern Cape • Kimberley: 59mm/hr	Free-State • Bethlehem: 60mm/hr • Bloemfontein: 67mm/hr	Limpopo • Tshipise: 50mm/hr
South African Province/Site	Western Cape • Cape Point: 20mm/hr • Cape Town: 25mm/hr • Beaufort: 37mm/hr	Mpumalanga • Ermelo: 76mm/hr • Belfast: 79mm/hr • Nelspruit: 78mm/hr	North West • Klerksdorp: 67mm/hr • Rustenburg: 70mm/hr

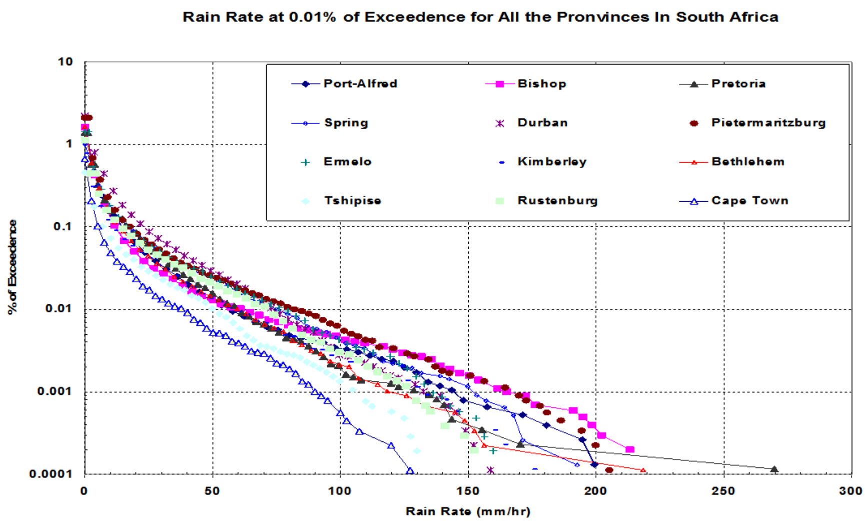

Figure 1: Average cumulative time distribution of the rain rate in all provinces of South Africa.

map. Figure 1 shows the average cumulative distributions for all the provinces in the region with their rain rate at 0.01% of exceedence as presented in Table 1.

The 0.01% of exceedence is a critical threshold for the system designers or radio planning engineers in order to obtain better accuracy and link performance. The highest rain rate distributions are found in KwaZulu-Natal and Mpumalanga provinces and the lowest rain rate distribution is observed in the Western Cape.

3. RAINDROP SIZE DISTRIBUTION AND ITS MODEL

The second regional-based factor that contributes to the calculation of rain attenuation is raindrop size distribution. In Southern Africa little work has been done in this area. Owolawi [6] has pioneered the study of raindrop size distribution in the region. The work presented in [6] used the method of Maximum Likelihood Estimation (MLE) to estimate a rain drop size distribution for Durban. Two different conditions are considered for the two regimes presented in Table 2 [6].

The model drop size distribution is based on the three-parameter lognormal distribution. The limitations of the model are:

- a sudden peak is found in its transition between the two specified regimes which may lead to over-estimation of a specific rain attenuation;
- the amount of data used to propose the models is limited to one year;
- the correlation coefficient value of fitted γ is poor.

In the present work, a general rain dropsize distribution with two years data is used to overcome the limitations mentioned previously. In this work, the raindrop data acquisition method employed

Table 2: Classification of $N(D)$ based on the rain rate regime [6].

Rain Type	Diameter Range (mm)
Regime one	$0 < R \leq 20$
Regime two	$20 < R \leq 100$

is the same as presented in [6] with little modification. The two rain type regimes as presented in Table 2 are combined to determine the general model for Durban. The probability density function of the three-parameter lognormal distribution is still considered with a little modification of the distribution input variables. The three-parameter lognormal distribution is given as:

$$N(D) = N_T(D) \times pdf(D; \gamma, \mu, \sigma) \tag{1}$$

where the random variable mean droplet diameter, D, is said to have a three-parameter lognormal distribution if the random variable $Y = \ln(D-\gamma)$, where D is greater than γ, is normally distributed (μ, σ^2), and σ is considered to be greater than zero. The probability density function of the three-parameter lognormal distribution is then given by Pang et al. [7] as:

$$pdf(D; \gamma, \mu, \sigma) = \frac{1}{\sigma\sqrt{2\pi}\,(D-\gamma)} \exp \frac{-1}{2\sigma^2} [\ln(D-\gamma) - \mu]^2 \quad \gamma < D < \infty \quad \text{and} \quad \sigma > 0 \tag{2}$$

and Equation (2) will be zero if the condition in the equation is not met. Parameter σ^2 is the variance of Y; it defines the shape parameter of D, where μ is the mean of Y. In the improved version of the newly proposed distribution, the same estimator method is used, but $\gamma = 0$, and a generalized model is developed. The summarized models with their expressions based on lognormal and Maximum Likelihood principles are presented as follows and used to determine the specific rain attenuation:

$$N_T(D) = 220R^{0.392} \quad 1\,\text{mm/hr} < R \leq 100\,\text{mm/hr} \tag{3}$$

where the parameter $N_T(D)$ is the total number of drops of all sizes as a function of the drop diameter. The other lognormal parameters such as the mean (μ), is given as:

$$\mu = -0.267 + 0.137\ln(R) \quad 1\,\text{mm/hr} < R \leq 1000\,\text{mm/hr} \tag{4}$$

The parameter σ^2 depends on the rain rate and is given as follows:

$$\sigma^2 = 0.0772 - 0.00991\ln(R) \quad 1\,\text{mm/hr} < R \leq 100\,\text{mm/hr} \tag{5}$$

The method of moments is used by many authors such as Ajayi et al. [8] to model the distribution for the western part of Africa and Ong et al. [9, 10] for Singapore. The mathematical details of the method presented by Kozu et al. [11] is applied to South African raindrop data and the scattergram plots are presented in Figure 2. Figure 2 also details the lognormal parameters and their respective correlation coefficients. It is noted that the correlation coefficients for all lognormal parameters are weak. In principle, Equations (3), (4) and (5) are used to calculate the specific rain attenuations.

The expressions in (6), (7) and (8) are the results obtained using the method of moments as detailed in [11]:

$$N_T(D) = 212.27\,R^{0..3866} \quad 1\,\text{mm/hr} < R \leq 100\,\text{mm/hr} \tag{6}$$
$$\mu = -0.2812 + 0.1306\ln(R) \quad 1\,\text{mm/hr} < R \leq 1000\,\text{mm/hr} \tag{7}$$
$$\sigma^2 = 0.0859 + 0.00128\ln(R) \quad 1\,\text{mm/hr} < R \leq 100\,\text{mm/hr} \tag{8}$$

The main aim of this section is to summarize the expressions and parameters that will be used to derive specific rain attenuation and its coefficients. The procedures used to model these expressions and parameters are fully presented in [12]. In order to study the degree of signal degradation in the presence of rain, rain drops may be considered as spherical or non-spherical (oblate/spheroid) objects. In this work, two phases of the rain drop shapes will be studied with respect to their scattering amplitude.

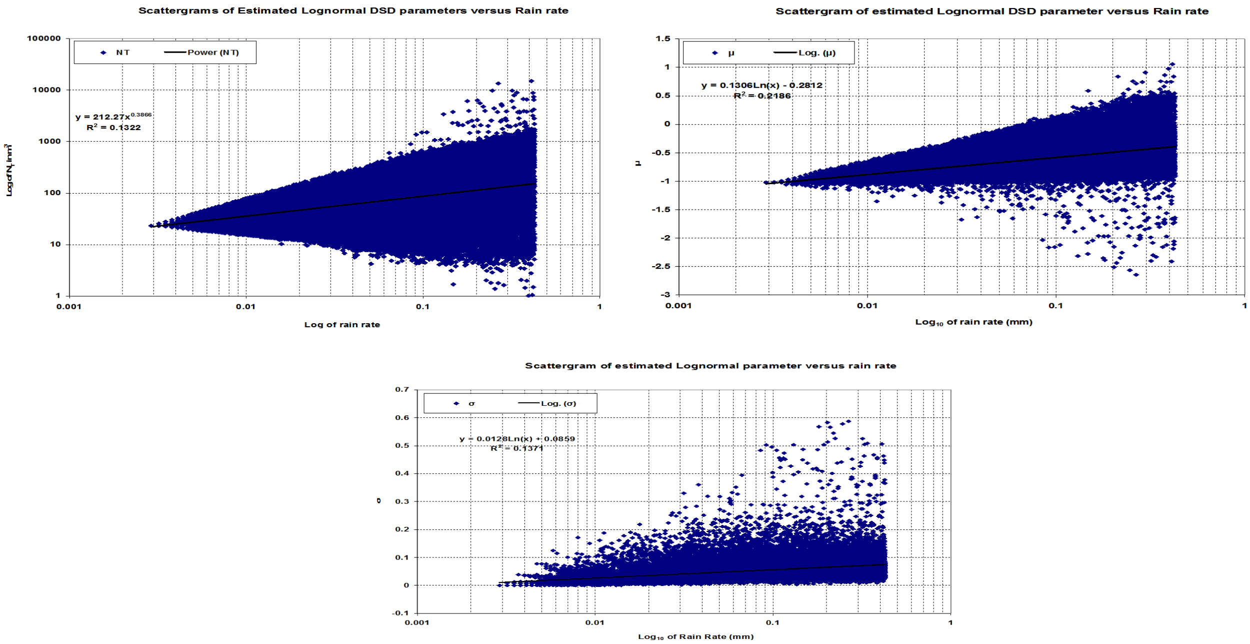

Figure 2: Scatter plots of estimated Lognormal parameters against rain rate.

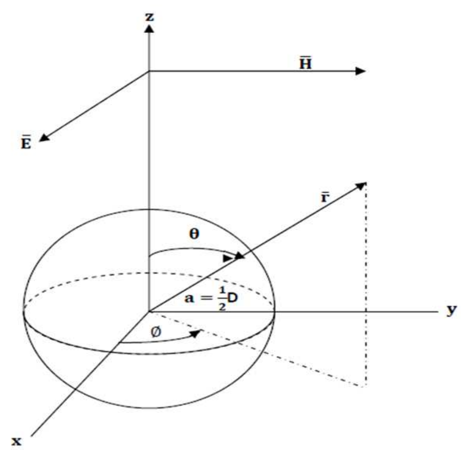

Figure 3: Electromagnetic plane Incident on spherical object.

4. RAIN: A SPHERICAL OBJECT

Each raindrop is made from material which can be classified as a lossy dielectric. Scattering and absorption are two main consequences of propagating electromagnetic waves through the rain. The magnitude of these two phenomena is based on the propagating frequency, the effective radius of the drops, rain water complex permittivity and orientation, or shape, of the raindrops.

To investigate rain attenuation, the first assumption is to consider the rain drop shape as spherical and then to use Mie's scattering technique to compute the scattering amplitude followed by the specific attenuation [3]. The details of Mie scattering theory are presented in [13].

Consider a spherically shaped raindrop incident on a plane EM wave in the Z-direction and framed in spherical coordinates r, θ, ϕ as presented in Figure 3.

Figure 3 shows a homogeneous sphere with radius r, complex refractive index m, and the size parameter, $x = ka\,(k = 2\pi/\lambda)$, where "$a$" is the radius of the sphere and "k" is the wave number in the medium. Considering the position of a target object, the total electric field is the sum of the incident field and the scattered field, given as:

$$E = E_o + E_0 f(x, m, \theta)\frac{e^{-jkr}}{jkr} \tag{9}$$

where $E_o = e^{-j(k\cdot r - w\,t)}$ is the incident electric filed amplitude of the wave and "w" is the angular frequency. The scattering matrix $f(x, m, \theta)$ depends on the scattering angle θ and the refractive index of the medium. The scattering matrix expressions and Mie coefficients which are used to calculate both scattered and internal fields of scattered objects are presented in [13]. The summarized expressions for the forward scattering problem, where its $\theta = 0°$ and backward scattering with $\theta = \pi$ radian, are given in (10). The forward scattering and backward scattering amplitudes are then given as:

$$\begin{aligned} f_1(0) = f_2(0) &= \frac{1}{2}\sum_{n=1}^{\infty}(2n+1)[a_n + b_n] = f(0) \\ -f_1(\pi) = f_2(\pi) &= \frac{1}{2}\sum_{n=1}^{\infty}(2n+1)(-1)^n[a_n - b_n] \end{aligned} \tag{10}$$

The scattering cross section, Q_{sca}, the potential area where the likelihood of EM waves could be scattered, is given as:

$$Q_{sca} = \frac{2\pi}{k^2}\sum_{n=1}^{\infty}(2n+1)\left(\lfloor a_n\rfloor^2 + |b_n|^2\right) \tag{11}$$

In the same way, the cross section $Q_{ext}(m^2)$ is given by:

$$Q_{ext}(m^2) = \frac{4\pi}{k^2}\mathrm{Re}f(0) = \frac{2\pi}{k^2}\mathrm{Re}\sum_{n=1}^{\infty}(2n+1)(a_n + b_n) \tag{12}$$

In this case, the sphere raindrop is absorbing, the general expression is given as: $Q_{abs} = Q_{ext} - Q_{sca}$ where Q_{abs}, Q_{ext} and Q_{sca} are absorption cross–section, extinction cross section and scattered cross-section, respectively.

The other properties that describe the spherical scattering are presented with expressions for backscattering (σ_b) and forward-scattering (σ_f) cross-sections.

- Backscattering cross-section:

$$\sigma_b = \frac{2\pi}{k^2}\left[|f_1(\pi)|^2 + |f_2(\pi)|^2\right] = \frac{\pi}{k^2}\left|\sum_{n=1}^{\infty}(-1)^n(2n+1)(a_n - b_n)\right|^2 \tag{13}$$

- Forward-scattering cross-section:

$$\sigma_f = \frac{2\pi}{k^2}\left[|f_1(0)|^2 + |f_2(0)|^2\right] = \frac{\pi}{k^2}\left|\sum_{n=1}^{\infty}(2n+1)(a_n - b_n)\right|^2 \tag{14}$$

5. RAIN: A NON-SPHERICAL OBJECT

In many cases, falling drops are not spherical in shape as a result of aerodynamics and gravitational pull. In most cases, the oblate spheroidal shape is assumed for the raindrop model as discussed earlier. The effectiveness of Mie computation is limited to the spherically shaped rain drops and small rain drop sizes. As the raindrops become larger, the effect of shape distortion is taken care of by employing an oblate spheroidal model to compute the rain scattering amplitude [14].

The work done by Pruppacher and Pitter (P-P) [15] presented an expression to describe the rain drop shape at a given terminal velocity with respect to the internal and external pressure on the surface of rain drops. This approach is considered and accepted by many researchers. In the work done by Oguchi [16], it is intended to solve a complex equation derived in the P-P method numerically with a range of 13 drop sizes and shapes in order to simplify the scattering problem with respect to engineering applications.

The specific attenuation is given by the expression:

$$A_o = 4.343 \times \int Q_t(a)n(a)da \ \ (\mathrm{dB/km}) \tag{15}$$

where Q_t is the total cross section, which is the sum of scattered power and power absorbed in the drops when the incident wave travelled through the rain-filled medium. Q_t is assumed using the expression :

$$Q_t = -(4\pi/k_0)\mathrm{Im}[\overline{a} \cdot f(K_1, K_2)] \tag{16}$$

It should be noted that $D = 2a$, where D is the raindrop diameter. Then Equation (15) can be re-written as:

$$A_{o_{h,v}} = 8.686 \times \int Q_t(D)n(D)dD = 8.686 \times \mathrm{Im}(k_{h,v}) \tag{17}$$

The phase shift is characterized by the expression:

$$\Phi_{0_{h,v}} = \frac{180}{\pi}\Re(k_{h,v}) \tag{18}$$

The attenuation of the signal over the path length of rain is then given as:

$$A_{h,v} = A_{0\,h,v} \times L_{\mathit{eff}} \ \ (\mathrm{dB}) \tag{19}$$

and

$$\Phi_{h,v} = \Phi_{0_{h,v}} \times L_{\mathit{eff}} \ \ (\mathrm{degree}) \tag{20}$$

In order to estimate the attenuation of a given path length, the effective path length is determined by using Rec. ITU-R P.530-13 for terrestrial links as presented in [17] and Rec. ITU-R P.618-10 for earth-space links. $k_{h,v}$ is the propagation constant given as $k_{h,v}$ and L_{eff} is the effective propagation path length as given in [17]:

$$L_{\mathit{eff}} = dr_{0.01} \tag{21a}$$
$$r_{0.01} = 1/(1 + d/d_0) \tag{21b}$$
$$d_0 = 35e_{0.01}^{-0.015R}, \quad R_{0.01} \leq 100\,\mathrm{mm/hr}; \tag{21c}$$
$$d_0 = 35e_{0.01}^{-1.5R}, \quad R_{0.01} \geq 100\,\mathrm{mm/hr}; \tag{21d}$$

where $R_{0.01}$ and $r_{0.01}$ are the rain rate and the reduction factor respectively with Equation (21) being valid for up to 60 km. If the effects of turbulence, updraft and downdraft and raindrop interaction are neglected, the rain rate is related to its drop size by the relation:

$$R \ (\mathrm{mm/hr}) = 6\pi \times 10^{-4} \int_0^\infty D^3 V(D)N(D)dD \tag{22}$$

where $V(D)$ is the terminal velocity and expressed with their respective values at different rain drop diameters.

6. MODELING OF SCATTERING AMPLITUDES

In estimating specific rain attenuation, forward scattering amplitude is used, being the imaginary part of the amplitude while the real part is often used to calculate the phase rotation of the electromagnetic wave. Figure 4 presents the real component of the scattering amplitude at different frequencies and orientations. Figures 4 and 5 depict scattering amplitudes as a function of the effective drop radius. The solution to both the real and imaginary part is derived by using the existing procedures or techniques: Mie scattering theory techniques [18], point-matching technique [19], perturbation method [20, 21] and Pruppacher-and-Pitter method [22, 23].

The scattering amplitude in both the real and imaginary components confirmed that all four approximation techniques are similar in distribution patterns and do not differ so much as revealed in the case of applying the Mie technique. The reason may be attributed to the suitability of Mie to the drops with small diameter and spherically shaped raindrops. In this paper, the method by Pruppacher-and-Pitter and Mie Scattering are modelled for both imaginary and real parts because of their accuracy and simplicity. Figure 5 shows the imaginary part of the scattering amplitude for similar conditions as mentioned above in the case of the real part of the amplitude. Figure 6 shows the modelling of scattering amplitude using the Pruppacher and Pitter technique. In Figure 6, it is noted that a power law can be used to express the relation between both real and imaginary scattering amplitudes versus equivolume drop radius. The samples presented in this paper are at frequencies of 11, 13, 19.3 and 34.8 GHz. The resulting power law expressions with their respective constants are given as:

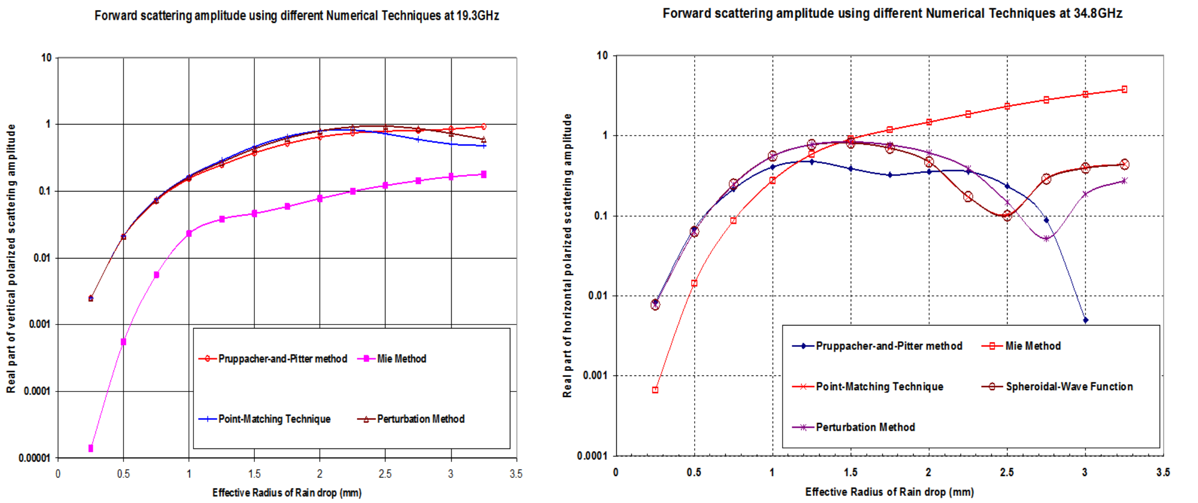

(a) (b)

Figure 4: (a) Vertically polarized at 19.3 GHz, and (b) horizontally polarized at 34.8 GHz.

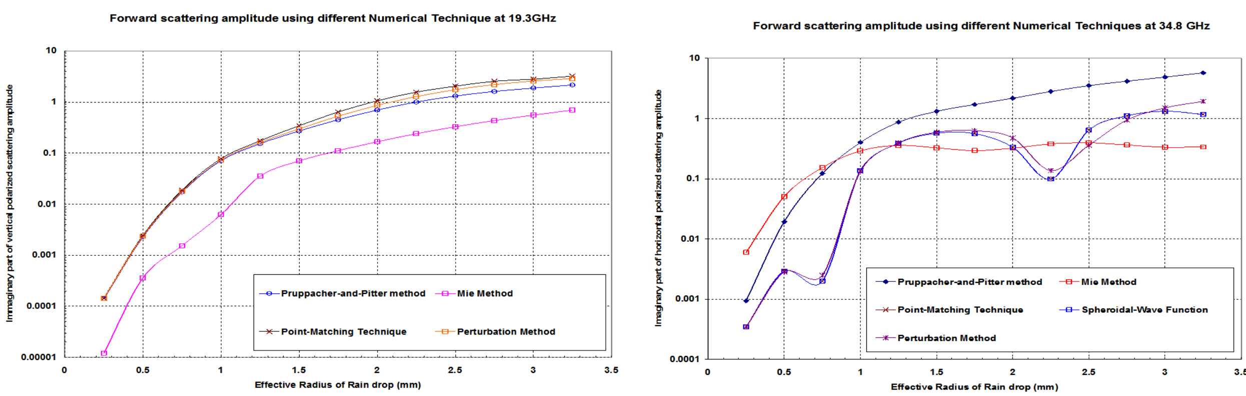

(a) (b)

Figure 5: (a) Vertically polarized at 19.3 GHz, and (b) horizontally polarized at 34.8 GHz.

Real part for both horizontal & vertical polarization.

$$\mathrm{Re} f_{v,h}(\phi = 0^0, \theta, a) = \hbar\ a^{\lambda} \tag{23}$$

Imaginary part for horizontal & vertical polarization.

$$\mathrm{Im} f_{v,h}(\phi = 0^o, \theta, a) = \ell\, a^{\partial} \tag{24}$$

Here $\hbar$, λ, ℓ and ∂ are constants that are associated with Equations (23) and (24) for different frequencies and polarizations as detailed in Table 3. Table 3 shows that the correlations are good and at best expressed with a 2nd order polynomial using correlation coefficient R^2 as a goodness of fit test. The least correlation coefficient R^2 value recorded is 0.90. At 34.8 GHz, the horizontal polarization has a least correlation coefficient using a power law, but for the second order polynomial, the fit performance is improved as presented in Equation (25).

$$\mathrm{Re} f_{v,h}\left(\phi = 0^0, \theta, a\right) = 0.1929a^2 + 0.6384a - 0.1323 \quad R^2 = 0.8594 \tag{25}$$

Although the intention of this paper is to determine the specific attenuation using forward scattering, it must be noted that the use of the power law is not as successful in case of backward scattering as it is when applied to forward scattering.

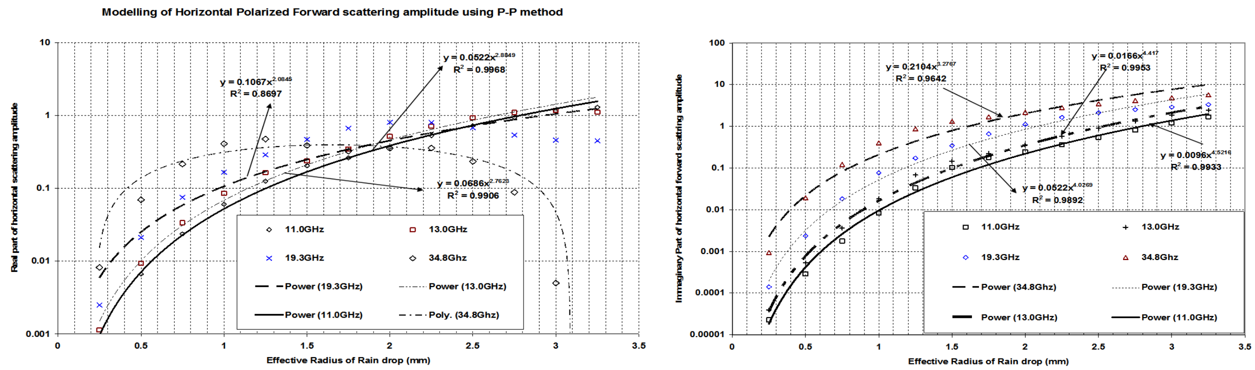

(a) (b)

Figure 6: (a) Real part and (b) imaginary part of forward scattering amplitude at a selected frequency.

Table 3: Forward scattering constants for both Real and Imaginary part at different polarizations.

Polarization/Frequency							
Real	$\hbar$	$\lambdabar$	$R^{2'}$	**Imaginary**	ℓ	∂	$R^{2'}$
Horizontal/11.0 GHz	0.0522	2.8849	0.9968	Horizontal/11.0 GHz	0.0096	4.5216	0.9933
Vertical/11.0 GHz	0.0436	2.645	0.9895	Vertical/11.0 GHz	0.008	4.2558	0.9872
Real	$\hbar$	$\lambdabar$	$R^{2'}$	**Imaginary**	ℓ	∂	$R^{2'}$
Horizontal/13.0 GHz	0.068	2.0845	0.9906	Horizontal/13.0 GHz	0.0166	4.417	0.9953
Vertical/13.0 GHz	0.0585	2.5935	0.9895	Vertical/13.0 GHz	0.0135	4.1207	0.989
Real	$\hbar$	$\lambdabar$	$R^{2'}$	**Imaginary**	ℓ	∂	$R^{2'}$
Horizontal/19.3 GHz	0.1067	2.0845	0.8697	Horizontal/19.3 GHz	0.0522	4.0269	0.9892
Vertical/19.3 GHz	0.0585	2.5935	0.9895	Vertical/19.3 GHz	0.0425	3.7929	0.986
Real	$\hbar$	$\lambdabar$	$R^{2'}$	**Imaginary**	ℓ	∂	$R^{2'}$
Horizontal/34.8 GHz	-	-	-	Horizontal/34.8 GHz	0.2104	3.2767	0.9642
Vertical/34.8 GHz	0.1985	1.6903	0.9113	Vertical/34.8 GHz	0.1833	3.167	0.9628

7. SPECIFIC RAIN ATTENUATION ESTIMATION

Specific rain attenuation γ_R (dB/km) is a fundamental factor used to determine rain attenuation at a defined distance. The specific attenuation coefficients due to rain are determined using the Equations (16) and (17) integrating over all the rain drop size data collected over a period of two years in Durban. The attenuation cross section Q_t is employed by using the classical methods of Pruppacher-and-Pitter and Mie. The power-law relation is used to determine specific rain attenuation expression with their respective coefficients at different frequencies as in [3]:

$$\gamma_R = a_{h(SA)} \cdot R^{b_{h(SA)}} \tag{26}$$

where $a_{h(SA)}$ and $b_{h(SA)}$ are power-law parameters derived for South Africa and presented in Table 4 where the R value denotes rain rate in mm/hr. The equivalent parameters are obtained by ITU-R and tabulated at defined frequencies [24].

Thus, the new expression is derived for $a_{h(SA)}$ and $b_{h(SA)}$ up to 100 GHz for horizontal polarization. The expressions are given for the horizontal polarization as:

$$a_{h(SA)} = 7 * 10^{-5} f^2 + 0.0015 f \quad \text{for 2 to 100 GHz} \tag{27}$$

$$b_{h(SA)} = -0.0059 f^2 + 0.1114 f + 0.7996 \quad \text{for 2 to 12 GHz} \tag{28}$$

$$b_{h(SA)} = 5 * 10^{-5} f^2 - 0.0105 f + 1.4138 \quad \text{for 13 to 100 GHz} \tag{29}$$

The least correlation coefficient for Equations (28) to (29) is 0.98 which shows the agreement of the expressions with the available data presented in Table 4. These expressions may be used more conveniently to estimate the specific rain attenuation in any of the provinces in South Africa.

It should be noted that $a_{h(SA)}$ and $b_{h(SA)}$ are dependent on rain drop size distribution for a defined region or site. In this work, the modified three-parameter lognormal model is used to derive the constants as presented in Equations (2) to (5). The reason for the method presented here, is to propose a rain attenuation model that uses complete rainfall rate distribution, elevation and frequency, and regional raindrop size data. In addition, the proposed model will significantly improve rain attenuation prediction error over the ITU-R models, using empirical data.

8. COMPARATIVE STUDIES OF SPECIFIC ATTENUATION MODEL

Figure 7 represents a comparison of the specific rain attenuation at 19 mm/hr and 100 mm/hr respectively using different rain drop size distributions and scattering amplitudes. Figure 7 presents an estimated specific rain attenuation against frequency, between 2 to 100 GHz.

In order to evaluate the amount of physical error in measurement, between proposed model and existing models, an absolute relative error is employed. The average absolute error shows that the average value between tests at 19 mm/hr (41.33%) is less compared to a situation at 100 mm/hr (85.67%). It shows that at lower rain rate, all the models performed uniformly well while at the higher rain rate, differences between the existing models and proposed model become evident. At 100 mm/hr, the least absolute error recorded is 18.91% (Proposed model-Nonspherical) while the average relative error is found to be more on the ITU-R model (137.99%). In the case of 19 mm/hr, the least absolute error is found in the proposed Model with 34.29% while the highest recorded relative error value is 51.38% also in the ITU-R model. Although the average differences recorded

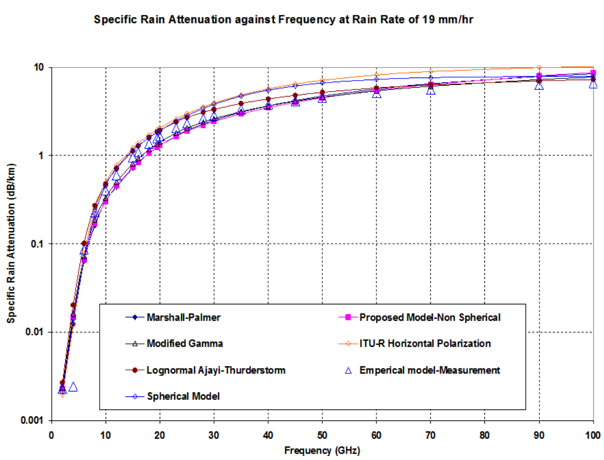

(a)

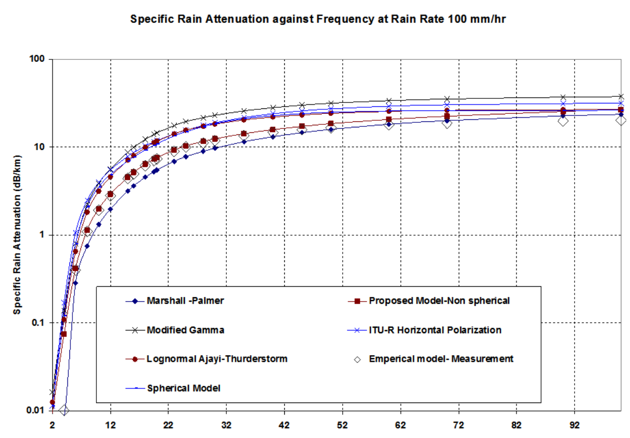

(b)

Figure 7: Specific rain attenuation (a) 19 mm/hr, (b) 100 mm/h.

Table 4: Comparison of ITU-R and derived values of a and b in South Africa at horizontal polarization.

Frequency (GHz)	$a_{h(ITU-R)}$	$a_{h(SA)}$	$b_{h(ITU-R)}$	$b_{h(SA)}$
2	0.000154	0.0001	0.963	1.0055
4	0.000650	0.0007	1.121	1.1276
6	0.00175	0.0019	1.306	1.2781
10	0.0101	0.008	1.276	1.3103
12	0.0188	0.0129	1.217	1.2895
15	0.0367	0.0226	1.154	1.2647
25	0.124	0.0744	1.061	1.1839
40	0.350	0.1949	0.939	1.0606
60	0.707	0.412	0.826	0.9445
70	0.851	0.412	0.793	0.9018
90	1.06	0.7638	0.753	0.8373
100	1.12	0.8758	0.743	0.8129

among the models are close as shown in Figure 7. Another comparative study is carried out when specific rain attenuation is plotted against rain rate as depicted in Figure 8.

In these two cases, the same absolute relative error is applied to evaluate the behaviour of the proposed models and the existing models against the empirical measurements. It is also confirmed that at the lower frequency, 10 GHz, (absolute relative error is 28.30%), i.e., the absolute relative error is less when compared to the case recorded at the higher frequency of 100 GHz, where the absolute relative error is 41.99%. At 10 GHz, the least relative error is recorded in the proposed model with the value of 18.10%, while most relative error is found with the Ajayi model (49.15%). The ITU-R model has the value of 31.63% while the closest to the least average relative error is obtained with the modified Gamma model (18.23%). At 100 GHz, the average relative errors increases progressively as follows: Proposed Model — 21.41%, Mashall-Palmer — 24.31%, Ajayi model — 24.51%, ITU-R model — 39.77%, and Modified Gamma — 99.90%. At this given frequency, the Ajayi model may be an alternative model to be used to describe the specific rain attenuation distribution while the modified Gamma model may not be the best for this region at this frequency.

9. APPLICATION OF THE PROPOSED MODELS

The proposed non-spherical rain attenuation model is compared with the measured rain attenuation done in 2004 at the University of KwaZulu-Natal, South Africa. The experimental setup and data collection procedures are reported by a few authors [25–27]. The link is set up between two of the campuses of the university. An Agilent 83018A microwave amplifier is used as a receiver and transmitter coupled with Valuline WR42/R220 parabolic antennas, each with 0.6 meter diameter. The receiver output is fed into a FS1Q40 spectrum analyzer in order to study the characteristics of the computed signal at both clear and non-clear air. The results are compared with the proposed non-spherical rain attenuation model and other existing models. Since the rain attenuation measurement transmitter propagates the signal in the horizontal polarization form, the comparative study is limited to the format as presented in Figure 9.

To test the goodness-of-fit of the measured data with the proposed and existing models, Root-Mean-Square (RMS) and Chi-Square tests were carried out and the statistical results are presented in Table 5. Although the Chi-square test indicated that all models may be used to predict the rain attenuation, based on the influence of the peak maximum, the RMS test was introduced to confirm this prediction. It affirmed the suitability of the non-spherical and modified Gamma rain attenuation models as suitable for Durban. In conclusion, the proposed non-spherical model may be appropriate for use in the South African region with minimum values for goodness-of-fit and ITU-R P.311-13. Thus, Table 1 and Equations (26)–(29) are employed to estimate the total attenuation for other provinces as presented in Figure 10.

Another method used in validating the proposed models has been recommended by ITU-R P.311-13 [28] and used by Abdulrahman et al. [29]. In this method, the same trend of comparative characteristics discussed using the goodness-of-fit test method, is observed.

Figure 10 represents rain attenuation versus propagating frequencies for both the Eastern Cape

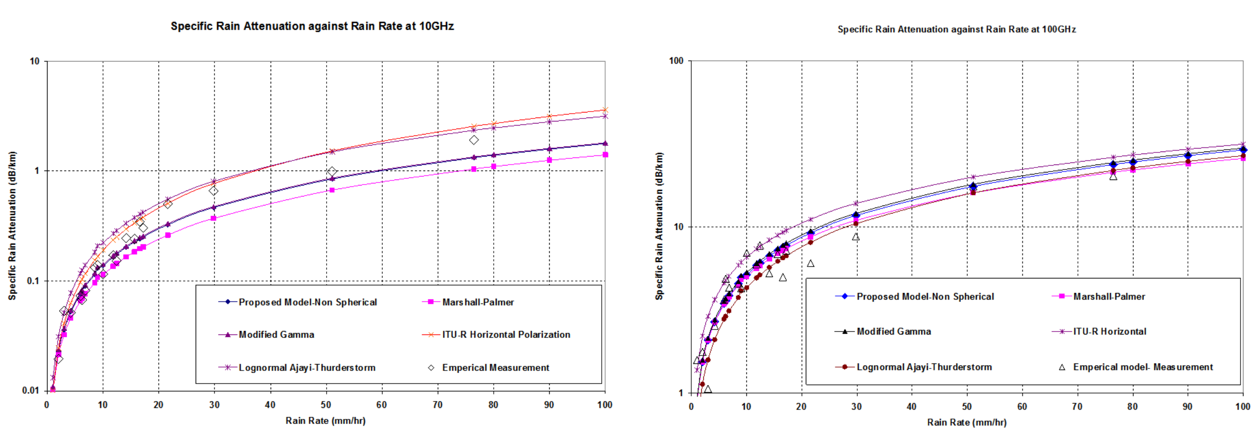

(a) (b)

Figure 8: Specific rain attenuation (a) 10 GHz, (b) 100 GHz.

Table 5: Goodness-of-fit test for rain attenuation models in Durban.

Test parameters	Non-Spherical Model	Marshall-Palmer model	Modified Gamma model	Lognormal-Ajayi et al. Model [30, 31]	ITU-R Model
RMS %	0.63	2.15	0.66	4.78	3.81
Chi-square Test (df=35.17) at 0.05 of probability	1.0544	7.8017	1.1067	33.18	14.97

Table 6: Validation of rain attenuation models in Durban using ITU-R P.311-13.

Test parameters	Non-Spherical Model	Marshall-Palmer model	Modified Gamma model	Lognormal-Ajayi et al. Model [30, 31]	ITU-R Model
μ_{ei}	8.37	19.30	8.46	41.51	14.88
σ_{ei}	0.26	0.29	0.26	0.32	0.67
D_{ei}	0.27	0.36	0.28	0.54	0.69

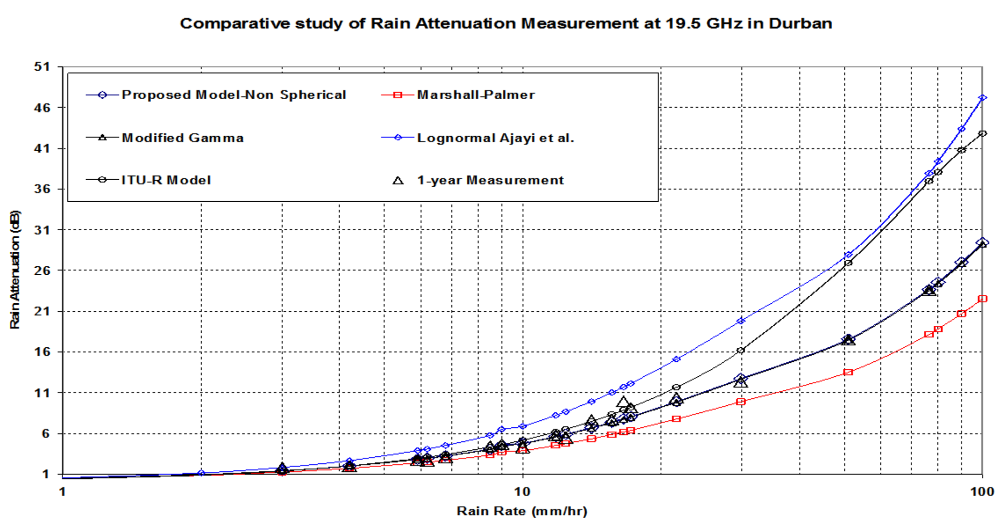

Figure 9: Rain attenuation on terrestrial 19.5 GHz link in Durban, South Africa.

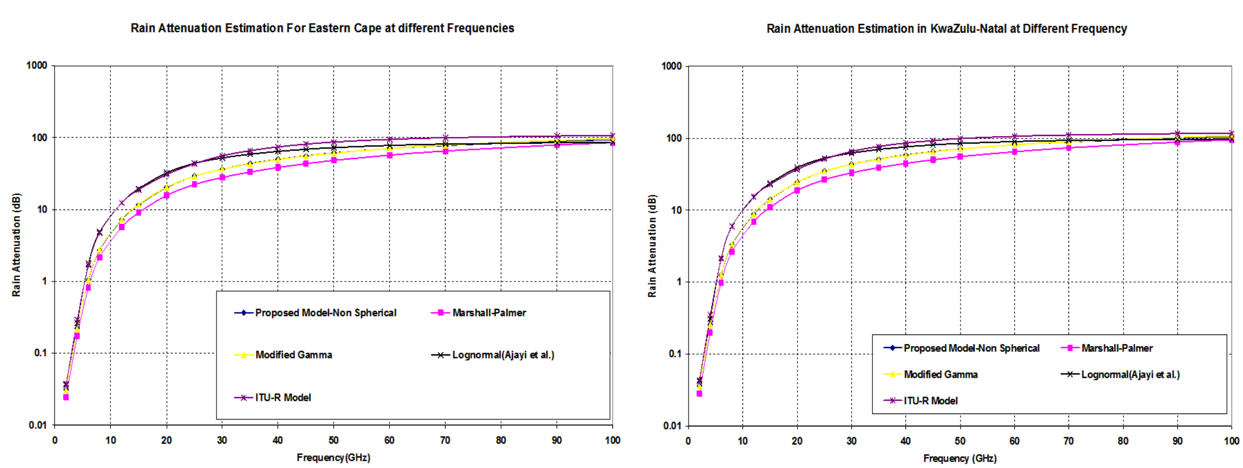

Figure 10: Rain attenuation at different frequency for Eastern Cape and KwaZulu-Natal province.

and KwaZulu-Natal provinces at the same propagation path length. In a practical scenario, rainfall distribution is not uniform along the path lengths that practically exceed 1 km. This is a result of variable raindrop size and rain rate. Thus, a physical transmission length is replaced with the effective path length. The average rain rate of 0.01% of exceedence considered and used to estimate the rain attenuation for the provinces in the country.

10. CONCLUSION

In this paper, we proposed a simple and regionally based model for the calculation of the specific rain attenuation at different rain rates and frequencies up to 100 GHz. The key parameters are "regional rain drop size distribution model" and "rain rate". The results presented in Figures 7–10 and Tables 5–6 show the suitability and adaptability of the model for the Southern African region with regards to the calculation of specific rain attenuation and thus total attenuation at a defined distance of less than 60 km. The statistical tests confirmed the suitability of other models such as the modified Gamma model but for the optimum calculation of the attenuation, a non-spherical rain attenuation model is suggested.

The result will serve as a good tool for radio planning engineers and technicians especially in the Southern African region where no comprehensive work has been carried out in the field of radio propagation through rain.

REFERENCES

1. Owolawi, P. A., "Rainfall rate probability density evaluation and mapping for the estimation of rain attenuation in South Africa and surrounding islands," *PIER Online*, Vol. 112, 155–181, 2011.
2. Moupfouma, F., "Improvement of a rain attenuation prediction method for terrestrial microwave links," *IEEE Transactions on Antenna and Propagation*, Vol. 32, No. 12, 1368–1372, 1984.
3. Olsen, R. L., D. V. Rogers, and D. B. Hodge, "The aR^b relation in the calculation of rain attenuation," *IEEE Transactions on Antenna and Propagation*, Vol. 26, No. 2, 318–329, 1978.
4. Crane, R. K., "Attenuation due to rain-A mini-review", *IEEE Transactions on Antenna and Propagation*, 751–752, Sep. 1975.
5. Owolawi, P. A., "Derivation of one-minute rain rate from five-minute equivalent for the calculation of rain attenuation in South Africa," *PIERS Online*, Vol. 7, No. 6, 524–535, 2011.
6. Owolawi, P. A., "Raindrop size distribution model for the prediction of rain attenuation in Durban" *PIERS Online*, Vol. 7, No. 6, 516–523, 2011.
7. Pang, W., P. Leung, W. Huang, and W. Liu, "On interval estimation of the coefficient of variation for three-parameter Weibull, lognormal and gamma distribution: A simulation-based approach," *European Journal of Operational Research*, Vol. 164, 367–377, 2005.
8. Ajayi, G. O., "Some aspects of tropical rainfall and their effect on microwave propagation," *Int. J. Satellite Commun.*, Vol. 8, 163–172, 1990.
9. Kumar, L. S., Y. H. Lee, and J. T. Ong, "Truncated gamma drop size distribution models for rain attenuation in Singapore," *IEEE Transactions of Antennas and Propagation*, Vol. 58, No. 4, Apr. 2010.
10. Kumar, L. S., Y. H. Lee, and J. T. Ong, "Two-parameter Gamma drop size distribution models for Singapore," *IEEE Transactions on Geoscience and Remote Sensing*, Vol. 549, No. 4, Sep. 2011.
11. Kozu, T. and K. Nakamura, " Rainfall parameter estimation from dual-radar measurements combining reflectivity profile and path-integrated attenuation," *J. Atmos. Ocean. Technol.*, Vol. 8, No. 2, 259–270, 1991.
12. Owolawi, P. A., "Characteristics of rain at microwave and millimetric bands for terrestrial and satellite links attenuation in South Africa and surrounding islands," Ph.D. Dissertation, School of Electrical, Electronics and Computer Engineering, University of KwaZulu Natal, Durban, South Africa, Jul. 2010.
13. Van de Hulst, H. C., *Light Scattering by Small Particle*, 143, John Wiley & Sons, Inc., New York, 1957.
14. Li, L. W., P. S. Kooi, M. S. Leong, and T. S. Yeo, "On the simplified expression of realistic raindrop shape," *Microwave Opt. Technol. Lett.*, Vol. 7, No. 4, 201–205, Mar. 1994.
15. Pruppacher, H. R. and R. L. Pitter, "A semi-emperical determination of the shape of cloud and rain drops," *J. Atmos. Sci.*, Vol. 28, 86–94, 1971.

16. Oguch, T., "Electromagnetic wave propagation and scattering in rain and other hydrometeor," *Proc. IEEE*, Vol. 71, 1029–1078, Sep. 1983.
17. Recommendation ITU-R P.530-13 (10/2009), "Propagation data and prediction methods required for the design of the terrestrial line of sight systems," Oct. 2009.
18. Deirmendjian, D., *Electromagnetic Scattering on Spherical Poly-dispersions*, Elsevier Publication Company, Inc., New York, 1966.
19. Oguchi, T. and Y. Hosoya, " Differential attenuation and differential phase shift of radio waves due to rain: Calculation at microwave and millimetre wave regions," *J. Rech. Atmos.*, Vol. 8, Nos. 1–2, 121–128, 1973.
20. Oguchi, T., "Attenuation of electromagnetic wave due to rain with distorted raindrops," *J. Radio Res. Labs.*, Vol. 7, 467–485, 1960.
21. Oguchi, T., "Attenuation of electromagnetic wave due to rain with distorted raindrops Part II," *J. Radio Res. Labs.*, Vol. 11, 19–44, 1964.
22. Oguchi, T., "Scattering properties of Pruppacher and-Pitter form rain-drops and cross polarization due to rain: Calculation at 11, 13, 19.3, and 34.8 GHz," *Radio Science*, Vol. 12, 41–51, 1977.
23. Oguchi, T., "Attenuation and phase rotation of radio waves dues to rain: Calculations at 19.3, and 34.8 GHz," *Radio Science*, Vol. 8, 31–38, 1973.
24. ITU-R P.838-3-8, "Specific attenuation model for rain for use in prediction methods," ITU, Geneva, Switzerland, 2008.
25. Naicker, K. and S. H. Mneney, "Propagation measurements and modelling for terrestrial line-of-sight links at 19.5 GHz," *IEEE Africon 2004*, Vol. 01, 95–100, Gaborone, Botswana, Sep. 2004.
26. Fashuyi, M. O. and T. J. Afullo, "Rain attenuation prediction and modelling for LOS terrestrial links in South Africa," *Radio Science*, Vol. 42, RS 5006, 2007.
27. Odedina, P. K. and T. J. Afullo, "Clear-air signal level measurement for microwave line-of-sight link application in South Africa," *SAIEE,* Vol. 101, No. 4, 132–139, Dec. 2010.
28. Recommendation ITU-R P.311-13, "Acquisition, presentation and analysis of data in studies of tropospheric propagation," ITU-R P Sers., Oct. 2009.
29. Abdulrahman, A. Y., T. A. Rahman, and S. K. A. Rahim, "A new rain attenuation conversion technique for tropical regions," *Progress In Electromagnetics Research B*, Vol. 26, 55–67, 2010.
30. Ajayi, G. O. and R. L. Olsen, "Modelling of tropical raindrop size distribution for microwave and millimeter wave applications," *Radio Science*, Vol. 20, 193–202, 1985.
31. Ajayi, G. O. and A. Adimula, "Variations in raindrop size distribution and specific attenuation in a tropical environment," *URSI Comm. F Symposium*, 811–814, La Londe-less Maures, France, Sep. 1989.

Six-port Based Wave Correlator with Application to Micro-displacement Measurement

N. Iwaki , F. Xiao, and T. Yakabe
The University of Electro-Communications, Japan

Abstract— As a remote sensing application of the six-port based wave-correlator (SPC), measuring the micro displacement of an object is discussed in this paper. This application indicates that it is applicable for various situations to measure the micro displacement. The SPC is a two-channel wave receiver for determining the vector relation, both amplitude and phase difference, between the two input signals by measuring the power levels. A measurement system with an MMIC SPC is developed, which includes differential amplifiers, AD converters, control circuits, and microwave components. In the preliminary experiments, the results of the micro displacement obtained are with a relative error within approximately 30% compared with the ideal values, which exemplifies the possibility of the developed measurement system in the practical application.

1. INTRODUCTION

Measurement techniques using one of the technologies of the six-port based wave-correlator (SPC) have been reported. For example, the applications of the SPC include finding beam direction [1], and measuring a very low velocity using the Doppler Effect [2]. As a remote sensing application of the SPC [3, 4], measuring the micro displacement of an object is discussed in this paper. One of the applications of this work is expected to predict landslide accidents by monitoring the micro displacement.

The SPC comprises two input channels, a signal source port and a measurement port, and four sidearm ports to which power detectors are connected. It can measure the vector relation, both amplitude and phase difference, between the two input signals by measuring the power levels of four sidearm ports [5]. The measurement system is developed, which includes differential amplifiers, AD converters, control circuits, and microwave components such as isolators, a small type oscillator, a directional coupler and two horn antennas.

The paper is organized as follows. First, the principle of measuring the micro displacement of an object is described. Next, the flow of signal processing in the system is shown. The third section includes a modern calibration method of the system containing the SPC. In the preliminary experiments, the results of measuring the displacement per 100 μm is shown. The results show that the measured displacement has a relative error within approximately 30% compared with the ideal values.

2. PRINCIPLE OF MICRO-DISPLACEMENT MEASUREMENT

Principle of measurement is shown in Figure 1. There are two horn antennas, one is as a transmitter and the other is as a receiver, and the moving object for which the micro displacement will be measured. The microwave is transmitted by the transmitter to irradiate the object. And the reflected wave is received by the receiver. The phase difference θ_1 between Tx and Rx is defined when the reflector is at position d_1. Next, the phase difference θ_2 is defined like θ_1 when the object is moved to position d_2. The relationship between the micro displacement $\Delta d\,(= d_2 - d_1)$ [m] and the variation of the phase difference $\Delta\theta\,(= \theta_2 - \theta_1)$ [rad] is shown in (1).

$$\Delta d = \frac{1}{2}\frac{\Delta\theta}{2\pi}\lambda \tag{1}$$

where, the wavelength λ is 3 cm in this report.

The scheme block diagram of the developed measurement system using an MMIC SPC is shown in Figure 2. The directional coupler divide the generated wave from the small type oscillator into two waves: one which is attenuated 20 dB enters the signal source port (P1) of the SPC and the other is transmitted by the transmitter to irradiate the object. The reflected wave from the object is received by the receiver and the wave enters the measurement port (P2) of the SPC. The SPC has a signal source port, a measurement port, and four sidearm ports. Structure of the MMIC SPC is shown in Figure 3. The MMIC SPC comprises four quadrature hybrids (Q), four diode detectors

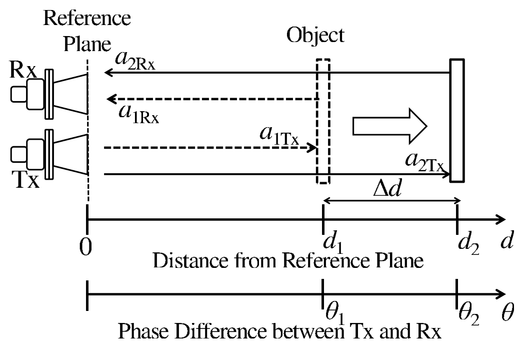

Figure 1: Principle of measuring the micro displacement using antennas.

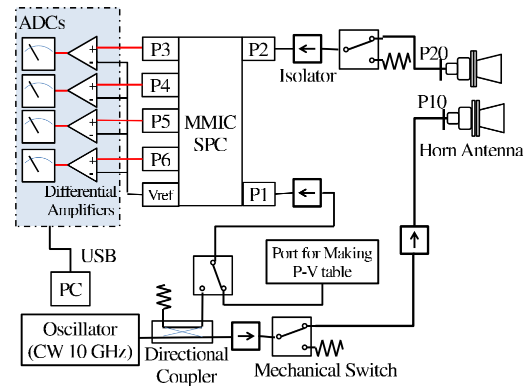

Figure 2: The scheme block diagram of the developed measurement system using the MMIC SPC.

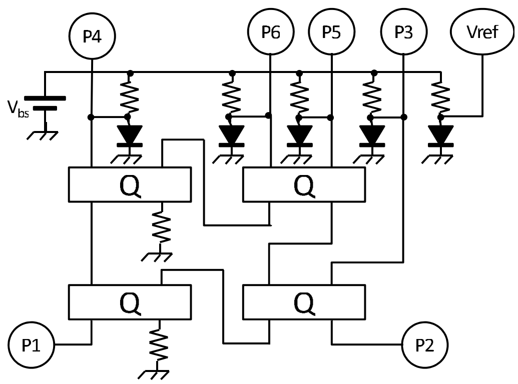

Figure 3: Structure of the MMIC SPC.

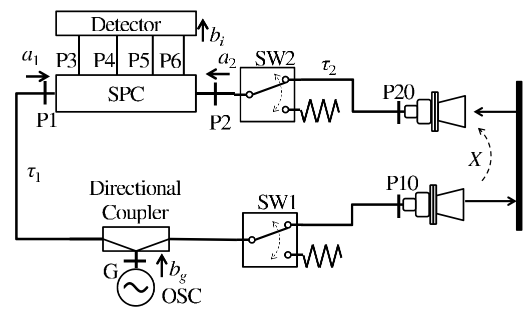

Figure 4: Signal flow block diagram.

and two terminations. The Vref port is a reference port to compensate the temperature changing of the MMIC SPC. Two input waves are mixed and delayed with four quadrature hybrids. The magnitude of the output powers which are converted to DC voltage by diode detectors is actually a function of the complex wave ratio. The output powers are amplified and converted to digital signals by circuits. A computer picks up these voltage data using serial interface communications. These voltage data are reconverted to power data based on the reference tables of power and voltage by the software. The micro displacement, relating complex wave ratio, is calculated by equations described in the next section and these port power data.

3. CALIBRATION THEORY

3.1. Determine the Complex Wave Ratio W

Signal flow block diagram of measurement is shown in Figure 4. Two incident waves are denoted by a_2 and a_1, by defining their complex wave ratio as $W = a_2/a_1$, then the four sidearm port power readings P_i, $(i = 3,\ 4,\ 5,\ 6)$ may be written as,

$$P_i = \alpha_i \left|A_i a_2 + B_i a_1\right|^2 = \alpha_i \left|a_1 B_i\right|^2 \left|\frac{A_i}{B_i} W + 1\right|^2, \quad (i = 3, 4, 5, 6) \tag{2}$$

$$_4P_i = \frac{P_i}{P_4} = \frac{\alpha_i \left|a_1 B_i\right|^2 \left|\frac{A_i}{B_i} W + 1\right|^2}{\alpha_4 \left|a_1 B_4\right|^2 \left|\frac{A_4}{B_4} W + 1\right|^2} = {}_4P_{\mathrm{ir}}\,{}_4T_i \left|\frac{1 + t_i W}{1 + t_4 W}\right|^2, \quad (i = 3, 5, 6) \tag{3}$$

where α_i are the power conversion parameters. A_i and B_i are complex constants, and ${}_4T_i$ and t_i are calibration parameters of the SPC. The reference port power ${}_4P_{\mathrm{ir}}$ are measured when SW1 and SW2 in Figure 4 are connected to the termination respectively. In this case, the sidearm P_4 is used for normalization port.

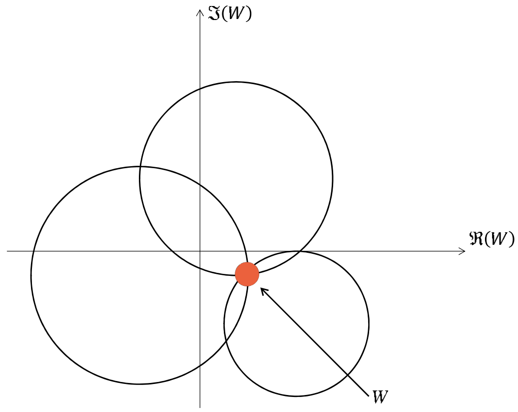

Figure 5: Determination of the complex wave ratio W.

Figure 6: A new tool to determine the t_i.

By expanding (3) into quadratic form, we have (4).

$$\left|W + \frac{z_i^*}{Q_i}\right|^2 = \frac{L_i Q_i + |z_i|^2}{Q_i} \qquad \begin{cases} L_i = \frac{{}_4P_i}{{}_4P_{\mathrm{ir}}} - {}_4T_i \\ Q_i = |t_i|^2\, {}_4T_i - |t_4|^2 \frac{{}_4P_i}{{}_4P_{\mathrm{ir}}} \\ z_i = t_i {}_4T_i - t_4 \frac{{}_4P_i}{{}_4P_{\mathrm{ir}}} \end{cases} \tag{4}$$

The equations mean three circles in the complex W plane with the centers $-z_i^*/Q_i$ and radii $\sqrt{(L_iQ_i + |z_i|^2)/Q_i^2}$. Sicne the locus of each circle represents the possible value for W, the complex W is the intersection of three circles as shown in Figure 5.

3.2. Determine the Calibration Parameters

The real ${}_4T_3$, ${}_4T_5$, ${}_4T_6$ which are the system parameters of the SPC are expressed,

$${}_4T_i = \frac{P_{i\mathrm{S}}/P_{4\mathrm{S}}}{{}_4P_{\mathrm{ir}}}, \tag{5}$$

where standard port power $P_{i\mathrm{S}}$ are measured when P10 and P20 in Figure 4 are connected to termination respectively. Meanwhile $\overline{P_{i\mathrm{S}}}$ are written as,

$$\overline{P_{i\mathrm{S}}} = \frac{P_i}{P_{i\mathrm{S}}} = |t_i W + 1|^2, \tag{6}$$

then by expanding (6) into quadratic form, we have (7) that are circles in the complex t_i plane similar to formula (4),

$$\frac{\overline{P_{i\mathrm{s}}^{(n)}}}{\left|W^{(n)}\right|^2} = \left|t_i + \frac{1}{W^{(n)}}\right|^2. \quad (i = 3, 4, 5, 6,\ n = 1, 2, 3) \tag{7}$$

t_i can be also determined if there are three standard of known W. Three lines of different length with known W are used before [6, 7]. In this work, a new method based on a new tool composed of the horn antennas that are used in the actual measurement, the reflector and the automatic stage is used, as shown in Figure 6. W of three points, corresponding to three arbitrary distances from the antennas to the reflector, are measured by a vector network analyzer. t_i can be determined by substituting the measured W for the $W^{(n)}$ in (7).

4. EXPERIMENT

Complex wave ratio is measured using the test setup shown in Figure 6 to calculate the displacement. Distance from the antennas to the reflector is changed between 150 mm and 185 mm and each position was measured at 100 µm intervals. The results of the complex wave ratio are shown in Figure 7 and the results of calculated displacement are shown in Figure 8. Further results of large range of distance between 150 mm and 360 mm are shown in Figure 9. According these results, the measured displacement has a relative error within approximately 30% compared with the ideal values. The direct wave from the transmitter to the receiver is thought to be the cause of the error.

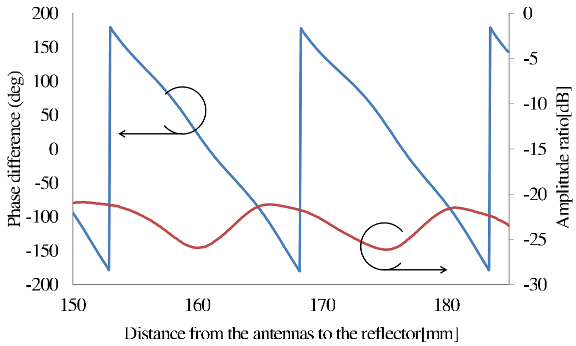

Figure 7: Complex wave ratio versus the distance between the antennas to the reflector.

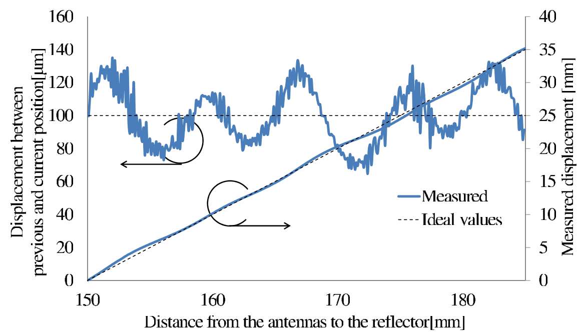

Figure 8: Calculated displacement.

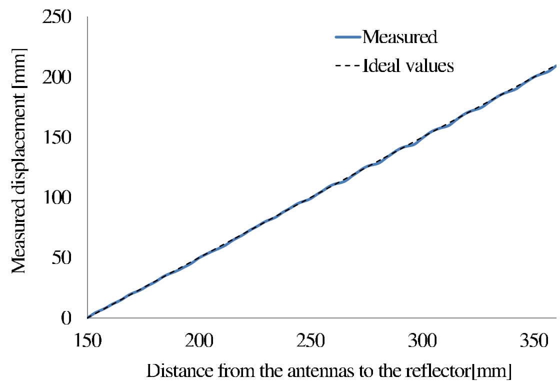

Figure 9: Calculated displacement for large range.

5. CONCLUSION

As a remote sensing application of the SPC, measuring the micro displacement has been discussed. The developed measurement can measure complex wave ratio easily. And the computed results of the micro displacement exemplified the possibility of the developed measurement system in the practical application. The results have some discrepancy as compared with the ideal values, and the improvement of the measurement accuracy will be further investigated.

REFERENCES

1. Yakabe, T., F. Xiao, K. Iwamoto, F. M. Ghannouchi, K. Fujii, and H. Yabe, "Six-port based wave-correlator with application to beam direction finding," *IEEE Trans. Instrum. Meas.*, Vol. 50, 377–388, Apr. 2001.
2. Xiao, F., F. M. Ghannouchi, and T. Yakabe, "Application of a six-port wave-correlator for a very low velocity measurement using doppler effect," *IEEE Trans. Instrum. Meas.*, Vol. 52, 297–301, Apr. 2003.
3. Iwaki, N. and T. Yakabe, "Study on the micro displacement sensor using the MMIC six-port correlator," *Technical Committee on Microwave Engineering*, 141–145, Oct. 2012.
4. Vinci, G., S. Lindner, F. Barbon, R. Weigel, and A. Koelpin, "Promise of a better position," *IEEE Microwave Magazine*, Vol. 13, S41–S49, Nov.–Dec. 2012.
5. Engen, G. F., "Application of an arbitrary 6-port junction to power-measurement problems," *IEEE Trans. Instrum. Meas.*, Vol. 21, No. 4, 470–474, Nov. 1972.
6. Yakabe, T., K. Hirose, H. Matsuura, K. Fujii, and F. Xiao, "An X-band MMIC six-port correlator based vector network analyzer," *2010 Conference on Precision Electromagnetic Measurements*, 714–715, Jun. 2010.
7. Akutsu, N., R. Matsuguma, N. Iwaki, and T. Yakabe, "A calibration method without a matched load for a six-port wave-correlator based VNA," *PIERS Proceedings*, 446, Kuala Lumpur, Malaysia, Mar. 27–30, 2012.

Uncertainty in Waveguide Vector Network Analyzer Measurements in the Frequency Range of D-band (110 GHz to 170 GHz)

Masahiro Horibe and Ryoko Kishikawa
National Metrology Institute of Japan
National Institute of Advanced Industrial Science and Technology, Japan

Abstract— We have evaluated the measurement uncertainty for rectangular waveguide Vector Network Analyzer (VNA) measurements in the frequency range of D-band, 110 GHz–170 GHz. We developed a new waveguide flange design for precise connections and dimensional measurements to establish traceability to the SI for standard line as a calibration standard in VNA measurements. As the result of evaluation for VNA and its standard, we estimated VNA measurement uncertainty in the D-band.

1. INTRODUCTION

In recent years millimeter-wave and sub-millimeter-wave signals have been used not only in radio astronomy but also in industrial telecommunications. In 2000's, prototype telecommunication system using D-band frequency base band has been developed and performed the field testing in Japan. In order to installing this type of new communication systems in to consumer field, testing regarding the radio law, relating the ITR-R recommendations, should be performed before using the system in a consumer field. This type of requirement is providing demands to develop the calibration standard and system for measurement instruments. For calibration of reflection coefficient in the test instruments, vector network analyzers are widely used. The use of millimeter-wave electronic instruments and systems has advanced rapidly and commercial Vector Network Analyzers are now operating up to 1100 GHz [1] with the result that national measurement standards must be extended for scattering parameter (S-parameter) measurements. Standards have been available for establishing measurement quality to frequencies beyond 110 GHz [2–4] but the extension above 110 GHz requires new technology.

For metrological purposes the fundamental measurements for rectangular waveguides have been the aperture dimensions (width and height). Thru-reflect-line (TRL) 'Line' standards are usually used as S-parameter measurement standards in VNA applications. At millimeter wave frequencies, accurate primary 'Line' standards based on dimensions alone pose a significant challenge and the National Metrology Institutes (NMIs) are developing S-parameter measurement systems and accompanying standards for establishing precision measurements at frequencies beyond 110 GHz [2–4] in Vector Network Analyzer (VNA) measurements. In the several hundred GHz band, a 3-dimensional coordinate measuring machine (3DCMM) can be used to measure the dimensions of the aperture.

This paper describes a technique for evaluating uncertainty in VNA measurements that have produced reliable S-parameter measurements in the D-band frequency. The new waveguide design and TRL "Line" standards are described. The results of mechanical measurements of "Lines" and test ports in the waveguide VNA are described. The influence of non-ideal TRL line characteristics on VNA measurement is discussed with uncertainty analysis of VNA measurement in the WM-1651 (WR-6) band (110 GHz–170 GHz).

2. WAVEGUIDES AND STANDARDS

The newly designed flange (Figure 1) makes precise alignments in the directions of the H-plane and E-plane of the aperture by a coupling ring attached to the outside circumference of each flange while two dowel holes provide precise angular alignment. Use of the newly designed flange achieves excellent connection repeatability at the waveguide interfaces of the test ports and finds a practical application in accurate VNA calibrations and measurements in the sub-millimeter wave band. Even if the newly designed flange [5] providing accurate connections, it was mechanically compatible with the MIL-DTL-3922/67C (UG-387) flange.

Precise connection was also required for measuring "Line" standards in TRL calibration of the VNA. Waveguide "Line" standards were developed to fit the newly designed flange and as above, the apertures of the "Line" standards were accurately centered by the use of a coupling ring. The "Line" standard fitted in this way made possible accurate TRL calibrations and accurate

Figure 1: WR-6 (WM-1651) waveguide straight section with newly designed flanges, alignment ring and waveguide shim. Flanges and shim are aligned by alignment ring.

Table 1: Lengths for line standards in the WM-250 band.

Description	Line Length [μm]	Frequency range as a TRL calibration standard [GHz] [7]	
		Minimum	Maximum
Line	728	110	170

Table 2: Line lengths.

Description	Line Length [μm]	Expanded uncertainty ($k = 2$) [μm]
Line	728.15	0.67

Table 3: Line aperture dimensions for TRL calibration in D-band.

Description	a [μm]	U ($k = 2$) [μm]	Δa [μm]	b [μm]	U ($k = 2$) [μm]	Δb [μm]
Line	1648.7	5.0	2.5	831.4	8.4	5.9

VNA measurements in D-band frequency. The length of the "Line" standard was chosen so that it typically provides a 90 degree phase change with respect to the through connection at the waveguide mid-band frequency (140 GHz in WM-1651 band) (Table 1) [6].

3. DIMENSIONAL MEASUREMENTS

3.1. Measurement System

Traceability to the international standards (SI) was established for S-parameter measurements via dimensional measurements of a waveguide line standard. Measurements of the height and width dimensions of the waveguide apertures were made by using a Mitutoyo LEGEX 322 three dimensional coordinate measuring machine (3DCMM) fitted with a 300 μm diameter ball-tip micro-stylus at standard conditions (23°C) of the electrical calibration laboratory.

The height (y-) and width (x-) dimensions of the rectangular aperture were measured at a series of approximately equally spaced locations across the aperture. Each measurement run therefore produced 4800 dimensional measurements, 1600 width values and 3200 height values. The systematic uncertainty from the measurement system was approximately 0.93 μm. Some dimensional variation of the aperture along the waveguide line added to the total measurement uncertainty. In most cases an additional uncertainty contribution was observed meaning roughness on waveguide aperture walls (Figure 2).

Measurements of the aperture corner radii of a WM-1651 waveguide line were made using the Keyence LT9010M laser interferometer with a specialized stage that can adjust the incident angle of the laser beam.

3.2. Aperture Dimensions

Measurements of the width at varying positions along the height and depth are shown in Figure 2. The expanded uncertainty of aperture measurements of Line is 5.0 μm for width dimension, a, and 8.4 μm for height dimension, b. The dominant sources of uncertainty in the dimensional measurements were increasing uniformity of the surface roughness on the aperture wall (over 6 µm [3]). Deviation, Δa and Δb, from the standard value defined in the IEEE standard P1785 [7] reaches 2.5 µm for a and 5.9 µm for b. The difference is taken into account in S-parameter calculations in Section 4.

3.3. Aperture Corner Radii

Cross-sectional views of the corners were obtained. The corner radius was fitted by a circle with mid-point radius values of 18.5 µm (minimum of 15 µm and maximum of 22 µm) at several positions along the "Line" length. The corner was no longer a right angle and the corner radii were not uniform at these positions. The variation was generally within ± 3.5 µm.

3.4. Difference of Center Positions for Test Ports and Line

Two 3DCMM measurements of center point are possible, one as defined with respect to the edges of the aperture and the other as defined with respect to the outer circumference of the flange. The differences between the aperture center and flange alignment center were obtained [8] and are summarized in Table 4. In the table x and y refer to the H-plane and E-plane directions, respectively, and $|\Delta x|$ and $|\Delta y|$ indicate the differences of the center positions between aperture and flange. In VNA measurements the center offsets of both test ports and "Line" provides H-plane and E-plane displacements at the waveguide mated interfaces. Such displacements at a mated interface produce reflections that increase VNA measurement uncertainty. H-plane displacement, δa_m, calculated by difference between both $|\Delta x|$ values of Port-1 and Port-2 is 2.4 µm. The resulting E-plane displacement, δb_m, is 2.3 µm.

4. CHARACTERIZATION

The S-parameter was estimated from the four mechanical measurements: width, height, corner radii and line length of the WM-1651 rectangular waveguide when connected in standard aperture size as defined in IEEE P1875 standard [6]. It was derived from a series expansion of the field in eigenmodes [9] by a Monte Carlo simulation involving 100,000 trials. S_{11} values for line standard with their associated uncertainties were calculated and are shown in Figure 3.

In the figure the calculated results of S_{11} are no longer zero at all frequencies (110 GHz to 170 GHz) due to the small deviation in aperture size compared to the values defined in the IEEE

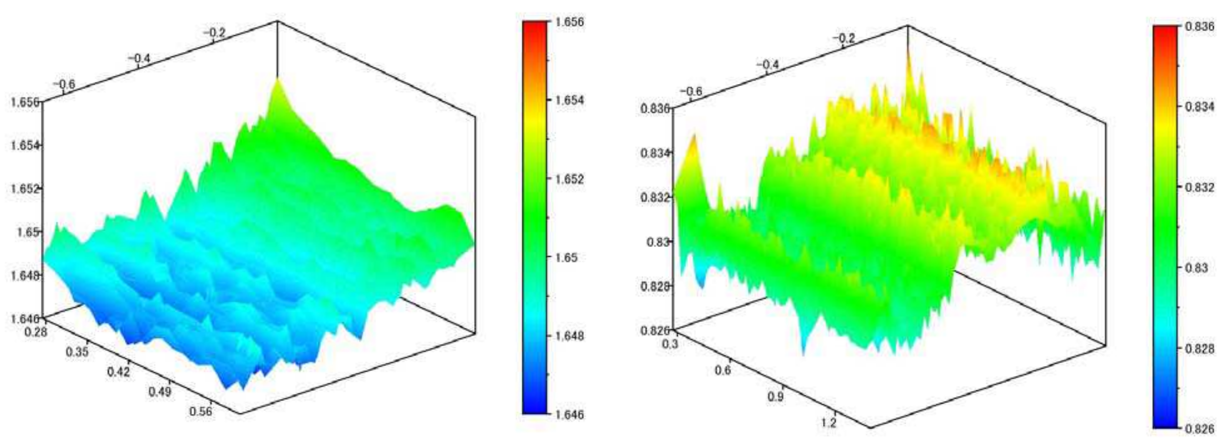

(a) (b)

Figure 2: Measurement results of aperture dimensions (a) width and (b) height for WM-1651 waveguide line standard.

Table 4: Difference of center position.

Description	Aperture center offset [µm]	
	$\lvert\Delta x\rvert$	$\lvert\Delta y\rvert$
Port-1	−3.1	−3.1
Port-2	−0.7	−0.8
Line	−1.6	−1.0

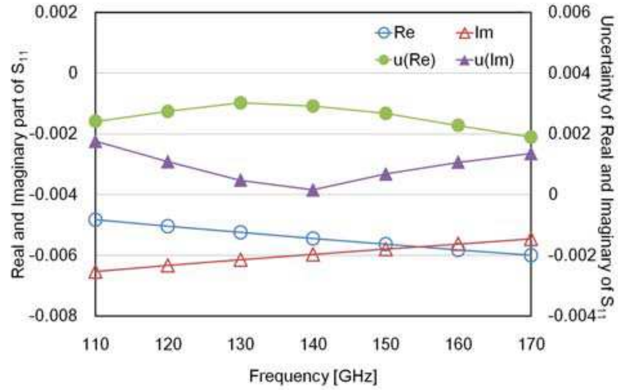

Figure 3: S_{11} and its uncertainty of TRL line ($L = 0.728\,\mathrm{mm}$). The open circular and triangular indicate calculated values of real and imaginary part of S_{11}, then, closed circular and triangular mean expanded uncertainty of real and imaginary parts of S_{11} of Line-1.

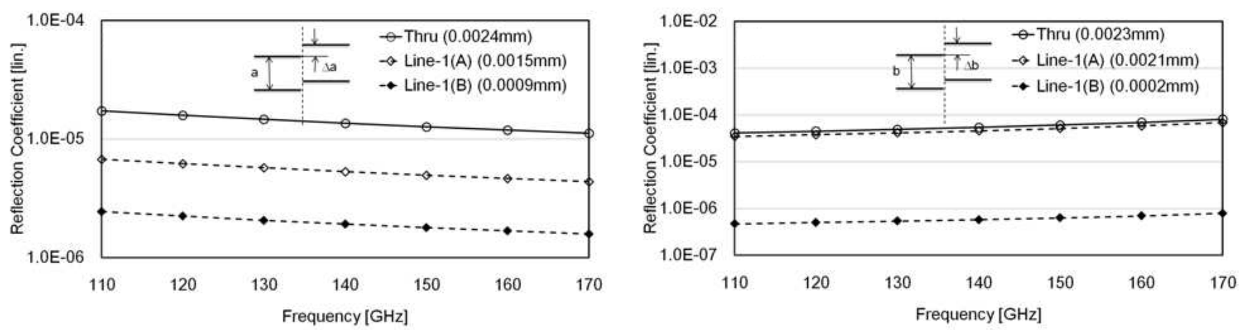

Figure 4: Calculated reflection characteristics from displacement of (a) H-plane and (b) E-plane. Values inside the blankets indicate displacement along with H- and E-plane.

standard.

The S-parameter expanded uncertainties, $U(\mathrm{Re})$ and $U(\mathrm{Im})$, for Line are also plotted in Figure 3. The expanded uncertainty is the same order of magnitude of the calculated values. This is because the uncertainties, $U(a)$ and $U(b)$, is approximately same as deviation, $|\Delta a|$ and $|\Delta b|$, in the dimensional measurements of the aperture. According to Refs. [3, 10] the width variation is a large contributor to the S_{11} uncertainty of the line standard when uncertainties in width and height are approximately equal.

The dominant effect in the millimeter waveband was usually the result of reflections caused by displacement of the apertures. The source consistently affecting the reflection coefficient was determined to be the difference between aperture center and flange center positions. This type of displacement produces reflection characteristics due to H- and E-plane displacements [10]. Figure 4 shows the calculated reflection characteristics provided from the H-plane and E-plane aperture displacements at the waveguide interface. In the figure reflection characteristics are shown for the all connection. However, magnitude of reflection characteristics was one order smaller than magnitude of S_{11} characteristics due to relatively small displacement values compared to aperture size.

5. VNA PERFORMANCE EVALUATION

5.1. Measurement Setup

The repeatability of connections was evaluated using a PNA Vector Network Analyzer from Agilent Technologies and a WR-6 (WM-1651) frequency extension module from Oleson Microwave Laboratory Inc. (OML). All results presented in this paper were obtained with an IF bandwidth of 100 Hz and a point averaging factor of 64. The system repeatability (system noise floor) was evaluated; the noise floor characteristics were 110 dB for transmission measurements.

5.2. TRL Calibration with Non-ideal TRL Line

A TRL calibration method theoretically provides accurate measurement in VNA. Ideal electrical characteristics (no reflection characteristics at the interfaces) are required in line standard. For practical use the waveguide line standard as the primary reference for VNA calibration is no longer ideal line standard. Non-ideal characteristics of line standards and through connections provide errors in the VNA [11]. Error sources of non-ideal characteristics are the value and uncertainty of S_{11}, H- and E-plane displacement at flange interface and mating repeatability of line and through connections. In other words, aperture size deviations, Δa and Δb, from the IEEE standard size are major contributor in VNA measurement uncertainty via values of S_{11} and S_{22} listed in Table 5. However, connection repeatability is particularly small contribution to a VNA measurement uncertainty due to use of newly designed flanges providing precise connections.

5.3. VNA Measurement Uncertainty

Measurement uncertainty was estimated from values and uncertainties of dimensional measurement results via the S-parameter calculation for the line standard [12].

The uncertainty budget at 170 GHz for S_{11} for one port devices with high reflection ($S_{11} = 1$) is listed in Table 5. S_{11} uncertainty was determined by reflection characteristics of line and interface for both line and through connections in the TRL calibration scheme. A major source of uncertainty of the S_{11} measurement was the value (0.0047) and uncertainty (0.0023) of S_{11} of line.

The uncertainty budget for S_{21} is listed in Table 6 in the case where $S_{11} = S_{22} = 0$ [lin.] and $S_{21} = 0$ [dB] at 170 GHz. In this case there was no contribution between port match and S_{ii} ($i = 1$, 2) of the device under test (DUT), and S_{21} uncertainty was determined by S_{21} repeatability of the through connection. S_{21} values of the line characteristic do not affect measurement uncertainty in the self calibration scheme.

The 3-dimensional plots in Figure 5 demonstrate the dependence of expanded uncertainty on

Table 5: Uncertainty budget for S_{11} measurement ($S_{11} = 1$, $S_{21} = S_{12} = 0$) at 170 GHz.

Uncertainty contributions		Value	Deviser	Uncertainty [lin.]	Uncertainty of S_{11} [lin.]
Line-1	Value of S_{11} or S_{22}	0.0081	$\sqrt{3}$	0.0047	0.0071
	Standard uncertainty of S_{11} or S_{22}	0.0023	1	0.0023	
	H-plane displacement at port-1 or -2	0.0000044	$\sqrt{3}$	0.0000025	
	E-plane displacement at port-1 or -2	0.000069	$\sqrt{3}$	0.000040	
	Flange mating repeatability of S_{11} or S_{22}	0.001	$\sqrt{10}$	0.00032	
	RMS of S_{11} or S_{22} contribution			0.0052	
Thru	H-plane displacement	0.000011	$\sqrt{3}$	0.0000064	0.00052
	E-plane displacement	0.000082	$\sqrt{3}$	0.000047	
	Flange mating repeatability of S_{11} ($= S_{22}$)	0.001	$\sqrt{10}$	0.00032	
	RMS of Thru contribution			0.00032	
Combined uncertainty from calibration					0.0071
Linearity			$\sqrt{3}$		0.0014
Noise Floor			$\sqrt{3}$		0.0000019
Standard uncertainty					0.0072
Expanded uncertainty ($k = 2$)					0.014

Table 6: Uncertainty budget for S_{11} measurement ($S_{21} = 0$ dB, $S_{11} = S_{21} = 0$) at 170 GHz.

Uncertainty contributions		Value	Deviser	Uncertainty [lin.]	Uncertainty of S_{21} [dB]
Thru	Flange mating repeatability of S_{21} ($= S_{12}$)	0.0010	$\sqrt{10}$	0.00032	0.0028
Linearity			$\sqrt{3}$		0.000
Noise Floor			$\sqrt{3}$		0.000016
Standard uncertainty					0.0028
Expanded uncertainty ($k = 2$)					0.0056

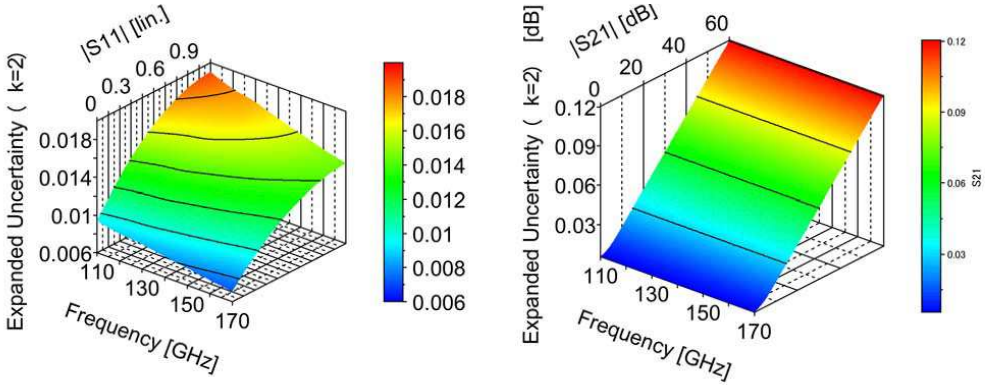

(a) (b)

Figure 5: Expanded uncertainty in VNA measurements in the D-band frequency range (a) S_{11}, (b) S_{12}.

the operating frequency and the characteristics of the DUT. The S_{11} measurement uncertainty ($5a$) grows large at the lower frequency limit or below 110 GHz. This is because the sensitivity to measurement uncertainty of the S_{11} value of the line standard increases at the lower frequencies. When the reflection characteristics are small the principal uncertainty contribution is the linearity of S_{21} for the DUT.

6. CONCLUSION

This paper has described a characterization for a waveguide line standard suitable for VNA calibrations in the frequency range from 110 GHz to 170 GHz. Even if line standard connecting test port the newly designed waveguide flange for metrology use provides good repeatability (less than 0.0010 of experimental standard deviation at 170 GHz). The newly designed flange produces the suppression of measurement errors systematically introduced by E-plane and H-plane displacements.

The scattering parameters for waveguide TRL line were calculated from electromagnetic theory. The uncertainty of the S-parameter of the line standard was calculated and its contribution to VNA measurement uncertainty was estimated. The major contribution to VNA measurement uncertainties is the aperture dimension difference of the waveguide line standard.

ACKNOWLEDGMENT

The work described in this paper was supported by the Industrial Technology Research Grant Program in 2009 from NEDO of Japan.

REFERENCES

1. Duan, Y. and J. L. Hesler, "Modular VNA extenders for terahertz frequencies," *20th Intl. Symp. on Space Terahertz Technology*, Charlottesville, VA, Apr. 20–22, 2009.
2. Ridler, N. M., R. G. Clarke, M. J. Salter, and A. Wilson, "Traceability to national standards for S-parameter measurements in waveguide at frequencies from 140 GHz to 220 GHz," *76th ARFTG Microwave Measurement Conference Digest*, 8–14, Marriott Suites on Sand Key, Clearwater Beach, FL, Dec. 2–3, 2010.
3. Horibe, M., R. Kishikawa, and M. Shida, "Complete characterization of rectangular waveguide measurement standards for vector network analyzer in the range of millimeter and submillimeter wave frequencies," *76th ARFTG Microwave Measurement Conference Digest*, 1–15, Marriott Suites on Sand Key, Clearwater Beach, FL, Dec. 2–3, 2010.
4. Williams, D., "500 GHz–750 GHz rectangular-waveguide vector-network-analyzer calibrations," *IEEE Trans. on Terahertz Sci. and Technol.*, Vol. 1, No. 2, 364–376, Nov. 2011.
5. Horibe, M. and K. Noda, "Modification of waveguide flange design for millimeter and submillimeter-wave measurements," *77th ARFTG Conference Digest*, 1–7, Jun. 2011.
6. Ridler, N. M., "Choosing line lengths for calibrating waveguide vector network analysers at millimeter and sub-millimetre wavelengths," *NPL Report TQE 5*, National Physical Laboratory, UK, Mar. 2009.

7. "IEEE standard for rectangular metallic waveguides and their interfaces for frequencies of 110 GHz and above," IEEE P1785, http://grouper.ieee.org/groups/1785.
8. Horibe, M. and N. M. Ridler, "Traceability via precision dimensional measurements of WM-864 (WR-03) waveguide standard shims including comparison between NPL and NMIJ," *79th ARFTG Microwave Measurement Conference Digest*, to be published.
9. Patzelt, H. and F. Arndt, "Double-plane step in rectangular waveguides and their application for transformers, irises, and filters," *IEEE Transactions on Microwave Theory and Techniques*, Vol. 30, No. 5, 771–776, May 1982.
10. Bannister, D. J., E. J. Griffin, and T. E. Hodgetts, "On the dimensional tolerances of rectangular waveguide for reflectmetry at millimetric wavelengths," *NPL Report DES 95*, National Physical Laboratory, UK, Sep. 1989.
11. Stumper, U., "Uncertainty of VNA S-parameter measurement due to nonideal TRL calibration items," *IEEE Trans. on Instrum. Meas.*, Vol. 54, No. 2, 676–679, Apl. 2005.

The Progress of Unmanned Aerial Vehicle Synthetic Aperture Radar Development for Environmental Monitoring

Yee Kit Chan, Voon Chet Koo, and Hean Teik Chuah
Faculty of Engineering & Technology, Multimedia University
Jalan Ayer Keroh Lama, Bukit Beruang, Melaka 75450, Malaysia

Abstract— Synthetic Aperture Radar (SAR) plays an invaluable role in disaster monitoring as well as military surveillance for the collection of all weather image data. In recent years, many countries have strived to develop high-resolution, multi-functional, airborne SAR systems with all-digital real-time imaging capabilities. In late 2007, the project to develop a UAVSAR system was initiated with joined collaboration with Agency Remote Sensing of Malaysia. The main objective of this project is to design and construct an imaging radar system with UAV as the platform. The SAR system is a C-band, single polarization, linear FM pulse radar system. This SAR system is designed to operate at low altitudes with low transmit power and small swath width in order to optimize the development cost and operating cost. This system will be used for monitoring and management of earth resources such as paddy fields, oil palm plantation and soil surface. A few flight missions have been conducted in Semprona and Mersing, Malaysia to verify the capability and performance of the sensor. This paper describes the development of the SAR sensor as well as the current status of the development.

1. INTRODUCTION

SAR is a technique which uses signal processing to improve the resolution [1, 2]. In SAR, forward motion of the actual antenna is used to "synthesise" a very long antenna. The concept of SAR can be traced back to the 1950s. In June 1951, Carl Wiley of Goodyear Aerospace Co, United States proposed the *Doppler beam sharpening system* which can be used to improve the azimuth resolution of the radar. Meanwhile, the Control Systems Laboratory of University of Illinois independently conducted a non-coherent radar experiment which confirmed that the Doppler frequency analysis method can really improve the azimuth resolution of the radar. This effort was continued by experimenting coherent radar with non-focused aperture synthesis methods and produced the first SAR image in July 1953 [3]. During the summer of 1953, American scientists presented a new concept of synthesis the real radar antenna to form a larger aperture by linear antenna array [1].

Since then, the principle of synthetic aperture and SAR have been recognized and supported with continuous development at research laboratories in various countries. In short, pulse compression technique and synthetic aperture technologies have greatly promoted the development of high-resolution imaging radars. The initial function of radar as a target detector has been migrated to the target imaging. SAR has its unique advantages in comparison with optical imaging, and it can provide a complementary and useful information to the optical sensor. With continuous development and improvement of the SAR technology, SAR resolution is finer and is approaching an optical sensor resolution. SAR as an active microwave remote sensor is able to extract a wide range of terrain and surface features. Its high resolution, large area of coverage, and all weather capability has aroused great interest of remote sensing scientists.

Microwave remote sensing is one of the major research areas conducted by a research group in Multimedia University, Malaysia, for the past 10 years or so. The design and development of the UAVSAR have been commenced in late 2007 by Remote Sensing Research Group of Multimedia University with joined collaboration with Agency Remote Sensing of Malaysia. The developed system is a single polarization, linear FM radar operating at C-band (5-cm wavelength) with low operation altitudes, low transmit power and small swath width in order to optimize the development cost and operating cost. This sensor have been test in a series of flight mission conducted in end of year 2010 at Mersing, Malaysia. During the Mersing Flight Mission, 6 flight measurements were successfully conducted. The processed SAR image shows clear signatures of river, roads, urban and forested areas [4].

In year 2011, second prototype of UAVSAR sensor has been design and developed to improved the some of the preformance of the existing SAR sensor. This paper outlines the development of the new SAR sensor as well as the current status of the development.

2. SYSTEM OUTLINE

The system specifications of the C-band UAVSAR system are summarized in Table 1. The development of UAVSAR system is presented in the subsequent section.

The major changes as compared to the previous C-band SAR system are: antenna elevation beamwidth is increased from 24° to 30° in order to accommodate larger swath width; introducing real time INS/GPS data display, real time SAR sensor monitoring, real time image processing and display in real time SAR processor; newly developed integrated software packet with SAR designer, simulator, processing and display features; as well as enhanced SAR chassis with flexible and removable cover and compartment for ease of maintenance and troubleshooting.

The UAVSAR Sensor can be functionally divided into a few assemblies: (i) RF section; (ii) FPGA-

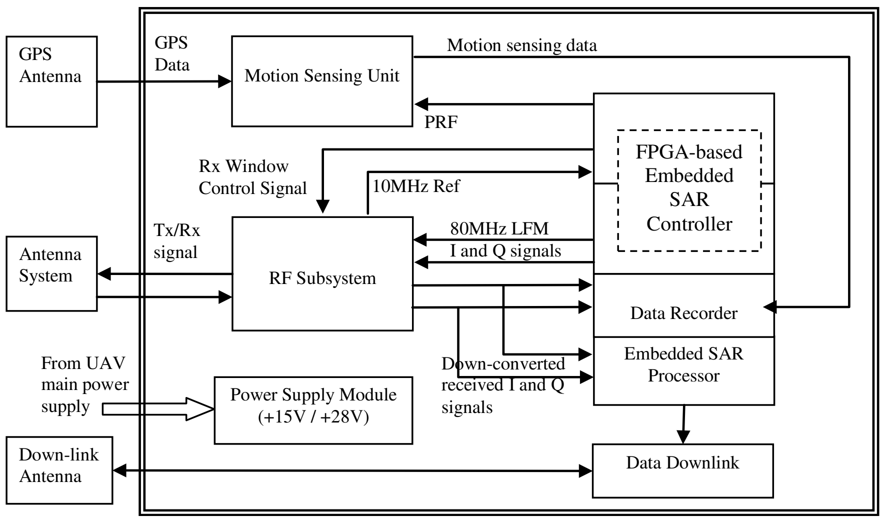

Figure 1: Block diagram of SAR sensor.

Table 1: UAVSAR system specifications.

System Parameters	Specifications
Mode of Operation	Stripmap
Operating Frequency	5.3 GHz (C-band)
Modulation	LFM Pulse
Bandwidth	80 MHz
Pulse Repetition Frequency	640–1000 Hz
Pulse Width	Variable pulse width of 1 µs to 10 µs
Polarization	VV
Antenna Gain	15 dBi
Antenna Size	$1\,\mathrm{m} \times 0.3\,\mathrm{m}$
Spatial Resolution	$2\,\mathrm{m} \times 2\,\mathrm{m}$
RCS Dynamic Range 30 dB	0 dB to -30 dB
SNR	> 10 dB
Platform Height, h	900–3000 m
Swath Width	607–2025 m
Nominal Platform Speed	32 m/s
Data Take Duration	1–2 hour (50 sec per scene)
Operating Platform	UAV, Aludra MK1 SE
Overall Sensor Weight	< 20 kg
Overall Sensor Dimension	$< 27\,\mathrm{cm}\ (W) \times 35\,\mathrm{cm}\ (L) \times 25\,\mathrm{cm}\ (H)$

based Embedded SAR Controller; (iii) Motion Sensor; (iv) Embedded SAR Processor; (v) Data Recorder and (vi) Antenna System. Each of these assemblies can be further divided into subassemblies and components. The block diagram of the sensor is shown in Figure 1.

All the UAVSAR system except the SAR antenna system and GPS antenna will be sat inside the UAV compartment. The SAR platform has been identified as the Aludra MK1 from Unmanned System Technology (UST), Malaysia. Figure 2 shows the image of Aludra MK1 platform. Figure 3 shows the

An housing has been redesigned and constructed to host all the unit in a limited working space for ease of accessing and maintenance of various sub-module of SAR system. Figure 3 shows the latest UAVSAR sensor. Figure 4 shows the microstrip antenna system employed in our UAVSAR system. In order to further reduce the hardware used in this system, a high performance FPGA board has been selected to perform the task of Chirp Generator, Timing and Control Unit, and Data Recorder where as the embedded SAR processor is implemented by a high performance single board computer.

3. FIELD MEASUREMENT

The latest field measurement has been successfully conducted at Mersing, Malaysia on July 2012 with primary objective is to verify the performance of new UAVSAR system. 6 flight measurements were successfully conducted during this flight mission. A total of about 339 sets of SAR raw data were collected. Figure 5 shows one of the samples of SAR images captured during the flight mission.

Figure 2: UAV employed in flight mission.

Figure 3: SAR sensor.

Figure 4: Antenna system.

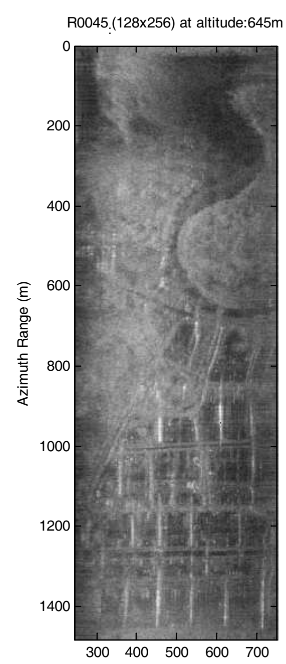

Figure 5: Example of SAR image generated.

4. CONCLUSION

The performance of newly designed and developed UAVSAR system has been verified in the recent flight test conducted in Mersing, Malaysia. A total of about 339 sets of SAR raw data were collected and the processed SAR images verified the capability of real time SAR processor. The achieved SAR images resolution is $3\,\mathrm{m} \times 3\,\mathrm{m}$ and clear signature of the earth terrain can be clearly observed.

ACKNOWLEDGMENT

This project is funded by Ministry of Science, Technology and Innovation, Malaysia.

REFERENCES

1. Curlander, J. C. and R. N. McDonough, *Synthetic Aperture Radar: System and Signal Processing*, A Wiley Interscience Publication, 1991.
2. Wiley, C. A., "Synthetic aperture radar — A paradigm for technology evolution," *IEEE Trans. Aerosp. Electron. Syst.*, Vol. 21, 440–443, 1985.
3. Ausherman, D. A., A. Kozma, J. L. Walkeretal, H. M. Jones, and E. C. Poggio, "Developments in radar imaging," *IEEE Trans. on Aerospace and Electronic Systems*, Vol. 20, No. 4, 363–440, 1984.
4. Chan, Y. K. and V. C. Koo, "The design and development of unmanned aerial vehicle synthetic aperture radar," *PIERS Proceedings*, 1236–1239, Suzhou, China, Sep. 12–16, 2011.

Development of an Integrated Velocity Compensation Timing and Control Unit for SAR

Huey Shen Boey, **Tien Sze Lim**, **Chua Ming Yam**, **and Voon Chet Koo**
Faculty of Engineering and Technology, Multimedia University
Jalan Ayer Keroh Lama, Melaka 75450, Malaysia

Abstract— This paper discusses the design and development of a Field Programmable Gate Array (FPGA) based integrated velocity compensation Timing and Control Unit (TCU) for high resolution Unmanned Aerial Vehicle (UAV) Synthetic Aperture Radar (SAR). The drift in instantaneous velocity has been an issue for SAR since the very beginning. These instabilities in azimuth parameters causes blurring and distortion of the final radar image. The aim of this advance TCU is to supply accurate and consistent signals to all needed modules of SAR while compensates for the instantaneous velocity error caused by the platform UAV.

1. INTRODUCTION

A Synthetic Aperture Radar (SAR) is a form of active remote sensing. It is an airborne or space-borne radar that utilizes its flight path along a synthetic length to simulate an extremely large antenna. SAR is usually preferred over its optical counterpart because SAR imaging is not affected by bad weather conditions and have a constant image resolution regardless of platform altitude in oppose to graphic imaging that is height dependent.

In the coverage of this research, a TCU is defined as a unit that commands and directs signals to trigger other devices or systems while manage and regulate the timing synchronization of those devices or systems. SAR uses the TCU as a signal generator for its transmitting signal and every other switching and triggering signal that is needed. This transmitting signal is also named the chirp signal and it contains a distinct waveform that easily recognizable to the receiver from the backscattered wave. The TCU will be in charge of supplying the chirp generator with the appropriate timings to house the chirp signal.

One of the main issues faced by SAR systems is the instability of the moving platform, which in this case is the UAV. Of all known motion errors, one motion error that has a direct relation to the timing parameters of SAR is the error in instantaneous carrier velocity as shown in Figure 1. This error causes image blur and is a major concern in SAR imaging. This issue is one of the main motivations in designing a TCU that is not only capable of supplying accurate signals to required modules, it is also capable of compensating for the error caused by instability in instantaneous velocity of the aircraft.

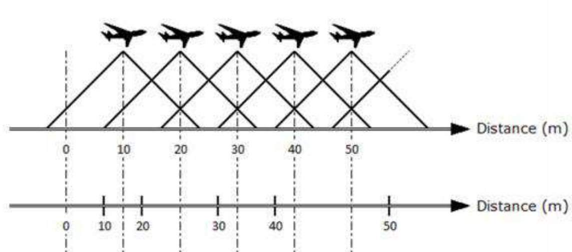

Figure 1: Comparison of ideal case UAV with real case scenario.

2. SAR TIMING SYSTEM

SAR is a coherent radar system; therefore its timing system has to be coherent and stable as well. This basically constitutes that digital pulse to pulse of the pulse train has to be coherent and in phase with one another. The concept of SAR is to calculate the distance of a particular target from the antenna. The distance of a target is given by:

$$R = \frac{c\Delta t}{2} \tag{1}$$

The factor of 1/2 in the equation denotes the time taken for the wave to travel to and back from the target. This is crucial in the calculation of the Pulse Repetitive Frequency (PRF) as shown in Figure 2.

The PRF is the frequency that the SAR transmits it chirp pulse train. The Pulse Repetitive Interval (PRI) is the interval in between each transmitting pulses and can be obtained from the inverse of the PRF. The chirp signal is embedded into the transmitting pulse which is denoted by τ in Figure 2. Backscattered signal will be received by the system and processed to produce the final SAR image.

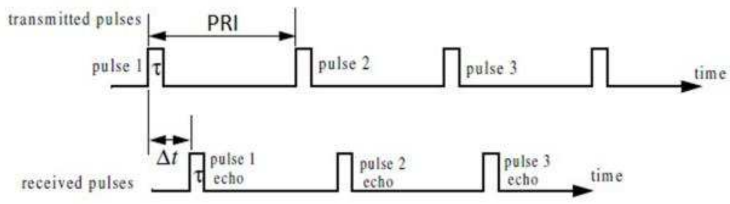

Figure 2: Basic pulses of SAR.

3. UNIT DESCRIPTION

The first function of the TCU is to supply accurate and consistent signals to required modules of SAR. Our SAR TCU is designed to fit with the requirements of the in-house SAR system. The TCU will be developed with FPGA using Altera's Development and Education Board 3 (DE3). FPGA is the choice platform as it has highly flexible programming capabilities making the TCU to be designed by virtually limitless approach and enables rapid prototyping. Furthermore it supports multiple programming languages such as Verilog, VHDL, Schematics and AHDL. The parameters that will be used by this TCU are as shown in Table 1.

Table 1: In-house digital SAR controller parameters.

Parameters	Value
Pulse Repetitive Frequency, PRF	640 Hz
Pulse Repetitive Interval, PRI	1.5625 ms
Pulse Length, τ	10 µs
STALO Frequency	10 MHz

Fundamentally, the TCU is designed using counters. The counters will self-increment until a particular state before resetting itself. Using this as the base, it is enhanced to self-update its counter status to generate at any particular PRI that is desired. This technique is described in Figure 3.

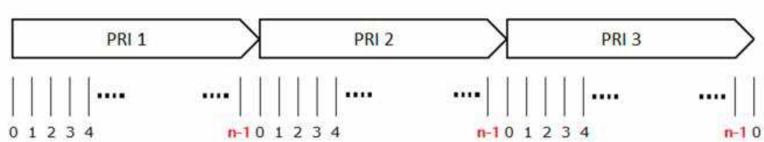

Figure 3: Generation of counter based PRI.

To compensate with the velocity error caused by the UAV, a motion compensation technique is implemented by adjusting the parameter of the TCU. This module is called the Velocity Error Compensator (VEC). The basic concept of implementing the VEC is to understand its relation to the geological sample spacing of each transmitting pulse as described below,

$$\Delta u = \frac{V}{PRF} \tag{2}$$

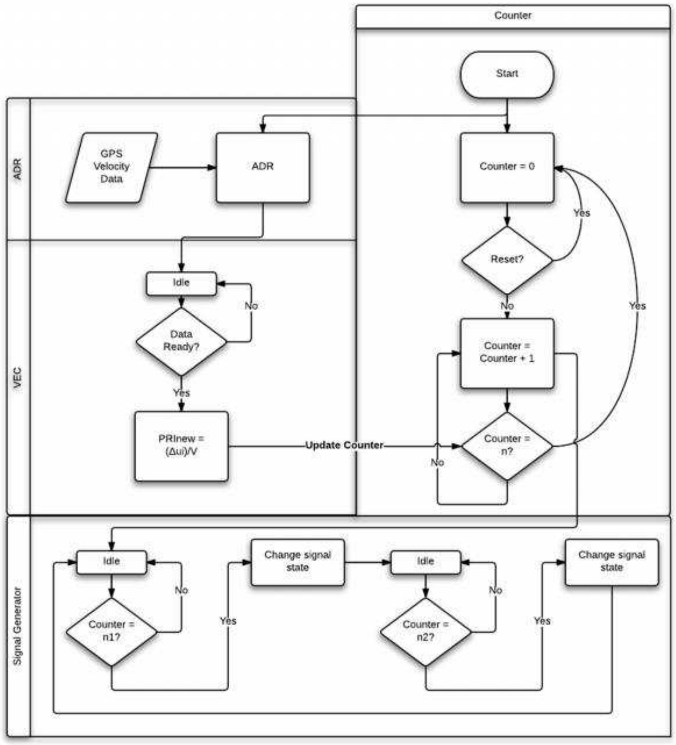

Figure 4: Block diagram of integrated velocity compensation timing and control unit.

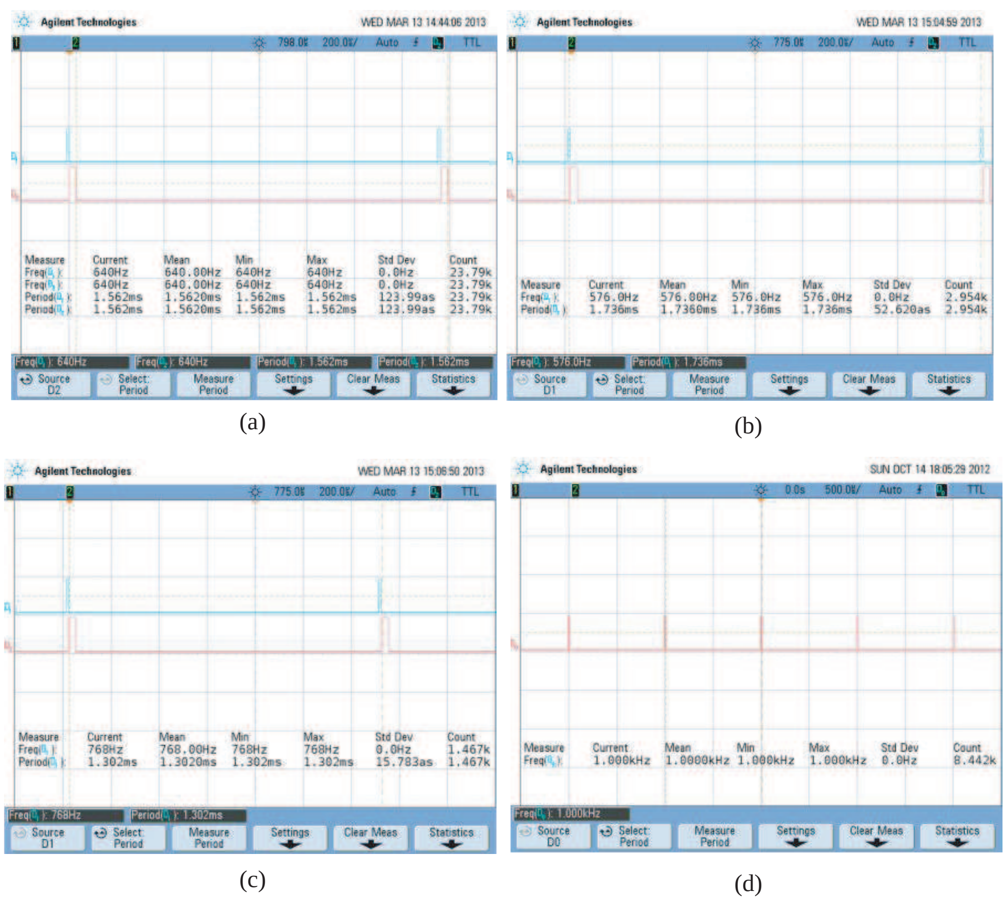

(a) (b) (c) (d)

Figure 5: (a) PRF at 30 m/s. (b) PRF at 27 m/s. (c) PRF at 36 m/s. (d) PRF at 50 m/s.

Ideally, to obtain a sharp and perfect SAR output image, the sample space is constant throughout the whole beam strip. However, it is understood that no platform is capable to move at a constant speed without error. Therefore, to reverse the error caused by the platform, an equal sampling space can be obtained by changing the PRF accordingly to accommodate for the instantaneous velocity changes. Taking into account the PRI which is primary used for the generation of the PRF, a new equation can be derived as,

$$PRF = \frac{\Delta u_i}{V} \tag{3}$$

By utilizing this concept, the PRF can be adjusted to accommodate with the velocity difference while maintaining the geological sample space in between each transmitting pulse. The block diagram of this advance TCU is as show in Figure 4.

4. RESULTS

A testbench is developed to test out the reliability and accuracy of the new advance TCU. The simulated testbench is set to have a UAV velocity of 30 m/s. To check for consistency, velocity errors are introduced (ranging from −10%, +20% and +67%) to the TCU and the output PRF is monitored. Collected data is compared to the calculated equivalent for verification. Figures 5(a) to (d) show the difference in frequency for velocity of 30 m/s, 27 m/s, 36 m/s and 50 m/s respectively.

5. CONCLUSION

An advance TCU is capable of supplying signals and compensate for instantaneous velocity error cause by the UAV. From the results of the testbench, it can be concluded that the advance TCU delivers accurate and consistent PRF while addresses the instantaneous velocity error by implementing proven error correction methods.

REFERENCES

1. Koo, V. C., Y. K. Chan, G. Vetharatnam, M. Y. Chua, C. H. Lim, C. S. Lim, C. C. Thum, T. S. Lim, Z. Bin Ahmad, K. A. Mahmood, M. H. Bin Shahid, C. Y. Ang, W. Q. Tan, P. N. Tan, K. S. Yee, W. G. Cheaw, H. S. Boey, A. L. Choo, and B. C. Sew, "A new unmanned aerial vehicle synthetic aperture radar for environmental monitoring," *Progress In Electromagnetics Research*, Vol. 122, 245–268, 2012.
2. Boey, H. S., T. Z. Lim, V. C. Koo, and W. L. Kung, "Development of a high precision timing and control unit for synthetic aperture radar," *2011 IEEE International RF and Microwave Conference*, 45–48, 2011.
3. Yeo, T. S., C. B. Zhang, Y. H. Lu, and T. Ren, "Development of a SAR digital system," *IEEE Aerospace and Electronic Systems Magazine*, 37–41, 1999.

Design and Development of a Sidelooking Microstrip Patch Antenna for Unmanned Aerial Vehicle Synthetic Aperture Antenna

Poi Ngee Tan, Yee Kit Chan, Tien Sze Lim, and Gobi Vetharatnam
Faculty of Engineering and Technology, Multimedia University
Jalan Ayer Keroh Lama, Bukit Beruang, Melaka 75450, Malaysia

Abstract— A microstrip patch antenna system with sidelooking characteristic is designed and developed for Unmanned Aerial Vehicle Synthetic Aperture Radar (UAVSAR). The Antenna Operates at C-band (5.3 GHz) with a minimum bandwidth requirement of 80 MHz. Several indoor measurements are performed to verify the performance of the developed microstrip patch antenna.

1. INTRODUCTION

Synthetic Aperture Radar (SAR) was first developed by Carl Wiley of Goodyear Corporation at early of 1950's and since then it has been developed rapidly all over the world [1]. Nowadays SAR has been utilized for various applications such as military observation, earth surface remote sensing, pollution monitoring [2] and etc.. Since SAR is an active sensor which generates its own sensing medium and in this case electromagnetic wave, hence it is able to operate regardless of the weather and lighting condition [3]. The electromagnetic signal can even penetrate through forest canopy, cloud and haze if the operating frequency is selected properly [4].

For airborne SAR application, the antenna size and weight is particularly restricted due to several issues such as: wind resistance, payload limitation and mounting space. The first SAR system adopts Yagi Uda Antenna with operating frequency of 900 MHz [4]. Slowly with the advancement of microwave technology the SAR operating frequency has been shifted to higher frequency region and microstrip patch antenna becomes the most popular choice of SAR antenna.

In year 2012, a probe fed microstrip patch dual antenna system has been developed for a C-band (5.3 GHz) Unmanned Aerial Vehicle Synthetic Aperture Radar (UAVSAR). The UAVSAR system adopts sidelooking stripmap scanning method with look angle of 24°. Table 1 shows the design specification of the UAVSAR antenna system.

Table 1: Design specifications of UAVSAR antenna.

Table Operating Mode	Stripmap
Operating Frequency	5.3 GHz
Azimuth Beamwidth	6°
Azimuth Look Angle	90°
Elevation Beamwidth	28°
Elevation Look Angle	24°
Polarization	VV

2. ANTENNA DEVELOPMENT

Microstrip square patch is adopted as the radiating element of UAVSAR antenna as it offers the ease of large array design and it can be modeled by transmission line modeling. The antenna consists of 3 layers where the top layer acts as radiating layer while the feeding network is located at the bottom layer and the middle layer acts as ground plane. The electromagnetic power is coupled from the feeding network to the radiating element via a copper probe which penetrates through the ground plane. Since the feeding network is located at the bottom layer therefore the spurious radiation from feeding network can be eliminated.

The elevation array consists of 6 radiating elements with $1/2\lambda$ spacing to form a radiation pattern with 24° look angle and beamwidth of 28°. Two 50 Ω feeding ports are assigned to distribute the electromagnetic signal to reduce power loss due to excessive long microstrip transmission line.

Microstrip T-junction power dividers are adopted in the feeding network to achieve desired excitation amplitude at each radiating elements.

The azimuth uniform linear array is formed by 12 array elements and a microstrip 3-way power divider is adopted to distribute the power equally to each of the array elements. A U-shaped microstrip feedline is integrated at the center output port of the 3-way power divider to achieve 0° phase difference at the radiating elements. The layout of microstrip 3-way power divider is shown in Figure 1. The azimuth array radiation pattern formed a pencil beam of 6° at broadside. Due to size limitation, the antenna panel is designed with additional pair of 'ear' to allocate the 3-way power divider and input connector. The transmit and receive antennas are allocated side by side with a total length of 1 meter as shown in Figure 2.

3. ANTENNA MEASUREMENT

The developed antennas are shown in Figure 3 where the antenna panels are installed side by side on aluminum casing where the 'ears' of antenna panels are covered by additional aluminum case. To eliminate the spurious radiation from the feeding network, a metal backplane is used to cover

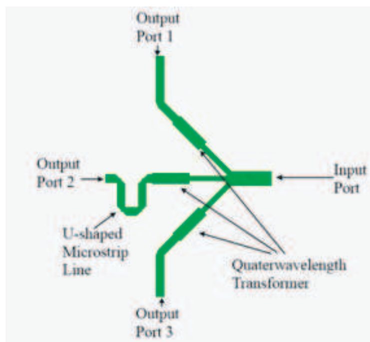

Figure 1: Layout of microstrip T-junction power divider.

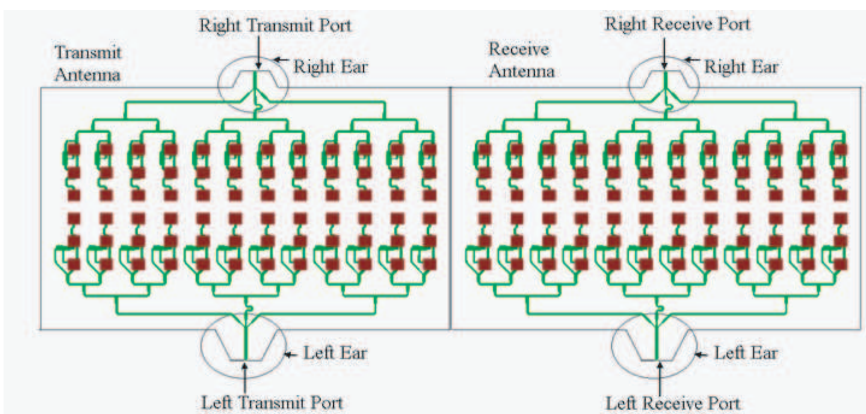

Figure 2: Top view of both transmit and receive antennas allocation.

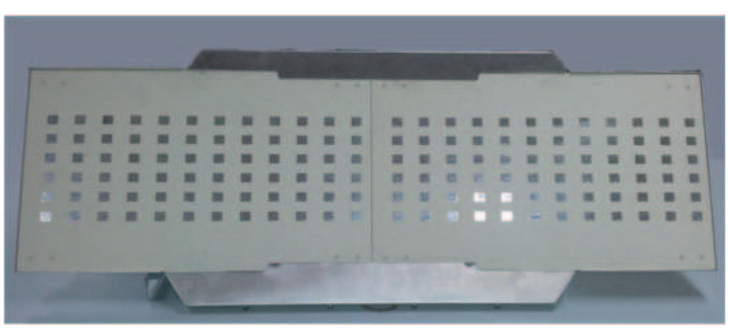

Figure 3: Top view of developed UAVSAR antenna with aluminum case.

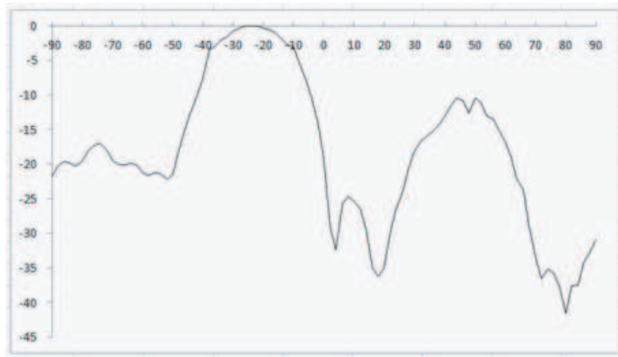

Figure 4: Measured radiation pattern of UAVSAR antenna.

the feeding network with a distance of $\lambda/4$. The total weight of the antenna is measured to be 4.66 kg including the aluminum case with total length of 1 meter and case thickness of 20 mm.

The return loss of the antenna at 5.3 GHz is measured to be -16.9 dB with operating bandwidth more than 80 MHz. The antenna radiation patterns are measured in anechoic chamber. Figure 4 shows the measured elevation radiation pattern of UAVSAR antenna beamwidth of 28° with main beam located at 24° off from nadir. The azimuth radiation pattern has a broadside look angle with beamwidth of 6°. The isolation of transmit and receive antenna is measured to be -41 dB at 5.3 GHz with antenna gain of 20.1 dB.

4. CONCLUSION

A C-band UAVSAR microstrip patch antenna has been designed and developed for UAVSAR application by using probe fed square patch. Both transmit and receive antennas are located side by side with high isolation between both antennas. Several indoor measurements are performed to confirm the performance of the developed UAVSAR antenna. The developed antenna is low profile, light weight and can be installed on UAV without additional tilting mechanism to perform UAVSAR flight measurement.

REFERENCES

1. Chan, Y. K. and S. Y. Lim, "Synthetic aperture radar (SAR) signal generation," *Progress In Electromagnetics Research B*, Vol. 1, 269–290, 2008.
2. Hovland, H. A., J. A. Johannessen, and G. Digranes, "Slick detection in SAR images," *Proceeding of the 1994 International Geoscience and Remote Sensing Symposium*, 2038–2040, 1994.
3. Berens, P., "Introduction to synthetic aperture radar," *Advanced Radar Signal and Data Processing*, 3-1–3-14, Educational Notes RTO-EN-SET-086, Paper 3, Neuilly-sur-Seine, France, 2006.
4. Chan, Y. K. and V. C. Koo, "An introduction to synthetic aperture radar (SAR)," *Progress In Electromagnetic Research B*, Vol. 2, 27–60, 2008.

High Speed AD DA for Synthetic Aperture Radar

Ming Yam Chua[1], **Voon Chet Koo**[1], **Heng Siong Lim**[1], **Huey Shen Boey**[1], **Yee Kit Chan**[1], **Chot Hun Lim**[1], **Tien Sze Lim**[1], **and Hean Teik Chuah**[2]

[1]Faculty of Engineering and Technology, Multimedia University, Malaysia
[2]University Tunku Abdul Rahman, Malaysia

Abstract— This paper discusses the design and development of High Speed (HS) Digital-to-Analog (DA) and Analog-to-Digital (AD) hardware. Both the modules are used in radar application, where HS-DA moduleis used to synthesize radar baseband waveform while the HS-AD module is used for baseband SAR signal digitization. In terms of total data throughput rate, HS-AD and HS-DA modulesaredesign with capabilityto deliverup to 500 MSPS and 420 MSPS total throughput rate, respectively. Both the modules are designed to interface with Altera Field Programmable Gate Array (FPGA) evaluation board through its High Speed Mezzanine Card (HSMC) interface. In prototyping, both the modules were fabricated on 4-layers FR4 Printed Circuit Board (PCB) substrate. A series of in lab measurement were conducted to verify the performance of both hardware modules.

1. INTRODUCTION

Multimedia University Malaysia has developed an Unmanned Aerial Vehicle based C-band Synthetic Aperture Radar (UAVSAR) in collaboration with Agency of Remote Sensing Malaysia (ARSM). The sensor was mounted on an Unmanned Aerial Vehicle (UAV) and used for monitoring and management of earth resources such as paddy fields, oil palm plantation and soil surface in future. The system operates in C-band (5.3 GHz) with 80 MHz of chirp bandwidth with configurable pulse duration of 0.5, 1, 2, 3, 4, 5, 8 and 10 µs.

Baseband SAR processor is essential in the SAR system. It is multi-functional which operates as abaseband signal synthesizer anda signal digitizer. As a signal synthesizer, it synthesis the required baseband waveform and timing signals, whereas a signal digitizer, it digitize the down-converted backscattered signal and perform front-end pre-processing. Figure 1 depicts the block diagram for the baseband SAR processor.

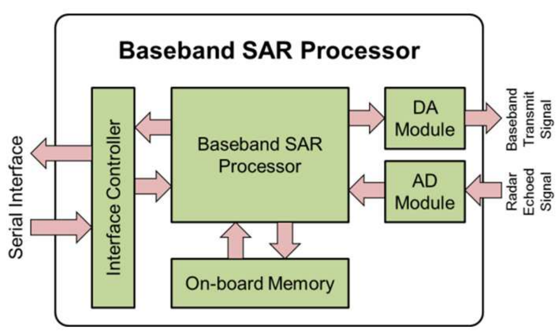

Figure 1: Block diagram of a baseband SAR processor.

The baseband SAR processor is built on an Altera DE3 FPGA development board. It supports interface to Personal Computer (PC) through Gigabit Ethernet transceiver with a High Speed Mezannine Connector (HSMC) interface. DA module synthesizes the baseband radar signal for Radio Frequency section while AD module digitizes the down-converted radar return signal and temporarily stored in on-board memory. Pre-processing is done in the baseband SAR processor. This paper will discuss the development work of the DA and AD module of the baseband SAR processor.

2. DA AND AD MODULES DESIGN

In typical pulse compression radar, range resolution is given as,

$$\Delta R = \frac{c\tau}{2} = \frac{c}{2B} \tag{1}$$

It is essential to increase the transmitted signal bandwidth so that better range resolution could be achieved [2]. The bottleneck in the current system configuration is the throughput rate of the DA and AD module. In order to increase the throughput rate of the DA and AD module, new modules are designed and fabricated as market readily solution does not exist.

The technical specifications of the modules are as listed in Table 1. In the DA module, two 14-bit AD9744 DACs are used with sampling rate of 210 MSPS. As for the AD module, two 12-bit LTC2242-12 ADCs are used, capable of digitize analog signal at 250 MSPS. Both the boards were compatible to interface with Altera HSMC interface.

For PCB stack-up, 4-layer stack-up configuration is being employed. All high speed clock and data traces were impedance controlled at $\sim 50\,\Omega$. The boards were prototyped on FR4 substrate with dielectric constant (ε_r) of 4.6.

Table 1: Specifications and PCB stack-up for HS-DA and HS-AD module.

Specifications		
DA module	Sampling rate	210 MSPS
	Resolution	14-bit
	Number of channel	2
	Interface to main board	Altera HSMC
AD module	Sampling rate	210 MSPS
	Resolution	12-bit
	Number of channel	2
	Interface to main board	Altera HSMC
PCB Stack-up	Layer	4
	Impedance control	$\sim 50\,\Omega$
	Substrate	FR4 $\varepsilon_r = 4.6$

3. PROTOTYPING WITH HIGH SPEED PCB CONSIDERATION

The designs were converted to PCB realization with various high speed PCB considerations. Impedance for all high speed traces were kept at $50\,\Omega$ for impedance matching. The board adopts separate analog and digital ground to reduce noise coupling from noisy digital circuit to analog circuit. For functionality testing prototype, both the boards were prototype on FR4 board.

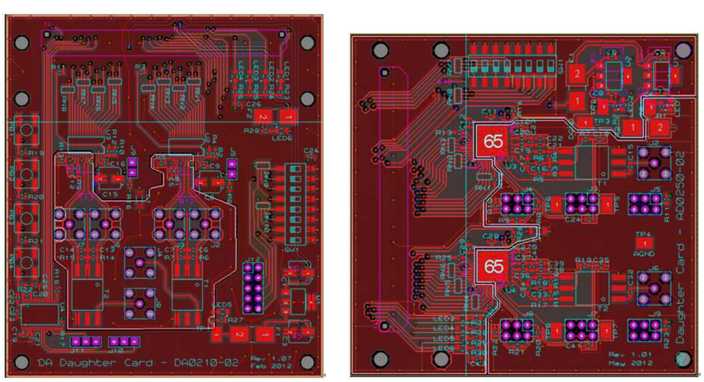

(a) (b)

Figure 2: PCB Layout. (a) HS-DA, (b) HS-AD.

4. PERFORMANCE EVALUATION

TWO tests were conducted for performance evaluation. In the first test, a signal synthesizer is built and the data pattern generated by the synthesizer is used to drive the HS-DA module [3, 4]. Figure 4 depicts the block diagram of the signal synthesizer.

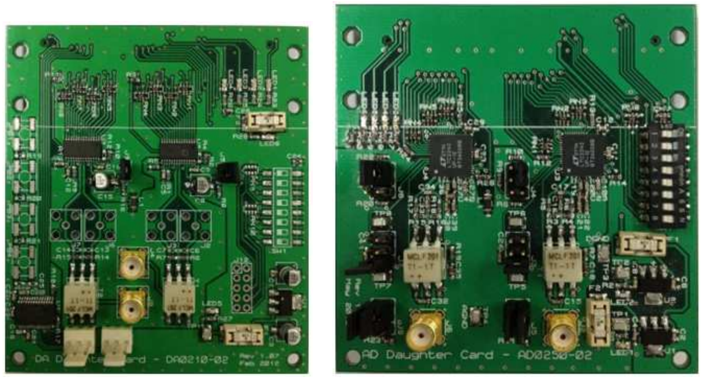

(a) (b)

Figure 3: Assembled prototype board. (a) HS-DA, (b) HS-AD.

The signal synthesizer was configured to generate a Linear Frequency Modulate (LFM) signal with frequency sweep from −100 MHz to −100 MHz (total bandwidth of 200 MHz). The baseband LFM signal were up-converted to 5.3 GHz using Quadrature Modulator (SSM0208MC2MDQ from Miteq). Figure 5(a) shows the recorded baseband signal in time domain while Figure 5(b) shows the spectrum of the up-converted signal. From the spectrum of the up-converted signal, it shows a total bandwidth of 200 MHz generated by the DA module.

For AD module evaluation, a loop back test wascarried out. The setup of the evaluation is shown in Figure 6. A function generator is used to generate a high frequency signal and fed into

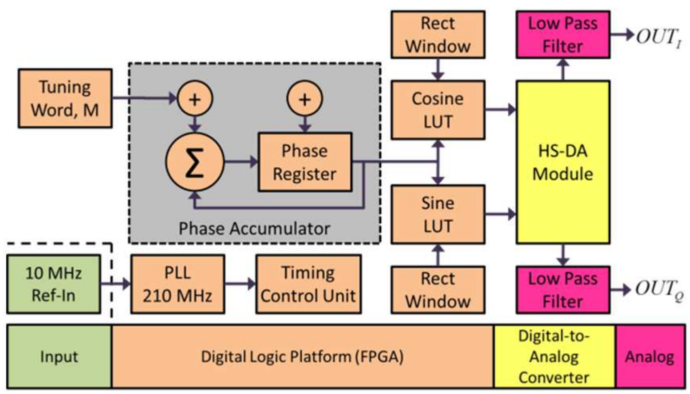

Figure 4: Block diagram of the signal synthesizer.

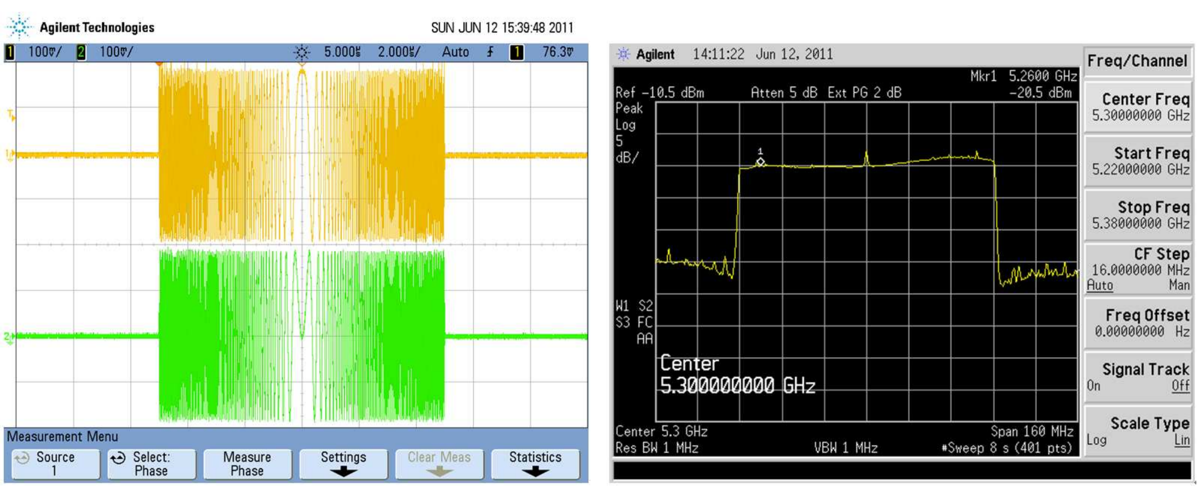

(a) (b)

Figure 5: (a) Baseband LFM signal in time domain. (b) Spectrum of the Up-converted signal.

the AD module. The clock required by the AD and DA module (200 MHz) wassupplied by the FPGA. Data captured by the AD module at every clock cycle were directly loop back to the data lines for the DA module. The output of the DA module was observed using an oscilloscope. The signal observed on the oscilloscope shows that the AD module is capable of digitizing the analog signal at 200 MSPS.

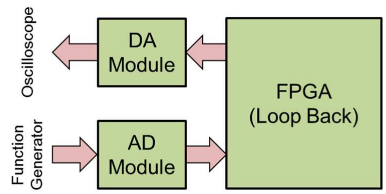

Figure 6: Loop back test for AD module evaluation.

5. CONCLUSION

This paper shows the development work for a HS-DA and HS-AD module developed for a baseband SAR processor. The results obtained from the performance evaluation shows that both the modules are functioning well.

ACKNOWLEDGMENT

The work is funded by Malaysian TM R&D research grant.

REFERENCES

1. Koo, V. C., Y. K. Chan, V. Gobi, M. Y. Chua, C. H. Lim, C. S. Lim, C. C. Thum, T. S. Lim, Z. Ahmad, K. A. Mahmood, M. H. Shahid, C. Y. Ang, W. Q. Tan, P. N. Tan, K. S. Yee, W. G. Cheaw, H. S. Boey, A. L. Choo, and B. C. Sew, "A new unmanned aerial vehicle synthetic aperture radar for environmental monitoring," *Progress In Electromagnetics Research*, Vol. 122, 245–268, 2012.
2. Chan, Y. K. and V. C. Koo, "An introduction to synthetic aperture radar (SAR)," *Progress In Electromagnetics Research B*, Vol. 2, 27–60, 2008.
3. Chua, M. Y. and V. C. Koo, "FPGA-based chirp generator for high resolution UAV SAR," *Progress In Electromagnetics Research*, Vol. 99, 71–88, 2009.
4. Chua, M. Y., H. S. Boey, C. H. Lim, V. C. Koo, H. S. Lim, Y. K. Chan, and T. S. Lim, "A miniature real-time re-configurable radar waveform synthesizer for UAV based radar," *Progress In Electromagnetics Research C*, Vol. 31, 169–183, 2012.

Realization of Interpolation-free Fast SAR Range-Doppler Algorithm Using Parallel Processing on GPU

Ozgur Altun[1], **Selcuk Paker**[2], **and Mesut Kartal**[2]

[1]Informatics Institue, Satellite Communication and Remote Sensing, Istanbul Technical University, Turkey
[2]Electrical and Electronic Engineering, Istanbul Technical University, Turkey

Abstract— In this work, a new interpolation-free fast Range-Doppler (RD) Synthetic Aperture Radar (SAR) algorithm has been developed using parallel processing on Graphical Processing Unit (GPU). Our main aim is increasing the performance of the RCMC step of RDA algorithm. Interpolation is the most used algorithm in order to realize RCMC process. But, the 2-D complex valued interpolation on RCMC step produces some computation errors and also needs extra processing because of the ambiguous search operations. In our work, we have developed Parallel-Discrete Fourier Transform (P-DFT) algorithm as an alternative to interpolation. We have performed P-DFT and Inverse Fast Fourier Transform on GPU respectively to get rid of the interpolation process. We have implemented interpolation and P-DFT algorithm in parallel on both CPU and GPU. Our tests show us the proposed algorithm provide us fast and more accurate results while processing RCMC step.

1. INTRODUCTION

Synthetic Aperture Radar (SAR) is a kind of high-resolution radar which can be applied widely in remote sensing and to acquire information about the Earth's surface from radar signals gathered by a moving platform such as an aircraft [1, 2]. Almost all SAR systems are designed to produce high-resolution images by synthesizing of the data obtained from moving platform. Because of the complex form of the radar signal and intensive floating-point operations, producing high-resolution requires more computations times.

Generally, real time processing of SAR images can be performed on Digital Signal Processor (DSP) and Field Programmable Gate Array (FPGA) systems. Due to difficulties of programming and debugging processes on DSP and FPGA other programming environment options should be considered [3]. For this reason, applications of SAR processing have been performed on the other processing environments such as CPU and GPU platforms. One of novel technique for SAR image processing is using Graphical Processing Unit (GPU) to obtain the high computation rate.

Many algorithms have been developed to process SAR images. In the SAR processing literature Range-Doppler, Chirp Scaling [4], Omega-K [1], SPECAN [1] and Extended Exact Transform Function (EETF) [5] and Frequency Scaling [6] are the most used algorithms. Due to the intensive computation, these algorithms require costly high performance computers. For this reason, GPU's are used to decrease the development environment costs and accelerate the all operation. The previous works on SAR processing algorithm by using GPU can be found in [7–9].

In this paper a new interpolation-free Range-Doppler Algorithm (RDA) is performed to process SAR raw data and acquire image. The main steps of RDA are range compression, transformation to Range-Doppler domain, Range Cell Migration Correction (RCMC), azimuth compression and transformation to spatial domain. All steps except for RCMC consist of Fourier and filter operations. Therefore, these are suitable for parallelization. Since RCMC process requires an appropriate search algorithm, it has a disadvantage of computational cost. In the SAR processing literature, many algorithms have been developed to process data in the RCMC step. However, developing an algorithm to process high amount of data in the RCMC step is an open problem and many researchers continue to study on. One of the possible ways to realization of RCMC process is the interpolation on Range-Doppler domain. But, interpolation based methods produce calculation error while processing data. As the migrated points can be calculated analytical, Discrete Fourier Transform (DFT) operation can be applied to get rid of interpolation process. In our works, we have performed Parallel-Discrete Fourier Transform (P-DFT) and Inverse Fast Fourier Transform (IFFT) operations respectively on the GPU instead of interpolation operation in order to decrease the calculation errors on the resultant image.

2. METHODOLOGY

We proposed an interpolation-free fast Range-Doppler SAR algorithm using parallel processing on the GPU. As we mentioned before, SAR raw data consist of huge amount of data. While processing RCMC step in the RDA, the data needs correction operation to regulate the position of the point in the processed data. Generally, interpolation based methods are used to realization of this process. The 2-D complex valued interpolation on RCMC step produces some computation errors and also needs extra processing because of ambiguous search operation. Although this computational requirement could be realized by using parallel processing, interpolation error would still remain on the results. To minimize these errors, DFT technique can be applied at the expense of additional computation cost. In our work, P-DFT and IFFT algorithms are used in RCMC step instead of classical interpolation algorithm. Usage of classical algorithms parallelization is not proper on CPU because of its small number of processing units and mathematical operation rate as compared with GPU. Implementation of the P-DFT algorithm on GPU also provides us fast implementation of processing step. On the other hand, all steps of RDA are transformed to simple multiplication operations to get rid of search operation in the interpolation. This allows us to increase the degree of parallelism. The block diagram of our proposed method are illustrated in Figure 1. To show the advantage of proposed method, we apply the P-DFT algorithm to a synthetic data obtained from a point scatterer model.

2.1. Range Cell Migration Correction

As known, synthetic aperture radars scan areas by use of propagation of signals and collect backscattered signals while the platform is moving. Due to the platform movement relative to the investigated area, the respected range changes with time [1]. This effect is named as Range Cell Migration (RCM). To put backscattered and migrated data in order, Range Cell Migration Correction (RCMC) operation should be applied to the data. RCMC is the key process to determine the performance of the RDA. Most common studies use interpolation to realize RCMC process.

2.2. RCMC Implementation with Classical Interpolation

In general case, the RCMC step of RDA uses nearest n neighbor interpolation method to regulate the position of the points in the radar image.

Classical interpolation process is used to determine desired number of nearest points according to selected reference point in the whole data. To do this, all data should be scanned and corresponding points must be determined. After that, average of the point values must be calculated to update the reference point with this calculation result. Similar process must be performed for all chosen data respectively. Therefore, mentioned method takes very long time. On the other hand, the interpolation operation results with calculation errors because of the pointwise convergence.

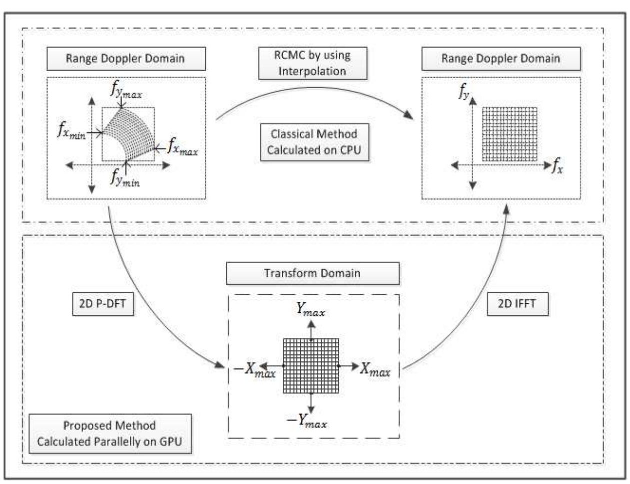

Figure 1: Block diagram of proposed method.

2.3. RCMC Implementation with P-DFT

In our study we proposed applying parallel DFT and IFFT operations respectively to realize RCMC process. Our aim is to minimize the calculation error and to reduce the processing time while performing RCMC process. To achieve this aim, GPU is used for computation and parallelization of DFT.

In order to apply P-DFT, we should regulate the position of points in the range doppler domain to use them in the transfer domain because of irregular distribution of the points. The size of the regularized data is equal to $N_{Range} \times N_{Azimuth}$. After the regulation process of point positions, we can use the position values as defined in Eq. (1). (see the block diagram of the proposed method, Figure 1)

$$X[i] = -X_{\max} + (i-1)\Delta X \qquad Y[i] = -Y_{\max} + (i-1)\Delta Y \tag{1}$$

where ΔX and ΔY are the distance between the positions of points in the transfer domain and can be calculated with Eq. (2).

$$\Delta X = \frac{2X_{\max}}{N_{Range}-1} \qquad \Delta Y = \frac{2Y_{\max}}{N_{Azimuth}-1} \tag{2}$$

In the Eq. (2) $X_{\max}$ and $Y_{\max}$ represent the maximum values in both X and Y axis in the transfer domain. These values can be calculated with Eq. (3).

$$X_{\max} = \frac{1}{2\Delta\hat{f}_x} \qquad Y_{\max} = \frac{1}{2\Delta\hat{f}_y} \tag{3}$$

where $\Delta\hat{f}_x$ and $\Delta\hat{f}_y$ represent the regular distances and can be calculated with Eq. (4).

$$\Delta\hat{f}_x = \frac{f_{x\max} - f_{x\min}}{N_{Range}-1} \qquad \Delta\hat{f}_y = \frac{f_{y\max} - f_{y\min}}{N_{Azimuth}-1} \tag{4}$$

After obtaining the regularized data in the transform domain, one can obtain the corrected data by simply applying the IFFT process.

3. GPU ARHITECTURE

One of the main purposes for processing of intensive data is to compute the result as fast as possible. To make real this purpose many technological advances have been developed. GPU is the one of the technology which has widely usage area in processing intensive data. In the GPU computing, CPU and GPU are used together in a heterogeneous co-processing computing model. In general, sequential operations are processed on CPU and parallel processing of data and acceleration are processed on GPU. To develop an application on the GPU several programming language have been produced. In our work, The Compute Unified Device Architecture (CUDA) [7] programming interface produced by NVDIA are used for developing application to perform our proposed algorithm on the GPU. CUDA programming interface is integrated into C programming language and called as CUDA C.

In the GPU Computing Architecture, programs are processed in host or kernel side. In the GPU computing concept, an operation processed on the CPU is called as host process. On the other hand each operation processed on the GPU is called as kernel process. The operation, which is desired to process on the GPU, is triggered by a host side operation. Due to the distinct memory structure between CPU and GPU, all of required data have to be copied from host process to the GPU device memory before execution of kernel operation. Also, results which are obtained after the execution of the kernel process have to be copied from GPU to host memory. The kernel operation is executed simultaneously by using many threads in parallel.

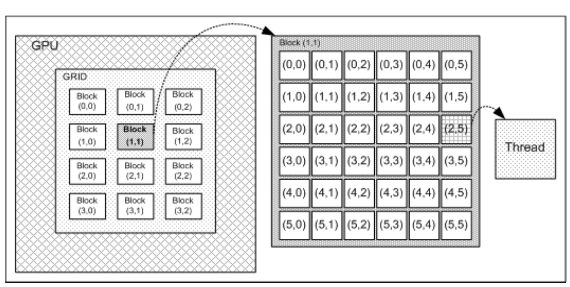

Figure 2: GPU grid, block and thread structure.

A GPU device includes grid, block and thread to parallelization of any operation. Each grids are managed by performed kernel. Each block is included by grid and all threads are operated within blocks. Figure 2 illustrates the grid, block and thread structure in the GPU. Before the execution of a kernel, block size and thread size have to be set up. This usage provides us $block\_size \times thread\_size$ threads in the kernel. This architecture also provides us optimization in parallel operations. On the other hand, processing mathematical operation rate is faster than CPU's rate. Especially array operation can be performed very fast and easily on the GPU. These advantages enabled us both fast and parallel processing on the huge amount of data.

4. EXPERIMENTAL RESULTS

In this paper, we have developed an algorithm to perform the RCMC process in parallel. We have performed parallel DFT operation on GPU to get rid of the intensive load of interpolation process. We have tested our algorithm on both CPU and GPU platform with using same parameters. Also, we have performed RCMC process by using nearest n neighbor interpolation method. All tests have been done with using three point scatter. To measure the performance of this our algorithm, we have used different size of input data and obtained performing times. All tests have been performed on the test environment as shown in Table 1.

Table 1: Test environment.

CPU	Intel Core i7-3820
CPU Frequency	3.6 GHz
CPU Cache	10 MB
Instruction Set	64-bit
RAM	64 GB
GPU	NVIDIA Tesla C2075
CUDA Cores	448
GPU Memory	6 GB GDDR5
GPU Memory Bandwidth	144 GB/sec
Operating System	64-bit Windows 7 Professional

To show the performance of this study, interpolation and P-DFT algorithms are processed on both CPU and GPU in parallel and results are obtained in seconds. We have used Open Message Passing Interface (OMPI) to parallelize interpolation and DFT algorithms on CPU. On the other hand, CUDA is used to process interpolation and DFT algorithm on GPU in parallel. We have used two types of data size to show the performance of algorithms. In our first experiment, we have set the data size $N_{range} = 128$ and $N_{azimuth} = 64$ to perform algorithms. After that, we have changed N_{range} and $N_{azimuth}$ as 1024 and 512 and all tests have been repeated respectively.

Table 2 shows us, P-DFT algorithm processing time is better than the interpolation. Also, we can clearly see that GPU produces results much faster than CPU. On the other hand, we can clearly determine that the processing time is growing considerably while the data size is increasing due to the complexity of these algorithms.

Table 2: Performance comparison between P-DFT and Interpolation.

	Interpolation		P-DFT Algorithm	
Data Size	CPU	GPU	CPU	GPU
128×64	7.05 s	4.46 s	3.28 s	3.20 s
1024×512	28719.00 s	1621.12 s	13267.59 s	1173.12 s

The acquired images after processing of RDA can be seen in Figure 3. The data size is selected as 128×64 to generate the illustrated images. The left image on the left shows us the result of RDA with using P-DFT and the other shows us the result of RDA with using interpolation while performing RCMC step. In Figure 3(b), calculation errors can be seen clearly on the image provided by using interpolation while performing RCMC step. However, we can see fast decay of echoes on the range and azimuth axis on Figure 3(a). Also, the point scatters have been seen clearly on the image provided by using P-DFT algorithm. In order to obtain the quality of the images, we have used only one scatter and we acquire almost same Peak Side Lobe Ratio (PSLR) value in range axis as $-13.00\,\mathrm{dB}$. Also, we determine that interpolation can produce inaccurate results if azimuth and range resolution are different.

Figure 3: Acquired images via P-DFT and Interpolation. (a) P-DFT results on GPU. (b) Interpolation results on GPU.

5. CONCLUSION

In this paper, we have presented a new interpolation-free Range-Doppler Algorithm (RDA) to process SAR data on GPU. We have focused on processing RCMC step while performing RDA algorithm. In this paper, we have developed P-DFT algorithm instead of interpolation. In order to compare the performance of P-DFT algorithm, nearest n neighbor interpolation method have been performed in parallel. All tests have been done on both GPU and CPU by using synthetic data obtained from a point scatterer model. Obtained results show us, performing P-DFT algorithm is faster than the interpolation. On the other hand, the obtained results provided by P-DFT are more accurate than the interpolation. The results also show us processing on GPU improves the performance of the algorithm. We have tested our algorithm with using two types of data size. Our results show us, the processing time is growing considerably while the data size is increasing. We can clearly determine that performing P-DFT algorithm on GPU is more suitable in order to process SAR data fast and get more accurate results.

REFERENCES

1. Cumming, I. G. and F. H. C. Wong, *Digital Processing Of Synthetic Aperture Radar Data: Algorithms And Implementation*, Ser. The Artech House Remote Sensing Library, Artech House, 2005.
2. Hartley, T. D. R., A. R. Fasih, C. A. Berdanier, F. Ozguner, and U. V. Catalyurek, "Investigating the use of GPU-accelerated nodes for SAR image formation," *IEEE International Conference on Cluster Computing and Workshops*, 1–8, 2009.
3. Peng, X., Y. Wang, W. Tan, W. Hong, and Y. Wu, "GPU acceleration of 3D SAR imaging using range migration techniques," *3rd International Asia-Pacific Conference on Synthetic Aperture Radar, APSAR*, 1–4, 2011.
4. Raney, R. K., H. Runge, R. Bamler, I. G. Cumming, and F. H. Wong, "Precision SAR processing using chirp scaling," *IEEE Transactions on Geoscience and Remote Sensing*, 786–799, 1994.
5. Eldhuset, K., "A new fourth-order processing algorithm for spaceborne SAR," *IEEE Transactions on Aerospace and Electronic Systems*, Vol. 34, No. 3, 824–835, July 1998.
6. Mittermayer, J., A. Moreira, and O. Loffeld, "Spotlight SAR data processing using the frequency scaling algorithm," *IEEE Transactions on Geoscience and Remote Sensing*, Vol. 37, No. 5, 2198–2214, September 1999.
7. Liu, B., K. Wang, X. Liu, and W. Yu, "An efficient SAR processor based on GPU via cuda," 1–5, Oct. 2009.
8. Zhao, S. and R. Wang, "A GPU based range-doppler algorithm for SAR imaging in opencl," 224–227, Oct. 2011.
9. Ning, X., C. Yeh, B. Zhou, W. Gao, and J. Yang, "Multiple-GPU accelerated range-doppler algorithm for synthetic aperture radar imaging," 698–701, May 2011.
10. NVIDIA CUDA: Compute Unified Device Architecture Programming Guide, NVIDIA Corporation, 2008.

Performance Analysis of DPCA Based SAR Moving Target Detection

Han Gao, **Jingwen Li**, **and Li Zhang**
School of Electronics and Information Engineering, Beihang University, China

Abstract— This paper analyzes the performance of SAR moving target detection based on displaced phase centre antenna (DPCA) method theoretically. The statistical models of multi-looked DPCA metric are established under hypotheses interference (stationary clutter plus noise) only case and the case moving target superimposed upon the interference. The probability density function (PDF) under interference only hypothesis is modified, compared with results from [1]. Under the alternative hypothesis, to represent more practical cases, several models of the metric dependent on the backscattering type and spatial dimension of the moving target are discussed [2], and corresponding PDFs ground on these models are derived in closed-form. The derived PDFs provide means to quantify the limits of performance and examine the capabilities of detection, which plays a significant role in system parameter design and algorithm selection.

1. INTRODUCTION

Synthetic Aperture Radar (SAR) is an advanced instrument to achieve ground scene imaging, not affected by weather, daytime and etc. Meanwhile, it also shows a lot of potential on moving target detection, which plays a significant role in martial threat and traffic control. To quantify the limits of performance and examine the capabilities of detection, performance analysis of SAR moving target detection is demanded. Motivated by this demand, the performance of DPCA based SAR moving target detection is theoretically analyzed in this paper, considering the effectiveness and widely usage of DPCA method. As multi-look process is commonly used for sparkle noise reduction after DPCA, it is taken into consideration as well, which increases the complexity but also practicability of the analysis.

It is found that the performance of detection is determined by the PDF of multi-looked DPCA metric [3]. Therefore, it is crucial for performance analysis to investigate on the PDFs under different statistical models. The statistical models of multi-looked DPCA metric are established under hypotheses interference only case and the case moving target superimposed upon the interference. Firstly, the PDF under interference only hypothesis is given, which modifies the results from [1]. Under the alternative hypothesis, to represent more practical cases, several models of the metric dependent on the backscattering type (deterministic or random target signal) and spatial dimension (compared to the multi-look resolution cell size) of the moving target are discussed [2], and corresponding PDFs ground on these models are derived in closed-form. Based on these PDFs, the dependences of the probability of detection (Pd) on SCR are investigated to illustrate the performance.

The rest of paper is organized as follow. The concept of DPCA based SAR moving target detection approach is briefly presented in Section 2. The statistical models of multi-looked DPCA metric are set up under both hypotheses in Section 3, with derivation of corresponding PDFs in closed-form. The measures of quality are depicted in Section 4, to illustrate the performance limits. Finally, the conclusion and the future work are given in Section 5.

2. CONCEPT

As a commonly used method, DPCA exploits the power difference for clutter suppression to achieve SAR moving target detection. Without loss of generalization, the dual-channel SAR system is considered in this paper. The two antennas are generally aligned along the direction of motion vector, so that each observes the scene from the same spatial position but at different times. The prescription for DPCA is to subtract the two data channels and apply some norm, the magnitude squared. Ideally, the signals from stationary clutter are suppressed to the noise floor of the radar, and only signals from moving targets with sufficient radial velocity remain [4]. Assuming that the two channels are co-registered by a time shift, the mathematical expression of DPCA metric is

$$M_{DPCA} = |z_1(k) - z_2(k)|^2 \tag{1}$$

To reduce the speckle, clutter suppressed data are frequently multi-look processed. This technique is achieved by calculating the average of n-look samples, assuming that the n-look samples are statistically independent. The mathematical expression of multi-processed DPCA metric is given as Equation (2), where n is the number of looks and k denotes the k-th one-look sample.

$$\bar{M}_{DPCA} = \frac{1}{n}\sum_{k=1}^{n} |z_1(k) - z_2(k)|^2 \tag{2}$$

3. STATISTICAL MODELS

Let Z_1 and Z_2 represent the two SAR complex images respectively, C_1 and C_2 the clutter signals, N_1 and N_2 the thermal noises, and S_1 and S_2 the SAR images of the moving target. The remainder of this paper assumes two channels have been co-registered, and signals can be modeled as follows:

$$\begin{aligned} Z_1 &= \begin{cases} C_1 + N_1 + S_1 & \text{target superimposed upon interference} \\ C_1 + N_1 & \text{interference only} \end{cases} \\ Z_2 &= \begin{cases} C_2 + N_2 + S_2 & \text{target superimposed upon interference} \\ C_2 + N_2 & \text{interference only} \end{cases} \end{aligned} \tag{3}$$

In the remainder of the paper, let σ^2denotes the variance, ρ the coherence, and the subscript of them indicates the discussed signal type.

3.1. Interference

Under homogeneous model assumption, $\mathbf{C} = [C_1, C_2]^T$can be modeled as a multivariate complex Gaussian random vector [6], where T denotes the transpose operator. N_1 and N_2 can be modeled as two additive (to the clutter) zero mean Gaussian complex processes independent of each other, and independent on the clutter. Assume that the power balance is achieved by channel balance which can be found in the literature [5]. Under interference only hypothesis, let $P = C + N$, the multi-looked DPCA metric is expressed as

$$\bar{M}_{DPCA} = \frac{1}{n}\sum_{k=1}^{n} |Z_1(k) - Z_2(k)|^2 = \frac{1}{n}\sum_{k=1}^{n}\left[(\mathrm{Re}\,(P_1(k) - P_2(k)))^2 + (\mathrm{Im}\,(P_1(k) - P_2(k)))^2\right] \tag{4}$$

As a linear function of a chi-square distributed variable, the PDF of $\bar{M}_{DPCA}$ is

$$f_{\bar{M}_{DPCA}}(m) = \left(\frac{n}{2\delta^2}\right)^n \cdot \left(\frac{m^{n-1}}{\Gamma(n)}\right) \cdot \exp\left(-\frac{nm}{2\delta^2}\right) \tag{5}$$

where $\delta^2 = (\sigma_c^2 + \sigma_n^2)(1 - \frac{\sigma_c^2}{\sigma_c^2+\sigma_n^2}\rho_c \cos\varphi)$. As ground clutter considered here, assume $\varphi = 0$.

3.2. Target

3.2.1. Deterministic Target Model

Let $\mathbf{S} = \beta[1 \;\; e^{j\theta}]^T$ denotes the target. β is the magnitude determined by RCS and θ is the difference of Doppler phases between two channels. Without loss of generality, the Doppler phase of S_1 is set to zero. Under this deterministic model assumption, the multi-looked DPCA metric is expressed as

$$\begin{aligned} \bar{M}_{DPCA} &= \frac{1}{n}\sum_{k=1}^{n} |Z_1(k) - Z_2(k)|^2 \\ &= \frac{1}{n}\sum_{k=1}^{n}\left[(\mathrm{Re}(P_1(k) - P_2(k)) + \beta(k)(1 - \cos\theta(k)))^2 + (\mathrm{Im}(P_1(k) - P_2(k)) - \beta(k)\sin\theta(k))^2\right] \end{aligned} \tag{6}$$

As a linear function of a non-central chi-square distributed variable, the PDF of $\bar{M}_{DPCA}$ is

$$f_{\bar{M}_{DPCA}}(m) = \frac{1}{2}\left(\frac{nm}{\lambda\delta^2}\right)^{\frac{n-1}{2}} \cdot \left(\frac{n}{\delta^2}\right) \cdot \exp\left\{-\frac{\lambda + nm/\delta^2}{2}\right\} \cdot I_{n-1}\left(\sqrt{\frac{nm\lambda}{\delta^2}}\right) \tag{7}$$

where $\lambda = \frac{2}{\delta^2}\sum\limits_{k=1}^{n} (\beta(k))^2 (1 - \cos(\theta(k)))$ is noncentrality parameter.

3.2.2. Gaussian Target Model

In practice, for target consisting of several scattering centres within a multi-look cell, it is evitable that the amplitudes fluctuate with the look of angle. For a more precisely modeling, the Gaussian target model is used, which assumes that the target fluctuates with the slow time [3]. Unlike the case of deterministic target model, the format of PDF is dependent on the target size, which will be discussed after.

Let $\mathbf{S} = [\,S_1 \;\; S_2\,]$ denotes the target. It is generally assumed that $\rho_s = \rho_c$, ignoring time de-correlation [2]. $\mathbf{S}$ satisfies multi-variable Gaussian distribution, with covariance matrix

$$\mathbf{K}_S = \beta^2 \begin{bmatrix} 1 & \rho_s e^{j\theta} \\ \rho_s e^{-j\theta} & 1 \end{bmatrix} \tag{8}$$

For a ideal case that the dimension of moving target is on the order of the multi-look cell size, the multi-looked DPCA metric is

$$\begin{aligned} \bar{M}_{DPCA} &= \frac{1}{n}\sum_{k=1}^{n} |Z_1(k) - Z_2(k)|^2 \\ &= \frac{1}{n}\sum_{k=1}^{n}\Big[(\mathrm{Re}(P_1(k) - P_2(k) + S_1(k) - S_2(k)))^2 + (\mathrm{Im}(P_1(k) - P_2(k) + S_1(k) - S_2(k)))^2\Big] \end{aligned} \tag{9}$$

with PDF of $\bar{M}_{DPCA}$ being

$$f_{\bar{M}_{DPCA}}(m) = \left(\frac{n}{2\delta^2}\right)^n \cdot \left(\frac{m^{n-1}}{\Gamma(n)}\right) \cdot \exp\left(-\frac{nm}{2\delta^2}\right) \tag{10}$$

When the target occupies L cells, smaller than n, the model in Equation (10) should be reformed as

$$\begin{aligned} \bar{M}_{DPCA} &= \frac{1}{n}\sum_{k=1}^{n} |Z_1(k) - Z_2(k)|^2 \\ &= \frac{1}{n}\sum_{k=1}^{L}\Big[(\mathrm{Re}(P_1(k) - P_2(k) + S_1(k) - S_2(k)))^2 + (\mathrm{Im}(P_1(k) - P_2(k) + S_1(k) - S_2(k)))^2\Big] \\ &\quad + \frac{1}{n}\sum_{k=L+1}^{n}\Big[(\mathrm{Re}(P_1(k) - P_2(k)))^2 + (\mathrm{Im}(P_1(k) - P_2(k))^2\Big] \end{aligned} \tag{11}$$

The PDF of $\bar{M}_{DPCA}$ is expressed in an integral which can only be approximated by numerical integration.

$$f_{\bar{M}_{DPCA}}(m) = \frac{\frac{n}{2\delta_2^2} \cdot \exp\left\{-nm/2\delta_2^2\right\}}{\Gamma(L)\Gamma(n-L)} \int_0^{\frac{nm}{2\delta_1^2}} x^{L-1} \cdot \left(\frac{nm}{2\delta_2^2} - \frac{\delta_1^2}{\delta_2^2}x\right)^{n-L-1} \cdot \exp\left\{-\frac{nm}{2\delta_2^2}\right\} dx$$

where $\delta_2^2 = \delta^2$, $\delta_1^2 = \delta_2^2 + \sigma_s^2\,(1 - \rho_s \cos\theta)$.

4. PERMORMANCE

Setting the probability of false alarm $P_{fa} = 10^{-5}$, $\rho_c = 0.95$, $\theta = 1.3\,\mathrm{rad}$, Figure 1 depicts the Pd versus SCR under deterministic target model. (a), (b) is when target size is on the order of the multi-look cell size, and (c), (d) is when target size is smaller with L being the target dimension. It is shown that under deterministic target model the expectation of metric is related to the target's amplitudes and Doppler phases within multi-look cells. However, the spatial size (compared with the multi-look cell size), will only change the noncentrality parameter, which will affect the expectation and variance slightly, but not the format and shape of PDF. Affected by the length limits, results under Gaussian target model are not presented, but they could easily be computed based on corresponding PDFs. It is shown that under Gaussian target model the spatial size is crucial, which will change the format and shape of PDF at all.

It is demonstrated from the simulation that the performance will benefit from an appropriate number of looks, and multi-look cell size close to target spatial size improve the performance most.

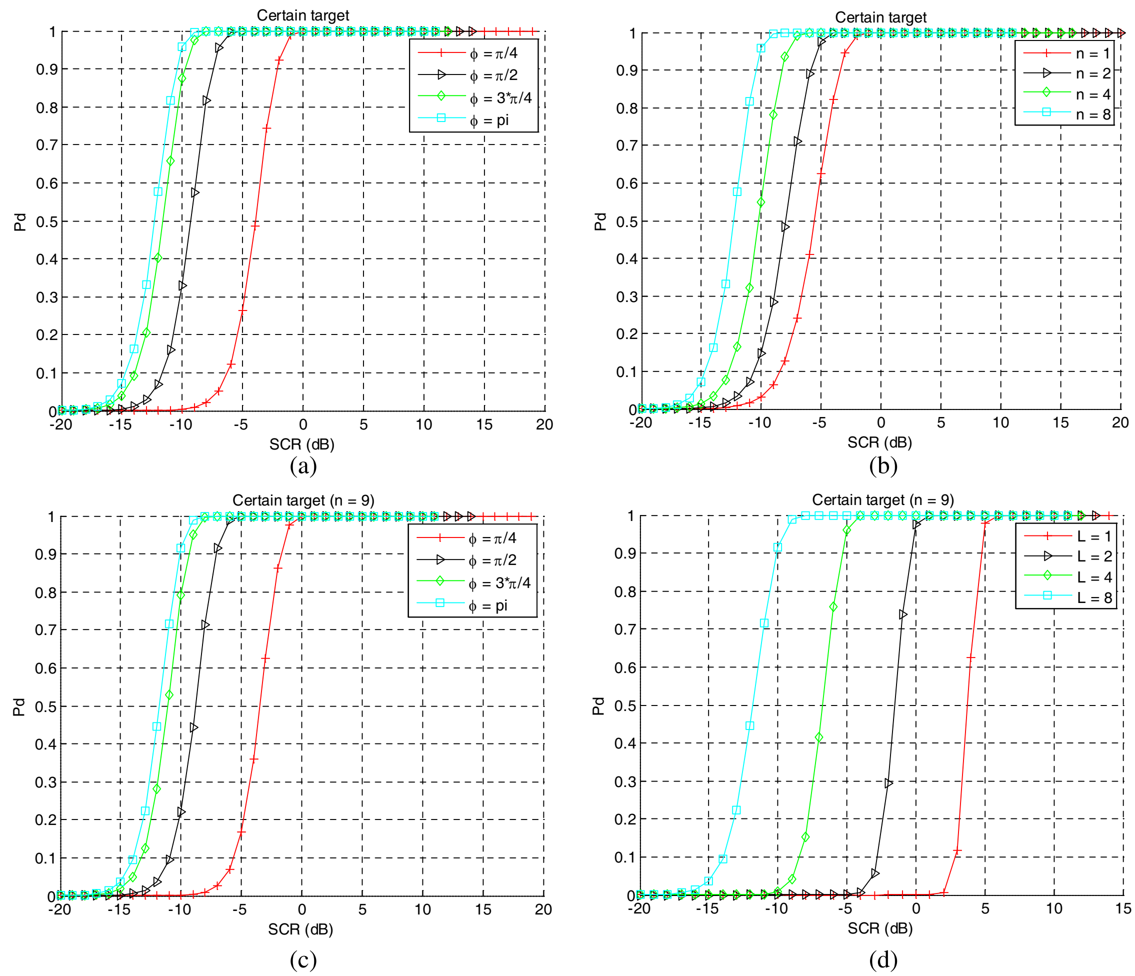

Figure 1: Pd versus SCR for varying Doppler phases and number of look.

5. CONCLUSIONS

In this paper, performance of DPCA based SAR moving target detection is analyzed theoretically. To achieve this, statistical models of multi-looked DPCA metric, under interference only and target superimposed upon interference hypotheses, are established. Especially, the backscattering type and spatial size of target are also considered to establish statistical models. Based on these models, dependence of Pd on SCR is obtained to illustrate the performance of detection, which will play a significant role in system parameter design and algorithm selection. Future work will be focused on optimizing the multi-look number to improve performance, with prior knowledge on the size of interested target.

REFERENCES

1. Liu, C. F., G. S. Liao, and C. Zeng, "Canonical framework for ATI and DPCA," *Proceedings of International Conference on Wireless Communication, Networking and Mobile Computing*, 714–717, September 2007.
2. Gierull, C. H., "Moving target detection with along-track SAR interferometry," Technical Report TR 2002-084, Defence Research and Development Canada (DRDC), August 2002.
3. Gierull, C. H., "Statistical analysis of multilook SAR interferograms for CFAR detection of ground moving targets," *IEEE Trans. Geosci. Remote Sensing*, Vol. 42, No. 4, 691–701, April 2004.
4. Sikanet, I. C., "A Detection of ground moving objects with synthetic aperture radar," Thesis, University of Ottawa, Ottawa, Canada, 2004.
5. Gierull, C. H., "Digital channel balancing of along-track interferometric SAR data," Technical Meomorandum TM 2003-024, Defence Research Eastablishment Ottawa (DREO), March 2003.
6. Chiu, S. and C. Liveingstone, "A comparison of displaced phase centre antenna and along-track interfermetry techniques for radarsat-2 ground moving target indication," *Can J. Remote Sensing*, Vol. 31, No. 1, 37–51, 2005.

Microstrip Slot Antenna for Mobile Base Station

Mohamed S. El-Gendy, Haythem H. Abdullah, and Esmat A. Abdallah
Electronics Research Institute, Dokki, Giza, Egypt

Abstract— A multi-band dual-polarized microstrip slot antenna for mobile base stations is proposed. The antenna is operating at the bands of GSM900 (0.87–0.96) GHz, DCS1800, PCS1900, and UMTS2100 (1.71–2.17) GHz used in mobile base stations. It is fabricated using the low cost FR4 dielectric substrate. The antenna is based on two orthogonal diamond cross slots etched on the ground plane and incorporates a two orthogonal microstrip feeding lines placed underneath the FR4 substrate material on the opposite side of the ground plane to achieve dual polarization. The measured isolation characteristics for the proposed antenna between the two ports do not exceed −30 dB within the operating bands. The front-to-back ratio is greater than 17 dB at GSM900, 20 dB at both DCS1800 and PCS1900 and 14 dB at UMTS2100. Average antenna gains about 7.9 dBi and 7.1 dBi have been obtained for lower and upper bands, respectively. The design is dedicated to the single array element which will be incorporated in an array in order to construct the base station antenna.

1. INTRODUCTION

In modern mobile base stations communication systems, operators require much larger bandwidths or dual frequency behavior due to capacity problems in the conventional base station transceiver systems such as GSM900 band. Because of this fact, much work has been devoted to increase the bandwidth or to obtain dual frequency characteristics of the microstrip antennas. An additional licenses for multi-bands operating frequency such as DCS1800 (Digital Cellular system), PCS1900 (Personal Communications Service) and UMTS2100 (Universal mobile Telecommunication system) are used to overcome these problems. Also, dual feed transceiver systems are facing the problem of poor isolation between the transmitting and the receiving ports. One of the most important parameter is the front-to-back ratio (FBR) which is almost achieved on one band and deteriorates on the other.

Very few designs with dual-band dual-polarized operations have been reported for application in mobile communication systems. The reported design in [1] demonstrates a dual band dual polarized patch antenna, the first band covers GSM900 and the second band covers DCS1800, PCS1900 and UMTS2100. The radiating element is double-sided notch patches that can resonate in the operating bands. The antenna provides two orthogonal linear polarizations with isolation of 30 dB between the ports for each of these bands. The antenna dimension is about $290 \times 220 \times 21.8\,\text{mm}^3$. The gain of this antenna is about 11.8 dBi and 7 dBi for lower and upper bands, respectively.

Caso et al. [2] introduces a dual-polarized wideband stacked patches fed through a slot-coupling technique [3], where two stacked resonant patch are coupled to the feeding line through a square ring slot. The antenna operates in the GSM1800-1900 band (1710–1910 MHz), UMTS2100 band (1920–2170 MHz), ISM band (2400–2484 MHz), and UMTS 3G band (2500–2690 MHz). The antenna element is placed in an array of 2×1 with 22 dB isolation between ports in the whole frequency band of interest. So, that the antenna has slightly poor isolation between the two operating ports. The antenna array gain is between 8 dBi and 11 dBi in the entire band of interest.

The antenna in [4] operates in two separate frequency bands, including 820–960 MHz and 1710–2170 MHz, which cover CDMA, GSM900, PCS1900, and UMTS2100. The design is an array consists of six elements with two larger patches for the lower band and four smaller patches for the upper band. Each patch element is excited from the side by two orthogonal L-shaped probes, for $\pm 45^\circ$ polarizations. A novel combination technique to achieve the optimization of both the element geometry and array layout of multiband BTS array antennas has been introduced in [5].

In this paper, a multi-band dual-polarized microstrip slot antenna for mobile base stations is proposed for the new generations of mobile phone communications. The antenna is suitable for transmitting and receiving operations at the operating bands of GSM900 (0.87–0.96) GHz, GSM1800, PCS1900, and UMTS2100 (1.71–2.17) GHz in mobile phone base stations. The measured isolation characteristics do not exceed −30 dB. The front-to-back ratio is about 17 dB at GSM850/GSM900, 24 dB at both GSM1800 and PCS1900 and 14.6 dB at UMTS2100. The overall antenna dimension is about $300 \times 300 \times 73.175\,\text{mm}^3$. The proposed antenna has simple structure, and low cost due to the use of FR4 substrate layers in comparison with similar designs done in this area. Anther advantage of the proposed antenna is the use of only one port for each polarization feed at all three frequency bands and utilizing a total of only two feeding ports.

2. ANTENNA DESIGN AND CONFIGURATION

The geometry of the proposed microstrip slot antenna is shown in Fig. 1. The proposed antenna is composed of multi layers of substrates. To reduce the cost of antenna fabrication and makes it more rigid in construction, FR4 substrates are utilized. The overall antenna dimensions are about $300 \times 300 \times 73.175\,\text{mm}^3$. The dimensions of the ground plane with the cross slot are $140 \times 140\,\text{mm}^2$. As seen from Fig. 1, the antenna consists of six layers; 4 FR4 dielectric layers with dielectric constant $\varepsilon_r = 4.5$ and dielectric thickness 1.5 mm. Two air/foam layers ($\varepsilon_r = 1$). One foam layer is placed between the receiving feed layer and the FR4 dielectric substrate layer of the first. The second foam layer is placed between the first reflector and the FR4 dielectric substrate of the second reflector. In order to achieve dual polarized operation, the etched cross slots on the ground plane is placed between two orthogonal microstrip feed layers. The transmitting/receiving feed layer consists of an input microstrip line with $50\,\Omega$ width branched to two $100\,\Omega$ microstrip lines look like U-shape that excite the radiating slot symmetrically. Since the two feeding network layers are separately isolated so, no air bridge may be used. The radiation layer consists of two diamond cross slots etched on the metallic ground plane. The choice of the diamond shape slot is to match the required bands used in mobile base station. The most important parameter is the front to back ratio which is almost achieved on one band and deteriorates on the other. The problem of the front-to-back ratio is solved by placing two reflectors underneath the radiating slot. The first square reflector of side length $0.6\lambda_{0U}$ is placed at $\lambda_{0U}/4$ apart from the radiating slot at 1800 MHz (λ_{0U} is the wavelength at the upper frequency band). The second square reflector of side length $0.9\lambda_{0L}$ is placed at $\lambda_{0L}/4$ apart from the radiating slot at 900 MHz (λ_{0L} is the wavelength at the lower frequency band).

The antenna dimensions shown in Fig. 1 are: $W_{50\,\Omega} = 2.82\,\text{mm}$, $W_{100\,\Omega} = 0.64\,\text{mm}$, $L_{S1} = L_{S2} = 107\,\text{mm}$, $W_{S1} = W_{S2} = 11\,\text{mm}$, $L_G = W_G = 110\,\text{mm}$, $S_{mw1} = S_{mw2} = 18\,\text{mm}$, $L_s = 35\,\text{mm}$, $L_p = W_p = 99\,\text{mm}$, $h_1 = h_2 = h_4 = h_6 = 1.5\,\text{mm}$, $\varepsilon_{r1} = \varepsilon_{r2} = \varepsilon_{r4} = \varepsilon_{r6} = 4.5$, $h_3 = 35\,\text{mm}$, $h_5 = 32\,\text{mm}$, $\varepsilon_{r3} = \varepsilon_{r5} = 1$.

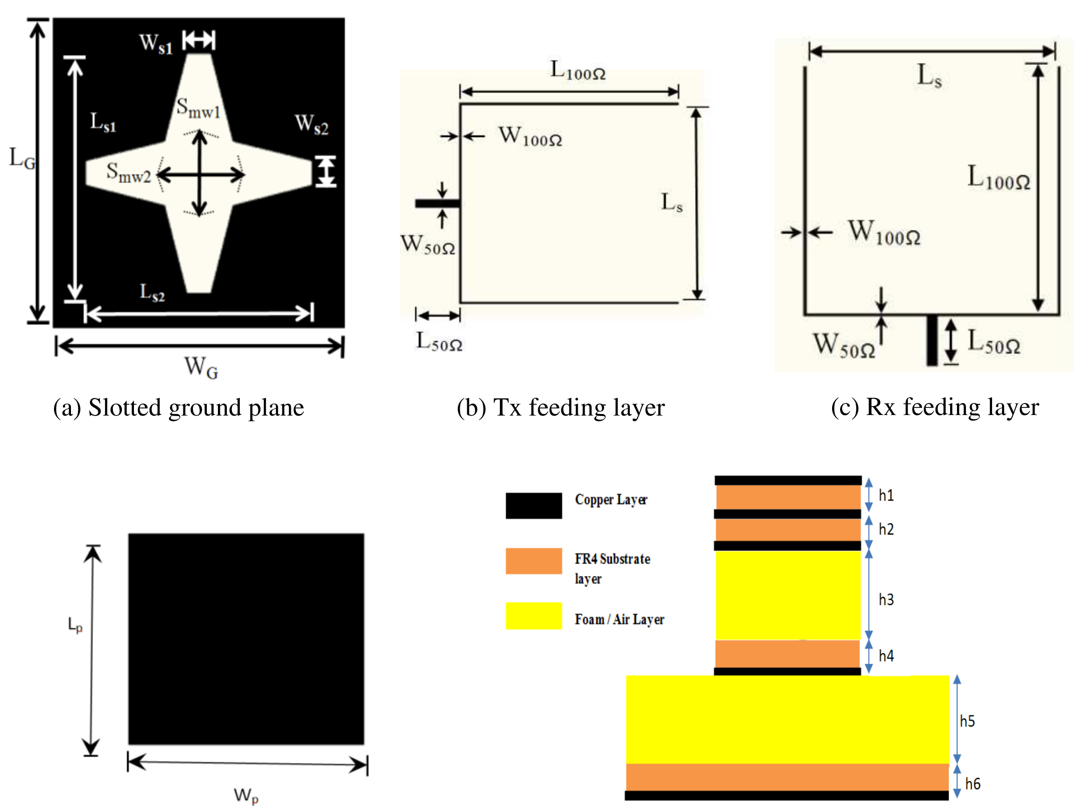

(a) Slotted ground plane (b) Tx feeding layer (c) Rx feeding layer
(d) First reflector (e) Side view

Figure 1: Antenna layers and its side view.

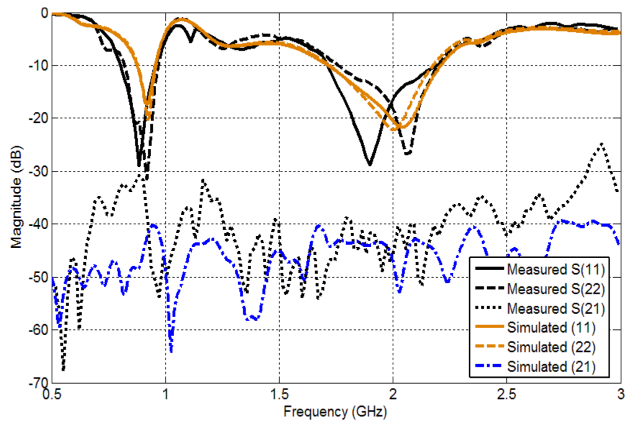

Figure 2: Measured and simulated results of return loss and insertion loss for the two ports.

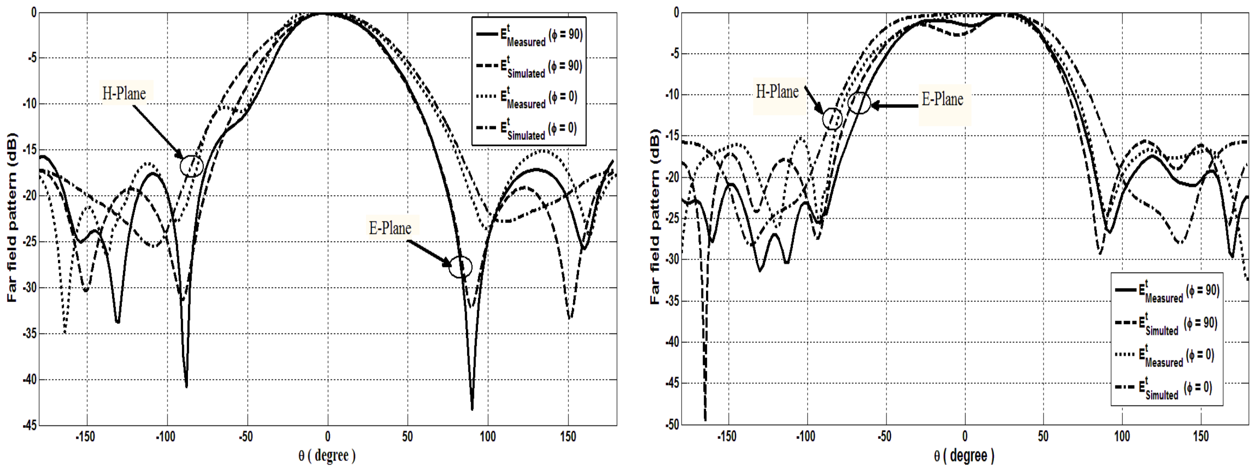

(a) (b)

Figure 3: Measured and simulated radiation pattern (E-plane and H-plane) at: (a) 925 MHz, (b) 1940 MHz.

3. RESULTS AND DISCUSSIONS

A prototype of the single element antenna with optimized dimensions has been simulated using CST STUDIO SUITE ver. 2012 and then fabricated. Fig. 2 depicts the simulated return loss for both Tx/Rx sides and the simulated isolation characteristics between the two ports compared to the measured results.

As shown in Fig. 2, the measurement results of the proposed antenna cover the GSM850, GSM900, GSM1800, PCS1900, and UMTS2100 bands at both ports. The antenna is measured using vector network analyzer Agilent: 8719ES. The measured results in Fig. 2 show 160 MHz -10 dB impedance bandwidth (VSWR $\leq$2) at both GSM850 and GSM900 while it shows 523 MHz -10 dB impedance bandwidth (VSWR $\leq$ 2) for GSM1800, PCS1900 and the UMTS2100. The measured isolation between the two ports is better than 30 dB at lower band (GSM850/GSM900) and is better than 40 dB at the upper bands (DCS1800, PCS1900 and the UMTS2100). Front-to-back ratio (FBR) is an important parameter for the antenna used in base stations. The front-to-back Ratio at the lower band (GSM850/GSM900) is about 17 dB and its range over the upper band varies from 14.6 dB to 24 dB. The measured radiation pattern is compared with the simulated one at the two operating bands as shown in Fig. 3.

4. CONCLUSIONS

A prototype of the antenna element with optimized dimensions has been simulated using CST STUDIO SUITE ver. 2011 and fabricated using photolithographic process. The measured results of the proposed antenna cover the GSM850, GSM900, GSM1800, PCS1900, and UMTS2100 bands at both ports and have good agreement with the simulated one The measured isolation between the two ports is better than 30 dB at lower band and is better than 40 dB at the upper band. The radiation pattern is measured and compared to the simulated results where a good agreement is noticed at the lower and the upper bands.

ACKNOWLEDGMENT

This work is done under the contract between the National Telecom Regulatory Authority (NTRA), Ministry of Communications and Information Technology (MCIT), Egypt and the Electronics Research Institute (ERI), Ministry of Scientific Research, Egypt.

REFERENCES

1. Nikmehr, S. and K. Moradi, "Design and simulation of triple band GSM900/DCS1800/UMTS2100 MHz microstrip antenna for base station," *IEEE International Conf. on Communication Systems (ICCS)*, 113–116, 2010.
2. Caso, R., A. A. Serra, M. R. Pino, P. Nepa, and G. Manara, "A wideband slot-coupled stacked-patch array for wireless communications," *IEEE Antenna and Wireless Propagation Letters*, Vol. 9, 986–989, 2010.
3. Caso, R., A. A. Serra, M. Pino-Rodriguez, P. Nepa, and G. Manara, "A square ring slot feeding technique for dual-polarized patch antennas," *Proc. IEEE Antennas Propag. Soc. Int. Symp.*, 1–5, Charleston, SC, Jun. 2009.
4. Li, P. and K. M. Luk, "Novel wideband dual-frequency patch antenna array for dual-polarization operation," *Proceedings of the 2005 Asia-Pacific Microwave Conference*, Suzhou, Dec. 2005.
5. Starke, P. L. and G. G. Cook, "Optimized design of multi-band cellular base station antenna array for GSM and UMTS deployment," *IET Microwave, Antennas and Propagation*, Vol. 3, No. 2, 333–347, Mar. 2009.

Resonance Absorption in Multilayered Bi-gratings

Y. Okuno[1], **S. Bai**[1], **T. Suyama**[1], **Q. Zhao**[2], **and X. Xu**[3]

[1]Graduate School of Science and Technology, Kumamoto University, Kumamoto 860-8555, Japan
[2]School of Engineering, Kumamoto University, Kumamoto 860-8555, Japan
[3]School of Engineering, Kyushu Sangyo University, Fukuoka 813-0004, Japan

Abstract— We numerically solved the problem of plane-wave diffraction in multilayered doubly periodic gratings consisting of thin layers made of metal or dielectric. In solving the problem, we employed a computational technique based on modal expansion. Taking a sandwiched structure Vacuum/Ag/SiO_2/Ag/Vacuum for an example, we observed: (1) excitation of a SISP mode at the lit surface of the 1st Ag layer with strong field enhancement for thick enough Ag layer case; (2) excitation of coupled SPR modes (SRSP or LRSP) at each surface between vacuum and Ag layers with strong field enhancements for thin enough Ag layer cases no matter with the thickness of SiO_2 layers; (3) enhancements of field at surfaces between Ag and SiO_2 layers in some cases related with the thickness of SiO_2 layers. The coupled plasmon modes were resulted by the resonance waves excited on four surfaces in these cases.

1. INTRODUCTION

In our previous study we examined the excitation of coupled plasmon modes in a thin-film grating made of a metal [1]. When the metal is thick, e.g., more than ten times the skin depth, the plasmon can be excited on the lit surface alone. This is termed a single-interface surface plasmon (SISP). When the thickness is decreased, the plasmon can be seen also on the other surface of the film. The two plasmon waves interact each other to form two coupled plasmon modes called short-range and long-range surface plasmon (SRSP and LRSP) [2].

In the present research we consider a sandwiched structure: metal/dielectric/metal, which is interesting for the application in development of optical equipment for example improving sensitivity of clinical sensing.

2. FORMULATION AND METHOD OF SOLUTION

In this section, we first formulate the problem of diffraction by multilayered bi-gratings shown in Fig. 1(a). After formulating the problem, we state a method of solution based on a modal-expansion approach.

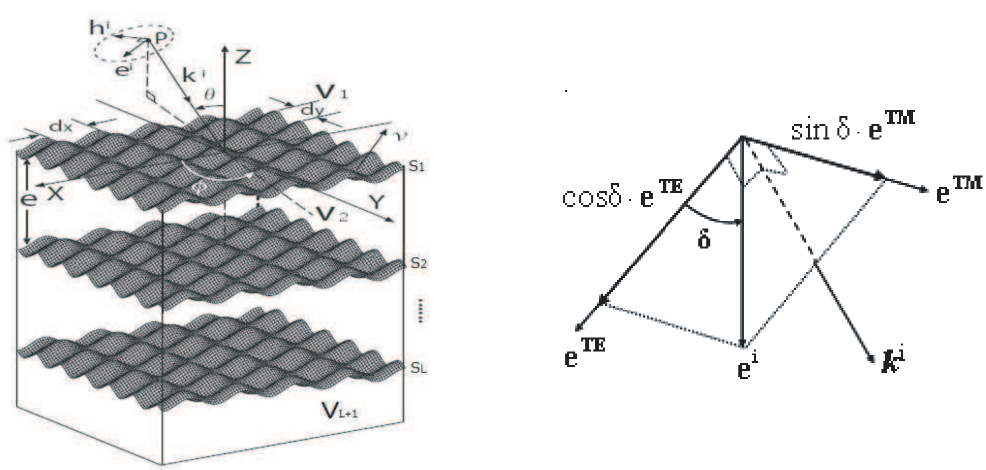

(a) (b)

Figure 1: (a) Schematic representation of multilayered bi-gratings with an incident light ($\mathbf{V}_1$: $\{\mathbf{P}\ |Z>S_1(X,Y)\}$, V_{L+1}: $\{\mathbf{P}\ |Z<S_L(X,Y)\}$); (b) Definition of a polarization angle.

2.1. Incident Wave

The electric and magnetic field of an incident light are given by

$$\begin{bmatrix} \mathbf{E}^i \\ \mathbf{H}^i \end{bmatrix} (\mathbf{P}) = \begin{bmatrix} \mathbf{e}^i \\ \mathbf{h}^i \end{bmatrix} \exp(i\mathbf{k}^i \cdot \mathbf{P}) \tag{1}$$

where $\mathbf{e}^i$ and $\mathbf{h}^i$ are the electric- and magnetic-field amplitude; $\mathbf{k}^i = [\alpha, \beta, -\gamma]$ is the incident wavevector with $\alpha = n_1 k \sin\theta \cos\phi$, $\beta = n_1 k \sin\theta \sin\phi$, $\gamma = n_1 k \cos\theta$, $k = 2\pi/\lambda$ and n_1 is the relative refractive index of region V_1; $\mathbf{P} = (X, Y, Z)$ is an observation point; λ is the wavelength of the incident wave; θ is the incident angle between the Z-axis and the incident wave-vector; ϕ is the azimuth angle between the X-axis and the plane of incidence.

The amplitude of the incident electric field can be decomposed into TE- (TM-) component, which means the electric (or magnetic) field is perpendicular to the plane of incidence. To do this, we define two unit vectors $\mathbf{e}^{\mathrm{TE}}$ and $\mathbf{e}^{\mathrm{TM}}$ that span a plane orthogonal to $\mathbf{k}^i$. Hence, the amplitude $\mathbf{e}^i$ in (3) is decomposed as

$$\mathbf{e}^i = \mathbf{e}^{\mathrm{TE}} \cos\delta + \mathbf{e}^{\mathrm{TM}} \sin\delta \tag{2}$$

where the symbol δ is the polarization angle between $\mathbf{e}^i$ and $\mathbf{e}^{\mathrm{TE}}$ shown in Fig. 1(b).

2.2. Diffracted Wave

We seek for the diffracted fields $\mathbf{E}_l\,(\mathbf{P})$ and $\mathbf{H}_l\,(\mathbf{P})$ in each region. These should satisfy the following requirements.

(C1) The Helmholtz equations in each region;

(C2) Radiation conditions: The diffracted waves in V_1 (or V_{L+1}) should propagate or attenuate in the positive (or negative) Z-direction;

(C3) Periodicity conditions: Each component of the diffracted electric and magnetic field should satisfy

$$f\,(X + d, Y, Z) = \exp\,(i\alpha d)\, f\,(X, Y, Z)\,, \tag{3}$$
$$f\,(X, Y + d, Z) = \exp\,(i\beta d)\, f\,(X, Y, Z) \tag{4}$$

where α and β are the phase constants in X and Y.

(C4) Boundary conditions: The tangential components of electric and magnetic fields are continuous across the boundaries S_l.

2.3. Method of Solution

We solve the problem above using Yasuura's method of modal expansion [4]. To do this, we first define the set of modal functions; next we construct approximate solutions in terms of finite modal expansions with unknown coefficients; and, finally we determine the coefficients applying the boundary conditions.

Modal functions: Because the diffracted waves have both TE- and TM-components, we need TE and TM vector modal functions in constructing the solutions. Here we employ the functions derived from the Floquet modes (separated solutions of the Helmholtz equations satisfying the periodicity (C3) and the radiation conditions (C2) if necessary). The modal functions for electric fields for each region are given by

$$\boldsymbol{\varphi}^{\mathrm{TE,TM}\pm}_{\ell mn}(\mathbf{P}) = \mathbf{e}^{\mathrm{TE,TM}\pm}_{\ell mn} \exp(i\mathbf{k}^i \cdot \mathbf{P}) \tag{5}$$

where, $m, n = 0, \pm1, \pm2, \ldots$ and $l = 1, 2, \ldots, L, L+1$, and wavevectors in (5) are defined by

$$\mathbf{e}^{\mathrm{TE}\pm}_{\ell mn} = \frac{\mathbf{k}^{\pm}_{\ell mn} \times \mathbf{i}_Z}{\left|\mathbf{k}^{\pm}_{\ell mn} \times \mathbf{i}_Z\right|}, \quad \mathbf{e}^{\mathrm{TM}\pm}_{\ell mn} = \frac{\mathbf{e}^{\mathrm{TE}\pm}_{\ell mn} \times \mathbf{k}^{\pm}_{\ell mn}}{\left|\mathbf{e}^{\mathrm{TE}\pm}_{\ell mn} \times \mathbf{k}^{\pm}_{\ell mn}\right|} \tag{6}$$

and

$$\mathbf{k}^{\pm}_{\ell mn} = [\alpha_m, \beta_n, \pm\gamma_{\ell mn}]\,, \quad \alpha_m = \alpha + \frac{2m\pi}{d_x}, \quad \beta_n = \beta + \frac{2n\pi}{d_y}, \quad \gamma_{\ell mn} = \left(n_\ell^2 k^2 - \alpha_m^2 - \beta_n^2\right)^{1/2} \tag{7}$$

where $\mathrm{Re}(\gamma_{\ell mn}) \geq 0$ and $\mathrm{Im}(\gamma_{\ell mn}) \geq 0$. We use the modal functions defined in equations from (5) to (7) to construct approximations of diffracted electric fields. For the Accompanying magnetic fields, we employ

$$\boldsymbol{\psi}_{\ell mn}^{\mathrm{TE,TM}\pm}(\mathbf{P}) = \frac{1}{\omega\mu_0}\mathbf{k}_{\ell mn}^{\pm} \times \boldsymbol{\varphi}_{\ell mn}^{\mathrm{TE,TM}\pm}. \tag{8}$$

Approximate solutions: To satisfy the radiation condition (C2), the approximate solution in V_1 should have a form of finite linear combination of up-going modal functions with unknown coefficients. Likewise, the solution in V_{L+1} must be a linear combination of down-going modal functions. The solution in V_l, however, must have both up- and down-going waves. To show the travelling direction of a modal function, we use superscripts $^+$ and $^-$ representing up- and down-going waves. Here, we form approximate solutions for the diffracted electric and magnetic fields in V_l:

$$\begin{aligned}\begin{pmatrix}\mathbf{E}_{\ell N}^{d}\\ \mathbf{H}_{\ell N}^{d}\end{pmatrix}(\mathbf{P}) = &\sum_{m,n=-N}^{N} A_{\ell mn}^{\mathrm{TE}+}(N)\begin{pmatrix}\phi_{\ell mn}^{\mathrm{TE}+}\\ \psi_{\ell mn}^{\mathrm{TE}+}\end{pmatrix}(\mathbf{P}) + \sum_{m,n=-N}^{N} A_{\ell mn}^{\mathrm{TM}+}(N)\begin{pmatrix}\phi_{\ell mn}^{\mathrm{TM}+}\\ \psi_{\ell mn}^{\mathrm{TM}+}\end{pmatrix}(\mathbf{P})\\ &+\sum_{m,n=-N}^{N} A_{\ell mn}^{\mathrm{TE}-}(N)\begin{pmatrix}\phi_{\ell mn}^{\mathrm{TE}-}\\ \psi_{\ell mn}^{\mathrm{TE}-}\end{pmatrix}(\mathbf{P}) + \sum_{m,n=-N}^{N} A_{\ell mn}^{\mathrm{TM}-}(N)\begin{pmatrix}\phi_{\ell mn}^{\mathrm{TM}-}\\ \psi_{\ell mn}^{\mathrm{TM}-}\end{pmatrix}(P) \quad (\ell = 1, 2, \ldots, L+1)\end{aligned} \tag{9}$$

where N denotes the number of truncation.

Boundary matching: Because the approximate solutions satisfy the requirements (C1), (C2), and (C3) by definition, the unknown coefficients $A_{\ell mn}^{\mathrm{TE}\pm}(N)$ and $A_{\ell mn}^{\mathrm{TM}\pm}(N)$ are determined such that the solutions satisfy the boundary conditions (C4) in an approximate sense. In the Yasuura's method [4], the least-squares method is employed to fit the solution to the boundary conditions. That is, we find the coefficients that minimize the weighted mean-square error by

$$\begin{aligned} I_N = &\int_{S_1'} \left|\mathbf{v} \times \left[\mathbf{E}_{1N}^{d} + \mathbf{E}^{i} - \mathbf{E}_{2N}^{d}\right](s_1)\right|^2 ds + |\Gamma_1|^2 \int_{S_1'} \left|\mathbf{v} \times \left[\mathbf{H}_{1N}^{d} + \mathbf{H}^{i} - \mathbf{H}_{2N}^{d}\right](s_1)\right|^2 ds\\ &+\sum_{\ell=2}^{L}\left\{\int_{S_l'} \left|\mathbf{v} \times \left[\mathbf{E}_{\ell N}^{d} - \mathbf{E}_{\ell+1 N}^{d}\right](s_\ell)\right|^2 ds + |\Gamma_\ell|^2 \int_{S_l'} \left|\mathbf{v} \times \left[\mathbf{H}_{\ell N}^{d} - \mathbf{H}_{\ell+1 N}^{d}\right](s_\ell)^2\right| ds\right\} \end{aligned} \tag{10}$$

where S_1' denotes one-period cells of the interface S_ℓ, Γ_ℓ is the intrinsic impedance of the medium in V_ℓ and $\mathbf{v}$ is a unit normal vector of each boundary.

To solve the least-squares problem on a computer, we need a discretized form of the problem. We first discretize the weighted mean-square error I_N by applying a two-dimensional trapezoidal rule where the number of sampling points is chosen as $2(2N+1)$ [5–8]. We then solve the discretized least-squares problem by the QR decomposition method. Computational implementation of the least-squares problem is detailed in the literature [8].

3. NUMERICAL RESULTS

The multilayered bi-gratings is made by 2 layers: Ag/SiO_2/Ag/. The incident light is a TM-polarized plane wave with a 650 nm wavelength. The relative refractive index of Vacuum = 1, $n_{\mathrm{Ag}} = 0.07 + 4.2i$ and $n_{\mathrm{SiO_2}} = 1.5$. The periods of two directions $d_x = d_y = 556$ nm. We consider 3 types of gratings with different thickness pairs of each region: (A) $e_{\mathrm{Ag}} = e_{\mathrm{SiO_2}} = 27.8$ nm; (B) $e_{\mathrm{Ag}} = 27.8$ nm, $e_{\mathrm{SiO_2}} = 278$ nm; and (C) $e_{\mathrm{Ag}} = 278$ nm $e_{\mathrm{SiO_2}} = 27.8$ nm. We will then calculate the diffraction efficiencies and field distributions of these gratings.

Figure 2 shows the (0, 0)-th order reflection and transmission coefficient as functions of the incident angle θ for 3 types of gratings with the azimuth angle $\phi = 45°$

Five dips are observed on reflection curves throughout Figs. 2(a)–2(c) the field distributions of the total electric fields in the vicinity of the SiO_2 layer for these dips are shown in Figs. 3(a)–(e). Distances in the Z direction are normalized by the wavelength.

For type A shown in Fig. 2(a), two dips (dip 1 at $\theta = 10.6°$ and dip 2 at $\theta = 12.5°$) are observed on reflection curve and the transmission coefficient also increases at the same time. Figs. 3(a) and 3(b) show the field distributions for dips 1 and 2. Strong field enhancements are observed at each surface between Vacuum and Ag layers for either of the two dips. The interaction of SPRs excited on these surfaces result in the coupled plasmon modes (SRSP or LRSP).

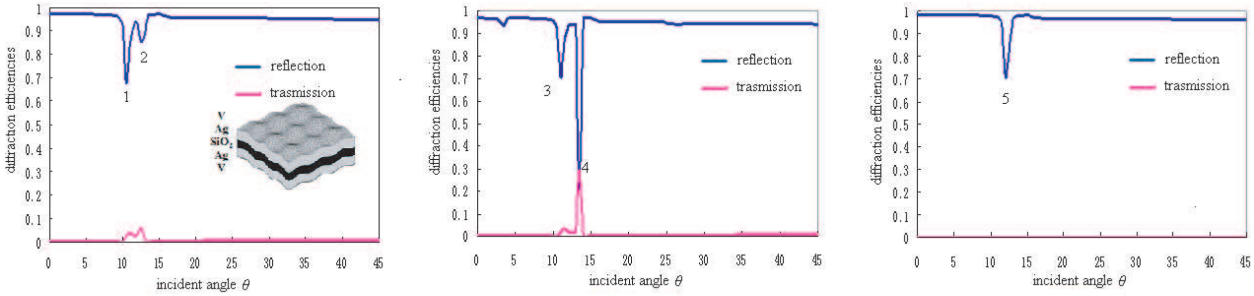

(a) Type A (b) Type B (c) Type C

Figure 2: The (0, 0)-th order reflection and transmission coefficient for 3-layers doubly periodic gratings with 3 types of thickness pairs.

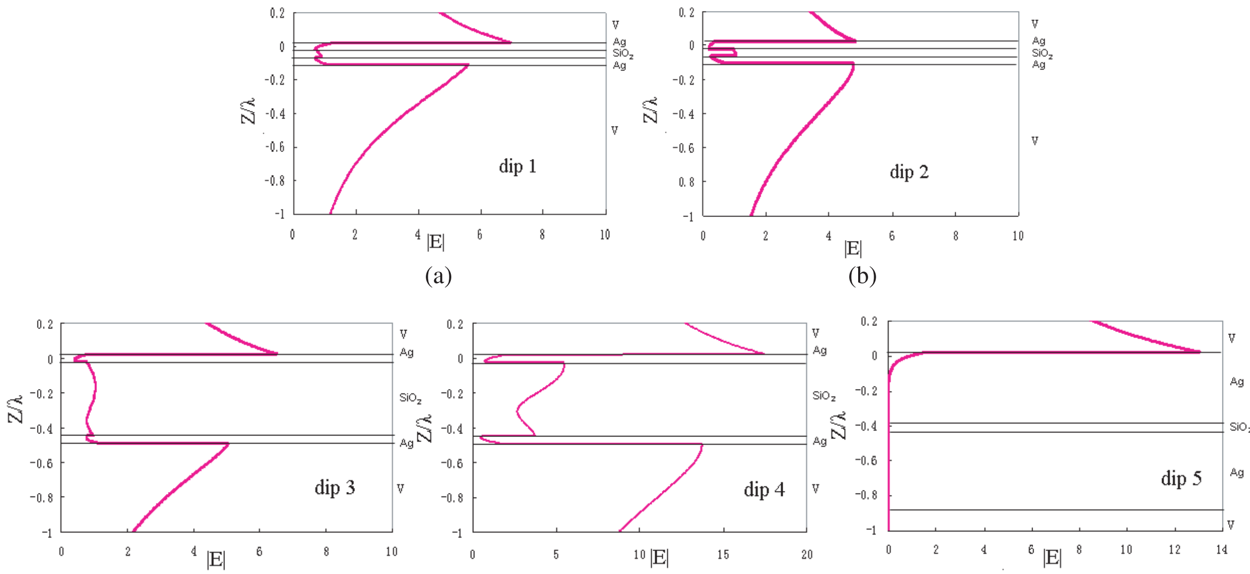

(a) (b)

(c) (d) (e)

Figure 3: Field distributions correspond to five dips.

For type B shown in Fig. 2(b), two dips (dip 3 at $\theta = 11.1°$ and dip 4 at $\theta = 13.5°$) are observed on reflection curve and the transmission coefficient increases at the same time. Reflection at dip 4 is much lower than that of dips 1 and 2 accompanying change of the thickness of SiO_2. Figs. 3(c) and 3(d) show the field distributions for dips 3 and 4. Strong field enhancements are observed at each surface between Vacuum and Ag layers similar to that of type A. In addition, fields enhance strongly at two surfaces between Ag and SiO_2 for dip 4 at the same time. This means coupled plasmon modes are resulted by resonance waves excited at four surfaces.

For type C shown in Fig. 2(c), one dip (dip 5 at $\theta = 12.0°$) is observed on reflection curve and the transmission coefficient keep to zero. Fig. 3(e) shows the field distribution for dip 5. Field enhanced only on the lit surface and quickly attenuates through the 1st Ag layer as shown in Fig. 3(e). This indicates the excitation of SISP.

4. CONCLUSIONS

We solved the problems for 3-layered thin-layer bi-gratings. By calculating the diffraction efficiency and field distributions, we showed that the SPR phenomenon excited and we observed: (1) excitation of a SISP mode at the lit surface of the 1st Ag layer with strong field enhancement for thick enough Ag layer case; (2) excitation of coupled SPR modes (SRSP or LRSP) at each surface between vacuum and Ag layers with strong field enhancements for thin enough Ag layer cases no matter with the thickness of SiO_2 layers; (3) enhancements of field at surfaces between Ag and SiO_2 layers in some cases related with the thickness of SiO_2 layers. The coupled plasmon modes were resulted by the resonance waves excited on four surfaces in these cases. In future, we plan to study applications for multilayered bi-gratings such as improving the sensitivity of a bio-sensor by determining changes of SPRs excited at different layers' surfaces.

REFERENCES

1. Suyama, T., Y. J. Zhang, Y. Okuno, Z. Q. Luo, and T. Matsuda, "Surface plasmon resonance absorption in a multilayered bigrating," *PIERS Online*, Vol. 6, No. 1, 76–80, 2010.
2. Hibbins, A. P., W. A. Murray, J. Tyler, S. Wedge, W. L. Barnes, and J. R. Sambles, "Resonant absorption of electromagnetic fields by surface plasmons buried in a multilayered plasmonic nanostructure," *Phys. Rev. B*, Vol. 74, No. 073408, 2006.
3. Ahn, J. H., T. Y. Seong, W. M. Kim, T. S. Lee, I. Kim, and K. S. Lee, "Fiber-optic waveguide coupled surface plasmon resonance sensor," *Optics Express*, Vol. 20, No. 19, 21729–21738, 2012.
4. Okuno, Y., "Mode-matching method," *Analysis Methods for Electromagnetic Wave Problems*, E. Yamashita, Ed., 107–138, Artech House, Boston, 1990.
5. Yasuura, K. and T. Itakura, "Approximation method for wave functions (I)," *Kyushu Univ. Tech. Rep.*, Vol. 38, 72–77, 1965.
6. Yasuura, K. and T. Itakura, "Approximation method for wave functions (II)," *Kyushu Univ. Tech. Rep.*, Vol. 38, 378–385, 1966.
7. Yasuura, K. and T. Itakura, "Approximation method for wave functions (III)," *Kyushu Univ. Tech. Rep.*, Vol. 39, 51–56, 1966.
8. Matsuda, T. and Y. Okuno, "Numerical evaluation of plane-wave diffraction by a doubly periodic grating," *Radio Sci.*, Vol. 31, 1791–1798, 1966.

Applications of the High-order Method in Dielectric Material

M. Zhu[1], **L. Zhao**[2], **and Q. S. Cao**[1]

[1]College of Electronic and Information Engineering
Nanjing University of Aeronautics and Astronautics, Nanjing 210016, China
[2]Nanjing ASSEN Environment Technology Co. Ltd., Nanjing 210042, China

Abstract— Recently, some important contributions have been made to the time domain scheme in computational electromagnetic field and much progress has been made to improve the finite-difference time-domain (FDTD) method. Among all these schemes, the high-order finite-difference time-domain (HO-FDTD) method has become an essential scheme for modern problem of moderately high frequency or a large domain in nature, especially the large computational involving complex geometries and dielectric material slab. In this paper, we have introduced the HO-FDTD method which apply the Taylor series to instead the time and space derivatives and attach high accurate. The applications of the HO-FDTD scheme has been studied and discussed in dielectric material slab. Reflect coefficients can be obtained from the simulation of the material slab structure and used to measure the accurate of the method. The simulation results have been presented and compared with those of the classical FDTD and Multi-resolution time domain (MRTD) methods in a material slab geometric model. The comparison results show that the HO-FDTD method is well consistent with the analytical results and more accuracy than the other two methods. Further more, the comparisons of the HO-FDTD and MRTD method have been shown in this paper, and obtained that the HO-FDTD method presents the better accurate than MRTD method. Finally, we apply the different spatial stencil size of the HO-FDTD method in the same dielectric material slab simulation and observe that the large spatial stencil size present the better result. All these conclusions show that the HO-FDTD scheme is a powerful, efficient and precise to treat with the dielectric material problem.

1. INTRODUCTION

The Yee's finite-difference time-domain (FDTD) [1] method is a significant method used to solve the computational electromagnetic problem. However, it is known that the dispersion error of the FDTD method is large, so the HO-FDTD method [2] was proposed to increase the dispersion error, which employing the Taylor series to replace the temporal and spatial derivatives. A fourth-order in time and space of the HO-FDTD method was applied in lossless cold plasma and obtained the better dispersion characteristic in [3]. M. F. Hadi and M. P. May presented a new hybrid scheme FDTD (2, 4) to demonstrate for modeling electrically large structures with high-phase accuracy [4]. A HO-FDTD (2, 4) scheme with the second-order accuracy in time and fourth-order in space is discussed in [5], and numerical results proved that the method is suitable for wide-band modeling and coarse-grid calculating and can be reduced the numerical dispersion. A HO-FDTD ($2M$, 4) scheme has been used to compare with the standard FDTD and HO-FDTD (4, 4) methods, the HO-FDTD ($2M$, 4) presents the higher accuracy and saves memory space and CPU time by choosing suitable meshes and bandwidth M [6]. A HO-FDTD (2, 4) method with reduced dispersion error has been developed and implemented in [7], which can enable the mitigation of phase inaccuracies around specific directions of propagation. The multi-resolution time domain (MRTD) method is proposed by M. Krumpholz and L. P. B. Katehi, which expanded in terms of scaling and wavelet functions [8]. The MRTD method and HO-FDTD are both higher accuracy methods, so we will compare them with each other in this paper.

In summary, the theory of the HO-FDTD method will be introduced in Section 2. The applications of the method in dielectric material slabs will be discussed and the comparison between the HO-FDTD and MRTD methods will be investigated in Section 3. Conclusions will be given in Section 4.

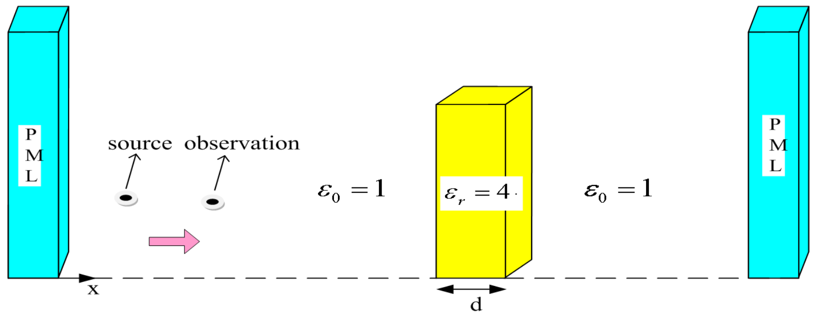

Figure 1: The structure of the dielectric material slab.

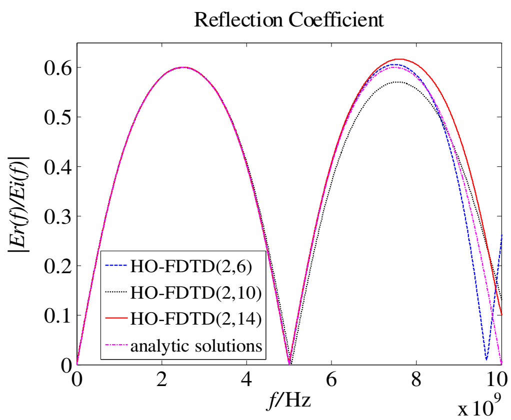

Figure 2: Magnitude of reflection coefficients for different method.

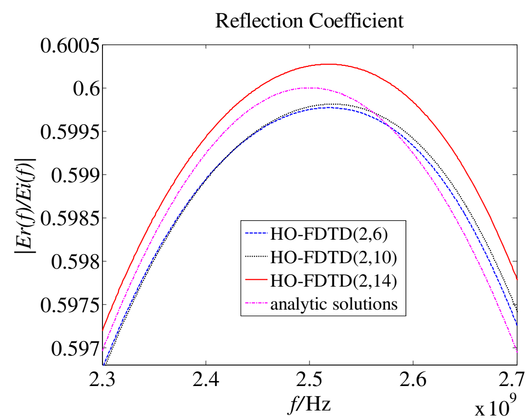

Figure 3: A Partial enlarged figure of Fig. 2.

Table 1: Coefficients for RK-HO-FDTD method.

	(2, 4)	(2, 6)	(2, 10)	(2, 14)	(2, 16)
a (1)	1.125	1.171875	1.211242676	1.228606224	1.23409107
a (2)	−0.041667	−0.06510416677	−0.0897216797	−0.102383852	−0.106649846
a (3)		0.00468750000	0.0138427734	0.0204767704	0.0230363667
a (4)			−0.00176565988	−0.00417893273	−0.0053423856
a (5)			0.000118679470	0.000689453549	0.00107727117
a (6)				−0.0000769225034	−0.000166418878
a (7)				0.00000423651475	0.0000170217111
a (8)					−0.000000852346421

2. THE HO-FDTD METHOD

In a source-free homogeneous isotropic and one-dimensional the Cartesian coordinate medium, the update equations of the HO-FDTD (2, 2 m) [9] can be written as

$$E_y^{n+1}(i) = E_y^n(i) - \frac{\Delta t}{\varepsilon \Delta x} \sum_{v=1}^{m} a(v) \left(H_z^{n+1/2}(i+v-1/2) - H_z^{n+1/2}(i-v+1/2) \right) \quad (1)$$

$$H_z^{n+1/2}(i+1/2) = H_z^{n-1/2}(i+1/2) - \frac{\Delta t}{\mu \Delta x} \sum_{v=1}^{m} a(v) \left(E_y^n(i+v) - E_y^n(i-v+1) \right) \quad (2)$$

where E and H are the electric and magnetic filed, Δt is the time step size, Δx, Δy is the spatial step size, ε is the permittivity, μ is the permeability, the coefficients $a(v)$ [9] listed is Table 1, c is the light speed in vacuum.

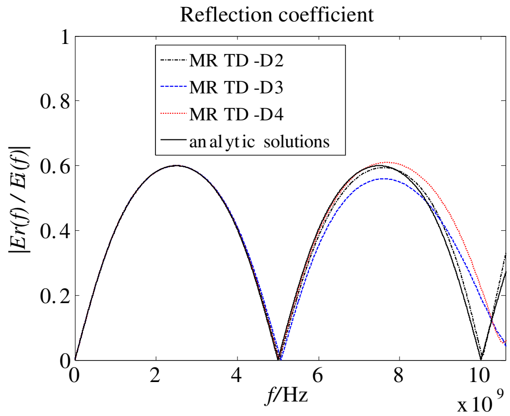

Figure 4: Magnitude of reflection coefficients for different method.

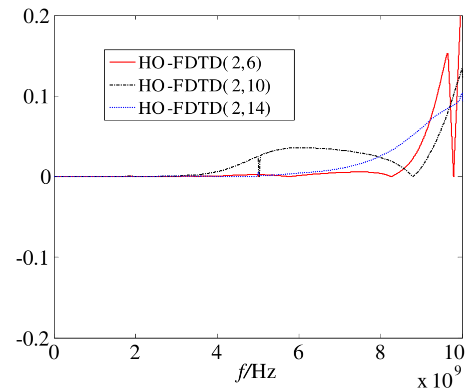

Figure 5: Errors of the HO-FDTD method.

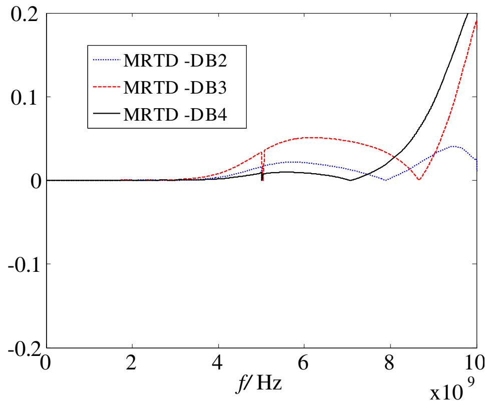

Figure 6: Errors of the MRTD method.

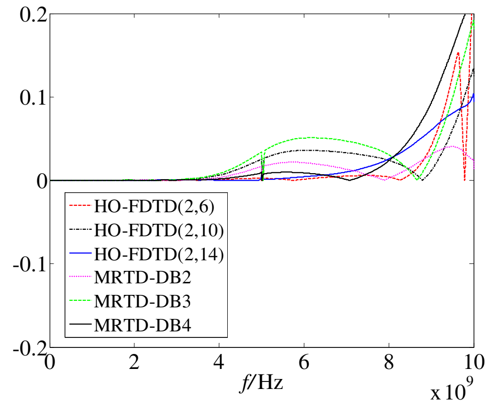

Figure 7: Errors of the different method.

3. SIMULATIONS AND RESULTS

We consider a dielectric material slab in one dimension as shown in Fig. 1. The thickness of the slab is 7.5×10^{-3} m, the relative permittivity of the slab is 4, and the air is 1. We defined the spatial step size is $\Delta x = \Delta y$, and the total computational domain is discretized as $\Delta x = \lambda/5$, which λ is the wavelength in the media and corresponds to the concerned maximum frequency $f_{\max} = 12$ GHz.

The reflection coefficients of the simulation with different spatial stencil size of the HO-FDTD method are shown in Fig. 2. The analytical solution is the Mie series solution. As shown Fig. 2, we can see that different spatial stencil size has the different accuracy and the HO-FDTD method (2, 14) is the better than other counterparts. Fig. 3 is the partial enlarged of the Fig. 2. The MRTD methods with different Daubechies scaling functions are plotted in Fig. 4 and the MRTD-D4 (MRTD-D4 refer to the MRTD method based on the Daubechies 4 scaling function) is more accuracy. Figs. 5–7 describe the errors between different method and the analytical solution, from these figures, we can clearly obtain that: for the HO-FDTD method, the larger the spatial stencil size can decrease the numerical dispersion error; for the MRTD method, the same conclusion can be drawn that the MRTD-D4 has the lower error than that of the other MRTD methods. The comparisons of the HO-FDTD and MRTD method in Fig. 6 show that the HO-FDTD methods present the better numerical dispersion than the MRTD counterparts.

4. CONCLUSIONS

In this paper, we have introduced the HO-FDTD method and presented the applications of the method which used in the dielectric material slab, and compared with the MRTD method. The experiments show that the larger spatial stencil size of the method can reduce the numerical dispersion error and present the better characteristic. From the comparison, we found that the HO-FDTD method has the lower error than their counterpart MRTD method. The results show that the HO-FDTD method is a powerful and efficient scheme in electromagnetic area.

ACKNOWLEDGMENT

The work was supported by the Funding of Jiangsu Innovation Program for Graduate Education and the Fundamental Research Funds for the Central Universities under Contract cxzz12-0156.

REFERENCES

1. Yee, K. S., "Numerical solution of initial boundary value problems involving Maxwell's equations in isotropic media," *IEEE Trans. Antennas Propag.*, Vol. 14, No. 3, 302–307, May 1966.
2. Fang, J., "Time domain finite difference computation for Maxwell's equation," Ph.D. Dissertation, University of California at Berkeley, CA, 1989.
3. Yong, J. L., "A higher order FDTD method for EM propagation in a collisionless cold plasma," *IEEE Trans. Antennas Propag.*, Vol. 44, No. 9, 1283–1289, 1996.
4. Hadi, M. F. and M. P. May, "A modified FDTD (2, 4) scheme for modeling electrically large structures with high-phase accuracy," *IEEE Trans. Antennas Propag.*, Vol. 45, No. 2, 254–264, 1997.
5. Lan, K., Y. W. Liu, and W. G. Lin, "A higher order (2, 4) scheme for reducing dispersion in FDTD algorithm," *IEEE Trans. Electronmagn. Compat.*, Vol. 41, No. 2, 160–165, 1999.
6. Shao, Z. H. and Z. X. Shen, "A generalized higher order finite-difference time-domain method and its application in guided-wave problems," *IEEE Trans. Microwave Theory Tech. Compat.*, Vol. 51, No. 3, 856–861, Mar. 2003.
7. Zygiridis, T. T. and T. D. Tsiboukis, "A dispersion-reduction scheme for the higher order (2, 4) FDTD method," *IEEE Trans. Magnetics*, Vol. 40, No. 2, 1464–1467, Mar. 2004.
8. Krumpholz, M. and L. P. B. Katehi, "MRTD: New time-domain schemes based on multiresolution analysis," *IEEE Trans. Microwave Theory Tech.*, Vol. 44, 555–571, Apr. 1996.
9. Zhang, J. and Z. Chen, "Low-dispersion super high-order FDTD schemes," *IEEE Antennas and Propagation Society International Symposium,* Vol. 3, 1510–1513, 2000.

Assessment of Decoupling between MRI Array Elements at 300 MHz

M. Kozlov and R. Turner
Max Planck Institute for Human Cognitive and Brain Sciences, Leipzig, Germany

Abstract— We numerically assessed the decoupling between magnetic resonance imaging (MRI) array elements at 300 MHz. The array was loaded by a typical human head model. A fine-tuning strategy, which mimics commonly used optimization during fabrication, was applied to arrays with inductive decoupling networks between adjacent elements. Element matching (S_{xx}) could also be optimized for an array lacking such decoupling networks. However, a single-resonance S_{xx} spectrum does not provide reliable evidence of low level array element coupling. It is not easy to define the lowest limit for element coupling that does not affect array performance. For a given array configuration and a given set of excitation modes, the power reflected by the entire array provides an excellent figure-of-merit for net array decoupling and circuit-level transmit performance.

1. INTRODUCTION

Magnetic resonance imaging (MRI) 7 T (300 MHz) RF arrays can provide a relatively uniform transmit magnetic near field with appropriate adjustment of the magnitude and phase. This adjustment process is commonly referred to as RF shimming [1]. Most developed RF shimming procedures require array elements to be well decoupled (isolated) from each other, in order to operate independently.

The level of decoupling between MRI array elements is commonly assessed by examining the frequency sweep of each array element's reflection coefficient (S_{xx}) and coupling coefficients (S_{xy}) for each adjacent element pair with a network analyzer. If S_{xx} shows a single resonance, without splitting, it is usually considered that 7 T array elements are decoupled well enough [1]. We investigated the consequences for RF transmit performance of different levels of coupling between array elements, in conditions where the frequency sweep of S_{xx} for each array element gave a single resonance.

2. METHOD

Our investigation was performed using RF circuit and 3-D EM co-simulation. This allows the effects of decoupling conditions on the RF transmit performance to be studied on the basis of only one multi-port 3-D EM simulation for a given array geometry. The fundamentals of the co-simulation work-flow have been described in our previous reports [2, 3]. The RF circuit simulator was Agilent ADS 2011.10, and Ansoft HFSS 14 was chosen as the 3-D EM tool.

Seven Tesla (300 MHz) MRI arrays investigated comprised eight identical planar single loop radiative elements of length 100 mm, mounted on a cylindrical acrylic former with diameter of 250 mm. The angular size of the loops was varied from 40 degrees (the closest element spacing) to 17.5 degrees (the largest gap between elements). The loops were made of rectangular copper strip, 5 mm by 0.045 mm (Fig. 1). The arrays were locally shielded by a cylindrical copper sheet 300 mm long, with diameter of 350 mm. 12 distributed capacitors were placed in each radiative element, in positions shown as orange patches on the copper strip in Fig. 1, to provide tune, shunt, and distributed capacitor functionality. The realistic 3-D EM model of the arrays included all construction details for the radiative elements, simulated with precise dimensions and material electrical properties. The scanner gradient shield was included in the numerical domain. However, neither RF cable traps nor coax cable interconnection wiring were included in the model.

We investigated two array element arrangements: a) inductive decoupling networks were placed between each adjacent radiative element, and b) no dedicated decoupling networks were used.

The load utilized was the multi-tissue Ansoft human body model, cut in the middle of the torso, with a scaling factor $X = 0.9$, $Y = 0.9$, $Z = 0.9$ (simulating an average head). The model was placed symmetrically in the array transverse plane.

To obtain values of fixed and variable array components — decoupling inductors, distributed, tune and match capacitors — we used two circuit-level optimization (fine-tuning) strategies [3]. The first strategy, which mimics commonly used optimization during fabrication, was applied for the arrays with inductive decoupling networks. Set of optimization criteria was defined (at the

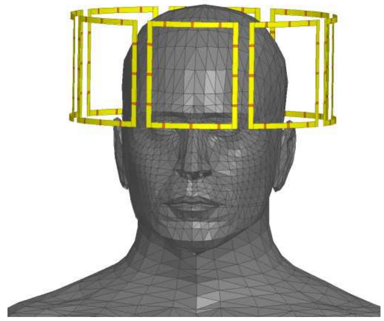

Figure 1: Array geometry setup. Only radiative elements and human model are shown.

desired frequency F_{MRI}) as: a) the actual S_{xx} must be less than a target value S_{xx_t}, for each array element; b) the actual S_{xy} must be less than a target value S_{xy_t}, for each adjacent element. Hence an error or cost function (EF), which was minimized, was

$$EF = \sum_{xx\_i=1}^{8} W_{xx\_i} \left|S_{xx\_i} - S_{xx\_t}\right|^2 + \sum_{xy\_i=1}^{8} W_{xy\_i} \left|S_{xy\_i} - S_{xy\_t}\right|^2 \tag{1}$$

where: w_{xx_i} — weighting factor for the reflection coefficient S_{xx_i} of the individual array element "i", w_{xy_i} — weighting factor for the reflection coefficient S_{xy_i} of the "i" decoupled pair of array elements.

The second optimization strategy, which required that the actual S_{xx} must be less than a target value S_{xx_t}, was applied to arrays with no dedicated decoupling network between adjacent elements. EF was defined as

$$EF = \sum_{xx\_i=1}^{8} W_{xx\_i} \left|S_{xx\_i} - S_{xx\_t}\right|^2 \tag{2}$$

Both optimizations were performed in two steps: 30,000 random tries, followed by the "Quasi-Newton" optimization method until no further improvement was possible. S_{xx_t} was -50 dB, S_{xy_t} was -20 dB and all weighting factors were equal to 1.

Circuit-level parameters evaluated were S_{xx}, S_{xy}, the power reflected by the entire array ($P_{\text{array\_refl}}$), and each element's Q_{load}, the value of loaded quality factor for the radiative elements for circular polarized (CP) excitation mode, calculated at a level -3 dB using the frequency dependence of the currents through radiative elements.

Widely used for indirect evaluation of the inherent coil losses produced by lossy lumped elements (e.g., capacitors and inductors), dielectrics, and conductors ($P_{\text{array\_internal}}$) and the power absorbed by the entire load (P_{load}) [5], the $Q_{\text{load}}/Q_{\text{unload}}$ ratios are not tabulated here, because $P_{\text{array\_internal}}$ and P_{load} were directly evaluated from volume and surface loss densities. It should also be noted that the use of $Q_{\text{load}}/Q_{\text{unload}}$ can provide misleading values for $P_{\text{array\_internal}}$ and P_{load} at 300 MHz. The reasons for this are as follows: a) both for unloaded and loaded coils, radiation losses and the coupling between array elements differ significantly; b) the coupling between power supply and coil is altered by coil loading, which can invalidate the general requirement of critical coupling that enables calculation of the Q-factor; and c) the reflected power $P_{\text{array\_refl}}$ is not taken into account. In our investigation Q_{load} is used only for estimation of how large mismatch can be, due to imperfect tuning, between the array central operating frequency and the Larmor magnetic resonance frequency (F_{MRI}).

The entire human brain was defined as the volume of interest (VOI). Array near field properties were evaluated by considering the values of a) $B_1{+}_V$, transverse magnetic field magnetic field component with clockwise circular polarization (B_1+) averaged over the VOI; b) $B_1{+}_V/\sqrt{P_{\text{transmit}}}$, array transmit performance; c) P_V, the power deposited in the VOI; d) $B_1{+}_V/\sqrt{P_V}$, the VOI excitation efficiency. Performance measures were calculated when CP excitation (1 W power with a sequential 45 degree phase increment) and some other excitation modes were applied to the arrays. Array transmit power (P_{transmit}) was always 8 W.

3. RESULTS AND DISCUSSION

Both circuit-level optimizations resulted in a single resonance for S_{xx} (Fig. 2), with a minimum which was always below -40 dB at MRI operation frequency (F_{MRI}), for all array elements in all array geometries. The worst case S_{xy} was in the range of 14.7 dB to 16.9 dB for the arrays with inductive decoupling networks, and -5.4 dB to 6.4 dB without such a network. For each of these cases the first value shown is for a loop of 40 degree angle and the second is for a 17.5 degree angle.

For the first optimization strategy and for the arrays with inductive decoupling networks, the best achievable S_{xy} was defined by the level of resistive and capacitive coupling. The larger the space between circumferentially adjacent elements, the smaller was the value of the best achievable S_{xy}.

With strong inter-coil coupling, the excitation power delivered to a single coil element was further distributed through several other elements, thus exciting a large sample volume. This resulted in significantly decreased Q_{load} for the array without decoupling networks, relative to the array with decoupling networks. The reduction of the Q_{load} resulted in broadening of the still single-resonance S_{xx} spectrum.

The array properties that were most sensitive to element coupling were: the power absorbed by the load (P_{load}), the power reflected by the entire array ($P_{\text{array\_refl}}$) (Fig. 3) and the frequency at which the current I_{elem} through a given array element approached its maximum (F_{Imax}). These properties were closely related to each other, such that $P_{\text{array\_refl}}$ approached its minimum (in the best case 0% of P_{transmit}) at F_{MRI}, P_{load} approached its maximum at F_{MRI}, and $F_{\text{Imax}} = F_{\text{MRI}}$. This condition provided the best $B_1{+}_V/\sqrt{P_{\text{transmit}}}$ for given array geometry and element material properties.

The closest element spacing resulted in a large $P_{\text{array\_refl}}$. For the array without decoupling networks, $P_{\text{array\_refl}}$ was 48% of P_{transmit} for loop angular size of 17.5 degrees, and 71% of P_{transmit} for a loop angle of 40 degrees. For the array with inductive decoupling networks, the $P_{\text{array\_refl}}$ was 3% and 5% of P_{transmit} respectively.

F_{Imax} values were not identical for all array elements (Fig. 3(b)), but the dependences on element coupling were very similar. For the array without decoupling networks, the closest element spacing resulted in a large value of $F_{\text{Imax}} - F_{\text{MRI}}$, which was 2.8 MHz and 18.8 MHz, for loop angular sizes of 17.5 degrees and 40 degrees respectively. For estimation of array transmit performance, $F_{\text{Imax}} - F_{\text{MRI}}$ should be used together with the Q_{load}, because the larger the Q_{load}, the more severe

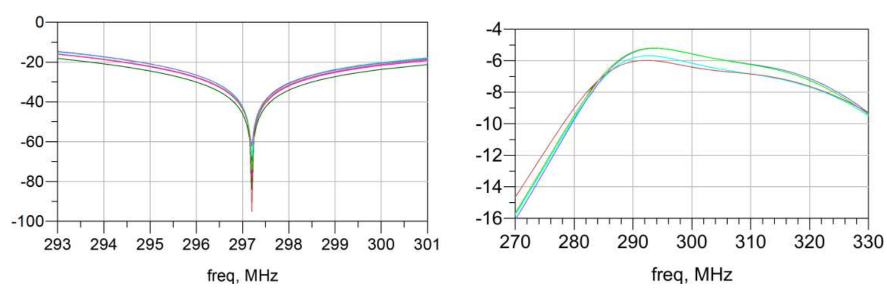

(a) (b)

Figure 2: S parameter data: (a) S_{xx}, (b) S_{xy}.

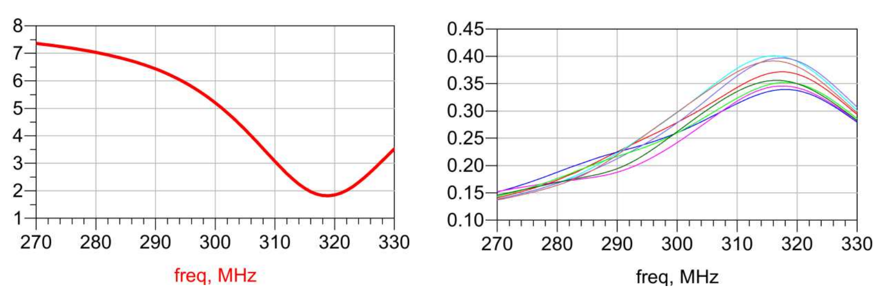

(a) (b)

Figure 3: Circuit-level data: (a) $P_{\text{array\_refl}}$, (b) currents through loop elements.

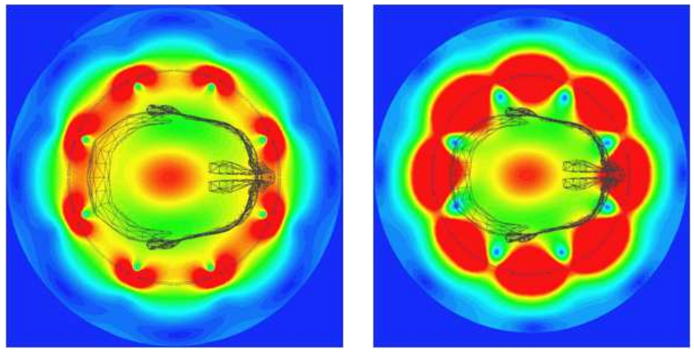

(a) (b)

Figure 4: B_1+ slices rescaled to individual maximum. The angular size of the loops: (a) 40°, (b) 22.5°.

the array transmit performance degradation, for a given $F_{\text{Imax}} - F_{\text{MRI}}$.

For single channel excitation, B_1+ within the central transverse slice differed significantly for arrays with and without decoupling networks. But for CP excitation, B_1+ had nearly the same profile within this slice and $B_1+_V/\sqrt{P_V}$ was nearly the same for arrays with the same geometry with and without decoupling networks. However, due to the large difference in $P_{\text{array\_refl}}$ and consequently P_V, there were significant differences in peak B_1+_V and $B_1+_V/\sqrt{P_{\text{transmit}}}$.

The angular size of the loops signicantly influenced on B_1+ inperiphery of head but near field remained near the same in the centre of the head (Fig. 4).

Simulating a dual-element array with no decoupling network, we obtained a single resonance S_{xx} when S_{xx} was minimized. This optimization resulted in $S_{21} = -2.3\,\text{dB}$, and different values of tune and match capacitors for each loop element. Because the coupling between the corresponding elements for an 8 element cylindrical array with the same loop size and geometrical spacing was $-5.6\,\text{dB}$, we can conclude that if there is asymmetrical tuning, or if coupling within the array has cylindrical symmetry, so that coupling to left and right adjacent elements is equalized, the spectrum of S_{xx} can remain non-split, as it is for a single element or an high level decoupled array.

When circuit-level performance optimization is performed for a fabricated array or in the numerical domain, in general, there is no need to measure or to calculate the combined 3-D EM fields, because the magnetic field generated by each coil element is defined by the current through it. The currents and the quantity $F_{\text{Imax}} - F_{\text{MRI}}$ for each array element can be monitored using current probes or pick-up loops, or calculated using an RF circuit simulator. On-bench there is one significant drawback in the use of these quantities — all the array elements must be excited simultaneously with amplitudes and phases similar to those used in the actual MRI scan application. If only one element is excited, the spectrum (and F_{Imax}) of the current through the elements changes significantly, compared with simultaneous excitation (e.g., F_{Imax} can shift by up to 27 MHz, 10% of F_{MRI}).

There is no simple relationship between array element matching, adjacent element coupling and $P_{\text{array\_refl}}$ for specific excitation modes

$$P_{\text{array\_refl}} = a^H \times S^H \times S \times a, \tag{3}$$

where a — excitation vector, S — entire scattering matrix, subscript "^{H}" represents complex conjugate transpose. $P_{\text{array\_refl}}$ depends not only on the excitation mode, but also on the number of array elements. Thus a given level of element coupling can result in a negligible $P_{\text{array\_refl}}$ for an array with small number of elements, but a substantial $P_{\text{array\_refl}}$ for an array with large number of elements. It is not easy to define a lower limit for element coupling that does not affect array performance.

On-bench measurement of the entire S parameter matrix can be done significantly more easily than simultaneous array excitation and current probe measurement. Using Equation (3), $P_{\text{array\_refl}}$ can be calculated for all given excitation modes by most up-to-date network analyzers. Therefore $P_{\text{array\_refl}}$ is the easiest and most reliable figure of merit for assessment of the quality of decoupling between array elements.

4. CONCLUSIONS

Neither the profile of B_1+ within the central transverse slice for CP mode excitation, nor a single resonant S_{xx} spectrum, can be used as reliable evidence of a low level of coupling between array elements. The dependence of S_{xy} on $B_1+_V/\sqrt{P_{\text{transmit}}}$ is not sensitive enough for reliable optimization of array transmit properties. Because $B_1+_V/\sqrt{P_V}$ is nearly the same for arrays with the same geometry, $B_1+_V/\sqrt{P_{\text{transmit}}}$ depends heavily on $P_{\text{array\_refl}}$ for a given excitation mode. Therefore, in a given configuration and set of excitation modes, $P_{\text{array\_refl}}$, which can be obtained in the numerical domain and also by using the available MRI scanner safety monitoring system, provides an excellent figure-of-merit for array decoupling and circuit-level transmit performance.

REFERENCES

1. Gilbert, K. M., A. T. Curtis, J. S. Gati, L. M. Klassen, L. E. Villemaire, and R. S. Menon, "Transmit/receive radiofrequency coil with individually shielded elements," *Magn. Reson. Med.*, Vol. 64, No. 6, 1640–1651, 2010.
2. Kozlov, M. and R. Turner, "Fast MRI coil analysis based on 3-D electromagnetic and RF circuit co-simulation," *J. Magn. Reson.*, Vol. 200, 147–152, Sep. 2009.
3. Kozlov, M. and R. Turner, "Multi-mode optimization of a near-field array," *Proceedings of the 42nd European Microwave Conference*, 309–212, Amsterdam, The Netherlands, 2012.
4. Gilbert, K. M., J. G. Belliveau, A. T. Curtis, J. S. Gati, L. M. Klassen, and R. S. Menon, "A conformal transceive array for 7 T neuroimaging," *Magn Reson Med.*, Vol. 67, No. 5, 1487–1496, 2012.
5. Lemdiasov, R., A. Obi, and R. Ludwig, "A numerical postprocessing procedure for analyzing radio frequency MRI coils," *Concepts in Magnetic Resonance Part A,* Vol. 38A, No. 4, 133–147, 2011.

Circularly Polarized Patch Antenna Based on Chiral Metamaterial

Yahong Liu, Ying Qi, Kun Song, Shuai Gu, and Xiaopeng Zhao
Smart Materials Laboratory, Department of Applied Physics
Chang'an Campus, Northwestern Polytechnical University, Xi'an 710129, China

Abstract— In this paper, a circularly polarized (CP) patch antenna with chiral metamaterial (CM) has been proposed. The proposed antenna is consisted of conventional linearly polarized (LP) patch antenna and CM. The proposed antenna operated at the frequency where CM resonates. The antenna performances have been studied. The study results show that the patch antenna can present CP characteristics when the CM cover is placed above the conventional LP rectangular patch antenna. A simple approach for achieving CP antenna has been provided in the present paper.

1. INTRODUCTION

Circularly polarized (CP) antennas have been received considerable attention for the applications in the fields of wireless mobile communications, radar detection and so on. CP antennas can provide better mobility and weather penetration than linearly polarized (LP) antennas [1]. A conventional method to construct a patch antenna with CP radiation is to produce two degenerate orthogonal modes with equal amplitude and 90° phase difference on the radiating element. However, CP antenna often needs dual-fed or multi-fed mechanism [2–4]. The feeding network complicates the CP antenna design and fabrication.

Recently, chiral metamaterial (CM) has been attracted interests due to its unique properties, such as negative refraction, electromagnetic activity, and circular dichroism. Tretyakov [5] firstly proposed CM which can realize negative refraction due to their strong optical activity. Pendry [6] and Monzon [7] also demonstrated CM is alternative route toward negative refraction CM may have paved a simple way for designing CP antenna.

2. ANTENNA DESIGN

The proposed antenna is consisted of conventional rectangular LP patch antenna and CM. In the proposed antenna, we use wheel-like CM proposed by Chang [8]. The CM is composed of two layers copper wheel on both sides of the substrate. The upper wheel is an enantiomeric form of the bottom one, with a relative twist of 45°. The design antenna is operated at about 7 GHz. Using commercial software CST microwave studio basing on a finite integration technique, an accurate modal analysis of the conventional LP rectangular patch antenna is carried out to determine the patch dimension of 11.9 mm × 13.4 mm. The dimension of plane ground is the same to that of substrate with 37 mm × 37 mm. The substrate is chosen as Teflon with relative permittivity $\varepsilon_r = 2.65$ (tangential loss of 0.009) and 0.8 mm thickness. A 50 Ω coaxial probe used to feed the antenna was situated at $(-0.9, -2)$ in the cartesian coordinates. The designed antenna operates at frequency where CM resonates. The substrate of the CM is the same to that of antenna. The CM used in the proposed antenna is consisted of 5 × 5 unit cells. The corresponding geometric parameters of CM which resonates at 7 GHz are as follows: $a_x = a_y = 7.4$ mm, $r = 2.8$ mm, $g = 0.2$ mm and $w = 0.2$ mm. The copper has a thickness of 0.035 mm. The distance between the LP patch antenna and CM influences antenna performances. Employing CST microwave studio, the optimal distance of about 0.6λ is obtained. The prototype of the proposed antenna is shown in Fig. 1.

In this paper, the simulations were studied with CST Microwave Studio. In the simulations, a LP electromagnetic wave is incident on the CM; the unit cell boundary conditions were applied to the x and y directions and absorbing boundary conditions were applied to the z direction. In the experiment, the results are measured by using an AV 3629 (45 MHz–40 GHz) vector network analyzer with two standard horn antennas.

3. ANTENNA PERFORMANCES

Figure 2 shows the antenna reflection coefficient. It can be seen that the antenna operates at 7 GHz for the simulation. Whereas the measured result shows the antenna operates at 7.22 GHz, which shifts to high frequency as compared to the simulated one. The discrepancy between the measured

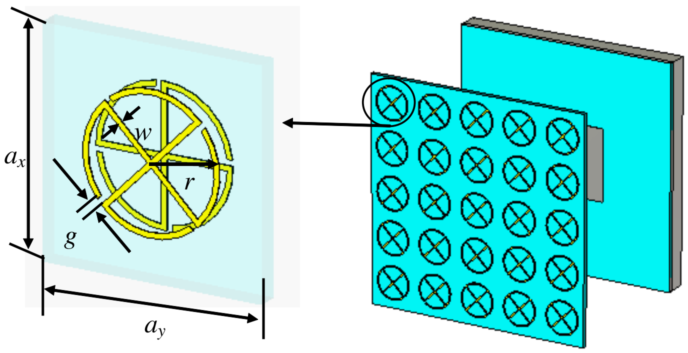

Figure 1: The prototype of the proposed CP antenna.

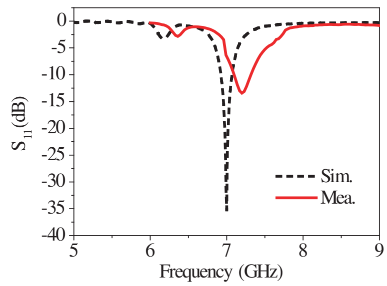

Figure 2: The reflection coefficient of the proposed antenna.

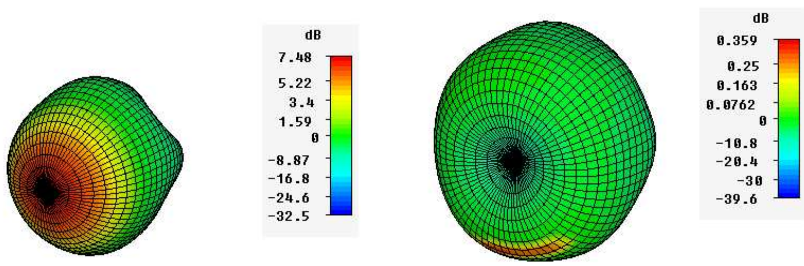

(a) (b)

Figure 3: The radiation patterns of the proposed antenna with CM. (a) LCP and (b) RCH.

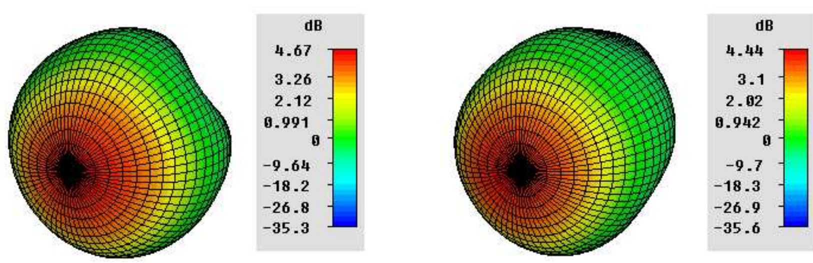

(a) (b)

Figure 4: The radiation patterns of the conventional antenna without CM. (a) LCP and (b) RCH.

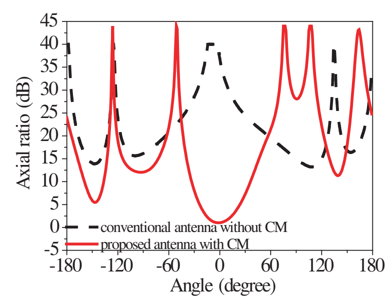

Figure 5: The comparative antenna axial ratio.

and simulated results may be due to the fabrication tolerance and the Teflon board material where the actual dielectric constant is a little different from the value used in the simulations.

The antenna radiation patterns are shown in Fig. 3. It presents that the gain of LCP component is 7.48 dB and the gain of RCP component is 0.359 dB. The LCP gain is much higher than that of RCP component, which implies the antenna with CM presents the LCP characteristics. RCP radiation characteristics can be achieved by simply flipping the CM cover by 180°.

Figure 4 gives the radiation pattern of the conventional patch antenna without CM cover. It can be seen that the gain of LCP component is 4.67 dB and the gain of RCP component is 4.44 dB. The LCP gain is the same to that of RCP component, which implies the conventional antenna presents the LP characteristics. It can be concluded that antenna polarization mode can be changed from LP mode to CP mode due to the CM.

In order to explore the polarization properties of the antennas, Fig. 5 shows the simulated axial ratio. It can be observed that the antenna axial ratio is 40 for the conventional LP antenna without CM, whereas the axial ratio for the antenna with CM is 1.039. It is demonstrated that the introduction of CM can reduce antenna axial ratio greatly.

4. CONCLUSIONS

In this paper, a CP patch antenna based on CM has been proposed. The antenna polarization mode can be changed from LP mode to CP mode due to the introduction of the CM is significant. Nowadays, with the technological development in wireless mobile communications, CP antennas have captured more and more attention. It can be expected that the proposed CP patch antenna has the potential application in the field of communications, radar detection, and among others.

ACKNOWLEDGMENT

This work is supported by the National Natural Science Foundation of China under Grants 11204241, 50936002, and by the NPU Foundation for Basic Research under Grant JC201154.

REFERENCES

1. Garg, R., R. Bhartia, I. Bahl, and A. Ittipiboon, *Microstrip Antenna Design Handbook*, 493–520, Artech House, Boston and London, 2001.
2. Bao, X. L. and M. J. Ammann, "Comparison of several novel annularring microstrip patch antennas for circular polarization," *Journal of Electromagnetic Waves and Applications*, Vol. 20, No. 11, 1427–1438, 2006.
3. Tong, K. F. and J. J. Huang, "New proximity coupled feeding method for reconfigurable circularly polarized microstrip ring antennas," *IEEE Trans. Antennas Propag.*, Vol. 56, 1860–1866, 2008.
4. Yang, S. S., A. A. Kishk, and K. Lee, "Wideband circularly polarized antenna with L-shaped slot," *IEEE Trans. Antennas Propag.*, Vol. 56, No. 6, 1780–1783, 2008.
5. Tretyakov, S., I. Nefedov, A. Sihvola, S. Maslovski, and C. Simovski, "Waves and energy in chiral nihility," *Journal of Electromagnetic Waves and Applications*, Vol. 17, No. 5, 695–706, 2003.
6. Pendry, J. B., "A chiral route to negative refraction," *Science*, Vol. 306, 1353–1355, 2004.
7. Monzon, C. and D. W. Forester, "Negative refraction and focusing of circularly polarized waves in optically active media," *Phys. Rev. Lett.*, Vol. 95, 123904, 2005.
8. Ye, Y., X. Li, F. Zhuang, and S. W. Chang, "Homogeneous circular polarizers using a bilayered chiral metamaterial," *Appl. Phys. Lett.*, Vol. 99, 031111, 2011.

Simulation of the Noise Induced by Corona Discharges on a Ground VHF Antenna

Mingtian Wang[1], **Alexandre Chabory**[1], **and Jean-Pierre Boeuf**[2]

[1]ENAC, TELECOM-EMA, 7 Avenue Edouard Belin, Toulouse F-31055, France
[2]LAPLACE, Paul Sabatier University, Toulouse, France

Abstract— A jamming phenomenon has been observed on a ground station working in the VHF aeronautical frequency-band (118–134 MHz). We attest corona discharges are possibly the source of noise by means of on-site measurements. In order to predict the noise level, we propose a model which consists in two parts: an electrostatic simulation to localize the corona discharges, and a simulation in the frequency domain to evaluate the noise at the antenna ports. The agreement between simulation and measurement is good.

1. INTRODUCTION

A jamming phenomenon has been experienced by the french civil aviation authority (DGAC) on a ground station working in the VHF aeronautical frequency-band (118–134 MHz). This has yielded troubles in air-ground communications. This phenomenon appears in the presence of a strong natural electrostatic field, and is probably due to corona discharges located near the ground antennas. The corona discharges can be sources of VHF and HF noise. This is notably known for antennas onboard aircrafts and for antennas placed near high-voltage transmission lines [1–3].

In this paper, we attest that the noise source is probably corona discharges by means of on-site measurements. Besides, a model is proposed to predict the level of noise introduced by corona discharges at the output of VHF ground antennas. It consists of two parts: an electrostatic simulation to localize where corona discharges occur, and a simulation in the frequency domain to evaluate the noise at the antenna ports.

In the first section, the jamming phenomenon and the measurement to identify its origin are presented. In the second and the third sections, both parts of the model are presented. In the last section the simulation results are compared with measurements.

2. PRESENTATION OF THE JAMMING PHENOMENON AND ITS ORIGIN

The ground station working in the VHF aeronautical frequency band is constituted by a 40-meters high metallic pylon presented in Figure 1. There are two types of VHF antennas on the pylon. On top are placed ground-plane antennas. On lower positions are placed two circular arrays of dipoles with reflectors. They are located 3 m and 10 m below the top.

In order to find the origin of the noise, on-site measurements of the ambient electrostatic field have been performed by means of an electric field mill which is placed below the pylon, on the roof

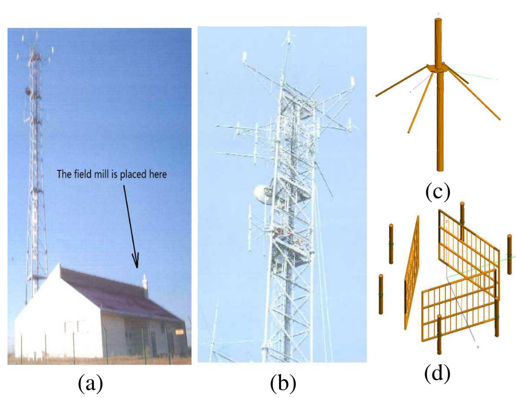

Figure 1: Configuration: (a) ground station; (b) pylon and antennas; (c) ground-plane antenna and (d) circular array of dipoles with reflectors.

of the building represented in Figure 1(a). During several days, the antenna output signal and the electrostatic field have been recorded and compared.

A representative case of measured data is displayed in Figure 2 for the antenna output power and electrostatic field.

The results show that there exists a clear correlation between both measurements. The level of noise always increases simultaneously with the electrostatic field, and the two phenomena last the same time. It should be noticed that this correlation between both measurements has been observed many times in the measured data. Thus, electrostatic discharges, and more particularly corona discharges may be the source of noise.

3. ELECTROSTATIC SIMULATION

Now that we have found a possible origin for the jamming phenomenon, the next work is to search for a method to predict the noise. In order to do that, an electrostatic simulation is performed to locate the place where the electrostatic field is the strongest. That is also the place where corona discharges most probably occur. For the electrostatic simulation, we suppose that the charge density is negligible in the atmosphere before the discharges occur, so the electrostatic simulation can be expressed via the Laplace's equation $\nabla^2 V = 0$. The models of the pylon and the antenna are presented in Figure 3.

The model of the pylon is based on the pylon of the ground station which has been presented in the previous section. The pylon has a 4 m high lightning conductor on top. The ground plane antennas and the dipoles of the circular arrays are represented by metallic cylinders.

We assume the computation volume is a box with the pylon at its centre. For the boundary conditions, two electrodes are defined as shown in Figure 3: a sky electrode associated with the charged cloud located above the pylon, and a ground electrode constituted by the pylon and the ground. The potential difference between both electrodes is fixed so that the ambient electrostatic field corresponds to the real case. Then we assume that the computation domain is large enough, and the lateral boundaries are placed far enough from the pylon, so that the horizontal component of the electrostatic field is zero on the surface of the lateral boundaries, which corresponds to Neumann boundary conditions for the potential. The numerical simulation is realised via Comsol and is thus based on the finite element method.

From [2] and the experimental result in Figure 2(b), the ambient electrostatic field can reach a level of 20 kV/m, and the distance between the sky electrode and the ground is 60 m in our case, therefore the potential difference between electrodes is set to $20\,\text{kV/m} \times 60\,\text{m} = 1.2 \times 10^6\,\text{V}$. The result of the electrostatic simulation is presented in Figure 4.

The result shows that the place with the strongest electrostatic field is the tip of the lightning conductor. Compared with the other places, the electrostatic field around the upper tips of the ground plane antennas is also relatively strong, but weaker than the field of the lightning conductor.

In order to locate the places where the corona occurs, the critical electric field of corona ignition shoud be evaluated. The Peek's formula is used to evaluate the corona inception electric field E_c

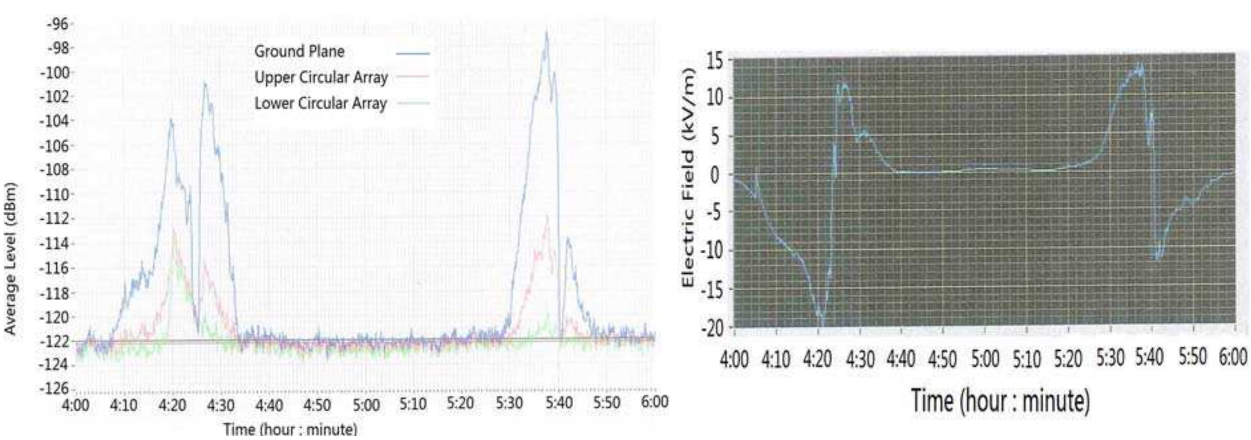

(a) (b)

Figure 2: Comparison between noise (dBm) received by (a) the VHF antennas and electrostatic field (kV/m) measured by the field mill.

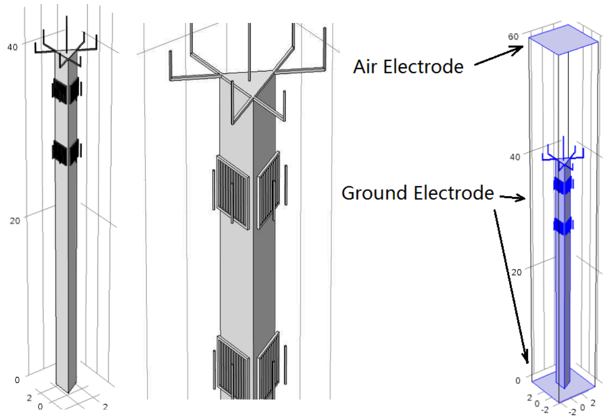

Figure 3: Model for the electrostatic simulation: (a) complete pylon; (b) antennas; (c) computation volume and electrodes.

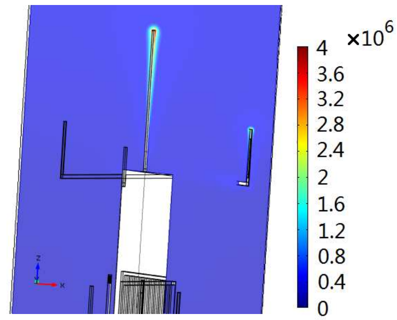

Figure 4: Electrostatic field near the top of the pylon (V/m).

as [8]

$$E_c = E_0 \delta \left(1 + \frac{0.301}{\sqrt{\delta r}}\right) \tag{1}$$

where $E_0 = 29.8\,\mathrm{kV/cm}$, r is the radius of the conductor in cm, δ is the ratio of air density to the normal density corresponding to $p = 760$ Torr and $T = 25°\mathrm{C}$. In our case, the radius of the lightning conductor is 5 cm, and we assume that $\delta = 1$, so the critical electric field $E_c = 33.8\,\mathrm{kV/cm} = 3.38 \times 10^6\,\mathrm{V/m}$.

The simulation result in Figure 4 shows that the surface of the tip of the lightning conductor is the only place where the electric field is stronger than the critical electric field. Thus the top of the lightning conductor is the place where the corona discharges most probably occurs.

4. SIMULATION IN THE VHF FREQUENCY DOMAIN

In the previous section, the place where corona discharges occur has been found. We are going to perform the simulation in the VHF frequency domain to verify the noise level generated by corona discharges.

The simulations in the VHF frequency domain are performed via Feko. We model the pylon as a wire structure because the section of the tubes is small compared with the wavelength (2 m). Both types of VHF ground antennas are modeled so as to obtain realistic matchings and radiation patterns. The voltage standing wave ratio (VSWR) and the gain patterns are presented in Figure 5. For both types of antennas, the VSWR is below 1.5 in all the aeronautical VHF frequency bandwidth. Besides, in the horizontal plane, the radiation patterns are quasi omnidirectional. In the vertical plane, the half-power beamwidths are about 70° and 90° for the ground plane and circulare array, respectively.

The corona discharges in the VHF band are represented by short electric dipoles [4] placed where the corona discharge would occur, i.e., on the top of the lightning conductor.

In [6], the current of the corona discharge can be represented by the following equation

$$I(t) = K I_p \left(e^{-\alpha t} - e^{-\beta t}\right), \tag{2}$$

where $I(t)$ is the current of the corona discharge, I_p is the peak value of the corona discharge current, α and β are constants, and K is a coefficient depending on α and β. In [6], the following values are found by means of measurements: $\alpha = 0.01\,\mathrm{ns}^{-1}$, $\beta = 0.0345\,\mathrm{ns}^{-1}$, $K = 2.34$. In [7], a representative value of the peak corona discharge current is estimated as $I_p = 10\,\mathrm{mA}$. From a Fourier transform of (2), we find that the corona discharge current in the VHF band is about $1\,\mu\mathrm{A}$. Based on the experimental results of [4, 5], we assume that the corona current is concentrated in an area about 5 cm around the corona point. Thus the dipolar moment is chosen to be $5 \times 10^{-8}\,\mathrm{A} \cdot \mathrm{m}$.

To determine the noise introduced by the corona discharges, we simulate the power at the antenna ports when they are excited by the short dipoles.

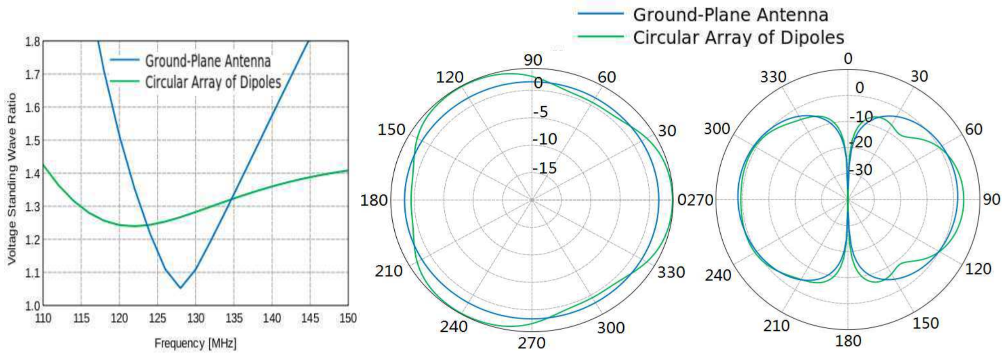

(a) (b) (c)

Figure 5: Matching and gain patterns of models of both antennas: (a) voltage standing wave ratio; (b) gain pattern (dBi) in the horizontal; (c) in the vertical plane.

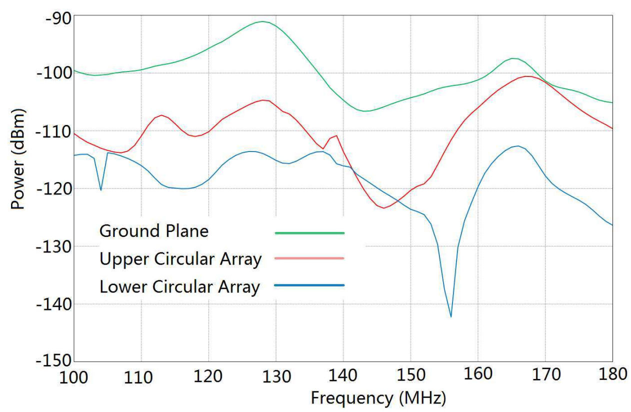

Figure 6: Power received at the ports of the antennas in the VHF frequency domain (dBm).

5. COMPARISON WITH THE EXPERIMENTAL RESULTS

The simulation result in the VHF frequency domain is presented in Figure 6. In the aeronautical VHF band, the noise received by the ground plane antenna located on the top of the pylon can reach −91 dBm. The antenna output noise measured during the experiments has been presented in Figure 2. In this figure, the maximal noise received by the ground plane VHF antenna in the VHF band is about −96 dBm. Thus there is a good agreement between the simulation result and the experimental one.

6. CONCLUSION

The corona discharges have been found as a possible origin of the jamming phenomenon observed on a ground station working in the VHF aeronautical frequency-band. A model has been proposed to predict the noise level induced by corona discharges at the ports of the VHF antennas. The place where the corona discharges occurr has been localized via an electrostatic simulation. The simulation results of the received noise level at the ports of the antennas are in good agreement with the measurements.

ACKNOWLEDGMENT

The authors acknowledge the financial support of PRES University of Toulouse, Région Midi-Pyrénées and DGAC (french civil aviation authority).

REFERENCES

1. Fu, H., Y. Xie, and J. Zhang, "Analysis of corona discharge interference on antennas on composite airplanes," *IEEE Transactions on Electromagnetic Compatibility*, Vol. 50, No. 4, 822–827, Nov. 2008.

2. Page, H. and D. J. Whythe, "Corona and precipitation interference in v.h.f. television reception," *Proceedings of the Institution of Electrical Engineers*, Vol. 114, No. 5, 566–576, May 1967.
3. Olsen, R. G. and B. O. Stimson, "Predicting VHF/UHF electromagnetic noise from corona on power-line conductors," *IEEE Transactions on Electromagnetic Compatibility*, Vol. 30, No. 1, 13–22, Feb. 1988.
4. Wilson, P. F. and M. T. Ma, "Fields radiated by electrostatic discharges," *IEEE Transactions on Electromagnetic Compatibility*, Vol. 33, No. 1, 10–18, Feb. 1991.
5. Fujiwara, O., "An analytical approach to model indirect effect caused by electrostatic discharge," *IEICE Transactions on Communications*, Vol. E79-B, No. 4, 483–489, Apr. 1996.
6. Rakoshdas, B., "Pulses and radio-influence voltage of direct-voltage corona," *IEEE Transactions on Power Apparatus and Systems*, Vol. 83, No. 5, 483–491, May 1964.
7. Janischewskyj, W. and A. Arainy, "Corona characteristics of simulated rain," *IEEE Transactions on Power Apparatus and Systems*, Vol. 100, No. 2, 539–551, Feb. 1981.
8. Xu, M., Z. Tan, and K. Li, "Modified peek formula for calculating positive DC Corona inception electric field under variable humidity," *IEEE Transactions on Dielectrics and Electrical Insulation*, Vol. 19, No. 4, 1377–1382, Aug. 2012.
9. McLean, K. J. and I. A. Ansari, "Calculation of the rod-plane voltage/current characteristics using the saturated current density equation and Warburg's law," *IEE Proceedings A Physical Science, Measurement and Instrumentation, Management and Education — Reviews*, Vol. 134, No. 10, 784–788, Dec. 1987.

Novel Design of Site Source for Radiation and Conduction Emission Test

Dau-Chyrh Chang[1], **Chih-Hung Lee**[2,3], **and Tsung-Yuan Yang**[3]

[1]Oriental Institute of Technology, Taiwan
[2]Yuan Ze University, Taiwan
[3]Electronics Testing Center, Taiwan

Abstract— The electronic devices monitoring of electromagnetic interferences (EMI) has therefore emerged as a major issue for radiation emission (RE) and conduction emission (CE) test, while it must be performed under specialized conditions for EMI measurements. The standard EMI radiation sources will be generated from the harmonic generator in this paper. The oscillator sources used a 16 MHz crystal oscillator together with designed circuit integrate into Hex Inverter Buffer SN74AS04N to generate the fast transition speed of trapezoidal waveforms. The oscillator sources are combined a switching power supply of noise generation and without the LISN (Line Impedance Stabilization Network) for conducted emission test. The noise coupling to generated the AC power of the harmonics during 150 kHz to 30 MHz. A high performance dipole antenna has been implemented as the radiating structure for the signal source and the measurement has been performed in the frequency range 30 MHz to 1 GHz. For application of the novel site source for the monitor of daily test site RE and CE, repeated tests were carried out to check the frequency, power stability and polarization symmetrical of the site source.

1. INTRODUCTION

Site source create harmonic frequencies from which one frequency can be selected with a narrow filter and then filtered out, which look like a comb when viewed on a spectrum analyzer. It is a source for producing fundamental frequency components and multiple harmonic components. From an input signal by crystal oscillator, this generator provides an effective method for generating frequency harmonics. The site source can produce harmonics of frequency step sizes up to the maximum range of operation. Typically, these generators are used for frequency multipliers, frequency synthesizers, built-in-self-test (BIST) sources, and test equipment.

2. DESIGN OF THE SITE SOURCE

The standard EMI radiation sources will be generated from the harmonic generator in this paper. This generator is a device that generates radio frequencies, which are capable of inductively heating metals to high temperatures. Figure 1 shows as using a 16 MHz crystal oscillator with inverter buffer (SN74AS04N) designed circuit integrates to generate the fast transition speed of trapezoidal waveforms and combined a switching power supply of noise generation for conducted emission test. The site source no need battery operated to eliminate for interconnecting cables which could provide the radiated signal and noise coupling. The output level of the site source is fixed and has minimum variation, the frequency range is 150 kHz to 30 MHz for conducted emission test and 30 MHz to 1000 MHz for radiated emission test. When a high performance dipole antenna is affixed atop this generator, the antenna radiates reference signals. The antenna structure, return loss and radiation patterns of simulation results show as the Figure 2.

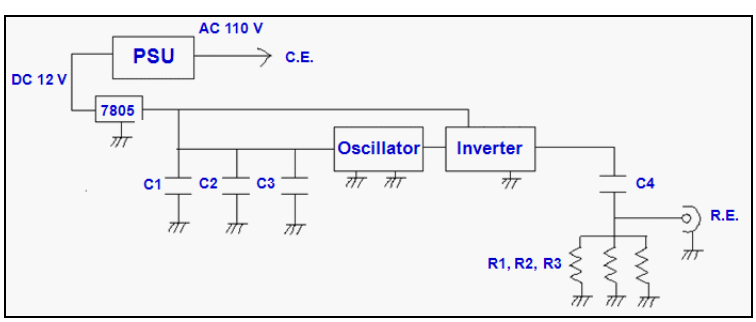

Figure 1: Schematic diagram of the circuit.

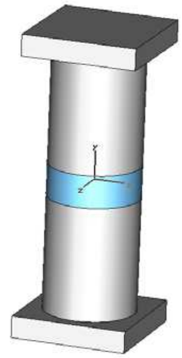

(a)

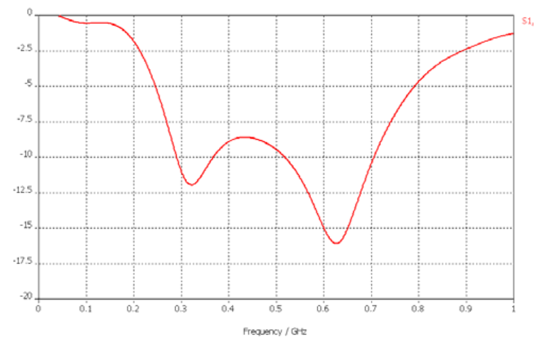

(b)

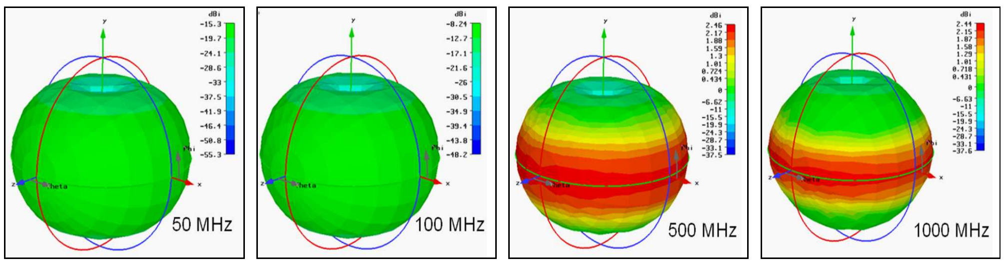

(c)

Figure 2: Simulation results. (a) Dipole antenna structure, (b) return loss, (c) radiation patterns.

(a) Vertical

(b) Horizontal

Figure 3: Testing environment in 10 m chamber.

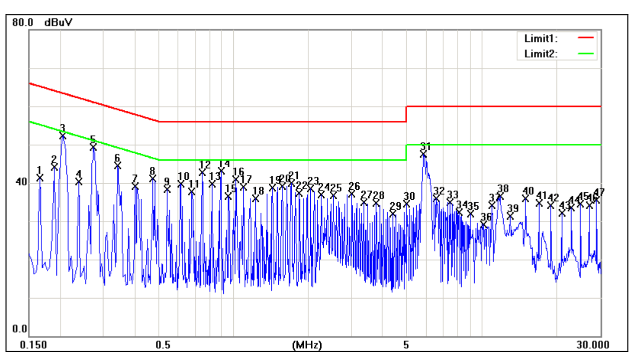

Figure 4: CE measurement result.

3. MEASUREMENT RESULTS

The electronic devices monitoring of EMI has therefore emerged as a major issue for radiation emission (RE) and conduction emission (CE) test, while it must be measured at semi-anechoic chamber during 10 meter distance. Figure 3 is the test environment of Electronics Testing Center, Taiwan. A tracking generator can be used with a spectrum analyzer to check the dynamic responses

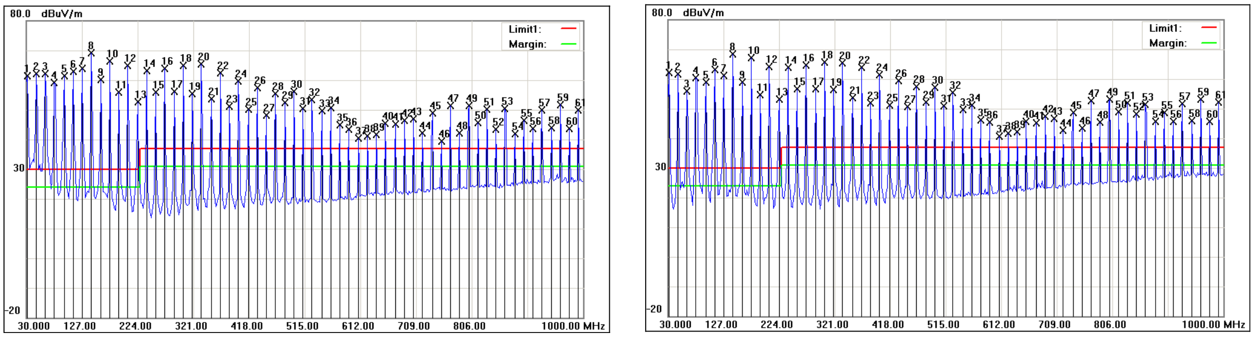

(a) Vertical polarization (b) Horizontal polarization

Figure 5: RE measurement result.

of frequency-sensitive devices, such as transmitter isolators, cavities, ring combiners, duplexers, and antenna systems. The noise coupling to generated the AC power of the harmonics during 150 kHz to 30 MHz. The CE test result show as the Figure 4. About the RE testing, both of the vertical and horizontal polarization can be measured by frequency responses of circuit on oscilloscopes that is a multiple (harmonic) from the 30 MHz to 1000 MHz, its show as in Figure 5.

4. CONCLUSIONS

The standard EMI site source have been generate in this paper. It can be used for radiation and conduction emission test from 150 kHz to 30 MHz and 30 MHz to 1000 MHz. The fundamental frequency components and multiple harmonic components are very stable and symmetry which on the vertical and horizontal polarization. For application of the novel site source for the monitor of daily test site RE and CE, repeated tests were carried out to check the frequency, power stability and polarization symmetrical of the site source.

REFERENCES

1. Reader, H. C., D. F. Williams, P. D. Hale, and T. S. Clement, "Comb-generator characterization," *IEEE Trans. Microwave Theory & Tech.*, Vol. 56, No. 2, 515, Feb. 2008.
2. Mullner, W., A. Kriz, and P. Preiner, "Comb generator measurement technique," *10th International Conference on Electromagnetic Interference & Compatibility*, 291–295, Austrian Research Centers GmbH-ARC, 2008.
3. Maas, S., *Nonlinear Microwave Circuit*, Artech House, Norwood, 1988.
4. Rubiola, E., *Phase Noise and Frequency Stability in Oscillators*, Cambridge University Press, 2010.
5. Bvalanis, C. A., *Antenna Theory: Antenna Theory Analysis and Design*, John Wiley & Sons, 1997.
6. Balanis, C. A., *Advanced Engineering Electromagnetics*, John Wiley and Sons, New York, 1989.
7. Osabe, K., T. Komatsuzaki, and K. Tamara, "Correlation test among EMI measurement sites using a comb generator," *IEEE International Symposium on EMC*, Vol. 2, 945–948, 2000.

The Analysis of Antenna Performance due to PCB Grounding Effect from the EMC Bead Device

Hsiao-Bin Liang[1], **Cheng-Wei Chen**[1], **Dau-Chyrh Chang**[2]
Ming-Ching Yen[2], **and Yu-Ling Chou**[1]

[1]Climax Technology Co., Ltd, Taiwan
[2]Oriental Institute of Technology, Taiwan

Abstract— The bead impact on the performance of on-board monopole antenna is analyzed in this work. The simulated and measured results of an on-board PCB monopole antenna with and without beads between the groundings are compared comprehensively. The return loss, efficiency, radiating pattern of the monopole antenna, and the current density of antenna's groundings under the condition of bead is attached and not are presented and analyzed in this study.

1. INTRODUCTION

For improving the EMC property of PCB, keeping ground separate for sensitivity and noise portion of circuitry is one of the simplest and most effective methods of noise suppression [1–3]. However, the SMD (Surface Mount Device) bead device [4], which is usually adopted for connecting different property of groundings and executing the function of noise suppression, sometimes has obviously influence on the monopole antenna in specific circumstance. In this work, the PCB in a wireless alarm product has two different types of groundings, digital and RF, with an on-board monopole antenna on it is analyzed. The device connecting between different properties of groundings is called bridge. In the following section, the simulated current density of the PCB and comprehensive performances of on-board monopole are presented and analyzed while the bead device and 0 ohm resistor (i.e., equivalent to no grounding separating) is adopted as bridge.

2. CHARACTERISTIC OF BEAD

The SMD beads are made of ferrite material and commonly used to prevent EMI/RFI problem in PCB design. Ferrite beads are used to form a passive low-pass filter characteristic. The geometry and electromagnetic properties of coiled wire over the ferrite bead result in impedance for high-frequency signals, attenuating high frequency EMI/RFI electronic noise. The energy is either reflected, or dissipated as low level heat. The diagram and 3D structure of SMD ferrite bead are shown in Fig. 1.

The SMD bead used in this work is measured and extracted on a PCB, which is shown in Fig. 2(a). The 2-port s-parameter is measured and the reference plane is calibrated by the open pad of the PCB by R&S VNA ZVB-4. Then the impedance (Z), resistance (R) and reactance (X)

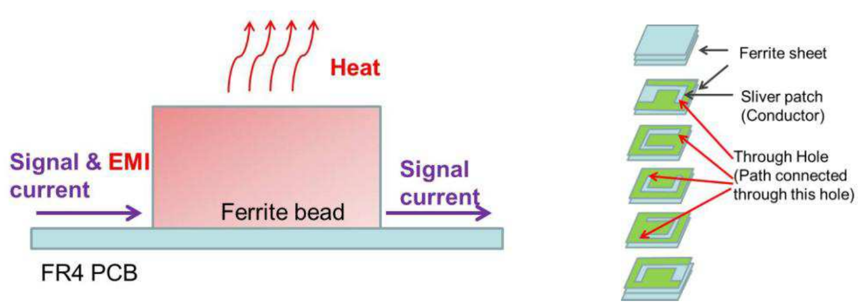

(a) (b)

Figure 1: The diagram of (a) a bead on PCB, (b) 3-D structure inside a bead.

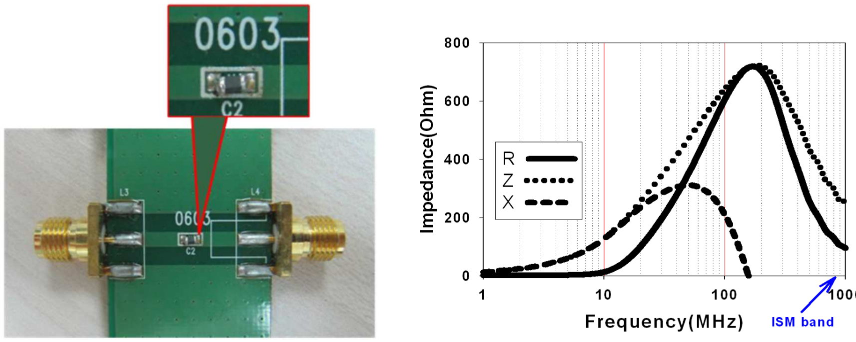

(a) (b)

Figure 2: SMD bead. (a) The photo of SMD bead under test. (b) The extracted impedance (Z), resistance (R) and reactance (X) of a bead.

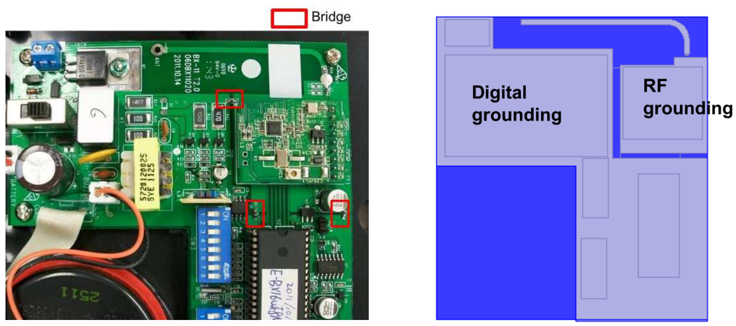

(a) (b)

Figure 3: The PCBA of this work. (a) Photo. (b) 3-D model setup in the GEMS.

of a bead can be extracted by

$$R = \mathrm{Re}\left(\frac{1}{Y_{12}}\right) \tag{1}$$

$$X = \mathrm{Im}\left(\frac{1}{Y_{12}}\right) \tag{2}$$

$$R = \sqrt{R^2 + X^2} \tag{3}$$

The characteristic of Z, R and X versus frequency is plotted in Fig. 2(b). As can be seem, the impedance increases as the frequency increases, reaches the peak value of 720 ohm at 174 MHz, then decreases with the increasing of frequency. The operation frequency of on-board monopole antenna is 868 MHz (ISM band). The impedance, resistance and reactance of bead at this frequency are 262, 109 and −238 ohm respectively.

3. ON-BOARD MONOPOLE ANTENNA SIMULATION

The simulation of current density for this work is operated by GEMS. The picture of PCBA is shown in Fig. 3(a) and the 3-D model setup in GEMS is shown in Fig. 3(b). There are three bridges between the RF grounding and digital ground. The bridges can be SMD beads or SMD 0 ohm resistors. The simulated current densities at 868 MHz for those two conditions are presented in Fig. 4. Fig. 4(a) demonstrates the current density of the PCB groundings with beads as bridge while Fig. 4(b) demonstrates that with 0 ohm resistors as bridge. As can be seen, the groundings with beads have weaker current density than 0 ohm one while the on-board monopole antenna is proceeding radiating. This is because the beads, which perform the impedance of 262 ohm at 868 MHz, degrade the activity of on-board monopole antenna's mirror current.

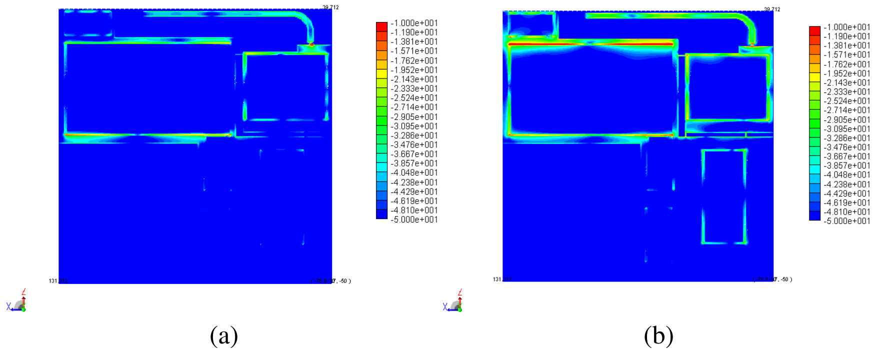

Figure 4: The simulated current density of (a) adopting beads as bridge, (b) adopting 0 ohm resistors as bridge.

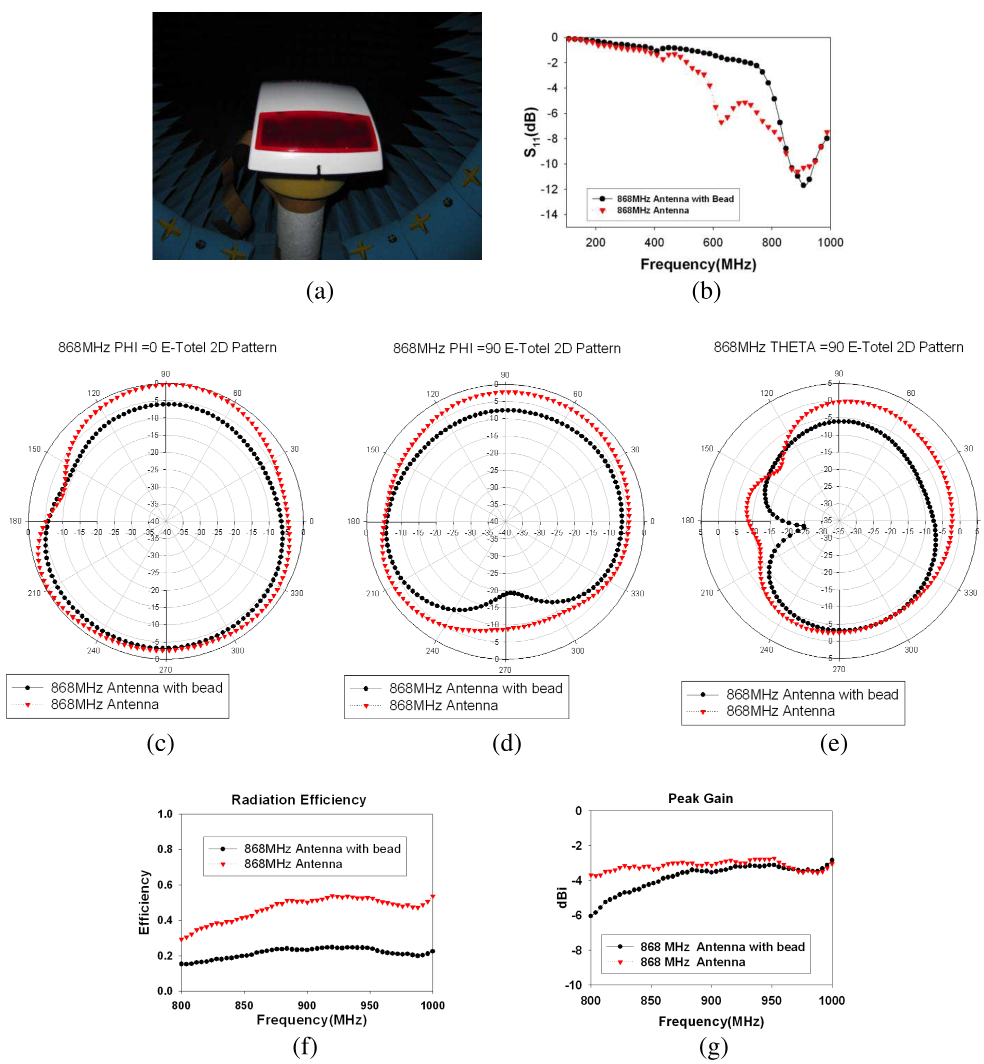

Figure 5: The measured results and comparison of on-board monopole antenna in this work. (a) Measurement setup in SATIMO chamber. (b) Measured return loss. (c) Radiation pattern at X-Z plane. (d) Radiation pattern at Y-Z plane. (e) Radiation pattern at X-Y plane. (f) Radiation efficiency and (g) peak gain.

4. MEASUREMENT AND COMPARISON OF ON-BOARD MONOPOLE ANTENNAS

The PCBA with its case, a wireless security alarm box, is setup in the SATIMO antenna fast measurement system for measuring the performance of monopole antenna with bead and 0 ohm resistor as the grounding bridges. The comprehensive comparison of measured performances for on-board monopole antenna is presented in Fig. 5. From those measured results, it can be observed that the antenna with 0 ohm as bridge connection for groundings has better performance than bead one.

5. CONCLUSIONS

The on-board monopole antenna adopting beads as groundings connection, i.e., bridge, obtains lower performance than the antenna without beads (i.e., 0 ohm resistor as bridge). The simulations of current density demonstrate that the beads still make the groundings high impedance at RF frequency range then reduce the performance of monopole antenna. This analysis will give a practical message for the engineers who are engaging in EMC design-in/debug and antenna design for optimizing the performance of PCBs.

REFERENCES

1. Montrose, M. I., *EMC and the Printed Circuit Board: Design, Theory, and Layout Made Simple*, IEEE Press, Wiley-Interscience, New York, 1998.
2. Pan. W., D. Pommerenke, S. Xu, and J. Jia, "PCB ground fill design guidelines for radiated EMI," *IEEE International Symposium on Electromagnetic Compatibility, 2008. EMC 2008*, Nos. 18–22, 1–6, Aug. 2008.
3. Lee, D.-H., Y.-S. Shin, C.-G. Kim, J.-H. Song, J.-K. Wee, J.-M. Lee, and J.-S. Seol, "Design of multiple power domains based on ground separation technique for low-noise and small-size module," *2012 Asia-Pacific Symposium on Electromagnetic Compatibility (APEMC)*, 805–808, May 21–24, 2012.
4. Damnjanovic, M. S., L. D. Zivanov, A. M. Maric, G. J. Radosavljevic, A. B. Menicanin, N. V. Blaz, and S. M. Djuric "Characterization of ferrite surface mount bead using S-parameters," *2010 8th International Symposium on Intelligent Systems and Informatics (SISY)*, Nos. 10–11, 357–360, Sep. 2010.

Design, Analysis and Implementation of RF/MMW Passive Circuits for Combining Yagi Antennas Using Mixed-mode *S*-parameters Concept

Hsiao-Bin Liang[1], **Dau-Chyrh Chang**[2], **Cheng-Wei Chen**[1], **and Chih-Ying Lin**[1]

[1]Climax Technology Co., Ltd, Taiwan
[2]Oriental Institute of Technology, Taiwan

Abstract— Two PCB Yagi Uda antennas are combined by power dividers and baluns (balance-to-unbalance) to enhance the radiation angle of a wireless communication system. The passive RF front-end circuits, power divider and balun, are implemented by lumped (SMT device) and distributed (transmission line) architecture then analyzed/characterized by mixed-mode s-parameters. Also, the Yagi antenna, which is implemented by means of differential structure, dipole, is also characterized by mix-mode s-parameter. Finally, the comprehensive performances of Yagi Uda antennas coordinating with lumped and distributed circuits are measured, analyzed and compared.

1. INTRODUCTION

For wireless communication system, the interface circuit design between antenna and RF front-end circuit is essential. Implementing antennas and passive RF/MMW circuits by PCB (printed circuit board) is the most simple and economic way to save BOM (bill-of-materials) then achieve cost-down purpose. However, due to insufficient PCB area and long wavelength of lower frequency band application (such as 868 MHz ISM band with 168 mm wavelength, respect to FR4 PCB with dielectric constant of 4.4), realizing passive RF/MMW circuits by distributed architecture is almost impossible for compact size wireless product design. To this end, the lumped RF/MMW circuits are the area-efficient way to be adopted for this condition. In this paper, the passive RF/MMW circuits, such as power divider and balun, are designed and implemented to combine two Yagi Uda antennas [1] for enhancing the radiation angle of wireless communication system. For convenience, the Yagi antennas combined with distributed and lumped RF/MMW circuits are noted as "Double Yagi" and "Double Yagi_sp" respectively in this paper. The performance of Yagi Uda antennas are measured by fast antenna measurement system, SATIMO. The s-parameters of passive RF/MMW circuits, balun and power divider, are measured by multi-port vector network analyzer, ZVB-4, then characterized and analyzed by mixed-mode s-parameters [2].

2. THE DOUBLE YAGI AND DOUBLE YAGI_SP

In Figure 1, the Double Yagi is designed with two Yagi Uda antennas feeding by baluns respectively and then combined with a power divider. Each Yagi Uda antenna has a driven element (folded dipole), reflector and four directors on the top layer of two-layer stack PCB. The PCB's dielectric constant is 4.4 and thickness is 0.8 mm. The bottom layer of the PCB is its associated ground layer. The RF/MMW circuits, baluns and power divider, are designed by distributed architecture [3] on the top layer. The layout of Double Yagi_sp is shown in Figure 2. The baluns and power divider are designed by lumped architecture [4] and implemented with SMT devices of 0402 size. Due to lumped circuit design, the area of baluns and power divider is substantially reduced then benefiting five directors for Yagi Uda antenna, which is one more than that of Double Yagi under the same PCB area. The SMT devices are mounted on top layer of PCB, the same layer of Yagi Uda antennas. The copper around the SMT devices are defined to be ground plane and connected with bottom layer with drills for averaging ground potential.

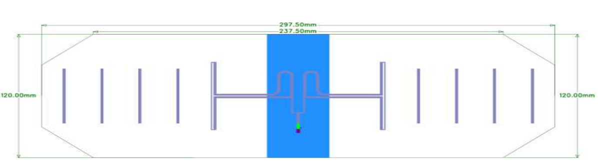

Figure 1: Layout of double Yagi.

Figure 2: Layout of double Yagi_sp.

The two-port s-parameters of Yagi Uda antennas for Double Yagi and Double Yagi_sp are measured by multi-port VNA, R&S ZVB4, then transformed into mixed-mode s-parameters by the equation as [2]:

$$S_{dd11} = \frac{1}{2}\left(S_{11} - S_{12} - S_{21} + S_{22}\right) \tag{1}$$

where the S_{dd11} is the differential input return loss of an Yagi Uda antenna. The setup and measured results for s-parameters are shown in Figure 3. From Figure 3(c), we can obtain that the differential input impedance of the Yagi Uda antenna is roughly around 70 ohm around the operation frequency, 1.9 GHz.

The passive performances (antenna pattern, efficiency and peak gain) of Yagi Uda antennas for Double Yagi and Double Yagi_sp are measured by fast antenna measurement system, SATIMO, which is shown in Figure 4.

3. POWER DIVIDERS AND BALUNS

In order to achieve the purpose of power splitting/combining and differentially feeding interface of folded dipole antenna, designing a RF power divider and two baluns is necessary for this work. The circuit diagram for this purpose is shown in Figure 5. Here, we implemented RF power divider and balun in the form of distributed and lumped architecture for Double Yagi and Double Yagi_sp, respectively.

Figure 6 reveals the implementation and measurement of power divider and baluns by distributed circuit architecture on two-layer FR4 PCB, which consumes PCB area of 50 mm × 35 mm. In the meanwhile, the circuits are also realized in the form of lumped elements. The schematic, photo and measured results are shown in Figure 7. The area of lumped architecture is 5 mm × 10 mm, which is only 1/35 area consumption of distributed one. The insertion loss of power divider coordinating with one balun, that is, the single-to-differential end insertion loss (S_{ds21}) from the RF input to one of the feed-in of folded dipole antenna for distributed and lumped architecture at 1.9 GHz are

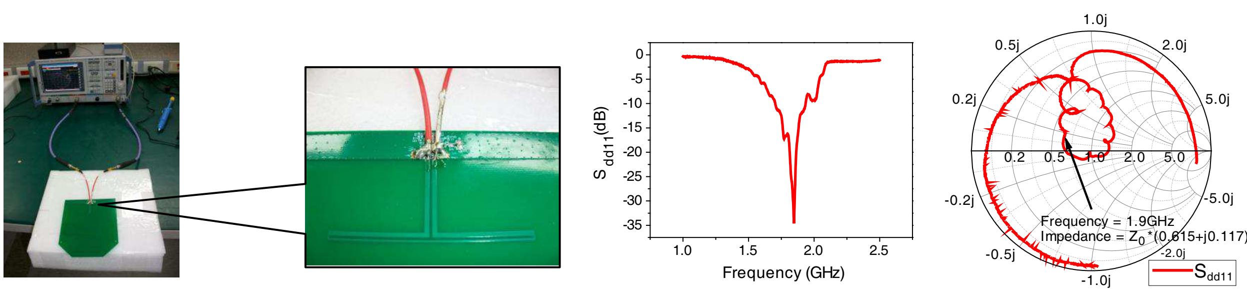

(a) (b) (c)

Figure 3: Mixed-mode s-parameters measurement of Yagi Uda antennas for Double Yagi and Double Yagi_sp. (a) Setup of measurement, (b) the differential input return losses, S_{dd11}, and (c) the differential input impedance respect to normalized differential $Z_0 = 100$ ohm.

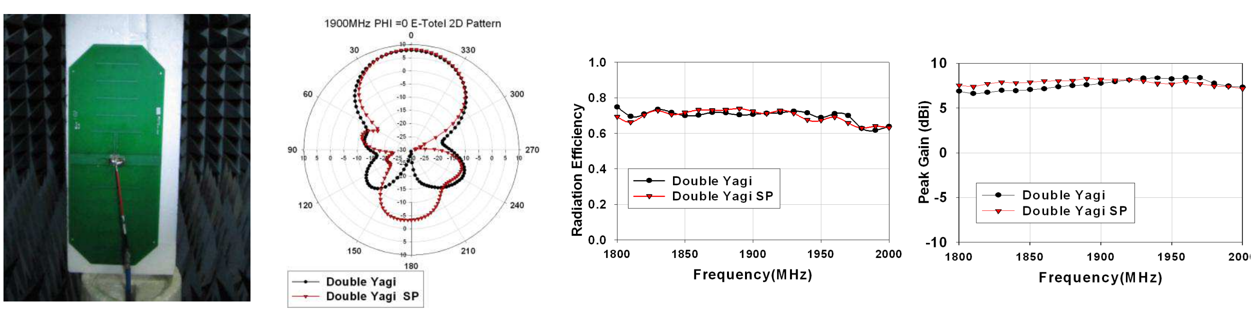

(a) (b) (c) (d)

Figure 4: Passive measurement of Yagi Uda antennas for double Yagi and double Yagi_sp. (a) Setup of antenna measurement in SATIMO system, (b) the measured antenna patterns at 1.9 GHz, (c) efficiencies and (d) peak gains.

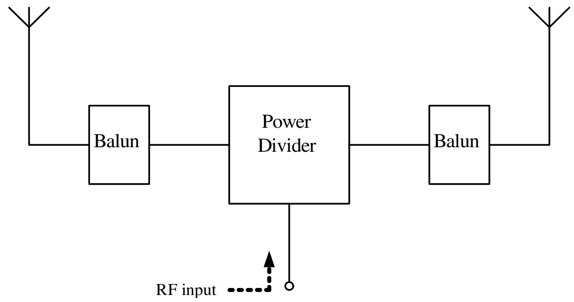

Figure 5: The diagram of the interface between RF input and feed-in of antennas for Double Yagi and Double Yagi_sp.

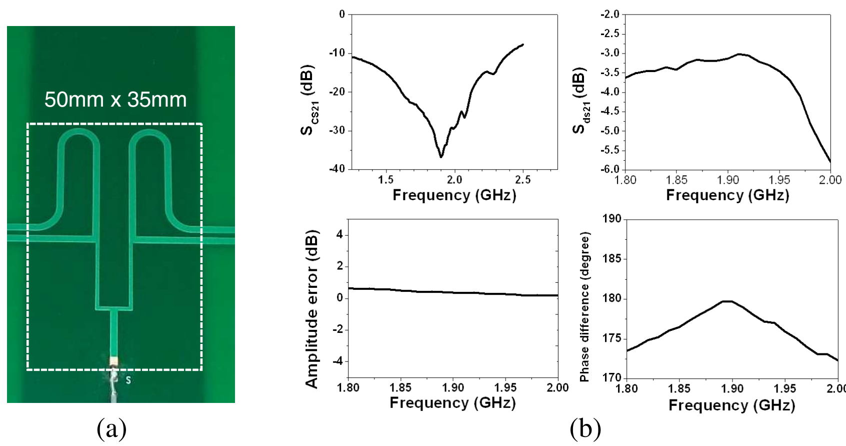

Figure 6: Distributed balun and power divider on a 2-layer FR4 PCB. (a) Photo of PCB and (b) measured results.

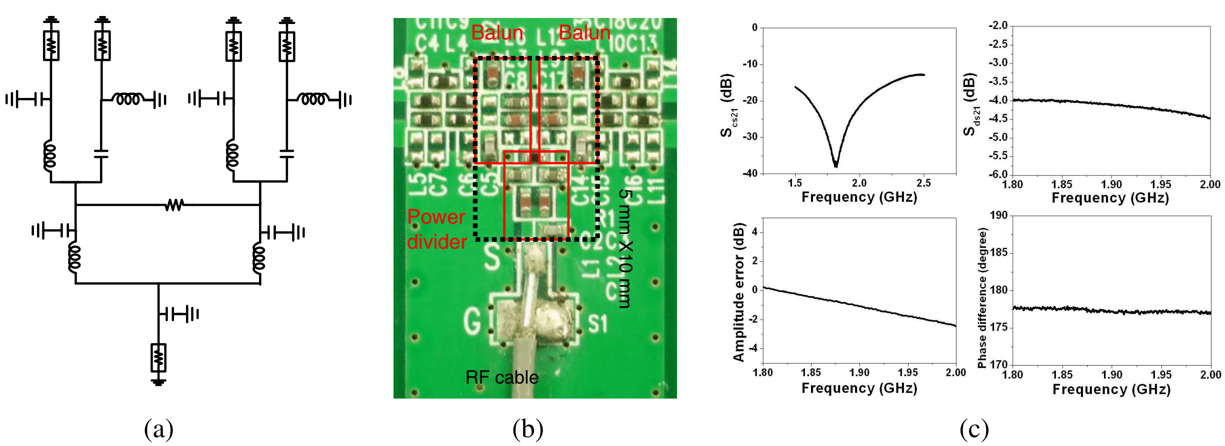

Figure 7: Lumped balun and power divider. (a) Schematic, (b) photo of PCBA and (c) measured results.

0.3 dB and 1.1 dB, respectively. Note that the half power, 3 dB, due to power splitting by power divider should be compensated from the measured results, in Figure 6(b) and Figure 7(c).

4. YAGI ANTENNAS COMBINING WITH DISTRIBUTED AND LUMPED CIRCUITS

The photos of Double Yagi and Double Yagi_SP are shown in Figures 8(a) and (b) respectively. The comprehensive comparison of measured results, radiation pattern, radiation efficiency and peak gain are presented in Figures 8(c), (d) and (e).

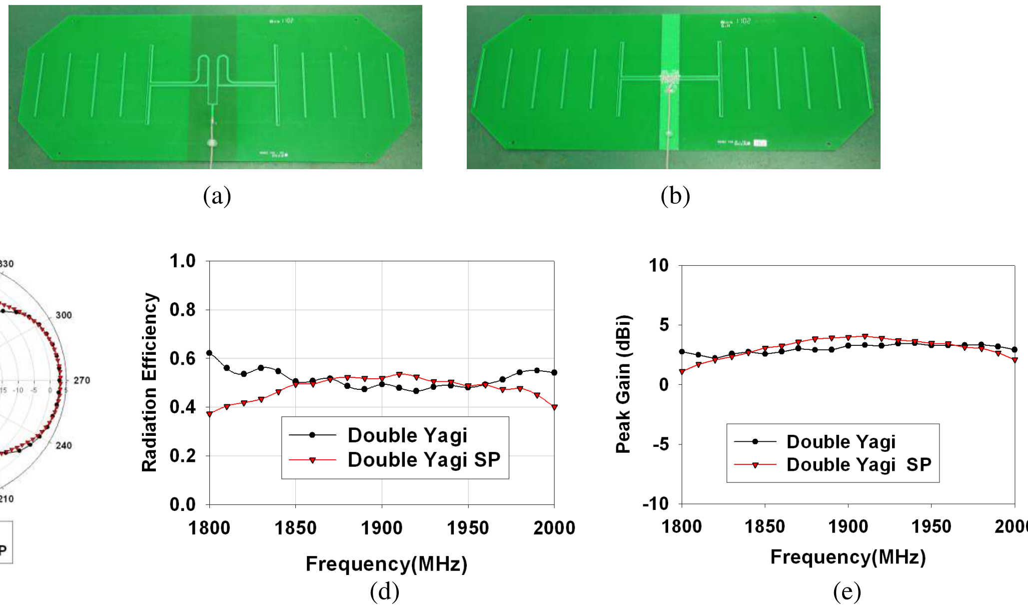

Figure 8: The measured results of double Yagi and double Yagi_sp. (a) PCB photo of double Yagi, (b) PCB photo of Double Yagi_sp, (c) radiation pattern of X-Z plane at 1.9 GHz, (d) efficiency, (e) peak gain.

5. CONCLUSIONS

Yagi Uda antennas are implemented, measured and analyzed by mix-mode s-parameters. The RF/MMW circuits, power divider and balun are also implemented in lumped and distributed architecture then analyzed by mix-mode s-parameters. Finally, the performance of Yagi Uda antennas coordinating with distributed and lumped RF/MMW circuits are measured by SATIMO, fast antenna measurement system, then compared. This work reveals the trade-off among performance, area consumption and BOM (bill-of-materials) cost in RF design, which responses the saying "There is no best, only the most suitable design in RF field".

REFERENCES

1. Kraus, J. D. and R. J. Marhefka, *Antennas for All Applications*, 3rd Edition, Mc Graw Hill, 2003.
2. Willian, R. E., S. Bob, and M. T. Bruce, *Microwave Differential Circuit Design Using Mixed-mode S-parameters*, Artech House, Inc., 2006.
3. Pozar, D. M., *Microwave Engineering*, John Wiley and Sons, Inc., 1998.
4. Bakalski, W., W. Simburger, H. Knapp, H.-D. Wohlmuth, and A. Scholtz, "Lumped and distributed lattice-type LC-baluns," *2002 IEEE MTT-S International Microwave Symposium Digest*, Vol. 1, 209–212, 2002.

A Low Cost Elliptical Dipole Antenna Array for 60 GHz Applications

Jianjun Xu and Weidong Wang
Wireless Information Network Laboratory, University of Science and Technology of China, China

Abstract— A low cost 4×4 elliptical dipole antenna array etching on the double sides of a dielectric substrate working at 60 GHz spectral range is presented in this paper. The feed network of the array consists of an exponentially taperd balun and linerly taperd T-junctions. For the purpose of gain improvement and structure support, a reflect plane is placed $\lambda/4$ away from the substrate and a rohacell foam is sandwiched between the substrate and the reflect plane, also additional metal strips are added to the periphery of the substrate to surpress surface wave and improve the gain slightly. Good agreement is achieved between simulations and measurements. The simulated S_{11} parameter shows the 16 elements antenna array has a bandwith of 57 GHz to 66 GHz with a maximal gain of 19 dBi.

1. INTRODUCTION

As the demand of high speed data transmission increases, attention is transfered to the license free 60 GHz spectrum. Many contries have regulated their own spectral allocation within this frequency range. According to the standard of IEEE 802.15.3C, four channels are distributed among 57–66 GHz and for many contries, there are two channels frequency range (59–63 GHz) overlapped all over the world. Moreover, more and more appilications in this frequency range are emerging. A good example is a wireless local area network with a data rate of 1.5 Gbps which would enable for exmaple a transfer of an uncompressed video signal between a video player and a television. However, the significant oxygen attenuation of signal in this spectral range and broad bandwidth requirement both put forward new chanllenges for antenna design.

Microstrip antenna has so many advantages in wireless communication like low cost, compact, easy to manufacture and so on, that it has attracted many attentions from researchers. Also, many aperture coupled microstrip patch antennas on LTCC process are proposed in recent years [1]. To overcome the inherent disadvantages of narrow bandwith and surface wave loss, many works have been done like taking advantage of stacked patch [2] or opening an air cavity in the multilayer substrates [3, 4]. However, these method always comes to a price that the complexity and fabrication cost rises. In order to design a millmeter antenna with low complexity and cost and meanwhile has the bandwith of over 7 GHz around 60 GHz and an overall gain of more than 15 dBi to fulfill the link demand, a microstrip elliptical dipole antenna array is designed.

2. ANTENNA DESIGN

2.1. Dipole

Compared with classical microstrip patch antennas, dipole is endowed with a broad bandwith [5]. Therefore, the design of a broadband microstrip dipole with relative high gain becomes critical. Among microstip dipole antennas, there are also many different types of it which mainly vary with the shape of radiation element such as circular, elliptical and so on. In this work, elliptical shape is choosen as the basic radiation element since it has two paremeters to adjust comparing with circular shape which only has one paremeter — radius. It's easy to change the resonance frequency by different assignment of the length of the long axis of the ellipse; also, the short axis length has a great effect on the impedance of the dipole and carefull choice can result in a great bandwidth. The proposed microstrip elliptical dipole is shown in Fig. 1.

The antenna comprises of three parts. The first part is a dieletric substrate with metal layer on both sides upon which will the antenna pattern be etched. Although very low thicness dieletric substrate like 5 mil is available in manufacturing market, it is too thin to acomplish the task of support and it requires a very high precision fabrication process. Any deformation or distortion will greatly degrade the performance of the antenna, so an alternative solution — a 10 mil RT5880 ($\varepsilon_r = 2.2$) dieletric substrate with copper foil of 17 µm thickness on both sides is selected to hold the the antenna firmly. The antenna pattern is fabricated on this dieletric substrate with the symmetrical radiating part of the dipole located on different sides of the substrate for the convenience of layout of feed network. The second part of the antenna is a reflect plane located

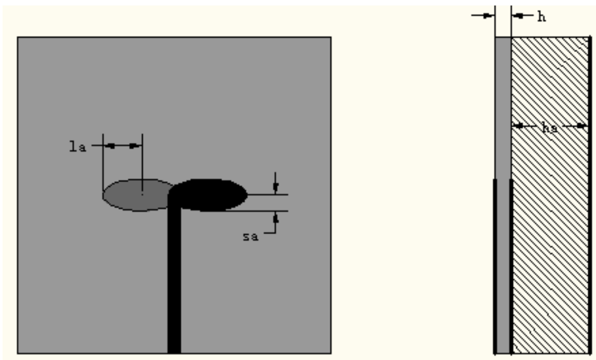

Figure 1: Model of the elliptical dipole.

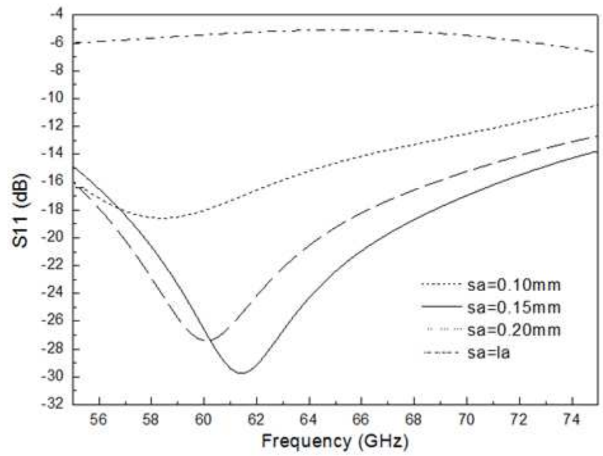

Figure 2: S_{11} parameters of the elliptical dipole with reflect plane.

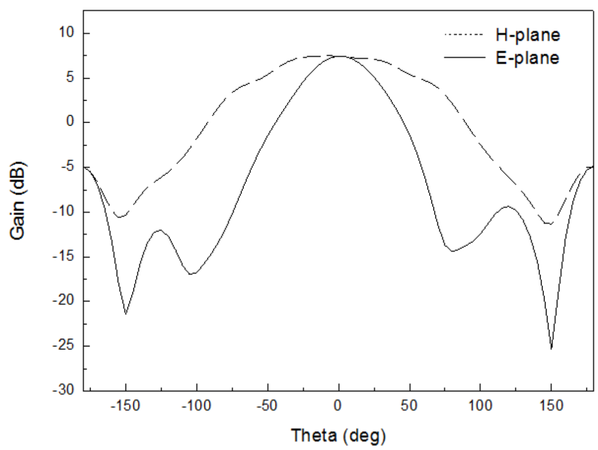

Figure 3: Radiation pattern of the elliptical dipole with reflect plane at 60 GHz.

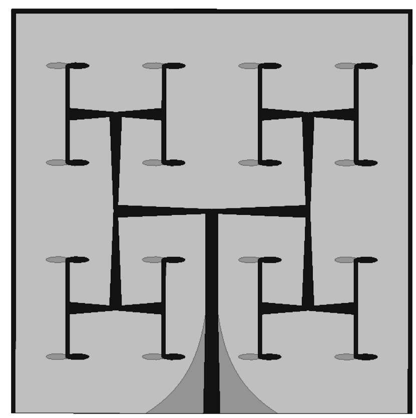

Figure 4: 16 elements antenna array model.

$\lambda/4$ away from the substrate to increase the directivity of the antenna, and the third part of this antenna is a ROHACELL foam with dieletric constant approximating 1 sandwiched between the substrate and the reflect plane.

The key parameters of the dipole are shown in the model. Since the thickness of the substrate and the foam is fixed to $h = 0.254$ mm (10 mil) and $h_a = 1.25$ mm ($\lambda/4$) separately, it is of great importance to adjust sa and la carefully. As has been mentioned above, la mainly determines resonance frequency and sa mainly effects the impedance of the dipole. In the 60 GHz spectral range, arm length of a half wavelength dipole is usually 1.25 mm, so la is assigned to 0.62 mm. In order to achieve a broad bandwidth, different sa ($sa = 0.10$ mm, $sa = 0.15$ mm, $sa = 0.20$ mm, $sa = la$) has been experimented and the result is illustrated in Fig. 2. As shown in the result, when $sa = 0.15$ mm, the antenna has a bandwidth of over 20 GHz (from 55 GHz to 75 GHz).

The simulated radiation pattern of the elliptical dipole is shown in Fig. 3. With a reflect plane, a peak gain of 7.5 dBi is achieved which makes it a good candidate for the configuration of antenna array.

2.2. Antenna Array

To fulfil the specifications of the link budget, the antenna gain has to be increased by placing several dipoles into an array configuration. Based on the link budget calculations for a 60 GHz gigabit link over a short distance [6], it seems that the number of radiating elements in the array should be at least 16 to obtain an adequate antenna gain, of about 15 dBi. With an overall size of 20×20 mm, the proposed 16 elements antenna array model is shown in Fig. 4.

In order to maximize the gain of the array, the distance between the radiation element should be around λ. In this case, the element distance along x axis and y axis is 4.8 mm to achieve the largest gain and relative low sidelobe level.

On the other hand, the overall realized gain of the array is also influenced by the feed loss of the feed network. It has been measured that the conductor loss of the microstrip line is in the order of 1.2 dB/cm at 60 GHz [4]. Therefore, the optimization of the feed network is of great importance. In this work, the feed network accomplish the task of power dividing and impedance match. The feed network consists of several equal power split T junctions where the 75 Ω line splits into two 150 Ω line since the port impedance of the ellipical dipole is 150 Ω.

In order to make the antenna be able to connect to coxial cable, an exponentially taperd balun is designed to transfer the unbalance current of the coxial cable to the balance current of the antenna array. The balun also undertakes the work of impedance matching. At one end of this balun, it's a microstrip line with 50 Ω port impedance, and on the other end, it's a balanced line with 75 Ω port impedance. The simulated result of the balun is displayed in Fig. 5.

From the simulated result of this balun, it can be seen that the balun has a good impedance match and a relative low conductor loss in the whole bandwidth.

3. RESULTS

The simulated S_{11} parameter of this antenna is shown in Fig. 6. From this figure, it can be seen the antenna array matches well among the frequency range of 57–66 GHz. The simulated radiation pattern of this antenna array at 60 GHz is illustrated in Fig. 7 and Fig. 8. It has a narrow beam pointing towards z direction with 15 degree half power beamwidth. Moreover, there is a symmetrical side lobe of less than −10 dB 15 degree apart from the main lobe in E-plane and a very low side lobe in h plane. Although surface wave is very weak compared with microstrip patch antennas,

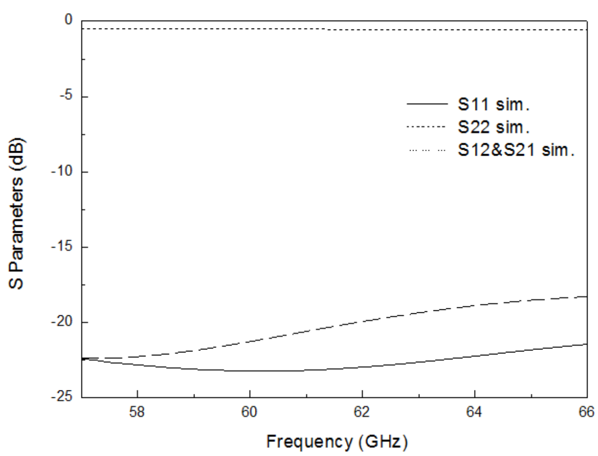

Figure 5: Simulated S parameters of the balun.

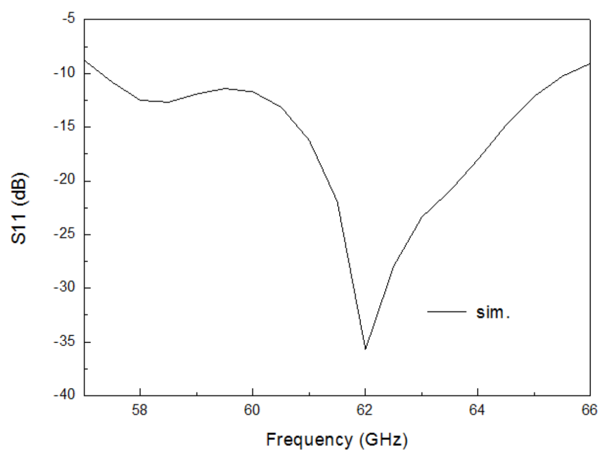

Figure 6: Simulated S_{11} parameter of the antenna array.

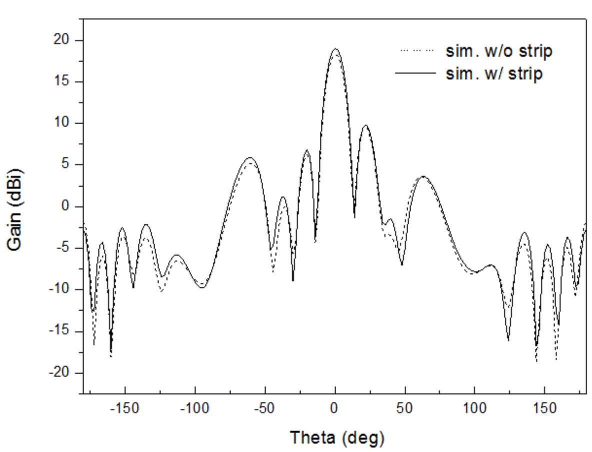

Figure 7: Simulated E-plane radiation pattern of antenna array with and without strip at 60 GHz.

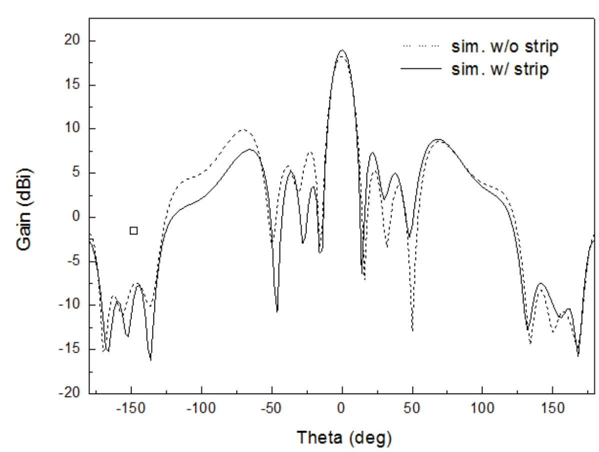

Figure 8: Simulated H-plane radiation pattern of antenna array with and without strip at 60 GHz.

it is unavoidably excited and propagates along the surface of the substrate which will not radiate in the disired direction and will decrease the efficiency of the antenna. Under this consideration, additional metal strips are added to the periphery of the substrate on both sides of it to cut down the propagation of the surface wave. The simulated result that the addition of this metal strip has the effect of slight increase in gain can also be seen in Fig. 7 and Fig. 8.

4. CONCLUSIONS

Microstrip elliptical dipole antenna and 16 elements planar array operating at 60 GHz frequency band have been designed, fabricated and tested. Different shapes of ellipse have been experimented and the result shows that short axis length of ellipse has a great effect on the bandwidth of dipole and should be carefully chosen. The interval distance of array element is optimized to achieve the largest gain and a relative low side lobe level. Moreover, an additional strip is added to the periphery to suppress surface wave effect and increases the gain slightly. All the effort results in a low cost 16 elements microstrip elliptical dipole antenna array with a bandwith of 57 GHz–66 GHz and a maximal gain of 19 dBi.

REFERENCES

1. Yamada, A., Y. Amano, E. Suematsu, and H. Sato, "A patch antenna array on a multi-layered ceramic substrate for 60 GHz applications," *31st European Microwave Conference*, 1–4, Sep. 24–26, 2001.
2. Woojin, B., B.-S. Kim, K.-S. Kim, M.-S. Kang, and M.-S. Song, "60 GHz 2×4 low temperature co-fired ceramic cavity backed array antenna," *IEEE Antennas and Propagation Society International Symposium, 2009, APSURSI '09*, 1–4, Jun. 1–5, 2009.
3. Vettikalladi, H., L. Le Coq, O. Lafond, and M. Himdi, "High-efficient slot-coupled superstrate antenna for 60 GHz WLAN applications," *Proceedings of the Fourth European Conference on Antennas and Propagation (EuCAP)*, 1–5, Apr. 12–16, 2010.
4. Lamminen, A., J. Saily, and A. R. Vimpari, "60-GHz patch antennas and arrays on LTCC with embedded-cavity substrates," *IEEE Transactions on Antennas and Propagation*, Vol. 56, No. 9, 2865–2874, Sep. 2008.
5. Estañ, C., K. Dombrowski, V. Branković, and D. Radović, "Antenna solutions for UWB communication devices in 60 GHz range," *Future Network and Mobile Summit*, 1–8, Jun. 16–18, 2010.
6. Smulders, P., H. Yang, and I. Akkermans, "On the design of low-cost 60-GHz radios for multigigabit-per-second transmission over short distances [Topics in Radio Communications]," *IEEE Communications Magazine*, Vol. 45, No. 12, 44–51, Dec. 2007.

Reconfigurable Monopole Antenna for WLAN/WiMAX Applications

Hashimu Uledi Iddi[1,2], **M. R. Kamarudin**[1], **T. A. Rahman**[1], **and Raimi Dewan**[1]

[1]Wireless Communication Centre (WCC), Faculty of Electrical Engineering
Universiti Teknologi Malaysia, Malaysia
[2]College of Information and Communication Technologies
University of Dar es Salaam, P. O. Box 35131, Dar es Salaam, Tanzania

Abstract— In this paper, a simple reconfigurable monopole antenna for WLAN/WiMAX application is presented. The proposed antenna has been designed and compared to a three patch strips triple band monopole antenna which operate at 2.45 GHz, 3.5 GHz and 5.8 GHz frequency bands. The antenna has been simulated using CST software studio and fabricated on FR4 substrate. The proposed antenna provides triple bands in which the bandwidth of 367 MHz for 2.45 GHz, 799 MHz for 3.5 GHz and a bandwidth of 3.47 GHz for 5.8 GHz has been obtained. The results show that the measured and simulated return loss characteristic of the optimized antenna satisfies the requirement of the 2.4/5.8 GHz WLAN and 3.5 GHz WiMAX antenna application. The proposed reconfigurable antenna is low profile, compact and small in size and show good performance for WLAN/WiMAX bands. There is good agreement between the measurement and simulation results in terms of return loss and radiation pattern.

1. INTRODUCTION

With the current research trends which require more than one wireless application in one device, has increase the demand on the design of multiband and reconfigurable antennas for wireless application. Reconfigurable antennas usually have the capability in which more than one resonance frequency could be achieved. Using switches different shapes of the radiating element can be created to excite different frequencies.

Most of researches in multiband antenna design for wireless communication focused on planar monopole antenna due to its low cost, good radiation pattern and simple in fabrication [1–3]. There are various techniques which are used to design of multi-band antenna for wireless communication application which includes use of different shapes such as E-shape [4], B-shape monopole [5] and use of slot [6].

However, all these techniques used to design dual or multiband antenna can provides fixed frequency characteristics. Therefore, in this paper, a simple reconfigurable monopole antenna has been investigated and compared with the triple band monopole antenna. The proposed reconfigurable antenna is low profile, compact and small in size compared to the conventional triple band monopole antenna and show good performance for WLAN/WiMAX bands. There is good agreement between the measurement and simulation results in terms of return loss and radiation pattern.

2. ANTENNA DESIGN

The geometry and dimension of the proposed antenna is shown in Figures 1(a)–(b). Figure 1(a) and Figure 1(b) show the geometry of the triple-band antenna and reconfigurable antenna respectively. The antenna comprised of copper strip which contribute to the three resonance frequency of the proposed antenna. The antenna has been designed using CST Microwave studio software. The substrate used is FR4 with permittivity of 4.5, loss tangent of 0.019 and thickness of 1.6 mm. It has been observed that the resonance frequency of the proposed antenna is influenced by the copper strip length of the antenna which is approximately quarter wavelength of the operating frequency. In proposed antenna only strip $A \rightarrow B \rightarrow C$ of the triple band antenna has been used to design reconfigurable antenna which is connected by two switches. In simulation copper strip has been used as switch when it is on state and off state when it is ignored. The optimal design of the proposed antenna has small overall dimension of $20 \times 35 \times 1.6\,\mathrm{mm}^3$ for triple band antenna and $15 \times 33 \times 1.6\,\mathrm{mm}^3$ for the reconfigurable antenna. The prototype of the triple-band antenna is shown in Figure 2.

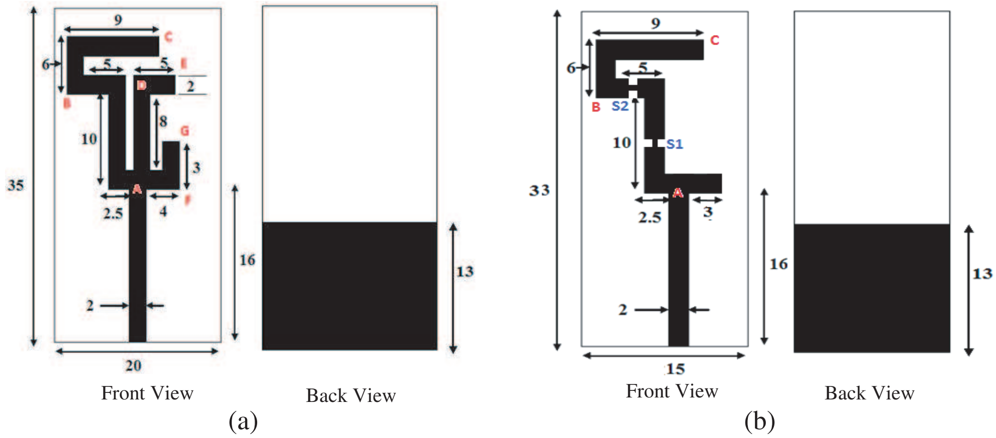

Figure 1: Geometry of (a) triple band monopole antenna and (b) reconfigurable monopole antenna.

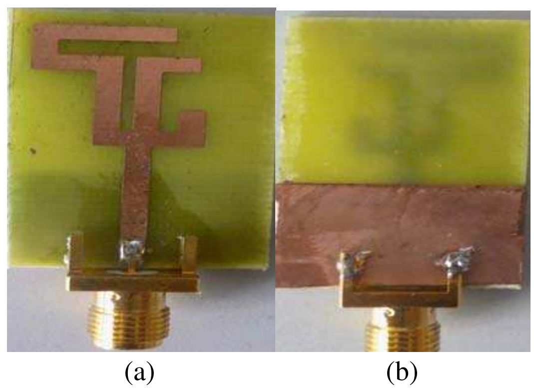

Figure 2: Prototype of triple band monopole antenna. (a) Front view and (b) back view.

3. RESULTS AND DISCUSSION

The reconfigurable monopole antenna has been analyzed and compared to the triple band monopole antenna which provides the same three frequency band. In the triple band antenna analysis, it has been observed that the first resonance frequency is obtained from the patch strip $A \rightarrow B \rightarrow C$ at 2.43 GHz with the return loss value of 15.2 dB. The second resonance frequency is obtained by additional of patch strip at a resonance frequency of 3.52 GHz with the return loss of 23.7 dB and the third resonance frequency is obtained by the strip $A \rightarrow F \rightarrow G$ at 5.8 GHz with the return loss value of 18.65 dB. The proposed reconfigurable monopole antenna is constructed based on the copper strip $A \rightarrow B \rightarrow C$ of the triple band antenna which provides the first resonance frequency. To make it configurable switch 1 and switch 2 has been introduced which make copper strip $A \rightarrow B \rightarrow C$ to be configured to provide additional 3.5 GHz and 5.8 GHz resonance frequencies.

Figure 3(a) shows the comparison between the simulated and measured return loss results of the proposed triple band monopole antenna. It can be seen that the measured and simulated return loss characteristic of the optimized antenna are in good agreement and satisfies the requirement of the 2.4/5.8 GHz WLAN and 2.3/3.5 GHz WiMAX antenna application. Figure 3(b) shows the simulated results of the proposed reconfigurable monopole antenna. The result shows different return loss characteristic of the proposed reconfigurable antenna when first when switch 1 is off or both switch 1 (S1) and switch 2 (S2) are ON and secondly, when switch 1 is ON and switch 2 is OFF. As it can be observed from Figure 3(b) when switch 1 is OFF, the antenna provides -10 dB bandwidth of 367 MHz for 2.45 GHz frequency band and when both switch 1 and switch 2 are ON, the proposed antenna provides -10 dB bandwidth of 799 MHz for 3.5 GHz frequency band and a bandwidth of 3.47 GHz for 5.8 GHz frequency band when switch 1 is OFF and switch 2 is ON.

The simulated radiation pattern of the proposed antenna has been analyzed and compared to the triple band monopole antenna. The E-plane and H-plane radiation pattern of the proposed reconfigurable antenna and triple-band monopole antenna at 2.45 GHz, 3.5 GHz and 5.8 GHz of have been investigated. Figure 4 shows the comparison of the E-plane radiation pattern of the proposed

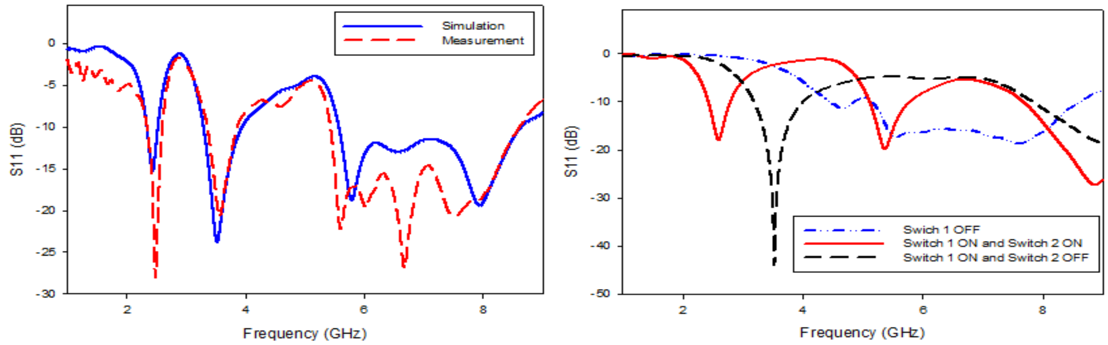

(a) (b)

Figure 3: (a) Measured and simulated return loss of triple band monopole antenna and (b) simulated return loss of reconfigurable antenna for different states of the switches.

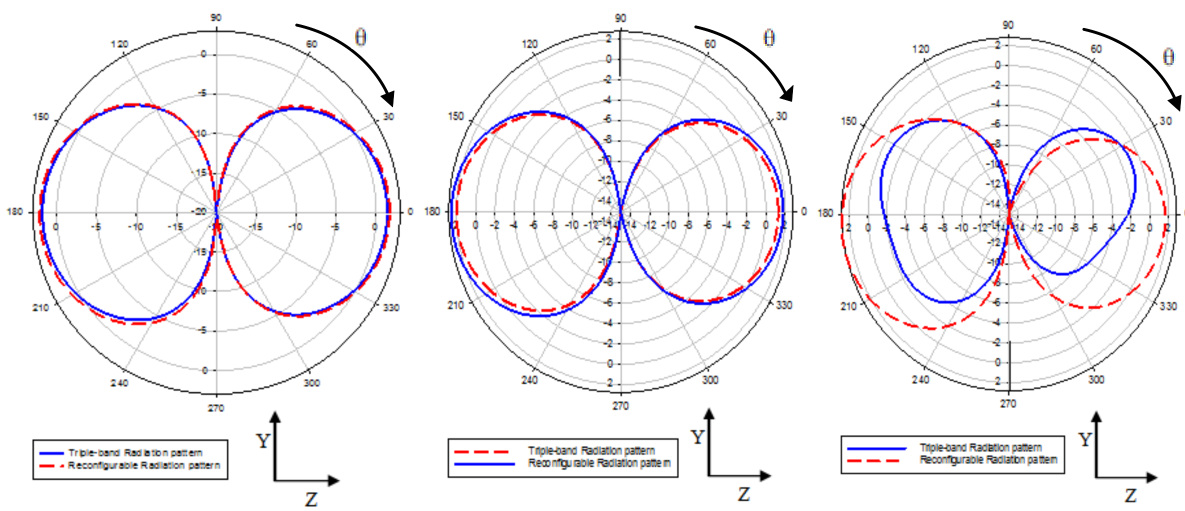

(a) (b) (c)

Figure 4: Comparison of simulated E-plane radiation pattern of the triple-band monopole antenna and proposed reconfigurable antenna at (a) 2.45 GHz, (b) 3.5 GHz, (c) 5.8 GHz.

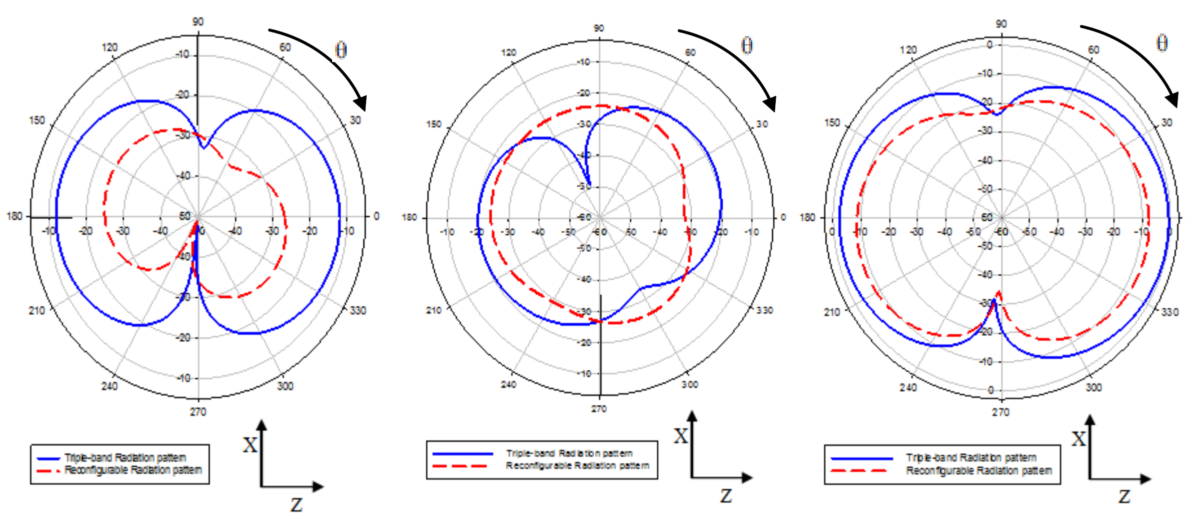

(a) (b) (c)

Figure 5: Comparison of simulated H-plane radiation pattern of the triple-band monopole antenna and proposed reconfigurable antenna at (a) 2.45 GHz, (b) 3.5 GHz, (c) 5.8 GHz.

antenna and triple-band antenna at 2.45 GHz, 3.5 GHz and 5.8 GHz frequency band. It can be seen that the E-plane radiation pattern is bi-directional and similar in shape with exceptional of radiation pattern at 5.8 GHz which have some deviation between the two antenna. Figure 5 shows H-plane radiation pattern at 2.45 GHz, 3.5 GHz and 5.8 GHz frequency bands. It can be seen that H-plane radiation pattern are close to omnidirectional and have similar shape between the two antennas.

4. CONCLUSION

In this paper a simple reconfigurable monopole antenna for WLAN/WiMAX application has been presented and compared with triple band monopole antenna in term return loss and radiation pattern performance. The proposed antenna provides the -10 dB bandwidth of 367 MHz for 2.45 GHz, 799 MHz for 3.5 GHz and a bandwidth of 3.47 GHz for 5.8 GHz which is better compared to that triple band monopole antenna which provides bandwidth of 200 MHz, 640 MHz, and 3.04 GHz for 2.45 GHz, 3.5 GHz and 5.8 GHz respectively. The reconfigurable monopole antenna has reduced size compared to the triple-band monopole antenna; however, the performance of the reconfigurable monopole antenna provides better result in term of return loss and radiation pattern.

ACKNOWLEDGMENT

The authors would like to thank to Ministry of Higher Education (MOHE) and UTM GUP (vote 01H00) and vote 00G36 for sponsoring this work. Besides, thanks to the members of Wireless Communication Center (WCC), UTM for helping and providing resources to enable this work to be completed. Finally, a special thanks goes to University of Dar es Salaam (UDSM) for the scholarship.

REFERENCES

1. Antoniades, M. A. and G. V. Eleftheriades, "A compact monopole antenna with a defected ground plane for multi-band applications," *IEEE Antennas and Propagation Society International Symposium 2008, AP-S 2008*, 2008.
2. Aghda, M. R., M. R. Kamarudin, and H. U. Iddi, "M-shape surrounded with ring patch wideband monopole printed antenna," *Microwave and Optical Technology Letters*, Vol. 54, No. 2, 482–486, 2012.
3. Zhang, G.-M., J.-S. Hong, B.-Z. Wang, Q.-Y. Qin, B. He, and D.-M. Wan, "A novel planar monopole antenna with an H-shaped ground plane for dual-band WLAN applications," *Journal of Electromagnetic Waves and Applications*, Vol. 21, No. 15, 2229–2239, 2007.
4. Jing, S., Y. Yin, A. Sun, Y. Wei, and Y. Yang, "Compact E-shaped monopole antenna for dual-band WLAN applications," *2011 IEEE International Conference on Microwave Technology & Computational Electromagnetics (ICMTCE)*, 2011.
5. Iddi, H. U., M. R. Kamarudin, T. A. Rahman, and R. Dewan, "Design of dual-band B-shaped monopole antenna for MIMO application," *2012 IEEE Antennas and Propagation Society International Symposium (APSURSI)*, 2012.
6. Zhang, S.-M., F.-S. Zhang, W.-M. Li, W.-Z. Li, and H.-Y. Wu, "A multi-band monopole antenna with two different slots for WLAN and WiMAX applications," *Progress In Electromagnetics Research Letters*, Vol. 28, 173–181, 2012.

RF Transmit Performance Comparison for Several MRI Head Arrays at 300 MHz

M. Kozlov and R. Turner
Max Planck Institute for Human Cognitive and Brain Sciences, Leipzig, Germany

Abstract— We numerically investigated several transmit arrays used for magnetic resonance imaging (MRI) at 300 MHz. The array was loaded by a typical human head model. For each array two independent optimization strategies were applied to fine-tune the circuit-level array performance. For excitation in the circular polarization mode, the design of the head array element — whether loop, strip line, or locally shielded microstrip — had no significant impact on entire brain RF inhomogeneity, transmit and safety excitation efficiencies for the entire brain, although magnetic field and SAR profiles vary with element design. Delivery of the maximal fraction of transmit power to the brain ensured the best transmit performance.

1. INTRODUCTION

Despite several optimistic claims that single-row array designs deliver high (or sometimes even optimal) transmit performance for 7 T (300 MHz) magnetic resonance imaging (MRI), there is no consensus why a given design might be better than others. It is difficult to compare literature values for transmit performance, because data for the dependences of the transverse magnetic field magnetic field component with clockwise circular polarization ($\mathbf{B}_1+$) on array transmit power ($\mathbf{P}_{\text{transmit}}$) and array power budget are rarely reported, especially when arrays are loaded by a human subject.

It has recently been shown that the transmit performance of 300 MHz MRI head arrays benefits from a dual-row array configuration, but there is no reliable answer for the question: "What is the optimal design of a radiative element in a dual-row array?". We expect that radiative elements that provide optimal performance in a single row array would also be good candidates for radiative elements in a dual-row array. In previous work we developed a 3D-EM RF circuit co-simulation approach [1] that closely corresponds to the fabrication steps of an MRI array. Our numerical simulation goal in this study was: to compare RF transmit performance data for several single-row head array designs: loops [2] and strip lines [3], and the locally shielded microstrip coil design [4].

For many research and clinical MRI applications so far, the workhorse for driving a multi-channel transmit array has been a single power amplifier, followed by a power splitter and phase shifter. Dual-row arrays can significantly improve $\mathbf{B}_1+$ field homogeneity when circular polarized (CP) excitation is applied to each row, and the two rows are excited with different phases. With this in mind, in the present study we have mainly used the CP excitation mode, with 8 and 16 channel arrays, for which respectively 1.0 or 0.5 W power was applied to each port ($\mathbf{P}_{\text{transmit}} = 8\,\text{W}$), with a sequential 45 or 22.5 degree phase increment. We also explored the effect of global optimization of amplitude and phase for each array element on transmit performance.

2. METHOD

The fundamentals of the RF circuit and 3-D EM co-simulation work-flow have been described in our previous report [1]. The RF circuit simulator was Agilent ADS 2011.10, and Ansoft HFSS 14 was chosen as the 3-D EM tool. The realistic 3-D EM model of the array included the scanner gradient shield (with diameter of 683 mm and length 1200 mm), scanner bore (with diameter of 900 mm and length 3366 mm) and all radiative element construction details, simulated with precise dimensions and material electrical properties. All capacitors, feed and decoupling networks were substituted as 3-D EM lumped ports. This allows different tuning, feeding and decoupling conditions to be studied on base only one multi-port 3-D EM simulation. Neither RF cable traps nor coax cable interconnection wiring were included in the 3-D EM model. Common-current suppression was assumed to be ideal.

The load utilized was the multi-tissue Ansoft human body model, cut in most cases in the middle of the torso, with a scaling factor $X = 0.9$, $Y = 0.9$, $Z = 0.9$ (simulating an average head). The model was placed symmetrically in the array transverse plane. When the radiated power ($\mathbf{P}_{\text{radiated}}$) of an array was higher than 10% of $\mathbf{P}_{\text{transmit}}$, the entire human body model was simulated.

The strip-line array of Adriany [3] was simulated in two modifications: the original design, and one with a local shield of diameter 325 mm and length 250 mm, to check the proposal by Wu [5] for performance improvement.

In the RF circuit domain, substituted components were connected to the corresponding ports of the S-parameter simulation block representing the array 3-D EM model. To obtain values of variable array components — decoupling inductors, tune and match capacitors — we used two circuit-level optimization (fine-tuning) strategies [6]. The first strategy, optimization based on S-parameters, mimics the commonly used tuning during coil fabrication, where capacitive or inductive decoupling networks are used for decoupling adjacent elements. Set of optimization criteria was defined (at the desired frequency F_{MRI}) as: a) the actual reflection coefficient ($\mathbf{S}_{xx}$) must be less than a target value $\mathbf{S}_{xx\_t}$, for each array element; b) the actual coupling coefficient ($\mathbf{S}_{xy}$) must be less than a target value $\mathbf{S}_{xy\_t}$, for each adjacent element. Hence an error or cost function (EF), which was minimized, was

$$EF = \sum_{xx\_i=1}^{Ne} \mathbf{w}_{xx\_i} \left|\mathbf{S}_{xx\_i} - \mathbf{S}_{xx\_t}\right|^2 + \sum_{xy\_i=1}^{Ndp} \mathbf{w}_{xy\_i} \left|\mathbf{S}_{xy\_i} - \mathbf{S}_{xy\_t}\right|^2 \tag{1}$$

where: $\mathbf{w}_{xx\_i}$ — weighting factor for the reflection coefficient $\mathbf{S}_{xx\_i}$ of the individual array element "i", $\mathbf{w}_{xy\_i}$ — weighting factor for the reflection coefficient $\mathbf{S}_{xy\_i}$ of the "i" decoupled pair of array elements, Ne — number of array elements, Ndp — number of array element decoupled pairs.

The second strategy, optimization based on the power reflected by the entire array ($\mathbf{P}_{\text{array\_refl}}$), minimized $\mathbf{P}_{\text{array\_refl}}$ with no dedicated decoupling network for CP excitation mode. Here EF was defined as

$$EF = \left|\mathbf{P}_{\text{array\_refl}}\right|^2 \tag{2}$$

We use the following abbreviations for array configurations: "**Pm**" denotes an array without decoupling network when optimization based on $\mathbf{P}_{\text{array\_refl}}$ was applied, "**ID**" denotes an array with inductive decoupling network when optimization based on S-parameters was applied, "**CD**" denotes an array with capacitive decoupling network when optimization based on S-parameters was applied.

After each co-simulation, the electrical (**E**) and magnetic (**H**) fields (on an equidistant 1 mm mesh) for all independently excited radiative elements were exported from HFSS to temporary ASCII files, and then converted into files in Matlab format. The spatial-average 10-gram specific absorption rate ($\mathbf{SAR}_{10g}$) was calculated using an in-house MATLAB procedure, developed consistently with the draft IEEE/IEC 62704-1 and validated by means of an IEEE TC 34 interlab comparison study [7].

The results reported were obtained under the following conditions: a) the values of the fixed capacitors were not limited to the commercially available range, b) zero tolerance in component values was assumed, c) circuit-level optimization reached global minimum.

For each array and tuning arrangement we analyzed quantities related to the power budget, obtained by direct calculation from volume and surface loss densities or wave quantities: a) $\mathbf{P}_{\text{array\_refl}}$; b) $\mathbf{P}_{\text{radiated}}$; c) $\mathbf{P}_{\text{array\_internal}}$, the inherent coil losses produced by lossy lumped elements (e.g., capacitors and inductors), dielectrics, and conductors; and d) $\mathbf{P}_{\text{load}}$ the power absorbed by the entire load.

The entire human brain was defined as the volume of interest (**VOI**). Array transmit properties were evaluated by considering the values of a) $\mathbf{B}_1{+}_V$, $\mathbf{B}_1+$ averaged over the brain, and its root-mean-square inhomogeneity ($\mathbf{IB}_1{+}_V$ evaluated as a percentage "%"); b) $\mathbf{B}_1{+}_V/\sqrt{\mathbf{P}_{\text{transmit}}}$, array transmit performance; c) $\mathbf{P}_V$, the power deposited in the **VOI**; d) $\mathbf{E}_V{=}\mathbf{B}_1{+}_V/\sqrt{\mathbf{P}_V}$, the **VOI** excitation efficiency; e) $\mathbf{SAR}_{10g}$, the peak SAR averaged over 10 gram; and f) $\mathbf{B}_{V\_sar}{=}\mathbf{B}_1{+}_V/\sqrt{\mathbf{SAR}_{10g}}$, the safety excitation efficiency.

$\mathbf{IB}_1{+}_V$ global optima, which were constrained by a set of $\mathbf{B}_1{+}_V$, were evaluated by a Matlab procedure based on the "patternsearch" function that forms part of the Matlab Global Optimization Toolbox™. It should be noted that no proof was obtained that a global optimum was reached for a given $\mathbf{B}_1{+}_V$. Global optimum conditions were evaluated for two cases: a) the power delivered to each array element was fixed and only excitation phase values were optimized. This case mimicked excitation of an array by a single power amplifier followed by a power splitter and phase shifters; b) all values of power and phase were optimized, in this case mimicking excitation of an array by independent power amplifiers.

3. RESULTS AND DISCUSSION

For "**ID**" and "**CD**" arrays the magnitude of all values of $\mathbf{S}_{xx}$ and $\mathbf{S}_{xy}$ was lower than -20 dB and -15 dB, respectively. In contrast, "**Pm**" arrays exhibited high coupling between coil elements, and pure $\mathbf{S}_{xx}$ matching. But for this method of tuning, the maximum current in the radiative elements occurred exactly at the MRI resonance frequency, and transmit performance was close to optimal for the CP excitation mode (Table 1).

The distance between head model and all the arrays investigated was more than 10 mm. Detailed analysis of electrical field showed that the non-conservative electrical field dominated for all these arrays.

For all arrays investigated, with CP excitation there was no striking difference in $\mathbf{B}_1+$ distribution within the central transverse slice, when the data were rescaled to the maximum value calculated in the brain (Figs. 2 and 3). The simulated central transverse slice and whole brain inhomogeneity also varied only slightly (Table 1).

On the basis of the $\mathbf{B}_1+$ slice profiles for single channel excitation, it would be hard to predict the nearly equal shape and homogeneity of $\mathbf{B}_1+$ over the central transverse slice (Figs. 1 and 2) and the entire brain for "**Pm**", "**CD**", and "**ID**" loop arrays. For single channel excitation of "**Pm**" arrays, the currents through the radiative elements and correspondently $\mathbf{B}_1+_V$ were both very small, because about 70% of $\mathbf{P}_{\text{transmit}}$ was then reflected. However, with CP excitation of "**Pm**" arrays, $\mathbf{B}_1+_V$ was higher than $\mathbf{B}_1+_V$ obtained with either "**CD**" or "**ID**" arrays. The reason for this phenomenon is the high level of constructive **H** and **E** field interference found with CP excitation of "**Pm**" arrays. **E** and **B** fields can be independently constructive and destructive at the same point in space, but on average — averaging the field interference over the entire human brain — both fields are consistent: high **B** field constructive interference coincides with high **E** field constructive interference.

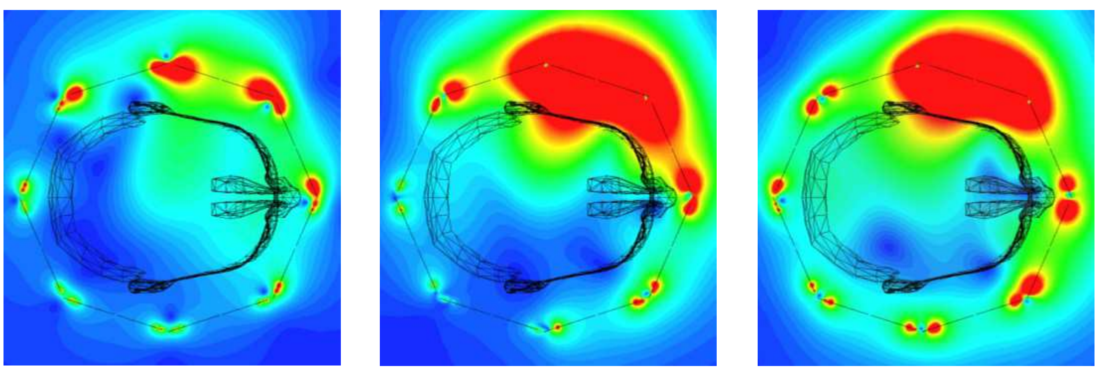

(a) (b) (c)

Figure 1: Loop array single element excitation. $\mathbf{B}_1+$ slices rescaled to individual maximum: (a) "**Pm**", (b) "**CD**", and (c) "**ID**".

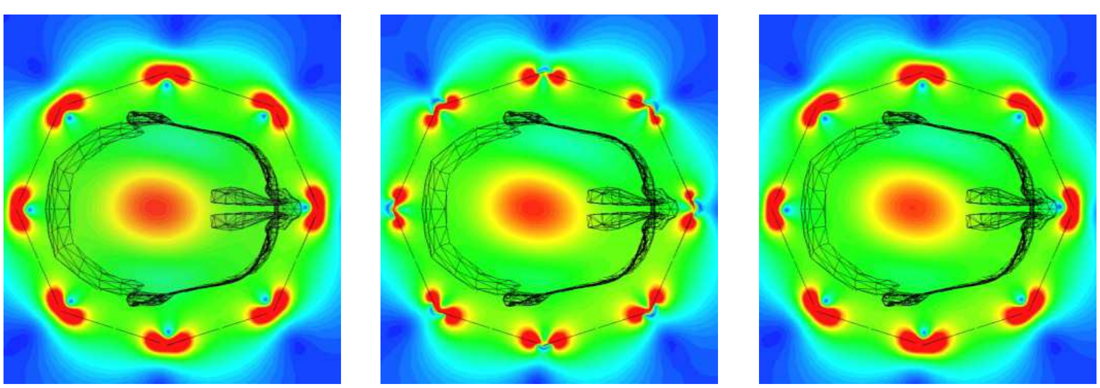

(a) (b) (c)

Figure 2: Loop array CP mode excitation. $\mathbf{B}_1+$ slices rescaled to individual maximum: (a) "**Pm**", (b) "**CD**", and (c) "**ID**".

(a) (b)

Figure 3: 16 element stripline. $\mathbf{B}_1+$ slices rescaled to individual maximum.

Table 1: Simulation data for $\mathbf{P}_{\text{transmit}} = 8\,\text{W}$.

Design	microstrip "Pm"	microstrip coil original	16 element stripline "CD"	16 element stripline "CD" shielded	8 element Loop "Pm"	8 element Loop "ID"	8 element loop shielded "Pm"	8 element loop shielded "ID"
$\mathbf{P}_{\text{array\_refl}}$, W	0.05	3.8	0.6	0.39	0	0.56	0	0.25
$\mathbf{P}_{\text{radiated}}$, W	0.25	0.12	2.33	0.44	0.63	0.82	0.07	0.08
$\mathbf{P}_{\text{array\_internal}}$, W	2.06	1.12	1.39	1.49	0.21	0.25	0.34	0.42
$\mathbf{P}_{\text{load}}$, W	5.64	2.96	3.68	5.67	7.16	6.37	7.59	7.25
$\mathbf{P}_{\text{V}}$, W	1.89	1.01	0.93	1.82	2.67	2.40	2.78	2.65
$\mathbf{B}_1+_{\text{V}}$, μT	1.29	0.93	0.96	1.29	1.57	1.48	1.62	1.58
$\mathbf{SAR}_{10\text{g}}$, W/kg	2.84	1.70	1.64	3.3	4.07	4.09	4.54	4.44
$\mathbf{B}_1+_{\text{V}}/\sqrt{\mathbf{P}_{\text{transmit}}}$, μT/√W	0.46	0.33	0.34	0.45	0.55	0.52	0.57	0.56
$\mathbf{E}_{\text{V}}$, μT/√W	0.94	0.93	0.99	0.95	0.96	0.95	0.97	0.97
$\mathbf{B}_{1\text{V}}$ sar, μT/√(W/kg)	0.77	0.72	0.75	0.71	0.77	0.73	0.76	0.75

The results presented in Table 1 were obtained for the conditions that the Q factor of all capacitors is equal 1000, and the inductor is simulated as lossless. When the capacitor Q factor was decreased, and inductor losses were included, $\mathbf{B}_1+_V$ was reduced and $\mathbf{P}_{\text{array\_internal}}$ was increased. Variation of the losses in decoupling networks and capacitors (for example due to use of a capacitor with another Q factor) had a significant influence on the second adjacent element coupling (consequently on $\mathbf{P}_{\text{array\_refl}}$) and these losses become dominant in high current (high loaded Q) designs, which finally results in relative low transmit performance, estimated as $\mathbf{B}_1+_V/\sqrt{\ }\mathbf{P}_{\text{transmit}}$. However, this did not have a significant impact on the homogeneity over the entire brain and the mean ratios $\mathbf{B}_1+_V/\sqrt{\mathbf{P}_V}$ and $\mathbf{B}_1+_V/\sqrt{\mathbf{SAR}_{10g}}$.

Although the variability of the entire array performance (estimated as the ratio $\mathbf{B}_1+_V/\sqrt{\ }\mathbf{P}_{\text{transmit}}$) was more than 72% (peak to peak) for all arrays analyzed, the ratio of $\mathbf{B}_1+_V/\sqrt{\mathbf{P}_V}$ was equal to $0.96\,\mu\text{T}/\sqrt{\text{W}}$, with only $+/-4\%$ variation. The ratio $\mathbf{B}_1+_V/\sqrt{\mathbf{SAR}_{10g}}$ also varied only slightly. Assuming ideal common current suppression, the local shield improved strip based array performance mainly because it simultaneously reduced $\mathbf{P}_{\text{radiated}}$ significantly (from 29% to 6% of $\mathbf{P}_{\text{transmit}}$), and increased both $\mathbf{P}_{load}$ and the ratio $\mathbf{P}_V/\mathbf{P}_{load}$ (from 25% to 32%). For a loop array the influence of the local shield on transmit performance was negligible for the "Pm" condition, because any reduction of the relatively small $\mathbf{P}_{\text{radiated}}$ (8% of $\mathbf{P}_{\text{transmit}}$) was accompanied by an increase of $\mathbf{P}_{\text{array\_internal}}$ and a slight decrease of the ratio $\mathbf{P}_V/\mathbf{P}_{load}$ from 37.3% to 36.6%. Addition of the shield barely affects $\mathbf{P}_V$. For the "ID" arrangement, the shield improves $\mathbf{B}_1+_V/\sqrt{\mathbf{P}_{transmit}}$ by 8%, because use of the shield reduced not only $\mathbf{P}_{\text{radiated}}$ but also $\mathbf{P}_{\text{reflected}}$.

When the "patternsearch" procedure was applied for "**ID**" and "**CD**" arrays and all values of power and phase were optimized, reduction of $\mathbf{IB}_1+_V$ for a given $\mathbf{B}_1+_V$, which was obtained for CP excitation, was minimal (less than 10%). When $\mathbf{B}_1+_V$ was constrained to attain a value after optimization, defined to be greater than its value for CP excitation, there were solutions where $\mathbf{B}_1+_V$ was increased by about 6% and $\mathbf{IB}_1+_V$ was unaffected. Thus, for the array investigated, the global optimization of amplitude and phase for each array element resulted in a very narrow trade-off for $\mathbf{B}_1+_V$ and its homogeneity.

4. CONCLUSIONS

For CP mode excitation of the entire brain, the dominance of non-conservative fields and delivery of the maximal fraction of transmit power to the brain ensure the best transmit performance, estimated as $\mathbf{B}_1+_{\text{brain}}/\sqrt{\mathbf{P}_{\text{transmit}}}$. Changes in array geometry and different array circuit-level performance optimizations have a very weak influence on the mean (integrated) ratios $\mathbf{B}_1+_{\text{brain}}/\sqrt{\mathbf{P}_{\text{brain}}}$ and $\mathbf{B}_1+_{\text{brain}}/\sqrt{\mathbf{SAR}_{10g}}$, although the $\mathbf{B}_1+_{\text{brain}}$ and SAR profiles vary. For comparisons of array transmit performance and SAR obtained by numerical simulation, consideration of both $\mathbf{P}_{\text{reflected}}$ and $\mathbf{P}_{\text{array\_internal}}$ is very important, because $\mathbf{P}_{\text{reflected}}+\mathbf{P}_{\text{array\_internal}}$ can be as great as 37% of $\mathbf{P}_{\text{transmit}}$ for arrays investigated. Manual tuning of a fabricated array is non-ideal. Analysis of near-field transmit properties, obtained for numerical tuning conditions similar to that of a constructed array, is important in order to conclude that an array is robust. Final decisions regarding coil design should include consideration of these factors.

REFERENCES

1. Kozlov, M. and R. Turner, "Fast MRI coil analysis based on 3-D electromagnetic and RF circuit co-simulation," *J. Magn. Reson.*, Vol. 200, 147–152, Sep. 2009.
2. Kozlov, M. and R. Turner, "Comprehensive analysis of transmit performance for an 8-element loop MRI RF coil at 300 MHz," *Proceedings of the 40th European Microwave Conference*, 328–331, Paris, France, 2010.
3. Adriany, G., P. F. van de Moortele, J. Ritter, S. Moeller, E. J. Auerbach, C. Akgün, C. J. Snyder, T. Vaughan, and K. Ugurbil, "A geometrically adjustable 16-channel transmit/receive transmission line array for improved RF efficiency and parallel imaging performance at 7 Tesla," *Magn. Reson. Med.*, Vol. 59, No. 3, 590–597, 2008.
4. Weisser, A. and T. Lanz, "A volume head array with 8 transmit/receive channels for 7 T," *Proceedings of the 14th ISMRM*, 2591, Seattle, Washington, USA, 2006.
5. Wu, B., C. Wang, D. A. Kelley, D. Xu, D. B. Vigneron, S. J. Nelson, and X. Zhang, "Shielded microstrip array for 7 T human MR imaging," *IEEE Trans. Med. Imaging.*, Vol. 29, No. 1, 179–184, 2010.
6. Kozlov, M. and R. Turner, "Multi-mode optimization of a near-field array," *Proceedings of the 42nd European Microwave Conference*, 309–212, Amsterdam, The Netherlands, 2012.
7. Monebhurrun, V., Y. Braux, H. Devos, M. Kozlov, W. Simon, and T. Wittig, "An interlaboratory comparison of SAR calculations using a CAD phone: A new step towards standardized procedures," *Proceedings of the BEMS2012*, 315–317, Australia, Jun. 2012.

Pulse Train Distributed Magnetic Field Generated from High Strength Concrete Using Magnetized Olivine Stone Aggregate

K. Mohri[1,4], M. Sasaki[2], T. Uemura[3], Y. Mohri[4], M. Yamada[5], and T. Kato[6]

[1]Nagoya Industrial Science Research Institute (NISRI), Nagoya 464-0819, Japan
[2]Shinchita Concrete Kogyo Corp., (NCC), Chita 478-0041, Japan
[3]Tsuruta Sekizai Corp., Nagoya 456-0024, Japan
[4]MI Institute, Nagoya 468-0028, Japan
[5]Faculty of Science and Technology, Meijo University, Nagoya 468-8502, Japan
[6]Graduate School of Engineering, Nagoya University, Nagoya 464-8603, Japan

Abstract— A new method for production of the high-strength concrete using the magnetized olivine stone as the aggregate is presented, which revealed a compressive strength of around 85 N/mm^2 at 13 weeks measurement. The alternative pulse train distributed magnetic field generated from the high strength concrete increased its density and strength with promotion of the solidification due to a possible inverse magnetostrictive effect of the magnetite, which promoted further the concrete solidification (positive feedback). An example of growth promotion of a plant on the concrete board is shown with the bio-activation magnetic field due to the magneto-protonics principle. The electromagnetic microwave interception efficiency of the high-strength mortar is more than 2 times higher than that of non-magnetized mortar.

1. INTRODUCTION

We report a new method for production of the high-strength concrete with around 85 N/mm^2 (around 8.66 kgf/mm^2) compressive strength at 13 weeks measurement using magnetized olivine stones as the coarse aggregate with the ordinary Portland cement. The strong solidification of the concrete is considered due to a catalytic activity of the free proton generated in the concrete moving water which is relatively suffered with an extremely low frequency (ELF) magnetic field in an alternative pulse train distributed magnetic field (APTD-magnetic field, for short) of the magnetized olivine aggregate stones (the magneto-protonics principle) [1]. We newly found a positive feedback phenomenon of a mutual reinforcement of the surface APTD-magnetic field with increasing of the density and the amplitude and the solidification with increasing the compressive stresses in the concrete. This is considered due to the inverse-magnetostrictive effect of the magnetite having a positive magnetostriction in the olivine stone. A switching phenomenon of the APTD-magnetic field pattern ranging whole area of a concrete rod surface was found with application of an alternate magnetic field at one edge of the rod.

An example of the bio activity effect of the high-strength concrete generating the APTD-magnetic field is shown for earlier growth of three vegetable plants on a concrete board on the basis of the magneto-protonics principle [2, 3], in which the free proton generated in bio-cell water running through the APTD-magnetic field reinforces the production of the adenosine-tri-phosphate (ATP) at the mitochondria.

A thin mortar board made with the ordinary Portland cement and magnetized olivine powder as the fine aggregate showed a high ability of the electromagnetic microwave interception efficiency for around 600 MHz band of 2 times higher than that of conventional non-magnetized mortar.

2. EXPERIMENTS

We have carried out a concrete sample test on January–April, 2012 at the Sinchita-concrete Kogyo Co., Japan (www.aiweb.or.jp/kumiai/C036/ch/sinchita.htm) using four kinds of samples with the concrete ingredients as illustrated in Table 1. Figure 1 represents measured results of the compressive strength of the four kinds of samples A-1, A-2, A-3, and A-4 measured at 1 week (1 W), 4 weeks (4 W), 8 weeks (8 W), and 13 weeks (13 W) using a compressive strength tester (AC-2000S III; TAKES-GROUP LTD., Japan).

Mixing times were 30 seconds for the mortar, and another 80 seconds for the concrete followed with 5 min. for aging. We obtained high values of the compressive strength of 85 N/mm^2 for A-4, and 82 N/mm^2 for A-2 at 13 W measurement, that are around 33% for A-4 and 28 % for A-2 higher than that of the conventional concrete A-1.

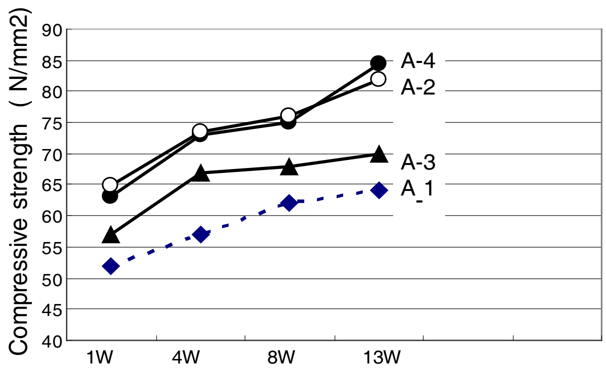

Figure 1: Increasing characteristics of the compressive strength of four kinds concrete samples with time up to 13 weeks: A-1: conventional, A-2: with magnetized aggregate, A-3: with magnetized water, and A-4: with magnetized aggregate and magnetized water.

Table 1: Concrete sample ingredients.

Sample	Water (20°C)	W/C (%)	Cement	Fine Aggregate	Coarse Aggregate	Concrete Mixture
A-1	4.5 kg	30	15 kg	20 kg	25 kg	0.15 kg
A-2	4.5	30	15	20	25 mag-A	0.15
A-3	4.5 mag-w	30	15	20	25	0.15
A-4	4.5 mag-w	30	15	20	25 mag-A	0.15

mag-A: magnetized olivine crashed stone aggregate ($5 \sim 20$ mm length)
mag-w: magnetized tap water with dipped magnetized olivine stones

Conventional static reaction equations for concrete solidification with the hydration:
$2(3CaO \cdot SiO_2) + 6H_2O \rightarrow 3CaO \cdot 2SiO_2 \cdot 3H_2O + 3Ca(OH)_2$
$2(2CaO \cdot SiO_2) + 4H_2O \rightarrow 3CaO \cdot 2SiO_2 + 3Ca(OH)_2$
$3CaO \cdot Al_2O_3 + 6H_2O \rightarrow 3CaO \cdot Al_2O_3 \cdot 6H_2O$
$4CaO \cdot Al_2O_3 \cdot 6H_2O + CaSO_4 + H_2O \rightarrow 3CaO \cdot Al_2O_3 3CaSO_4\ 32H_2O$
$4CaO \cdot Al_2O_3 \cdot Fe_2O_3 + 2Ca(OH)_2 + 10H_2O \rightarrow 3CaO \cdot Al_2O_3 \cdot 6H_2O + 3CaO \cdot Fe_2O_3\ 6H_2O$
should be considered in dynamical sense to be promoted using a hydration energy of the hydrogen-bond energy of a proton (H^+) with around 20 kJ/mol. Therefore, the generation of the free proton in the concrete water due to gathering same sized water clusters $H_3^+O(H_2O)n$ during running through the APTD-magnetic field promotes the concrete solidification.

3. MUTUAL POSITIVE FEEDBACK OF APTD-MAGNETIC FIELD AND SOLIDIFICATION

We found a new phenomenon of a mutual reinforcement of the concrete solidification with time and generation of the concrete surface APTD-magnetic field. Figure 2 illustrates measured results of the APTD-magnetic field generated from a magnetized concrete board of 60 cm length, 18 cm width, and 3 cm thickness made of same ingredients to A-4 in Table 1. Number of pulses increased from 13 at one day to 24 at 7 days that suggested a mutual positive feedback of the reinforcement for the generation of the APTD-magnetic field promoting solidification of the concrete with the free proton and the solidification with increasing the in-plane compressive stresses which reinforce the inverse-magnetostrictive effect for the magnetite in the olivine stones, where the magnetostriction λ of the polycrystalline magnetite (Fe_3O_4) is $\lambda = (2/5)\ \lambda_{100} + (3/5)\ \lambda_{111} = 41\ \times 10^{-6}$ with $\lambda_{100} = -19 \times 10^{-6}$ and $\lambda_{111} = 81 \times 10^{-6}$.

The generation of the APTD-magnetic field is due to the adjacent-magnetization reversal effect among olivine stones having the saturation magnetization Ms of $2 \sim 50$ emu/gr depending on the content rate of Fe_3O_4 (Ms = 0.6 T) and the coercivity Hc of $110 \sim 130$ Oe [1].

Figure 3 illustrates self organization characteristics of the APTD-magnetic field generated from a magnetized concrete bar crammed in a vinyl pipe of 40 cm length and 2 cm diameter.
triggered with a pulse magnetic field Hp at one end of the pipe. Re-self organization of the pulse train distribution occurred through whole range for the pipe with the left edge triggering as shown

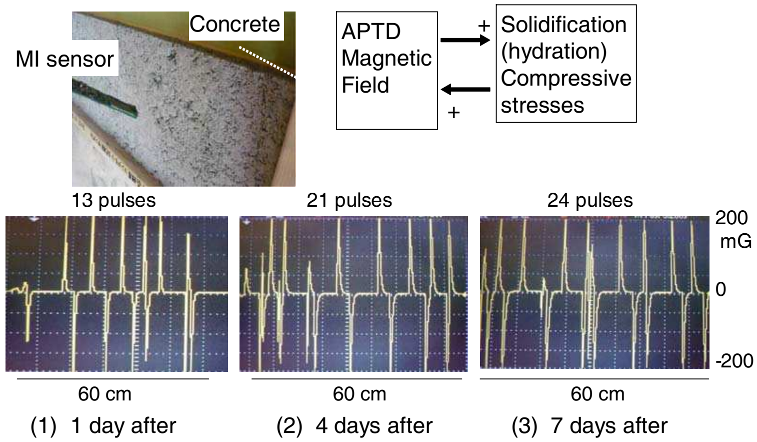

Figure 2: Measured APTD-magnetic field generated from a concrete board of 60 cm length, 18 cm width, and 3 cm thickness made of concrete ingredients same to the A-4 at 1 day after (1), 4 days after in (2), and 7 days after in (3).

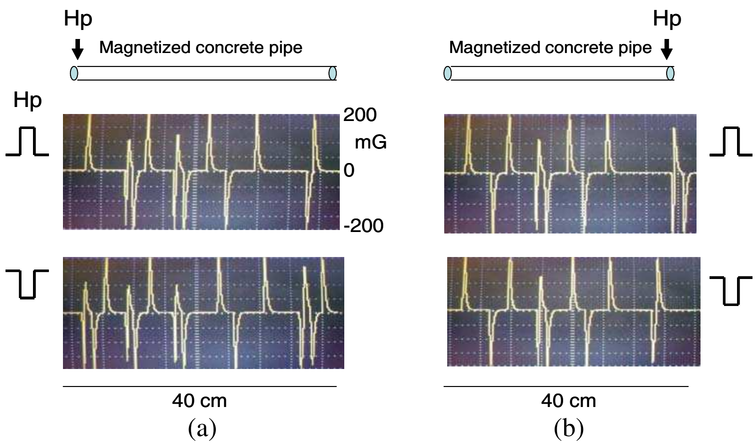

Figure 3: Alternate self organization of the APTD-magnetic field generated from a surface of a magnetized concrete crammed vinyl pipe of 40 cm length and 2 cm diameter triggered with a pulse magnetic field Hp at one end of the pipe: (a) Re-self organization through whole length of the pipe triggered at the left end, and (b) partial re-self organization at the right hand region triggered at the right end.

in (a), while a partial re-self organization occurred at a right hand area with the right edge triggering in (b) probably due to smaller Ms group stones area.

4. BIO ACTIVATION EFFECT OF APTD-MAGNETIC FIELD ON HIGH-STRENGTH CONCRETE

The APTD-magnetic field is useful to promote the production of the bio-cell energy material adenosine-tri-phosphate (ATP) at the mitochondria based on the magneto-protonics principle, in which the free proton H^+ is generated in a bio-water composed of the water cluster $H_3^+O(H_2O)n$, $n = 1, 2, \ldots$ during moving through the APTD-magnetic field (relative an extremely low frequency magnetic field) [2].

Figure 4 represents a photograph of Za-sai vegetable cultivation in which three pot plants on the magnetized high-strength concrete board generating the APTD-magnetic field are growing earlier than that of the reference.

5. ELECTROMAGNETIC WAVE ABSORPTION OF MAGNETIZED MORTAR BOARD

We found electromagnetic microwave absorption characteristics of a magnetized mortar of 4 mm thickness and 100 mm square made of ordinary Portland cement and magnetized olivine powder as illustrated in Figure 5. A microwave (magnetic wave) interception efficiency ability of the magnetized mortar for 600 MHz band showed −5 dB which is 2 times higher due to the vertical-

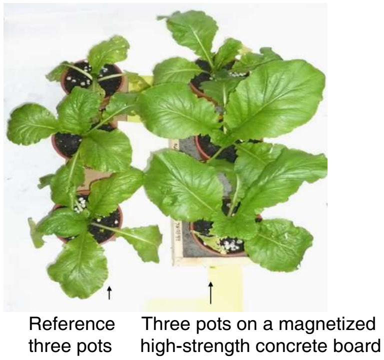

Figure 4: Vegetable plant cultivation on a magnetized high-strength concrete.

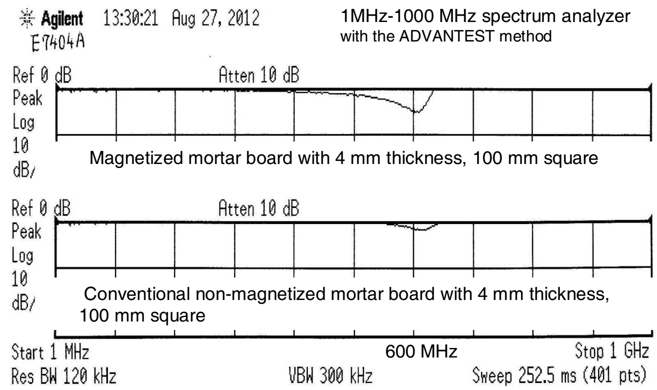

Figure 5: Microwave absorption of a magnetized thin mortar board.

plane magnetization vector precession loss than that of a conventional non-magnetic mortar.

6. CONCLUSIONS

Basic properties of newly developed high-strength concrete and mortar using the magnetized olivine aggregates are presented concerning (1) the compressive strength growth to 85 N/mm^2 and its mechanism based on the magneto-protonics principle, (2) a mutual positive feedback of reinforcing of the concrete solidification with increasing the in-plane compressive stresses and the generation of vertical-plane APTD-magnetic field and its mechanism, (3) self organization phenomena of the APTD-magnetic field generation with a mutual magnetization reversal among the magnetized olivine stones, (4) a bio-activation of a vegetable plant growth promotion on the magnetized concrete board based on the ATP production promotion with the magneto-protonics principle, and (5) a microwave interception efficiency of a thin magnetized mortar with 2 times higher than that of conventional mortar. The new high-strength concrete and mortar are expected to be suitable for contribution to the earthquake-proof and disaster prevention agricultures.

REFERENCES

1. Mohri, K., T. Uchiyama, M. Yamada, T. Watanabe, Y. Inden, T. Kato, and S. Iwata, "Arousal effect of physiological magnetic stimulation on elder person's spine for prevention of drowsiness during car driving," *IEEE Trans. Magn.*, Vol. 47, No. 10, 3066–3069, 2011.
2. Mohri, K. and M. Fukushima, "Milligauss magnetic field triggering reliable self organization of water with long range ordered proton transport through cyclotron resonance," *IEEE Trans. Magn.*, Vol. 39, No. 5, 3328–3330, 2003.
3. Mohri, K., Y. Inden, M. Yamada, and Y. Mohri, "Health recovery effect of physiological magnetic stimulation on elder person's immunity source area with transition of ECG and EEG," *PIERS Proceedings*, 240–244, Kuala Lumpur, Malaysia, Mar. 27–30, 2012.

Arousal Effect of Physiological Magnetic Stimulation on Car Driver's Pit of Stomach Evaluated with Electroencephalogram Using Driving Simulator

Y. Mohri[1], **M. Yamada**[2], **K. Sakai**[2], **W. Kato**[2], **K. Mohri**[3], **and T. Uchiyama**[4]

[1]MI Institute, Nagoya 468-0028, Japan
[2]Faculty of Science & Technology, Meijo University, Nagoya 468-8502, Japan
[3]Nagoya Industrial Science Research Institute (NISRI), Nagoya 464-0819, Japan
[4]Graduate School of Eng., Nagoya University, Nagoya 464-8603, Japan

Abstract— A new effective and safe arousal method is presented for car drivers with application of a physiological magnetic stimulation (PMS) to their pit of the stomach using a magnetic necklace-pendant made of magnetized olivine sintered particles. A relatively large magnetic field generated from the pit of the stomach was detected using the pico-Tesla resolution MI magnetic sensor, which is remarkably changed in the time series pattern with application of the PMS. The arousal effect was evaluated considering a transition of the defined arousal index of $(\alpha+\beta)/(\delta+\theta)$ for detected four points electroencephalogram (EEG) for 8 subjects before and after application of the PMS on a driving simulator. Arousal effect for 15 subjects with the spine PMS was also evaluated.

1. INTRODUCTION

We have reported an effective and safe arousal method for car drivers with a physiological magnetic stimulation (PMS) applying a pulse train distributed static magnetic field generated from a magnetized olivine stone crammed pipe set along their spine [1–3], in which the arousal effect has been evaluated with a defined arousal index $\beta/(\delta+\theta)$ for detected four points electroencephalogram (EEG) on a driving simulator. In this case, we obtained a clear arousal effect for elderly person subjects over 40 ages, whilst results were not so clear for younger generation subjects for the arousal index in the EEG experiments.

We have further found a new special area at the pit of driver's stomach for an effective PMS position considering a relatively large magnetic field generation detected with a pico-Tesla MI magnetic sensor [2]. A clear arousal effect was obtained for 8 person subjects with $20 \sim 72$ ages for a defined arousal index $(\alpha+\beta)/(\delta+\theta)$ for detected four points electroencephalogram (EEG) measured with and without application of the PMS setting a necklace-pendant made of magnetized olivine sintered particles on the pit of their stomach at a driving simulator. A similar arousal effect was also obtained for 15 subjects in the case of PMS setting a magnetized olivine stone crammed pipe fixed in a vest along their spine position.

2. BIO-MAGNETIC FIELD GENERATED FROM PIT OF THE STOMACH

We found that the bio-magnetic field generated from the pit of the stomach (MPG, for short) [2] is an independent magnetic field from the bio-magnetic field generated from the heart (the magneto-cardiogram; MCG) showing different response characteristics for the PMS. Figure 1 illustrates measured results of simultaneous detection of the MCG and the MPG for a 71 age man subject using two pico-Tesla resolution MI magnetic sensors [2]. The subject quietly lies on his stomach on a wooden bed having a slit for setting of two MI sensor heads. A PMS is applied with 10 min. stroking a magnetized olivine stone crammed pipe on his back for fixing two sensing points of the heart and pit of the stomach positions. A remarkable difference of the time series waveform before and after the PMS is observed for the MPG in (b), whilst almost no change for the MCG in (a). Figure 2 represents the FFT frequency spectrum for the MCG and MPG time series illustrated in Figure 1, in which the ratio of the spectrum integration value for the frequency band $3 \sim 13$ Hz after and before the PMS is 0.98 for the MCG, and 1.74 for the MPG. That is, almost no change occurs in the MCG for the PMS.

On the other hand, the MPG sensitively respond to the PMS possibly due to the physiological functions of the aorta and the vein adjusting whole body blood flow, and the celiac plexus adjusting all viscera. Source origin of the MPG is considered due to the ion flow in the smooth muscle organ of the aorta and the vein. The position of the pit of the stomach is called as the middle jiao in

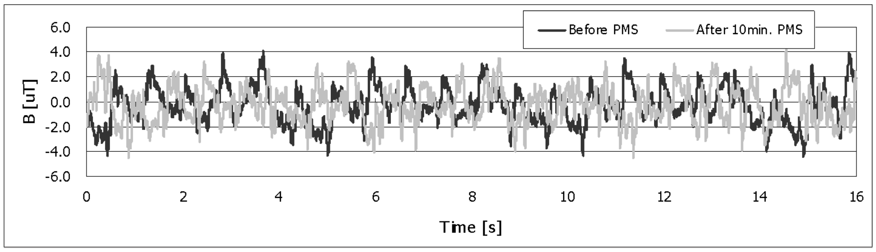

(a) Magneto-cardiogram (MCG)

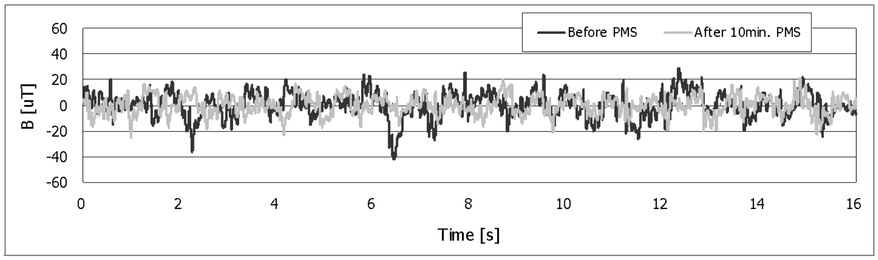

(b) Magneto-pit of the stomach-gram (MPG)

Figure 1: Simultaneously measured MCG and MPG for 71 age man before and after PMS.

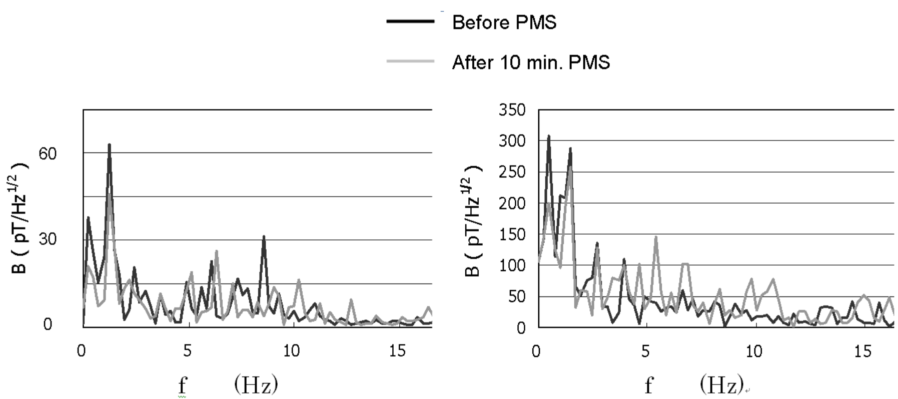

(a) Magneto-cardiogram (b) Magneto-pit of stomach-gram

Figure 2: FFT frequency spectrum of MCG and MPG time series illustrated in Figure 1: (a) for MCG, and (b) for MPG.

the san-jiao (the three heaters in the Chinese medicine). Therefore, we newly choose the pit of the stomach as an important position of the PMS for an effective and safe arousal for car drivers in addition to the spine position.

3. EXPERIMENTAL PROCEDURES

3.1. EEG Measurement Method Concerning Car Driving Behavior

According to the purpose to detect EEG as reflection of car driving behavior concerning the arousal, we adopted a method to measure the EEG at four points of a top head close to the forehead, a right head, a left head, and a back head of a subject with closing eyes due to detect bio signal of both consciousness and unconsciousness just after a driving behavior using the driving simulator considering the afterimage combined with the kinesthetic memory.

Table 1 shows a sequence for each set of driving task followed with EEG measurement for each subject without and under PMS. We set a 10 min. city driving for finding a change in EEG through a careful driving behavior. We also set one time 20-min. highway night driving through simple curved road in which almost all subjects tend to feel sleepy.

Table 1: Sequence for driving task followed with EEG measurements.

I	II		III	
EEG-1 (3 min) (Before driving)	City driving (10 min)	EEG-2 (3 min)	Highway night driving (20 min)	EEG-3 (3 min)

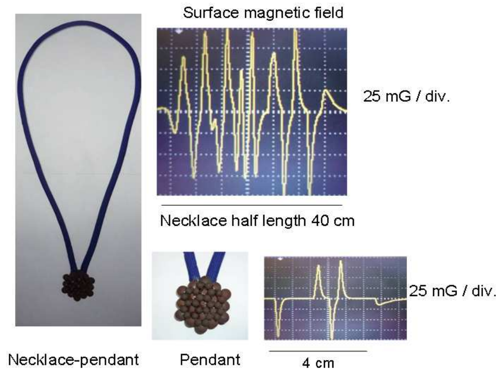

Figure 3: Necklace-pendant generating pulse train distributed surface magnetic field.

3.2. Physiological Magnetic Stimulation Method for Arousal at Pit of the Stomach

There are two main requisite conditions of stimulation for car drivers with effectiveness and safety in non-disturbance for any normal driving ability. Car drivers are simultaneously supported and controlled with two different nervous systems of the cerebral cortex nervous system which operates information processing gathering signals from five sense organs and simultaneously generates command signal for four limbs muscles (consciousness control), while instincts including sleep, arousal, respiration, body temperature, and blood flow are controlled with the brain stem nervous system (unconsciousness control system) affecting the cerebral cortex function as peripheral nerves. And these arousal functions are supported with active blood flow driven with the cell energy ATP in the whole body, in which the shortage of production of the ATP increases the generation of the fatigue materials in the blood vessels inducing the sleepiness. Therefore, we tried to activate a pair of the biggest blood vessels the aorta and the vein in the pit of the stomach. An effective stimulation for arousal should be on the basis of the physiology rather than stimulation for the cerebral cortex with alarm signals such as electronic sound, flash light, and strong smelling perfume spray that often result in dangerous so-called “rebound sleepiness” during car driving. We newly made a necklace-pendant crammed with magnetized olivine sintered particles of around 6 mm diameter as shown in Figure 3. An alternate pulse train distributed surface magnetic field is generated with around 3 cm interval on the necklace, and around 1 cm interval on the pendant. We predict a generation of the free proton in the bio materials and cells such as the blood plasma, hematid, and leucocyte running through the pulse train magnetic field resulting an exposure to an extremely low frequency (ELF) magnetic field due to the magneto-protonics principle [4, 5], in which the ATP production at the mitochondria is reinforced with the proton flow and the bio cells are activated to overcome the driver’s sleepiness. A dummy necklace-pendant with the same size and the same weight is made of non-magnetic particles of Al_2O_3.

3.3. Driving Simulator

We used a driving simulator having a large display showing realistic driving environment with two small displays of a room mirror and a side mirror made by Mitsubishi Precision Co., Japan (D3sim) and set in Meijo University [1, 3]. Driver’s face is monitored by an infrared micro camera system. Four EEG electrode positions are selected considering the relation between driving motion and cerebral functional area such as the motor area, the motor association area, the somatosensory area and the visual association.

4. EXPERIMENTAL RESULTS

We measured a feature of car driving motion in four points EEG measurement for 8 subjects with the magnetized necklace-pendant PMS as shown in Figure 3, and 15 subjects with the magnetized

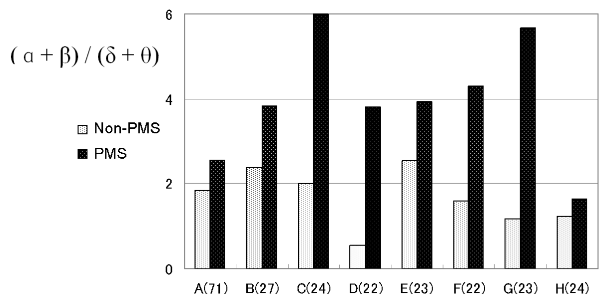

Figure 4: Bar graph of the arousal index $(\alpha+\beta)/(\delta+\theta)$ for 8 subjects for EEG measurements with and without the PMS on the driving simulator.

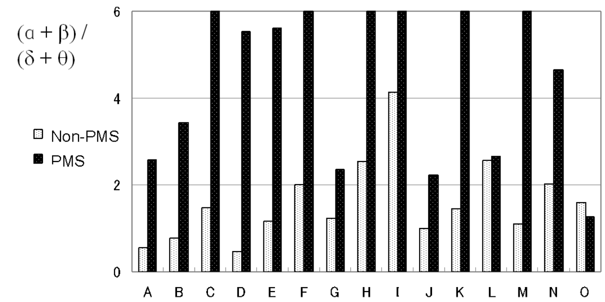

Figure 5: Bar graphs of the arousal index $(\alpha+\beta)/(\delta+\theta)$ for 15 young subjects with and without the PMS for the spine.

pipe PMS [3] on the spine position according to the driving task schedule as illustrated in Table 1. An EEG meter made by Inter Cross Co., Japan; inter cross-410, with the sampling frequency 1000 Hz, and the amplifier gain of 100 is used. We newly defined an arousal index $(\alpha+\beta)/(\delta+\theta)$ instead of the former arousal index $\beta/(\delta+\theta)$ by adding the passive arousal EEG wave α with the active arousal wave β considering an international standard on the arousal in the sleepiness medical treatment on the basis of α wave.

Figure 4 illustrates bar graphs of the analyzed arousal index $(\alpha+\beta)/(\delta+\theta)$ for 8 subjects A(72) to H(24). EEG measurements for each subject were carried out in different two days with one day for the PMS and another day for non-PMS. The subject was announced nothing which necklace-pendant is magnetized or not for the blind test. Remarkable arousal effect was obtained for the all 8 subjects of one elderly man and 7 younger men.

Figure 5 represents bar graphs of the arousal index $(\alpha+\beta)/(\delta+\theta)$ for EEG measurements for 15 young person subjects of 20 to 24 years old with and without the spine PMS using a vest fixing a flexible vinyl pipe crammed with the magnetized olivine particles along the spine position. A dummy vest is made of the Al_2O_3 particles pipe. Each object was announced nothing on which is a magnetized pipe for the blind test.

Remarkable arousal effect was obtained for 13 subjects, a slightly inverse effect was for 1 subject, and a slight effect was for 1 subject. A clear arousal effect was resulted using the vest type PMS tool probably due to a reliable application of the PMS with always fixing to the driver's spine position in stead of setting the magnetized pipe on the driver's seat [1]. A similar bio-activation effect of the PMS at the aorta and vein area would be estimated from both the spine and the pit of the stomach due to the magnetic field influence ranging around 20 cm.

5. CONCLUSIONS

(1) It is considered that a definition of car driver's arousal index using a form $(\alpha+\beta)/(\delta+\theta)$ is reasonable, which matches measured results of four point EEG FFT frequency spectrum to the subjective evaluation.

(2) A relatively large bio-magnetic field (MPG) was detected at the pit of the stomach which sensitively responds to the PMS, while no response occurred in the MCG.

(3) A PMS using a necklace-pendant made of the magnetized olivine sintered particles with setting on the pit of the stomach of car driver is considered to be highly effective and safe to prevent drowsiness during driving.

(4) A new measurement method for the EEG of car drivers with eyes closing and rest just after stopping a car utilizing the afterimage and the kinesthetic memory which produces valuable information of car driver's EEG signal.

(5) A vest type PMS tool with fixing a flexible pipe crammed with magnetized olivine sintered particles along the spine position is reasonable for reliable application of the PMS to driver's spine position.

ACKNOWLEDGMENT

The authors wish to express their gratitude to Mr. M. Matsubara, of Shinko Yogyo Co., Japan for his presentation of the sintered magnetized olivine particles.

REFERENCES

1. Mohri, K., T. Uchiyama, M. Yamada, T. Watanabe, Y. Inden, T. Kato, and S. Iwata, "Arousal effect of physiological magnetic stimulation on elder Person's spine for prevention of drowsiness during car driving," *IEEE Trans. Magn.*, Vol. 47, No. 10, 3066–3069, 2011.
2. Mohri, K., T. Uchiyama, M. Yamada, Y. Mohri, K. Endo, T. Suzuki, and Y. Inden, "Physiological magnetic stimulation for arousal of elderly car driver evaluated with electro-encephalogram and spine magnetic field," *IEEE Trans. Magn.*, Vol. 48, No. 11, 3505–3508, 2012.
3. Mohri, Y., M. Yamada, K. Endo, T. Suzuki, and K. Mohri, "Arousal effect of physiological magnetic stimulation on car driver's spine evaluated with electroencephalogram using driving simulator," *PIERS Proceedings*, 245–249, Kuala Lumpur, Malaysia, Mar. 27–30, 2012.
4. Mohri, K. and M. Fukushima, "Milligauss magnetic field triggering reliable self-organization of water with long range ordered proton transport through cyclotron resonance," *IEEE Trans. Magn.,* Vol. 39, No. 5, 3328–3330, 2003.
5. Mohri, K., Y. Inden, M. Yamada, and Y. Mohri, "Health recovery effect of physiological magnetic stimulation on elder Person's immunity source area with transition of ECG and EEG," *PIERS Proceedings*, 240–244, Kuala Lumpur, Malaysia, Mar. 27–30, 2012.

Speed-feedback, Direct-drive Control of a Low-speed Transverse Flux-type Motor with Large Number of Poles for Ship Propulsion

Y. Yamamoto[1], **T. Nakamura**[2], **Y. Takada**[1], **T. Koseki**[1], **Y. Aoyama**[3], **and Y. Iwaji**[3]

[1]The University of Tokyo, Japan
[2]West Japan Railway Company, Japan
[3]Hitachi Research Laboratory, Hitachi, Ltd., Japan

Abstract— In this paper, direct-drive transverse flux-type motors (TFMs) with large pole numbers have been proposed for electric ship propulsion. The propulsion motors are required for low-speed drive. In speed-feedback control at low-speed region, however, it is difficult to obtain enough speed information from encoder due to its low resolution. Consequently, the stability of the system tends to get remarkably worse. For that reason, Dual Sampling rate Observer (DSO) is applied to the control system to resolve such problem in feedback control. The validity of the proposed system is verified through the comparison of experimental results with/without DSO.

1. INTRODUCTION

Electric propulsion (EP) in marine industry has been developed due to savings in energy and maintenance requirements. Conventional EP systems composed of motors with gearboxes have complicated mechanism and improvement in efficiency and reliability were restrictive. Thus, the direct-drive (DD) motors have been given attention. In order to achieve high torque at low speed, prototype models with large number of poles taking advantage of TFMs, which have controllable pole pitch and are suitable for such application, have been proposed and created.

Basically, control of the motor is consisted of speed feed-back loop using encoder pulse information. In low-speed region, however, the stability of drive system is lost due to insufficient resolution of the encoder. As a solution for this critical problem, we demonstrate the validity of DSO based on simulations and experiments.

2. DETERMINATION OF MOTOR PARAMETERS FOR CONTROL SYSTEM DESIGN

Identification of parameters used in control of the motor is conducted in following steps by finite element analysis (FEA) and experiments. As for FEA, linkage flux in the armature winding with/without current flow is estimated from 3-D numerical study. Then, induced voltage, torque coefficient and inductance are estimated by no-load flux waveform, absolute value and phase difference of flux between no load and load [1].

On the other hand, determination of parameters based on experiments is conducted based on basic theory of synchronous machine. Armature resistance, inductance and coefficient of induced voltage/torque are obtained from DC voltage-drop method, sigle-phase AC static test and no-load test using another motor respectively. Comparison of parameters calculated by FEA and experiments is shown in Table 1. The experimetal values are relatively high compared to FEA values due to dispersion of materials and building factors, but it is practical solution to design control system and estimate characteristic before creating prototype model.

In the following sections, parameters based on experiments are used for design of control systems. Experimental setup in this paper is shown in Figure 1.

Table 1: Comparison of parameters identified by FEA and experiments in the prototype model.

Symbol	Description	FEA	Experiments
R_a	Armature resistance	$7.58\,\Omega$	$8.06\,\Omega$
L_d, L_q	d-axis/q-axis inductance	142 mH	112 mH
K_e	Back EMF coefficient	0.208 Vs/rad	0.191 Vs/rad
K_t	Torque coefficient	5.20 Nm/A	4.76 Nm/A
$2p$	Pole numbers	50 poles	
J_r	Rotor Inertia	0.003261 kgm^2	

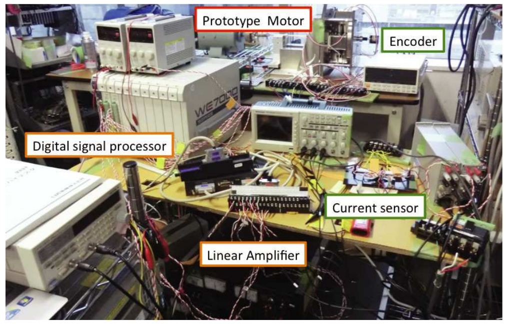

Figure 1: Experimental setup in motor-drive system.

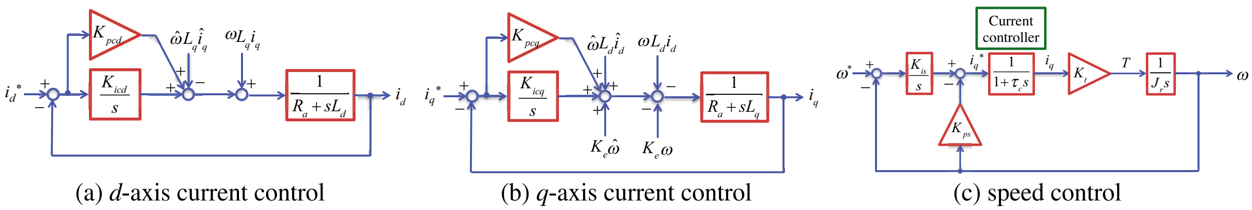

Figure 2: Block diagram in each control system.

3. DESIGN AND TESTS OF CONTROL SYSTEM BY COEFFICIENT DIAGRAM METHOD (CDM)

The design of control system is conducted based on rotational *d*-*q* coordinates. The system is composed of cascade control based on current and speed feed-back control systems on the assumption that each feed-back information is obtained from current sensor or encoder. Current control system is *d*-axis current zero and speed control system is configured by regarding the current control system as first-order lag system by using CDM.

3.1. Determination of Controller Gains in the Feed-back Control System [2]

Current controller is composed of P-I control so that *d*-axis and *q*-axis currents can follow commands for each current. Interference in each axis current is disregarded due to decoupling by feed-forward compensation of reference signals. Speed controller is consisted of I-P control with two feed-back loop by regarding current controller as first-order lag system to realize reduction of overshoot, simultaneously achieve quick response and describe as simple system without zero point. The block diagram of the system is shown in Figure 2. Transfer functions $G_{cm}(s)$ and $G_s(s)$ in the current/speed controller are giving in as Equation (1).

$$G_{cm}(s) = \frac{i_m}{i_m^*} = \frac{1}{K_{icm}} \cdot \frac{K_{icm} + K_{pcm}s}{1+\frac{R_a+K_{pcm}}{K_{icm}}s+\frac{L_m}{K_{icm}}s^2}, \quad G_s(s) = \frac{\omega}{\omega^*} = \frac{1}{1+\frac{K_{ps}}{K_{is}}s+\frac{J_r}{K_tK_{is}}s^2+\frac{J_r\tau_c}{K_tK_{is}}s^3} \tag{1}$$

In Equation (1), index m, i_m, i_m^*, K_{pcm}, K_{icm}, L_m, ω, ω^*, τ_c, K_{ps} and K_{is} represent *d*-axis or *q*-axis physical amount, real current, command of the current, proportional and integral gains of current controller, inductance, electrical angular velocity, command of the angular velocity, equivalent time constant in the current control, proportional and integral gains of speed controller respectively. Kessler method, one of CDMs, is applied to denominator polynomial of the transfer function. Each controller gain is determined as shown in Equation (2).

$$K_{pcm} = \frac{2L_m}{\tau_c} - R_a, \quad K_{icm} = \frac{2L_m}{\tau_c^2}, \quad K_{ps} = \frac{J_r}{2K_t\tau_c}, \quad K_{is} = \frac{J_r}{8K_t\tau_c^2} \tag{2}$$

where, equivalent time constant in the speed control is four times of that in the current control. Each gain is determined as shown in Table 2 by above procedure. In ideal differential of deviation, however, control system is easy to become unstable due to excessive amplification of high frequency component and insufficient energy in pulse output when the deviation causes change like step input. Therefore, lagged derivative is applied to the system. Furthermore, the system is composed of digital control, so transformation from continuous system to discrete system is conducted by first approximation of Taylor's expansion of Z-transform.

Table 2: Controller gains in cascade control system detected by Kessler method.

Parameters	Current Controller	Speed Controller
Proportional gain	$K_{pc} = 8.06$	$K_{ps} = 0.0246$
Integral gain	$K_{ic} = 1160$	$K_{is} = 0.443$
Equivalent time constant	$\tau_c = 13.9$ msec.	$\tau_s = 55.6$ msec.
Control period	$T_s = 0.100$ msec.	

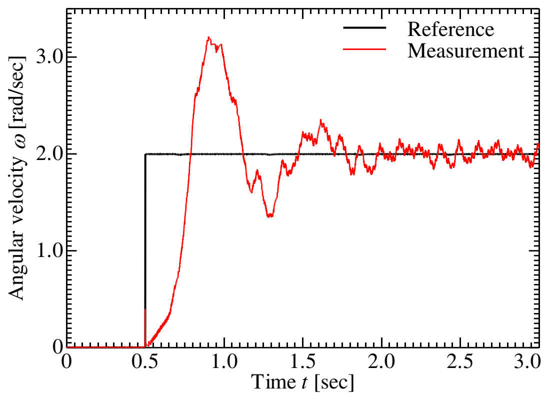

Figure 3: Response with feed-forward (FF) compensation.

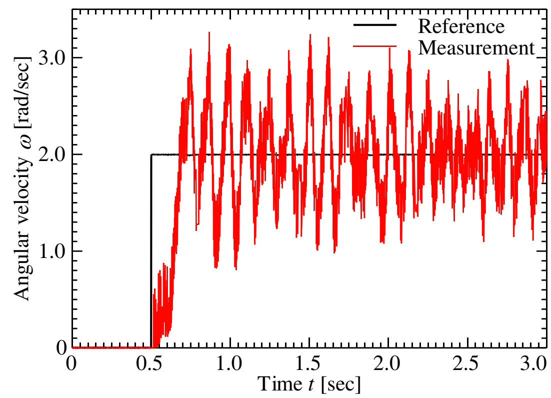

Figure 4: Response without FF compensation.

3.2. Inspection of Control System Based on CDM through Experiments

Figure 3 shows system response when the speed signal is calculated by lagged derivative. The speed signal follows the command, however steady-state characteristics including setting time and overshoot are poor. As shown in Table 1, the number of poles is fifty so that the motor requires high torque at low speed. On the other hand, resolution of encoder is limited due to its number of pulse per revolution. As a result, reliability of control using speed calculated from finite difference of encoder pulse might decrease due to its insufficient information in low speed region. In the control using only feed-back loop, speed signal fluctuates vigorously as shown in Figure 4 for a long period of time. Thus, feed-forward compensation contributes to reduction of oscillation in steady state to a certain extent as shown in Figure 3. In order to improve low-speed drive control, however, it is essential to apply additional solution.

4. DESIGN AND VERIFICATION OF CONTROL SYSTEM USING DSO THROUGH THE TESTS

In Section 3, it is impossible to estimate speed by difference method in every control period in low speed region, resulting in lost of stability of control system due to insufficient encorder pulse. Consequently, we use DSO which has the potential to realize low-speed drive without changing any hardware. Its objective is to give controller position and speed in such low speed region by both state estimation with model of controlled object and correcting error of the estimation in obtaing pulse information.

4.1. Determination of Observer Gain in Current-type DSO [3, 4]

Position θ, angular velocity ω from encorder and disturbance torque T_d are chosen as state variables and a state equation is described. After that, it is necessary to convert to discrete system in order to conduct online calculation by a computer [5]. Current-type DSO, one of derivation of the current-type observer, is consisted of encoder pulse cycle T_1, control period T_2 and an iteger N defined as ratio of T_1 to T_2 as shown in Figure 5.

When $T_1 < T_2$, DSO operates as the usual current-type observer with discrete cycle T_2. Otherwise, DSO is operated at following two manners. In only any one time per N samples, state estimation is corrected by real output value. In another case ($N - 1$ samples), state estimation is conducted by using one earlier estimated values and input values. Consequently, DSO is expected to make determination of observer gains easier as well as to correct current state estimate by error calculated in current sample.

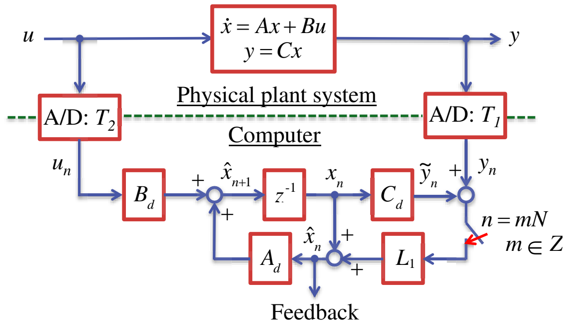

Figure 5: Configuration of Current-type DSO.

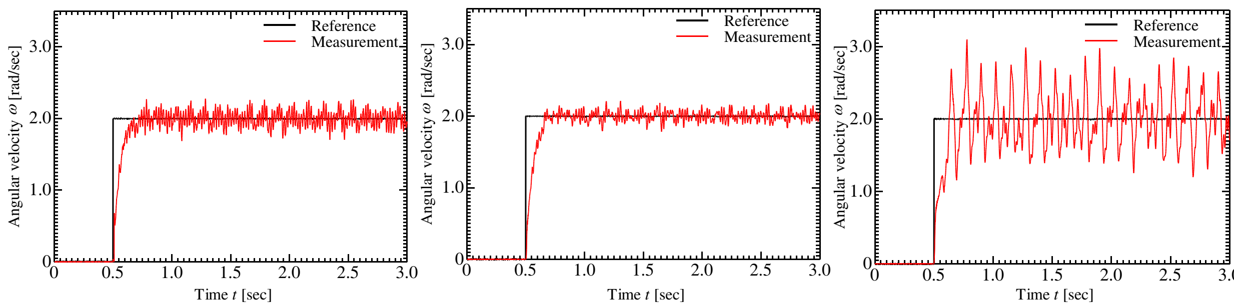

(a) τ_{ob} =4.0 msec. (b) τ_{ob} =8.0 msec. (c) τ_{ob} =20.0 msec.

Figure 6: Response with DSO.

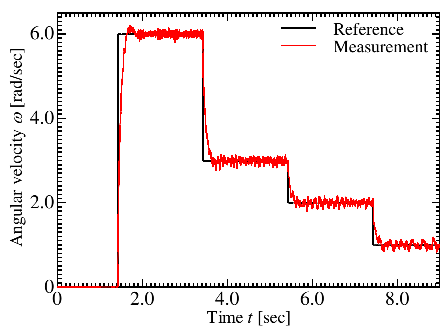

Figure 7: Variable speed control with DSO.

The observer gains of DSO are determined based on period of encorder pulse T_1, but it is difficult to predict appropriate pole assignment in discrete Z plane. In this paper, appropriate obserber gains in Z plane are obtained by converting poles s_i $(i = 1 \sim 3)$ as fixed with CDM in Section 3. The observer gain matrix L_1 is designed so as to fulfill characteristic equation under absolute value of all poles in Z plane of less than 1 in Equations (3) and (2).

$$\det\left[zI - \{A_d - L_1 C_d A_d\}\right] = 0, \quad |z| < 1 \tag{3}$$

$$L_1 = \begin{bmatrix} l_1 \\ l_2 \\ l_3 \end{bmatrix} = \begin{bmatrix} -e^{-4T_1/\tau_c} + 1 \\ \frac{1}{2T_1}\left[3\left(e^{-4T_1/\tau_c} + 1\right) - 2\left\{\left(e^{-3T_1/\tau_c} + e^{-T_1/\tau_c}\right)\cos\left(\sqrt{3}T_1/\tau_c\right) + e^{-2T_1/\tau_c}\right\}\right] \\ -\frac{J_r}{T_1^2}\left(e^{-2T_1/\tau_c} - 1\right)\left\{e^{-2T_1/\tau_c} + 1 - 2e^{-T_1/\tau_c}\cos\left(\sqrt{3}T_1/\tau_c\right)\right\} \end{bmatrix} \tag{4}$$

4.2. Observations on Applicability of DSO through the Experiments

It is important to choose equivalent time constant of DSO. In short time constant, effect of correction on position signal increases and estimation works well for disturbance due to its large gains. On the other hand, in long time constant, the gains are small and the effect of correction is poor. Moreover, it is sensitive to noise, error, disturbance and variation of parameters, so we decide the gains through the experiments. Time constant of observer τ_{ob} is chosen as 8.0 msec, which gives low fluctuation and relatively good response in the tests as shown in Figure 6.

The validity of DSO for variable speed control is verified at low speed as well as high speed as shown in Figure 7. DSO is one of the effective solutions for motor called for low-speed drive by only changing software without adding special hardware.

5. CONCLUSION

A systematic method to determine controller gains in cascade control based on CDM and observer gains in DSO has been described. The observer gains of DSO can be obtained easily by converting appropriate poles in s plane. The application of the proposed DSO has solved the problem of instability caused by coarse encoder pulsed in low speed drive, which often occurs in low speed direct drive motors with large number of poles.

ACKNOWLEDGMENT

We would like to thank the members of Hitachi Research Laboratory for their technical advice and supprt of this research and those of MT Drive, ACM and Shin-Etsu Chemical for manufacturing the experimental machine.

REFERENCES

1. Morimoto, S., Y. Takeda, and T. Hirasa, "Parameter measurement of PM motor in dq equivalent circuit," *IEEJ Trans. Industry Applications*, Vol. 113, No. 11, 1330–1331, 1993.
2. Manabe, S., "Application of coefficient diagram method to dual-control-surface missile," *15th IFAC Symposium on Automatic Control in Aerospace*, 499–504, 2001.
3. Yusuke, K. and Y. Hori, "Instantaneous speed observer with improved disturbance rejection performance based on higher order dynamics," *IEEJ Trans. Industry Applications*, Vol. 112, No. 6, 539–544, 1992.
4. Lilit, K. and T. Koseki, "Precise speed estimation from a low-resolution encoder by dual-sampling-rate observer," *IEEE/ASME Trans. Mechatronics*, Vol. 11, No. 6, 661–670, 2006.
5. Farzad, N. and M. Gene, *Digital Control Using Digital Signal Processing*, Prentice Hall, Inc., PTR, 1999.
6. Nakamura, T., T. Koseki, and Y. Aoyama, "A low-speed high-torque permanent magnet synchronous motor — Reducing cogging torque and eddy current loss," *Journal JSAEM*, Vol. 20, No. 2, 410–415, 2012.

A 2.4 GHz Array Combination High-power Amplifier

Chien-Hua Lai and Jeng-Rern Yang
Microwave Laboratory, Department of Communication Engineering
Yuan Ze University, Jhongli City, Taoyuan Country 320, Taiwan

Abstract— The purpose of this study was to design a 2.4 GHz class-A RF power amplifier following the Taiwan Semiconductor Manufacturing Company (TSMC)'s 0.18 μm Process. A high-pass filter was employed for front-end matching, and a load-pull method was used for back-end matching. Matching design was conducted for a 2.4 GHz band. The output power of this power amplifier design was 2.6 dBm. The $P_{1\,dB}$ compression point was 16 dBm, the power-added efficiency (PAE) was 18.4%, and the power-gain was 11 dB. For an overall supply voltage of 3.1 V, the overall power consumption was approximately 1.8 mW. The area of the chip was approximately 0.63 mm × 1.3 mm, achieving front-end and back-end matching.

1. INTRODUCTION

With the rapid growth in wireless technology, demand exists for endless highpower transceivers to achieve low-cost, low-power applications that enhance system functions. In radio frequency (RF) systems, the power amplifier is the key circuit that receives conversion mixer signals; therefore, a highefficiency RF power amplifier is crucial for saving power consumption. Gradually, 4G LTE has become mainstream for mobile broadband, and RF power transmitters are a key component of mobile broadband devices. Therefore, determining how to use RF CMOS technology to achieve a highpower, highperformance transmitter is a crucial issue to the development of mobile communication technology. In this section, this study proposes a circuit that is a highly linear, low-voltage, high-gain, amplifier array system fully-integrated, bias classification A, 2.4 GHz design band power amplifier that can be applied to an LTE system (700 MHz to 2.7 GHz). The circuit was designed for fully integrated power amplifiers. To prevent the problems of an excessively large area created in the past when excessive inductance of power transmitter circuits was used to achieve the desired watt level, this study employed a side-by-side array, combining the electrical currents gathered in the amplifiers and using the positive and negative signal conversion between the n-channel metal-oxide semiconductors (NMOS) and p-channel metal-oxide semiconductors (PMOS) to save driver area. With this method the entire area used is smaller than the combined area of traditional power amplifiers.

2. CIRCUIT TOPOLOGY AND ANALYSIS

2.1. The Main Schematic of the PA

The main circuit schematic and structure is shown in Figure 1. The input side is a high-pass filter with a parallel capacitor and inductor. In the middle section or intermediate stage, an array with multiple NMOS and PMOS is used to collect the electrical current after signal conversion. For the output side, a Balun transformer is employed to output the collected electrical current at high power.

In this circuit, C1 and L1 represented the high-pass filter combination Twelve NMOS and PMOS in the middle array were employed for a total of 24 MOS electrical current collectors; a

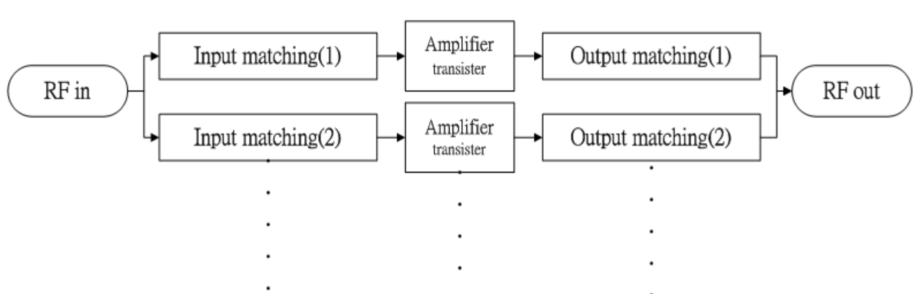

Figure 1: Traditional circuit.

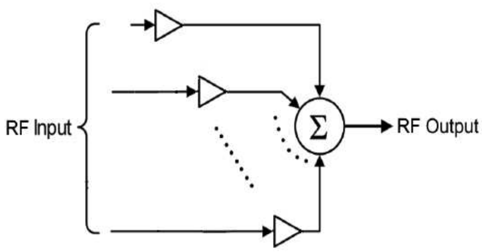

Figure 2: Conceptual structure.

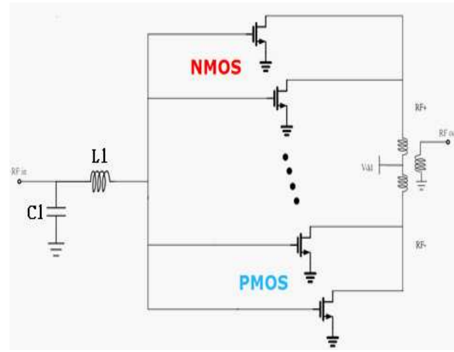

Figure 3: Primary circuit.

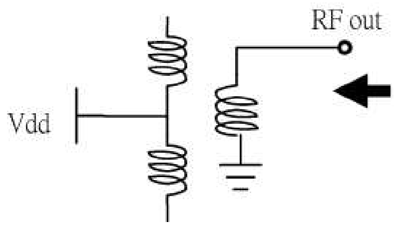

Figure 4: Output inductor central tap.

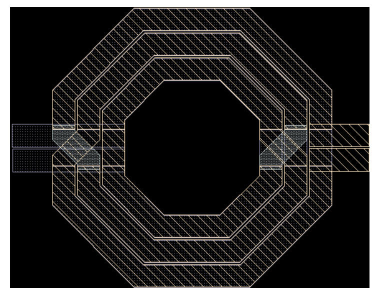

Figure 5: Free-coil inductor.

Table 1: Primary parameters of the free-coil inductor.

Frequency (GHz)	Inductance (nH)	Q
2.4	0.33	2.5

Table 2: Secondary parameters of the free-coil inductor.

Frequency (GHz)	Inductance (nH)	Q
2.4	3.02	10.05

Balun transformer wrapped in two metal layers was used on the back end; and 3.1 V of bias was added to the central tap.

2.2. Input Matching Circuit

The input matching circuit comprised inductor L1, capacitor C1, and Cgs and achieved a 2.4 GHz matching frequency. The input impedance expression shows the following:

$$Z_{\text{in}}=\frac{1}{\text{SC}_1}//\left\{\text{SL}_1+\left\{\left[\frac{1}{\text{SC}_{\text{gsn1}}}//\frac{1}{\text{SC}_{\text{gsn2}}}//\frac{1}{\text{SC}_{\text{gsn3}}}//\dots\right]//\left[\frac{1}{\text{SC}_{\text{gsp1}}}//\frac{1}{\text{SC}_{\text{gsp2}}}//\frac{1}{\text{SC}_{\text{gsp3}}}//\dots\right]\right\}\right\}$$

After simplification, the actual matching part was $50\,\Omega$, the virtual matching part was 0, and the same results were produced with minimal fine-tuning, verifying the feasibility of the front matching circuit.

2.3. Amplifier Circuit

The circuit was designed as a classA power amplifier. To satisfy the bias control and transistor voltage swing crash limitations for class-A, the NMOS transistors and PMOS gate terminal bias were at the appropriate positions, the drain terminal bias was at 3.1 V, and each group of transistors consumed 28.3 mA of electrical current. Additionally, the transistor array arrangement was divided into upper and lower circuits to reduce the load carried by the transmission line regarding current. This circuit design used ADS software to simulate the transistor output power and corresponding efficiency and to identify the point of resistance that could achieve the optimal power output and efficiency. The resulting system was then used to design the power amplifier.

Table 3: Performance summary and comparison to other wideband 0.18 mm CMOS LNAS.

	Simulation
VDD (V)	3.1
Total current (mA)	602
Frequency (GHz)	2.4
S_{11} (dB)	−18.7
S_{21} (dB)	11
Output Power (dBm)	26
MAX PAE (%)	18.4

Figure 6: Output power.

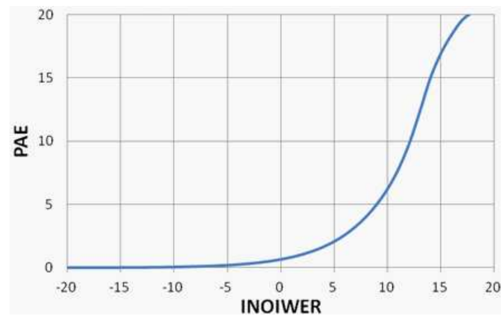

Figure 7: PAE.

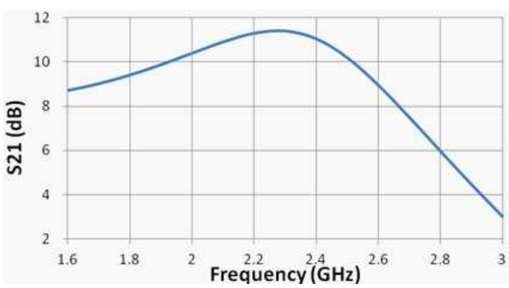

Figure 8: (S_{21}).

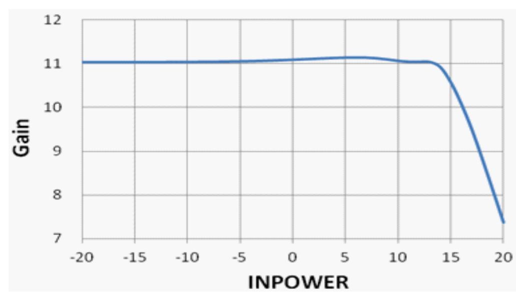

Figure 9: $P_{1\,dB}$ (NF).

2.4. Output Matching Circuit

The optimal relationship between the transistor and resistor was identified using amplification circuit selection. For the output matching circuit, the optimal resistance point of a central tap inductor under a 2.4 GHz band was adopted, which could also reduce the area, as shown in Figure 4.

For a direct current, the transistor current must pass through the output central tap inductor. Because power amplifiers have a high current consumption rate, the maximum width of the inductance component in the TSMC model is only 15 μm, which cannot hold the amount of current created in this design. Therefore, a transformer was added to the output end to achieve the required current load (Figure 5). This free-coil inductor used Metal 6 and Metal 4 layers as the signal and current paths. A wire of 30 μm in width, with a 30 μm coil radius, was wrapped three times using the center point as radius to produce the inductance required for this circuit. The final output was transformed from a dual-end to a single-end signal.

3. SIMULATED RESULTS

Graphs of the simulation results for this circuit show that a 3.1 V VDD bias was used and 1.8 W of power was consumed. For output power simulations and measurement results, when simulating 2.4 GHz, the maximal output power was 26 dBm and the maximal power-added efficiency (PAE) was 18.4%. The simulation result for $P_{1\,dB}$ was 16 dBm, S_{11} was −18.7 dB, S_{22} was −13.1 dB, and S_{21} was 11 dB. The power amplifier distribution graph is shown in Figure 5. The total chip area

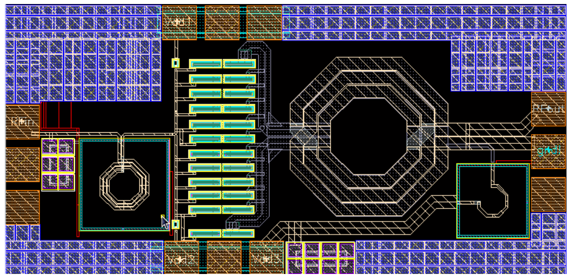

Figure 10: Layout.

was $0.633 \times 1.315\,\mathrm{mm}^2$. By arranging the NMOS and PMOS transistors in an array and adding a bypass capacitor to all PADs connected to the electrical supply the signal was able to flow toward the chip ground. The five graphs and figures below show the output power, PAE, circuit gain, and $P_{1\,\mathrm{dB}}$ of the circuit at 2.4 GHz frequency. They indicate that it is not necessary for the optimal output resistance point to be of identical resistance to the optimal PAE resistance point. Therefore, one of the two parameters must be selected during design.

4. CONCLUSION

RF power transmitters are a key component of mobile broadband devices. Therefore, determining how to use RF CMOS technology to achieve a highpower, highperformance transmitter is a crucial issue for the development of mobile communication technology. To prevent the problems of excessively large areas created previously when excessive inductance of power transmitter circuits was used to achieve the desired watt level, this study replaced the driver transformer with positive and negative signals between the NMOS and PMOS. Using this method the entire area was smaller than that of conventional power amplifiers. Finally, a freecoil inductance transformer was used to output the collected electrical current, approximately achieving the desired watt level. The output power for this power amplifier design was 2.6 dBm, the $P_{1\,\mathrm{dB}}$ compression point was at 16 dBm, the PAE was 18.4%, and power gain was 11 dB. For an overall supply voltage of 3.1 V, the overall power consumption was approximately 1.8 mW. The area of the chip was approximately $0.63\,\mathrm{mm} \times 1.3\,\mathrm{mm}$.

ACKNOWLEDGMENT

The authors would like to thank the Chip Implementation Center (CIC) of the National Science Council, Taiwan, R.O.C., for supporting the TSMC 0.18 μm 1P6M CMOS Process.

REFERENCES

1. Chen, M.-P., C.-H. Shih, W. Chang, and C. Lien, "A 2.5 GHz CMOS power amplifier for WiMAX application," *2010 International Conference on Green Circuits and Systems (ICGCS)*, Jun. 21–23, 2010.
2. Choi, K., D. H. Shin, and C. P. Yue, "A 1.2-V, 5.8-mW, ultra-wideband folded mixer in 0.13 IJ.I11 CMOS," *IEEE Radio Frequency Integrated Circuits (RFIC) Symposium*, 489–492, Jun. 3–5, 2007.
3. Shahani, A. R., D. K. Shaeffer, and T. H. Lee, "A 12 mw wide dynamicrange CMOS front-end for a portable GPS receiver," *IEEE J. Solid State Circuits*, Vol. 32, No. 12, 2061–2070, 1999.
4. Vidojkovic, V., J. Tang, A. Leeuwenburgh, and A. van Roermund, "A low-voltage folded-switching mixer in 0.18-μm CMOS," *IEEE J. Solid State Circuits*, Vol. 40, No. 6, 1259–1264, Jun. 2005.

Design and Optimization of Carrier Suppression Circuit for UHF RFID Reader Applications

You Bin, Quliang Yu, Mingzhu Zhou, and Xiaohong Zhang
Key Laboratory of RF Circuits and Systems, Ministry of Education
Hangzhou Dianzi University, Hangzhou 310018, China

Abstract— In this paper, a new design is proposed to optimize 902 MHz–928 MHz UHF RFID reader systems. With coupler RCP890A05, captured TX Signal after being attenuated and Reversed-Phase, is superimposed on leakage signal, at best, two LO signals will offset each other. When only using a circulator or directional coupler, isolation is always insufficient, then TX-to-RX leakage signal lead to saturation of the low noise amplifier or demodulator. This scheme adopts relatively simple circuit design; on one hand it will not increase the cost and circuit complexity, on the other hand reader performance is significantly improved, and more than 60–70 dB isolation is acquired.

1. INTRODUCTION

Because of its unique advantages, RFID gradually replace barcode system; Expand from EAS to warehousing, logistics, and charges. Along with the rapid rise of Internet of Things program, RFID begin to accelerate and penetrate into all aspects of human life [1].

A passive RFID system consists of reader and matching tag. The working principle is the reader activates passive tags first, and then continues to send carrier signal to provide energy to tag [2]. The tag send back Modulated signal after being activated. Compared with general mobile communication system, a significant difference is passive RFID system has relatively simple tag structure, just make a simple modulation with carrier signal. There is no new carrier frequency generated in the entire process. It means that the carrier frequency of the reflected signal and transmit carrier frequency is identical. Therefore it leads into a serious interference which limits passive RFID system performance — the carrier leakage.

For example, in the most widely used single antenna transceiver circuit, transmitter and receiver isolation generally adopt circulator or directional coupler, such as AS3992 Series RFID chip [3], usually achieves transceiver isolation by circulator. The structure is shown in Figure 1.

The theory isolation of a circulator is about $20 \sim 40$ dB; it is always insufficient for a transceiver, supposing that Transmitter power is 1 W, 6 dBi antenna aerial gain, reflected signal intensity of Mainstream tags is about -75 dBm 10 meters away, take isolation intermediate value of circulator 30 dB. Leak carrier, superimposed on -75 dBm reflected signal, it is about 0 dBm now. In terms of the receiver, in order to improve the ability of identifying weak signal and reduce noise figure, First-class general access low-noise amplifier; but 0 dBm basic input has been reached or even more than a low-noise amplifier 1 dB compression point. So the receiver designer usually had to abandon LNA and demodulates received signal directly. On the other hand, reflection carrier caused by the antenna mismatch and background reflection caused by the also leak to the receiver, sometimes it may cause receiver blocking [4].

To achieve ideal isolation effects, predecessors had put forward a variety of solutions. There are three main current carrier suppression circuit now. The first one is a typical structure, the feature of this structure is attenuating and inverting Coupled transmitted carrier, then we get coupled carrier and leak carrier, which are equal amplitude and opposite phase, then synthesize them together through a Power combiner, they will offset each other. Tested under experimental conditions, this program reaches 70 dB isolation. The disadvantage is the control circuit requires higher, because phase and amplitude have to be adjusted at the same time [5–7].

The second scheme uses a mismatch directional coupler, changing the impedance of the coupling end to adjust reflection coefficient, when amplitude and phase appropriate, leakage carrier will be offset. The disadvantage of program two firstly is a certain degree attenuation of the useful signal, then increasing the Noise figure at the same time, it is difficult to Control impedance mismatch, the circuit is still relatively complex [8–11].

The third is a leaked carrier offset improved program, inserting the circuit as shown in Figure 2 into Figure 1 between circulator and low noise amplifier. The use of the power splitter ensure a stable amplitude relationship among the upper and lower two-way signal. After setting the gain ratio of the amplifier and limiter between, signal amplitude of the upper and lower two-way don't need further adjustment.

To cope with the use of the limiter, AGC and power amplifier is added in front of this circuit. noise figure of AGC is usually larger, usually higher than 8 dB. Second, the use of the power splitter attenuate return signals about 3 dB, the above bring negative impact to the receiver [12].

2. SIGNAL THEORETICAL ANALYSIS

After analysis of the mathematical model of carrier suppression, we found that carrier leakage suppression degree mainly depends on two variables, carrier amplitude and the phase difference between way A and B in Figure 3.

Assuming that the transmitter leakage to the received carrier signal is

$$S_{CW}(t) = A\cos(\omega_c t)$$

RFID tags reflection to effectively signal the receiving end is

$$S_{REF}(t) = g(t)\sin(\omega_c t + \varphi)$$

Then the received signal is the superposition of the two

$$S(t) = S_{CW}(t) + S_{RE}(t)$$

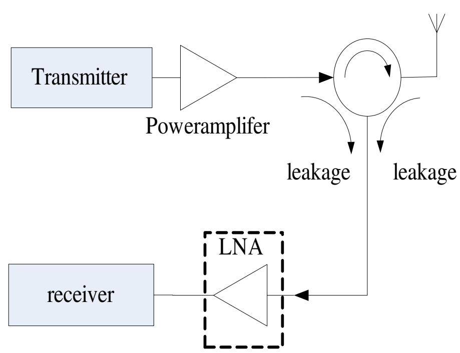

Figure 1: Transceiver structure with a circulator.

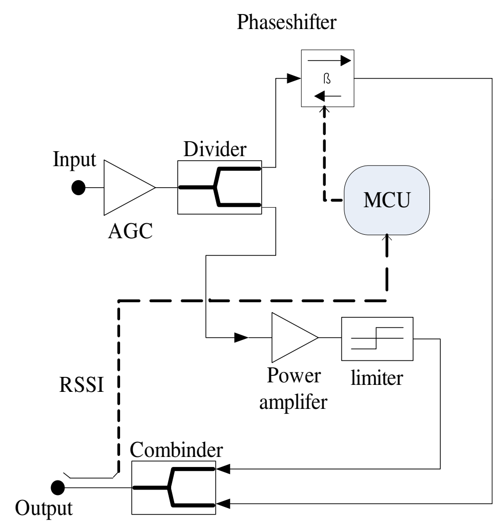

Figure 2: Improved carrier suppression circuit.

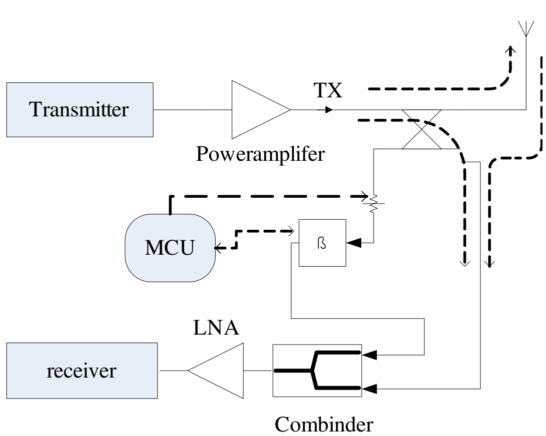

Figure 3: Carrier suppression circuit schematics.

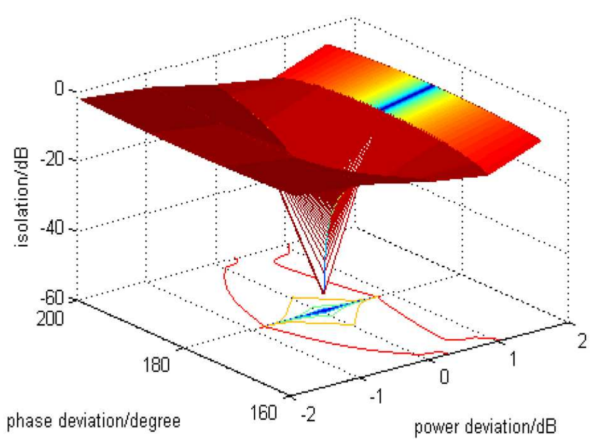

Figure 4: Phase and power changes on isolation effect.

where A represents the amplitude of the leakage carrier signal ω_c represents carrier frequency; φ represents tag returned signal phase, which is related to the tag distance; $g(t)$ means Effective tag Information. Under normal conditions, the label reflected signal is very weak, superimposed on top of the strong carrier signal.

Set the coupling carrier signal after attenuation and phase shift is $S_{DE}(t) = A_1 \cos(\omega_c t + \theta)$, A_1 represents the magnitude of the attenuated coupling carrier, θ is the coupling carrier phase, their numerical range can be adjusted respectively through the attenuator and phase shifter. The receiver input signal $S(t)$ is superimposed with the coupled carrier, so LNA input signal is

$$S_{rec} = S_{DE}(t) + S(t)$$
$$S_{rec} = A\cos(\omega_c t) + A_1 \cos(\omega_c t + \theta) + Bg(t)\sin(\omega_c t + \varphi)$$

where signal $g(t)\sin(\omega_c t+\varphi)$ is effective, carrier suppression effect depends on the signal amplitude of the sum of the first two. That is

$$S_{leak} = A\cos(\omega_c t) + A_1 \cos(\omega t + \theta)$$

Signal simulation results.

Ideally, if $A = A_1$, $\theta = \pi$, the leak carrier will be fully offset. But it is difficult to achieve absolute equal amplitude and phase contrast, amplitude and phase fluctuations impact on the suppression results intensely, under certain conditions we even get an opposite effect. Using matlab for mathematical analysis of the Influence brought by Amplitude and phase error, as shown in Figures 4 and 5.

3D graphics in Figure 4 visual display phase and amplitude changes on the effect of isolation, X-axis takes ± 2 dB power deviation, indicating power difference between leakage carrier and coupling carrier (). Y-axis represents the phase θ scilicet, phase difference between leakage carrier and coupling carrier, 180-degree is an Ideal situation, and 20 degrees of deviation is taken in the figure. Surface value corresponding to the longitudinal axis indicates isolation.

Figure 5 clearly shows the projection of the surface in Figure 4, we can name it equivalent isolation curve, which Lists the amplitude and phase accuracy range to reach -5 dB, -10 dB, -20 dB, -30 dB isolation. Figure 5 clearly shows that within ± 5 dB power and degree deviation, more than 15 dB isolation could still be reached. In the practical application, we hope to obtain 30 dB or more isolation at least. Then phase deviation must be controlled ∓ 2 degrees or less, the magnitude of deviation no more than ∓ 0.5 dB, the above two conditions are indispensable, so we need to adjust the amplitude and phase more accurately.

3. THE EXPERIMENTAL RESULTS

Carrier suppression focuses on the amplitude and phase control, the coupling carrier amplitude is generally 20 dB higher than the leaked carrier. Attenuate coupled Carrier with Voltage controlled attenuator. MCU control the attenuation voltage of the voltage-controlled attenuator, guarantee two-way power equal. When receives a signal, if the antenna position is fixed, the main leakage carrier phase is also fixed.

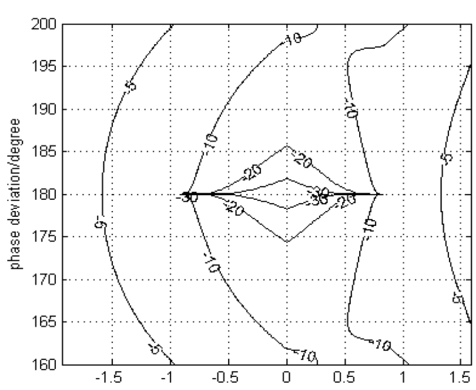

Figure 5: Equivalent isolation curve.

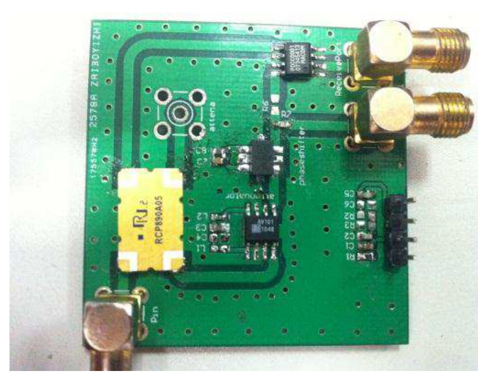

Figure 6: Photograph of the Carrier suppression circuit structure.

Figure 7: Isolation effect without the carrier suppression.

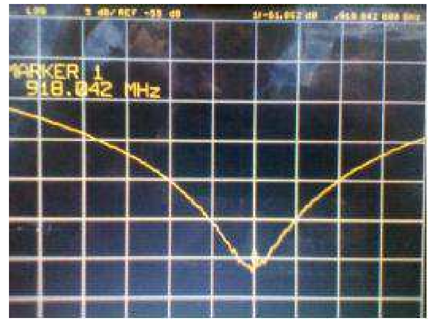

Figure 8: Isolation effect with the carrier suppression.

We select phase shifter PS088-315 produced by Skyworks, attenuator AV101-12, power synthesizer MAPDCC0001 produced by MACOM, and directional coupler RCP890A05 to verify abovementioned program, test results obtained in use of Vector network analyzer as shown in Figures 7 and 8.

Test pass-band 900 MHz $\sim$ 930 MHz, we can see the isolation is 27.9 dB when without carrier suppression circuit (coupler isolation is only 26 dB, attenuation exists in circuit), as shown in Figure 7, adjust control voltage of phase shifter, we can observe within the whole pass band, isolation are below -60 dB, and jitter is very small, as shown in Figure 8.

4. CONCLUSIONS

This paper introduces a kind of low cost, simple carrier suppression circuit structure. Theoretical analysis shows that this scheme can greatly increase the isolation effect; and circuit test results confirm that, in practical application, the whole system isolation reached 60–70 dB, and the isolation effect is relatively stable. In short, it shows excellent performance in the entire bandwidth range.

ACKNOWLEDGMENT

This work was supported in part by Zhejiang Province Key Science and Technology Innovation Team (No. Gk110908002) the Zhejiang Provincial Natural Science Foundation of China under Grant No. Y1110991, the National science foundation of China under Grant No. 61102027.

REFERENCES

1. Curty, J.-P., M. Declercq, C. Dehollain, and N. Joehl, *Design and Optimization of Passive UHF RFID Systems*, Springer Science Business Media, 2007.
2. Part 6C: Parameters for Air Interface Communications at 860 MHz to 960 MHz, ISO/IEC Standard 18000-6C, Jan. 7, 2012.
3. Lei, Q., G. Wang, and D. Wang, "Design of a handheld UHF RFID reader for the internet of things," *Computer and Management (CAMAN), 2011 International Conference on Digital Object Identifier*, 1–4, 2011.
4. Radio-Frequency Identification for Item Management — Part 6: Parameters for Air Interface Communications at 860 MHz to 960 MHz, ISO/IEC Standard 18000-6, 2010.
5. Jung, J.-W., H.-H. Roh, J.-C. Kim, H.-G. Kwak, M. S. Jeong, and J.-S. Park, "TX leakage cancellation via a micro controller and high TX-to-RX isolations covering an UHF RFID frequency band of 908–914 MHz," *IEEE Microw. Wireless Compon. Lett.*, Vol. 18, No. 10, 710–712, Oct. 2008.
6. Xiong, T., X. Tan, J. Xi, and H. Min, "High TX-to-RX isolation in UHF RFID using narrowband leaking carrier canceller," *IEEE Microw. Wireless Compon. Lett.*, Vol. 20, No. 2, 124–127, Feb. 2010.
7. Villame, D. P. and J. S. Marciano, "Carrier suppression locked loop mechanism for UHF RFID readers," *IEEE Int. RFID Conf.*, 141–145, Apr. 2010.
8. Kim, W., M. Lee, J. Kim, H. Lim, J. Yu, B. Jang, and J. Park, "A passive circulator with high isolation using a directional coupler for RFID," *IEEE MTT-S Microw. Symp. Dig.*, 1177–1180, Jun. 2006.

9. Bai, P., Y. Yin, and X. Yang, "A novel RX-TX front-ends for passive RFID reader with high isolation," *IEEE Int. Microw., Antenna, Propag. and EMC Technol. for Wireless Commun. Symp.*, 332–335, 2007.
10. Brauner, T. and X. Zhao, "A novel carrier suppression method forRFID," *IEEE Microw. Wireless Compon. Lett.*, Vol. 19, No. 3, 128–130, Mar. 2009.
11. Jung, S.-C., M.-S. Kim, and Y. Yang, "A reconfigurable carrier leakagecanceller for UHF RFID reader front-ends," *IEEE Circuits Syst. I: Reg. Papers*, Vol. 58, No. 1, 70–76, Jan. 2011.
12. Jung, J.-Y., C.-W. Park, and K.-W. Yeom, "A novel carrier leakage suppression front-end for UHF RFID reader," *IEEE Transactions on Microwave Theory and Techniques*, Vol. 60, No. 5, May 2012.

Implementation of a Compact RF Module by Analysis and Fabrication for Organic Substrate with Embedded Passives

Jong-In Ryu, Jong Min Yook, and Dongsu Kim
Package Research Center, Korea Electronics Technology Institute, South Korea

Abstract— This paper presents embedded passives in organic substrate. By using this technology, a compact module for a Bluetooth and GPS are implemented in this paper. A compact module for a Bluetooth and GPS by using embedded passives as system-on-package (SoP) technology. In order to implement a compact module, interposer with fine line/pitch and embedding technology are proposed. Capacitors are embedded in printed-circuit-board (PCB). A Bluetooth IC and a GPS IC are mounted in interposer.

In order to obtain the effect of embedded capacitors, embedded capacitors and surface mounted capacitors are simulated and compared. Embedded capacitor is better than surfaced mounted capacitor in wide frequency range. Two representative modules for Bluetooth/GPS with SMT and with SoP are designed and compared. Almost 50% size reduction is obtained by SoP.

Tx power and Rx sensitivity are given as 6 dBm and −72 dBm, respectively. The received signal strength of GPS is −155.7 dBm/Hz, respectively. Actually, Bluetooth and GPS are well performed in commercial field.

1. INTRODUCTION

In the booming market of wireless communication, many companies of wireless device spend a lot of effort to the cost of their products, with at the same time an increase of the performance and a reduction of size. Multi-function, compact size, good performance, and convergence of technology are demanded in components, modules, mobile device, portable devices, and appliance.

Users want small, cheap, convenient, and multi-function. Compact design is main issue in portable device. Many researchers, universities and engineers have been studied in order to satisfy these requirements. As a result, system-on-chip (SoC), System-in-package (SiP), package-on-package (PoP), and system-on-package (SoP) are representative approaches in order to highly integrate many function as compact size [1, 2]. SoC has been introduced in field of semi-conductor and it is invented in one material as example as silicon or GaAs. SiP has been driven by packaging research group and it contains more than two heterogeneous semi-conductors with wire-bonding or solder bump. PoP is a simple combination among package modules. SoP has been leaded and proposed by package group with embedding ICs, passive components, and system. Process is segmented into polymer, silicon, and low-temperature co-fired ceramic (LTCC). Normally, LTCC technology is mainly issued to integrate components due to high integration. LTCC substrate is so difficult to embed ICs in substrate so that organic substrate is vividly researched [3–5]. Therefore, embedding components in organic substrate has been studied [6–9].

In this paper, the module for GPS and Bluetooth are presented. The proposed module is miniaturized by SoP technology. Many capacitors are embedded in substrate and interposer is employed. The proposed module is designed and implemented.

2. DESIGN

Capacitors as 2.2 μF, 1 μF, 470 nF, 100 nF, 22 pF, 10 pF, so on are fully embedded in PCB as organic substrate and total number of embedded capacitors is 17 in this paper as depicted in Fig. 1(a). Capacitors are embedded in printed-circuit-board (PCB). A Bluetooth IC and a GPS IC are mounted in interposer. In side view, ICs, interposer substrate, and a PCB with capacitors are sequentially located from top and bottom as shown in Fig. 1(b). This module is composed of a Bluetooth IC, a GPS IC, interposer with 30 μm line width, and 17 shunt capacitors.

Capacitors are embedded by using chip-first process so capacitors are located in the middle of PCB substrates. Chip-first process means that embedded components are first laminated and next PCB process goes on. The substrate is composed of Ajinomoto-bonding-film (ABF) and FR4 as epoxy core with the cavity to embed capacitors. ABF is very convenient to embedding ICs because of good adhesive to silicon. ABF is suitable for the fine line formation and thin substrate by using semi additive process. The dielectric constant of the FR4 and ABF in PCB substrate is 4.5 and 3.3, respectively. Drilling via by UV laser and Cu pattern plating processes are employed

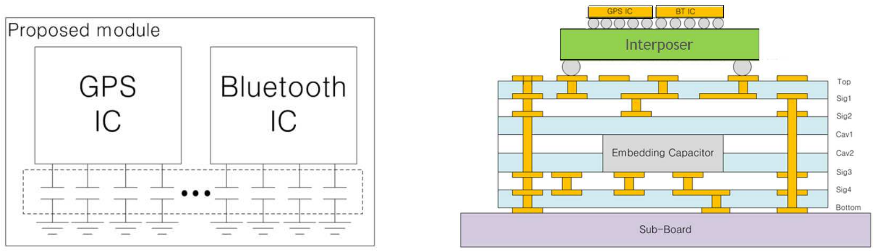

(a) (b)

Figure 1. (a) A block diagram and (b) cross section for a proposed SoP module.

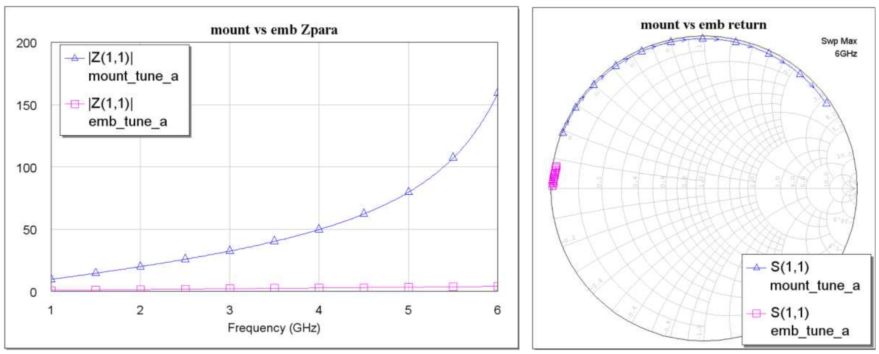

(a) (b)

Figure 2. (a) Z-parameter and (b) S-parameter in smith chart.

to interconnection between the pad of an IC and formed patterns. A planar surface and void free cavity filling are processed by vacuum lamination. After lamination and laser drilling, Cu plating and etching processes are performed. The fabricated process for a presented module is explained in follow as : 1) ABF film is prepared. 2) Drilling vias to align the position of an IC, An embedded IC is mounted on ABF. 3) Removing carrier film of ABF. 4) FR4 core with cavity for an embedded IC and two ABFs for top-side and down-side are simultaneously laminated. 5) UV laser drills into the Pads of IC and through via. 6) Cu is plated and pattern is formed on ABF. 7) Two ABFs in top-side and bottom-side are laminated as 2nd process, and through-vias and blind-vias are drilled and plated. 8) Two ABFs in top-side and bottom-side are laminated as 3rd process, and vias and pattern are plated in organic substrate.

Before fabricating module, the effect of embedded capacitors are simulated and compared by Sonnet program. The mounted capacitor and embedded capacitor are compared. The results are analyzed in view of Z-parameter and S-parameter. Fig. 2 shows the simulated results. Red line and blue line express embedded capacitor and mounted capacitor, respectively. 100 nF is tested and embedded capacitor has almost constant value from 1 GHz to 6 GHz as shown in Fig. 2. 10 pF is also tested. Mounted capacitor and embedded capacitor have 1 GHz and 5 GHz self resonant frequency. Embedded capacitor has good self resonant frequency. Therefore, embedded capacitor is better than surfaced mounted capacitor in wide frequency range.

3. FABRICATION AND MEASUREMENT

Figure 3(a) shows fabricated substrate with embedded capacitors. The proposed module is fabricated by proposed process as shown in Fig. 3(b). The size of module is given as 12 mm × 7 mm and the size of this interposer is given as 9.6 mm × 4.9 mm. A Bluetooth IC and a GPS IC is mounted on interposer. The side view of the implemented module is depicted in Fig. 3(c).

In order to check the performance and size for embedded modules, two representative modules for Bluetooth/GPS with SMT and with SoP are designed and compared. The size of module with SMT and SoP are as 15 mm × 10 mm and 12 mm × 7 mm, respectively. Almost 50% size reduction is obtained by SoP as shown in Fig. 4.

A presented module for Bluetooth/GPS was measured by using step attenuator, spectrum analyzer, Bluetooth test program, and GPS signal of field. In order to perform Bluetooth, two test

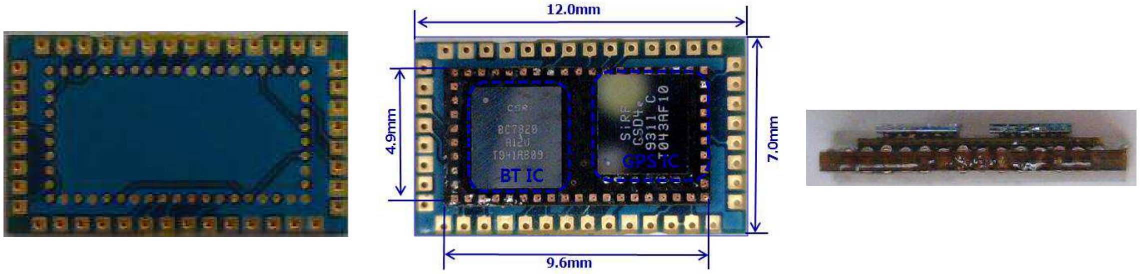

(a) (b) (c)

Figure 3. (a) Fabricated substrate with embedded capacitors and (b) fabricated bluetooth/GPS module, and (c) side view of the module.

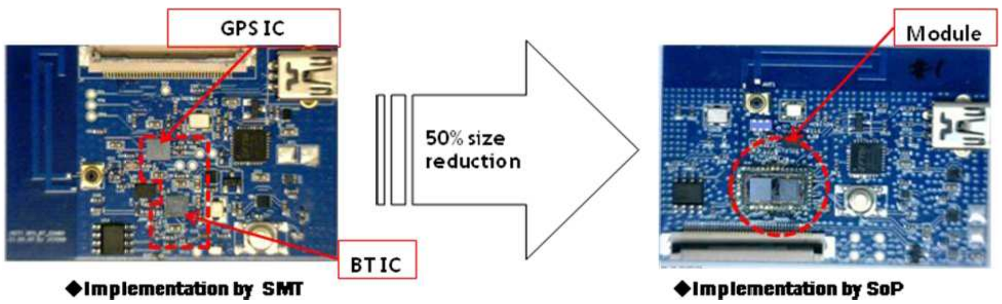

Figure 4. Module in comparison with SMT and SoP.

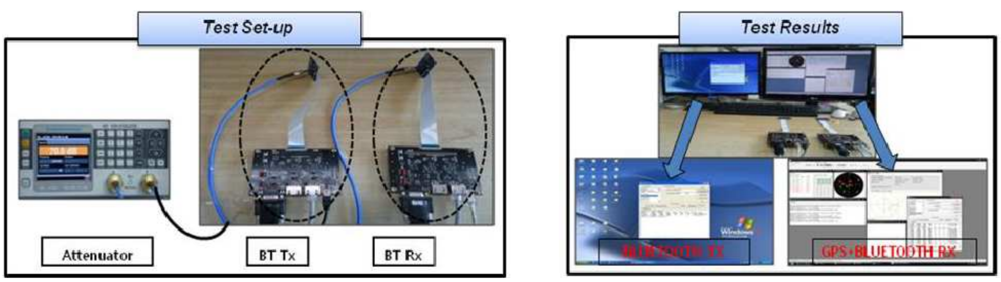

Figure 5. Test set-up and test results.

devices are communicated with each other to measure sensitivity by adopting non-signaling method as shown in Fig. 5. Two devices are connected through attenuator as air interface. The value of attenuator is raised as if distance is increased because distance means the RF loss between antennas in view of RF system. Tx power and Rx sensitivity are given as 6 dBm and −72 dBm, respectively. The received signal strength of GPS is −155.7 dBm/Hz, respectively. Actually, Bluetooth and GPS are well performed in commercial field.

4. CONCLUSIONS

A presented module for Bluetooth/GPS was designed and implemented by lamination process with polymer material. Various capacitors were embedded in PCB in this paper. Fine line was realized in interposer substrate. Implemented modules with SMT and with SoP were compared in size. This paper presented that SoP technology was better than SMT technology in a view of size. Implemented module had good performance and slim size.

REFERENCES

1. Fontanelli, A., "System-in-package technology: Opportunities and challenges," *Proc. 9th Int. Sym. on Quality Electronic Design*, 589–593, 2008.
2. Lenihan, T. G. and E. J. Vardaman, "Worldwide perspectives on SiP market: Technology trends and challenges," *Proc. 7th Int. Conf. on Electronics Packaging Technology*, 2006.

3. Kim, D., D. H. Kim, G. H. Baek, J. I. Ryu, C. D. Park, C. S. Kim, I. S. Song, and J. C. Kim, "Front-end moudle for Wi-Fi and WiMAX dual-mode system," *Microwave and Optical Technology Letters*, Vol. 52, No. 3, 753–757, Mar. 2010.
4. Ryu, J., J. Moon, D. Kim, and J. C. Kim, "Implementation of the front-end module with a power amplifier for dual-band wireless LAN," *Proc. Eur. Microwave. Conf.*, 1357–1360, 2009.
5. Radosavljevic, G. J., L. D. Zivanov, W. Smetana, A. M. Maric, M. Unger, and L. F. Nad, "A wireless embedded resonant pressure sensor fabricated in the standard LTCC technology," *IEEE Sensor Journal*, Vol. 9, No. 12, 1956–1962, 2009.
6. Tummala, R. R., M. Swaminathan, M. M. Tentzeris, J. Laskar, G.-K. Chang, S. Sitaraman, D. Keezer, D. Guidotti, Z. Huang, K. Lim, L. Wan, S. K. Bhattacharya, V. Sundaram, F. Liu, and P. M. Raj, "The SOP for miniaturized, mixed-signal computing, communication, and consumer systems of the next decade," *IEEE Trans. on Advanced Packaging*, Vol. 27, No. 2, 250–267, 2004.
7. Ulrich, R., "Embedded resistors and capacitors for organic-based SOP," *IEEE Trans. on Advanced Packaging*, Vol. 27, No. 2, 326–331, 2004.
8. Ryu, J., D. Kim, S. H. Park, J. C. Park, and J. C. Kim, "Investigation of an embedded RF switch IC in printed circuit board," *Proceeding of the Electrical Design of Advanced Packaging and Systems Symposium*, 81–84, 2008.
9. Ryu, J., S. Park, J. Moon, D. Kim, J. C. Kim, and N. Kang, "Implementation of a front-end-module by embedding a RF switch IC and a power amplifier in printed-circuit-board," *Proceeding of the Electric Components and Technology Conf.*, 1920–1923, 2009.

Propagation Characteristics of the Meandered Defected Ground Structure

Wan-Ti Wang, Tzu-Hsiung Lin, and Chien-Jen Wang
Department of Electrical Engineering, National University of Tainan, Tainan, Taiwan

Abstract— In this paper, a meander-shaped slotted-ground-plane resonator has been proposed to show a compactness and wide rejection band. The meandered slot disturbs the surface current distribution in a ground plane so that the frequency response of a transmission line can be changed. Unlike a conventional slot in a ground plane acting a stop band, the meandered slot possesses multi-band frequency-rejection characteristics. By merging several bands into one band, the meandered-slot resonator provides a wideband resonator with low insertion loss and very sharp cutoff frequency response. The phenomenon the rejection bands are theoretically analyzed by utilizing magnetic field distribution. Detailed discussions for important dimensional parameters are determined.

1. INTRODUCTION

A microstrip slotted-ground-plane bandstop resonator with a compact size and spurious suppression has attracted a growing amount of interest in the field of radio frequency/microwave circuit design. Such resonators are widely used in designs for low-pass filter, power dividers, power amplifiers, frequency multipliers and so on. The resonator, which has a patterned slot in the backside metallic ground plane, can exhibit stopband characteristics. This slot disturbs the shield current distribution in the metallic ground plane, and this disturbance changes the frequency characteristics of the transmission line, modelled as inductance and capacitance. By employing circuit analysis theory, an equivalent resonance circuit of the slotted-ground-plane resonator is derived and lumped-element parameters are extracted. The lumped element construct an LC tank, and then a stopband effect is obtained.

By changing the shape of a slot, the equivalent inductance and capacitance will be tuned so that the frequency response of the transmission line is controlled. Earlier research has proposed various topologies of the slotted-ground-plane resonator, such as dumbbell-shaped [1, 2], alphabet-shaped (H, I, V, U) [3–5], spiral-shaped [6] and interdigital [7] slots, The slot shape has an influence on the sharpness of the transition and rejection bandwidth [1]. In order to obtain better inductive loading and to further miniaturise the resonator, the dumbbell-shaped slot has been replaced by the H-shaped slot (H-slot) [3]. Moreover, the geometrical dimension of the U-and V-slot resonators was parametrically investigated in [5], which found that the characteristics of the resonators, such as the resonance frequency, the rejection bandwidth and the quality factor (Q), are dependent on the structural parameters of the patterned slot. The dimensions of the slot length, width and the distance between two slots significantly affect the transfer response. The steep rejection characteristics are also observed by utilising the spiral-shaped slot [6]. Interdigital slots were introduced in [7], and the resonance frequency was easily adjusted by changing the distance between two conducting fingers.

A microstrip bandstop resonator with a slotted ground structure featuring compact size and a wide spurious-free passband was proposed in [8]. By embedding varactors in the slotted ground structure, tunable bandstop resonators are implemented, and these are used as harmonic traps and to improve the circuit performance of tunable amplifiers or antennas. The method of embedding isolated patches (islands) in the slotted-ground-plane resonator was proposed in [9], which described the effects of the frequency characteristics of the resonator on passive devices (resistors or capacitors) connecting the patches and the ground plane. An equivalent circuit consisting of a parallel LC resonance circuit and the open patches was shown in the same work, although it was accompanied by only a limited discussion of the geometrical parameters of the isolated patches (islands). However, the equivalent circuit of this resonator can be revised to meet various frequency characteristic.

In this paper, a meander-shape slotted-ground-plane resonator is shown to perform multi-band rejection characteristics in frequency response. Unlink a conventional slot in a ground plane acting a bandstop resonator, a meandered-shaped slot possesses multi-band frequency-rejection characteristics with a sharp transition knee.

2. A DEFECTED-GROUND-STRUCTURE MEANDERED RESONATOR

As shown in Figure 1(a), for the wideband defected-ground-structure resonator operated about at 3.0 GHz, an meandered-shaped slot etched in the ground plane and the dimensions of the slot are as following: $a = 20$ mm, $d = 12$ mm, $g = 1$ mm, $t_1 = 5$ mm and $t_2 = 6$ mm. The circuits in this paper are designed and fabricated on a high frequency printed circuit board FR4 with a relative dielectric constant of 4.4 and a thickness of 0.8 mm. The width of the transmission line is chosen for the characteristic impedance of a 50-Ω microstrip line.

In Figure 1(d), the simulated S-parameters of the meandered-shaped slot resonator are compares with the conventional dumbbell-shaped and H-shaped resonators (seeing Figures 1(b) and (c)) having same size. The first resonance frequencies of the H-shaped and meander-shaped resonators are operated about at 3.0 GHz. The first resonance frequency of the dumbbell-shaped resonator is resonated at 3.65 GHz. The 10-dB rejection bandwidth of the meander-shaped slot resonator is 3.14 GHz wider than those (2.48 and 1.21 GHz) of the dumbbell-shaped slot and H-shaped slot resonators. It is also observer that the attenuation rate and the harmonic suppression of the meandered-shaped resonator are superior to the other ones.

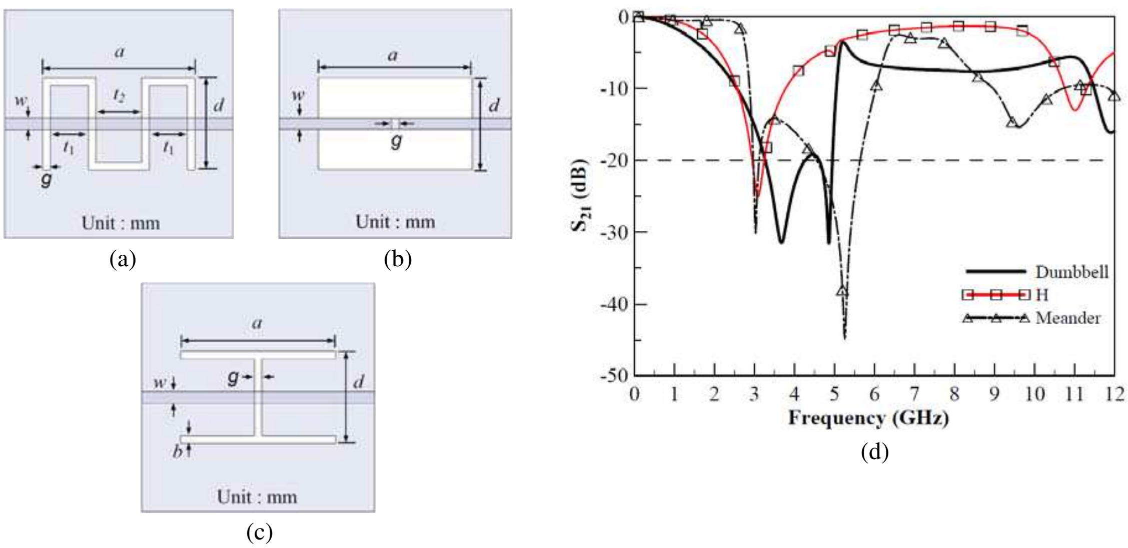

Figure 1: (a) Proposed meandered defected-ground-structure resonator, (b) dumbbell-shaped resonators, (c) H-shaped resonators where $a = 20$, $d = 12$, $w = 1.5$, $g = 1$, $b = 1$, $t_1 = 5$, $t_2 = 6$ and (d) simulated S_{21} of the meandered-shaped slot, dumbbell-shaped slot and H-shaped slot resonators.

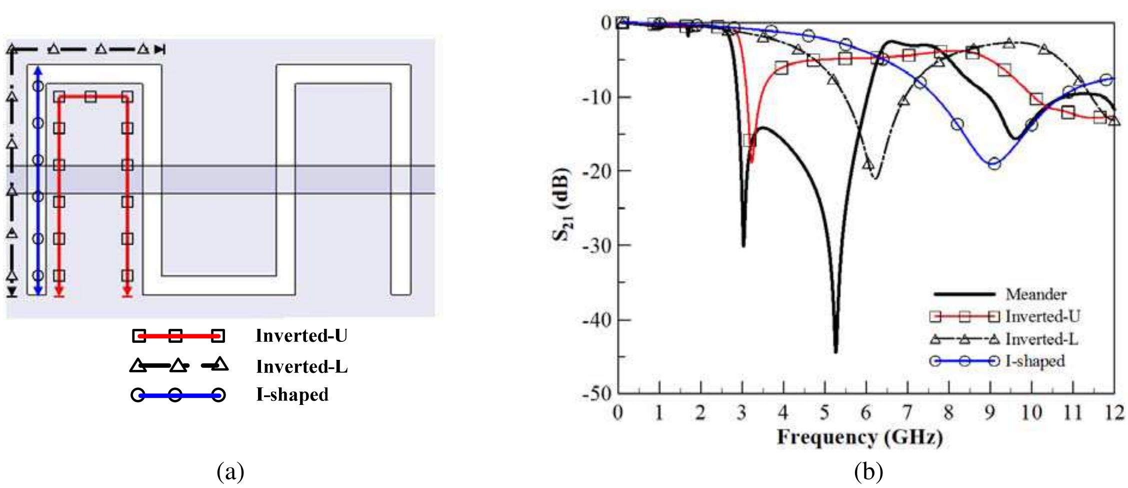

Figure 2: (a) Three resonant paths of the meandered-slot resonator and (b) simulated S-parameters of the defected-ground-structure resonators, including the meandered, inverted-U, inverted-L and I resonators.

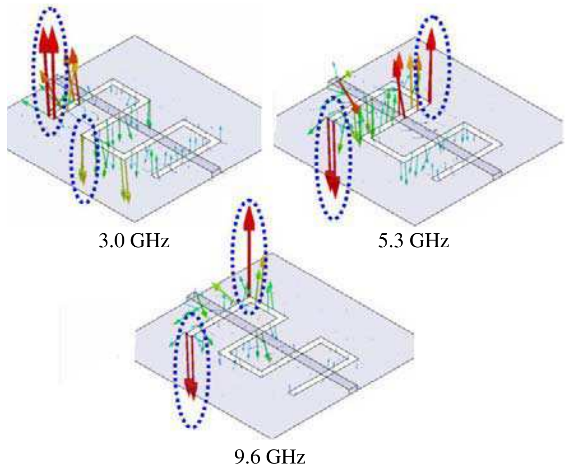

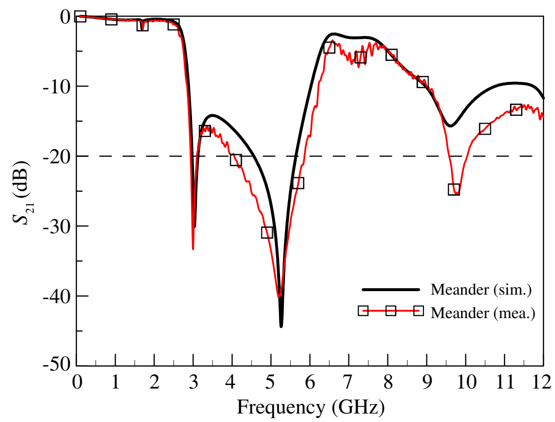

Figure 3: (a) Distributions of the magnetic field of the meandered resonator at three different operated frequencies and (b) comparison of simulated and measured S-parameters of the simple meandered-slot resonator.

3. RESONANCE ANALYSIS

As shown in Figure 1(d), below 12 GHz, there are three resonances for the meander-shaped resonator. The three resonances are at 3.0, 5.3 and 9.6 GHz, which are excited by the inverted-U, inverted-L and I paths shown in Figure 2(a).

Figure 2(b) is the simulated S_{21}-parameters of the defected-ground-structure resonators for different slot topologies, including the meandered, inverted-U, inverted-L and I resonators. From the simulated results in the Figure 2(b), the lower transmission zero at 3.0 GHz is excited by the inverted-U slot, the second transmission zero is generated by the inverted-L slot, and the third transmission zero is determined by the I slot. The discrepancy of the resonance frequency between the single and meandered resonators may be attributed to the mutual coupling effect of the slot trace.

Figure 3(a) is the distributions of the magnetic field of the meandered resonator at 3.0, 5.3 and 9.6 GHz. It is found that, for the magnetic field, a distance between two maximum out-of-phase vectors is half-wavelength, which is the resonant path of the defected-ground-structure resonator.

4. RESULTS AND DISCUSSIONS

The line width was chosen to be the characteristic impedance of 50-Ω microstrip line for simulation. In order to investigate the influence of the slot width which is related to the gap capacitance, the whole dimension of the meandered resonator was kept constant to $20 \times 12\,\mathrm{mm}^2$ for all three cases.

It is noted that increasing the slot width (g) results in decrease of t_2 when t_1 is fixed. The simulated results are illustrated in Figure 4(a). From this figure, one clearly observes that decreasing the slot width increases the effective capacitance of the resonator which introduces the cutoff characteristics at transmission zeros. As the etched width of the slot is decreased, the effective capacitance increases, and it gives rise to a lower cutoff frequency, as seen in Figure 4(a). An additional transmission zero is excited around 1.8 GHz because of the resonance of the whole meandered slot path. The additional transmission zero is insignificant and useless so that it should be avoided to be excited.

We now investigate the influence of the resonant slot path, which is to change the length of t_1 with same dimension ($20 \times 12\,\mathrm{mm}^2$) of the whole unit circuit. Note that g is fixed by 1 mm and t_2 is varied. The simulated transfer characteristics of the test circuit by varying t_1 are shown in Figure 4(b). The additional transmission zero around 1.8 GHz is easily generated for two cases of $t_1 = 3$ and 5 mm. Due to the increase of the resonant path of the inverted-U resonator, the transmission zero at 3.0 GHz shifts down as t_1 increases. It is interesting that the resonance frequency of the transmission zero at 5.3 GHz also reduces when t_1 is 3 mm. The reason of this phenomenon results from the change of the resonator at this operated frequency. The resonant path for large t_1 is inverted-L, but one for small t_1 is inverted-J. When t_1 changes from 5 mm to 3 mm, one maximum magnetic fields is moved from the right corner of the inverted-U slot to the

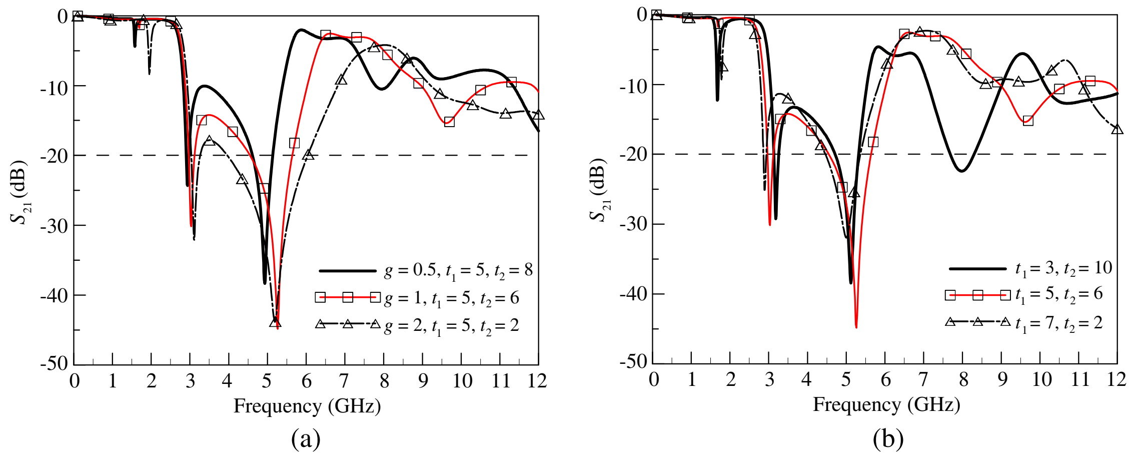

Figure 4: (a) Comparison of simulated transfer characteristics of the meandered resonator when changing the slot width g and (b) simulated transfer characteristics of the test circuit by varying t_1 when the slot width g is fixed by 1 mm.

cross point of the microstrip line and the slot. The resonant path increases so that the frequency reduction of the transmission zero is achieved, Figure 3(b) shows good agreement between the simulated and measured has been observed.

5. CONCLUSIONS

A compact meander-slotted-ground-plane resonator with multi-band frequency-rejection characteristics has been presented and demonstrated in this paper. Comparisons of the conventional dumbbell-shaped and H-shaped resonators (seeing Figures 1(b) and (c)), the proposed meandered slot provides a wideband resonator with low insertion loss and very sharp cutoff frequency response.

REFERENCES

1. Abdel-Rahman, A. B., A. K. Verma, A. Boutejdar, and A. S. Omar, "Control of bandstop response of Hi-Lo microstrip low-pass filter using slot in the ground plane," *IEEE Trans. Microw. Theory Tech.*, Vol. 52, No. 3, 1008–1013, Mar. 2004.
2. Safwat, A. M. E., F. Podevin, P. Ferrari, and A. Vilcot, "Tunable bandstop defected ground structure resonator using reconfigurable dumbbell-shaped coplanar waveguide," *IEEE Trans. Microw. Theory Tech.*, Vol. 54, No. 9, 3559–3564, Sep. 2006.
3. Mandal, M. K. and S. Sanyal, "A novel defected ground structure for planar circuits," *IEEE Microw. Wireless Comp. Lett.*, Vol. 16, No. 20, 93–95, Feb. 2006.
4. Chen, H. J., T. H. Huang, C. S. Chang, L. S. Chen, N. F. Wang, Y. H. Wang, and M. P. Houng, "A novel cross-shaped DGS applied to design ultra-wide stopband low-pass filters," *IEEE Microw. Wireless Comp. Lett.*, Vol. 16, No. 5, 252–254, May 2006.
5. Woo, D. J., T. K. Lee, J. W. Lee, C. S. Pyo, and W. K. Choi, "Novel U-slot and V-slot DGSs for bandstop filter with improved Q factor," *IEEE Trans. Microw. Theory Tech.*, Vol. 54, No. 6, 2840–2847, Jun. 2006.
6. Liu, H. W., T. Yoshimasu, and L. L. Sun, "CPW bandstop filter using periodically loaded slot resonators," *Electron. Lett.*, Vol. 42, No. 6, 352–353, Mar. 2006.
7. Balalem, A., A. R. Ali, J. Machac, and A. Omar, "Quasi-elliptic microstrip low-pass filters using an interdigital DGS slot," *IEEE Microw. Wireless Comp. Lett.*, Vol. 17, No. 8, 586–588, Aug. 2007.
8. Wang, X. H., B. Z. Wang, H. Zhang, and K. J. Chen, "A tunable bandstop resonator based on a compact slotted ground structure," *IEEE Trans. Microw. Theory Tech.*, Vol. 55, No. 9, 1912–1918, Sep. 2007.
9. Kim, J., J. S. Lim, K. Kim, and D. Ahn, "Effects of a lumped element on DGS with islands," *IEEE MTT-S Int. Microw. Symp. Dig.*, 1145–1148, 2006.

Wideband Leveling Amplifier Design Using 0.18 μm CMOS Process

Guan-Shian Li[1], **Chin-Ying Huang**[2], **Robert Hu**[2], **and Chung-Ping Chen**[2]

[1]College of Electrical Engineering and Computer Science, NTU, Taiwan
[2]College of Electrical and Computer Engineering, NCTU, Taiwan

Abstract— This manuscript reports the development of leveling amplifier, or known as active gain equalizer designed using commercial 0.18 μm CMOS process. Similar to a distributed amplifier, this circuit uses artificial transmission lines to achieve broadband input and output matching; each of the gain cells utilizes two cascode amplification stages to sustain wideband gain performance. Allowing attenuation of the input transmission line to be frequency-dependent, where the shunt admittance G comes from a resistor in series with a capacitor, this equalizer's gain slope can be adjusted. On the other hand, the output transmission line will be altered by the capacitors attached to the gate nodes of the output common-gate transistors, and that in turn shifts the equalizer's cutoff frequency In the simulation, the high-frequency gain can be lifted from 15 dB up to 30 dB in small steps, while the cutoff frequency can be finessed within 1 GHz. Small input and output reflection coefficients are also observed, and the port isolation is better than 40 dB across the bandwidth.

1. INTRODUCTION

Since the performance of active and passive circuits in most receiver front-ends is frequency dependent — usually the attenuation will be more pronounced as frequency increases, a wideband gain equalizer or leveling amplifier has to be used for gain compensation. To have good input and out matching, resistors have to be employed in the passive gain equalizer design; however, the use of resistor itself also implies the equalizer's loss cannot be neglected; more amplifiers therefore have to be inserted into the system [1]. Active leveling amplifier, on the other hand, can achieve good input and output matching and, with positive gain, additional amplification stages are not in need. Though the leveling amplifier's power handling capability is quite limited as compared with its passive counterpart, this does not become an issue in our receivers where the detected signal is very weak. Unlike most commercial leveling amplifiers that have octave bandwidth, our DC-8.7 GHz version is extremely wideband in term of the relative bandwidth. This is made possible with the use of distributed amplifier [2, 3]. By making the property of the input and output transmission lines to be frequency-dependent and adjustable, both the gain slope and the exact gain bandwidth can be changed whenever deemed necessary. In the following, the gain cell and transmission lines will be discussed to explain how the intended features can be achieved; preliminary simulation results using TSMC 0.18 μm CMOS process will then be presented.

2. DC-8.7 GHz LEVELING AMPLIFIER DESIGN

Two cascode amplification stages are used for the gain cell, as shown in Fig. 1. An inductor L_1 (and L_2 too) is inserted between the drain of common-source and the source of common-gate transistors for high frequency gain boosting as this inductor could form a short transmission line with drain and source parasitic capacitors. Without L_1 or L_2, the mere existence of these two capacitors will cause gain degradation at high frequency. The employment of gate inductor L_3 is to introduce negative output impedance for the gain cell so that it can alleviate the loss of the output transmission line, though too large the value of L_3 will definitely cause instability.

The input artificial transmission line is made of the periodic LC's, where the L comes from the spiral inductor while the C is mainly the gate-source capacitance of the common-source transistor. The corresponding line impedance Z_0 and cutoff frequency can be easily calculated. To have discernible gain slope, we intentionally introduce the frequency-dependent loss into the line, as shown in Fig. 2(a), where R is the channel resistance of the transistor and C_{DC} is the DC-blocking capacitor. With control signal applied, the transistor can be switched ON (lossy line) or OFF (lossless). With appropriate selection of the controlled transistors along the input transmission line, the gain slope can thus be adjusted. On the other hand, the exact bandwdith of the amplifier can be changed by finessing the cutoff frequency of the output transmission line. As shown in Fig. 2(b), the DC-blocking capacitor C'_{DC}, once the control transistor is turned ON, will affect the line's unit capacitance through the existance of gate-drain capacitance C_{gd} of the output transistor. Due to

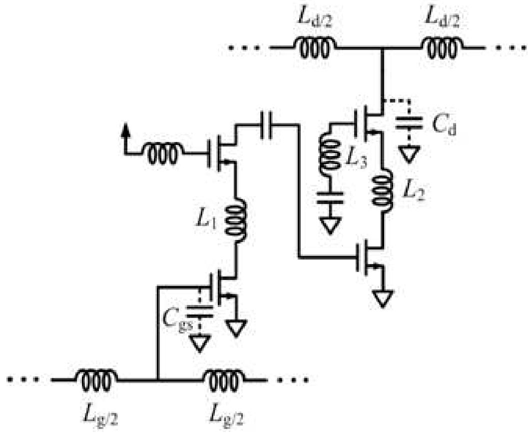

Figure 1: Schematic of the gain cell which is made of two cascode amplification stages.

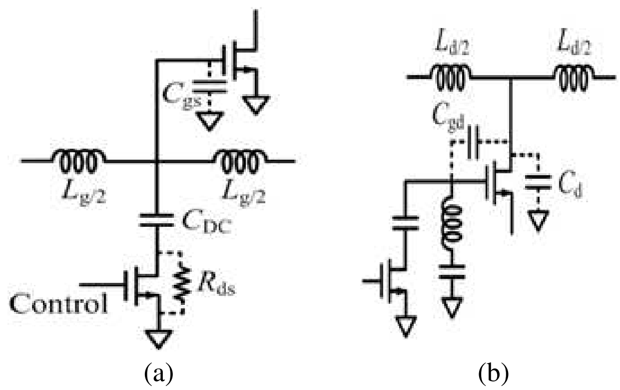

Figure 2: Input and output transmission lines. (a) Input transmission line where the frequency-dependent admittance G is made of R_{ds} and C_{DC}. (b) Output transmission line where the shunt capacitance C will be affected by gate-node capacitance.

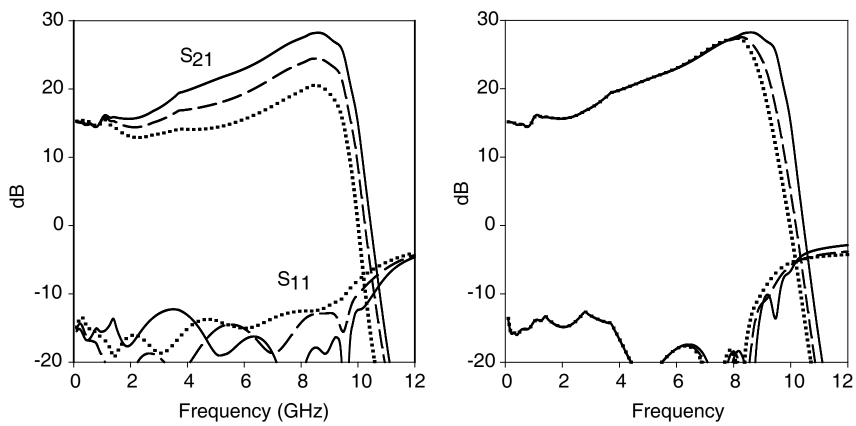

Figure 3: Simulated results for gain-slope and cutoff-frequency tuning.

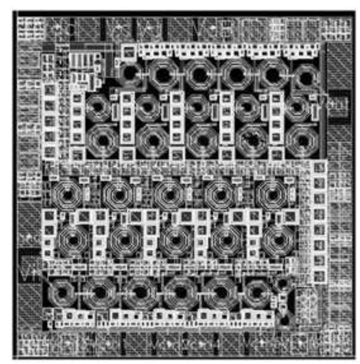

Figure 4: Layout of the DC-8.7 GHz leveling amplifier designed with 0.18 µm CMOS process.

the the small value of C'_{DC}, the channel resistance of the control transistor can be neglected here. Fig. 3 demonstrates the simulated gain-leveling capability. With different control transistors turned ON, the gain slope can be changed while the input matching is always maintained. It is observed that the cutoff frequency will also increase as gain slope increases. However, the cutoff frequency can be re-adjusted via the second set of control transistors working on the output transmission line. Again, output matching is rarely affected during the operation. Fig. 4 is the layout of the DC-8.7GHz leveling amplifier designed using TSMC 0.18 µm CMOS process.

3. CONCLUSIONS

In this paper, a DC-8.7 GHz active leveling amplifier using TSMC 0.18 µm CMOS process has been designed. By inserting periodic shunt RC circuits along the input artificial transmission line, the gain slope of the amplifier can be adjusted, with gain at 8.7 GHz changed by more than 10 dB. Likewise, with variable capacitors linked to the output transmission line, this circuit's cutoff frequency can be fine-tuned within 1 GHz range. The underlying mechanisms have been clearly explored and buttressed by simulated results.

ACKNOWLEDGMENT

The authors would like to thank Kung-Long Wu and Dean Chang for the fruitful discussions. This paper is supported in part by the National Science of Council, R.O.C., under the contract NSC101-2221-E009-170.

REFERENCES

1. Teng, H.-F., J.-C. Wu, T.-H. Chiueh, and R. Hu, "The design of wideband DC-35 GHz modules for 78113 GHz receiver array," *PIERS Proceedings*, 1229–1232, Kuala Lumpur, Malaysia, Mar. 27–30, 2012.
2. Huang, J.-Y., D.-C. Niu, R. Hu, and C.-F. Jou, "The design of 40 GHz active power splitter," *PIERS Proceedings*, 1381–1384, Kuala Lumpur, Malaysia, Mar. 27–30, 2012.
3. Huang, J. Y., H.-I. Wu, R. Hu, C. F. Jou, and D.-C. Niu, "A DC20 GHz CMOS active power divider design," *Proceedings of Asia Pacific Microwave Conference (APMC)*, 524–526, Yokohama, Japan, Dec. 2011.

FPGA Implementation and Verification of Reed-Solomon Code in SDR System

Yi Hua Chen, Chang Lueng Chu, and Chun Chun Yeh
Institute of Information and Communication Engineering
Oriental Institute of Technology, New Taipei City, Taiwan

Abstract— This study used the LabView FPGA to implement two Reed-Solomon codes (R-S code), R-S (31, 15, 8) and R-S (63, 47, 8) using $m = 8$ on the NI SDR PXIe-5641R FPGA module. Besides providing a detailed discussion on the encoding and decoding mechanism of R-S code, this study completed software simulation and hardware verification of R-S code. When the error probability is 10^{-4}, the coding gain of R-S (31, 15, 17) [10] using $m = 5$ can be up to 2 dB, R-S (31, 15, 8) using $m = 8$ can be up to 2.5 dB, R-S (63, 47) [11] can be up to 1.5 dB and R-S (63, 47, 8) using $m = 8$ can be up to 3.5 dB. The result indicates that the R-S (63, 47, 8) implemented in this study has the best power-saving capacity. Comparing the error performance, when the E_b/N_0 is fixed at 5 dB, the error probability of R-S (31, 15, 17) [10] is 10^{-2}; the error probability of R-S (63, 47) [11] is much greater than 10^{-1}; the error probability of R-S (31, 15, 8) code is small greater than 10^{-3}; and the error probability of R-S (63, 47, 8) code is small less than 10^{-4}, indicating that the R-S (63, 47, 8) implemented in this study has the best correction capacity.

1. INTRODUCTION

Forward error correction (FEC) schemes, different from the source coding for data compression, ensure the correctness of transmission data by restoring the destroyed data. It can be classified into block code and convolution code. Reed-Solomon code is a kind of block code [1, 2]. In December 1958, I. S. Reed and G. Solomon [3, 4] completed in M. I. T. Lincoln Laboratory the "polynomial code in the finite field". The advantages of R-S code include its effective resistance to packet data loss during the network transmission process and its excellent error correction capability. Its disadvantage is the need to use large Galois Field (GF) to establish the long R-S code [5, 6]. Larger number of bits in symbol will result in greater order of power in the information polynomial and higher complexity level of decoding calculation. The algebraic decoding method is commonly used in decoding process [7, 8]. This study used the algebraic BMA algorithm [9] for decoding computation. The error probability was compared with that in Ref. [10], and the LabView simulation was compared with the implementation in LabView FPGA to analyze the effectiveness.

The SDR system used in this study is composed of modules including controller (NI PXIe-8106), transceiver (5641R), down-converter (5600), up-converter (5610). 5641R is an IF transceiver of bandwidth at 20 MHz equipped with DSP optimized Xilinx Virtex-5 SX95T FPGA with IF frequency input and output interface that can be interfaced with analog up and down converter to capture and generate RF signals. The FPGA interface card can be programmed through LabView FPGA to execute complex modulation and signal processing of the hardware.

2. REED-SOLOMON CODES DESIGN PRINCIPLES

2.1. Reed-Solomon Codes Encoding

Reed-Solomon codes are non-binary cyclic codes with symbols made up of m-bit sequences, where m is any positive integer having a value greater than 2. All the symbol of the $m = 8$ R-S codes generated by the primitive polynomial $p(x) = x^8 + x^4 + x^3 + x^2 + 1$ is shown in Table 1.

In general, Reed-Solomon codes can be expressed as R-S (n, k, t) codes, where n is the total number of code symbols in the encoded block, k is the number of data symbols being encoded, t is the symbol-error correcting capability of the code, and $n - k = 2t$ is the number of parity symbols. The code minimum distance is given by $d_{\min} = 2t + 1$. For $m = 8$, the codeword length $n = 2^m - 1 = 255$, parity symbols $2t = n - k = 239$, code minimum distance, $d_{\min} = 2t + 1 = 17$.

Figure 1 shows the R-S code structural diagram. The decoding and encoding require 256 GF elements, which can be directly produced by a table circuit. Each codeword block, consisting of source information, $V(x)$ and protective symbols, is known as the parity check messages, $P(x)$. The generating polynomial $g(x)$ produced according to the number of correcting symbol, t can be represented as $g(x) = (x + \alpha)(x + \alpha^2)\ldots(x + \alpha^{2t})$; as $t = 8$ in this study, $g(x) = (x + \alpha^1)(x +$

Table 1: Code symbols of GF (2^8).

Power of α	Vectors over GF(2^8)	Power of α	Vectors over GF(2^8)	Power of α	Vectors over GF(2^8)	Power of α	Vectors over GF(2^8)
0	00000000	α^{33}	00100111	α^{67}	11000010	α^{101}	00100010
α^{0}	00000001	α^{34}	01001110	α^{68}	10011001	α^{102}	01000100
α^{1}	00000010	α^{35}	10011100	α^{69}	00101111	α^{103}	10001000
α^{2}	00000100	α^{36}	00100101	α^{70}	01011110	α^{104}	00001101
α^{3}	00001000	α^{37}	01001010	α^{71}	10111100	α^{105}	00011010
α^{4}	00010000	α^{38}	10010100	α^{72}	01100101	α^{106}	00110100
α^{5}	00100000	α^{39}	00110101	α^{73}	11001010	α^{107}	01101000
α^{6}	01000000	α^{40}	01101010	α^{74}	10001001	α^{108}	11010000
α^{7}	10000000	α^{41}	11010100	α^{75}	00001111	α^{109}	10111101
α^{8}	00011101	α^{42}	10110101	α^{76}	00011110	α^{110}	01100111
α^{9}	00111010	α^{43}	01110111	α^{77}	00111100	α^{111}	11001110
α^{10}	01110100	α^{44}	11101110	α^{78}	01111000	α^{112}	10000001
α^{11}	11101000	α^{45}	11000001	α^{79}	11110000	α^{113}	00011111
α^{12}	11001101	α^{46}	10011111	α^{80}	11111101	α^{114}	00111110
α^{13}	10000111	α^{47}	00100011	α^{81}	11100111	α^{115}	01111100
α^{14}	00010011	α^{48}	01000110	α^{82}	11010011	α^{116}	11111000
α^{15}	00100110	α^{49}	10001100	α^{83}	10111011	α^{117}	11101101
α^{16}	01001100	α^{50}	00000101	α^{84}	01101011	α^{118}	11000111
α^{17}	10011000	α^{51}	00001010	α^{85}	11010110	α^{119}	10010011
α^{18}	00101101	α^{52}	00010100	α^{86}	10110001	α^{120}	00111011
α^{19}	01011010	α^{53}	00101000	α^{87}	01111111	α^{121}	01110110
α^{20}	10110100	α^{54}	01010000	α^{88}	11111110	α^{122}	11101100
α^{21}	01110101	α^{55}	10100000	α^{89}	11100001	α^{123}	11000101
α^{22}	11101010	α^{56}	01011101	α^{90}	11011111	α^{124}	10010111
α^{23}	11001001	α^{57}	10111010	α^{91}	10100011	α^{125}	00110011
α^{24}	10001111	α^{58}	01101001	α^{92}	01011011	α^{126}	01100110
α^{25}	00000011	α^{59}	11010010	α^{93}	10110110	α^{127}	11001100
α^{26}	00000110	α^{60}	10111001	α^{94}	01110001	α^{128}	10000101
α^{27}	00001100	α^{61}	01101111	α^{95}	11100010	α^{129}	00010111
α^{28}	00011000	α^{62}	11011110	α^{96}	11011001	α^{130}	00101110
α^{29}	00110000	α^{63}	10100001	α^{97}	10101111	α^{131}	01011100
α^{30}	01100000	α^{64}	01011111	α^{98}	01000011	α^{132}	10111000
α^{31}	11000000	α^{65}	10111110	α^{99}	10000110	α^{133}	01101101
α^{32}	10011101	α^{66}	01100001	α^{100}	00010001	α^{134}	11011010

Power of α	Vectors over GF(2^8)	Power of α	Vectors over GF(2^8)	Power of α	Vectors over GF(2^8)	Power of α	Vectors over GF(2^8)
α^{135}	10101001	α^{165}	10010001	α^{195}	01100100	α^{225}	00100100
α^{136}	01001111	α^{166}	00111111	α^{196}	11001000	α^{226}	01001000
α^{137}	10011110	α^{167}	01111110	α^{197}	10001101	α^{227}	10010000
α^{138}	00100001	α^{168}	11111100	α^{198}	00000111	α^{228}	00111101
α^{139}	01000010	α^{169}	11100101	α^{199}	00001110	α^{229}	01111010
α^{140}	10000100	α^{170}	11010111	α^{200}	00011100	α^{230}	11110100
α^{141}	00010101	α^{171}	10110011	α^{201}	00111000	α^{231}	11110101
α^{142}	00101010	α^{172}	01111011	α^{202}	01110000	α^{232}	11110111
α^{143}	01010100	α^{173}	11110110	α^{203}	11100000	α^{233}	11110011
α^{144}	10101000	α^{174}	11110001	α^{204}	11011101	α^{234}	11111011
α^{145}	01001101	α^{175}	11111111	α^{205}	10100111	α^{235}	11101011
α^{146}	10011010	α^{176}	11100011	α^{206}	01010011	α^{236}	11001011
α^{147}	00101001	α^{177}	11011011	α^{207}	10100110	α^{237}	10001011
α^{148}	01010010	α^{178}	10101011	α^{208}	01010001	α^{238}	00001011
α^{149}	10100100	α^{179}	01001011	α^{209}	10100010	α^{239}	00010110
α^{150}	01010101	α^{180}	10010110	α^{210}	01011001	α^{240}	00101100
α^{151}	10101010	α^{181}	00110001	α^{211}	10110010	α^{241}	01011000
α^{152}	01001001	α^{182}	01100010	α^{212}	01111001	α^{242}	10110000
α^{153}	10010010	α^{183}	11000100	α^{213}	11110010	α^{243}	01111101
α^{154}	00111001	α^{184}	10010101	α^{214}	11111001	α^{244}	11111010
α^{155}	01110010	α^{185}	00110111	α^{215}	11101111	α^{245}	11101001
α^{156}	11100100	α^{186}	01101110	α^{216}	11000011	α^{246}	11001111
α^{157}	11010101	α^{187}	11011100	α^{217}	10011011	α^{247}	10000011
α^{158}	10110111	α^{188}	10100101	α^{218}	00101011	α^{248}	00011011
α^{159}	01110011	α^{189}	01010111	α^{219}	01010110	α^{249}	00110110
α^{160}	11100110	α^{190}	10101110	α^{220}	10101100	α^{250}	01101100
α^{161}	11010001	α^{191}	01000001	α^{221}	01000101	α^{251}	11011000
α^{162}	10111111	α^{192}	10000010	α^{222}	10001010	α^{252}	10101101
α^{163}	01100011	α^{193}	00011001	α^{223}	00001001	α^{253}	01000111
α^{164}	11000110	α^{194}	00110010	α^{224}	00010010	α^{254}	10001110

$\alpha^2)\ldots(x+\alpha^{16})$. The encoding is to acquire the residual, $P(x)$ of the long division of $V(x)$ and $g(x)$. In order to ensure that the sum of $V(x)$ and $P(x)$ can be divided by $g(x)$ without remainder, the order of $V(x)$ should be increased The encoding equation is as shown in (1):

$$Codewords = x^{2t} \cdot V\left(x\right) + \left\{V\left(x\right) \cdot x^{2t}\right\} \bmod\ g\left(x\right) \tag{1}$$

This paper implements an R-S encoder. The design process is as follows: establish GF (2^m) table (Table 1), calculate the coefficients of generating polynomial $g(x)$, and calculate the modules by dividing $g(x)$ shown as Fig. 2.

2.2. Reed-Solomon Codes Decoding

Some of the codeword will result in error during the transmission process; the received message symbol will be different from the original sending message. In order to identify the locations and values of the error symbols, the process is as follows: syndrome calculator, error location by Chien search algorithm, error values of relevant location using the Forney algorithm The complete R-S code decoding flowchart is shown in Fig. 3.

First, upon receiving the message, Syndrome calculator reveals whether the message contains any error. If syndrome is zero, it means that the message is correct. Syndrome calculator divides the received message by generating polynomial, and it is equivalent to input all the factors of $g(x)$ including α, $\alpha^2, \ldots, \alpha^{2t}$ into $r(x)$. If the calculation result is zero, it means that there is no error.

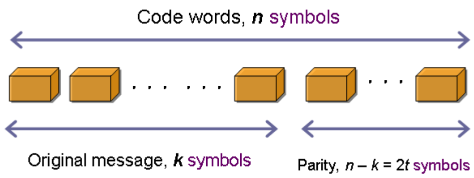

Figure 1: R-S code bit architecture SEM.

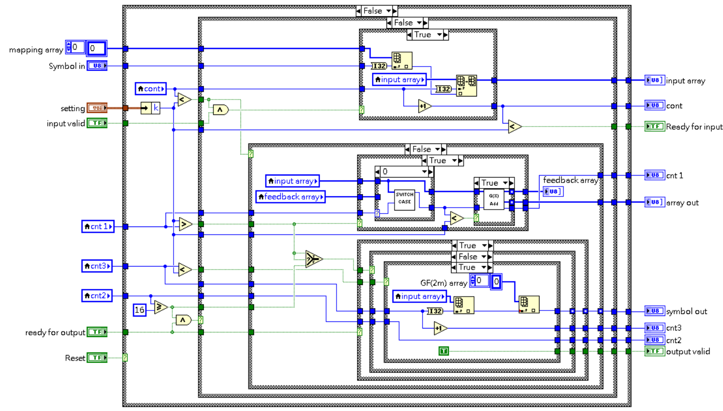

Figure 2: Reed-Solomon Encoder.

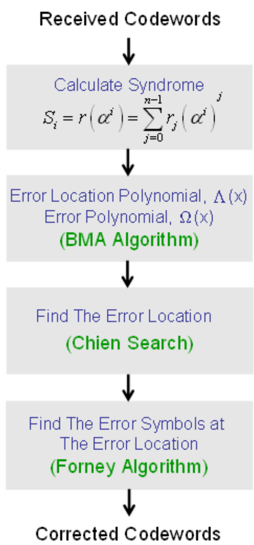

Figure 3: R-S code decoding process diagram.

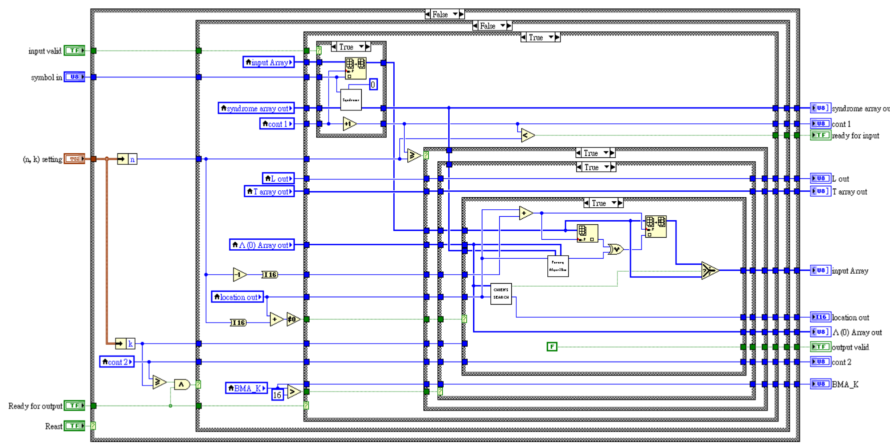

Figure 4: LabView FPGA reed-solomon codes decoding circuit.

The Syndrome calculator is shown in (2):

$$S_i = r\left(\alpha^i\right) = \sum_{j=0}^{n-1} r_j \left(\alpha^i\right)^j \quad 1 \le i \le 2t \tag{2}$$

The calculation of error polynomial is the core processing of the entire Reed-Solomon Coding. The BMA algorithm uses repeated iterated calculation to calculate the correction polynomial as shown in (3). Λ^k is the correction polynomial, k is the times of iteration, Δ^k is the Delta polynomial.

$$\sigma(x) = \Lambda^k(x) = \Lambda^{k-1}(x) - \Delta^k \mathrm{T}^{k-1}(x) \tag{3}$$

Chien search then is to find out all the locations of the error symbols by putting all α^{-i} ($i = 0$ to 20) into the error location polynomial $\sigma(x)$. If the result is zero, it indicates that α^{-i} is the root of the error location equation $\sigma(x) = 0$, the value of i represents the location of the error symbol of the received message polynomial $r(x)$. Combining the syndrome polynomial and error location polynomial, we define a key equation, $\Omega(x)$, as shown in (4).

$$\Omega(x) = [\sigma(x) \cdot S(x)] \bmod X^{2t} = \sum_{i=0}^{t-1} \Omega_i X^i \tag{4}$$

By Forney Equation (4), dividing the first order differentials of $\sigma(x)$, we can get the error vector $E(x)$ (5). Finally, according to the error vector $E(x)$, we can correct the values of the error symbols at the error locations indicated by Chien search method to restore the original accurate message.

$$E_i = \frac{\Omega\left(\alpha^{-i}\right)}{\alpha^{-i}\cdot\sigma'\left(\alpha^{-i}\right)} = \frac{\Omega\left(\alpha^{-i}\right)}{\alpha^{-i}\cdot\sigma_{odd}\left(\alpha^{-i}\right)} \tag{5}$$

3. IMPLEMENTATION OF REED-SOLOMON CODES

The encoding part establishes the primitive polynomial table to set the parameters. R-S decoding program contains sub-programs of the four steps of syndrome, error location, Chien search and Forney algorithm. The error location uses the BMA algorithm and Chien search are the most complex. In programming the calculation process, the script file should be broken into a few sub-programs separately for the application in BMA algorithm. Chien search works along with the final Forney algorithm program. As it may take up large amount of hard disc space, the Boolean elements are generated by programs to comply with its characteristics. The sub-programs are completed and summarized as shown in Fig. 4. Coupled with some judgment and control pins, the entire decoding can be executed. During the decoding process, after executing a block, the program needs to be reset to enter into next block, thus, the program needs to make automatic judgment. The decoding sequence is syndrome value, BMA, Chien search and Forney algorithm.

The result of the compiling verification of the 5641R FPGA module of LabView FPGA code shows that the Total Slice use rate is 6.8% (997 out of 14720) the use rate of the Slice Register is 2%(1167 out of 58880) and the use rate of the Slice LUTs is 4.5% (2642 out of 58880). Table 2 shows the Reed-Solomon code optimization efficiency.

4. SOFTWARE VERIFICATION OF REED-SOLOMON CODES

The error performance of R-S codes of (31, 15, 8) with BPSK modulation in AWGN environment is shown in Fig. 5. When the error probability is 10^{-4}, the R-S (31, 15, 8) coding gain can be up to 2 dB.

Regarding the R-S (31, 15, 17) codes used by Lin, 17 is $d_{\min}$, $d_{\min} = 2t + 1$, therefore, $t = 8$ and the R-S (31, 15, 8) in this study are the same codes. However, $m = 5$, it indicating that a symbol contains that is consisted of 5 bits and can correct 40 error bits; while can be corrected. The method proposed in this study can correct 64 error bits. If the E_b/N_0 is kept at 5 dB in the same AWGN channel environment, the error probability of R-S (31, 15, 8) is about 10^{-3} (blue solid square), and the error probability of R-S (31, 15, 17) is about 10^{-2} (the green circle) [10], it means

Table 2: Reed-Solomon code optimization efficiency.

Reed-Solomon Code Optimization efficiency								
LabView FPGA Code	Adders/Subtractors	Multiplexers	Counters	Registers	Comparators	Xors	Latches	Tristates
Reed-Solomon Code	17	19	6	643	12	11847	1	89
BMA	9	19	6	636	8	3290	1	89
Chien's & Forney	9	2	6	634	10	8291	1	89
Syndrome	7	2	6	636	8	282	1	89

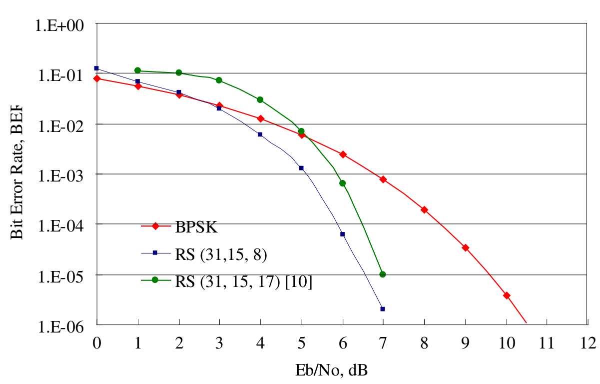

Figure 5: Reed-Solomon codes (31, 15, 8) error probability performance analysis.

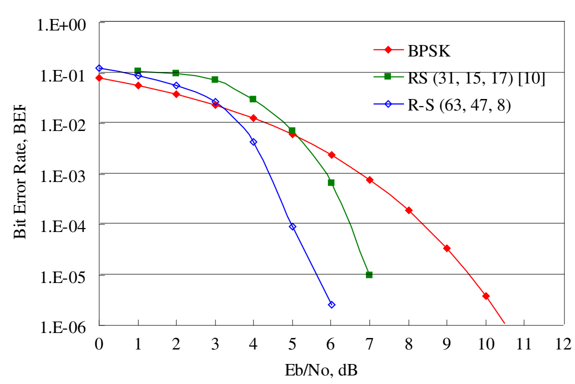

Figure 6: Reed-Solomon codes (63, 47, 8) error probability performance analysis.

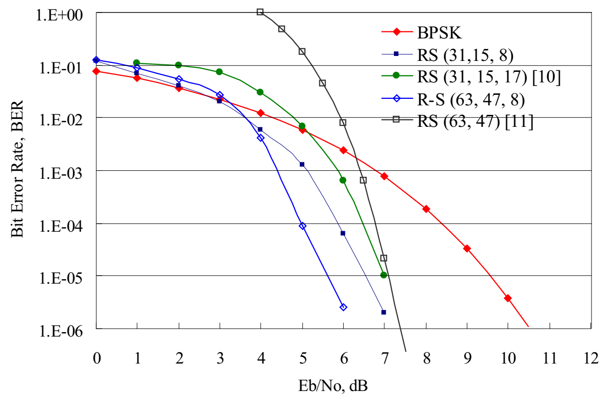

Figure 7: Reed-Solomon codes error probability performance analysis.

the error probability of R-S (31, 15, 8) is lower than that of R-S (31, 15, 17) by about 10^{-1} at the same transmission power.

The error performance of R-S codes of (63, 47, 8) with BPSK modulation in AWGN environment is shown in Fig. 6.

The E_b/N_0 thresholds of BPSK R-S (63, 47, 8) (blue empty diamond) is at 3.2 dB. In addition, when the error probability is 10^{-5}, the R-S (63, 47, 8) coding gain can be up to 4 dB.

If the E_b/N_0 is kept at 5 dB in the same AWGN channel environment, the error probability of R-S (63, 47, 8) is about 10^{-4} (blue empty diamond), nevertheless, the error probability of R-S (31, 15, 17) is about 10^{-2} (the green square) [10], it means the error probability of R-S (63, 47, 8) is lower than that of R-S (31, 15, 17) by about 10^{-2} at the same transmission power. At same bit error probability $P_b = 10^{-5}$, the E_b/N_0 value of R-S (31, 15, 17) is 7 dB, yet, the E_b/N_0 value of R-S (63, 47, 8) is 5.5 dB. There is a 1.5 dB difference between them.

In Fig. 7, we compare both R-S (31, 15, 8) and R-S (63, 47, 8) codes implemented in this study with R-S (31, 15, 17) [10] and R-S (63, 47) [11] codes, and find out the best power-saving code among the four. When the error probability is 10^{-4}, the coding gain of R-S (31, 15, 17) [10] using $m = 5$ can be up to 2 dB, R-S (31, 15, 8) using $m = 8$ can be up to 2.5 dB, R-S (63, 47) [11] can be up to 1.5 dB and R-S (63, 47, 8) using $m = 8$ can be up to 3.5 dB. The result indicates that the R-S (63, 47, 8) implemented in this study has the best power-saving capacity.

As well in Fig. 7, Comparing the error performance, when the E_b/N_0 is fixed at 5 dB, the error probability of R-S (31, 15, 17) [10] is 10^{-2}; the error probability of R-S (63, 47) [11] is much greater than 10^{-1}; the error probability of R-S (31, 15, 8) code is small greater than 10^{-3}; and the error probability of R-S (63, 47, 8) code is small less than 10^{-4}, indicating that the R-S (63, 47, 8) implemented in this study has the best correction capacity.

REFERENCES

1. Lin, S. and D. J. Costello, Jr., *Error Control Coding Second Edition*, 2nd Edition, 237–251, Pearson Prentice Hall, United State of America, 2004.
2. Sklar, B., *Digital Communications Fundamentals and Applications*, 2nd Edition, 437–460, Prentice Hall PTR, Oct. 2005.
3. Hsu, C.-H., "Design of Reed-Solomon decoder and implement on FPGA," 7–22, Jun. 2007.
4. Hsueh, W.-L., "Reed-Solomon decoder hardware implementation for digital video broadcasting standard for terrestrial transmission (DVB-T) channel coding," 35–51, Jun. 2005.
5. Almeida, G. M., "A Reed-Solomon algorithm for FPGA area optimization in space application," *Second NASA/ESA Conference on Adaptive Hardware and System*, 2007.
6. Mahajan, S. and G. Singh, "Reed-Solomon code performance for M-ary modulation over AWGN channel," *International Journal of Engineering Science and Technology*, Vol. 3, 3739–3745, May 2011.
7. Liu, T. and C. Zhang, "Optimization design of Reed-Solomon decoder based on FPGA," *IEEE for the Central Universities*, HEUCF110802, 368–371, 2011.
8. Ardalan, S., K. Raahemifer, F. Yuan, and V. M. Geukov, "Reed-Solomon encoder & decoder design, simulation and synthesis," *IEEE CCECE 2003-CCGEI*, 255–258, May 2003.

9. Zhu, J. and X. Zhang, "Efficient Reed-Solomon decoder with adaptive error-correcting capacity," *19th Annual Wireless and Optical Communications Conference (WOCC)*, 2010.
10. Liu, C. Y. and S. Lin, "Turbo encoding and decoding of Reed-Solomon codes through binary decomposition and self-concatenation," *IEEE Transactions on Communications*, Vol. 52, No. 9, Sep. 2004.
11. Hu, T.-H. and M.-H. Chang, "Decoding shortened Reed-Solomon codes at bit level," *WSEAS Transactions on Communications*, Vol. 9, No. 11, Nov. 2010.

Design of a Bandwidth-enhanced Ultra Thin Metamaterial Absorber

Saptarshi Ghosh, Somak Bhattacharyya, and Kumar Vaibhav Srivastava
Department of Electrical Engineering, Indian Institute of Technology, Kanpur, India

Abstract— This paper presents a low-profile (single layer) circular metamaterial (MTM) microwave absorber structure based on electric field driven LC (ELC) resonator. The structure is simulated in HFSS solver giving rise to almost unity absorption (99.92%) at 11.22 GHz (X-band). Further a 2×2 array using two different variants of the same resonating structure (different number of concentric rings) has been studied, which shows two discrete absorption peaks. When these peaks are brought closer by optimizing its dimensions, the structure exhibits a bandwidth of 0.86 GHz (11.74–12.60 GHz) above 70% absorbance with two absorbance peaks at 12 and 12.5 GHz (95% and 93% absorbance respectively) and with minimum absorbance at 12.3 GHz (72% absorbance). This proposed bandwidth-enhanced MTM absorber can be used in stealth technology for both X and Ku bands for the application of battlefield and air borne radar. The proposed structure also shows high (94%) absorbance for angular incidence up to 50°.

1. INTRODUCTION

Electromagnetic (EM) metamaterials (MTM) are usually artificial composite materials consisting of periodic structural units much smaller than the wavelength of the incident radiation [1]. Because of some attractive properties of MTM structures that natural materials don't have, they can be applied in many fields, such as — negative refraction, perfect lens, cloaking, antenna miniaturization etc. in almost every technologically relevant spectral range — from radio wave, microwave, THz, MIR (mid-infrared), NIR (near-infrared), to the near optical frequency. EM microwave absorber [2] is one of the major applications of MTM which has several uses in different frequency ranges such as solar cell in infrared frequencies, reduction of Radar Cross Section in stealth technology in gigahertz domain and thermal detector at terahertz regime.

According to the effective medium theory, MTMs can be characterized by a complex frequency-dependent electric permittivity and magnetic permeability which can be tailored to minimize both transmittance and reflectance simultaneously at resonance frequency to obtain high absorption through resistive and dielectric loss. Split ring resonator (SRR) based MTMs were initially used as microwave absorbers [3], but Electric field driven (ELC) resonating structures [4] are now extensively used as absorbers since EM waves travel lesser distance in ELC compared to the conventional SRR based structure.

In this paper, an ELC driven bandwidth enhanced MTM absorber has been proposed based on double resonance. First, we have presented a single band circular MTM absorber, where absorption takes place at 11.22 GHz. After analyzing the structure, two different variants of the same structure has been taken in a 2×2 array, which gives two distinct absorption peaks. Then the dimensions of the array structure are optimized to bring the peaks closer which exhibits a full width at half maximum (FWHM) of 8.69% around 12.17 GHz with a minimum value of 72% at 12.30 GHz for normal incidence.

2. DESIGN OF THE STRUCTURE

The proposed MTM structure consists of two conductive copper layers (conductivity of 5.8×10^8 S/m) separated by a lossy dielectric substrate FR-4 (relative permittivity $\varepsilon_r = 4.4$ and dielectric loss tangent $\tan\delta = 0.02$) [5]. The bottom layer is completely grounded and the top layer consists of a number of concentric copper rings, each connected with its successive ring by a small strip as shown in Figure 1(a). The dimensions of the top copper layer along with the directions of electric field, magnetic field and wave propagation have also been shown in this figure.

When a wave is incident on the interface of two media, the absorbance in the second medium can be expressed as in (1), where $Z(\omega)$, $A(\omega)$, $|S_{11}|^2$ and $|S_{21}|^2$ are the input impedance, absorbance, reflected power and transmitted power respectively at an angular frequency ω.

$$A(\omega) = 1 - |S_{11}|^2 - |S_{21}|^2 \tag{1}$$

Since the structure is completely copper backed, $|S_{21}| = 0$ and thus (1) is reduced to

$$A(\omega) = 1 - |S_{11}|^2.$$

Now, when EM wave is incident on the structure, the electric field is coupled with the top ELC structure, which controls the electric permittivity $\varepsilon(\omega)$ and the anti-parallel current between the top layer and the metal ground plane can be coupled with the magnetic field which controls the magnetic permeability $\mu(\omega)$ of the resonating structure. Thus by tuning the physical parameters of the top copper layer and the thickness of the dielectric substrate, the electric and magnetic fields can be highly coupled in a particular frequency range where the input impedance $Z(\omega)$ as given in (2) can be matched with free space impedance η_0 at the interface resulting minimization of S_{11} of the structure as deduced in (3) [6].

$$Z(\omega) = \sqrt{\frac{\mu_r\mu_0}{\varepsilon_r\varepsilon_0}} = \eta_0\sqrt{\frac{(1+S_{11}^2)-S_{21}^2}{(1-S_{11}^2)-S_{21}^2}} \tag{2}$$

$$S_{11} = \frac{Z(\omega)-\eta_0}{Z(\omega)+\eta_0} \quad (\text{Since } |S_{21}| = 0) \tag{3}$$

To understand the mechanism of high absorption (due to ohmic and dielectric loss), we consider the effective refractive index $n(\omega)$ of the structure as given in (4), where k is the wave number and t is the thickness of the structure [6].

$$n(\omega) = \frac{1}{kt}\cos^{-1}\left[\frac{1}{2S_{21}}\left(1-S_{11}^2-S_{21}^2\right)\right] \tag{4}$$

Since $S_{21} = 0$, the effective refractive index of the structure can't be accurately determined from (4). Therefore, we can roughly estimate $n(\omega)$ from its relation with the scattering parameters as in (5) [7].

$$e^{inkt} = \frac{S_{21}}{1-S_{11}\frac{Z-1}{Z+1}} \tag{5}$$

Now, in order to make right side of (5) zero, the imaginary part of refractive index $n(\omega)$ should be very high, which ensures that the wave attenuates significantly as propagating through the MTM absorber.

The equivalent LC-circuit analysis of the structure in Figure 1(a) shows that the circular rings provide the effective inductance L and the gaps between the concentric rings provide the effective capacitance C. By tuning the geometrical dimensions (radius of the rings r and the gap widths w), we can adjust the resonance peaks as desired.

Now when we take two different variants (different number of concentric rings, radii and gap lengths) of the same structure in a 2×2 array such that 1st and 4th structures are same and 2nd and 3rd structures are of similar type as shown in Figure 1(b), then each set of the two structures give distinct resonance peaks independently. Now, when the dimensions of those structures are optimized to bring the peaks closer, a broadband absorber can be realized as shown in Figure 4 [8].

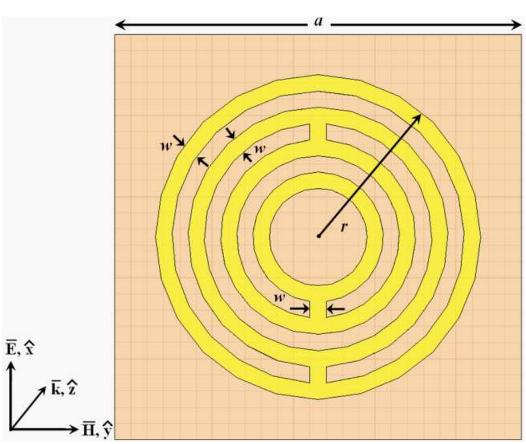

(a)

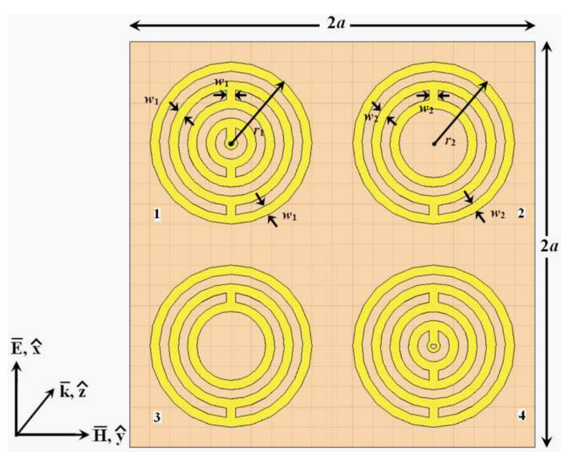

(b)

Figure 1: (a) Proposed single band structure; the parameters are $w = 0.2\,\text{mm}$, $r = 1.8\,\text{mm}$, and $a = 5\,\text{mm}$. (b) Proposed bandwidth-enhanced structure; the parameters are $w_1 = 0.23\,\text{mm}$, $w_2 = 0.23\,\text{mm}$, $r_1 = 1.8\,\text{mm}$, $r_2 = 1.8\,\text{mm}$, and $2a = 10\,\text{mm}$.

3. SIMULATED RESULTS

The simulation of the structure is carried out by using Finite Element Based solver High Frequency Structure Simulator (HFSS) where Periodic Boundary Conditions (PBC) are used with wave vector being perpendicular to the plane of the structure and electric field and magnetic field are parallel with the x-axis and y-axis respectively. The simulation of the first proposed structure shows a minimum of S_{11} at 11.22 GHz at the value of -30.93 dB as shown in Figure 2(a). The corresponding absorbance is obtained as 99.92% with a full width at half maximum (FWHM) equal to 4.27% around the absorption frequency as shown in Figure 2(b).

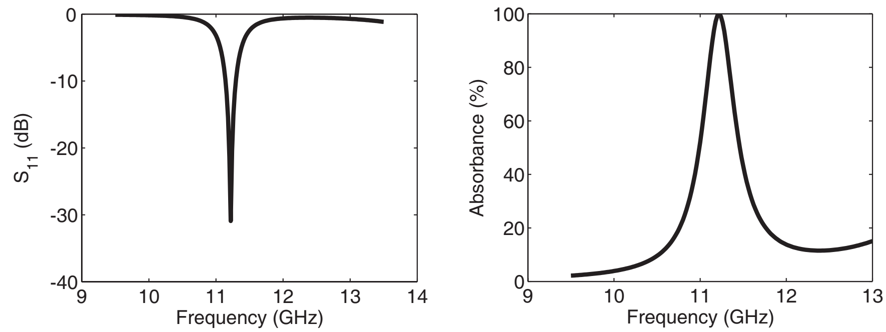

(a) (b)

Figure 2: (a) Reflection coefficient S_{11} (dB) and (b) absorbance (%) for the proposed single band structure as shown in Figure 1(a).

The dielectric and ohmic loss of the single band structure has been shown in Figure 3 which also ensures that the maximum absorption takes place at the absorption frequency 11.22 GHz.

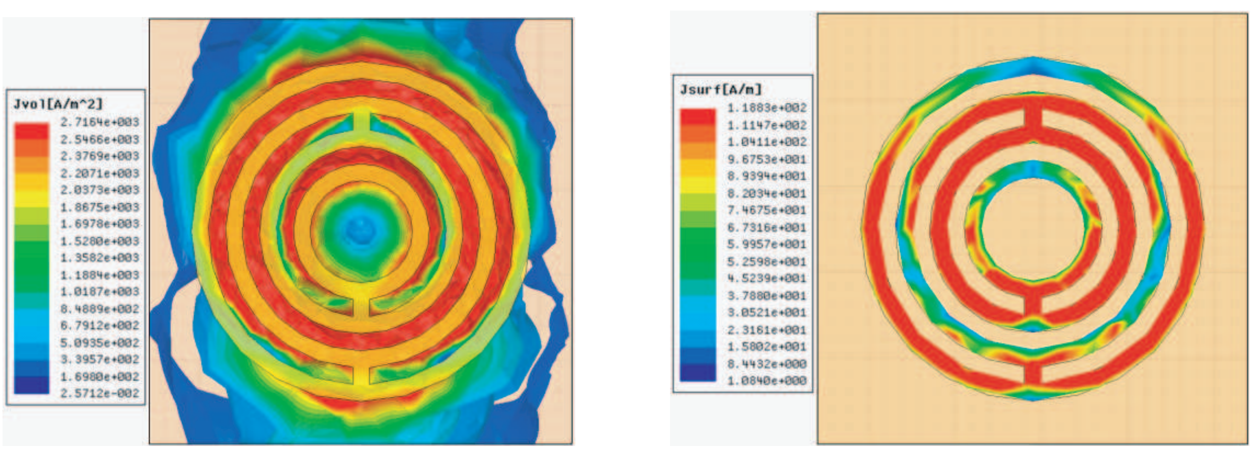

(a) (b)

Figure 3: (a) Dielectric loss and (b) ohmic loss of single band structure at frequency 11.22 GHz.

Now, when we simulate the proposed 2×2 unit cell array resonating structure using the same boundary conditions as above, there is a bandwidth enhancement as shown in Figure 4, where the structure exhibits a broadband of 0.86 GHz (11.74–12.60 GHz) above 70% absorbance with two absorbance peaks at 12 and 12.5 GHz (peak absorbance 95% and 93% respectively) with the minimum absorbance at 12.3 GHz (72% absorbance).

Since $S_{21} = 0$, the input impedance $Z(\omega)$ as given in (2) can be reduced to

$$Z(\omega) = \eta_0 \frac{1 + S_{11}}{1 - S_{11}}. \tag{6}$$

The real and imaginary parts of the input impedance are calculated for both the single band and the bandwidth-enhanced structure (shown in Figure 1) and shown in Figure 5.

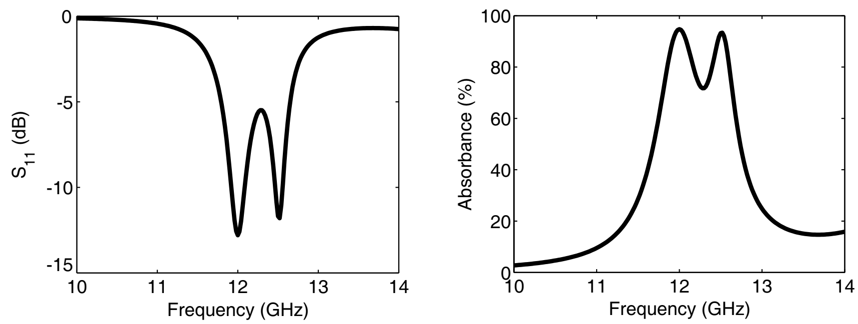

(a) (b)

Figure 4: (a) Reflection coefficient S_{11} (dB) and (b) absorbance (%) for the proposed bandwidth-enhanced structure as shown in Figure 1(b).

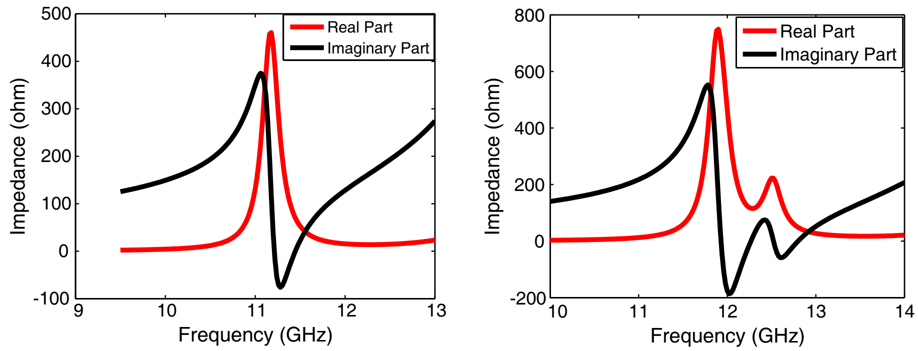

(a) (b)

Figure 5: Impedance plot of the proposed (a) single-band and (b) bandwidth-enhanced structure.

The proposed single band MTM structure is highly absorptive with wide incident angle ranging from 0° to 50° for oblique incidence of electric field as well as for different polarizations of electric field as shown in Figure 6.

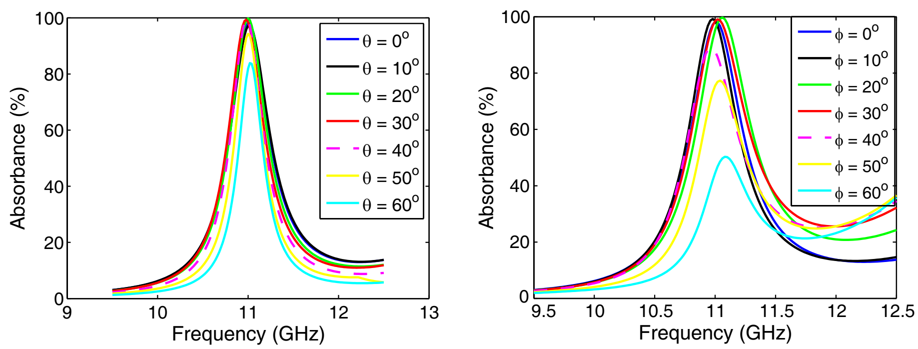

(a) (b)

Figure 6: (a) Oblique incidence (θ-variation) for variation of E-field at constant phi ($\phi = 0°$) angle and (b) normal incidence for variation of E-field along phi (ϕ) for constant theta ($\theta = 0°$) angle at absorption frequency 11.22 GHz.

4. CONCLUSION

In this paper, we propose an ultra thin ELC driven microwave absorber having a total thickness of 1.07 mm ($\sim \lambda/25$). By optimizing the dimensions of the resonating structures, the absorption peaks are brought closer to realize bandwidth- enhanced absorption with a FWHM of 8.69% around 12.17 GHz. The single band structure (as shown in Figure 1(a)) also gives above 94% absorbance for changing the angle of incident of wave vector up to 50°. This proposed bandwidth-enhanced MTM absorber can be used in stealth technology for both X and Ku bands for the application of battlefield and air borne radar.

ACKNOWLEDGMENT

The authors want to acknowledge all the members of Microwave Circuit Laboratory and Microwave Metamaterial Laboratory for their continuous support and IIT Kanpur for the financial assistance.

REFERENCES

1. Veselago, V. G., "The electrodynamics of substances with simultaneously negative value of ε and μ," *Sov. Phys. Usp.*, Vol. 10, No. 4, 509–514, 1968.
2. Schurig, D., J. J. Mock, and D. R. Smith, "Electric-field-coupled resonators for negative permittivity metamaterials," *Applied Physics Letters*, Vol. 88, 041109, 2006.
3. Bilotti, F., L. Nucci, and L. Vegni, "An SRR-based microwave absorber," *Microwave and Optical Technology Letters*, Vol. 48, No. 11, 2171–2175, Nov. 2006.
4. Landy, N. I., S. Sajuyigbe, J. J. Mock, D. R. Smith, and W. J. Padilla, "Perfect metamaterial absorber," *Physical Review Letters*, Vol. 23, 207402, 2008.
5. Li, M. H., L. H. Yang, B. Zhou, X. P. Shen, Q. Cheng, and T. J. Cui, "Ultrathin multiband gigahertz metamaterial absorbers," *Journal of Applied Physics*, Vol. 110, 014909, 2011.
6. Smith, D. R., D. C. Vier, T. Koschny, and C. M. Soukoulis, "Electromagnetic parameter retrieval from inhomogeneous metamaterials," *Physical Review E*, Vol. 71, 036617, 2005.
7. Chen, X. D., T. M. Grzegorczyk, B. I. Wu, and J. A. Kong, "Robust method to retrieve the constitutive effective parameters of metamaterials," *Physical Review E*, Vol. 70, 016608, 2004.
8. Lee, J. and S. Lim, "Bandwidth-enhanced and polarization-insensitive metamaterial absorber using double resonance," *Electronics Letters*, Vol. 47, 8–9, 2011.

Investigation of Parasitic Effects Induced by the Ground on LTCC Passive Components

Runiu Fang[1], **Min Miao**[1,2], **and Yufeng Jin**[1]

[1]National Key Laboratory of Science and Technology on Micro/Nano Fabrication
Peking University, Beijing, China
[2]Institute of Information Microsystem, Beijing Information Science and Technology University, China

Abstract— In this paper, the ground-induced parasitic effects on LTCC capacitors and inductors are studied. On the basis of the proposed circuit models, the effects are discussed and explained, and the results are verified by the FEA simulation. In terms of capacitors, the ground may serve for an extra electrode, couple with the existing ones, and cause discrepancy between effective capacitance seen at different ports. For inductors, the introduction of ground decreases both the effective inductance and the quality factor due to great negative mutual inductance induced into the component, and for both passive components, these effects are more obvious with a closer proximity of the ground.

1. INTRODUCTION

In the past decade, LTCC (Low Temperature Co-fired Ceramic) based module is considered as an alternative for the traditional silicon-based RF module, with lower cost and higher quality factor. Multilayer LTCC integrated passives have been demonstrated as a favorable option to realize passives of both high inductance or capacitance and high quality factor [1]. The increasing operation frequency and demand of high density integration of RF modules cause severe coupling and crosstalk problems between components, which can be dissipated to a great extent by inserting ground planes. Therefore, effects of ground planes on LTCC passives, mainly capacitors and inductors, need to be investigated.

[2] presents a thoroughly study on LTCC passive library, in which the ground-induced effect on inductors is concluded. However, the mechanism behind the conclusion is not well explained. Besides, the effects on capacitors is not investigated. In this paper, the ground-induced parasitic effects on LTCC capacitors and inductors are discussed and explained respectively. In terms of capacitors, the ground-induced effects cause the discrepancy between effective capacitance seen at different ports. The coupling between the electrode of the capacitor and the ground adds to the effective capacitance, and is strengthened with the closer proximity of the ground. For LTCC inductors, decreasing the distance between ground and inductor leads to both a lower effective inductance and quality (Q) factor, and the self resonant frequency (SRF) is slightly increased. For RF applications, these effects can be exploited to achieve specific designing scheme or at least need to be addressed during the design process of passive components.

2. CAPACITORS

Capacitors are extensively used in decoupling, filter, tuning and rectifying circuits. The LTCC capacitor is generally implemented as parallel plate capacitors by screen printing silver/gold film served as platy electrodes on different layers. Fig. 1(a) illustrates the three-dimensional views of a double-plate capacitor, also known as Metal-Insulator-Metal Capacitor. Besides, multilayer configurations such as triple-plate and quadruple-plate capacitor configuration, known as VIC (vertically interdigitated capacitors) are also widely used [2]. Compared with double-plate capacitors, the size of VIC can be much smaller as multiple electrodes are assigned on more layers.

For LTCC capacitors configuration, the ground serves as the shielding plane and return path of the current, blocking electromagnetic leakage, and hence guarantee the signal and power integrity of the system. However, the insertion of the ground inevitably induces parasitic effects to passive components. To investigate these effects of the ground on the capacitors, an equivalent lumped circuit model is applied as shown in Fig. 1(b). The resistance R_1, R_2 and the inductance L_1, L_2 represent the parasitic resistance and inductance. The capacitance C_S denotes the designed capacitance, while the capacitance C_G represents the parasitic capacitance between the electrode and the ground.

Impact of C_S and the parasitic elements should be all taken into account, especially for high frequency applications, the latter ones can be more dominant. Through applying the simplified

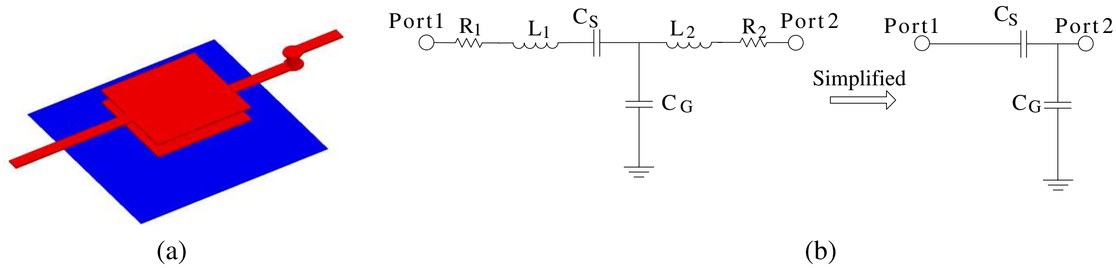

Figure 1: (a) Three-dimensional views of a double-plate capacitor. (b) Schematics of lumped circuit model of LTCC capacitors.

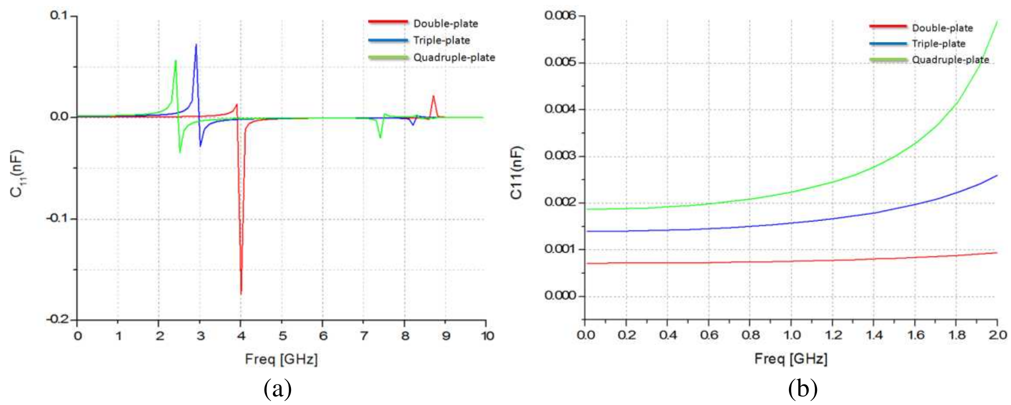

Figure 2: Simulated effective capacitance in the frequency range of (a) 0–10 GHz and (b) 0–2 GHz.

Table 1: Effective capacitance seen at different ports with different D_G.

D_G	0.5 mm	0.4 mm	0.3 mm	0.2 mm	0.1 mm
C_{11} (pF)	0.70	0.71	0.71	0.72	0.76
C_{22} (pF)	0.90	0.93	0.99	1.12	1.55

circuit model shown in Fig. 1(b), the effective capacitance is derived from Y_{11} and Y_{22} of the two-port admittance matrix given by $Y_{11} = \frac{1}{j\omega C_S}$, and $Y_{22} = \frac{1}{j\omega C_S} + \frac{1}{j\omega C_G}$ respectively.

Due to the asymmetric nature of the circuit, the effective capacitance seen at port 1 and port 2 shown in Fig. 1(b) is different, and the discrepancy between is caused by the ground. C_{11} represents the effective capacitance seen at port 1 given by $C_{11}(\omega) = -1/\omega \mathrm{Im}|Y_{11}|$, and C_{22} represents the effective capacitance seen at port 2 given by $C_{22}(\omega) = -1/\omega \mathrm{Im}|Y_{22}|$. The angular frequency ω is given by $2\pi f$ where f is the frequency. In our case for the double-plate capacitor, the C_{11} is smaller than C_{22} by the value of C_G.

The conclusion is verified by the electromagnetic FEA simulator, HFSS. Dupont 951AT tapes are utilized. The tapes have a dielectric constant of 7.8 and a loss tangent of 0.0015 at 100 MHz. The electrodes are squares with the side length of 0.8 mm and the distance between of 0.1 mm. Table 1 gives the value of C_{11} and C_{22} of the capacitor. The parameter D_G denotes the distance between the lower electrode of the capacitor and the ground. The effective capacitance is extracted at 10 MHz where effects of parasitic inductance can be ignored. As shown in Table 1, C_{22} is larger than C_{11}, and the difference between them is increasing when D_G decreases. According to our circuit model, the difference between them is equal to the value of C_G illustrated in Fig. 1(a) and is generally inversely propositional to D_G. The slight increase of C_{11} with the decreasing D_G is due to the relatively small coupling between the upper electrode and the ground. In conclusion, the parasitic effect of the ground is more obvious with a closer proximity of the ground.

Figure 2 shows the simulated C_{11} of double-plate, triple-plate and quadruple-plate LTCC capacitors up to 10 GHz. The self resonant frequency (SRF), which determines the usable frequency range of the component, decreases with the increasing number of plates, which is essentially caused by the increase of capacitance. The simulated C_{11} within the SRF range (0–2 GHz) is shown in Fig. 2(b). Note that the effective capacitance generally exhibits the linear increase with the number of plates over the frequency range, and for triple-plate capacitors, the lowest electrode is connected to port 1, thus the effective capacitance of C_{11} is larger than C_{22} because of the ground coupling. The simulated result indicates a C_{11} of 1.54 pF and C_{22} of 1.27 pF at 10 MHz for triple-plate capacitors. For the same reason, C_{11} should be smaller than C_{22} for quadruple-layer capacitor, which is verified by the results of $C_{11} = 1.90$ pF and $C_{22} = 2.18$ pF at 10 MHz.

3. INDUCTORS

Inductors is one of key components of every RF/microwave circuit, particularly in voltage control oscillator (VCO), power amplifier, low noise amplifier and filter. To evaluate the ground-induced parasitic effects on LTCC inductors, three indicators, namely the effective inductance, the quality (Q) factor and the SRF are utilized.

Figure 3(a) shows the model of a common LTCC spiral inductors. We apply the simplified π circuit model to LTCC inductors as shown in Fig. 3(b). The inductance L_S represents the inductance of the system, including the inductance of spiral inductors, conductor lines and mutual inductance between conductors. The resistance R_1 and R_2 represent the resistance of the conductor lines. Capacitance C_S and C_{G1}, C_{G2} represent the capacitance between different turns of the spiral inductor and capacitance between ground and the spiral inductor respectively. Considering the lossless circuit, the admittance matrix is as

$$\begin{bmatrix} Y_{11} & Y_{12} \\ Y_{21} & Y_{22} \end{bmatrix} = \begin{bmatrix} j\omega C_{G1} + j\omega C_S + \frac{1}{j\omega L_S} & -j\omega C_S - \frac{1}{j\omega L_S} \\ -j\omega C_S - \frac{1}{j\omega L_S} & j\omega C_{G2} + j\omega C_s + \frac{1}{j\omega L_S} \end{bmatrix} \tag{1}$$

The two shunt capacitance C_{G1}, C_{G2} is extracted as

$$C_{G1} = \frac{Y_{11}(\omega) + Y_{12}(\omega)}{j\omega} \tag{2}$$

$$C_{G2} = \frac{Y_{22}(\omega) + Y_{21}(\omega)}{j\omega} \tag{3}$$

According to the definition, the effective inductance seen at port 1 is given by $L_{eff} = \frac{\mathrm{Im}\left[\frac{1}{Y_{11}}\right]}{\omega}$, and L_S is calculated as

$$L_S = \frac{\omega_{rp}^2 - \omega^2}{\omega\omega_{rp}^2 \mathrm{Im}[Y_{11}(\omega) + Y_{22}(\omega)] + \frac{\omega_{rp}^2}{L_{eff}}}, \tag{4}$$

where ω_{rp} is the angular frequency when $\mathrm{Im}[Y_{12}]$ becomes zero.

The admittance matrix is obtained through simulation of HFSS. The width of conductor lines is 0.1 mm and the pitch between them is 0.25 mm. The ground locates under the inductor. In order to examine the effect of the ground, cases of different distance between the ground and the inductor are investigated. The Q factor is given by $\mathrm{Im}[1/Y_{11}]/\mathrm{Re}[1/Y_{11}] = -\mathrm{Im}[Y_{11}]/\mathrm{Re}[Y_{11}]$ based on its definition. Notice that when Q factor becomes zero, which means the reactance ($\mathrm{Im}[Y_{11}]$) of the circuit is zero, the circuit is working under its SRF.

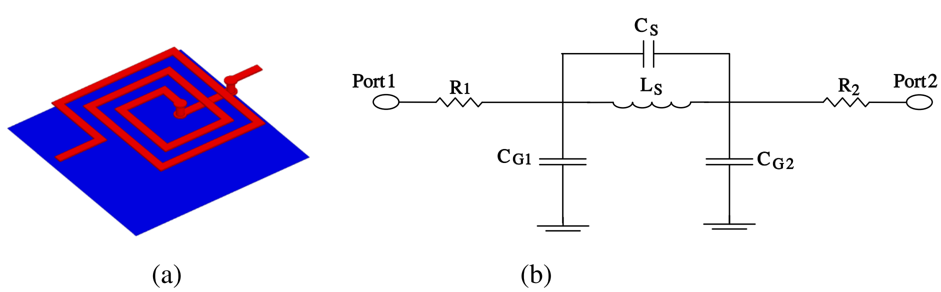

Figure 3: (a) Three-dimensional view and (b) schematics of lumped circuit model of LTCC spiral inductors.

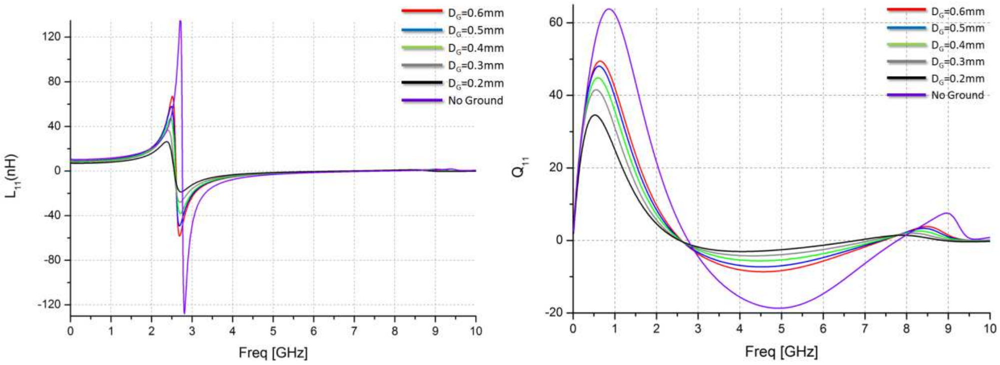

(a) (b)

Figure 4: Simulated (a) effective inductance and (b) Q factor of different D_G.

Table 2: Extracted results of the inductor.

item / D_G (mm)	C_{G1} (pF)	C_{G2} (pF)	L_{eff} (nH)	L_S (nH)	SRF (GHz)	$Q_{\max}$	$f_{Q\max}$ (GHz)	$J_{\max}$ (A/m^2)
0.6	0.44	0.39	9.79	9.50	2.60	49	0.72	5.53
0.5	0.47	0.42	9.39	9.30	2.58	48	0.62	8.23
0.4	0.51	0.48	8.99	8.93	2.58	44	0.60	9.61
0.3	0.59	0.59	8.23	8.24	2.55	41	0.55	15.62
0.2	0.74	0.82	7.10	7.13	2.55	34	0.52	35.38

Table 2 summarizes the extracted data of the cases of different distance between the ground and the inductor, D_G, The results clearly indicate that the decreasing D_G makes the effective inductance, L_{eff} smaller, and L_{eff} is extracted at the frequency point of maximum Q factor, $f_{Q\max}$.

Figure 4 presents the results of simulated effective inductance seen at port 1, L_{11} in the cases of different D_G. The effective inductance increases with the frequency before the SRF point. The increasing D_G leads to both higher effective inductance and higher Q factor, while the SRF is almost kept the same. Considering the infinite-distance ground case, the benefits of a far-away ground are more obvious. As is shown in Fig. 4, the case of the infinite-distance ground and the case of $D_G = 0.6$ mm exhibit Q factor of 65 and 49 and SRF of 2.76 GHz and 2.61 GHz respectively.

The extracted results also show that as D_G decreases, the shunt capacitance C_{G1} and C_{G2} will increases, while the system inductance, L_S will decreases, which are explained as follows. On one hand, the increasing shunt capacitance resulted from a closer ground is beneficial to the effective inductance L_{eff} seen at ports, because the shunt capacitors are in paralleled with the spiral inductor, which will increase the input impedance, and consequently increase the effective inductance. On the other hand, Close proximity of the ground to the inductor reduces the system inductance due to the negative mutual coupling caused by the current flowing in the ground in the opposite direction to the inductor current flow [3]. Table 2 present the maximum value of the induced eddy current density, $J_{\max}$ of different ground position, and $J_{\max}$ is increasing rapidly when ground is placed nearer, which implies the mutual inductive coefficient is increasing rapidly with the closer proximity of the ground. According to the extracted effective inductance, L_{eff} in Table 2, we can conclude that the negative mutual inductance is more dominant in affecting the effective inductance.

4. CONCLUSIONS

In conclusion, we have investigated the ground-induced parasitic effects on LTCC capacitors and inductors. The effects are discussed and explained on the basis of the proposed lumped circuit models, and are verified by the FEA simulation. For capacitors, the ground may serve for an extra electrode, couple with the existing ones, and cause discrepancy between effective capacitance seen at different ports. For inductors, the introduction of ground decreases both the effective inductance and the quality factor due to great negative mutual inductance induced into the component.

ACKNOWLEDGMENT

The work presented here has been co-funded by National Natural Science Foundation of China (Project. No. 61176102 "LTCC Micromachined Accelerometer". 60976083 "Micromachined THz waveguide embedded into LTCC substrate, corresponding functional devices and process" and 60501007 "Bulk Micromachined Tunable Microwave filter"), and Chinese National High-tech R&D Program (863 Program, Project No. 2007AA04Z352, "Micro/Nano Vacuum Packaging Technology based on LTCC substrate"), Funding Project for Academic Human Resources Development in Institutions of Higher Learning Under the Jurisdiction of Beijing Municipality, (Project. No. PHR201108257, "Research on Technical Basics for three-dimensional system-in-package") and also supported by Beijing Natural Science Foundation (Project No. 3102014 "Microfabrication of cooling microtube network embedded into multilayer substrate for system-in-package"), China. In addition, research funding from National S&T Major Project with the contract No. 2009ZX02038 "Key technologies for high-density 3-dimensional system-in-package" is greatly acknowledged.

REFERENCES

1. Brown, R. L., A. A. Shapiro, and P. W. Polinski, "Integration of passive components into MCMs using advanced low-temperature cofired ceramics," *International Journal of Microcircuits and Electronic Packaging*, Vol. 16, No. 4, 328–338, 1993.
2. Sutono, A., et al., "High-Q LTCC-based passive library for wireless system-on-package (SOP) module development," *IEEE Transactions on Microwave Theory and Techniques*, Vol. 49, No. 10, 1715–1724, 2001.
3. Remke, R. L. and G. A. Burdick, *Spiral Inductors for Hybrid and Microwave Applications*, 1974.

Microwave Optoelectronic Oscilator for Distribuited Receivers Operating Remotely

Larissa Aguiar Dantas de Britto,
Débora Maria Souza Morais, and Gefeson Mendes Pacheco
Microwave and Opto-Electronic Department, Aeronautics Technical Institute
Avenida Brigadeiro Eduardo Gomes, São José dos Campos, São Paulo, Brazil

Abstract— This paper describes the first results related to the implementation of a system combining microwave and photonic technologies in Brazil. Such combination comes from an circuit for radio frequency signals generation known as Optoelectronic Oscillator. Starting from a configuration previously presented in the literature, a small and innovative change in the oscillator feedback loop was proposed. The characterization of the photonic circuit reveals output signal amplitude of -27 dBm, line width less than 30 kHz and the phase noise better than -90 dBc/Hz for 1 MHz deviation. The obtained results are discussed in the spite of the previous theoretical analysis of the OEO and prospective applications for remote signal receivers.

1. INTRODUCTION

The combination of the low attenuation fiber-optics signal transmission and the microwave technology maturity is very attractive technology for high data capability telecommunication systems, to avoid EMI problems and when a complex high frequency system is operated remotely.

Considering receiver systems for radar and telecommunications it is importante to consider the oscillators sources. Radio frequency generation has been an important field of research and development since the beginning of the electronic engineering. The frequency, frequency stability and spectral characteristics are the most important parameters for all oscillators in a general point of view. The high frequency signal generation is generally accomplished by a master oscillator followed by a frequency multiplier circuit. Such multiplier contributes to increase the noise of the generated signal [1, 2]. The directly signal generation at high frequencies can be carried out by optical technics eliminating, in this way, the mentioned noise degradation. Such technical solution is also compatible with fiber-optics systems and long distance transmission. In this paper are presented the first results of high frequency generation by an optical oscillator with a small change from the initial idea proposed by early authors. Starting with an optical link discussion it is shown the oscillator configuration and results are presented. The final aim and next steps are pointed out together the conclusions.

2. OPTOELETRONIC OSCILATOR

The optoelectronic generation of microwave by optical oscillator, was first reported during the 90 [3]. Optoelectronic Oscillator, OEO, is a ring optical circuit with a fiber-optic length closing the feedback path. Such feedback length determines a time delay that defines the frequency step at the radio frequency output spectrum. As previously mentioned by the first authors the optoelectronic oscillator has a dual output. One, in the optical domain, that can be used to send a microwave signal along an optical fiber link and the other one that is in a radio frequency domain output that releases an electrical high frequency signal.

This paper brings smalls but important changes from the first OEO reported before. The used delay element was not a fiber-optic but a coaxial cable after the photodetector. This is different of the previous proposed setup because, in this case, the delay occurs at the radio frequency domain and not at the optical domain within the fiber-optic. Instead a dual output MZ optical modulator it was used a single output modulator followed by a directional coupler with 30/70 ratio for the outputs.

It is clear that a fiber-optic length delay will be obtained with less weight and volume than that one from coaxial cable, if one considers the same delay time τ. The use of a coaxial cable replacing the optical fiber is based on the two following points.

1. A high standard signal, with low noise phase, is not always necessary.
2. The fiber optic is a very temperature sensitivity component and the effects of radiation in space are not completely understood.

3. A small coaxial cable length (1 m) results on a cheap, stable and reliable delay component that can be easily constructed.

Changing, from a dual output modulator, for a single output one it was obtained a cost reduction even when one consider a OEO with only a radio frequency output without the directional coupling.

If one consider the OEO as an optical link plus a feedback loop it was possible to evaluate the net gain along the feedback loop necessary to generate the RF signal. The Figure 1 presents a such optical link scheme and the actual components.

Following the optical link analysis [4, 5] it is possible to calculate the minimum gain of the feedback loop to satisfy the oscillating state needs [6].

The optical gain of the optical link is given by the following equation

$$G_T = 10 \cdot \log(g_{Tms}) \tag{1}$$

where

$$g_{Tms} = \frac{4 \cdot S_{mz}^2 \cdot r_d^2 \cdot R_{mz}^2 \cdot T_F^2}{[(R_s + R_{mz})^2 + (\omega \cdot C_{mz} \cdot R_s \cdot R_{mz})^2] \cdot [1 + 4 \cdot (\omega \cdot C_D \cdot R_L)^2]} \tag{2}$$

And

$$S_{mz} = \frac{\pi \cdot T_{mz} \cdot P_{cw} \cdot R_s}{2 \cdot V_\pi} \tag{3}$$

The terms are: s_{mz} (slope efficiency of the Mach-Zehnder), R_s (ohmic resistance of the modulation source), ω (angular frequency), C_D (the photodetector junction capacitance), R_L (resistance of the laser), r_d (responsiveness of the optical receiver), C_{MZ} (capacitance of the Mach-Zehnder), P_{cw} (the laser optical power), T_{mz} (transmission coefficient of the optical Mach-Zehnder modulator) and T_F (coefficient of optical transmission between devices modulation and detection).

On the Table 1 are presented all the numerical values used for calculate the optical link gain according the above equations.

For P_{cw} equal to 19 mW it was obtained a -31.5 dB gain, for 10 mW the gain is equal to -25.9 dB.

The current diagram OEO constructed is shown in the Figure 2, where the optical domain is differentiated of electrical domain.

For each one domain there is an innovative change as pointed early.

The MZ is a single output one followed by a directional coupler. The delay line is obtained with a coaxial cable (on the electrical domain after the photodetector). Taking in account the

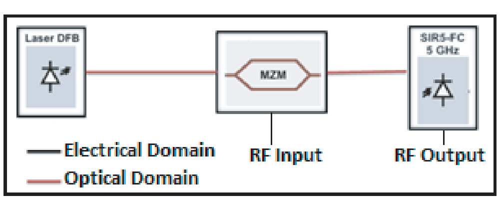

Figure 1: Optical link.

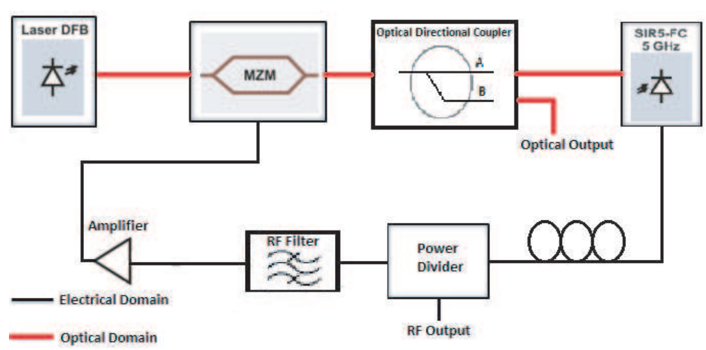

Figure 2: Scheme of OEO.

Table 1: Numerical values of gain parameters.

$T_{mz} = 0.4074$	$\omega = 6.283 \times 10^9$ rad/s
$P_{cw} = 10$ m ou 19 mW	$C_{mz} = 8.33 \times 10^{-12}$ F
$R_s = 50\,\Omega$	$R_{mz} = 50$
$V_\pi = 5.7$ V	$C_D = 0.3 \times 10^{-12}$ F
$S_{mz} = 56.35^{-3}$	$R_L = 50\,\Omega$
$r_d = 1$	$T_F = 0.79$

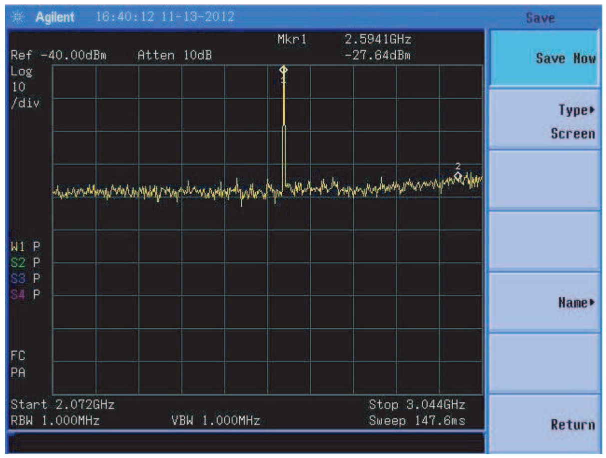

Figure 3: OEO output.

previous gain calculation it was selected a 40 dB amplification gain for the feedback loop gain (on the electrical domain).

On the Figure 3 it is possible to see the OEO radio frequency output.

On the Figure 3 it is shown a 2.5 GHz component at the RF output. The line width is less than 30 kHz and the output is equal -27 dBm. Such signal is also on the optical domain to be transmitted by an optical link from the optical output of the OEO.

3. CONCLUSIONS

The OEO is a technical solution for high frequency signal generation. The characteristics of the generated signal can match high standards and the choice of its components must take in account the final and specific use. Signal generation with frequency up to 3 GHz was observed with a feedback loop element made of a coaxial cable instead a fiber-optic length as previous works. An optical coupler was used instead a double output modulator. Such differences of previous works are innovative contributions in the field of OEO and cost reduction of such oscillator.

As the generated signal can be directly transmitted by a fiber optic (from the optical output of the OEO) the OEO can be used for a heterodyne microwave receptor as reference remotely oscillator. Such application is under investigation and the level requirements for a optical link are considered in the sense of spurious free dynamic range, SFDR, and noise figure, NF.

In nowadays there are efforts to use as laser source of the oscillator an VCSEL laser as others authors (7) for weight, size and energy consumption reducing.

ACKNOWLEDGMENT

The authors wish to acknowledge the Brazilian Space Agency, AEB, and the National Space Research Institute, INPE — for financial support of this work.

REFERENCES

1. Pan, S. and J. Yao, "Optical clock recovery using a polarization-modulator-based frequency-doubling optoelectronic oscillator," *Journal of Light wave Technology*, Vol. 27, No. 16, Aug. 2009.
2. Chang, W. S. C., *RF Photonics Technology in Optical Fiber Links*, Cambridge University Press, 2002.
3. Yao, X. S. and L. Maleki, "Optoelectronic microwave oscillator," *Optical Society of America*, Vol. 13, No. 8, 1725–1735, Aug. 1996.
4. Cox, C. H., *Analog Optical Links: Theory and Practice*, Cambridge University Press, 2004.
5. Junior, E. C. P., "Estudo e caracterização da transmissão de sinais de rádio frequência e microondas por meio de fibra óptica," 2010.
6. Sedra, A. S. and K. C. Simith, *Microelectronic Circuits*, 4th Edition, Oxford University Press, 1998.
7. Bacou, A. H., J. C. Mollier, and A. Rissons, "2.49 GHz low phase-noise optoelectronic oscillator using 1.55 μm VCSEL for avionics and aerospace applications," *SPIE Photonics West*, San Jose, USA, Jan. 19–24, 2009.

LTE Mixer Array of 0.5 W High Output Power

Pang-Hsing Chen, Yen-Heng Chen, and Jeng-Rern Yang
Microwave Laboratory, Department of Communication Engineering
Yuan Ze University, Jhongli City, Taoyuan Country 320, Taiwan

Abstract— The proposed design was applied to a 1.7 GHz mixer array power amplifier in an LTE system. The proposed design uses mixer units as array combinations and achieves combination by converging output currents at the mixer output point, utilizing the Balun transformer to convert double-ended signals to single-ended signals. In transmitter applications, a power amplifier designed using this method can realize a transmitter front-end circuit with a fully integrated CMOS and 0.5 W of input power. The results of the 16-unit simulation were as follows: the output power was 27 dBm and the power-added efficiency (PAE) was 19%. There was an overall supply voltage of 3 V, and the chip's area was approximately 1.512×1.285 mm.

1. INTRODUCTION

The power amplifier and up-converter are typically designed separately in CMOS RF front-end circuits. Regarding amplifiers, advancements in manufacturing techniques has caused the CMOS manufacturing process to improve from 0.18 μm to 0.13 μm, and even 35 nm. Because of its advantage of continuously decreasing size, the low-cost CMOS process can use a large amount of transistors to solve previously encountered design problems, therefore attaining a high, and possibly even a Watt-level, output power. In addition, regarding supply voltages, GSM and GPRS require peak-to-peak voltages of approximately 20 V. However, 0.18 μm transistors have the disadvantage of a low breakdown voltage, and their maximum drain voltage is 2 V, which only provides approximately 10 W of power. Therefore, the electrical impedance conversion method must be used at the output end to alter relationships with output voltage and current.

The proposed design is applied to the mixer array power amplifier in LTE systems. The design uses mixer units as array combinations and achieves combinations by converging the output currents at the mixer output point, using the Balun transformer to convert double-ended signals to single-ended signals. In transmitter applications, power amplifiers that are designed using this method can directly replace previous mixers and power amplifiers. In addition, because the mixer unit does not employ inductance, the area is not excessively large.

2. CIRCUIT DESIGN

As shown in Figure 1, the IF and LO signals enter the mixer separately to up-convert. Then, currents i_0, $i_1 \ldots i_n$ are converged at the output point into i_{out}, and the matching output circuit is used for combination before output is achieved.

2.1. The Mixer Unit

Consequently, mixer units are designed and arranged into arrays. Because mixer units with small areas are preferred in the selection of single mixer units, a traditional double-balanced Gilbert cell mixer (Figure 2) was selected. Figure 3 shows the design with the mixer unit output altered to

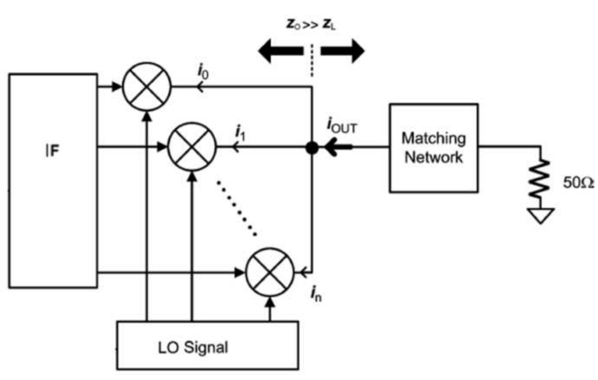

Figure 1: The mixer array structure schematic.

feature an additional level of a common-source amplifier and current converging methods. The common-source amplifier amplifies mixer signals and current shunts. Figure 4 shows the output power of a single mixer unit, and the output power is 14.5 dBm. Figure 5 shows the conversion gain, and the 1 dB compression point is 12 dBm.

2.2. The Balun Transformer Output

Figure 7 shows the structure of the array and the matching output network. For the mixers that were converged using currents, the observation of impedance was simpler. The key to this phenomenon

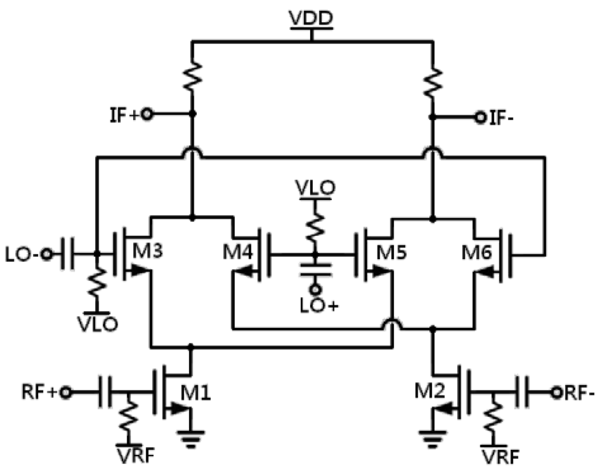

Figure 2: Traditional mixer.

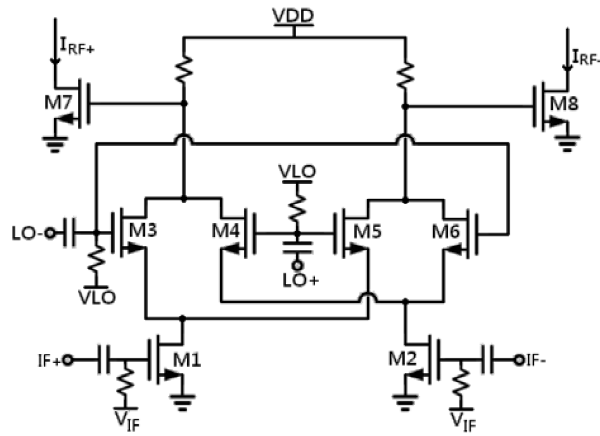

Figure 3: Current output mixer.

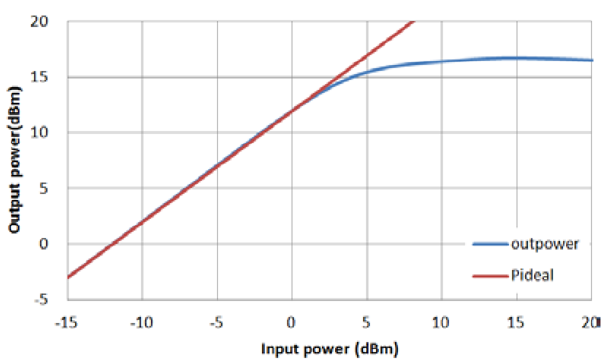

Figure 4: Up-converter unit (output power @ P1 dB).

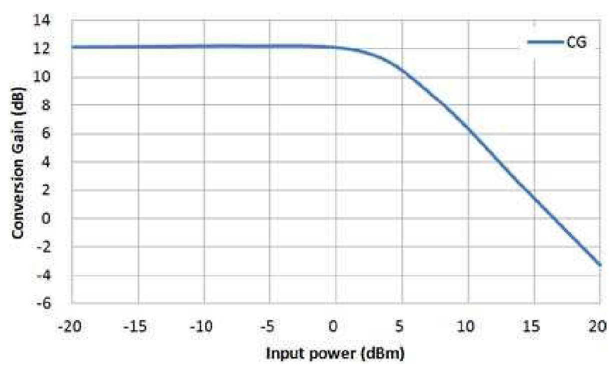

Figure 5: The correlation between the conversion gain and the input power of the up-converter unit (P1 dB).

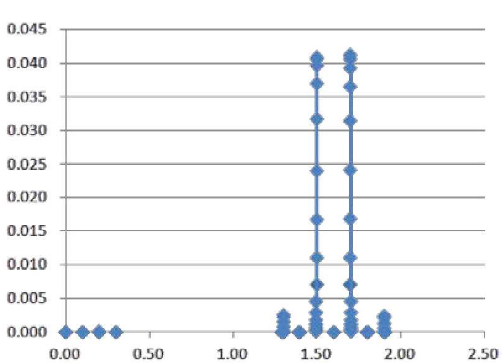

Figure 6: The output frequency spectrum of up-converter unit.

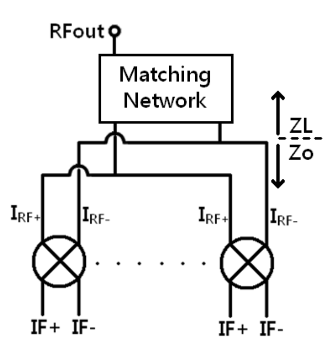

Figure 7: The overall array structure schematic.

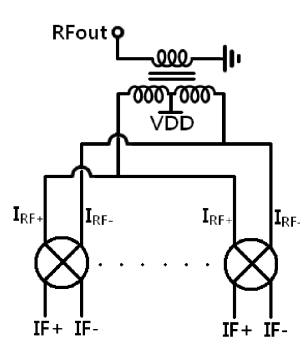

Figure 8: The overall array structure and output Balun transformer.

was that the observed output load Z_L in the mixer array must be sufficiently small. With 16 units, the output load must be approximately 6 ohm, and Z_0 is typically 50 ohm. The mixer array current output of the proposed design requires convergence of the output current of each unit. Therefore, output convergence is accomplished using the Balun transformer, which not only converges currents and combines power, but converts impedances and transforms the differential signals of the mixer to single-ended signals. Compared with original mixers that required inductances for matching, convergence using this method reduces the area that was required for previous methods. As shown in Figure 8, the output currents of all of the mixer units I_{RF+}, I_{RF-} were separately converged to the two ends of the Balun for conversion into single-ended RF signals for outputs.

Regarding the design of the Balun transformer, because the proposed design is primarily intended for use in power combining outputs, a highly coupling Finlay-winding Balun transformer was selected. For use as a Balun, the main coil employs symmetrical wiring and applies bias voltage to the center of the main coil to complete the design of the converged current output. Figure 9 shows a traditional transformer and the center-tapped bias voltage Balun transformer of the proposed design. The turn ratio can be calculated based on an equation. Because it is difficult to achieve large inductance values in integrated circuits, the inductance value can be independently adjusted to an appropriate value:

$$N = \frac{N_S}{N_{P1}} = \frac{N_S}{N_{P2}} = \sqrt{\frac{L_S}{L_P}} \tag{1}$$

In addition, because the main coil has two ends, the actual inductance value ratio should be

$$N = \frac{N_S}{N_{P1} + N_{P2}} \tag{2}$$

Figures 10–12 show simulations and layouts using a 2-unit Balun transformer. If the number of units is increased to 8 or 16, line width and current strength problems should be considered to avoid line widths that are too narrow to tolerate strong currents. In a 16-unit circuit, the turn ratio should be adjusted to 2.5 : 1, and the line width should be 35 µm — the maximum acceptable width in the manufacturing process. In addition, the routing from the bias voltages to the Balun transformer should be separated into 2 routes with line widths of 35 µm that converge into the Balun transformer to prevent routing intolerance to excessive currents.

3. SIMULATED RESULTS

All of the simulations used Agilent ADS to complete the design of the circuit. A TSMC 1P6M 0.18-µm CMOS standard manufacturing process component model was employed to perform the simulations. In addition, a PAD equivalent circuit was added to simulate parasitic effects. For the layouts, because the array units are mixers, the design must be more symmetric, and excessively long routings should be avoided. All of the simulation results were obtained from the maximum unit number (16 units).

(1) Output S parameter

Figure 13 shows the simulation of the output S parameter, which reached −20 dB at 1.7 GHz.

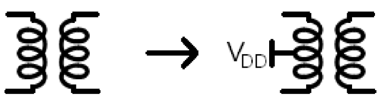

Figure 9: The traditional transformer and the center-tapped bias voltage Balun transformer.

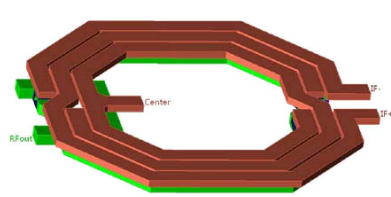

Figure 10: The 3D layout of 2-unit array Balun transformer.

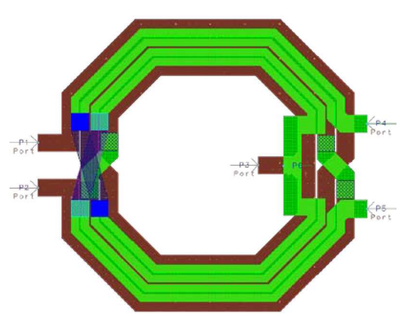

Figure 11: The 2D layout of 2-unit array Balun transformer.

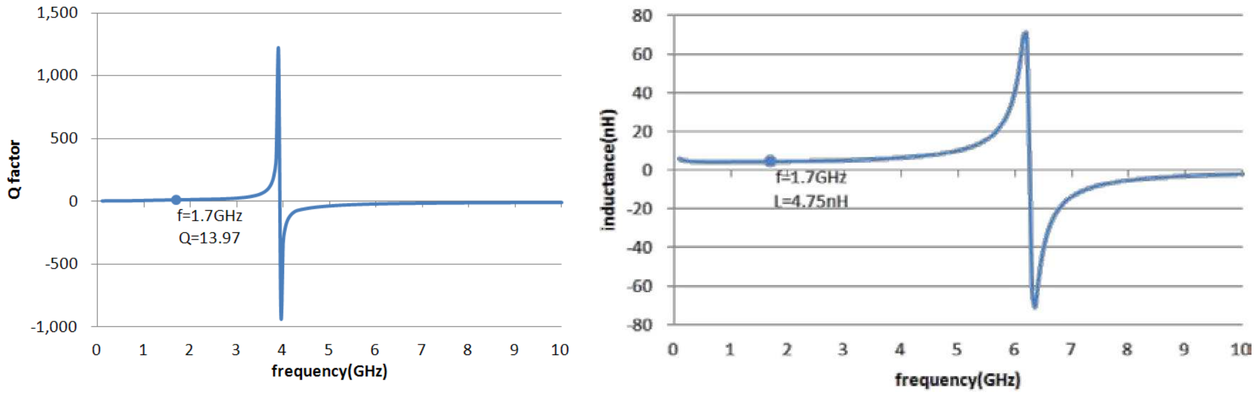

Figure 12: The Q factor and inductance simulations of the 2-unit array main coil.

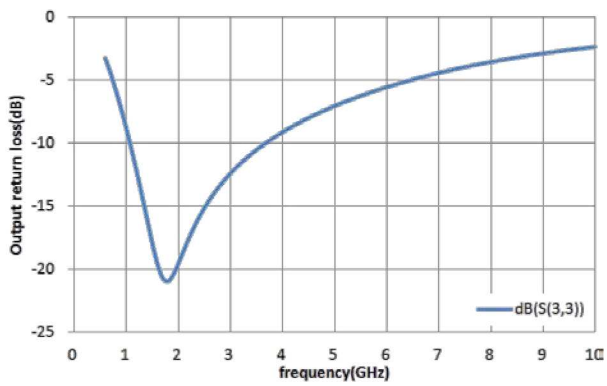

Figure 13: Output reflection coefficients.

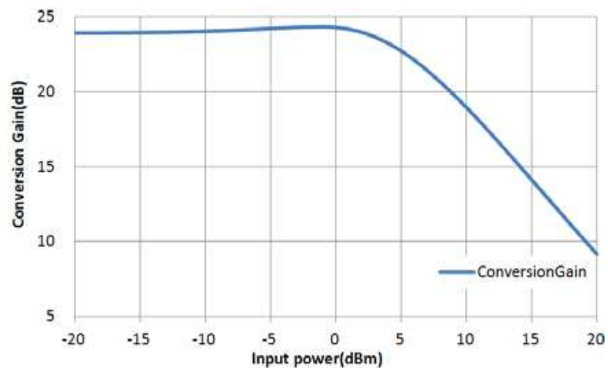

Figure 14: Conversion gain.

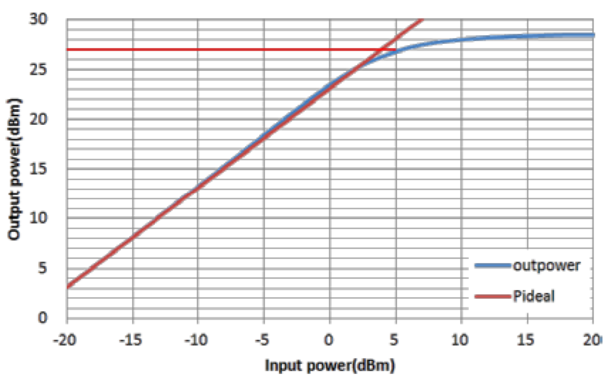

Figure 15: Output power.

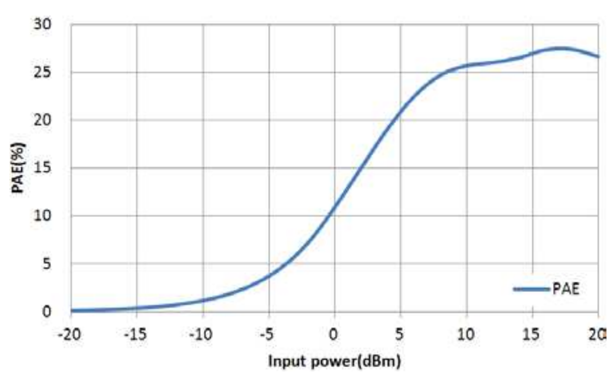

Figure 16: PAE(%).

(2) Conversion gain

The conversion gain was 24 dB at 1.7 GHz, and the P1 dB was 4 dBm. Figure 14 shows the correlation between the conversion gain and input power.

(3) Output power

The output power was 27 dBm (0.5 W) at P1 dB and 1.7 GHz. Figure 15 shows the correlation between the output power and input power.

(4) Power-added efficiency

Figure 16 shows the power-added efficiency (PAE) at 1.7 GHz, which was approximately 19% at P1 dB.

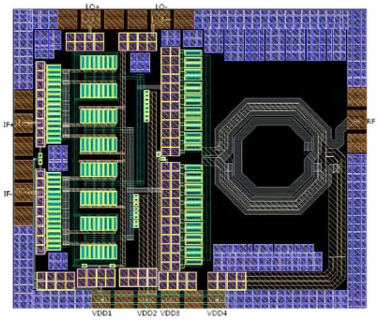

Figure 17: The layout of the low-voltage broadband mixer ($1.512 * 1.285\,\text{mm}^2$).

Table 1: Simulation results.

	Simulation
Frequency (GHz)	1.7 GHz
Conversion Gain (dB)	24
S_{33} (dB)	< -20 dB
P1 dB	+4 dBm
Pout@P1 dB	+27 dBm
PAE	19%
Chip size	$1.512 * 1.285$
Voltage supply	3 V

4. CONCLUSION

The primary focus when designing the mixer array power amplifier was to utilize the array to obtain an output power of approximately 0.5 W, even in CMOS manufacturing processes that have transistor breakdown voltages of only 2 or 3 V. In addition, using the advantages inherent in Balun transformer impedance conversion, double-to-single ended signal conversion, and area saving, a transmitter front-end circuit with a fully integrated CMOS and a 0.5 W output power was produced. Regarding the design of the Balun transformer, because of its use in combining large current convergence power, the simulation and layout line widths of the inductance and the Q values of the single coils should be considered.

ACKNOWLEDGMENT

The authors want to thank the Chip Implementation Center (CIC) of the National Science Council, Taiwan, R.O.C., for supporting the TSMC 0.18-μm 1P6M CMOS process.

REFERENCES

1. Kozlowski, M., "Whats the deal with version of LTE 4G network," 2011.
2. 3GPP, Overview of 3GPP Release 8 V0.2.3.
3. Chang, C.-H., "A brief talk about the LTE bands," Apr. 9, 2011.
4. http://temiac.ee.ntu.edu.tw/files/archive/245_6a6f8d5c.pdf.
5. Cobler, K., "Interoperability and QoS in LTE networks," Oct. 12, 2010.
6. Cripps, S. C., *RF Power Amplifier for Wireless Communications*, Artech House, 1999.
7. Gonzalez, G., *Microwave Transistor Amplifier*, Prentice Hall, 1997.
8. Bevilacqua, A. and A. M. Niknejad, "An ultrawideband CMOS low noise amplifier for 3.1–10.6 GHz wireless receivers," *IEEE Journal of Solid State Circuits*, Vol. 39, No. 12, 2259–2268, 2004.

Design of a Highly Linear Low-noise Amplifier with Noise and Distortion Cancelation

Pang-Hsing Chen and Jeng-Rern Yang
Microwave Laboratory, Department of Communication Engineering
Yuan Ze University, Jhongli City, Taoyuan Country 320, Taiwan, R.O.C.

Abstract— This study presents a highly linear low-noise amplifier with noise and distortion canceling. The circuit design of this amplifier focuses on the realization of high linearity and low-noise amplification. An operation within LTE frequency bands (0.7–2.6 GHz) produces a noise level of 2.3–3.1 dB; IIP3 was +8 dBm at a center frequency of 1.7 GHz, and P1 dB was −10 dBm at 1.7 GHz, with an operating voltage of 1.3 V. However, enhancement of linearity in an NMOS design may result in additional power consumption. Therefore, this design involved using a PMOS and an NMOS that could cancel second-order harmonic distortion, and the supply of single current could reduce power consumption. The circuit area is $0.86 \times 0.63\,\mathrm{mm}^2$.

1. INTRODUCTION

A low-noise amplifier (LNA), which is the first-stage active amplifier circuit in a receiver front-end circuit, is used to receive and amplify weak signals while reducing potential noise. According to the definition of the noise figure in an overall circuit, the noise of an LNA can directly influence the noise level and sensibility of a receiver, and a higher gain in an LNA can further restrain the gain of a back-end circuit.

Based on this description, the primary goal of an LNA design is to reduce the noise figure as much as possible, and to reduce back-end noise. However, the gain of an LNA design must not be too low, and an increase of the gain causes a decrease of linearity and an increase in power consumption. Power consumption and circuit area must be minimized to reduce the cost of mainstream circuit designs. Satisfying all of the demands is a challenge; therefore, a trade-off must be made.

2. CIRCUIT TOPOLOGY AND ANALYSIS

2.1. Main Schematic of the LNA

The circuit design of this amplifier focuses on the realization of high linearity and low-noise amplification. The circuit design involves using a noise canceling structure to cancel the noise of the transistors. As a result of the phase difference between the noise and signals, the noise of an LNA can be effectively reduced. At the input, a PMOS was connected serially to the NMOS, which was used as a CG amplifier; and a low gain in the distortion canceling structure could be slightly offset by supplying the same current for two transistors. This structure can also cancel distortions. A traditional distortion canceling structure can only cancel a third-order distortion, and it cannot effectively improve IIP3. Therefore, a PMOS was used to replace either the primary or the secondary transistor to use its characteristic in high-order transconductance. Consequently, third-order distortions could be cancelled, second-order distortions could be partially cancelled, and linearity was increased. In addition, source degradation inductors were used to increase linearity further. Fig. 1 shows the overall schematic of the LNA design, with an input impedance of 1/gm in the input impedance matching circuit composed of L_1 and C_G amplifiers, and with an output impedance matching circuit working as the load of resistances.

2.2. Noise Canceling

In the small-signal analysis performed in this study, the small signal, entering from the input, was amplified non-invertedly by transistors M_1 and M_5; and the small signal was amplified invertedly by M_2 and M_3. Thus, no phase difference was in the output. In the noise analysis performed in this study, the phases of the noise current, produced by M_1 and M_5, were opposite in the source and in the drain, and the two phase-opposite noises were still opposite in phase after being amplified invertedly by M_2 and M_3. Therefore, phase opposition can be used for noise cancelation.

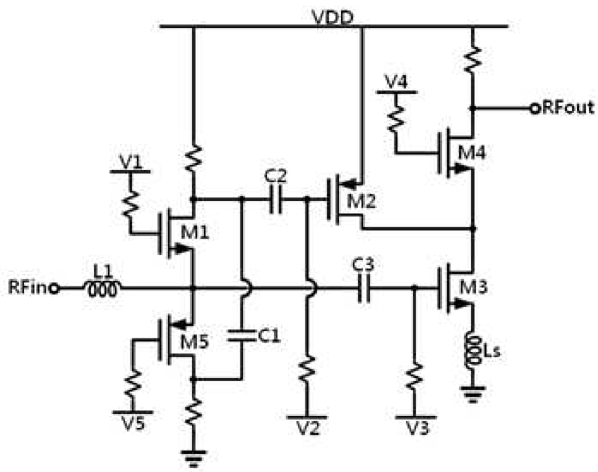

Figure 1: Main schematic of the LNA.

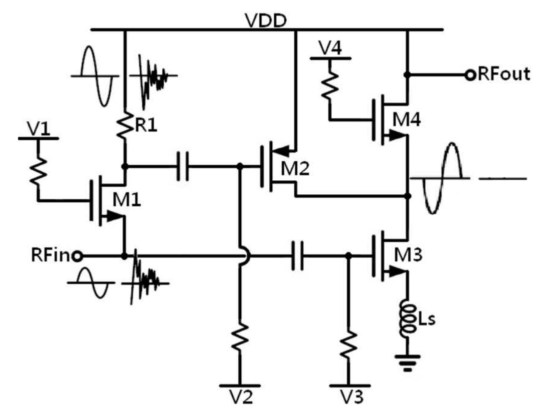

Figure 2: Schematic diagram of noise cancelation.

Theoretically, the noise in this noise canceling structure could be deduced as follows:

$$F = 1 + \frac{g_{m2}^2 R_1 + \left(\frac{\gamma}{\alpha}\right)\left(g_{m1} R_T^2 \left(g_{m2}\frac{R_1}{R_2} - g_{m3}\right)^2 + g_{m2} + g_{m3}\right) + \frac{1}{R_L}}{R_L^{-2} R_S^{-1} \times (R_S || R_{in})^2 \times A_v^2} \tag{1}$$

$$R_T = R_S || \frac{r_{o1}}{1 + \frac{R_1}{R_S}} || \frac{1}{g_{m1}} || \left(\frac{g_{m3} L_S}{c_{gs3}}\right) \tag{2}$$

$$R_{in} = \frac{R_1 + r_{o1}}{1 + g_{m1} r_{o1}} || \left(\frac{g_{m3} L_S}{c_{gs3}}\right) \tag{3}$$

$$A_v = -\left(g_{m3} + g_{m2}\left(\frac{1 + g_{m1} r_{o1}}{1 + \frac{r_{o1}}{R_1}}\right)\right) \times R_L \tag{4}$$

Using the above equations revealed that the noise was mainly influenced by R_1, M_1, M_2, and R_L, and the noise canceling equation was the relationship between g_{m2} and g_{m3} in (1):

$$\delta = \frac{R_s g_{m3}}{R_1 g_{m2}} - 1 \tag{5}$$

$R_1 \times g_{m2} = R_S \times g_{m3}$ was the optimal condition for noise canceling performance, but the above values of the transistors, resistors, and bias voltages should be adjusted to ensure the optimal effect because of the impedance changes at high frequencies.

2.3. Distortion Cancelation

The distortion of amplified signals often results from varying performance levels of transistors when using different bias voltages and when the current in the active region enters the non-linear region. Referring to this CG amplifier as an example, the drain current includes not only the original amplified signal but also the non-linear drain current caused by non-linear transduction. The relationship between non-linear drain current and non-linear transduction could be expressed by a Taylor series:

$$i_{ds} = g_m \times v_{gs} + \frac{g_m'}{2!} \times v_{gs}^2 + \frac{g_m''}{3!} \times v_{gs}^3 + \ldots \tag{6}$$

As illustrated in Fig. 3, C_1 and C_x were parasitic capacitances, and C_{gs3}, L_s, and $g_{m3}L_s/C_{gs3}$ were the equivalent model of the input impedance for M_3. Calculating the KCL of the circuit by using the Volterra series also produced the results of g_{m2}, which was the third-order distortion voltage, the relationship of g_{m3}, and the relationships of the third-order transduction coefficients,

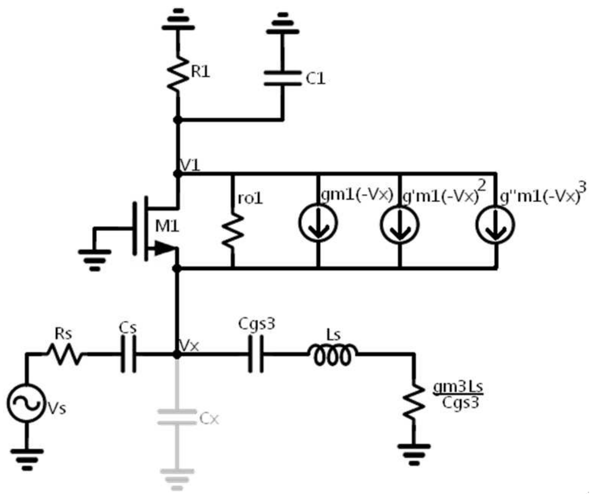

Figure 3: Distortion analysis of common-gate.

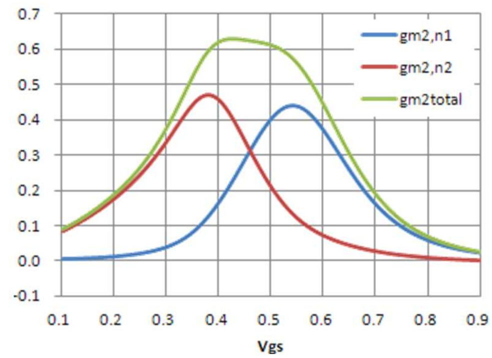

Figure 4: 2rd distortion of parallel NMOS.

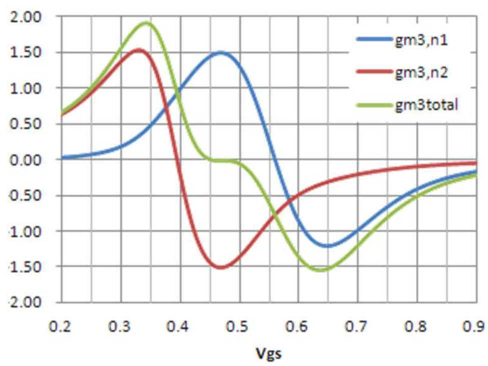

Figure 5: 3rd distortion of parallel NMOS.

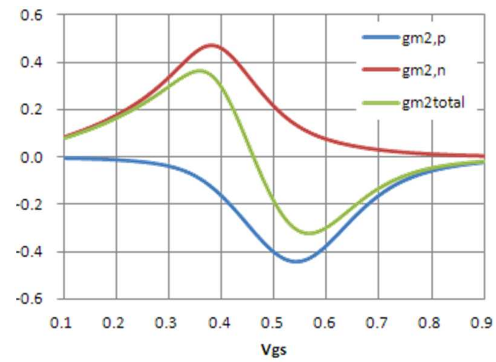

Figure 6: 2rd distortion of parallel PMOS.

g''_{m2} and g''_{m3}:

$$\frac{g_{m3}}{g_{m2}} = \frac{R_1}{R_S || \frac{g_{m3}L_s}{C_{gs3}}} \tag{7}$$

$$\frac{g''_{m3}}{g''_{m2}} = -\frac{R_1}{1/g_{m1}} \tag{8}$$

By using various bias voltages, the distortion transduction coefficient differs in magnitude; therefore, a distortion structure could perform the third-order distortion cancelation by adjusting the distortion transconductance of the two transistors to improve the effectiveness of IIP3 when paralleled with the transistors.

2.4. Co-current of a PMOS and Inductors Connected in Series

In this circuit, M_2 was a PMOS in which the drain was connected to M_3; and M_2 and M_3 shared the same current to cancel third-order distortion. When an NMOS is the selection of transistors, the direction of the M_4 current is $i_4 = i_2 + i_3$; for transistors that are replaced by using the PMOS, the M_4 current is $i_4 = i_3 - i_2$, as shown in (9). This enabled the cancelation of the NMOS with the second-order transduction coefficient of the PMOS. In addition, not only that second-order distortion was not produced, but also the result partially cancels second-order distortion further. Figs. 4 and 5 show the simulation of the second- and third-order transduction coefficients of the two NMOSs connected in parallel. Figs. 6 and 7 show the improved canceling simulation results of the second- and third-order distortion coefficients of the PMOS and NMOS connected in parallel. In accordance with the variation of frequency, (3.23) varies because of the variation of impedance. Therefore, an inductance connected in series with the source of M_3 decreases the frequency variation

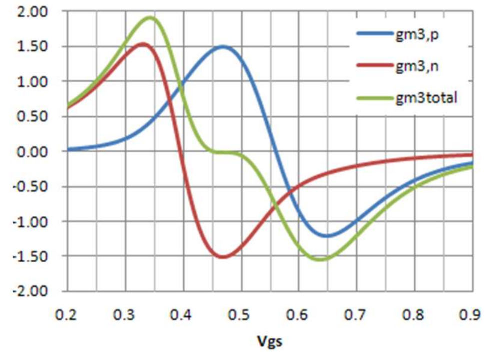

Figure 7: 3rd distortion of parallel PMOS.

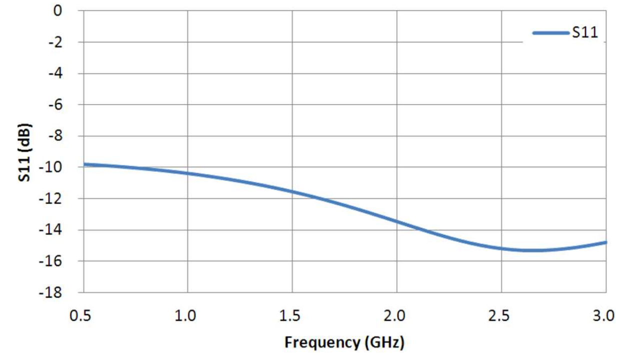

Figure 8: S_{11}.

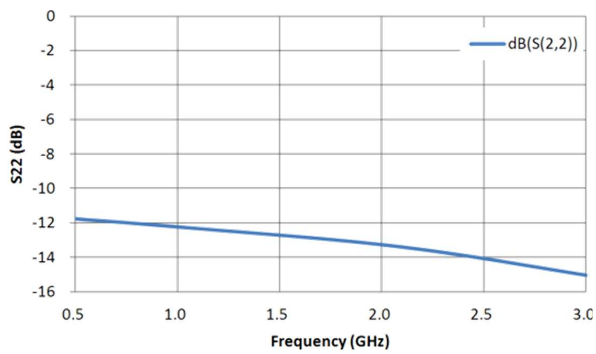

Figure 9: S_{22}.

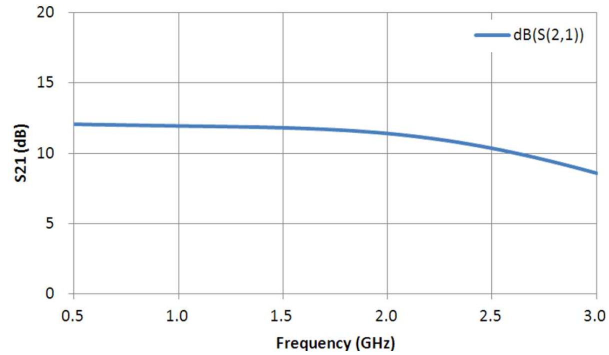

Figure 10: S_{21}.

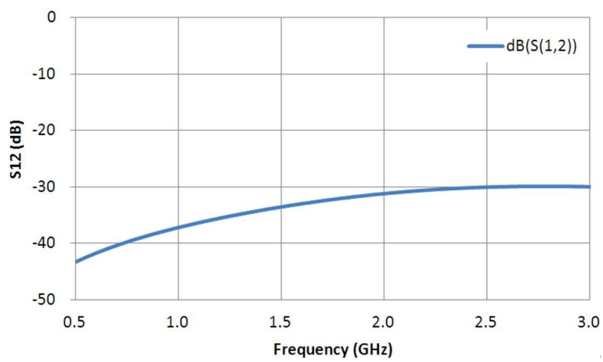

Figure 11: S_{12}.

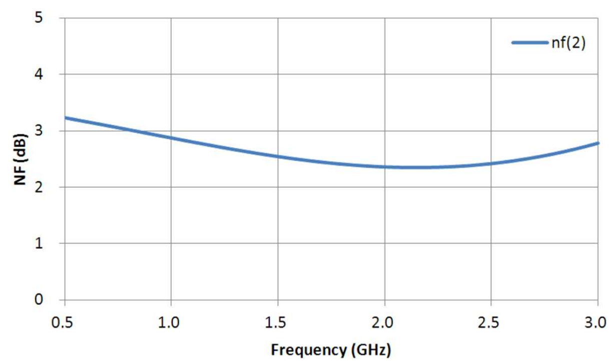

Figure 12: NF.

caused by distortion cancelation.

$$\begin{aligned} i_{out} &= i_{ds,n} - i_{sd,p} = g_{m,n} \cdot (-v_{in}) + \frac{g'_{m,n}}{2} \cdot (-v_{in})^2 + \frac{g''_{m,n}}{6} \cdot (-v_{in})^3 \\ &\quad - \left(g_{m,p} \cdot v_{in} + \frac{g'_{m,p}}{2} \cdot v_{in}^2 + \frac{g''_{m,p}}{6} \cdot v_{in}^3 \right) \\ &= -(g_{m,n} + g_{m,p}) \cdot v_{in} + \frac{g'_{m,n} - g'_{m,p}}{2} \cdot v_{in}^2 - \frac{g''_{m,n} + g''_{m,p}}{6} \cdot v_{in}^3 \end{aligned} \tag{9}$$

3. SIMULATED RESULTS

Agilent ADS and Momentum were used for circuit design and simulation in this study. TSMC 1P6M 0.18 μm CMOS model simulation was conducted; and, considering the parasitic effect of the PAD, a PAD equivalent circuit was incorporated in the simulation. The operating voltage was set at 1.3 V, with a total power consumption of 12 mW. Figs. 8–14 show the simulation results, including the S-parameter (return loss in the input and output, forward gain, and isolation), noise

Table 1: Low noise amplifier simulation result.

Parameters	Simulation Result
Frequency (GHz)	0.7–2.6 GHz
Supply Voltage	1.3 V
Gain (dB)	10.2–12.2
S_{11} (dB)	< -10
S_{22} (dB)	< -10
NF (dB)	2.3–3.1
P_1 dB (dBm)	-10@1.7 GHz
IP3 (dB3)	8@1.7 GHz
Power Dissipation (mW)	12

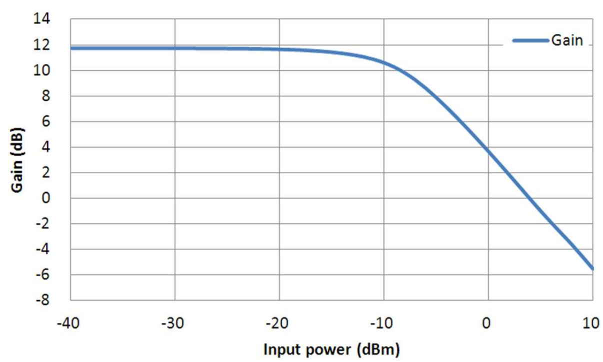

Figure 13: P1 dB (@1.7 GHz).

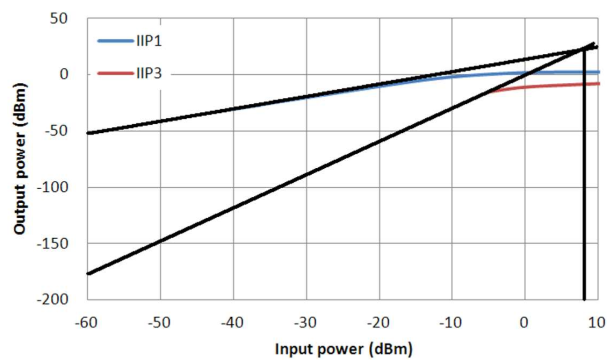

Figure 14: IP3 (@1.7 GHz).

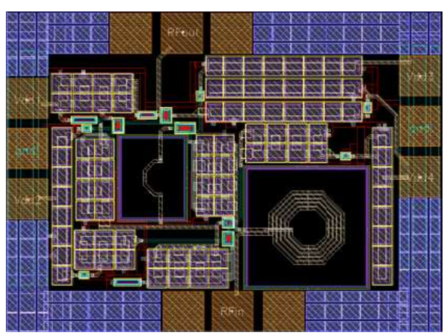

Figure 15: Layout (area: $0.86 \times 0.63\,\text{mm}^2$).

figures, P1 dB compression points, and performance of IP3. Fig. 15 shows the schematic of the circuit, with an area of $0.86 \times 0.63\,\text{mm}^2$.

4. CONCLUSION

The design focus of this circuit design is to enhance linearity and suppress noise, which was 2.3–3.1 dB in the LTE frequency bands (0.7–2.6 GHz). IIP3 was +8 dBm at a center frequency of 1.7 GHz; and PldB was −10 dBm with an operating voltage of 1.3 V. Although linearity is improved by using an NMOS, additional power consumption might occur. Therefore,a co-current PMOS and a co-current NMOS that can cancel second-order harmonic distortion were adopted in this design to reduce power consumption.

ACKNOWLEDGMENT

Special thanks to the support of the R.O.C. National Science Council and the National Chip Implementation Center (CIC), as well as the TSMC 0.18 μm 1P6M CMOS manufacturing process.

REFERENCES

1. Shen, H., L.-W. Yang, and X. Lv, "A 0.13 μm CMOS low-voltage high-linearity mixer for UWB receiver," *International Conference on Microwave and Millimeter Wave Technology, ICMMT'07*, 1–4, Apr. 18–21, 2007.
2. Bruccoleri, F. and E. A. M. Klumperink, "Noise canceling in wideband CMOS LNAs," *2002 IEEE International ISSCC*, Vol. 1, 406–407, 2002.
3. Liao, C.-F. and S.-I. Liu, "A broadband noise-canceling CMOS LNA for 3.1–10.6-GHz UWB receivers," *JSSC*, Vol. 42, 329–339, 2007.
4. Brandolini, M., P. Rossi, D. Manstretta, and F. Svelto, "Toward multistandard mobile terminals-fully integrated receivers requirements and architectures" *IEEE TMTT*, Vol. 53, 1026–1038, 2005.

A Tunable Dual-band Bandpass Filter with Two Independently Tunable Passbands

D.-H. Jia, Q.-Y. Feng, X.-G. Huang, and Q.-Y. Xiang
School of Information Science and Technology
Southwest Jiaotong University, Chengdu, Sichuan 610031, China

Abstract— In this paper, a novel tunable dual-band bandpass filter is proposed. Based on two quarter-wavelength resonators and one half-wavelength resonator, dual-band character is designed by introducing two independent coupling paths. Therefore, the whole filter structure can be divided into two parts and designed respectively. The Transmission Zeros (TZs) are derived through simulation. By varying the reverse bias voltage applied to the varactor diodes connected to the resonators, each passband can be tuned independently. Finally, the simulation results of the dual-band tunable filter shows a first tunable passband constant fractional-bandwidth range of $4.35\pm0.35\%$, a center frequency of 1.25–1.75 GHz, a insertion loss of 4.25–2.16 dB, and a second passband absolute-bandwith of 80 ± 5 MHz, a center frequency of 1.83–2.27 GHz, a insertion loss of 2.75–1.97 dB.

1. INTRODUCTION

Due to their potential to significantly reduce the overall size and complexity of modern multiband communication systems, RF tunable filters are becoming an active research topic [1–3]. However none of the above works addressed the design of two tunable passbands. There have been several papers [4–8] working on the design of tunable dual-band bandpass filters. However, [4–6] focused on the design of fixed first passband and tunable second passband. Little attention has been done on independent dual-band tuning [7] demonstrated a varactor-tuned dual-band tunable BPF that both passbands can be tuned independently, and this design had a large circuit size, large number of varactor diodes, large insertion loss. In [8], the authors presented a tunable dual-band BPF based on two varactor-tuned resonators. The proposed filter structure offered the possibility of two tunable passbands, with a fixed first passband and controllable second passband or both passbands tuned together. Nevertheless, its two passbands could not be tuned independently with any influence on the other passband.

In this paper, a reconfigurable dual-band BPF with two tunable passbands characteristics is presented. Each passband can be controlled independently and has tiny influence on the other passband while tuning the frequency. The dual-band character is due to the two independent coupling schemes that don't disturb with each other. The first passband is controlled by the input/output couplings and two varactor-loaded open-loop resonators, meanwhile, the second passband is determined by the input/output couplings and the half-wavelength resonator. The filter can be divided into two independent filters completely and be analyzed.

2. FILTER DESIGN

Figure 1 shows the layout of the proposed reconfigurable dual-band bandpass filter. The dual-band bandpass filter consists of two $1/4$ wavelength varactor-loaded open-loop resonators, one $1/2$ wavelength resonator and the coulping input/output. Two chip capacitors C_g are adopted to enhance the tuning range and return loss. As the two quarter resonators and the half-wavelength resonator are only coupled with the in/out ports, the filter structrure can be devided into two independent filters with the original parameters, as shown in Figures 2(a) and (b).

First of all, for the two-order BPF as shown in Figure 2(a), the overall admittance matrix of capacitively loaded coupled resonator is

$$[Y] = \begin{bmatrix} Y_{11} & Y_{12} \\ Y_{21} & Y_{22} \end{bmatrix} \tag{1}$$

For the above admittance matrix, three conditions must be satisfied. One is the resonance condition and the others are the coupling condition, Q_{ext}. The conditions are

$$\mathrm{Im}(Y_{11}(\omega_0)) = 0 \quad \frac{\mathrm{Im}(Y_{12}(\omega_0))}{b} = K_{12} \quad Q_{ext} = \frac{b}{\mathrm{Re}\,[Y_{11}(\omega_0)]} = \frac{g_0 g_1}{\Delta} \tag{2}$$

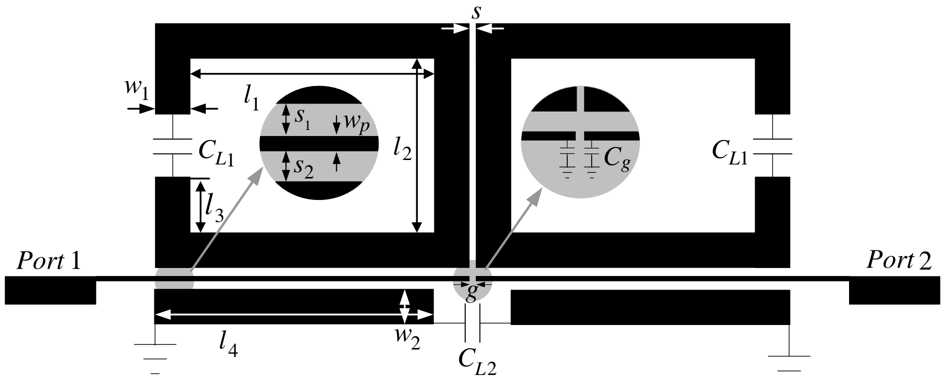

Figure 1: Layout of the tunable dual-band bandpass filter.

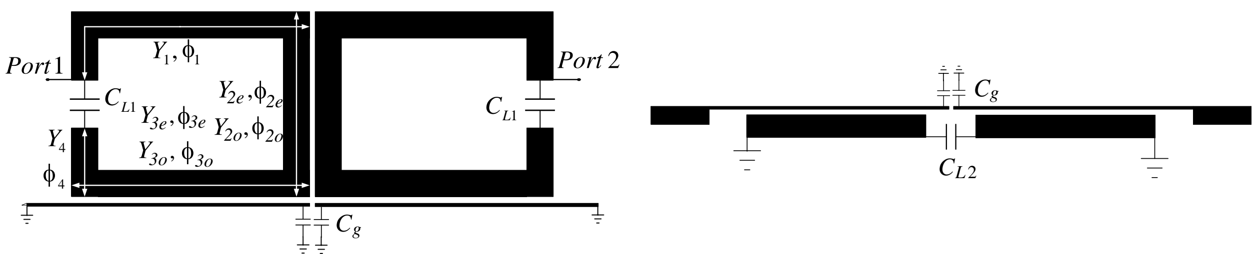

(a) (b)

Figure 2: (a) Layout of Filter I. (b) Layout of Filter II.

where

$$b = \frac{\omega_0}{2}\frac{\partial \mathrm{Im}(Y_{11}(\omega_0))}{\partial \omega} \quad K_{12} = \frac{\Delta}{\sqrt{g_1 g_2}} \tag{3}$$

Constant fractional-bandwidth tunablity demands that firstly the overall coupling efficient, K_{12}, should keep constant during the tuning range. Secondly, Q_{ext} should be in small variation with frequency in the tuing range. Only with the two conditions were satisfied, can we obtain a nice constant fractional-bandwidth. To demonstrate the performance of the tunable two-order constant fractional-bandwidth filter — Filter I, the simulation results of the Filter I are given in Figures 3(a) and (b) on an $\varepsilon_r = 2.65$, $h = 0.5$ mm F4B-2 substrate.

Then the tunable one-oder filter — Filter II detemine the second passband, as shown in Figure 2(b). Its center frequency is mainly controlled by the length l_4 of the resonantor, and the Q_{ext} determains the bandwidth of the passband. The detailed method to extract the Q_{ext} is shown in [9]. Its tunablity simulated results are shown in Figures 4(a) and (b).

Thirdly, the TZs mecharism is analyzed under simulation as Figure 5 shown. Hence, the mechanism producing each passband and transmisson zeros is readily discovered. It is observed that the dual-pand characteristics is achieved by combining two independent bandpass filter together and the TZ1 and TZ2 are generated by the Filer I and cross couplings, respectively.

From the analysis above, we can achieve a tunable dual-band BPF Filter with a predefined constant fractional-bandwidth tunable first passband and a tunable second passband with constant absoult bandwidth.

3. VERIFICATION BY SIMULATION

To demonstrate the performance of the proposed filter, a tunable filter is designed and simulated. The dimensions for the filter are presented in Table 1 for $\varepsilon_r = 2.65$, $h = 0.5$ mm. The load capacitors C_{L1} and C_{L2} are implemented with lump chip capacitors ($1.5 \times 0.7\,\mathrm{mm}^2$), where SMV 1405 abrupt junction tuning varactors of SKYWORKS in SC-79 package have been used as the tuning elements. The single capacitance is 0.63 pF and 2.67 pF at 30 V and 0 V bias, respectively. The dc bias is done by using a 100 KΩ resistor and an ATC chip capacitor between the DC voltage and the open ends of the resonator. $V1$ and $V2$ are the bias voltage of C_{L1} and C_{L2}, respectively. The capacitor-varactor series connection hardly changed the overall capacitance with the chip capacitor value 15 pF. The C_g is selected as 1 pF as a tradeoff between tunability and loss.

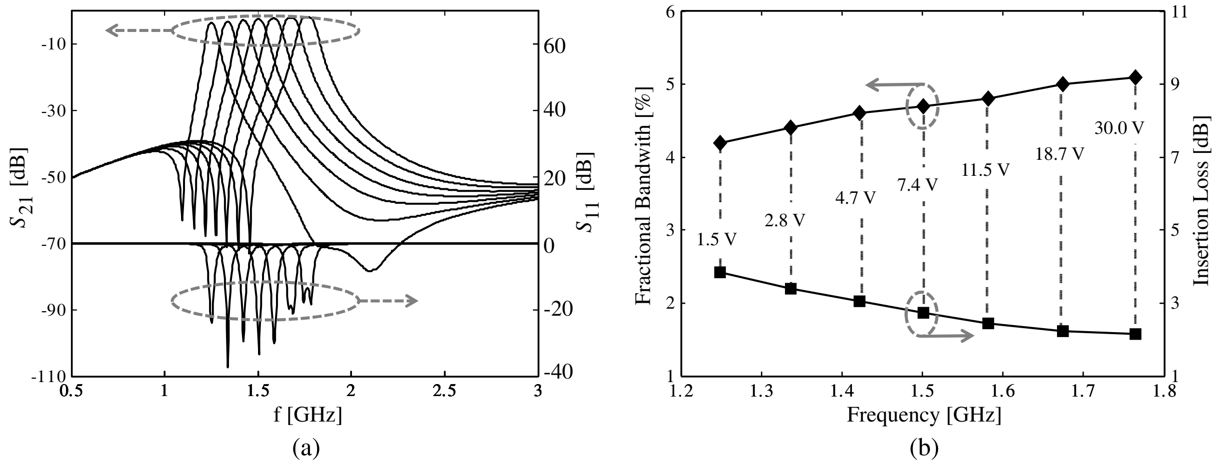

Figure 3: (a) Simulated S-parameters of Filter I. (b) Simulated insertion loss and 3-dB bandwidth of Filter I.

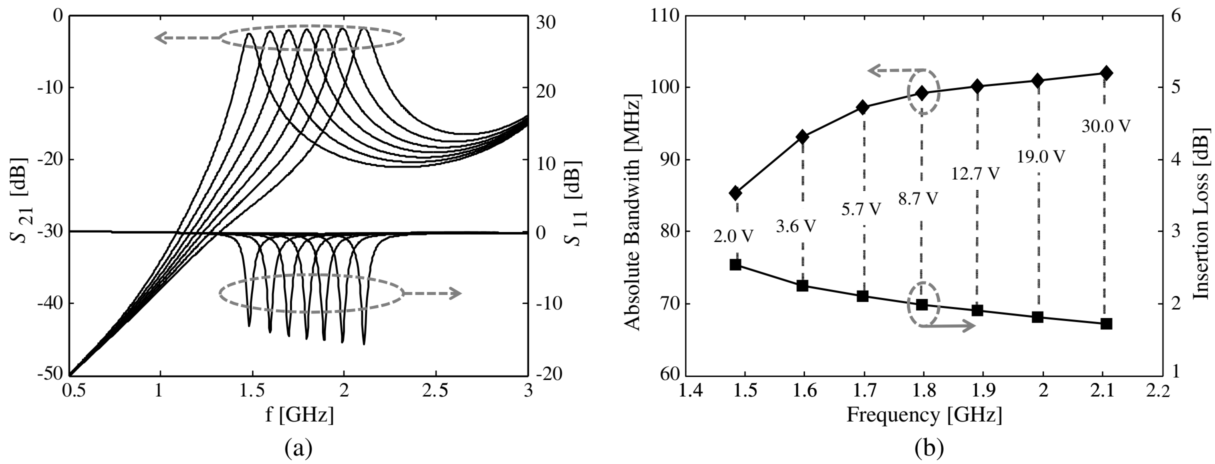

Figure 4: (a) Simulated S-parameters of Filter II. (b) Simulated insertion loss and 3-dB bandwidth of Filter II.

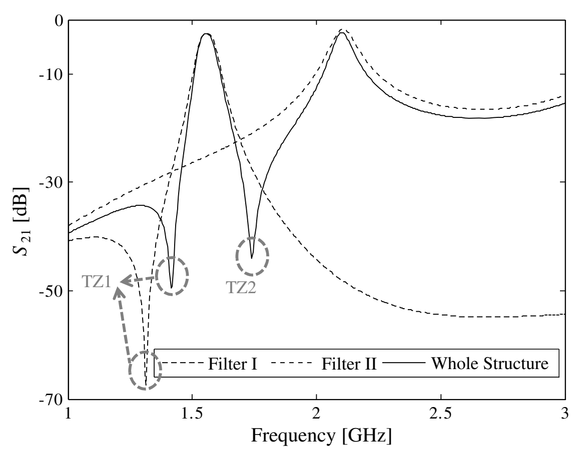

Figure 5: Simulated S_{21} of Filter I, Filter II and whole structure.

The simulated results are shown in Figure 6. As Figure 6(a) shown, the firsr passband shows a constant fractional-bandwidth range of 4.35±0.35%, a center frequency of 1.25–1.75 GHz, a insertion loss of 4.25–2.16 dB while the bias voltage $V1$ changes from 30 V to 1.5 V and the bias Voltage $V2$ keep constant at 30 V. Among the first passband tuning process, the second passband shows a small variation with center frequency of 2.27 GHz, absolute bandwidth of 83 ± 3 MHz, an insertion loss

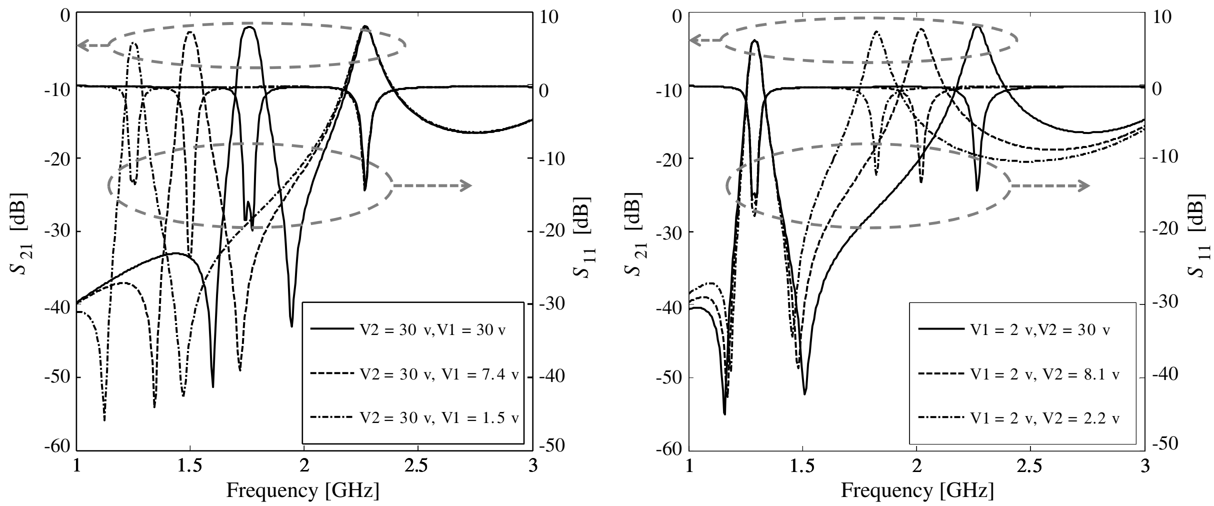

(a) (b)

Figure 6: Layout of the bandwidth tunable bandpass filter without harmonic suppression.

Table 1: Critical dimensions of the bandwidth tunable BPF with harmonic suppression (Unit: mm).

l_1	l_2	l_3	l_4	w_1	w_2	w_p	s_1	s_2	s	g
11.8	6.9	2.2	15.1	2.0	2.0	0.3	0.1	0.2	0.2	0.2

of 2 dB. The tunability of second passband is shown in Figure 6(b). The second passband shows an absolute-bandwith of 80 ± 5 MHz, a center frequency of 1.83–2.27 GHz, a insertion loss of 2.75–1.97 dB while the $V2$ tunes from 30 V to 2.2 V and the $V1$ keep constant at 2 V. The first passband almost keep constant during the second passband tuning with a center frequency at 1.29 GHz, a fractional-bandwidth of 4%, an insertion loss of 3.91 dB.

4. CONCLUSION

In this paper, a dual-band bandpass filter with two independent tunable passbands is demonstrated. Introduced with two independent coupling paths, the filter shows the unique property that each passband can hardly be influenced while tuning the other passband. This design method is verified by simulation results and shows good performance. In the future, the use of RF MEMS will significantly enhance the performance of the filters.

ACKNOWLEDGMENT

This work is supported by the National Natural Science Foundation of China (NNSF) under Grant 60990320, 60990323; 61271090, and the National 863 Project of China under Grant 2012AA012305, and Sichuan Provincial Science and technology support Project under Grant 2012GZ0101, and Chengdu Science and technology support Project under Grant 12DXYB347JH-002.

REFERENCES

1. Sang-June, P. and G. M. Rebeiz, "Low-loss two-pole tunable filters with three different predefined bandwidth characteristics," *IEEE Transactions on Microwave Theory and Techniques*, Vol. 56, 1137–1148, 2008.
2. Wang, X. G., X. H. Cho, and S. W. Yun, "A tunable combline bandpass filter loaded with series resonator," *IEEE Transactions on Microwave Theory and Techniques*, Vol. 60, 1569–1576, 2012.
3. Lacorte Caniato Serrano, A., F. Salete Correra, T. P. Vuong, and P. Ferrari, "Synthesis methodology applied to a tunable patch filter with independent frequency and bandwidth control," *IEEE Transactions on Microwave Theory and Techniques*, Vol. 60, 484–493, 2012.
4. David, G., L. Antonio, M. Esther, M. Diego, and L. Pradell, "Tunable dual-band bandpass filter for wlan applications," *Microwave and Optical Technology Letters*, Vol. 51, 2025–2028, 2009.

5. Zhang, X. Y. and Q. Xue, "Novel centrally loaded resonators and their applications to bandpass filters," *IEEE Transactions on Microwave Theory and Techniques*, Vol. 56, 913–921, 2008.
6. Chaudhary, G., H. Choi, Y. Jeong, J. Kim, D. Kim, and J. C. Kim, "Design of dual-band bandpass filter using DGS with controllable second passband," *IEEE Microwave and Wireless Components Letters*, Vol. 21, 589–591, 2011.
7. Djoumessi, E. E., M. Chaker, and K. Wu, "Varactor-tuned quarter-wavelength dual-bandpass filter," *IET Microwave, Antennas & Propagation*, Vol. 3, 117–124, 2009.
8. Chaudhary, G., Y. Jeong, and J. Kim, "Harmonic suppressed dual-band bandpass filters with tunable passbands," *IEEE Transactions on Microwave Theory and Techniques*, Vol. 60, 2115–2123, 2012.
9. Hong, J. S. and M. J. Lancaster, *Microstrip Filters for RF/Microwave Applications*, Wiley, New York, 2001.

A Constant Absolute Bandwidth Tunable Combline Bandpass Filter

X.-G. Huang, Q.-Y. Feng, Q.-Y. Xiang, and D.-H. Jia
School of Information Science and Technology
Southwest Jiaotong University, Chengdu, Sichuan 610031, China

Abstract— This paper presents a novel two-pole constant absolute bandwidth tunable combline bandpass filter with controllable coupling coefficient. The combline bandpass filter can be divided two parts: coupling section and non-coupling section. By controlling the length ratio of the coupling section and non-coupling section while maintaining the total length unchanged, the external quality Q_{ext} maintain stationary and the coupling coefficient k can be tuned to desirable values to meet the requirement of constant absolute bandwidth. The filter is designed on F4b-2 substrate with $\varepsilon_r = 2.65$ and 0.5 mm. The measured results show that the frequency can be tuned from 1.13 to 1.53 GHz with a 3-dB absolute bandwidth 80 ± 4 MHz. The tested results show good agreement with the simulated results.

1. INTRODUCTION

Electronically tunable/reconfigurable filters are essential components for reconfigurable front-ends since they can significantly reduce the system size, complexity and cost. Recently, numerous literatures fix their attentions on tunable filter, most of which can be classified into three categories according to the content: controlling the center frequency [1, 2]; (2) controlling the bandwidth at a fixed centre frequency [3–5]; and (3) simultaneous controlling bandwidth and center frequency [6, 7].

Tunable filters with constant absolute bandwidth had been paid more attentions. Various planar structures for tuning have been reported: In [8], the low-loss tunable filters with three different fractional-bandwidth variations by adjusting the independent electric and magnetic coupling coefficients between two resonators are reported. Then, dual-mode microstrip resonators are proposed to develop constant absolute bandwidth filters [9, 10]. The corrugated microstrip coupled lines was used to control the coupling coefficient, resulting in a constant absolute bandwidth tunable filter [11]. In [12], the $\lambda/2$ resonator and λ resonator are proposed to design constant absolute bandwidth. The combline structures have been used to design tunable filters with controllable bandwidth for a long time [9]. However, bandwidth control is usually realized by adding the tunable element in the coupling spacing to adjust the coupling coefficient, which results in a high complex of tuning.

In this paper, a constant absolute bandwidth tunable filter is designed and fabricated based on microstrip combline. Benefiting from the length ratio of the coupling section and non-coupling section, the coupling coefficient could be tuned while keeping the resonant frequency and external quality unchanged. This circuit has good performance in terms of bandwidth variation and physical size.

2. TUNABLE FILTER DESIGN

Figure 1(a) shows the conventional tunable microstrip combline filter employs a varactor diode as the tuning element, which is connected to the coupling line via a dc block capacitor. The entire combline resonator is coupled. In this design, unlike the conventional tunable combline filter, the combline resonator can be divided two parts: coupling section and non-coupling section, as shown in Figure 1(b). Figure 1(c) illustrates the electrical circuit model of the filter. The filter can be treated as a symmetrical two-port network, and the even- and odd-mode analytical method is adopted to investigate the mechanism of the proposed design. The admittances matrix seen from port A and B defined by

$$Y = \begin{bmatrix} Y_{11} & Y_{12} \\ Y_{21} & Y_{22} \end{bmatrix} \tag{1}$$

$$Y_{11} = Y_{22} = (Y_{re} + Y_{ro})/2 + j\omega C_L \tag{2}$$

and

$$Y_{12} = Y_{21} = (Y_{re} - Y_{ro})/2 \tag{3}$$

$$Y_{re} = Y_{0e}\frac{-jY_0 \cot\theta_1 + jY_{0e}\tan\theta_t}{Y_{0e} + Y_0 \cot\theta_1 \tan\theta_t} \tag{4}$$

and

$$Y_{ro} = Y_{0o}\frac{-jY_0 \cot\theta_1 + jY_{0o}\tan\theta_t}{Y_{0o} + Y_0 \cot\theta_1 \tan\theta_t} \tag{5}$$

where $\theta_t = \theta_2 - \theta_1$, $\theta_1 = \beta L_1$, $\theta_2 = \beta L_2$ (β is the propagation constant) and Y_{0o}, Y_{0e} and Y_0 denote the odd-even-mode admittance of the coupling section and the characteristic admittance of the non-coupling section, respectively.

The resonant frequency, external quality Q_{ext} and coupling coefficient k_{21} of the proposed circuit in can be calculated as

$$\mathrm{Im}[Y(\omega_0)] = 0 \tag{6}$$

$$Q_{ext} = \frac{b}{\mathrm{Re}\left[Y_{11}\left(\omega_0\right)\right]} \tag{7}$$

$$k_{21} = \frac{\mathrm{Im}\left[Y_{12}(\omega_0)\right]}{b} \tag{8}$$

where the slope parameter (b) can be derived as

$$b = \frac{\omega_0}{2}\left.\frac{\partial \mathrm{Im}\left[Y_{11}\left(\omega_0\right)\right]}{\partial\omega}\right|_{\omega=\omega_0} \tag{9}$$

Given parameters of the filter, the variation of resonant frequency with capacitance of the varactor diodes and tuning range can be obtained by solving the Equation (6). The variation of the bandwidth vary with resonant frequency depends on the Q_{ext} and k_{12}, which can be obtained by solving the Equations (7) and (8).

Figure 2 is plotted by using (7) and (8), where the C_{ratio} of C_L is 2.8 (0.95–2.67 pF). It is clear that the coupling coefficient should be inversely proportional to the centre frequency within the tuning range. Using the proposed configuration, the dimensions are as follows: $W_1 = 1.5$ mm, $W_2 = 0.6$ mm, $L_2 = 25.5$ mm, $S_2 = 0.2$ mm. The value of the coupling coefficient k_{12} is affected by

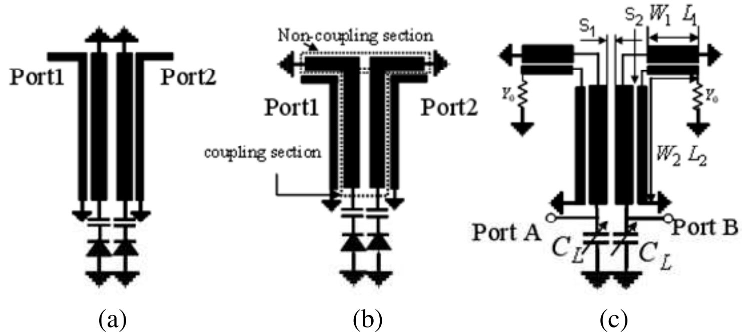

Figure 1: Structures of conventional and proposed tunable combline filter: (a) Conventional tunable combline filter, (b) proposed tunable combline filter, (c) equivalent circuit of the proposed filter.

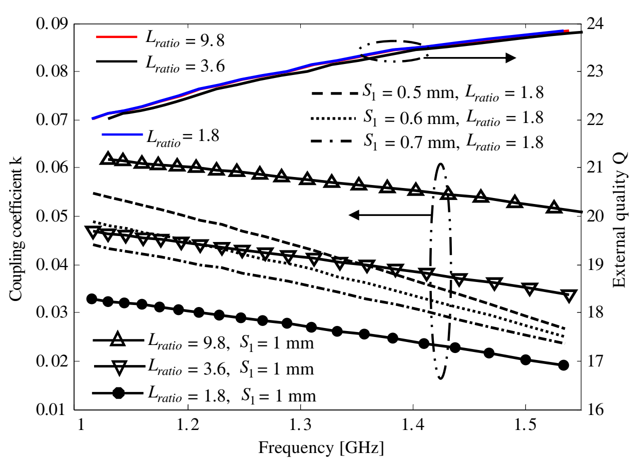

Figure 2: Coupling coefficients as a function of the centre frequency under different L_{ratio} and S_1.

the C_L under different coupling and non-coupling length ratio L_{ratio} ($L_{ratio} = (L_2 - L_1)/L_1$) and coupling spacing S_1 as shown in Figure 2. The slopes of k_{12} are nearly same under different L_{ratio}, whereas the slopes of k are different under various S_1, especially at the high frequency. The tuning frequency and the external quality remain the same duo to the total length L_2 keeping unchanged. Thus, the constant absolute bandwidth can be met by choosing the suitable L_{ratio} and coupling spacing S_1.

3. FABRICATION AND MEASUREMENTS

To verify the predictions, the proposed tunable filter is fabricated on the F4B-2 substrate with a dielectric constant of 2.65, dielectric loss tangent of 0.001 and the thickness of 0.5 mm. By optimizing the parameters, the length ratio and coupling spacing are 3.6 and 0.7 mm. The terminal loaded capacitors CL realized by connecting a hyperabrupt junction tuning varactor diode (SMV1405-SC79). The varactor capacitance is 0.63 pF and 2.67 pF at 30 V and 0 V reverse bias, respectively. DC-biasing scheme was realized by a 15 pF chip capacitor between the short and open ends of the resonator. To minimize any RF signal leaking on the bias pads, the bias circuit was done using two 100 K resistors to reduce the RF-signal leakage through the bias network. The S-parameters of the filter were measured with an Agilent E5071C vector network analyzer.

Figure 3(a) shows the fabricated tunable filter. The whole physical size is $25 \times 43\,\text{mm}^2$. The measured S_{21} and S_{11} are plotted in Figure 3(b). The measured and simulated 3-dB bandwidth and insertion loss are shown in Figure 4. The measured frequency tuning is 1130–1530 MHz with an insertion loss of 3.6–4.6 dB. Especially, the absolute bandwidth of the filter is about 80 ± 4 MHz across the whole tuning range, which could be considered constant absolute bandwidth. The insertion loss would be mainly attributed to the conductor and the finite Q of varactor diode. The measured return loss is better than 10 dB over the whole center frequency tuning range. The reverse

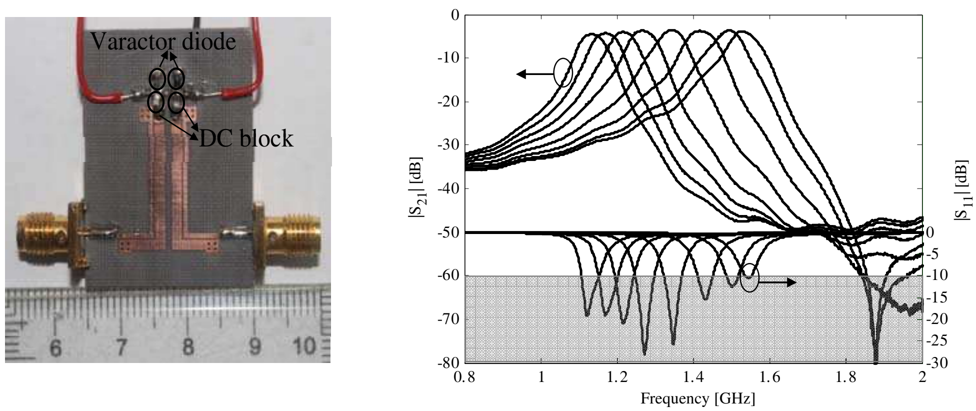

(a) (b)

Figure 3: (a) Photograph of the fabricated filter and (b) measured S-parameter of the tunable filter.

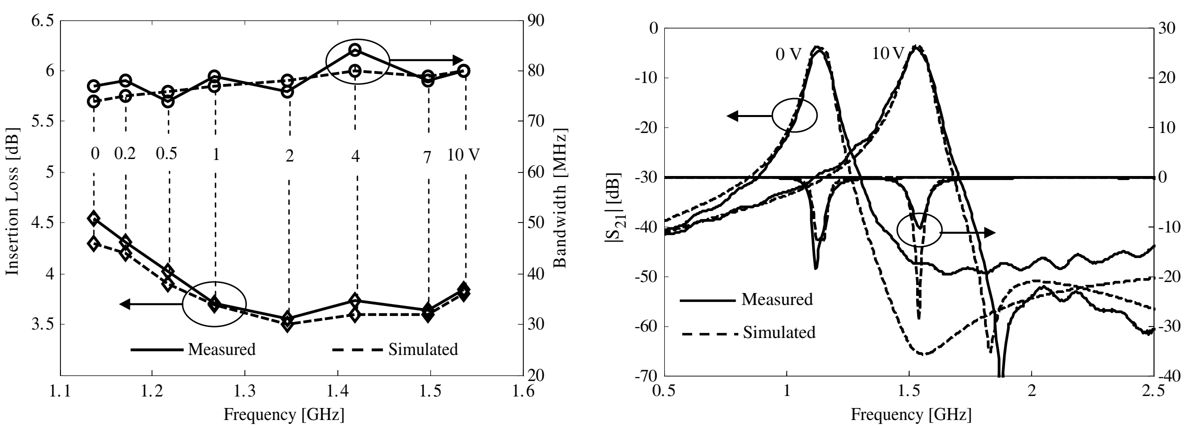

(a) (b)

Figure 4: (a) Measured and simulated insertion loss and 3-dB bandwidth of the constant absolute-bandwidth filter, (b) measured and simulated S-parameters.

voltage applied on the varactors range from 0 to 10 V, resulting in the capacitance changing from about 0.95 to 2.67 pF. The simulated responses of this filter obtained by Sonnet and Advanced Design System (ADS) simulators, which shows good agreement with measured results as shown in Figure 4(b).

4. CONCLUSIONS

In this paper, a constant absolute bandwidth tunable filter is designed and implemented using novel combline. The configuration of the proposed filter has controllable coupling coefficient to meet the requirement of absolute bandwidth. The demonstrated tunable filter presents a continuous tuning rang from 1130 to 1530 MHz with acceptable insertion loss, and the 3-dB bandwidth is 80 ± 4 MHz across the entire tuning range. The insertion loss could be improved by using MEMS technology, high temperature superconductivity (HTS) technology or negative resistance circuit.

ACKNOWLEDGMENT

This work was partly supported by the National Natural Science Foundation of China (NNSF) under Grant 60990320, 60990323, 61271090, the National 863 Project of China under Grant 2012AA0123-05, Sichuan Provincial Science and technology support Project under Grant 2012GZ0101, Chengdu Science and technology support Project under Grant 12DXYB347JH-002, and the "2013 Doctoral Innovation Funds of Southwest Jiaotong University" and "the Fundamental Research Funds for the Central Universities".

REFERENCES

1. Xiang, Q.-Y., Q. Y. Feng, and X.-G. Huang, "Half-mode substrate integrated waveguide (HMSIW) filters and its application to tunable filter," *Journal of Electromagnetic Waves and Applications*, Vol. 25, Nos. 14–15, 2043–2053, 2011.
2. Xiang, Q.-Y., Q. Y. Feng, X.-G. Huang, and D.-H. Jia, "Substrate integrate waveguide filters and mechanical/electrical reconfigurable half-mode substrate integrated waveguide filters," *Journal of Electromagnetic Waves and Applications*, Vol. 26, No. 13, 1756–1766, 2012.
3. Huang, X.-G., Q. Y. Feng, and Q.-Y. Xiang, "Bandpass filter with tunable bandwidth using quadruple-mode stub-loaded resonator," *IEEE Microwave and Wireless Components Letters*, Vol. 22, 176–178, 2012.
4. Liu, B., F. Wei, H. Zhang, X.-W. Shi, and H.-J. Liu, "A tunable bandpass filter with switchable bandwidth," *Journal of Electromagnetic Waves and Applications*, Vol. 25, Nos. 2–3, 223–232, 2011.
5. Park, W.-Y. and S. Lim, "Bandwidth tunable and compact band-pass filter (BPF) using complementary split ring resonators (CSRRS) on substrate integrated waveguide (SIW)," *Journal of Electromagnetic Waves and Applications*, Vol. 24, Nos. 17–18, 2407–2417, 2010.
6. Manuel, S. R., G. G. Roberto, J. I. Alonso, and B. R. Cesar, "Tunable combline filter with continuous control of centre frequency and bandwidth," *IEEE Transactions on Microwave Theory and Techniques*, Vol. 53, 191–199, 2005.
7. Zhang, X. Y., Y. B. Zhang, X. Y. Wang, and B.-J. Hu, "Tunable bandpass filter with continuously-tuned center frequency and bandwidth," *Journal of Electromagnetic Waves and Applications*, Vol. 26, Nos. 8–9, 1048–1058, 2012.
8. Park, S. J. and G. M. Rebeiz, "Low-loss two-polo tunable filters with three different predefined bandwidth characteristics," *IEEE Transactions on Microwave Theory and Techniques*, Vol. 56, 1137–1148, 2008.
9. Tang, W. X. and J. S. Hong, "Varactor-tuned dual-mode bandpass filters," *IEEE Transactions on Microwave Theory and Techniques*, Vol. 58, 2213–2220, 2010.
10. Athukorala, L. and D. Budimir, "Compact second-order highly linear varactor-tuned dual-mode filters with constant bandwidth," *IEEE Transactions on Microwave Theory and Techniques*, Vol. 59, 2214–2220, 2011.
11. EI-Tanani, M. A. and G. M. Rebeiz, "Corrugated microstrip coupled lines for constant absolute bandwidth tunable filters," *IEEE Transactions on Microwave Theory and Techniques*, Vol. 58, 956–963, 2010.
12. Liu, B., F. Wei, Q.-Y. Wu, and X.-W. Shi, "A tunable bandpass filter with constant absolute bandwidth," *Journal of Electromagnetic Waves and Applications*, Vol. 25, Nos. 11–12, 1596–1604, 2011.

Digital Predistortion for RF Power Amplifiers Based on Enhanced Orthonormal Hermite Polynomial Basis Neural Network

X. H. Yuan, Q. Y. Feng, T. J. Zeng, and H. B. Ma
School of Information Science and Technology
Southwest Jiaotong University, Chengdu, Sichuan 610031, China

Abstract— In this paper, a novel digital baseband predistorter for RF power amplifiers (PAs) based on enhanced orthonormal Hermite polynomial basis neural network (EOHPBNN) is proposed. Digital predistortion technique based on neural network has been a hot topic in recent years, but the commonly used neural network predistorters employs feedforward neural networks (FNNs) with sigmoid function as the hidden neurons' activation function, which have limited linearization performance. The new proposed predistorter utilizes an orthonormal Hermite polynomial basis neural network where the orthonormal Hermite polynomial terms are chosen as the hidden neurons' activation functions. Taking advantage of the universal approximation capability of Hermite polynomial, the EOHPBNN predistorter shows superior linearization performance to the traditional NN-based predistorter. Also, the design of the EOHPBNN predistorter is combined with the AM/AM and AM/PM distortion characteristics, showing an improved linearization performance. The experimental results on a class-AB power amplifiers using wideband CMMB test signal demonstrate the excellent linearization performance.

1. INTRODUCTION

RF Power amplifiers (PAs) are essential components in wireless communication systems, which boost the radio signal to sufficient power level for transmission through the air interface from the transmitter to the receiver. However, PAs are inherent nonlinear devices and the nonlinearities generates amplitude and phase distortions (i.e., AM/AM and AM/PM distortions) at the output of PAs [1–3], resulting in adjacent channel interference and degradation of bit-error rate (BER) performance. High spectrally efficient signals employed in modern wideband communication systems, such as WCDMA, WiMAX, are more vulnerable to PAs nonlinearities due to their high peak-to-average power ratio (PAPR). Thus, it is necessary to compensate for the nonlinearities of PAs to comply with the linearity requirements imposed by regulatory bodies.

Currently, linearization of PAs using digital baseband predistortion has been widely studied in the literature and has been widely used in wireless communication systems [4–14]. For a digital predistorter, one of the crucial tasks is to find a good model to approximate the inverse of the PA nonlinearity. There are many techniques proposed to perform the digital predistortions. Generally these can be categorized into two classes: lookup tables (LUTs) and behavioral models. The LUT-based predistorter is simple in implementation and capable of approximating any nonlinear function, but plenty of memory is needed to accurately linearize a PA system and consequently the convergence rate is slow [12]. On the other hand, many types of behavioral model based digital predistorter have been proposed and evaluated, such as polynomial model, Volterral model [11], memory polynomial model [8–10], Wiener model, etc.. All these models have their advantages and disadvantages and a comparative overview has been presented in [14]. Over the last decade, neural network (NN) has been successfully applied to PA behavioral modeling and predistortion linearization [14, 15]. For its universal approximation capability, neural network based models are seen as a potential alternative to PA modeling and predistortion. Most neural network based PA models and predistorters utilize feedforward multilayer perceptron with sigmoid activation function and back propagation algorithm, which suffer from limited linearization performance and slow convergence rate. In this paper, a novel enhanced orthonormal Hermite polynomial basis neural network (EOHPBNN) predistorter is proposed. The EOHPBNN predistorter employs the orthonormal Hermite terms as its activation functions, exhibiting more accurate linearization performance. More over, the distortion mechanism is taked into account and combined with the EOHPBNN predistorter.

2. EOHPBNN PREDISTORTER

In this paper, we propose a novel enhanced orthonormal Hermite polynomial basis neural network (EOHPBNN) based predistorter to linearize PAs. Similar to the RVTDNN model presented in [15], the EOHPBNN predistorter is constructed as a multilayer feedforward network with in-phase and quadrature components as its inputs and outputs, and an additional tapped delay line (TDL) is applied at the input side to account for the memory effects of PAs. However, contrary to commonly used feedforward networks, this newly proposed EOHPBNN predistorter uses a set of orthonormal Hermite polynomial basis functions, taking advantage of their excellent approximation performance, as the activation functions in the hidden layer with the aim of obtaining better performance in terms of accuracy and convergence [16]. The orthogonal Hermite polynomials are defined as follows:

$$\begin{cases} H_0(x) = 1 \\ H_1(x) = 2x \\ H_n(x) = 2xH_{n-1}(x) - 2(n-1)H_{n-2}(x) \end{cases} \tag{1}$$

where $H_i(x)$, $i = 0, 1, 2, \ldots$, is the ith-order term of the orthogonal Hermite polynomial. It should be noted that the terms are orthogonal with each other and there is a recursive relationship between the terms, which helps to alleviate the computational burden. Based on the representations given above, the orthonormal Hermite polynomials used in this paper are defined as:

$$h_n(x) = a_n H_n(x)\varphi(x) \quad n = 0, 1, 2, \ldots \tag{2}$$

where

$$a_n = (n!)^{-1/2}\pi^{1/4}2^{-(n-1)/2} \tag{3}$$

$$\varphi(x) = 1/\sqrt{2\pi}\, e^{-x^2/2} \tag{4}$$

The orthonormal Hermite terms are also orthogonal and have the property of universal approximation, i.e., they have the capability of approximating any real function of interest to any desired accuracy. In the proposed EOHPBNN behavioral model in this paper, the terms $h_n(x)$, $n = 0, 1, 2, \ldots$, are chosen as the activation functions of the hidden neurons of the neural network. The orthonormal Hermite terms are assigned from the lowest order term to the higher order ones in the hidden neurons, as shown in Figure 2.

In addition, the EOHPBNN predistorter is also motivated from the measured dynamic AM/AM and AM/PM characteristics, as shown in Figure 1. It can be seen that the AM/AM and AM/PM conversion characteristics are no longer smooth curves, which suggests that the PA has significant memory effects and also that the small signal response of PA is more affected by the memory

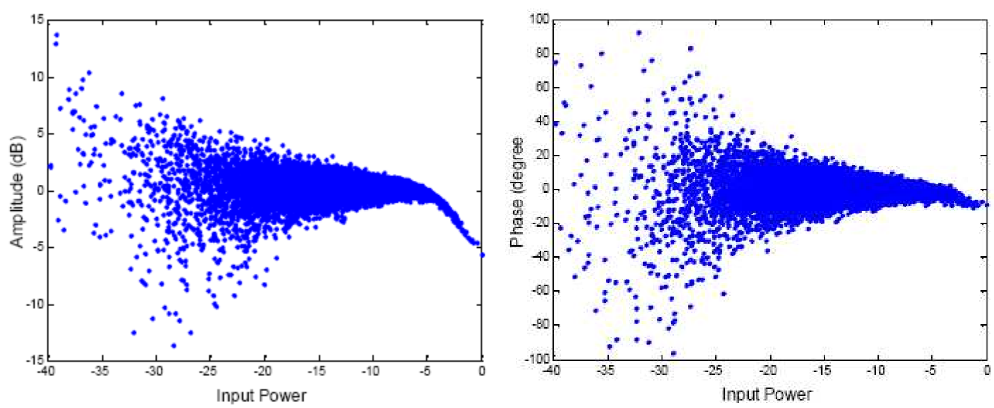

(a) (b)

Figure 1: Dynamic AM/AM and AM/PM characteristics.

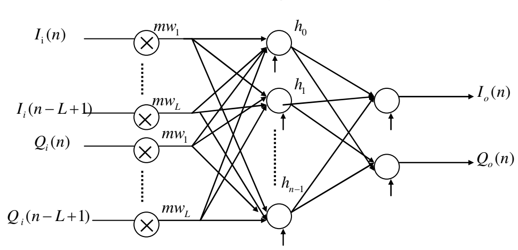

Figure 2: EOHPBNN based predistorter.

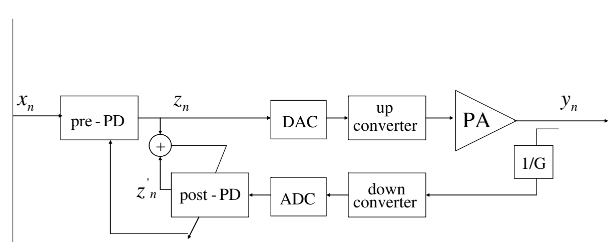

Figure 3: Block diagram of the experimental setup.

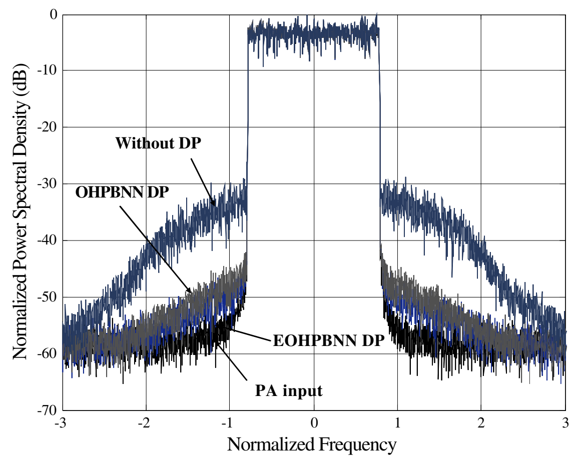

Figure 4: PSD comparison of the PA input, PA output without DP, PA output with EOHPBNN DP and PA output with OHPBNN DP.

effects than the large signal when PA is driven by wideband signals [15]. Thus there are some distinctions existing in the distortion mechanisms between the small and large signals. By means of utilizing a set of fuzzy membership functions to represent the degree of memory effects and then to weight the input data, these distinctions are reflected in our EOHPBNN predistorter to enhance the linearization performance. To account for the influence of PA memory effects on various signal magnitude, a commonly used Gaussian membership function, which here represents the extent of memory effects, are defined as follows:

$$m = \exp\left(-\frac{\rho^2}{cm_1}\right) \tag{5}$$

where ρ is the normalized amplitude of input signal. c and m_1 are constant and adjustable variable respectively. m represents the degree of memory effects for input signal with normalized amplitude ρ. m is then used to define the following Gaussian membership functions:

$$mw_l = \exp\left(-((l-1)/L)^2/mm_2\right) \quad l = 0, 1, \ldots, L-1 \tag{6}$$

where L is the total number of in-phase (or quadrature) input data. l is the index of input and m_2 is the adjustable variable. The values mw_l are used to weight the input signal, as shown in Figure 2.

From Equations (5), (6) and Figure 2, it can be seen that, if the input signal is small, the value of m is large, indicating significant memory effects, and the historical inputs are weighted with large fuzzy weights thus imposing great influence on the instant output. While if the input amplitude is large, it suffers less affection of historical inputs.

3. VALIDATION RESULTS

The experimental validation of the proposed EOHPBNN predistorter was conducted on a class-AB power amplifier with an average output power of 50.4 dBm using MMB (Mobile Multimedia Broadcasting) signal. The signal bandwidth is 7.56-MHz. Figure 3 shows the block diagram of experimental setup and learning architecture.

In order to demonstrate the performance improvement of the EOHPBNN predistorter, another predistorter based on the orthonormal Hermite polynomial basis neural network (OHPBNN) without using the fuzzy membership functions weighting the input data is constructed and tested. Figure 4 presents the power spectral density (PSD) comparison for the PA input, PA output without predistorter, PA output with EOHPBNN predistorter and OHPBNN predistorter. These experimental results clearly show that the two digital predistorters can greatly suppress the out-band spectrum regrowth. More over, the EOHPBNN predistorter is able to further linearize the PA output signals.

4. CONCLUSIONS

In this paper, a novel enhanced orthonormal Hermite polynomial basis neural network (EOHPBNN) predistorter is proposed and experimentally validated. The EOHPBNN predistorter utilizes orthonormal Hermite polynomial terms as the hidden layer's activation functions and motivated from the dynamic AM/AM and AM/PM characteristics, thus exhibiting superior linearization performance. The experimental validation was conducted on a class-AB power amplifiers using wideband CMMB test signal.

ACKNOWLEDGMENT

This work is supported by the National Natural Science Foundation of China (NNSF) under Grant 60990320, 60990323; 61271090, and the National 863 Project of China under Grant 2012AA012305, and Sichuan Provincial Science and technology support Project under Grant 2012GZ0101, and Chengdu Science and technology support Project under Grant 12DXYB347JH-002. The authors would also like to express their gratitude to Dr. Liangchen Zhou for his affording the experimental data and valuable discussions on this paper.

REFERENCES

1. Vuolevi, J. and T. Rahkonen, *Distortion in RF Power Amplifiers*, Artech House, London, MA, 2002.
2. Kennington, P. B., *High Linearity RF Amplifier Design*, Artech House, Boston, MA, 2000.
3. Thein, T. T., C. L. Law, and K. Fu, "Frequency domain dynamic thermal analysis in GaAs HBT for power amplifier applications," *Progress In Electromagnetics Research,* Vol. 118, 71–87, 2011.
4. Moazzam, M. R. and C. S. Aitchison, "A low third order intermodulation amplifier with harmonic feedback circuuitry," *IEEE Trans. Microw. Theory Tech.*, Vol. 2, No. 10, 827–830, 1996.
5. Yang, Y., Y. Y. Woo, and B. Kim, "Optimization for error canceling loop of the feedforward amplifier using a new system-level mathematical model," *IEEE Trans. Microw. Theory Tech.*, Vol. 51, No. 2, 475–482, 2003.
6. Cheong, M. Y., S. Werner, M. J. Bruno, J. L. Figueroa, J. E. Cousseau, and R. Wichman, "Adaptive piecewise linear predistorters for nonlinear power amplifiers with memory," *IEEE Trans. Circuits. Syst. I, Reg. Papers*, Vol. 59, No. 7, 1519–1532, 2012.
7. Kim, J. and K. Konstantinou, "Digital predistortion of wideband signals based on power amplifier model with memory," *Electron. Lett.*, Vol. 37, No. 23, 1417–1418, 2001.
8. Ding, L., G. T. Zhou, D. R. Morgan, Z. X. Ma, J. S. Kenney, J. Y. Kim, and C. R. Giardina, "A robust digital baseband predistorter constructed using memory polynomials," *IEEE Trans. Commun.*, Vol. 52, No. 1, 159–165, 2004.
9. Morgan, D. R., Z. Ma, J. Kim, M. G. Zierdt, and J. Pastalan, "A generalized memory polynomial model for digital predistortion of RF power amplifiers," *IEEE Trans. Signal Process.*, Vol. 54, No. 10, 3852–3860, 2006.
10. Zhu, A. D. and T. J. Brazil, "An adaptive Volterra predistorter for the linearization of RF high power amplifiers," *IEEE MTT-S Int. Microw. Symp. Dig.*, 461–464, July 2002.
11. Muhonen, K. J., M. Kavehrad, and R. Krishnamoorthy, "Look-up table techniques for adaptive digital predistortion: A development and comparison," *IEEE Trans. Veh. Technol.*, Vol. 49, No. 5, 1995–2002, 2000.
12. Hong, S. C., Y. Y. Woo, J. H. Kim, J. H. Cha, I. Kim, J. H. Moon, J. Y. Yi, and B. Kim "Weighted polynomial digital predistortion for low memory effect Doherty power amplifier," *IEEE Trans. Microw. Theory Tech.*, Vol. 55, No. 5, 925–931, 2007.
13. Rawat, M. and F. M. Ghannouchi, "Distributed spatiotemporal neural network for nonlinear dynamic transmitter modeling and adaptive digital predistortion," *IEEE Trans. Instrum. Meas.*, Vol. 61, No. 3, 595–608, 2012.
14. Pedro, J. C. and S. A. Maas, "A comparative overview of microwave and wireless power-amplifier behavioral modeling approaches," *IEEE Trans. Microw. Theory Tech.*, Vol. 53, No. 4, 1150–1163, 2005.
15. Liu, T. J., S. Boumaiza, and F. M. Ghannouchi, "Dynamic behavioral modeling of 3G power amplifiers using real-valued time-delay neural networks," *IEEE Trans. Microw. Theory Tech.*, Vol. 52, No. 3, 1025–1033, 2004.
16. Lin, F. J., "Tracking control of thrust active magnetic bearing system via Hermite polynomial-based recurrent neural network," *Electric Power Applications, IET*, Vol. 4, 701–714, 2010.

Design of Parallel FFT Based on FPGA in the Field of Software Radio

G. C. Wan, Y. Q. Zhang, and M. S. Tong
Department of Electronic Science and Technology, Tongji University
4800 Cao'an Road, Shanghai 201804, China

Abstract— Most of the high-speed signal processing functions in software radio are used to realize the transformation between time domain and frequency domain by Discrete Fourier Transform (DFT) first. However the time consuming in calculation of DFT is too large to apply in practice so that Fast Fourier Transform (FFT) is proposed. In this work, we develop a design of parallel FFT in which the data exported by every butterfly processing element flow to the next level directly without storage in order to avoid data stack. The method of data truncation is to obtain the high 16 bits of the data exported by every multiplier and to halve the calculation results of butterfly elements at each level.

1. INTRODUCTION

Software radio is a kind of communication technology of radio system based on software-defined radio rather than hard-wired radio. Though Software radio has good application prospect in theory, its practical use is still limited due to its very high requirement on the rate of signal processing. There are two key ideas of software radio: making A/D/A (analog to digital/digital to analog) converters as close to the antenna as possible and achieving as many radio functions as possible by software. One of the main techniques is high-speed signal processing including baseband processing, modulation, demodulation, coding, decoding and some other functions. Most of these functions are used to realize the transformation of signal between time domain and frequency domain by Discrete Fourier Transform (DFT) first. However the time consuming in calculation of DFT is too large to apply in practice so that Fast Fourier Transform (FFT) is proposed. FFT can reduce the computational cost by resolving a long sequence DFT into short sequences.

Field Programmable Gate Array is a good hardware choice to process the signal exported by the high-speed A/D because of its high efficiency based on Application Specific Integrated Circuit (ASIC) and its flexibility for system realization. Meanwhile, the FFT IP (intellectual property) core on FPGA provided by Xilinx is widely used to accomplish the FFT calculation. However the FFT IP core only supports serial input rather than parallel input. This disadvantage makes it inappropriate for high-speed signal especially in the field of software radio. Also, the design of distributing memory cell to every radix-2 butterflies occupies too much resource of FPGA.

To aim at the problems caused by serial FFT IP core, we develop a design of parallel FFT based on FPGA which can be more suitable for the field of software radio.

2. PARALLEL FFT AND REALIZATION ON FPGA

The formula of DFT is

$$X(k) = \sum_{n=0}^{N-1} x(n) e^{-jnk2\pi/N} = \sum_{n=0}^{N-1} x(n) W_N^{kn} \quad k = 0, \ldots, N-1 \tag{1}$$

where $x(n)$ is the input sequence, $X(k)$ is the output sequence, N is the transform size, $j = \sqrt{-1}$, and W_N^k is the rotation factor.

Figure 1 shows the 8 point FFT when using radix-2. The input is in bit-reversed order by binary method and the output is in normal order. In this parallel FFT, data exported by every butterfly processing element flow to the next level directly without storage in order to avoid data stack. If the synchronous sequential circuit is adopted, a set of calculation results will be exported at every clock tick that can greatly improve the speed of computation.

The top-down design method is adopted when the thought of modularization is applied to the FPGA. The module of butterfly is the core module of this parallel FFT. The basic flow chart is as shown in Figure 2.

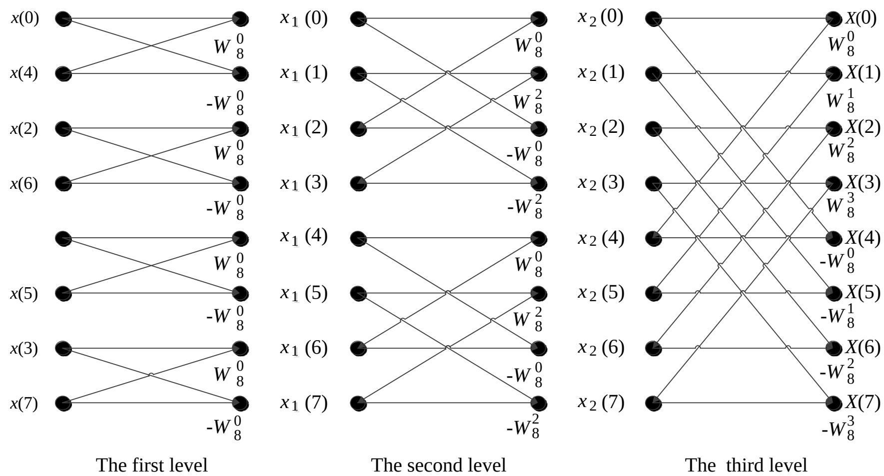

Figure 1: The flow chart of 8 point FFT.

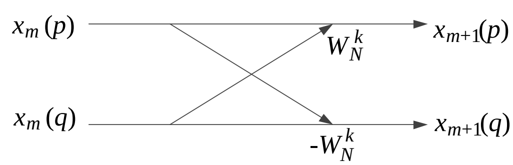

Figure 2: The butterfly processing element.

The $x_m(p)$ and $x_m(q)$ is the input data while $x_{m+1}(p)$ and $x_{m+1}(q)$ is the output data. is the rotation factor. The formula of this butterfly processing element is

$$\begin{cases} x_{m+1}(q) = x_m(p) - W_N^k x_m(q) \\ x_{m+1}(p) = x_m(p) + W_N^k x_m(q) \end{cases} \tag{2}$$

A multiplier, an adder and a subtractor constitute the inner structure of the butterfly processing element. When fixed-point operation is taken by FPGA, such as complex multiplication, the bit-wide of the data will double each time. Then the width of date exported by the last level of FFT will be $m_0 N + 2(N+1)$, where m_0 is the width of input data and N is the point of FFT. It is very clear that the data should be truncated to avoid the occupation of much resource of the devices. The method we use is to obtain the high 16 bits of the data exported by every multiplier and to halve the calculation results of butterfly elements at each level.

3. THE ROUNDING ERROR OF FFT

Comparing the rounding error of FFT which is caused by the multiplication and the error of DFT is very necessary. Every complex multiplication needs four multiplications of real numbers so that there will be four quantization errors. The assumptions about the statistics property of noise sources we make are:

- All of the 4 K errors are irrelated with each other and independent of the input sequence.
- The rounding error is a uniformly distributed random variable of which the variance is $\sigma_e^2 = 2^{-2b}/12$. It is assumed to be a signed number with b points.

When DFT is calculated directly, the variance of the error in one DFT calculation is

$$\sigma_\gamma^2 = 4N\sigma_0^2 = 2^{-2b}N/3 \tag{3}$$

which indicates that the round error is proportional to the transform size of DFT. The input sequence $x(n)$ must be scaled in order to avoid overflow.

$$|X(k)| \leq \sum_{n=0}^{N-1} |x(n)| < N \tag{4}$$

We assume the input sample can meet the limitation of dynamic range $|x(n)| \leq 1$. $|X(k)| < 1$ is guaranteed by dividing $x(n)$ by N. When the input sequence is a white noise sequence distributing in $(-1/N,\ 1/N)$, the power is

$$\sigma_x^2 = (2/N)^2/12 = 1/\left(3N^2\right) \tag{5}$$

while the power of output signal is

$$\sigma_X^2 = N\sigma_x^2 = 1/(3N) \tag{6}$$

Then the SNR (Signal to Noise Ratio) is

$$SNR = \sigma_X^2/\sigma_\gamma^2 = 2^{2b}/N^2 \tag{7}$$

When DFT is calculated by FFT, the flow chart will be simplified as shown in Figure 3.

In Figure 3, one calculation of the DFT sample has $\upsilon = \log_2 N$ steps. The rth step has $N/2^r = 2^{\upsilon - r}$ butterflies, and $r = 1, 2, \ldots, \upsilon$. Thus, the amount of butterflies in one DFT calculation is

$$1 + 2 + 2^2 + \ldots + 2^{\upsilon-2} + 2^{\upsilon-1} = 2^\upsilon - 1 = N - 1 \tag{8}$$

The output variance of rounding error is

$$\sigma_r^2 = 4(N-1) \cdot 2^{-2b}/12 \cong 2^{-2b}N/3 \tag{9}$$

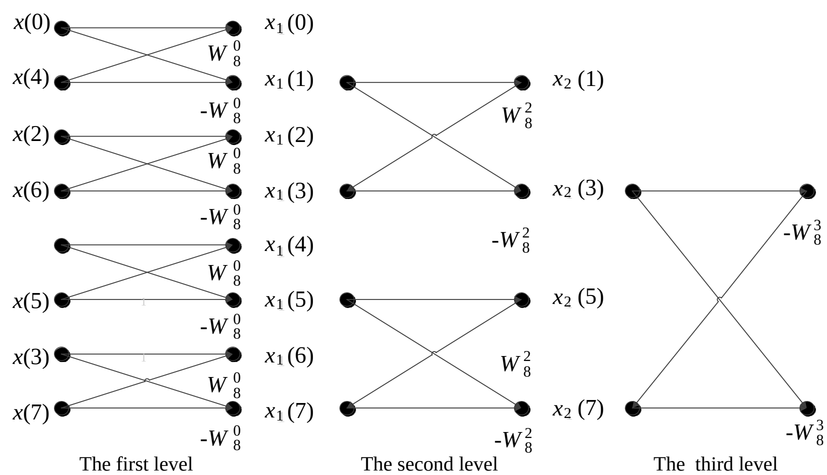

Figure 3: The simplified flow chart of 8 point FFT.

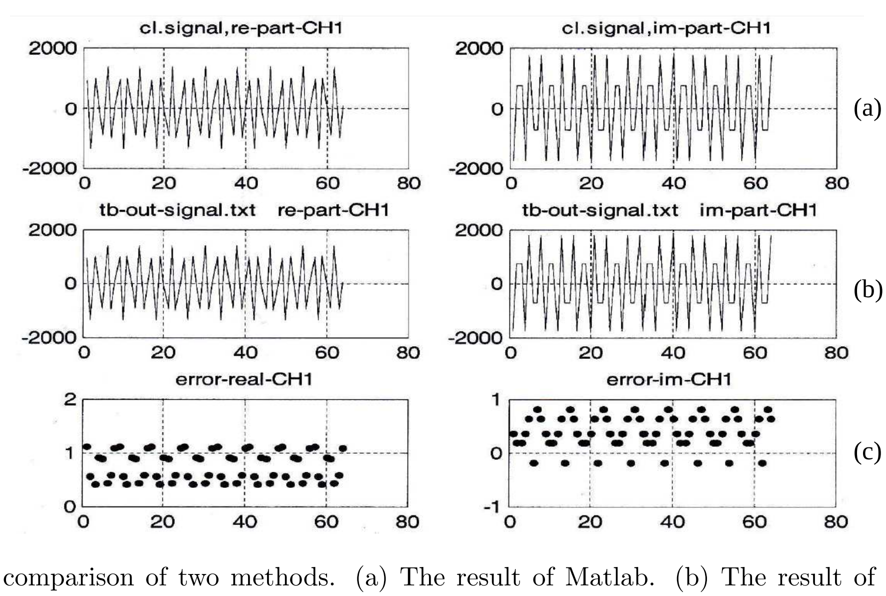

Figure 4: The comparison of two methods. (a) The result of Matlab. (b) The result of FPGA. (c) The errors.

If the calculation results of butterflies are halved at each level, the output variance of rounding error will be

$$\sigma_r^2 = (2/3) \cdot 2^{-2b}(1 - (1/n)) \cong (2/3) \cdot 2^{-2b} \tag{10}$$

Then the SNR will be

$$SNR = \sigma_x^2/\sigma_r^2 = 2^{2b}/(2n) \tag{11}$$

4. SIMULATION RESULTS

We create a signal with Matlab, of which the frequency is 10 MHz, the word length is 16 bit, and the sampling rate is 128 MHz. the 8-point FFT calculation with the full parallel FFT based on the FPGA is co-simulated in ModelSim and Matlab. The results of these two methods simulation are compared as shown in Figure 4.

5. CONCLUSIONS

The parallel FFT we designed based on FPGA is much faster than the commercial IP core. Though the parallel structure occupies many hardware resources, it can be applied in the practice with the development of FPGA. How to process the high-speed signal preferably is always one of the key problems in software radio, so this design has great application prospect in this field. This design still can be proved in many ways which our further work will focus on.

REFERENCES

1. Yeh, W. and C. Jen, "High-speed and low-power split-radix FFT," *IEEE Trans. Signal Processing*, Vol. 51, No. 3, 864–874, 2003.
2. Chang, Y. and K. K. Parhi, "An efficient pipelined FFT architecture," *IEEE Trans. Circuits & Systems-II: Analog & Digital Signal Processing*, Vol. 50, No. 6, 322–325, 2003.
3. Ma, Y. T. and L. Wanhammar, "A hardware efficient control of memory addressing for high performance FFT processors," *IEEE Trans. Signal Processing*, Vol. 48, No. 3, 917–921, 2000.
4. Tucky, C. J. W., "An algorithm for the machine calculation of complex fourier series," *Math. of Comput.*, Vol. 19, No. 90, 297–301, 1965.

A Correction Term for Maxwell's Equations Transformed between Galilean Reference Systems (Part I)

Namık Yener
Biomedical Engineering Department, Technology Faculty
Umuttepe Campus, Kocaeli University, Izmit, Kocaeli 41380, Turkey

Abstract— Two electromagnetic problems are solved in which Maxwell's equations are shown to need a correction term when their Lorentz transformation is taken between two Galilean reference systems. In the examples two relations exist between the wave number k' and frequency ω' in K' which is in uniform rectilinear motion with respect to K. One of these relations dictates the law by which k' and ω' abide on their path to zero. The other one which is the representation of Maxwell's second equation yields the unbalance between the two sides of this equation when the limit $\omega' \to 0$ and $k' \to 0$ is taken. This constitutes the first part of the two papers describing the work.

1. INTRODUCTION

We consider two examples which exhibit the need for a correction term in Maxwell's equations transformed between Galilean reference systems. The first one is presented in this paper and the second one in its companion [1].

For the first example we consider a Debye material with permittivity function given by

$$\varepsilon = \varepsilon_\infty + \frac{\varepsilon_d}{1 - j\omega\tau}. \tag{1}$$

We further assume $\varepsilon_\infty = \varepsilon_0$ where ε_0 is the permittivity of vacuum. We take this medium as medium (I) of an electromagnetic system in which another medium (II) that consists of a perfect electric conductor, is in uniform rectilinear motion with respect to medium (I) with speed v. Galilean reference frames K and K' are assumed to be attached to medium (I) and medium (II) respectively and the velocity boost is assumed to be along the Ox axis of a Cartesian coordinate system $Oxyz$. The interface of the two media is assumed to be an infinite plane perpendicular to the Ox axis. We further assume that there are no free charges in medium (I) when observed from K.

Considering plane wave solutions and in Maxwell's equations using jk for ∇ and $-j\omega$ for $\frac{\partial}{\partial t}$ and by employing primed quantities for K' and unprimed ones for K, under a Lorentz transformation [2], the frequencies and wave numbers will be related as follows:

$$\omega_i = \gamma(\omega' + vk'), \tag{2a}$$
$$\omega_r = \gamma(\omega' - vk'), \tag{2b}$$
$$k_i = \gamma\left(k' + \frac{\beta}{c}\omega'\right), \tag{3a}$$
$$k_r = \gamma\left(k' - \frac{\beta}{c}\omega'\right). \tag{3b}$$

In the above, subscripts i and r pertain to incident and reflected waves respectively, $\beta = v/c$, $\gamma = 1/\sqrt{1-\beta^2}$ where c is the speed of light in vacuum. We have assumed that the incident plane wave makes an angle of zero degree with the normal of the interface of the two media when observed from K'.

2. ELECTRIC CURRENT DENSITY VECTORS OBSERVED FROM K AND K'

Considering (1), the dispersion relation that medium (I) has, can be written as

$$k_i^2 = \omega_i^2\varepsilon_0\mu_0\left(1 + \frac{\varepsilon_d/\varepsilon_0}{1 - j\omega_i\tau}\right), \tag{4a}$$

for the incident wave, and as

$$k_r^2 = \omega_i^2\varepsilon_0\mu_0\left(1 + \frac{\varepsilon_d/\varepsilon_0}{1 - j\omega_r\tau}\right), \tag{4b}$$

for the reflected wave where μ_0 is the magnetic permeability of vacuum. Based on (4) then,

$$k_i^2 - k_r^2 = (\omega_i^2 - \omega_r^2)/c^2 + \mu_0 \left(\frac{\omega_i^2 \varepsilon_d}{1 - j\omega_i \tau} - \frac{\omega_r^2 \varepsilon_d}{1 - j\omega_r \tau} \right), \tag{5a}$$

$$k_i^2 + k_r^2 = (\omega_i^2 + \omega_r^2)/c^2 + \mu_0 \left(\frac{\omega_i^2 \varepsilon_d}{1 - j\omega_i \tau} + \frac{\omega_r^2 \varepsilon_d}{1 - j\omega_r \tau} \right), \tag{5b}$$

follow. Observing (2) and (3), from (5a)

$$\frac{\omega_i^2 \varepsilon_d}{1 - j\omega_i \tau} = \frac{\omega_r^2 \varepsilon_d}{1 - j\omega_r \tau}, \tag{6}$$

can be written. From (6), $\omega_i^2(1 - j\omega_r \tau) = \omega_r^2(1 - j\omega_i \tau)$ can be deduced which implies

$$(\omega_i + \omega_r) = j\tau\omega_i\omega_r. \tag{7a}$$

Consider the equality $\omega_i^2 j\tau + \omega_i\omega_r j\tau = j\tau\omega_i(\omega_i + \omega_r)$. This can be written in the form

$$-j\tau\omega_i^2 = -j\tau\omega_i 2\gamma\omega' + j\tau\omega_i\omega_r, \tag{7b}$$

when (2) is noted, or in the form

$$-j\tau\omega_i^2 = -j\tau\omega_i 2\gamma\omega' + (\omega_i + \omega_r) = 2\gamma\omega'(1 - j\tau\omega_i), \tag{7c}$$

upon using (7a) in (7b). On the other hand (7c) means

$$\frac{\omega_i^2 \varepsilon_d}{1 - j\omega_i \tau} = \frac{\varepsilon_d 2\gamma\omega'}{-j\tau}. \tag{7d}$$

If for the incident wave, we consider a plane wave solution in medium (I) as observed from K in the form of $\vec{E} = A_1' \exp[j(k_i x - \omega_i t)]\, \vec{a}_z$ where $\vec{a}_z$ is the unit vector along Oz, according to (1), the current density vector will be

$$\vec{J}_i = A_1' \exp[j(k_i x - \omega_i t)] \frac{-j\omega_i \varepsilon_d}{1 - j\omega_i \tau} \vec{a}_z. \tag{8}$$

Since the velocity boost is along Ox axis, and $\vec{J}_i$ has only an $\vec{a}_z$ component, under the Lorentz transformation,

$$\vec{J}_i' = \vec{J}_i = A_1' \exp[j(k_i x - \omega_i t)] \frac{-j\omega_i \varepsilon_d}{1 - j\omega_i \tau} \vec{a}_z \tag{9}$$

holds. Because of the phase invariance principle $j(k_i x - \omega_i t) = j(k' x' - \omega' t')$ is true and (9) can also be written as

$$\vec{J}_i' = A_1' \exp\left[j\left(k' x' - \omega' t'\right)\right] \frac{1}{\omega_i} \frac{\varepsilon_d 2\gamma\omega'}{\tau} \vec{a}_z, \tag{10}$$

also with the help of (7d).

3. RELATIONS BETWEEN ω' AND k'

For the incident and reflected waves, substitution of (2) and (3) in (4a) and (4b) yields the following two relations that k' and ω' must satisfy:

$$\left(k' + \frac{\beta}{c}\omega'\right)^2 = \frac{1}{c^2}(\omega' + vk')^2 \left[1 + \frac{\varepsilon_d/\varepsilon_0}{1 - j\tau\gamma(\omega' + vk')}\right], \tag{11a}$$

$$\left(k' - \frac{\beta}{c}\omega'\right)^2 = \frac{1}{c^2}(\omega' - vk')^2 \left[1 + \frac{\varepsilon_d/\varepsilon_0}{1 - j\tau\gamma(\omega' - vk')}\right]. \tag{11b}$$

By inspection of (11) it is possible to conclude that under the limit $\omega' \to 0$, one solution for k' also tends to zero. Under this limit and for this k' solution, the quantities $1 - j\tau\gamma(\omega' \mp vk')$ in (11) can be taken approximately equal to 1. Then, from addition of (11a) and (11b) under this condition,

$$k'^2 + \left(\frac{\beta}{c}\omega'\right)^2 \cong \frac{1}{c^2}\left[\omega'^2 + (vk')^2\right](1 + \varepsilon_d/\varepsilon_0), \tag{12}$$

will follow. Equation (12) shows that k'^2 is proportional to ω'^2 under the limit $\omega' \to 0$ and $k' \to 0$.

On the other hand substitution of (2) and (3) in (5b) yields, in the light of (7d),

$$k'^2 - \left(\frac{\omega'}{c}\right)^2 = \mu_0 \frac{2\gamma\varepsilon_d\omega'}{-j\tau}. \tag{13}$$

At this point it must be pointed out that having two relations (Equations (12) and (13)) and not one relation that k' and ω' must satisfy, is acceptable, because essentially we have two different dispersion relations connecting these two variables; one for the incident and the other for the reflected wave.

4. OBTAINING ELECTROMAGNETIC FIELDS OBSERVED IN *K* AND *K′*

Equation (13) indicates that there are two possible values for the variable k' which are negatives of each other. These correspond to the wave numbers of the incident ($+k'$) and reflected ($-k'$) waves observed from K'. Thus, through observing (2) and (3) and by the phase invariance principle, the total electric field vector measured from K can be expressed as

$$\vec{E} = E_z\vec{a}_z = \sum_{p=1}^{2} A_p^{'} \exp(jk_p^{'}x')\,\vec{a}_z \tag{14}$$

when the factor of $\exp(-j\omega' t')$ is suppressed. Therefore here $k'_1 = k'$ and $k'_2 = -k'$.

Now using the derivation of [1] between Equations (4) through (16) therein, which we do not repeat here for conciseness, we conclude,

$$E'_z = A'_1 \frac{2\omega'}{\gamma(\omega' + \beta ck')} \sinh(jk'x'), \tag{15}$$

and

$$\vec{B}' = -A'_1 \frac{2}{\gamma(\omega' + \beta ck')} \left[\vec{a}_y k' \cosh(jk'x')\right], \tag{16}$$

for the totals of incident and reflected waves.

When observed from K, medium (I) has a magnetic permeability μ_0 and a dielectric constant ε_0. When observed from K' it will still have the same permeability and dielectric constant although its conductivity will change. Under these permeability and dielectric constant value assumptions the electromagnetic field transforms consistently under a Lorentz transformation. Therefore when (16) is given,

$$\vec{H}' = -A'_1 \frac{2}{\mu_0\gamma(\omega' + \beta ck')} \left[\vec{a}_y k' \cosh(jk'x')\right], \tag{17}$$

will follow.

On the other hand, $\vec{J}'_i = \sigma'\vec{E}'_i$ where $\sigma' = -j\omega'(\varepsilon' - \varepsilon_0)$. Here ε' is the permittivity of medium (I) observed from K' and due to (13), it is given by $\varepsilon' = \varepsilon_0 - \frac{1}{\omega'^2}\frac{2\gamma\varepsilon_d\omega'}{j\tau}$. Therefore $\sigma' = \frac{2\gamma}{\tau}\varepsilon_d$ and

$$\vec{J}'_i = \sigma'\vec{E}'_i = \frac{2\gamma}{\tau}\varepsilon_d A'_1 \frac{\omega'}{\gamma\left(\omega' + \beta ck'\right)} \exp\left(jk'x'\right)\vec{a}_z = \frac{2\gamma}{\tau}\varepsilon_d A'_1 \frac{\omega'}{\omega_i} \exp\left(jk'x'\right)\vec{a}_z, \tag{18}$$

which is in agreement with Equation (10) and hence with Equation (9). This is a cross-check of the correctness of the Lorentz transformation of the electromagnetic field.

For medium (I) if we set up the second Maxwell equation for the incident wave observed from K', incorporating (15)–(18) in it, we will get:

$$\begin{aligned} &j\,\vec{a}_x k'_1 \times \left\{A'_1 \frac{1}{\mu_0\gamma(\omega' + \beta ck')} \left[-\vec{a}_y k' \exp(jk'x')\right]\right\} \\ &= -\left\{j\omega' A'_1 \frac{\omega'\varepsilon_0}{\gamma(\omega' + \beta ck')} - \frac{1}{\omega_i}\frac{\varepsilon_d 2\gamma\omega'}{\tau} A'_1\right\} \exp(jk'x')\vec{a}_z. \end{aligned} \tag{19}$$

Equation (10) is already contained in (18). Implicit in (19) is also the dispersion relation (13).

5. MAXWELL'S SECOND EQUATION UNDER THE LIMIT $\omega' \to 0$ AND $k' \to 0$

By Section 3 we know for certain that as $\omega' \to 0$ we can take $k' \to 0$. To determine the law by which ω' and k' abide on their path to zero we have two relations, namely Equations (12) and (13). From (13) one can infer that as ω' approaches zero, the second term on the left can be neglected when compared with the term on the right hand side and hence that k'^2 is proportional to ω'. But this argument can be true only if it is supported by the fact that k'^2 is *not* proportional to ω'^2 at the same time, because if k'^2 is proportional to ω'^2, then k'^2 too ought to be neglected when compared with the term on the right hand side. In such a case k' would be proportional to $\sqrt{\omega'}$ and from (13) we would have an equation of the form

$$0 \cong \mu_0 \frac{2\gamma\varepsilon_d\omega'}{-j\tau},$$

both sides of which would be equal when ω' tends to zero. However the point is that we have no supporting fact that k'^2 is *not* proportional to ω'^2. On the contrary, by Equation (12) k'^2 is proportional to ω'^2. Therefore as they approach zero k' and ω' are proportional.

We shall use this conclusion in assessing (19). Indeed because of this result the left hand side of (19) will vanish as $\omega' \to 0$ since its numerator is of the power two of ω' whereas its denominator is of the power of one of ω'. Similar argument shows that the first term on the right also vanishes whereas the second term approaches a constant value and does not vanish.

Hence we have a case where Maxwell's second equation is not satisfied and needs a correction term. This correction term that must be subtracted from Maxwell's second equation is temporally and spatially constant because it appears as a result of the limit operation $\omega' \to 0$ and $k' \to 0$.

This example shows that when the dielectric constant and magnetic permeability of medium (I) are that of vacuum, medium (II) is a perfect electric conductor, k' and ω' are proportional on their path to zero and this inconsistency emerges, then the correction term needed is equal to $\lim\limits_{\substack{\omega' \to 0 \\ k' \to 0}} \vec{J}'$.

A similar derivation will hold true for the reflected wave.

REFERENCES

1. Yener, N., "A correction term for Maxwell's equations transformed between Galilean reference systems (Part II)," *PIERS Proceedings*, Taipei, Taiwan, March 25–28, 2013.
2. Jackson, J. D., *Classical Electrodynamics*, John Wiley & Sons, Inc., New York, 1975.

A Correction Term for Maxwell's Equations Transformed between Galilean Reference Systems (Part II)

Namık Yener
Biomedical Engineering Department, Technology Faculty
Kocaeli University, Umuttepe Campus, Izmit, Kocaeli 41380, Turkey

Abstract— Two electromagnetic problems are solved in which Maxwell's equations are shown to need a correction term when their Lorentz transformation is taken between two Galilean reference systems. In the examples two relations exist between the wave number k' and frequency ω' in K' which is in uniform rectilinear motion with respect to K. One of these relations dictates the law by which k' and ω' abide on their path to zero. The other one which is the representation of Maxwell's second equation yields the unbalance between the two sides of this equation when the limit $\omega' \to 0$ and $k' \to 0$ is taken. This constitutes the second part of the two papers describing the work.

1. INTRODUCTION

In this Part II of the two paper series [1], we cite the second example where a correction term is needed for Maxwell's equations under Lorentz transformation.

2. SECOND EXAMPLE WHERE A CORRECTION TERM IS NEEDED FOR MAXWELL'S EQUATIONS UNDER LORENTZ TRANSFORMATION

In this section, we cite one other problem in which the above inconsistency is exhibited by Maxwell's equations. We consider a perfect electrically conducting medium (medium (II)) filling a half space $x' > 0$ to which is attached a Galilean reference system K' and a Lorentz medium (medium (I)) filling the space $x > -\infty$ to which is attached the Galilean reference system K. K' is in uniform rectilinear motion with respect to K with speed v along the Ox axis of the $Oxyz$ Cartesian coordinate system of K. For the incident wave observed from K, the Lorentz medium has the dispersion relation given by [2];

$$k_i^2 = \left(\frac{\omega_i}{c}\right)^2 \left(1 - \frac{b^2}{\omega_i^2 - \omega_0^2 + 2j\bar{\delta}\omega_i}\right), \tag{1}$$

whereas for the reflected wave one again has (1) but this time the subscript r will replace subscript i [3]. In addition the symbol $\bar{\delta}$ is used to denote the damping constant.

For a velocity boost along Ox under the Lorentz transformation [4], the following chain differentiation rules apply. (Here we have adopted the notation $\beta = v/c$, $\gamma = 1/\sqrt{1-\beta^2}$ with v as the relative speed of K' with respect to K and c as the speed of light in vacuum.):

$$\frac{\partial}{\partial x} = \gamma\frac{\partial}{\partial x'} - \gamma\frac{\beta}{c}\frac{\partial}{\partial t'}, \tag{2a}$$

$$\frac{\partial}{\partial t} = -\gamma\beta c\frac{\partial}{\partial x'} + \gamma\frac{\partial}{\partial t'}. \tag{2b}$$

In this paper primed quantities will pertain to K' whereas unprimed ones will pertain to K.

If for the incident and reflected waves, we consider plane wave solutions in medium (I) according to Equation (1) above and Equations (20) and (21) of [3] the dispersion relation becomes

$$k'^2 - \left(\frac{\omega'}{c}\right)^2 = -b^2\frac{\bar{b}}{\bar{b} + j\bar{\delta}}, \tag{3a}$$

under the condition that the wave vector in K' makes an angle of zero degree with the normal of the interface of medium (I) and (II) which is an infinite plane perpendicular to the Ox axis. The reader is referred to [3] for the meanings of various quantities in (1) and (3a). Only notice that in this paper we are assuming $c = c'$ vis-à-vis the speed of light in vacuum. Since relation (3a) is quadratic in k' it is to be expected that the wave number k' for medium (I) observed from K' has two roots. Hence we can write

$$E_z = \sum_{p=1}^{2} A'_p(\omega') \exp(jk'_{px'}x'). \tag{3b}$$

when the phase invariance principle is noted and the factor of $\exp(-j\omega' t')$ is suppressed. Thus the index p in (3b) takes on the values 1 and 2.

On the other hand the first Maxwell's equation is

$$\nabla \times \vec{E} = -\frac{\partial \vec{B}}{\partial t}. \tag{4}$$

Suppose $\vec{E} = E_z(t, x)\vec{a}_z$. From (4), we obtain,

$$\frac{\partial \vec{B}}{\partial t} = \frac{\partial E_z}{\partial x}\vec{a}_y. \tag{5}$$

Here $\vec{a}_y$ is the unit vector of the Cartesian coordinate system of K along the Oy axis.

Using (2), from (5) we get:

$$\frac{\partial \vec{B}}{\partial t} = -\left(\gamma\beta c\frac{\partial \vec{B}}{\partial x'} - \gamma\frac{\partial \vec{B}}{\partial t'}\right) = \vec{a}_y\left(\gamma\frac{\partial E_z}{\partial x'} - \gamma\frac{\beta}{c}\frac{\partial E_z}{\partial t'}\right). \tag{6}$$

The $\vec{a}_y$ component of (6) reads:

$$-\gamma\beta c\frac{\partial B_y}{\partial x'} + \gamma\frac{\partial B_y}{\partial t'} = \gamma\frac{\partial E_z}{\partial x'} - \gamma\frac{\beta}{c}\frac{\partial E_z}{\partial t'}. \tag{7}$$

Taking the Fourier transform of this equation with respect to t' and in it substituting (3b) we get:

$$-\gamma\beta c\frac{dB_y}{dz'} - \gamma j\omega' B_y = \gamma\sum_{p=1}^{2} jk'_{px'}A'_p\left(\omega'\right)\exp\left(jk'_{px'}x'\right) + \gamma\frac{\beta}{c}j\omega'\sum_{p=1}^{2}A'_p\left(\omega'\right)\exp\left(jk'_{px'}x'\right). \tag{8}$$

We find the following solution for the resulting differential Equation (8):

$$B_y = \sum_{p=1}^{2} B'_p\left(\omega'\right)\exp\left(jk'_{px'}x'\right) + B'_3\left(\omega'\right)\exp\left(-\frac{j\omega'}{\beta c}x'\right). \tag{9}$$

Here we disregard the last term because B_y must satisfy the same plane wave structure as E_z does and E_z does not support a third wave number as of this term (cf. Equation (3a)). This becomes clear when the second Maxwell's equation is considered in addition to (7), while the structure of (3a) is observed. Also:

$$B'_1 = -\frac{k'_{1x'} + \omega'\beta/c}{\beta ck'_{1x'} + \omega'}A'_1, \qquad B'_2 = -\frac{k'_{2x'} + \omega'\beta/c}{\beta ck'_{2x'} + \omega'}A'_2. \tag{10}$$

holds. Under the Lorentz transformation we also have [4],

$$E'_z = \gamma(E_z + vB_y). \tag{11}$$

Using (3a), (9), (10) and (11) one obtains:

$$E'_z = \gamma\left[A'_1\left(1 - v\frac{k'_{1x'} + \omega'\beta/c}{\beta ck'_{1x'} + \omega'}\right)\exp\left(jk'_{1x'}x'\right) + A'_2\left(1 - v\frac{k'_{2x'} + \omega'\beta/c}{\beta ck'_{2x'} + \omega'}\right)\exp\left(jk'_{2x'}x'\right)\right]. \tag{12}$$

The boundary condition $E'_{z'}|_{x'=0} = 0$ on the surface of the perfectly conducting half space that is the boundary between the two media, can now be expressed as:

$$A'_1\left(1 - v\frac{k'_{1x'} + \omega'\beta/c}{\omega' + \beta ck'_{1x'}}\right) = -A'_2\left(1 - v\frac{k'_{2x'} + \omega'\beta/c}{\omega' + \beta ck'_{2x'}}\right). \tag{13}$$

This can be re-expressed as:

$$A_1'\left(\omega' + \beta c k_{2x'}'\right) = -A_2'\left(\omega' + \beta c k_{1x'}'\right) \tag{14}$$

The fact that the reflected and incident waves observed from K' must have opposite directions implies that $k_{1x'}' = -k_{2x'}' = k_1'$. This is also seconded by the structure of (3a) which admits two k' values that are negatives of each other. Then (11) will yield the following expression for E_z':

$$E_z' = A_1' \frac{2\omega'}{\gamma\left(\omega' + \beta c k_1'\right)} \sinh\left(j k_1' x'\right). \tag{15}$$

Here A_1' is a constant to be determined by boundary conditions. Then from Maxwell's equations in K' one can get:

$$\vec{B}' = -A_1' \frac{2}{\gamma\left(\omega' + \beta c k_1'\right)} \left[\vec{a}_y k_1' \cosh\left(j k_1' x'\right)\right], \tag{16}$$

We take the dielectric constant and magnetic permeability of medium (I) as observed from K' equal to those of vacuum as they are when observed from K. The validity of this assumption is confirmed by the structure of the left side of (3a). We need one last check though to be assured that (3a) is indeed the Lorentz transform of (1). This check is seeing that the current density vectors in K and K' transform as per (1) and (3a).

Using a second subscript r for the reflected portion of corresponding vector, in K' the reflected current density vector will have the component;

$$J_{zr}' = j\omega' \left[\frac{b^2}{\omega'^2} \frac{\bar{b}}{\bar{b} + i\bar{\delta}}\right] \varepsilon_0 E_{zr}', \tag{17}$$

since $J_{zr}' = \sigma' E_{zr}'$ where $\sigma' = -j\omega'(\varepsilon' - \varepsilon_0)$. Here ε' is the permittivity of medium (I) observed from K' and it is equal to $\varepsilon_0 - \frac{b^2}{\omega'^2} \frac{\bar{b}}{\bar{b}+j\bar{\delta}} \varepsilon_0$ as per (3a).

To control if this current density vector (17) agrees with the one obtained from the Lorentz transformation of the corresponding vector in K, note that $\vec{J}_{zr} = \sigma E_{zr} \vec{a}_z = -j\omega_r(\varepsilon - \varepsilon_0) A_2' \vec{a}_z = -j\omega_r \frac{b^2 \varepsilon_0}{\omega_r^2 - \omega_0^2 + 2j\delta\omega_r} A_2' \vec{a}_z$. ($\vec{a}_z$ is the unit vector along the Oz axis.) But by virtue of Equations (24), (25) and (31) of [3], $\vec{J}_{zr} = jb^2 \frac{A_2'}{\omega_r} \frac{\bar{b}\varepsilon_0}{\bar{b}+j\bar{\delta}} = \vec{J}_{zr}'$ can be seen. This is true because the velocity boost is along Ox and $\vec{E}$ and $\vec{E}'$ have only $\vec{a}_z$ components and so do $\vec{J}$ and $\vec{J}'$. This is a confirmation of (3a) as the Lorentz transformation of the dispersion relation (1) when written for the reflected wave from K to K'.

Because in K' also magnetic permeability is μ_0, from (16),

$$\vec{H}' = -A_1' \frac{2}{\mu_0 \gamma(\omega' + \beta c k_1')} \left[\vec{a}_y k_1' \cosh(j k_1' x')\right], \tag{18}$$

will follow.

For medium (I), if we set up the second Maxwell equation for the reflected wave observed from K', incorporating (15)–(18) in it, we will get:

$$\begin{aligned} &-j\, \vec{a}_x k_1' \times \left\{-A_1' \frac{1}{\mu_0 \gamma(\omega' + \beta c k_1')} \left[\vec{a}_y k_1' \exp(-j k_1' x')\right]\right\} \\ &= -\left\{ j\omega' A_1' \frac{\omega' \varepsilon_0}{\gamma\left(\omega' + \beta c k_1'\right)} - j\omega' \left[\frac{b^2}{\omega'^2} \frac{\bar{b}}{\bar{b} + j\bar{\delta}}\right] \varepsilon_0 A_1' \frac{\omega'}{\gamma(\omega' + \beta c k_1')} \right\} \exp(-j k_1' x') \vec{a}_z. \end{aligned} \tag{19}$$

Let us examine (19) under the limit $\omega' \to 0$. Even though, because of (3a), $\omega' \to 0$ implies $k_1' \to 0$ too, it is not possible to determine from (3a) which law ω' and k_1' obey while on their path to zero. For example k_1' can be proportional to ω' or $\sqrt{\omega'}$. In the former case ${k_1'}^2$ can be incorporated into $(\frac{\omega'}{c})^2$ on the left side of (3a) and both sides of (3a) would vanish satisfying the equality. In the latter case ${k_1'}^2$ can be incorporated into $-b^2 \frac{\gamma\omega'}{\gamma\omega' + j\delta}$ on the right side of (3a) and again both sides of (3a) would vanish satisfying the equality.

But only utilizing the fact that $k_1' \to 0$ follows from $\omega' \to 0$ due to (3a) which fact is not questionable, we shall obtain below the law k_1' and ω' obey when they tend to zero. It will be found that k_1' is proportional to ω' on their path to zero.

Recalling (21) of [3], we have:

$$\omega_i = \gamma\left(\omega' + vk_1'\right), \tag{20a}$$
$$\omega_r = \gamma\left(\omega' - vk_1'\right). \tag{20b}$$

Notice that when ω' approaches zero, ω_i and ω_r also tend to zero. If we use (20) in (24) and (25) of [3], under the limits of $\omega_i \to 0$, $\omega_r \to 0$ which by (20) are true when $\omega' \to 0$ and $k_1' \to 0$, we get:

$$\lim_{\omega_i \to 0}\left[{k_1'}^2 - \left(\frac{\omega'}{c}\right)^2\right] = \lim_{\substack{\omega' \to 0 \\ k_1' \to 0}}\left[{k_1'}^2 - \left(\frac{\omega'}{c}\right)^2\right] \cong -\lim_{\substack{\omega' \to 0 \\ k_1' \to 0}} \frac{b^2}{c^2}\frac{\gamma^2\left(\omega' + vk_1'\right)^2}{-\omega_0^2}, \tag{21a}$$

$$\lim_{\omega_r \to 0}\left[{k_1'}^2 - \left(\frac{\omega'}{c}\right)^2\right] = \lim_{\substack{\omega' \to 0 \\ k_1' \to 0}}\left[{k_1'}^2 - \left(\frac{\omega'}{c}\right)^2\right] \cong -\lim_{\substack{\omega' \to 0 \\ k_1' \to 0}} \frac{b^2}{c^2}\frac{\gamma^2\left(\omega' - vk_1'\right)^2}{-\omega_0^2}. \tag{21b}$$

Subtraction of (21b) from (21a) yields $\lim_{\substack{\omega' \to 0 \\ k_1' \to 0}} \omega' k_1' \cong 0$ which is consistent with the above finding that $\omega' \to 0$ implies $k_1' \to 0$ too. Addition of (21a) and (21b) on the other hand yields,

$$\lim_{\substack{\omega' \to 0 \\ k_1' \to 0}} {k_1'}^2 = \lim_{\substack{\omega' \to 0 \\ k_1' \to 0}} \left(\frac{\omega'}{c}\right)^2 \frac{\omega_0^2 + b^2\gamma^2}{\omega_0^2 - b^2\gamma^2\beta^2}, \tag{22}$$

which shows that when $\omega' \to 0$ then $k_1' \to 0$ at the *same* speed since k_1' is proportional to ω' on their path to zero.

Then through making use of this fact we observe that under the limit $\omega' \to 0$ and $k_1' \to 0$ the left hand side of (19) will vanish because its numerator is of the power of two of k_1', whereas its denominator is a sum of power one of k_1' and one of ω'. On the right hand side, the first term will vanish because its numerator is of the power of two of ω', whereas its denominator is a sum of power one of k_1' and one of ω'. The second term though will not vanish because its numerator is of power three of ω' and its denominator is the product of power two of ω' and a sum of power one of ω' and power one of k_1'.

Thus we have a case where the second of Maxwell's equation does not hold true.

In fact the above sequence of arguments is essentially the same as the corresponding one in [1]. There too we had to be cautious in deciding whether k' is proportional to $\sqrt{\omega'}$ and upon deriving that k' is proportional to ω' we were led to the mismatch of the two sides of Maxwell's second equation.

In order to deal with this inconsistency in Maxwell's equations, we must subtract a spatially and temporally constant term equal to

$$\lim_{\substack{\omega' \to o \\ k_1' \to 0}} -j\omega'\left[-\frac{b^2}{\omega'^2}\frac{\bar{b}}{\bar{b} + j\delta}\right]\varepsilon_0 A_1' \frac{\omega'}{\gamma\left(\omega' + \beta c k_1'\right)}\left[\exp\left(-jk_1' z'\right)\right]\vec{a}_z, \tag{23}$$

from the right hand side of the second Maxwell's equation written in time-space domains. As discussed in [1] in this example too this corresponds to a term equal to $\lim_{\substack{\omega' \to 0 \\ k' \to 0}} \vec{J}'$.

A similar development will hold true for the incident wave.

3. CONCLUSIONS

Two examples have been presented in a series of two papers [1] in which Maxwell's equations need a correction term. In both examples two relations exist between k' and ω', the wave number and frequency in the Galilean reference frame K' which is in uniform rectilinear motion with respect to frame K. This is possible because there are two waves; one incident and one reflected in K'. One of these relations dictates the law by which k' and ω' abide on their path to zero. The other one is an outcome of Maxwell's second equation in K'. This law when applied on this said equation yields an unbalance between the two sides of the equation under the limit $\omega' \to 0$ and $k' \to 0$. In the two examples presented a term equal to $\lim\limits_{\substack{\omega' \to 0 \\ k' \to 0}} \vec{J}'$ has to be subtracted to balance the two sides.

REFERENCES

1. Yener, N., "A correction term for Maxwell's equations transformed between Galilean reference systems (Part I)," *PIERS Proceedings*, Taipei, Taiwan, March 25–28, 2013.
2. Oughstun, K. E. and G. C. Sherman, "Propagation of electromagnetic pulses ina a linear dispersive medium with absorption (the Lorentz medium)," *J. Opt. Soc. of America B*, Vol. 5, No. 4, 817–849, 1988.
3. Yener, N., "Non-constancy of speed of light in vacuum for different Galilean reference systems in case of an impulsive plane wave," *PIERS Proceedings*, 1638–1643, Xi'an, China, March 22–26, 2010.
4. Jackson, J. D., *Classical Electrodynamics*, John Wiley & Sons, Inc., New York, 1975.

A Large Tuning Range Ring VCO in 180 nm CMOS

Xuemei Lei[1,2], **Zhigong Wang**[1], **Lianfeng Shen**[1], **and Keping Wang**[3]

[1]School of Information Science and Engineer, Southeast University
Sipailou 2, Nanjing 210096, China
[2]College of Electronic Information Engineering, Inner Mongolia University
Daxuexilu, Hohhot 010010, China
[3]University of Washington, USA

Abstract— The phase noise requirements is decreased in some applications of short-range communication, data rates are low, and the channel spacing wide. This make a voltage-controlled ring oscillator is widely applied which need smaller chip area and larger tuning range. In the other hand the low supply voltage is trend of the electronic communications. Thus a large tuning range ring VCO base on a different cascade voltage logic delay cell is presented, which is suitable for low supply voltage. The delay cell is composed of a differential pair of NMOS transistors with a cross coupled load PMOS transistors, along with two PMOS transistors who change the current of output node. A new typical structure is suit for low supply voltage with large tuning range and less transistors. In SMIC 180-nm CMOS process, simulation results show the maximum oscillator frequency of the ring VCO is 6.9 GHz and the tuning range is from 75 MHz to 6.9 GHz with a worse phase noise level of 101.1 dBc/Hz at an offset of 10 MHz. Its maximum average power consumption is 5.18 mA from 1.8 V power supply and the minimum average power consumption is 0.10 mA from 0.7 V power supply. The core area is 50 μm × 35 μm in a 180-nm CMOS process.

1. INTRODUCTION

The VCO is a critical and essential component in modern wireless communication systems. CMOS VCOs with low power consumption, low phase noise, and wide tuning range, is demanded in the multi-standard wireless communication systems. The LC VCOs typically result in low phase noise along with a relatively small tuning range [1]. The small tuning range of the LC VCO results in the requirement for multiple VCOs with different center frequencies to cover a broadband system. And large layout area is need. At the same time, it is difficult to obtain a large quality factor of the inductor for most digital CMOS processes. Therefore, some extra processing steps may be required to assure good phase noise performance.

On the other hand the ring oscillator based VCOs typically exhibit a wide tuning range with low power and small layout areas, but with relatively poor phase noise [2]. But the phase noise requirements is decreased in some applications of short-range communication, data rates are low, and the channel spacing wide [3, 4]. This make a voltage-controlled ring oscillator is widely applied which needs smaller chip area and has a larger tuning range than the LC oscillator.

In this paper, a monolithic Ring VCO base on a different cascade voltage logic (DCVL) delay cell was developed. It employs a couple of PMOS to control the tuning range. At the same time the rail to rail voltage swing reduces the phase noise a little. The following part of the paper will show how the vco works. The Section 2 shows the delay cell design. Section 3 describe layout and the simulation results are also presented. Some final conclusions are presented in Section 5.

2. CIRCUITS DESIGN

Figure 1 show the circuit presented in [5]. The delay cell is composed of a differential pair of MN1 and MN2 with a cross coupled load (MP1 and MP2), along with two PMOS diode-connected devices (MP4 and MP5) whose current are controlled by another PMOS device (MP3). The ring VCO is composed of two delay cell. The operation of the cell can be described as follows: by changing the control voltage (Ctr) on the gate of MP3, the charge up current of the delay cell output load is changed. Therefore its delay time and thus the frequency of the whole VCO are controlled. The current of the diode connected devices (MP4 and MP5) is provided by MP3. They will always be in the saturation region and consume power more than MP3.

The circuit implement of proposed ring VCO are shown in Figure 2. Compare to Figure 1(a), the proposal delay cell change the charge up or down current of the delay cell output load by changing the control voltage (Ctr) on the gate of MP4 and MP5 instead of MP3. Thus, the delay cell is more suitable for low power application. And there delay cells is need to obtain large tuning range.

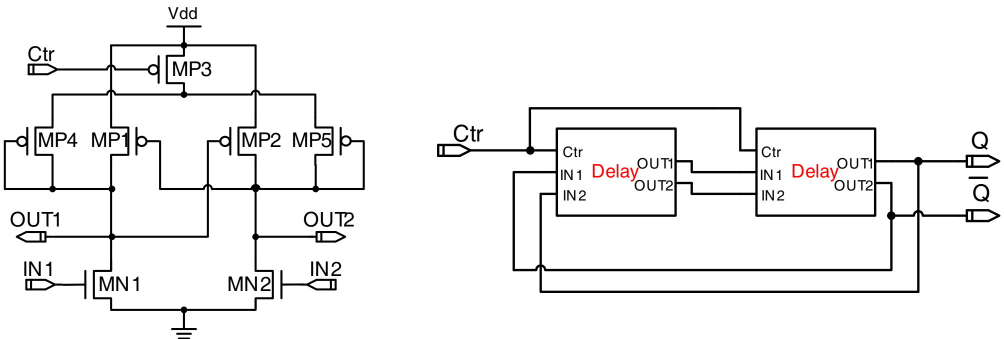

(a) delay cell (b) ring oscillator

Figure 1: Circuit implementation in [5]. (a) Delay cell and (b) ring oscillator.

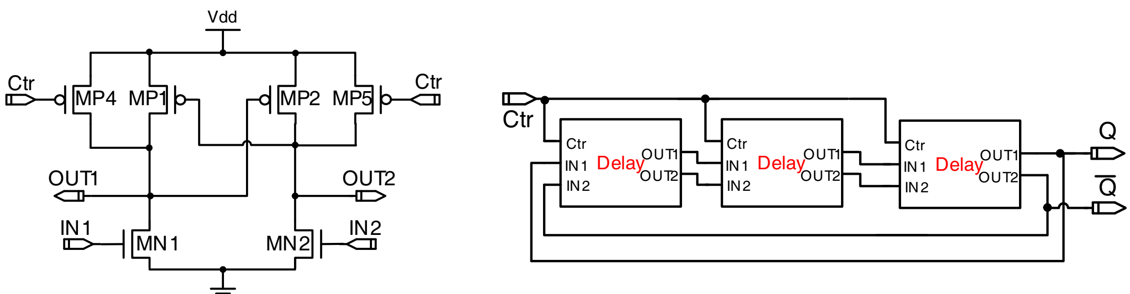

(a) delay cell (b) ring oscillator

Figure 2: Circuit implementation of the proposal ring VCO. (a) Delay cell and (b) ring oscillator.

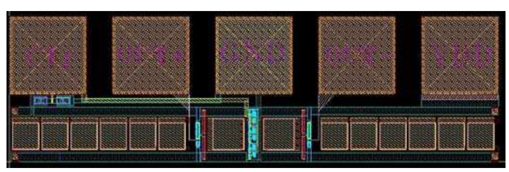

Figure 3: The layout of the proposed the proposal ring VCO.

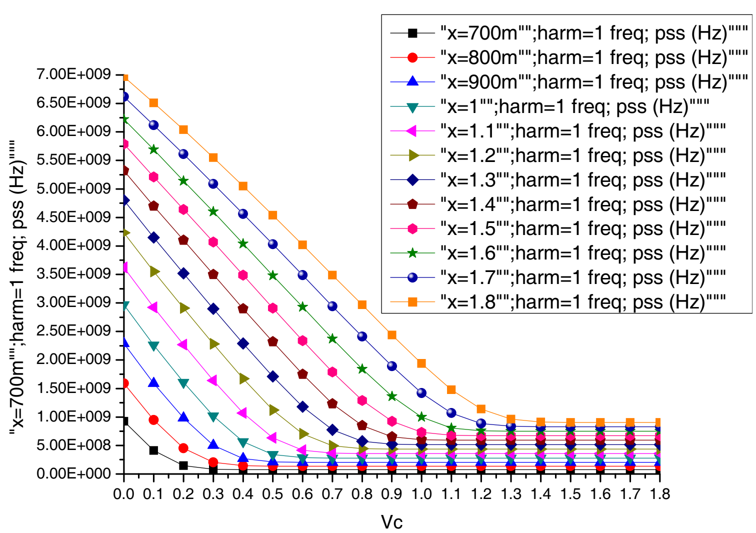

Figure 4: The simulated f-V curve of the proposed ring VCO.

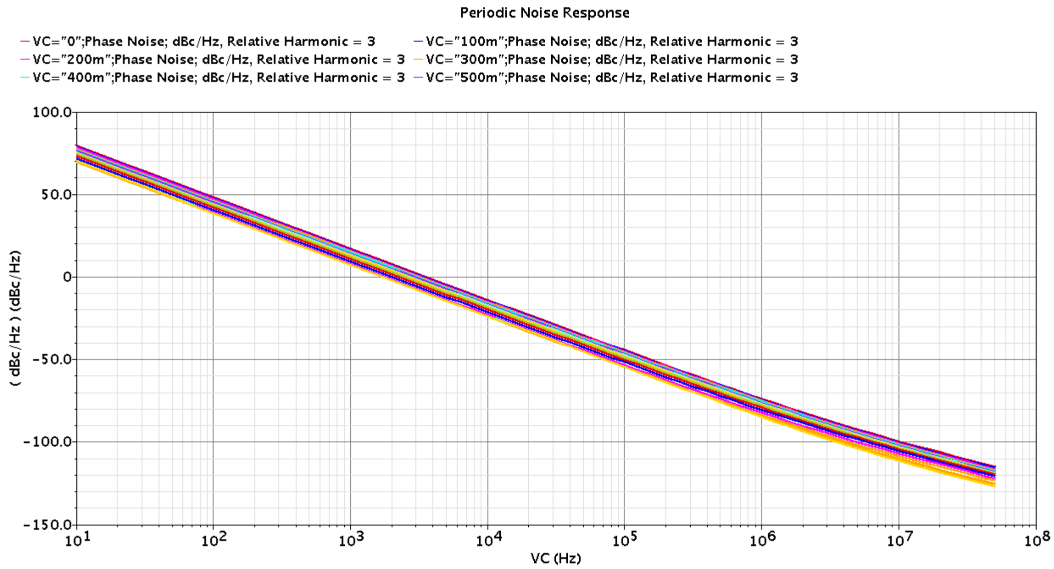

Figure 5: The simulated phase noise of the proposed ring VCO.

3. LAYOUT AND SIMULATION RESULTS

The proposed ring VCO is fabricated in SMIC 180-nm CMOS process. The layout of the ring VCO is showed in Fig. 3. The core area is 70 µm × 105 µm.

The ring VCO is simulated to operate with a frequency range from 75-MHz to 6.9-GHz while consuming a maximum power of 9.32 mW. Fig. 4 shows the simulated f-V curve of the proposed ring VCO. The oscillation frequency is change by the power supply and controlled voltage. The maximum oscillation frequency is with the largest power supply and lowest controlled voltage, and the minimum oscillation frequency is with the lowest power supply.

Figure 4 shows the simulated results of phase noise of the proposed ring VCO. The phase noise is change by the controlled voltage at the same offset. The phase noise becomes better when the controlled voltage is higher.

In SMIC 180-nm CMOS process, simulation results show the maximum oscillator frequency of the ring VCO is 6.9 GHz and the tuning range is from 75 MHz to 6.9 GHz with a worse phase noise level of 101.1 dBc/Hz at an offset of 10 MHz.

ACKNOWLEDGMENT

The authors gratefully acknowledge help and support from Li Zhang in design.

REFERENCES

1. Li, Z. and K. K. O, "A low-phase-noise and low-power multiband CMOS voltage-controlled oscillator," *IEEE Journal of Solid State Circuits*, Vol. 40, No. 6, 1296–1302, Jun. 2005.
2. Berny, A. D., A. M. Niknejad, and R. G. Meyer, "A 1.8 GHz LC VCO with 1.3 GHz tuning range and digital amplitude calibration," *IEEE Journal of Solid State Circuits*, Vol. 40, No. 4, 909–917, Apr. 2005.
3. Sharaf, K. M., "A CMOS fractional-N frequency synthesizer for low-power RF applications," *IEEE MEKECON 2002*, May 2002.
4. Chen, M., K. H. Wang, D. Zhao, L. Dai, Z. Soe, and P. Rogers, "A CMOS bluetooth radio transceiver using a sliding-IF architecture," *IEEE Custm Integrated Circuits Conference*, Mar. 2003.
5. Shing, W., T. Yan, and H. C. Luong, "A 900-MHz CMOS low-phase-noise voltage-controlled ring oscillator," *IEEE Transactions on Circuits and Systems — II: Analog and Digital Signal Processing*, Vol. 48, No. 2, 216–222, Feb. 2001.

A Planar MIMO Antenna for Mobile Phones

Di Wu[1], **S. W. Cheung**[2], **T. I. Yuk**[2], **and X. L. Sun**[2]

[1]City University of Hong Kong, Hong Kong, China
[2]The University of Hong Kong, Hong Kong, China

Abstract— This paper presents a MIMO antenna using planar technology for mobile phone applications in the next generation. The antenna is composed of two identical monopoles printed on the ground plane of a one-sided printed-circuit board (PCB). A parasitic element is used in each monopole to increase the operating bandwidth. Simulation results show that the antenna can be used to cover the UMTS-2100 systems. By cutting two slits on the ground plane, isolation between the two monopoles can be greatly enhanced for the frequency band. The MIMO antenna has a planar structure, so it is low profile with low cost for mobile phone applications.

1. INTRODUCTION

Multiple-input multiple-output (MIMO) system that utilizes multiple antennas to increase channel capacity without sacrificing additional spectrum or transmitted power has received a growing amount of interest in recent years. MIMO antenna technology can provide higher receiver gain, increased data rates, larger network throughput, and improved reliability through antenna diversity. However, to achieve these advantages, the MIMO antenna is required to have low mutual coupling between closely packed antenna elements, which is quite difficult to realize using the limited spaces of the handsets. Recently, there have been efforts on research in attempts to reduce the mutual coupling between elements in MIMO antennas [1–5]. However, most of these MIMO antennas are not designed for the mobile phone application, or could not be mass production.

In this paper, a MIMO antenna designed using planar technology for use in mobile phones is presented. The MIMO antenna is composed of two monopoles printed at the bottom of the mobile-phone ground plane. Two slits are cut on the PCB ground to reduce the mutual coupling and increase the isolation between the two elements. The EM simulation tool, CST, is used to study and design the MIMO antenna. Simulation results illustrate that the proposed planar MIMO antenna can be used to cover the UMTS-2100 system. A stub and two slits are used to increase the isolation between the two elements.

2. ANTENNA DESIGN

The geometry of the proposed MIMO antenna for mobile phone applications is shown in Fig. 1. The antenna was designed on a FR4 substrate with a dielectric constant of $\varepsilon_r = 4.4$, a loss tangent of 0.025 and a thickness of 0.8 mm. The antenna consisted of two planar L-shaped monopole elements and a ground plane all printed on one side of the substrate to achieve a good diversity performance and lower correlation coefficient [6]. The radiator occupied a total area of $14 \times 21\,\mathrm{mm}^2$. The two planar L-shaped monopole elements, monopoles #1 and #2 as shown in Fig. 1, were mirror images of each other on the substrate, hence complementing the radiation patterns of each other. Two

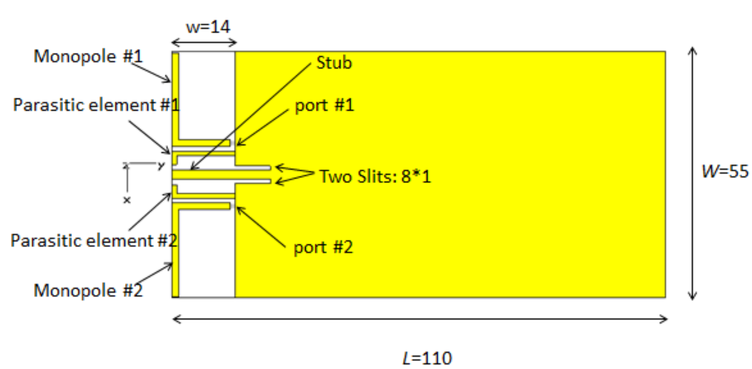

Figure 1: Geometry of proposed MIMO antenna.

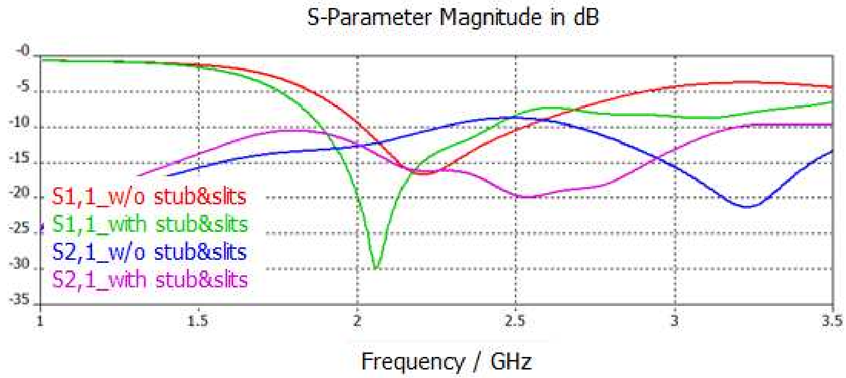

Figure 2: Simulated S parameters.

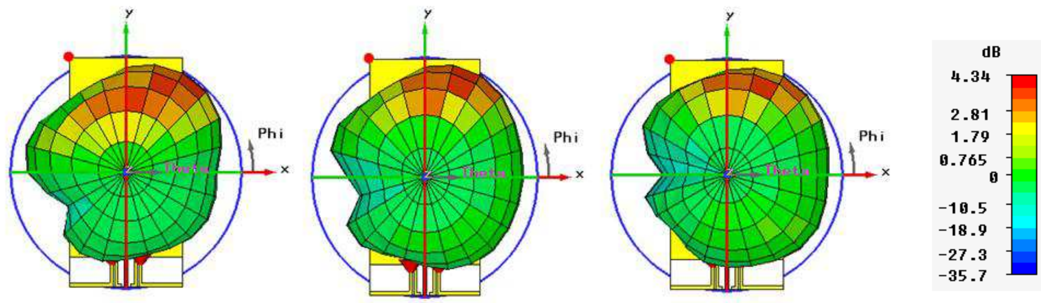

(a) 1.9 GHz (b) 2.4 GHz (c) 2.7 GHz

Figure 3: Simulated 3D-radiation pattern with port #1 excited.

symmetrical and identical L-shaped parasitic elements, parasites elements #1 and #2 as shown in Fig. 1, were placed near to the two monopole elements to widen the bandwidth. A ground stub was used to enhance the isolation between the two monopole elements. In order to achieve better isolation between the two monopole elements, two identical slits were cut on the ground plane. The length of the slit was quite critical to the performance. Computer simulation using the EM software CST was used for optimization of the slit and results showed the optimized dimension for the slit is $8 \times 1\,\mathrm{mm}^2$.

3. SIMULATION RESULTS

The proposed MIMO antenna was studied, designed and optimized using the EM simulation software CST. The simulated S parameters are shown in Fig. 2. Since the two monopole elements were identical and placed symmetrically to each other on the FR4 substrate, $S_{11} = S_{22}$ and also $S_{12} = S_{21}$. Thus we only show the results for S_{11} and S_{21} in Fig. 2. Without using the two ground stubs and slits, Fig. 2 shows that the MIMO antenna had an impedance bandwidth ($S_{11} < -10\,\mathrm{dB}$) of 1.9–2.4 GHz. The isolation (S_{21}) between the two input ports was only about $-8\,\mathrm{dB}$ from 2.3–2.4 GHz. However, with the uses of the ground stubs and slits, the antenna had an impedance bandwidth of 1.9–2.4 GHz which could be used to cover the UMTS-2100 system. The isolation between the two input ports in this bandwidth was also increased to more than $-15\,\mathrm{dB}$, which was also sufficient for MIMO operation.

Figures 3 and 4 show the simulated 3D-radiation patterns of the MIMO antenna when ports #1 or #2, respectively, was excited, at 1.9, 2.4 and 2.7 GHz. In simulation, when an input port was excited, the other port was terminated with a 50-Ω load. It can be seen in Figs. 3 and 4 that, by placing the monopole elements with mirror images of each other on the substrate, the antenna had different radiation patterns when either of the two ports was excited. The 3D-radiation patterns of each monopole element were complementary to each other. Hence, the MIMO antenna could be used for pattern diversity to overcome multipath fading in the wireless channels.

The simulated gains and efficiencies of the monopole elements are shown in Fig. 5. Because the two monopole elements were identical and placed symmetrically to each other on the substrate, the two monopoles should have the same gain and efficiency. Thus here again we only show the

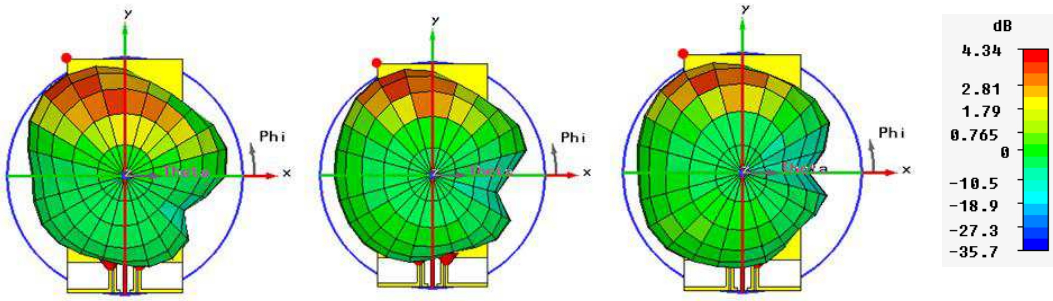

(a) 1.9 GHz (b) 2.4 GHz (c) 2.7 GHz

Figure 4: Simulated 3D-radiation pattern with port #2 excited.

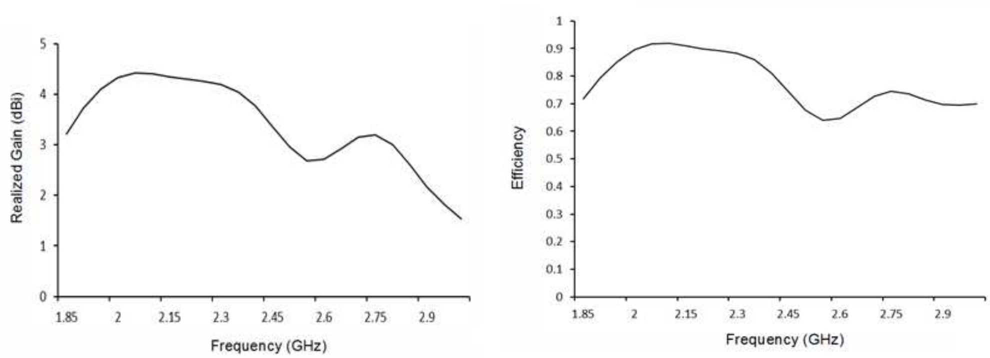

(a) (b)

Figure 5: (a) Realized gain and (b) efficiency of MIMO antenna with port #1 excited.

results when port #1 was excited. It can be seen in Fig. 5 that the antenna had the gain ranging from 4.1–4.4 dBi, with efficiency ranging from 85%–92% across the operating frequency band from 1.95–2.17 GHz.

4. CONCLUSION

A printed MIMO antenna consisted of two monopoles with parasitic elements was proposed in this paper. The antenna could be used for mobile terminals in the UMTS-2100 system. A stub and two slits cut on the ground plane were used to reduce the coupling and increase the isolation of the two elements. Results showed that the isolation of the proposed MIMO with stub and slits on the PCB ground was better than -15 dB in the operating frequency band.

REFERENCES

1. OuYang, J., F. Yang, and Z. M. Wang, "Reducing mutual coupling of closely spaced microstrip MIMO antennas for WLAN application," *IEEE Antennas and Wireless Propagation Letters*, Vol. 10, 2011.
2. Chung, K. and J. H. Yoon, "Integrated MIMO antenna with high isolation characteristic," *Electronics Letters*, Vol. 43, No. 4, 199–201, 2007.
3. Chiu, C. Y., C. H. Cheng, R. D. Murch, and C. R. Rowell, "Re-duction of mutual coupling between closely-packed antenna elements," *IEEE Transactions on Antennas and Propagation*, Vol. 55, No. 6, 1732–1738, 2007.
4. Minz, L. and R. Garg, "Reduction of mutual coupling between closely spaced PIFAs," *Electronics Lett.*, Vol. 46, No. 6, 392–394, Mar. 2010.
5. Diallo, A., C. Luxey, P. Le Thuc, R. Staraj, and G. Kossiavas, "Study and reduction of the mutual coupling between two mobile phone PIFAs operating in the DCS1800 and UMTS bands," *IEEE Transactions on Antennas and Propagation*, Vol. 54, No. 11, 3063–3074, Nov. 2006.
6. Ding, Y., Z. Du, K. Gong, and Z. Feng, "A novel dual-band printed diversity antenna for mobile terminals," *IEEE Transactions on Antennas and Propagation*, Vol. 55, 2088–2096, 2007.

CPW-coupled-fed Circular UWB Monopole Antenna

J. Zhang, S. W. Cheung, and T. I. Yuk
Department of Electrical and Electronic Engineering
The University of Hong Kong, Hong Kong, China

Abstract— In this paper, a coupled-fed monopole antenna with co-planar-waveguide (CPW) is proposed for ultrawide band (UWB) applications. The antenna is composed of a CPW feed line terminated with a trapezium patch on one side of the substrate and a radiator with a circular segment shape on the other side. With such configuration, there are many parameters such as the dimensions in the radiator, patch and feed line which can be used to optimize the design. Computer simulation is used to study the antenna and results show that the antenna has a large impedance bandwidth covering the frequency band from 2.7 to 11.4 GHz with return loss larger than 10 dB. The return loss, radiation pattern, peak gain, efficiency of the antenna are studied using computer simulation.

1. INTRODUCTION

Since the unlicensed frequency band from 3.1–10.6 GHz was released by the Federal Communications Commission (FCC) for unlicensed uses and low power applications in 2002 [1], ultrawide band (UWB) systems have received much attention. To design an UWB antenna for wireless devices is quite challenging because it has to satisfy the requirements such as wide impedance bandwidth, omnidirectional radiation pattern, constant gain, high radiation efficiency, constant group delay, low profile and easy manufacturing [2].

Monopole is a good candidate for the design of UWB antennas. Different radiator shapes, such as triangle, square, pentagon, hexagon, circle, ellipse, and ring [3–6] and various feeding structures such as microstrip [7, 8], co-planar-waveguide (CPW) [9] and coaxial [10] have been proposed for the designs of UWB monopole antennas.

In this paper, a monopole antenna with CPW-coupled-fed is proposed for UWB applications. This is an improved design with a smaller size compared with the design in [11–13] which used elliptical radiator. In the proposed antenna, the CPW feed line is terminated with a trapezium patch on one side of the substrate and a radiator with a circular segment shape on the other side. With such configuration, the dimensions in the radiator, the coupling patch and also the feed line can all be used to optimize the antenna. This gives the designers many choices to achieve the final design.

2. ANTENNA DESIGN

The configuration of the proposed antenna for studies is shown in Fig. 1, which was composed of a feeding structure on one side of the substrate and a radiator on the other side. The antenna was designed on a Rogers substrate, RO4350, with an area of $38 \times 30\,\mathrm{mm}^2$, a relative dielectric constant of 3.5, a thickness of 0.8 mm and a loss tangent of 0.003. The radiator had a simple circle-segment shape with radius of r and the distance from the chord to the centre of d. The feeding structure was a CPW terminated with a trapezium patch with a topline of w_3, a baseline of w_2 and a height of h, as shown in Fig. 1. The trapezium patch was used to couple the signal from the CPW to the radiator on the other side of the substrate. The width of the CPW feed line tapered from w_1 to w_2 for achieving good impedance match. The antenna was simulated and optimized in terms of large impendence bandwidth and good impedance matching performances. The optimized dimensions of the proposed antenna are listed in Table 1.

To better understand how different dimensions of the antenna affected the lower and higher cutoff frequencies of the antenna, a parametric study was carried out using computer simulation. Results showed that different dimensions had different effects. However, we could identify some dimensions which had significant effects on the lower and higher cutoff frequencies. This is briefly described as follows.

Simulation showed that the lower cutoff frequency of the antenna was mainly determined by the size of the radiator, i.e., the radius r of circular segment shape for the radiator. To illustrate this, we fixed the other dimensions of the antenna using the values listed in Table 1 and studied the effects of r on the bandwidth. The simulated return losses with different values of r are shown

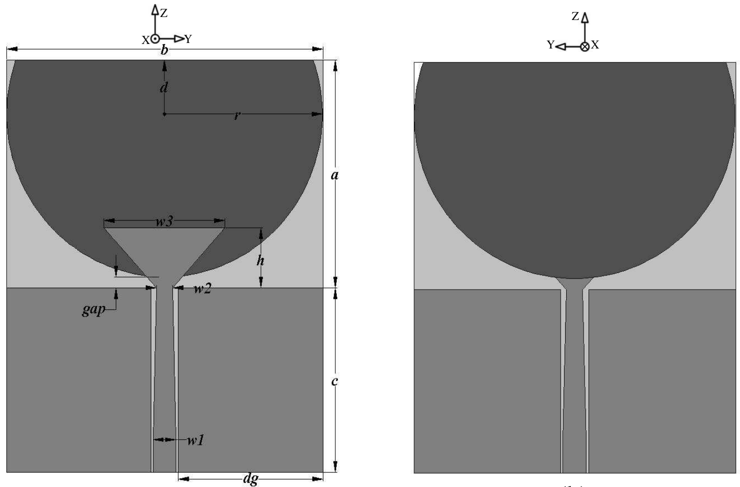

Figure 1: Configuration of proposed UWB antenna. (a) Top view. (b) Bottom view.

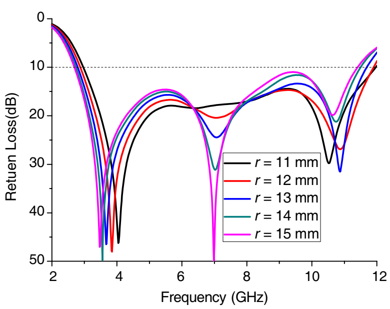

Figure 2: Simulated return loss with different values of r.

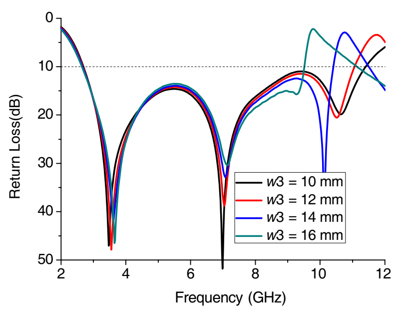

Figure 3: Simulated return loss with different values of w_3.

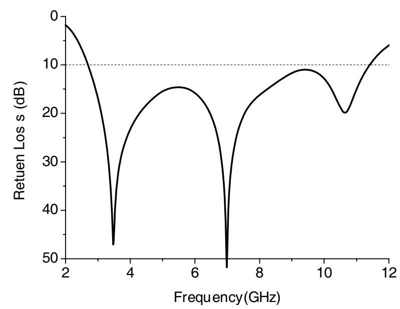

Figure 4: Simulated return loss of antenna.

Table 1: Dimensions of proposed antenna (mm).

r	d	w_1	w_2	w_3	h	gap	a	b	c	dg
18	5	2.2	1.5	10	5.5	1	21	30	17	1

in Fig. 2. It can be seen that the lower cutoff frequency was inversely proportional to the length r. Although it also shifted the high cutoff frequency down, another dimension, e.g., the length of the topline used in the patch, could be used to shift it up. Figure 3 shows the effect of w_3 on the higher cutoff frequency. Here again, the other dimensions of the antenna were fixed using the values in Table 1. It can be seen that the higher cutoff frequency was inversely proportional to w_3. Note that changing w_3 would not affect the lower cutoff frequency of the antenna.

3. RESULTS AND DISSCUSSIONS

With the use of the dimensions shown in Table 1, the simulated return loss of the antenna is shown in Fig. 4. It can be seen that, with return loss > 10 dB, the simulated impedance bandwidth was from 2.7 to 11.4 GHz, which was larger than the required UWB from 3.1–10.6 GHz.

The simulated radiation patterns of the antenna in the x-y, y-z planes at 3.0, 5.0, 8.0 and 10.0 GHz are shown in Fig. 5. At lower frequencies of 3, 5 and 8 GHz, the radiator patterns were quite omnidirectional in the x-y plane and had "dumb-bell" shape in the y-z plane, typical for monopole antennas. At the higher frequency of 10 GHz, fluctuations occurred in the radiation patterns, which were caused by the higher operation modes. The simulated peak gain and efficiency of the antenna are shown in Figs. 6 and 7, respectively. It can be seen in Fig. 6 that proposed antenna had a maximum peak gain of 5.3 dBi at the frequency of 10.3 GHz. The efficiency of the antenna within the pass band (2.7–11.4 GHz) was between 89.4% and 98.4% as can be seen in Fig. 7.

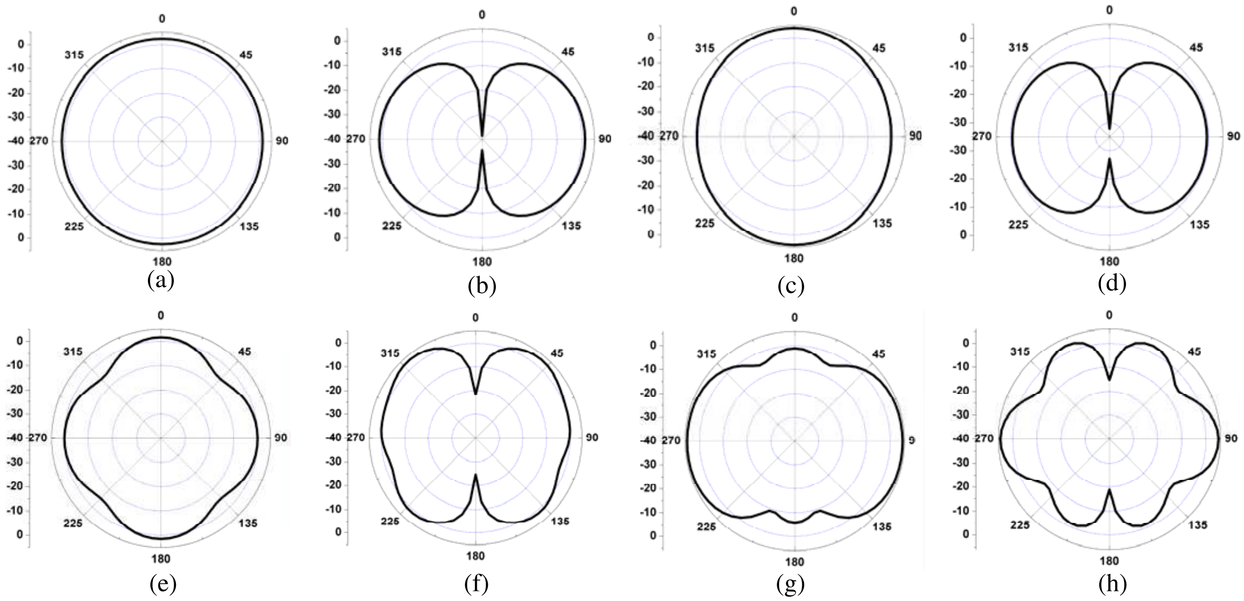

Figure 5: Simulated radiation patterns: (a) 3 GHz in x-y plane; (b) 3 GHz in y-z plane; (c) 5 GHz in x-y plane; (d) 5 GHz in y-z plane; (e) 8 GHz in x-y plane; (f) 8 GHz in y-z plane; (g) 10 GHz in x-y plane; (h) 10 GHz in y-z plane.

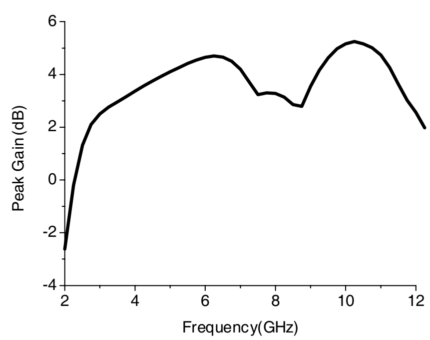

Figure 6: Simulated peak gains of antenna.

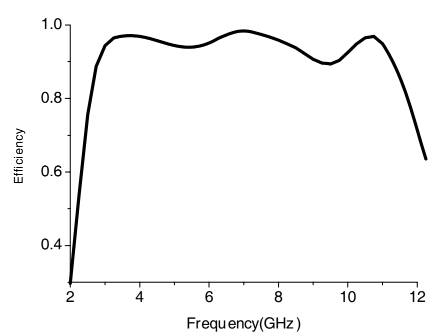

Figure 7: Simulated efficiency of antenna.

4. CONCLUSIONS

A simple monopole antenna with CPW-coupled-fed has been presented for UWB applications. The configuration provides many choices for designers in the designs of UWB antennas. For illustration, the radius of the radiator and topline of the coupling patch have been used to adjust the lower and higher cutoff frequencies of the antenna. The performances in terms of return loss, radiation pattern, peak gain and efficiency, of the antenna have been studied using computer simulation. Results have shown that the antenna can achieve a wide impedance bandwidth from 2.7 to 11.4 GHz with efficiency between 89% and 98.4%.

REFERENCES

1. Federal Communications Commission, First Report and Order, "Revision of Part 15 of the commission's rules regarding ultra-wideband transmission systems," FCC 02-48, Apr. 2002.
2. Ghavami, M., L. B. Michael, and R. Kohno, *Ultra Wideband Signals and Systems in Communication Engineering*, John Wiley and Sons, New York, USA, 2004.
3. Sun, Y. Y., S. W. Cheung, and T. I. Yuk, "Studies of planar antennas with different radiator shapes for ultra-wideband body-centric wireless communications," *PIERS Proceedings*, 1415–1419, Suzhou, China, Sep. 12–16, 2011.
4. Sun, Y. Y., S. W. Cheung, and T. I. Yuk, "Planar monopole ultra-wideband antennas with different radiator shapes for body-centric wireless networks" *PIERS Proceedings*, 839–843, Kuala Lumpur, Malaysia, Mar. 27–30, 2012.

5. Cheung, S. W., L. Liu, R. Azim, and M. T. Islam, "A compact circular-ring antenna for ultra-wideband applications" *Microwave and Optical Technology Letters*, Vol. 53, No. 10, 2283–2288, Oct. 2011.
6. Sun, Y. Y. M. T. Islam, S. W. Cheung, T. I. Yuk, R. Azim, and N. Misran, "Offset-fed UWB antenna with multi-slotted ground plane," *IEEE International Workshop on Antenna Technology (iWAT2011)*, 2011.
7. Liu, L., S. W. Cheung, and T. I. Yuk , "Bandwidth improvements using ground slots for compact UWB microstrip-fed antennas," *PIERS Proceedings*, 1420–1423, Suzhou, China, Sep. 12–16, 2011.
8. Weng, Y. F., S. W. Cheung, and T. I. Yuk, "Compact ultra-wideband antennas with single band-notched characteristic using simple ground stubs," *Microwave and Optical Technology Letters*, Vol. 53, No. 3, Mar. 2011.
9. Lee, S. H., J. K. Parka, and J. N. Lee, "A novel CPW-fed ultra-wideband antenna design," *Microwave and Optical Technology Letters*, Vol. 44, No. 5, Mar. 2005.
10. Zhang, Z. C., C. J. Guo, J. Ding, and Y. Su, "A novel printed UWB monopole antenna fed by coaxial cable," *International Conference on Microwave and Millimeter Wave Technology*, 25–27, 2010.
11. Zhang, J., X. L. Sun, S. W. Cheung, and T. I. Yuk, "CPW-coupled-fed elliptical monopole antenna for UWB applications," *IEEE Radio Wireless Week 2012 (RWW2012)*, Santa Clara, CA, USA, 2012.
12. Zhang, J., S. W. Cheung, and T. I. Yuk, "CPW-coupled-fed elliptical monopole UWB antenna with dual-band notched characteristic," *PIERS Proceedings*, 823–827, Kuala Lumpur, Malaysia, Mar. 27–30, 2012.
13. Zhang, J., X. L. Sun, S. W. Cheung, and T. I. Yuk, "CPW-coupled-fed elliptical monopole UWB antenna with simple dual-band notch design for WLAN band," *2012 IEEE International Symposium on Antennas and Propagation (2012 IEEE AP-S)*, 2012.

A Compact Branch-line Directional Coupler Using Lumped-element CRLH TLs

Y. F. Wu, J. Zhang, and S. W. Cheung
Department of Electrical and Electronic Engineering
The University of Hong Kong, Hong Kong, China

Abstract— In this paper, the design of a compact branch-line directional coupler using lumped-element composite right/left-handed transmission line (CRLH TL) is presented. The compactness is achieved by replacing the -90° right-handed transmission lines (RH TL) in a conventional branch-line directional coupler with 90° CRLH TLs implemented using lumped elements. Computer simulation is used to study the performance of the coupler and results show that the coupler has a bandwidth from 0.96 to 0.99 GHz, with $|S_{11}|$ and $|S_{41}|$ lower than -15 dB, $|S_{21}|$ and $|S_{31}|$ close to -3 dB, and a phase difference of 90° between ports 2 and 3. For comparison, a conventional branch-line directional coupler implemented using the RH TL and working at the same center frequency is also designed. Simulation results show that the proposed coupler can achieve a size reduction of 82.8% compared with the conventional RH TL branch-line directional coupler.

1. INTRODUCTION

The concept of metamaterials, commonly known as left-handed (LH) materials, was first investigated by Veselago in 1968 [1]. Metamaterials have negative permittivities and permeabilities which are not commonly found in nature. Although the properties of LH materials promised for a wide range of novel applications and devices, LH materials did not attract much attention until it was found that the materials could be realized using a general transmission-line (TL) approach [2] and these TLs are known as LH TLs. A practical LH TL has the right-handed (RH) effects, so a LH material realized using TLs is called a composite right/left-handed transmission line (CRLH TL). Due to the unique dispersion characteristic, CRLH TL can be used to design many different microwave components such as filters, diplexers and antennas with compact sizes [3–5].

Couplers are utilized in a variety of circuits including modulators, balanced amplifiers, balanced mixer and phase shifters in RF communication systems [6]. Branch-line couplers are -3 dB couplers with a 90°-phase difference at the outputs of the through and coupled ports. A conventional branch-line directional coupler consists of four $\lambda/4$-transmission lines which are connected together in a square format and so occupies quite a large area on a printed-circuit board (PCB) for low operating frequency.

In this paper, a novel design for a compact branch-line directional coupler using CRLH TL unit cells is presented. The CRLH TL unit cells are implemented using lumped elements to replace the four $\lambda/4$-transmission lines of a conventional branch-line directional coupler. Computer studies show that the proposed design can significantly reduce the area of the coupler by 82.8% when compared with the conventional design.

2. CONVENTONAL BRANCH-LINE DIRECTIONAL COUPLER

Figure 1 shows a conventional 3 dB-branch-line directional coupler, which consists of four transmission lines in a square shape. The two horizontal transmission lines, known as the horizontal branch lines, have a characteristic impendence of 35.35 Ω, while the two vertical transmission lines, known as the vertical branch lines, have a characteristic impendence of 50 Ω. The four ports are designed to have a characteristic impendence of 50 Ω. These four transmission lines have a length of $\lambda/4$ long, resulting in a phase shift of 90° at the other ends. As a result, there will be no signal at port 4. The signal input to port 1 will be divided equally at ports 2 and 3 [7].

Table 1: Dimensions of proposed unit cell (mm).

L_1	W_1	W_2	L_2	gap
3	1.8	3	15	1

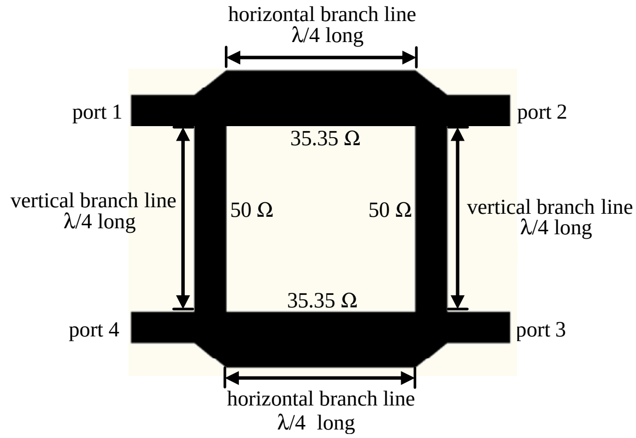

Figure 1: Conventional 3-dB branch-line directional coupler.

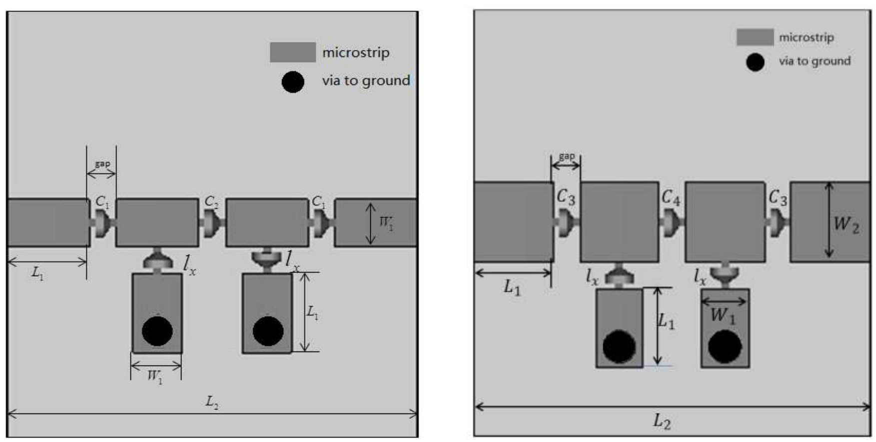

(a) (b)

Figure 2: Configurations of (a) 50-Ω vertical and (b) 35.35-Ω horizontal branch lines using lumped-element CRLH TL unit cells.

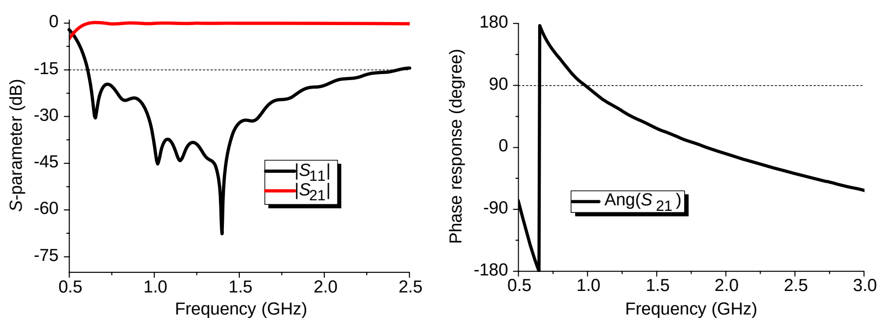

(a) (b)

Figure 3: Simulated (a) $|S_{11}|$ and $|S_{21}|$, and (b) phase response of 50-Ω vertical branch line.

3. BRANCH LINE DESIGN

In a conventional branch-line directional coupler shown in Figure 1, since the branch lines need to be $\lambda/4$ long, the overall size of the coupler will be quite large for low operating frequency. Here we propose to use CRLH TL unit cells implemented using lumped elements to replace these branch lines. The CRLH TL unit cells used to replace the 50-Ω vertical branch line and 35.35-Ω horizontal branch line in the conventional branch-line directional coupler of Figure 1 are shown in Figures 2(a) and 2(b), respectively [8, 9], where the stubs were connected to the ground plane on the other side of the substrate using vias. For illustration, we designed a coupler to operate at the frequency of around 1 GHz. Computer simulation was used to obtain dimensions of the

CRLH TL unit cells for the required phase shifts and impedance. The 50-Ω vertical branch line was designed on a Rogers substrate, RO4350B, with a relative dielectric constant of 3.5, thickness

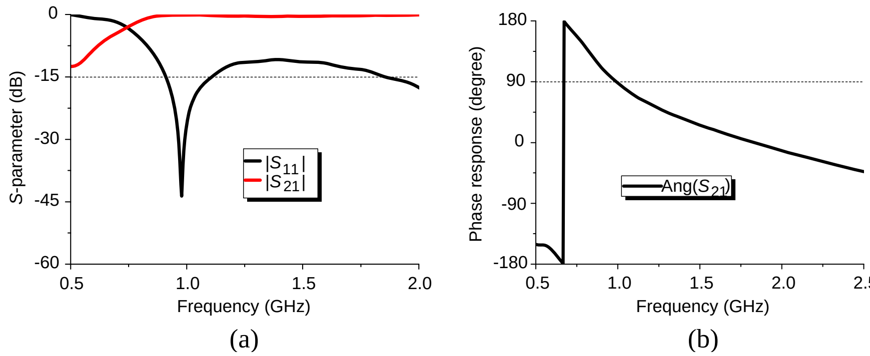

Figure 4: Simulated (a) $|S_{11}|$ and $|S_{21}|$, and (b) phase response of 35.35-Ω horizontal branch line.

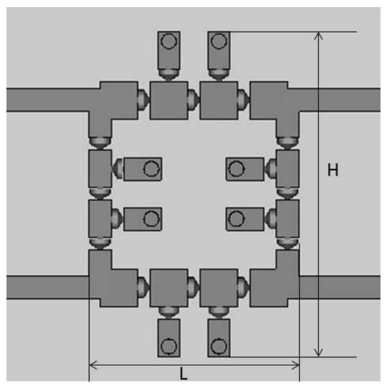

Figure 5: Proposed branch-line directional coupler.

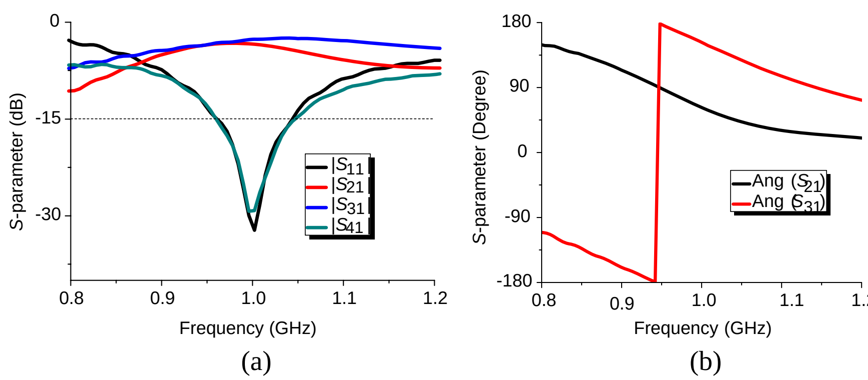

Figure 6: Simulated (a) S-parameter and (b) phase response of proposed branch line coupler.

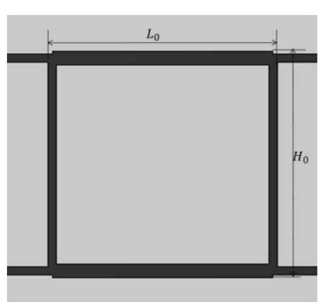

Figure 7: Configuration of conventional branch-line coupler.

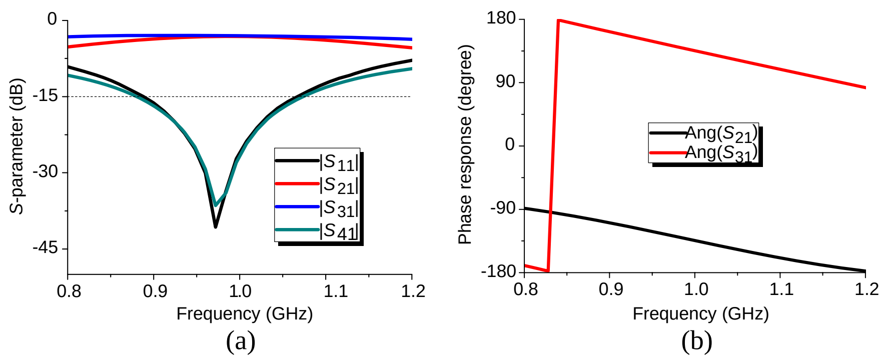

Figure 8: Simulated (a) $|S_{11}|$, $|S_{21}|$, $|S_{31}|$ and $|S_{41}|$, and (b) phase response of conventional branch line coupler.

of 0.8 and a loss tangent of 0.003. The detailed dimensions obtained for the 50-Ω vertical branch line shown in Figure 2(a) to have a phase shift of 90° and an impedance of $50\,\Omega$ at 0.98 GHz are listed in Table 1, with the required values for the components of $C_1 = 5.6\,\mathrm{pF}$, $C_2 = 3\,\mathrm{pF}$ and $L_x = 6.8\,\mathrm{nH}$. The simulated $|S_{11}|$ and $|S_{21}|$ are shown in Figure 3(a) and the simulated phase response is in Figure 3(b). It can be see that the branch line had a bandwidth from 0.6 to 2.4 GHz ($|S_{11}| < -15\,\mathrm{dB}$) and a phase shift of 90° at 0.98 GHz. Thus it can be used to design a branch-line directional coupler at 0.98 GHz. For the 35.35-Ω horizontal branch line shown in Figure 1, the width of the microstrip line needed to be increased from 1.8 to 3 mm in order to have an impedance of $50/\sqrt{2} = 35.35\,\Omega$. However, this change of dimension would alter operating frequency band of having the 90°-phase shift required in a branch-line coupler. To solve this problem, the values of the capacitors required to shift the operating frequency of having 90°-phase shift back to 0.98 GHz were obtained using computer simulation. Simulation showed that the required values for the components in the horizontal branch line were $C_3 = 3.6\,\mathrm{pF}$ and $C_4 = 10\,\mathrm{pF}$ and $L_x = 6.8$ nH. The simulated $|S_{11}|$, $|S_{21}|$ and phase response for the 35.35-Ω horizontal branch line are shown in Figure 4. Figure 4(a) shows that the horizontal branch line had a bandwidth ($|S_{11}| < -15\,\mathrm{dB}$) of 0.9–1.1 GHz and Figure 4(b) shows that the branch line had a phase shift of 90° at 0.98 GHz. Thus horizontal branch line satisfied the required characteristic to be used in a branch-line directional coupler. With the use of the 50-Ω vertical branch line and 35.35-Ω horizontal branch line shown in Figures 2(a) and 2(b), respectively, the branch-line directional coupler was designed as shown in Figure 5. The coupler had an area of $L \times H = 16.8 \times 26\,\mathrm{mm}^2 = 436.8\,\mathrm{mm}^2$. To save space, all stubs should be placed inside the square formed by the branches. However, to avoid the two stubs in the horizontal branches from touching each other, the stubs were placed outside the square.

4. RESULTS AND DISSCUSSIONS

The simulated S-parameter and phase response of the branch-line directional coupler are shown in Figure 6. It can be seen in Figure 6(a) that the impendence bandwidth of the coupler was about 30 MHz (0.96–0.99 GHz), with the $|S_{11}|$ and $|S_{41}|$ below $-15\,\mathrm{dB}$, and the $|S_{21}|$ and $|S_{31}|$ close to $-3\,\mathrm{dB}$. The phase difference between ports 2 and 3 was close to 90° as can be seen in Figure 6(b).

For comparison, a conventional branch-line directional coupler implemented using RL TLs and working at the same center frequency was also designed using computer simulation and the configuration is shown in Figure 7. The coupler occupied an area of $L_0 \times H_0 = 49.82 \times 50.98\,\mathrm{mm}^2 = 2539.8\,\mathrm{mm}^2$. The simulated S-parameter and phase response of the coupler are shown in Figure 8. It can be seen from Figure 8(a) that the coupler had a bandwidth of 140 MHz (0.92–1.06 GHz), with the $|S_{11}|$ and $|S_{41}|$ below $-15\,\mathrm{dB}$, the $|S_{21}|$ and $|S_{31}|$ close to $-3\,\mathrm{dB}$. Figure 8(b) shows that the phase difference between ports 2 and 3 was very close to 90°. Thus our proposed design occupied an area of only 17%, but had the bandwidth of about 21.1% of those of the conventional coupler.

5. CONCLUSION

A compact branch-line directional coupler using CRLH TL unit cells has been studied and designed using computer simulation. The CRLH TL unit cells are designed using lumped elements. For comparison, a conventional branch-line coupler implemented using transmission lines has also been designed and studied. Simulation results have shown that our proposed design can achieve an area reduction of 82% compared with a conventional branch-line coupler, but has a bandwidth of about

21% of it. So it is more suitable for narrowband operation.

REFERENCES

1. Veselago, V. G., "The electrodynamics of substances with simultaneously negative values of ϵ and μ," *Sov. Phys. Uspekhi*, Vol. 10, No. 4, 509–514, 1968.
2. Caloz, C., H. Okabe, T. Iwai, and T. Itoh, "Transmission line approach of left-handed (LH) materials," *Proc. USNC/URSI National Radio Science Meeting*, Vol. 1, 39, San Antonio, Texas, June 2002.
3. Byun, J., Y. I. Kwon, and H. Y. Lee, "Super compact UWB bandpass filter using unit-cell CRLH-TL based on via-pin capacitor," *European Microwave Conference, EuMC 2009*, 1389–1392, 2009.
4. Horii, Y., C. Caloz, and T. Itoh, "Super-compact multilayered left-handed transmission line and diplexer application," *IEEE Transactions on Microwave Theory and Techniques*, Vol. 53, No. 4, 1527–1534, 2005.
5. Lee, C.-J., K. M. K. H. Leong, and T. Itoh, "Composite right/left-handed transmission line based compact resonant antennas for RF module integration," *IEEE Transactions on Antennas and Propagation*, Vol. 54, No. 8, 2283–2291, 2006.
6. Lee, T. H., *Planar Microwave Engineering,* Cambridge University Press, UK, 2004
7. Fooks, E. H. and R. A. Zakarevicius, *Microwave Engineering Using Microstrip Circuits*, Prentice Hall, 1990.
8. Antoniades, M. A. and G. V. Eleftheriades, "A broadband Wilkinson balun using microstrip metamaterial lines," *IEEE Antennas Wireless Propag. Lett.*, Vol. 4, 209–212, 2005.
9. Tseng, C. H. and C. L. Chang, "A broadband quadrature power split-ter using metamaterial transmission line, *IEEE Microwave Wireless Compon Lett.* Vol. 18, 25–27, 2008.

Direction of Arrival Estimation Based on Maximum Likelihood Criteria Using Gravitational Search Algorithm

Ahmed Magdy, K. R. Mahmoud, S. G. Abdel-Gawad, and I. I. Ibrahim
Department of Electronics, Communications and Computers
Faculty of Engineering, Helwan University, Cairo, Egypt

Abstract— In this paper, a new heuristic optimization algorithm called Gravitational Search Algorithm (GSA) is proposed for Direction of Arrival (DOA) estimation method based on maximum likelihood (ML) criteria for a Uniform Circular Array (UCA) of 12 elements. The results are compared with those obtained using Particle Swarm Optimization (PSO) and MUSIC algorithms in terms of Root Mean Square Error (RMSE).

1. INTRODUCTION

In engineering applications, where an incoming wave is detected and/or measured by an antenna array, the associated signals at different points in space can be processed to extract various types of information including their direction of arrival (DOA). Algorithms for estimating the DOA in antenna arrays are often used in wireless communications to increase the capacity and throughput of a network [1]. DOA estimation is an important problem in many fields such as radar, sonar, radio, astronomy, under water surveillance and seismology to estimate the source location. One of the simplest versions of this problem is the estimation of the directions of arrivals (DOAs) of narrow-band sources where the sources are located in the far field of the sensor array [2, 3].

Previously, many high resolution suboptimal techniques have been proposed and analyzed such as signal parameters via rotational invariance technique (ESPRIT) [4] and multiple signal classification (MUSIC) which in some cases combined with special processor or with interference rejection [5, 6]. However, these techniques give better performance at high SNR only. DOA algorithms can be divided into three basic categories, namely, classical, subspace methods, and maximum likelihood (ML) techniques [7]. The ML method offers high performance due to its superior statistical performance compared to spectral based methods. The ML estimation is computed by maximizing the likelihood function or minimizing the negative likelihood function with respect to all unknown parameters, which may include the source DOA angles, the signal covariance, and the noise parameters. Generally, to obtain the exact ML (EML) solutions, the DOAs must be estimated by optimizing a complicated nonlinear multimodal function over a high-dimensional problem space.

There are different optimization techniques are considered in the previous literature to optimize the ML function [8–12]. In [8], a novel method to generate the optimum direction of arrival (DOA) estimation algorithm using genetic algorithm (GA) is proposed. In [9], an Alternating Projection (AP) ML optimization technique is presented for UCA. Particle swarm optimization had already used as a global optimization technique to estimate the DOA. In [10, 11], particle swarm optimization (PSO) provided better results than MUSIC and AP techniques. In [12] the ant colony optimization (ACO) is found to be able to provide similar performance to that of Multi Dimensional (MD)-MUSIC algorithm, while its computational cost is only 1/13 of MD-MUSIC algorithm. In [13], it is found that the ACO-MUSIC not only reduces the computational load greatly but also maintains the excellent performance of the original MUSIC. In [14], the exact maximum likelihood DOA Estimation using Bacteria Foraging Optimization (BFO) is proposed, it is found that the results obtained by BFO are more accurate than PSO in addition to achieving faster convergence.

Recently, Gravitational search algorithm (GSA) is considered as a new optimization technique based on the law of gravity and mass interaction [15]. A set of various standard benchmark functions were examined and in most cases the GSA provided superior or at least comparable results with Real Genetic Algorithm (RGA), PSO and CFO. In [16], a comparative performance of gravitational search algorithm and modified particle swarm optimization algorithm for synthesis of thinned scanned concentric ring array antenna is considered. It is found that, the GSA technique has better performance than the modified PSO algorithm in terms of computed final fitness values and computational time. In [17], a fully digital controlled reconfigurable concentric ring array antenna has been proposed using GSA. Results clearly showed a very good agreement between the desired and GSA synthesized pattern even with a 4-bit digital attenuator and a 5-bit digital phase shifter instead of a continuous phase shifter and an analog attenuator. In [18], GSA has been applied for the length and width calculations of the rectangular patch antenna under various resonant frequencies, substrate permittivity and thickness of the antenna.

In the DOA estimation, due to multimodal, nonlinear, and high-dimensional nature of the parameter space, the problem seems to be a good application area for GSA, by which the excellent performance of ML criteria can be fully explored. In this paper, the GSA optimization technique applied to ML criterion functions for accurate DOA estimation in Gaussian noise.

The paper is organized as follows. In Section 2, the signal model and estimation problem for EML and beamforming is explained. In Section 3, a brief description to the GSA algorithm is introduced. GSA based ML results and discussions are discussed in Section 4. Finally, Section 5 presents the conclusions.

2. SIGNAL MODEL AND ESTIMATION PROBLEM FOR MAXIMUM LIKELIHOOD AND BEAMFORMING

Data model for array is considered that, L narrowband sources from far fields in the directions of $\Theta = [\theta_1, \ldots, \theta_L]$ are impinging on the array consisting of N elements. The received signals are modeled as:

$$x(t) = A(\Theta)s(t) + n(t) \tag{1}$$

where $A(\Theta) = [a(\theta_1), \ldots, a(\theta_L)]$ is array manifold, $s(t) = [s_1(t), \ldots, s_L(t)]^T$ is the L source signals at time t, and $n(t)$ is the additive white Gaussian noise which is not correlated to the signals. A uniform circular array (UCA) is considered as shown in Figure 1.

The geometry consists of ($N = 12$) elements uniformly distributed with a ring radius $r = (6/2\pi)\lambda$. Where the distance between adjacent elements is $d = 0.5\lambda$, $\theta_0 = 2\pi/N$ is the angle between adjacent elements. θ is azimuth angle measured from the z-axis. The response of the nth sensor to the ith signal is given by:

$$a_n(\theta_i) = e^{j\Psi n(\theta_i)} \tag{2}$$

where Ψn is given by:

$$\Psi n = 2\pi r \cos(\theta - (n-1)\theta_0)/\lambda \tag{3}$$

and θ_i lies in $(-\pi, \pi)$.

Assuming that the signals $s(t)$ are deterministic and unknown sequence, the maximum likelihood estimation vector $\Theta = [\theta_1, \ldots, \theta_L]$ which called objective function in optimization technique of the DOA is given by [9]:

$$\theta = \arg \underbrace{\max}_{\theta} tr\{PA(\Theta)\hat{R}\} \tag{4}$$

where $PA(\Theta) = A(\Theta)(A(\Theta)^H A(\Theta))^{-1} A(\Theta)^H$ is the projection operator onto the space spanned based on the columns of the matrix $A(\Theta)$, $\hat{R} = (1/LD)\Sigma_{t=1}^{LD} X(t)X^H(t)$ is the sample covariance matrix and LD denotes the number of data snapshots.

3. GRAVITATIONAL SEARCH ALGORITHM OPTIMIZATION TECHNIQUE

Gravitational search algorithm (GSA) is a recently proposed method used on optimization problem based on the law of gravity and mass interaction [15]. The algorithm considers agents as objects

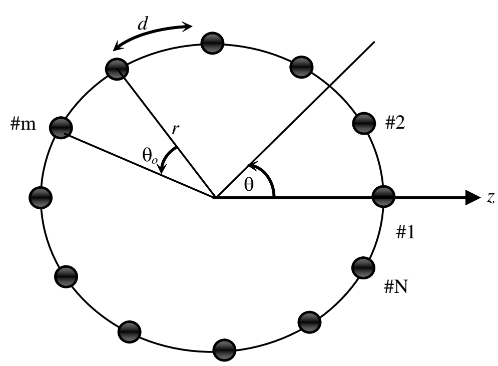

Figure 1: Geometry of the UCA with N elements.

consisting of different masses. Each agent in GSA is specified by four parameters: position of the mass in dth dimension, inertia mass, active gravitational mass and passive gravitational mass. The positions of the mass of an agent at specified dimensions represent a solution of the problem and the inertia mass of an agent reflect its resistance to make its movement slow. Both the gravitational mass and the inertial mass, which control the velocity of an agent in specified dimension, are computed by fitness evolution of the problem the positions of the agents in specified dimensions (solutions) are updated every iteration and the best fitness along with its corresponding agent is stored.

The first step in the GSA algorithm is to generate initial positions of the K number of agents randomly within the given search interval as below:

$$x_i = \left(x_i^1, \ldots, x_i^d, \ldots, x_i^k\right), \quad \text{for } i = 1, 2, \ldots, K \tag{5}$$

where, x_i^d represents the positions of the ith agent in the dth dimension and k is the space dimension. At each iteration, perform the fitness evolution for all agents and also compute the best and worst fitness defined as below (for minimization problems):

$$\text{best}\,(t) = \min_{j\epsilon\{1,\ldots,K\}} \text{fit}_j(t) \tag{6}$$

$$\text{worst}\,(t) = \max_{j\epsilon\{1,\ldots,K\}} \text{fit}_j(t) \tag{7}$$

where, $\text{fit}_j(t)$ represents the fitness of the jth agent at iteration t, $\text{best}(t)$ and $\text{worst}(t)$ represents the best and worst fitness at generation t. Compute gravitational constant G at iteration t using the following equation:

$$G\,(t) = G_0 e^{(\alpha t/T)} \tag{8}$$

In this problem G_0 is set to 100, α is set to 20 and T is the total number of iterations as considered in [15]. Then the mass of the agents (gravitational and inertia masses) can be calculated as:

$$M_{ai} = M_{pi} = M_{ii} = M_i; \quad i = 1, 2, \ldots, K$$

$$m_i\,(t) = \frac{\text{fit}_i\,(t) - \text{worst}_i(t)}{\text{best}\,(t) - \text{worst}(t)} \tag{9}$$

$$M_i\,(t) = \frac{m_i(t)}{\sum_{j=1}^{K} m_i(t)} \tag{10}$$

where, M_{ai} is the active gravitational mass of the ith agent, M_{pi} is the passive gravitational mass of the ith agent; M_{ii} is the inertia mass of the ith agent. Now, the accelerations of the ith agents at iteration t is calculated as below:

$$a_i^d(t) = \frac{F_i^d(t)}{M_{ii}(t)} \tag{11}$$

where, $F_i^d(t)$ is the total force acting on ith agent calculated as:

$$F_i^d\,(t) = \sum\nolimits_{i=1, j\neq 1} rand_j F_{ij}^d(t) \tag{12}$$

where $rand_j$ is a random number in the interval [0, 1]. $F_{ij}^d(t)$ is the force acting on agent 'i' from agent 'j' at dth dimension and tth iteration is computed as below:

$$F_{ij}^d\,(t) = G\,(t)\,\frac{M_{pi}(t)\,M_{aj}\,(t)}{R_{ij}\,(t) + \epsilon}\left(x_j^d\,(t) - x_i^d(t)\right) \tag{13}$$

where, $R_{ij}(t)$ is the Euclidian distance between two agents 'i' and 'j' at iteration t and $G(t)$ is the computed gravitational constant at the same iteration. ϵ is a small constant. Now, it is ready to compute the agents' velocity and position at next iteration $(t+1)$ using the following equation:

$$v_i^d\,(t+1) = rand_i v_i^d\,(t) + a_i^d\,(t) \tag{14}$$

$$x_i^d\,(t+1) = x_i^d\,(t) + v_i^d(t+1) \tag{15}$$

These steps will be repeated till the specified maximum iteration number is reached to terminate the optimization processes. To formulate the GSA algorithm for EML optimization to estimate source DOA's. Firstly, a population of agents is initialized in the search space with random positions and random velocities constrained between $-\pi$ and π in each dimension. The K dimensional position vector of the jth probe takes the form $\theta_j = [\theta_1, \ldots, \theta_L]$, where θ represents the DOAs. A probe position vector is converted to a candidate solution vector in the problem space through a suitable mapping. The score of the mapped vector evaluated by a likelihood function $f(ML)$ which is given above in (4) is regarded as the fitness of the corresponding agent. To evaluate the likelihood function $f(ML)$ required the data from all the elements of the array for LD number of snapshots ($LD = 1024$), are initialized for the optimization algorithm. By using algorithm agents with highest health will be obtained.

4. GSA-EML DOA ESTIMATION AND DISCUSSION RESULTS

Here we present a numerical example to demonstrate the performance of GSA based DOA estimation against PSO and MUSIC which is the best known and well investigated algorithm. The DOA estimation root-mean squared error (RMSE) is calculated as shown in Equation (5) to measure the performances of those methods.

$$RMSE = \sqrt{\frac{1}{L}\sum\nolimits_{l=1}^{L}\left(\hat{\theta}\left(l\right)-\theta\right)^2} \tag{16}$$

where L is the number of sources, $\hat{\theta}_n(l)$ is the estimate of the lth DOA achieved, θ is the true DOA of the lth source. The sources are equal power narrow-band emitters, and the noise is additive and uncorrelated from sensor to sensor and with the signals.

In beginning, the simulation introduces the MUSIC algorithm with power of incoming signal $P = 1$, variance of noise $N_0 = 1$, finally number of snapshots $LD = 1024$. Figures 2(a), (b), and (c) illustrate the DOA estimation RMSE values obtained using GSA-EML, PSO-EML, and MUSIC as a function of SNR for different number of sources. In Figure 2(a), a single signal impinging the array at 30°, however in Figure 2(b) three signals at −30°, 0°, and 30° are considered. It is clear that, as the number of impinging signals increase the RMSE decrease. For scenario #3, it is assumed that there are five signals impinging the array with small separation between them at 30°, 15°, 5°, 0°, and −30°. It is observed that as the SNR is increased, the performance of GSA algorithm is improved significantly, whereas the PSO algorithm show slightly changes at high SNR compared to the MUSIC which does not show any significant changes. In general, as can be seen from Figure 2, GSA-EML yields significantly superior performance over PSO-EML and MUSIC as a whole, by demonstrating lower DOA estimation RMSE. On the other hand, MUSIC produces less accurate estimates than PSO. Table 1 shows a comparison between the actual and estimated values of DOAs for the previous scenarios using GSA, PSO, and MUSIC. As can be seen only GSA can determine DOAs when number of sources increase as shown in final scenario. Figure 3 shows the relation between actual DOA and estimated DOA in the case of incoming signals from one, three, and five sources based on GSA technique. To validate the algorithm, a comparison between DOA estimation RMSE values of GSA-EML and previous published results [14] are illustrated in Figure 4. In this example, two uncorrelated sources impinge on 8-sensor UCA at 130° and 140° is considered with 1000 snapshots. It is shown that, the GSA-EML yields lower DOA estimation RMSE over other algorithms such as BFA, PSO, and MUSIC especially for SNR less than 0 dB.

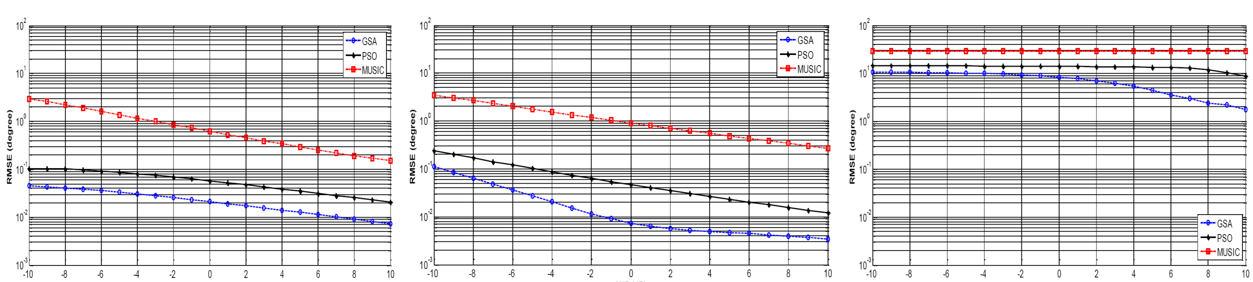

(a) Scenario #1 (b) Scenario #2 (c) Scenario #3

Figure 2: DOA estimation RMSE values of GSA-EML, PSO-EML, and MUSIC versus SNR.

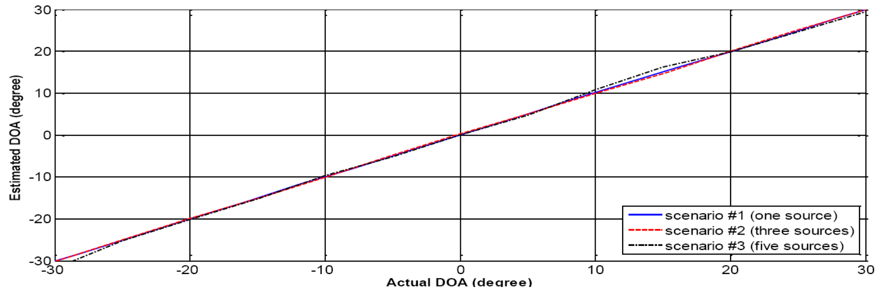

Figure 3: Comparison between actual and estimated DOA using GSA algorithm for different number of incoming signals.

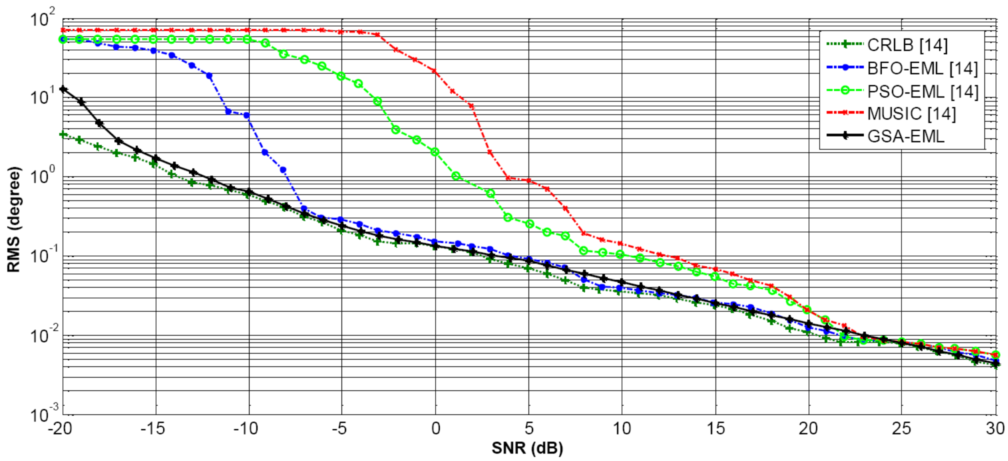

Figure 4: RMSE comparison between GSA-EML and previous published results [14].

Table 1: The comparison between the actual and estimated values of DOAs.

Scenario No.	Actual DOA	Estimated DOA		
		Music	PSO	GSA
Scenario #1	30°	29.8°	30.0487°	29.9948°
Scenario #2	30°	29.9°	30.0359°	29.9953°
	0°	0°	0.1183°	0.0715°
	−30°	−30.2°	−29.8313°	−30.1122°
Scenario #3	30°	29.2°	28.9888°	28.8962°
	15°	14°	13.1168°	14.6065°
	5°	Not detect	−19.5712°	2.7174°
	0°	1.5°	−0.6128°	−1.2915°
	−30°	−30°	−28.7704°	−29.6135°

The results are compared to Cramer-Rao Lower Bound (CRLB) which is the boundary of the DOA estimation RMSE. The GSA gives better performance than the PSO in terms of computed final fitness values and computational time where it required about 16 second for GSA to get the result compared to 58 second for PSO on a 32-bit Dell Vostro 1015 (Intel® Core™ 2 Duo CPU@ 2.1 GHz) 4G-RAM as shown in Table 1.

5. CONCLUSION

In this paper, GSA technique is proposed with UCA antenna system for enhancing the performance of DOA and adaptive beamforming in wireless communications. The technique is simple and appropriate for real time applications. Simulations of DOA estimation show accurate results even for a big set of simultaneously incident signals. Strategically pairing GSA with EML has the desired advantages over PSO based schemes and MUSIC. The GSA gives better performance than the PSO in terms of computed final fitness values and computational time.

REFERENCES

1. Akyildiz, I., W. Su, Y. S. Subramaniam, and E. Cayirci, "A survey on sensor networks," *IEEE Communications Magazine*, Vol. 40, No. 8, 102–114, Aug. 2002.
2. Foutz, J., A. Spanias, and M. K. Banavar, *Narrowband Direction of Arrival Estimation for Antenna Arrays*, Morgan & Claypool Publishers, 2008.
3. Ottersten, B., M. Viberg, P. Stoica, and A. Nehorai, "Exact and large sample ML techniques for parameter estimation and detection in array processing," *Radar Array Processing*, Simon Haykin, Ed., 99–152, Feb. 1993.
4. Roy, R. and T. Kailath, "ESPRIT-estimation of signal parameters via rotational invariance techniques," *IEEE Transactions on Acoustics, Speech and Signal Processing*, Vol. 37, No. 7, 984–995, Jul. 1989.
5. Eric, M. and B. Igric, "Practical implementation and performance estimation of MUSIC method implemented on signal processor TMS 320c30," *Scientific-technical Review*, Vol. LIV, No. 1, 2004.
6. Vesa, A., "Interference rejection in direction of arrival estimation using linear array antenna," *13th International Conference on Optimization of Electrical and Electronic Equipment (OPTIM)*, 1221–1225, 2012.
7. Stoica, P. and A. Nehorai, "Music, maximum likelihood and Cramer-Rao bound," *International Conference on in Acoustics, Speech, and Signal Processing*, Vol. 4, 2296–2299, Apr. 1988.
8. Karamalis, P. M., A. Kanatas, and A. Constantinou, "Direction of arrival estimation using genetic algorithm," *IEEE Vehicle Technology Conference (VTC 2001)*, 162–166, 2001.
9. Lee, J. H. and S. H. Jo, "On initialization of ML DOA cost function for UCA," *Progress In Electromagnetics Research M*, Vol. 3, 91–102, 2008.
10. Zeng, J., Z. He, and B. Liu, "Maximum likelihood DOA estimation using particle swarm optimization algorithm," *CIE International Conference on Radar*, 1–4, Oct. 16–19, 2006.
11. Panigrahi, T., A. D. Hanumantharao, G. Panda, B. Majhi, and B. Mulgrew, "Maximum likelihood DOA estimation in distributed wireless sensor network using adaptive particle swarm optimization," *International Conference on Communication, Computing* & *Security*, 134–137, 2011.
12. Jiao, Y., J. Huang, and Y. Hou, "Multidimensional MUSIC DOA estimation using ant colony optimization algorithm," *10th IEEE International Conference on Signal Processing (ICSP)*, 291–294, Oct. 24–28, 2010.
13. Yang, Y., Y. Hou, and X. Liu, "Two dimensional DOA estimation by ant colony optimization," *International Conference on Intelligent System Design and Engineering Application*, Vol. 2, 789–792, Oct. 13–14, 2010.
14. Hanumantharao, A. D., T. Panigrahi, U. K. Sahoo, G. Panda, and B. Suresh, "Exact maximum likelihood direction of arrival estimation using bacteria foraging optimization," *International Conference on Emerging Technologies (ICET 2011)*, 17–22, NIT Durgapur, Mar. 28–31, 2011.
15. Rashedi, E., H. Nezamabadi-Pour, and S. Saryazdi, "GSA: A gravitational search algorithm," *Information Sciences*, Vol. 179, No. 13, 2232–2248, 2009.
16. Chatterjee, A., G. K. Mahanti, and N. Pathak, "Comparative performance of gravitational search algorithm and modified particle swarm optimization algorithm for synthesis of thinned scanned concentric ring array antenna," *Progress In Electromagnetics Research B*, Vol. 25, 331–348, 2010.
17. Chatterjee, A., G. K. Mahanti, and P. R. S. Mahapatra, "Design of fully digital controlled reconfigurable dual-beam concentric ring array antenna using gravitational search algorithm," *Progress In Electromagnetics Research C*, Vol. 18, 59–72, 2011.
18. Altinoz, O. T. and A. E. Yilmaz, "Calculation of optimized parameters of rectangular patch antenna using gravitational search algorithm," *2011 International Symposium on Digital Object (INISTA)*, 349–353, Jun. 15–18, 2011.

Experimental Studies on Microwave Gunn Oscillator Based Modulator-demodulator Systems with Chaotic Modulating Signals

B. C. Sarkar[1], **T. Banerjee**[1], **S. Sarkar**[2], **C. Koley**[1], **and A. K. Guin**[1]

[1]Department of Physics, Burdwan University, India
[2]Electronics Department, Burdwan Raj College, India

Abstract— A technique of chaos-based communication using X-band microwave frequency channel has been experimentally studied. Chaotic signals of lower radio frequency (RF) region ($\sim 200\,\mathrm{kHz}$) is used to angle modulate an X-band Gunn Oscillator ($\sim 10\,\mathrm{GHz}$) by a bias tuning technique. The modulated microwave signal is detected in a phase discriminator type demodulator designed using an injection synchronized Gunn oscillator. Obtained results indicate that information bits encoded on low frequency RF chaotic signals could be transmitted and received through a microwave channel by an adequate modulation-demodulation process.

1. INTRODUCTION

Chaos-based secure communication systems have drawn much interest in recent years [1, 2]. In secure communication the privacy as well as the integrity of the transmitted message is to be ensured. In this respect, chaos-based techniques offer potential advantages over conventional one in terms of higher security of the information using simple hardware circuits [2–4]. Studies reported in the literature concerning chaos-based communication mainly concentrate on the two issues-process of synchronization of chaos and techniques of masking modulating signals with chaotic signals. A third issue which also demands attention is the type of the channel through which the signal is being transmitted. In most of the studies [2] a wire is used to transmit the chaotic signal, which is good for baseband communication systems, but that is not enough for band-pass high frequency (HF) communication technique. Communication in HF zone has advantages of high band width, low loss, high reliability, etc. [5]. Thus chaos based communication system in high frequency domain would result in added security and reliability. To realize a band-pass HF communication system with chaos, we have to choose a channel having efficient transmission characteristics. For wireless line-of-sight communication, it may be free space and for guided communication it may be waveguide or transmission line.

In the present paper, we report experimental studies on transmission and reception of chaos modulated RF signals through a microwave guided channel. To realize a transmitter, a free running GO is angle modulated with a low frequency RF chaos by bias tuning technique. Here the modulating chaotic signal is superimposed on the dc bias of the free running GO and one gets an frequency modulation (FM) type angle modulator. To combat the degrading effects of frequency drifting of a free running GO, a modulator with frequency stabilization arrangements has also been studied. Effectively, such a modulator behaves as phase modulation (PM) type modulator [6]. The demodulator system has been realized using an injection synchronized GO with some additional circuits. The rest of the paper is organized in the following way. The outlines of theoretical principles of the experimental work are described in Section 2. In Section 3, the set up for the hardware experiment is described along with a few comments on experimental observations. Finally some concluding remarks are given in Section 4.

2. THEORETICAL BASIS OF EXPERIMENTS PERFORMED

In this section, we describe outlines of the principle of operation of the GO based modulator and demodulator circuits studied in this paper. These circuits could be used to realize a microwave chaotic communication system.

2.1. GO Based Bias-tuned Modulator

The frequency of oscillation of an X-band GO depends on the cavity and the device (Gunn diode) parameters. The negative differential resistance of the device is primarily determined by the operating dc bias voltage and as such the parameters used in the mathematical model of the GO are sensitive to the changes of the operating dc bias. Hence it can be anticipated that the instantaneous frequency of the GO would be a function of the instantaneous dc bias. Based on this basic principle of a bias tuned modulator design, we have superimposed chaotic signals of lower RF range on the GO dc bias voltage by using a bias tee network. However to stabilize the carrier frequency of the angle modulated signal thus generated, the bias tuned GO has been made to operate in an injection synchronized mode to a stable microwave frequency signal. It is expected that a free running GO based bias-tuned FM modulator would have larger deviations for a given modulating signal amplitude than that of a modulator based on a frequency stabilized GO. The response of the later type modulator would be equivalent to a phase modulator having reduced perturbation due to inherent noise.

2.2. GO Based Injection Synchronized Demodulator

Using the principle of direct or injection synchronization of an oscillator, one can design a phase discriminator type [7] FM demodulator. If a GO be synchronized to an angle modulated signal of reasonably stable amplitude A and information modulated phase theta (θ), the output of the GO would have an instantaneous phase same as that of the injected signal having a time delay dependent on the system parameters. Thus, the real time product of the injected and the output signals of the demodulated GO would have a low frequency component proportional to the time derivative of the injected signal phase. Obviously, using a properly designed phase comparator circuit along with the injection synchronized GO, an FM demodulator could be realized with frequency stabilized and free running carrier signals.

2.3. Principle Adopted to Identify the Demodulated Chaotic Signal

In our experiment, the chaos signals of low RF frequencies have been used as the modulating signals. So, the detected chaotic signals must be identified as the modulating signals to ensure proper operation of the modulator-demodulator chain. For this purpose we have used the technique of representing the real time chaotic variables in the phase plane. The chaos signal used in the experiment has been taken from a single amplifier bi-quad (SAB) chaotic oscillator [8]. The phase plane representation of this chaos signal with its time delayed version at the transmitter end would represent its nature through the obtained strange attractor. The nature of the detected chaos is examined by getting the phase plane representation of the transmitted chaos and the detected chaos. If the nature of the strange attractor is equivalent to that obtained at the transmitting end with two versions of the modulating chaos, one can conclude that the detected chaos is also a time shifted version of the modulating chaos. The ability of the demodulator circuit in our experiment has been examined using above mentioned algorithm.

3. EXPERIMENTAL STUDY

The block diagram of the experimental arrangement to examine the response of the angle modulator is shown in Figure 1. In the actual hardware circuit, a low power X-band GO (GO1: VJU, Model No. X2152 Sl No. 1031) is used as bias tuned modulator. The modulating signal is added to the dc bias with the help of bias tee. The frequency stabilizing RF signal is injected to the modulator GO1 via an X-band circulator (SICO, Model No. XC621 Sl No. 440). A microwave signal source and the GO1 are connected at port 1 and port 2 of the circulator, respectively. For a modulator with free running GO, the port 1 of the circulator is terminated by a matched load. The output is taken out from the port-3 of the circulator and is examined by a spectrum analyzer (Rohde and Schwarz, FSL SA, 9 kHz–18 GHz). The block diagram of the demodulator circuit is shown in Figure 2. It consists of a low power X-band GO (GO2: VJU, Model No. X2152 Sl No. 1288), a microwave mixer consisting of a magic tee, two diode detectors and a difference amplifier [7]. The signals applied to and taken from GO2 (with the help of a circulator) are fed to E-arm and H-arm of the magic tee. The signals obtained from other two arms of the magic tee are detected with the

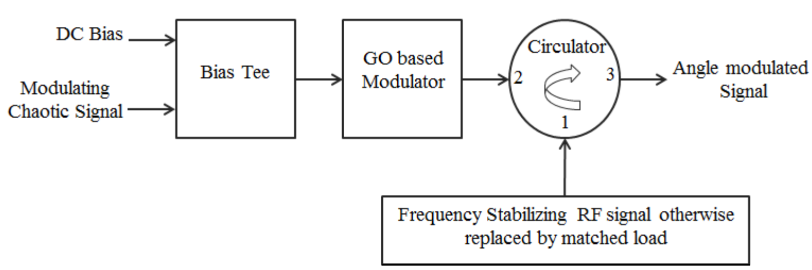

Figure 1: Simplified functional structure of GO based bias-tuned modulator.

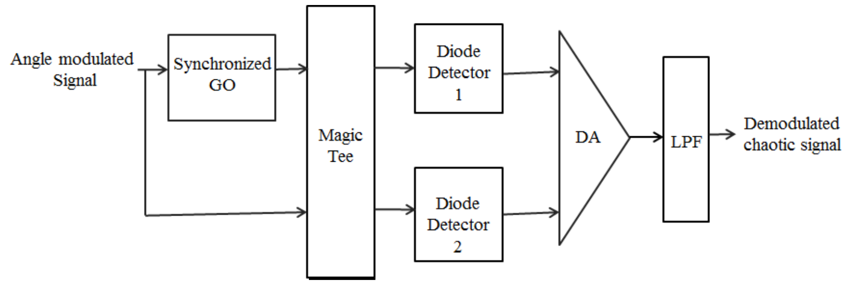

Figure 2: Simplified functional structure of GO based injection synchronized demodulator.

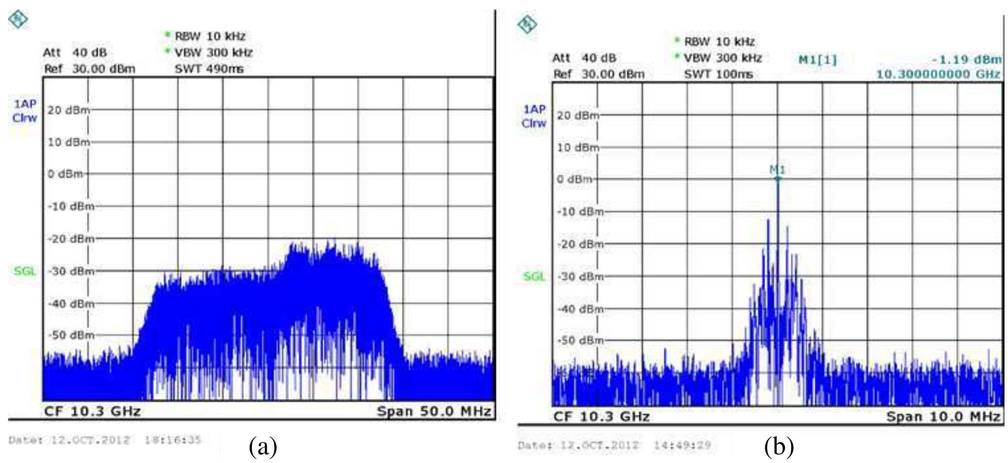

Figure 3: Experimentally obtained output spectra of chaos modulated signal of the GO based bias tuned modulator. (a) Modulation on a free running carriers. (b) Modulation on a frequency stabilized carriers.

help of diode detectors and their difference is taken as the detected signal. A SAB-based chaotic oscillator provides the low frequency chaos signal (CS) for modulation.

In the experiment, the free running carrier frequency of the modulator GO (MGO) is taken as 10.3 GHz. The frequency of the stabilizing microwave signal and the frequency of the demodulator GO (DGO) are also taken at this value. The DGO is made to synchronize with the modulated RF signal obtained from the MGO. The chaotic modulating signal is taken from a SAB based chaotic oscillator with center frequency kept at 190 kHz. The amplitude of the modulating chaos signal is varied to get different values of the modulation index. The dynamics of the chaotic signal generator can be examined by observing the phase plane diagram between two outputs of the circuit with the help of a CRO. In the transmitter section one of these two outputs of the chaos generator is used as the modulating signal. The spectra of the modulated signal free running carriers and with frequency stabilized are shown in Figures 3(a) and 3(b) respectively. For the frequency stabilized carrier, the width of the modulated signal spectrum is considerably less. This means that the frequency deviation with a given amount of modulating signal amplitude is small for a frequency stabilized GO. The detection ability of the detector can be understood by using the algorithm described in Section 2.3. The phase plane plots shown in Figure 4 show the attractor of the modulating chaos (Figures 4(a)) and those obtained by using transmitted and detected chaos. The detected chaos from the modulated signal with free running carrier is much distorted which is evident from the reconstructed attractor for this case (Figure 4(b)). The detected chaos from modulated signal with frequency stabilized carrier is considerably less distorted and so the reconstructed attractor (Figure 4(c)) is much similar to that obtained at the chaos generator. Figure 5(a) shows the spectrum of the modulating chaos. The spectra of the detected chaos from the modulated signal with free running carriers and with frequency stabilized are shown in Figures 5(b) and 5(c) respectively. It is evident from the obtained results that the demodulated chaos signal is similar to the modulating chaotic signal in both schemes.

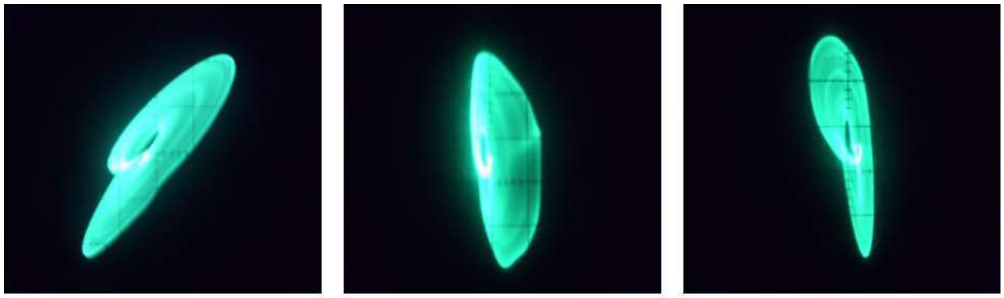

(a) (b) (c)

Figure 4: The oscilloscope trace of (a) the attractor of the modulating chaos, (b) the reconstructed attractor using transmitted and detected chaos with free running carrier, (c) the reconstructed attractor using transmitted and detected chaos with frequency stabilized carrier.

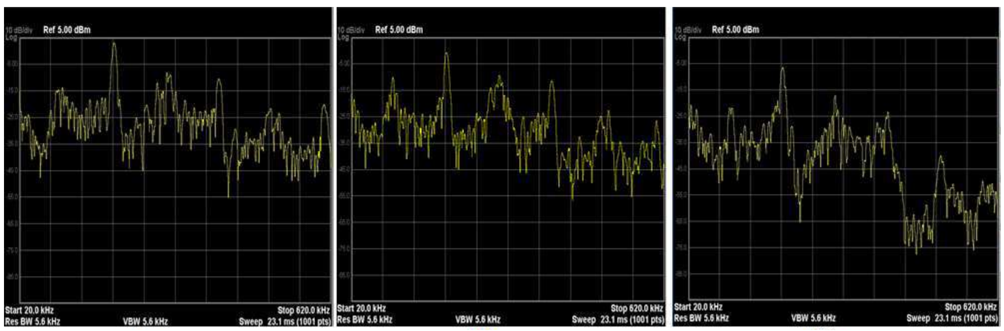

(a) (b) (c)

Figure 5: Experimentally obtained spectra of (a) the modulating chaos, (b) the detected chaos from the modulated signal on a free running carrier, (c) the detected chaos from the modulated signal on a frequency stabilized carrier.

4. CONCLUSION

The outcome of the whole study can be summarized as follows. A bias-tuned GO can be used as an angle modulator for chaotic modulating signals as well. If the frequency of the GO is stabilized by the technique of injection synchronization, the index of modulation would be less and hence the transmission bandwidth of the modulated signal would be of small width. The chaotically modulated microwave signal could be detected by the conventional injection synchronized FM detectors based on the principle of phase discrimination. The modulated signal on a frequency stabilized carrier provides less distorted demodulated signals. The modulator-demodulator chain introduces an additional phase shift and distortion signal components in the detected chaos signal. The obtained results would provide useful knowledge in the implementation of chaotic communication system at the microwave frequency region.

ACKNOWLEDGMENT

Authors acknowledge the financial support from DST (India) through sponsored projects in carrying out this work. They also acknowledge the financial support from the DAE (BRNS), India for developing the infrastructure required for the experiment.

REFERENCES

1. Kennedy, M. P., R. Rovatti, and G. Setti, *Chaotic Electronics in Telecommunication*, CRC Press, Boca Raton, 2000.
2. Yang, T., "A survey of chaotic secure communication system," *International Journal of Computational Cognition*, Vol. 2, 81–130, 2004.
3. Chen, T.-I. and T.-L. Liao, "Design of secure digital communication systems using chaotic modulation, cryptography and chaotic synchronization," *Chaos, Solitons and Fractals*, Vol. 24, 241–255, 2005.

4. Volkovskii, A. R., L. S. Tsimring, N. F. Rulkov, and I. Langmore, "Spread spectrum communication system with Chaotic frequency modulation," *Chaos*, Vol. 15, 1–6, 2005.
5. Sarkar, B. C., A. K. Guin, D. Ghosh, C. Koley, and T. Banerjee, "Experimental studies on a Chaos based communication system using microwave Gunn oscillator," *ICLMSC 2011 Proceedings*, 299–301, Burdwan University, India, Dec. 7–9, 2011.
6. Ching, T. W. and F. J. Rosenbaum, "Amplitude and frequency modulation of a waveguide cavity CW Gunn oscillator," *IEEE Trans. on Microwave Theory and Techniques*, Vol. 18, No. 11, Nov. 1970.
7. Sarkar, S., T. Banerjee, D. Mondal, and B. C. Sarkar, "Theory and performance of an electrically controlled microwave phase shifter," *Indian Journal of Pure and Applied Physics*, Vol. 43, 15–20, 2005.
8. Banerjee T., B. Karmakar, and B. C. Sarkar, "Single amplifier biquad based autonomous electronic oscillators for chaos generation," *Nonlinear Dynamics*, Vol. 62, 859–869, 2010.

Effects of Nonlinear Bias Tuning of X-band Gunn Oscillator Based Frequency Modulators

B. C. Sarkar, **T. Banerjee**, **A. K. Guin**, **and C. Koleye**
Department of Physics, Burdwan University, India

Abstract— The charecteristics of a frequency modulator based on bias tuned Gunn oscillators has been studied taking the nonlinear variation of oscillator frequency (ω) with bias voltage (V) into account. The dependence of ω on V by a finite order power series. The co-efficients used in the power series are estimated from experimental results of the bias tuning characteristics of the diode. Based on the proposed analytical relations, the shift has been expressed of centre frequency and the assymetry in power distribution in upper and lower side bands are analytically evaluated. This gives the proof of deleterious effects of nonlinear modulation. Results of hardware experiments confirm the analytical predictions.

1. INTRODUCTION

In conventional frequency modulators, the instantaneous frequency of the output signal is considered to be a linear function of the applied modulating signal [1–3]. As such, frequency adjusting parameters of the voltage controlled oscillator used in the frequency modulator are made to vary linearly with the modulating signal amplitude. Some parameters are the bias current or the bias voltage of the active circuit element, the reactors or resistors used to design frequency selective circuits etc. Gunn oscillators (GOs) are common devices used as frequency modulators in X-band microwave frequency [4, 5]. The negative differential resistance(NDR) of the GO is a function of the bias voltage and it plays important role to determine the condition of oscillation and frequency of oscillation of the oscillator [6, 7]. The variation of the bias voltage of a GO causes a change in the value of the NDR of the GO and as such the frequency of the GO becomes a function of the bias voltage. However, it is observed experimentally that the variation of the frequency with bias voltage is not linear for a reasonable change in the dc bias voltage. Thus the response of the bias controlled FM modulator (FMM), based on GO departs from that of a system having linear voltage sensitivity. The present paper aims to explore the effects of nonlinear voltage sensitivity of a GO based FM modulator analytically as well as experimentally. The study would help to generalize the effects of nonlinear frequency modulation [8–10]. The subsequent sections of the paper are organized as follows: In Section 2, an analytical approach for finding the frequency spectrum of a general nonlinear frequency modulator has been given. Section 3 proposes a mathematical relation connecting the bias voltage and the oscillation frequency of a GO and using it finds the response of GO based nonlinear FM modulator. Also reports the observation of a hardware experiment finding the characteristics of a GO based FMM. Finally some concluding remarks on the outcome of the work are given in Section 4.

2. ANALYTICAL APPROACH

The instantaneous angular frequency of a generic voltage controlled FMM is written as,

$$\omega_i(V_{dc} + \Delta v) = \omega_0(V_{dc}) + \Delta\omega(\Delta v) \tag{1}$$

Here, $\Delta\omega(\cdot)$ is a function of the argument and V_{dc} is the dc bias voltage applied to the active circuit element and it determines the free running (unmodulated) frequency ω_0 of the oscillator. Δv is the modulating voltage controlling the angular frequency of the modulator. In a linear modulator $\Delta\omega(\Delta v)$ would be taken as $K_{f1}\Delta v$, where K_{f1} is the linear voltage sensitivity factor (VSF). For a nonlinear FM Modulator (NFMM) one can write

$$\Delta\omega(\Delta v) = \sum_{n=1}^{\infty} K_{fn}(\Delta v)^n \tag{1a}$$

Here K_{fn} stands for nth order VSF. Depending upon the type of the NFMM, the values of K_{fn} would be different. In the case of tone modulation, one takes Δv as $a_m \cos\omega_m t$ and the instantaneous angular frequency becomes,

$$\omega_i(t) = \omega_0 + \sum_{n=1}^{\infty} K_{fn} a_m^n (\cos\omega_m t)^n \tag{2}$$

As a special case, we consider the nonlinearity upto cubic term and upon simplification we get,

$$\omega_i(t) = (\omega_0 + \omega_{d2}) + (\omega_{d1} + 3\omega_{d3})\cos\omega_m t + \omega_{d2}\cos(2\omega_m t) + \omega_{d3}\cos(3\omega_m t) \tag{2a}$$

Here ω_{dn} $(n = 1, 2, 3)$ represents nth order angular frequency deviation. The values of ω_{d1}, ω_{d2}, ω_{d3} are $K_{f1}a_m$, $K_{f2}a_m^2/2$ and $(K_{f3}a_m^3)/4$ respectively. The output signal of the NFMM would be written as,

$$e_{NFM}(t) = A_c \cos\left(\int \omega_i(t)\mathrm{d}t\right) \tag{3}$$

where A_c is the amplitude of the nonlinearly modulated FM (NFM) signal. After a little bit of simplification one gets,

$$e_{NFM}(t) = A_c \cos\left(\omega_c t + \sum_{n=1}^{3} m_{fn}\sin(n\omega_m t)\right) \tag{4}$$

Here we substitute $\omega_c = (\omega_0 + \omega_{d2})$ as the shifted average frequency and m_{fn} as the nth order modulation index parameter. The values of the index parameters are, $m_{f1} = \frac{\omega_{d1}+3\omega_{d3}}{\omega_m}$; $m_{f2} = \frac{\omega_{d2}}{2\omega_m}$; $m_{f3} = \frac{\omega_{d3}}{3\omega_m}$. The shift in average frequency is a result of the nonlinearity in the FNM modulator. The expression for $e_{NFM}(t)$ is written as,

$$e_{NFM}(t) = \text{real part of } \left[A_c \exp(j\omega_c t)\prod_{n=1}^{3}\exp(jm_{fn}\sin(n\omega_m t))\right] \tag{5}$$

To find the component signals of $e_{NFM}(t)$, one substitutes

$$\exp(jm_{fn}\sin(n\omega_m t)) = \sum_{k=-\infty}^{\infty} J_k(m_{fn})\exp(jkn\omega_m t) \tag{5a}$$

where $J_k(m_{fn})$ is the kth order Bessel function. Here one can write,

$$e_{NFM}(t) = \text{real part of } \left[A_c \prod_{n=1}^{3}\sum_{k=-\infty}^{\infty} J_k(m_{fn}\exp(j(\omega_c + kn\omega_m)t))\right] \tag{6}$$

Expanding this expression for different values of k and n, we estimate the amplitudes of component signals having frequency ω_c, $\omega_c + \omega_m$, $\omega_c - \omega_m$ etc. the amplitude of the signal of frequency ω_c is obtained as,

$$A_c' = A_c[J_0(m_{f1})J_0(m_{f2})J_0(m_{f3}) + J_1(m_{f1})J_1(m_{f2})J_1(m_{f3}) - J_1(m_{f1})J_1(m_{f2})J_1(m_{f3})] \tag{7a}$$

Note that, this expression has been obtained by taking $k = 0$, ± 1 only. In a similar way the amplitudes of first upper and lower side bands of the FM wave of frequencies $\omega_c + \omega_m$ and $\omega_c - \omega_m$ respectively are obtained as:

$$A_u' = A_c[J_1(m_{f1})J_0(m_{f2})J_0(m_{f3}) - J_0(m_{f1})J_1(m_{f2})J_1(m_{f3}) - J_1(m_{f1})J_1(m_{f2})J_1(m_{f3})] \tag{7b}$$

and

$$A_l' = -A_c[J_1(m_{f1})J_0(m_{f2})J_0(m_{f3}) + J_0(m_{f1})J_1(m_{f2})J_1(m_{f3}) + J_1(m_{f1})J_1(m_{f2})J_1(m_{f3})] \tag{7c}$$

It is observed that magnitudes of A_u' and A_l' are different and this is an important effect of the nonlinearity in the frequency modulator [8]. The relation (6) can be used to find the frequency spectrum of the nonlinear FM signal with multiple sidebands about the average central frequency. From the numerical computation of the amplitudes of a particular order sideband at the two sides of the average frequency, the detailed information about the asymmetry could be obtained.

3. RESPONSE OF A NONLINEAR GO BASED FM MODULATOR

The variation of bias voltage of a GO causes a nonlinear variation of the NDR and the device reactances as a result of which the angular frequency of oscillation of the GO (ω) changes with the bias voltage above threshold. Examining the experimentally obtained nature of the variation of ω with bias voltage (V) above the threshold value V_T. We propose a mathematical relation for ω as,

$$\omega(V) = \beta[1 - \exp -\alpha(V - V_T)] \tag{8}$$

where β and α are to be determined by the method of fitting between the experimental curve and the curve according to the Equation (8). In presence of the modulating voltage Δv with the dc bias voltage V_{dc}, we write putting $V = V_{dc} + \Delta v$,

$$\omega(V_{dc} + \Delta v) = \beta[1 - \exp -\alpha(V_{dc} - V_T + \Delta v)] \tag{9}$$

and equate the expression with

$$\omega_i(V_{dc} + \Delta v) = \omega_0(V_{dc}) + \sum_{n=1}^{\infty} K_{fn}(\Delta v)^n \tag{10}$$

to find the values of ω_0 and K_{fn} in terms of GO parameters α, β and $(V_{dc} - V_T)$. Then putting

$$K_0 = \exp -\alpha(V_{dc} - V_T) \tag{11a}$$

one gets,

$$\omega_0 = \beta(1 - K_0) \tag{11b}$$

and

$$K_{fn} = (-1)^{n+1} \frac{K_0 \beta \alpha^n}{n!} \tag{11c}$$

These values of K_{fn} are used to find the values of ω_{d1}, ω_{d2} and ω_{d3} mentioned in Section 2 and hence to get different orders of modulation indices for NFM output from the GO based modulator. Thus the output spectrum can be obtained from Equation (6) for particular values of modulating signal amplitude and the same can be compared with the experimentally obtained curves. Figure 1(a) shows the bias voltage-frequency curve for the GO (SICO, Model No-X2152, Sl No.-1287) with the cavity length fixed at 9.1 mm. Using the curve and converting the measured frequency into corresponding angular frequency we get the values of α and β as 0.8 and 62.7 respectively. We got the threshold voltage (V_T) as 7.2 volts. These values are used to get the numerically estimated frequency spectrum of the GO modulator with modulating signal amplitude applied at the bias terminal as $0.75\cos(2\pi 10^7 t)$. The experimentally obtained frequency of the modulator along with the corresponding numerically estimated are shown in Figures 2(a) and 2(b). The effects of the nonlinearity in the NFMM response are observed in the obtained figures.

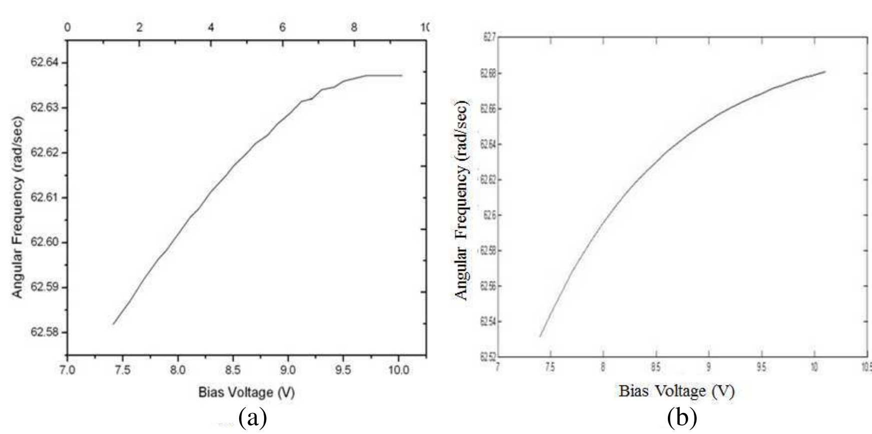

Figure 1: Frequency vs. bias voltage curve: (a) Experimental. (b) Numerical.

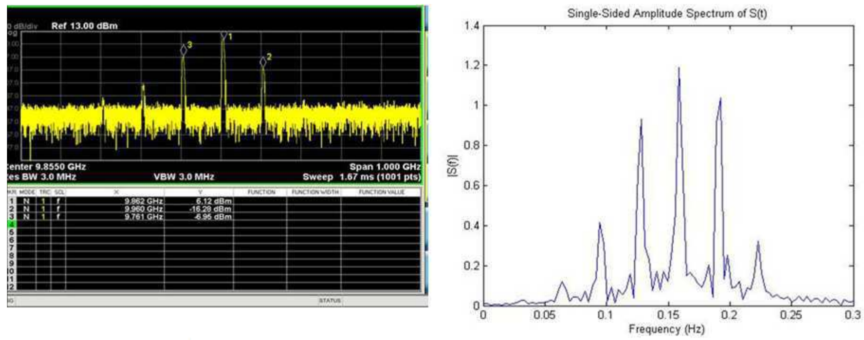

(a) (b)

Figure 2: Experimentally and numerically obtained frequency spectrum of the modulator: (a) Experimental. (b) Numerical.

4. DISCUSSION

The present work establishes both analytically and experimentally that due to nonlinear variation of the instantaneous frequency of an FM wave with the modulating signal,the powers of the same order upper and lower side bands would be different. Also the average frequency of the modulated signal would be different from the unmodulated carrier signal frequency. The study has been carried over on a bias-modulated Gunn Oscillator which has nonlinear frequency-vs-bias voltage dependence. It has been shown that the effect of the nonlinearity is more pronounced when the bias voltage is close to device threshold bias voltage (V_T) or considerably away from it. To design a linear FM modulator, the dc bias should be optimally chosen, moderately higher than V_T. In this paper the nonlinear variation of the frequency of oscillation with bias voltage has only been considered, the possible variation of the amplitude of oscillation has not been taken into account.

REFERENCES

1. Lathi, B. P., *Modern Digital and Analog Communication System*, 3rd Edition, Oxford University Press, 1998.
2. Kurokawa, K., "Injection locking of microwave solid state oscillator," *Proc. IEEE*, Vol. 61, 1386–1410, 1973.
3. Bestwick, P. R., P. S. Drinan, G. S. Hobson, P. N. Robson, M. Thomas, and R. Tozer, "Direct frequency modulation with CW Gunn and IMPATT Oscillators," *IEEE Journal of Solid State Circuits*, Vol. 8, 37–43, 1973.
4. Tsai, W. C. and F. J. Rosenbaum, "Amplitude and frquency modulation of wave guide cavity CW Gunn oscillator," *IEEE Transaction on Microwave Theory and Techniques*, Vol. 18, 877–884, 1970.
5. Martin, B. and G. S. Hobson, "High-speed phase and amplitude modulation of Gunn oscillator," *Electronics Letters*, Vol. 6, 244–246, 1970.
6. Sarkar, B. C., C. Koley, A. K. Guin, and S. Sarkar, "Some numerical and experimental observations on the growth of oscillation in an X-band Gunn oscillator," *Progress In Electromagnetic Research B*, Vol. 40, 325–341, 2012.
7. Sarkar, B. C., D. Sarkar, S. Sarkar, and J. Chakraborty, "Studies on the dynamics of bilaterally coupled X-band Gunn oscillator," *Progress In Electromagnetic Research B*, Vol. 32, 149–167, 2011.
8. Consolo, G., et al., "Combined frequency-amplitude nonlinear modulation: Theory and applications," *IEEE Transaction on Magnetics*, Vol. 46, 3629–3634, 2010.
9. Faulkner, E. A., "Frequency modulation sensitivity of Gunn oscillators," *Electronics Letters*, Vol. 5, 217–218, 1969.
10. Sudbo, A. and L. Bjerkan, "Nonlinear modulation response and relaxation oscillations in semiconductor injection LASER," *IEEE Journal of Quantum Electronics*, Vol. 19, 1542–1551, 1983.

Experimental Studies on the Nonlinear Interaction between a Chaotic Signal and a Periodic Signal at Microwave Frequency Range

B. C. Sarkar[1], **S. Sarkar**[2], **C. Koley**[1], **A. K. Guin**[1], **and T. Banerjee**[1]

[1]Department of Physics, Burdwan University, India
[2]Electronics Department, Burdwan Raj College, India

Abstract— Experimental studies on the interaction of a microwave chaotic signal (MCS) with a periodic Gunn oscillator (PGO) have been reported. Two characteristically different results have been obtained depending on the power and the frequency range of the MCS relative to those of the PGO. They are: (i) the output of the PGO becomes chaotic with similar spectral characteristics as that of the injected MCS; This happens in a synchronized state of the GO with the injected MCS, (ii) A broad band chaotic oscillations are observed at the PGO output having bandwidth larger than that of the injected MCS; This happens in a state of out-of-lock interaction between the PGO and the MCS.

1. INTRODUCTION

The problems of chaos based communication systems are being studied in last few decades [1, 2]. In this context, the application of microwave frequency chaotic signal has been proved to be potentially advantages [3, 4]. As such, generation of broad band microwave chaotic signal (MCS) has become an important technological challenge. Some novel techniques of MCS generation have been reported in the literature in the recent years using Gunn Oscillators (GOs), Colpitts oscillators etc.. In [5], a periodic GO (PGO) is made to oscillate in chaotic domain under the influence of one or more external RF signals. Another novel technique based on an under biased GO driven by a weak external RF signal has recently been proposed [6]. Depending on the magnitude of the applied dc bias and the frequency of the injected RF field, one gets chaotic signals of different power and bandwidth. The present work studies experimentally the interaction between an injected MCS and a PGO. Basically, this is a problem which explores the possibility of injection synchronization of a PGO with a chaotic signal having frequency components around that of the PGO. Due to the non linear nature of the oscillator circuit one can expect several interesting phenomena due to this interaction process. In a possible synchronized state of the PGO one would get output chaotic signal with enhanced power [7]. Also, in the non synchronized condition bandwidth enlargement can be expected due to the appearance of out of lock component signals [8, 9]. The rest of the paper is organised in the following way: In Section 2, theoretical principle behind the motivation of the experimental study has been given. Section 3 describes briefly the experimental arrangement along with the obtained results. A few concluding remarks are given in Section 4.

2. THEORETICAL PRINCIPLE OF EXPERIMENTS PERFORMED

The underlying principle of the experimental studies reported in this paper is the injection synchronization of a nonlinear oscillator to the external signals. A weak CW or modulated signal could be amplified by applying it to an oscillator of proper frequency and taking the output of the synchronized oscillator obtained there by. In the experiment, a low power chaotic signal having a continuous broad band around a frequency equal to that of a PGO has been injected into the PGO. In the condition of a possible synchronization, one would get chaotic oscillations at the output with enhanced power.

Also, in the unlocked state, one gets large number of discrete components at the output of the oscillator driven by a single frequency signal. Hence, when a chaotic signal would be used as the injecting signal, the output of the PGO would give a continuous spectrum, the bandwidth is expected to be broadened compared to the input chaos. The above mentioned points have been examined by hardware experiment in this work.

3. EXPERIMENTAL STUDIES

Figure 1 shows the functional block diagram of the experimental setup used in the study. In the hardware circuit, periodic and chaotic signals are generated in the wave guide based oscillators

GO2 and GO1 respectively. To produce MCS, GO1 (VJU, Model No. X2152, Sl No. 1031) is operated in the under biased condition (4.76 volts) in a cavity of resonant frequency ≈ 10.02 GHz. A weak (0 dBm) RF signal of frequency f_r (10.025 GHz) is injected into the GO1 cavity using an X-band circulator (SICO, Model No. XC621, Sl No. 439) from a microwave signal generator (Agilent N5183A). Adjusting the dc bias (V_B) and the cavity dimension, GO2 (VJU, Model No. X2152, Sl No. 1288) is made to operate with free running frequency (f_0) and output power 10 GHz and 7.39 dBm respectively. The nature of oscillations of the chaotic GO (CGO) and the PGO are observed with the help of a spectrum analyser (Rhode and Schwarz, FSL SA, 9 kHz–18 GHz) as shown in Figures 2(a) and 2(b) respectively. In the experiment, the chaotic signal is injected to the PGO using an attenuator to adjust the strength of the chaotic signal injected to the PGO. The output of the PGO is examined for different values of detuning (Δf) between f_0 and f_r. For the variation of the detuning, f_0 is varied by changing the position of the micrometer screw attached with the cavity. Some experimental observations are presented in Figure 3(a) to Figure 3(e).

The obtained results can be qualitatively summarized as follows:

1. When the magnitude of Δf $(= |f_r - f_0|)$ is large compared to the bandwidth of the chaotic signal, the bandwidth of the chaos remains almost unaffected but the spectral characteristics of the PGO becomes slightly broadened. This indicates a feeble interaction between two interacting signals.
2. With the gradual reduction of $|\Delta f|$, the interaction becomes more prominent resulting in the broadening of the continuous broadband spectrum of the chaotic signal. The spectrum of the PGO losses its identity and becomes a part of the resultant broad spectrum.
3. When $|\Delta f|$, is smal, i.e., f_r and f_0 are comparable, the bandwidth of the PGO output signal becomes of the same order of the original chaotic signal. This may be a case of synchronized state of the PGO with the injected chaotic signal.
4. The observations are qualitatively similar for positive and negative values of $|\Delta f|$. However, there is a quantitative asymmetry in the nature of the output spectra of the PGO on the two sides of f_r in terms of the amount of enhancement in the bandwidth and the power of the resultant chaos. Table 1 gives an estimation of the experimental observation regarding modification of the bandwidth of the chaotic signal due to interaction with PGO.

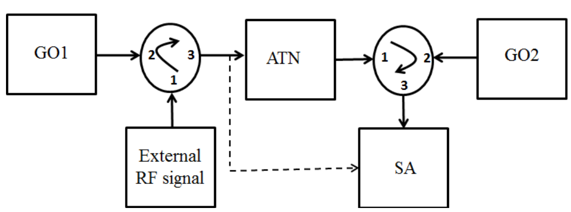

Figure 1: Functional block diagram of the experimental set up.

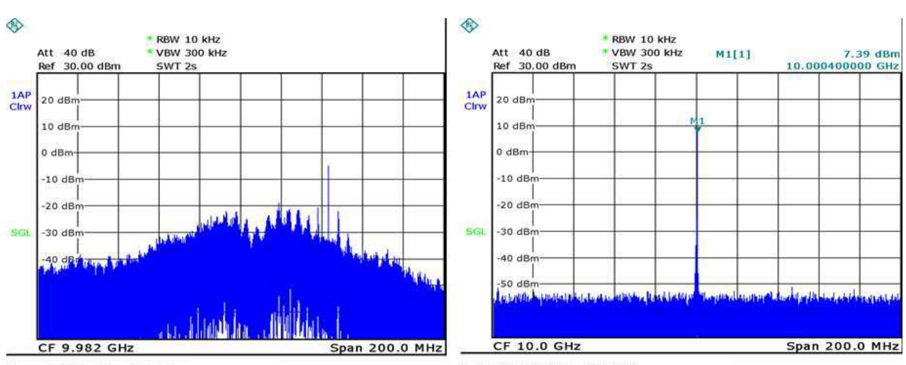

(a) CGO (b) PGO

Figure 2: The nature of output spectra of the GOs in isolated condition: (a) CGO (20 dBm bandwidth = 140 MHz), (b) PGO (output power $(P_0) = 7.39$ dBm, frequency $(f_0) = 10.0$ GHz).

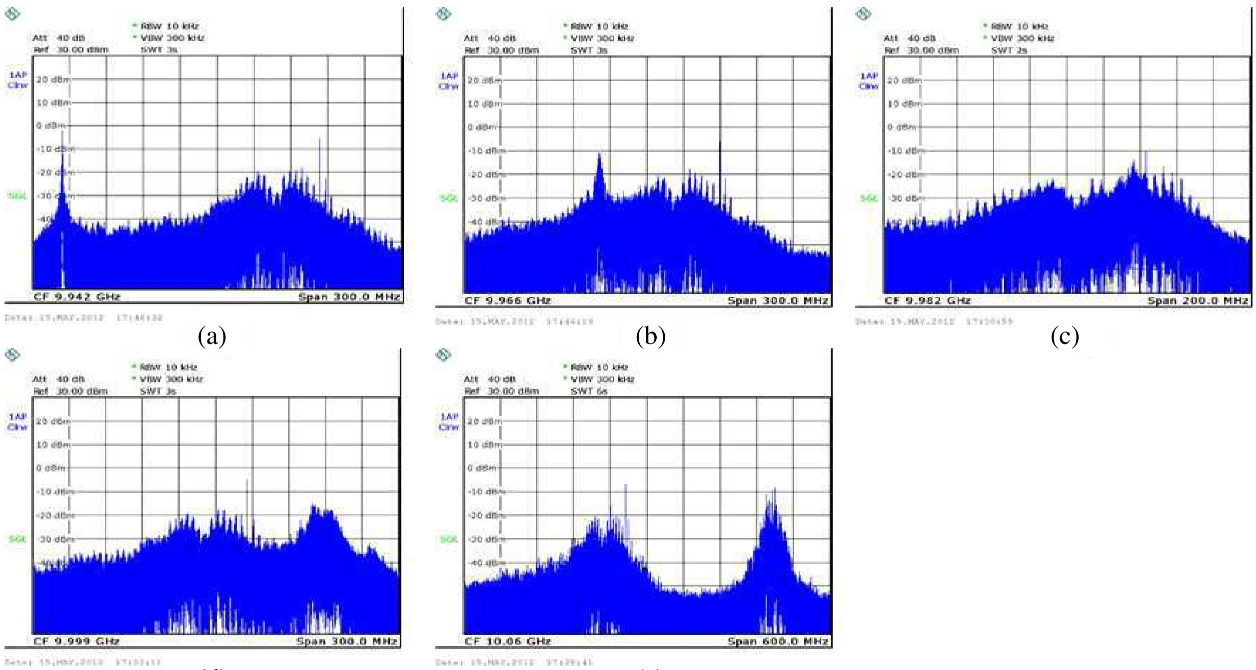

(a) (b) (c) (d) (e)

Figure 3: The nature of variation of the output spectra of the PGO due to interaction with the chaotic signal ($f_r = 10.025$ GHz), (a) $f_0 = 9.816$ GHz, (b) $f_0 = 9.925$ GHz, (c) $f_0 = 10.018$ GHz, (d) $f_0 = 10.089$ GHz, (e) $f_0 = 10.261$ GHz.

Table 1: Experimental observation regarding modification of the bandwidth of the chaotic signal due to interaction with PGO ($f_r = 10.025$ GHz).

f_0 **(GHz)**	Δf (GHz)	**20 dBm Bandwidth (GHz)**
9.816	0.209	130
9.925	0.100	170
10.018	0.006	140
10.089	0.064	200
10.261	0.236	130

4. CONCLUSION

Detailed experimental investigations on the nonlinear interaction of a microwave chaotic signal with a periodic signal have been done. In brief, the outcomes of the study can be summerised as (i) A PGO can be used to amplify the power of a chaotic signal of proper bandwidth and centre frequency based on the principle of lock-in amplifications; (ii) depending on the detuning between the frequency of the GO and the centre frequency of the chaotic oscillation, the nonlinear interaction between them broadens the bandwidth of the chaotic signal. This study has potential application in chaos based secured communication.

ACKNOWLEDGMENT

Authors acknowledge partial financial assistance from DAE, BRNS (India) and DST (India) through sponsored research projects in carrying out the work.

REFERENCES

1. Kennedy, M. P., R. Rovatti, and G. Setti, *Chaotic Electronics in Telecommunications*, Taylor and Francis, 2000.
2. Larson Lawrence, E., J.-M. Liu, and L. S. Tsimring, *Digital Communications Using Chaos and Nonlinear Dynamics*, Springer, 2006.

3. Qiao, S., Z. G. Shi, T. Jiang, and L.-X. Ran, "A new architecture of UWB radar utilizing microwave chaotic signals and chaos synchronization," *Progress In Electromagnetic Research*, Vol. 75, 225–237, 2007.
4. Shi, Z. G. and L. X. Ran, "Microwave chaotic Colpitts oscillator: Design, implementation and applications," *Journal of Electromagnetic Waves and Applications*, Vol. 20, No. 10, 1335–1349, 2006.
5. Chakravorty, J., T. Banerjee, R. Ghatak, A. Bose, and B. C. Sarkar, "Generating chaos in injection-synchronized gunn oscillator: An experimental approach," *IETE Journal of Research*, Vol. 55, 106–111, 2009.
6. Sarkar, B. C., C. Koley, A. K. Guin, and S. Sarkar, "Some numerical and experimental observations on the growth of oscillations in an X-band Gunn oscillator," *Progress In Electromagnetics Research B*, Vol. 40, 325–341, 2012.
7. Kurokawa, K., "Injection locking of microwave solid state oscillator," *Proc. IEEE*, Vol. 61, 1386–1410, 1973.
8. Razavi, B., "A study of injection pulling and locking in oscillators," *Proc. IEEE 2003 Custom Integrated Circuit Conference*, 305–311, 2003.
9. Banai, A. and F. Farzaneh, "Locked and unlocked behavior of mutually coupled microwave oscillators," *IEE Proc. Microwave*, Vol. 147, 2000.

FPGA Implementation of LDPC Encoder with Approximate Lower Triangular Matrix

Yi Hua Chen and Jheng Shyuan He
Institute of Information and Communication Engineering
Oriental Institute of Technology, New Taipei City, Taiwan

Abstract— This study used the weight (3, 6) approximate lower triangular regular parity check matrix to implement the LDPC encoding on the 5641R FPGA of the Software Define Radio system developed by National Instruments (NI) [1]. This study provided a detailed introduction to the encoding mechanism of the approximate lower triangular LDPC, and completed the implementation and verification of FPGA hardware.

1. INTRODUCTION

Shannon proposed the mathematical theories of communications in 1948 [2], arguing that the system capacity C of a channel perturbed by additive white Gaussian noise (AWGN) is a function of the received signal power S, the noise power N, and the receiver bandwidth W. It is possible to send information at the rate R, where $R \leqq C$, through the channel with an arbitrarily small error probability by using a sufficiently complicated coding scheme. In 1962, Gallager proposed Low Density Check Codes (LDPC) [3], which is a linear block codes [4], and proved that the data transmission rate of LDPC code can approach the Shannon capacity C.

2. BAPPROXIMATE LOWER TRIANGULAR LDPC ENCODING ARCHITECTURE

2.1. Characteristics of Low Density Parity Check Matrix *H*

LDPC code is a linear block code based on sparse check matrix. General block codes can be encoded and decoded by generating matrix and parity check matrix. The approximate lower triangular encoding method used in this study directly uses parity check matrix for encoding.

2.2. Encoding Steps of LDCP Check Matrix Based on Approximate Lower Triangular Structure

Compared with general linear block code encoding, LDPC encoding with lower triangular check matrix [5] and approximate lower triangular check matrix [6] carry out encoding directly by parity check matrix H. There are two types of encoding by lower triangular check matrix structure. The first is to use the Gaussian elimination to convert the check matrix H into lower triangular matrix structure (as shown in Fig. 1) before encoding. The encoding complexity is $O(n^2)$. n is the column of check matrix. However, lower triangular check matrix produced in this method is not consistent with the sparse characteristics. The second is to directly use a given lower triangular sparse check matrix for encoding, which may result in loss of encoding performance [7].

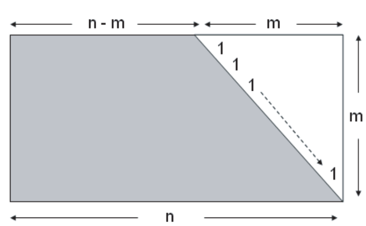

Figure 1: Lower triangular parity check matrix structural diagram.

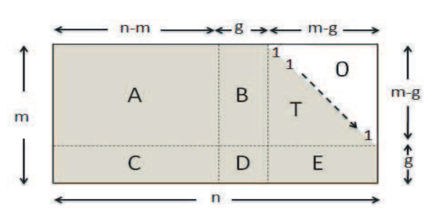

Figure 2: Structural diagram of approximate lower triangular matrix.

Approximate lower triangular LDPC encoding was proposed by Richardson and Urbanke in 2001. The encoding is to disintegrate the check matrix H of (1) into six (A, B, C, D, T, E) sparse sub-matrix before working out the redundant bit p_1, p_2 according to the characteristics of the six sparse sub-matrix to complete the encoding. The encoding complexity is $O(n + g^2)$, g is the row of matrix E. Compared with the lower triangular encoding matrix, the complexity is lower and the encoding is consistent with the sparse characteristics; hence, the encoding performance is relatively higher. The approximate lower triangular LDPC encoding is illustrated as below:

First, a standard original matrix is given as:

$$H = \begin{bmatrix} A_{(m-g)\times(n-m)} & B_{(m-g)\times g} & T_{(m-g)\times(m-g)} \\ C_{g\times(n-m)} & D_{g\times g} & E_{g\times(m-g)} \end{bmatrix} \tag{1}$$

The matrix finally can be used should be obtained by processing of four steps as follows:

Step1: Conduct column switching of the Matrix A and Matrix B of the original matrix with Matrix T. The switching results are: the diagonal lines of the Matrix T are all 1; the right upper corners are all 0 (as shown in Fig. 2).

Step2: For the convenience of solving the redundant vector p_1, Gaussian elimination computation of check matrix H. Matrix I in (2) represent the identity matrix.

$$\begin{bmatrix} I & 0 \\ ET^{-1} & I \end{bmatrix} \begin{bmatrix} A & B & T \\ C & D & E \end{bmatrix} = \begin{bmatrix} A & B & T \\ -ET^{-1}A + C & -ET^{-1}B + D & 0 \end{bmatrix} \tag{2}$$

Step3: After the Gaussian elimination computation, we define $\Psi = -ET^{-1}B + D$, and check whether Ψ is reversible. If it is irreversible, column switching with Matrix A should be redone.

Step4: After confirming $\Psi = -ET^{-1}B + D$ as reversible, the weights of parity check matrix can be converted into the weights of the original parity check matrix (3, 6) to complete the parity check matrix that can be encoded.

Codeword vector X is composed of two parts including the information vector m and redundant vectors (p_1, p_2). $HX^T = 0$ can lead to (3) (4) by inference:

$$Am^T + Bp_1^T + Tp_2^T = 0 \tag{3}$$

$$\left(-ET^{-1}A + C\right) m^T + \left(-ET^{-1}B + D\right) p_1^T = 0 \tag{4}$$

After obtaining by (3) (4) the redundant vectors (p_1, p_2), codeword $X = [m\ p_1\ p_2]$ can be obtained by adding the information vector m to complete the entire approximate lower triangular LDPC encoding process.

$$p_1^T = -\psi^{-1}\left(-ET^{-1}A + C\right) m^T \tag{5}$$

$$p_2^T = -T^{-1}\left(Am^T + Bp_1^T\right) \tag{6}$$

3. REALIZATION OF APPROXIMATE LOWER TRIANGULAR LDPC ENCODING IN FPGA

3.1. Tranforming Processes of the Approximate Lower Triangular Regular Parity Check Matrix

On the SDR platform of NI LabVIEW 5641R FPGA, we transform the original given weight (3, 6) parity check matrix into a weight (3, 6) approximate lower triangular regular parity check matrix to implement the LDPC encoding circuit. The number of row and column and parameter g of the approximate lower triangular matrix are $N = 12$, $M = 6$ and $g = 2$. The number of "1" in each column of the weight (3, 6) approximate lower triangular regular parity check matrix is fixed to 3, and 6 in each row. The weight (3, 6) approximate lower triangular regular matrix is divided into six sub-matrix of A, B, C, D, T, D, E (as shown in Fig. 3).

1	1	1	0	0	1	1	0	0	0	1	0
1	1	1	1	1	0	0	0	0	0	0	1
0	0	0	0	0	1	1	1	0	1	1	1
1	0	0	1	0	0	0	1	1	1	0	1
0	1	0	1	1	0	1	1	1	0	0	0
0	0	1	0	1	1	0	0	1	1	1	0

Figure 3: The original given weight (3, 6) parity check matrix.

The original given weight (3, 6) parity check matrix is converted into weight (3, 6) approximate lower triangular regular parity check matrix in the following four steps:

Step1: Rearranging the sequence of column into 1, 2, 3, 4, 5, 6, 7, 10, 11, 12, 8, 9, so as to transform the diagonal terms of the matrix T into "1".

1	1	1	0	0	1	1	0	**1**	0	0	0
1	1	1	1	1	0	0	0	0	**1**	0	0
0	0	0	0	0	1	1	1	1	1	**1**	0
1	0	0	1	0	0	0	1	0	1	1	**1**
0	1	0	1	1	0	1	0	0	0	1	1
0	0	1	0	1	1	0	1	1	0	0	1

Figure 4: Transforming the diagonal terms of the matrix T into “1”.

1	1	1	0	0	1	1	0	1	0	0	0
1	1	1	1	1	0	0	0	0	1	0	0
0	0	0	0	0	1	1	1	1	1	1	0
1	0	0	1	0	0	0	1	0	1	1	1
0	0	1	1	0	0	**1**	**1**	0	0	0	0
1	0	1	1	1	0	**1**	**1**	0	0	0	0

Figure 5: Simplified the check matrix with the Gaussian elimination scheme.

Step2: Using the Gaussian elimination to convert the upper check matrix H into the lower one with some modifications of the matrix C, D, E.

Step3: Define $\psi = -ET^{-1}B + D$. Interchange column 5 with column 8 of matrix D. So that matrix ψ become reversible.

1	1	1	0	0	1	1	0	1	0	0	0
1	1	1	1	1	0	0	0	0	1	0	0
0	0	0	0	0	1	1	1	1	1	1	0
1	0	0	1	0	0	0	1	0	1	1	1
0	0	1	1	0	0	**1**	**0**	0	0	0	0
1	0	1	1	1	0	**1**	**1**	0	0	0	0

Figure 6: Confirming the matrix is reversible.

Step4: Converting the upper check matrix H into a weight (3, 6) approximate lower triangular regular parity check matrix by rearranging the column into 1, 2, 3, 4, 10, 6, 7, 5, 11, 12, 8, 9.

1	1	1	0	0	1	1	0	1	0	0	0
1	1	1	1	0	0	0	1	0	1	0	0
0	0	0	0	1	1	1	0	1	1	1	0
1	0	0	1	1	0	0	0	0	1	1	1
0	1	0	1	0	0	1	1	0	0	1	1
0	0	1	0	1	1	0	1	1	0	0	1

Figure 7: Weight (3, 6) approximate lower triangular parity check matrix.

In the 5641R FPGA card, several Sub-VI programs are written to solve the redundant vectors p_1, p_2. First, the check matrix H is cut into 6 block matrices. Then, according to (5), p_1^T is disintegrated into three Sub-VI programs of Am^T, $ET^{-1}Am^T$, Cm^T. Multiply the Sub-VI programs of Cm^T and $ET^{-1}Am^T$ with $-\psi^{-1}$ to complete the p_1^T circuit (as shown in Fig. 8). Input p_1^T into (6), by multiplying the two Sub-VI programs of Am^T, $B\ p_1^T$ with $-T^{-1}$, the p_2^T circuit can be obtained (as shown in Fig. 9).

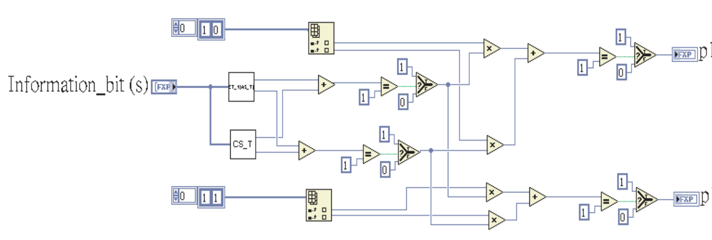

Figure 8: Redundant vector p_1^T circuit diagram.

Since the p_1, p_2 calculation process is considerably complex; circuits of p_1^T, p_2^T are set as Sub-VI programs for simplification. Finally, by adding the transparent information vector m, the encoding systematic codeword X can be obtained (as shown in Fig. 10).

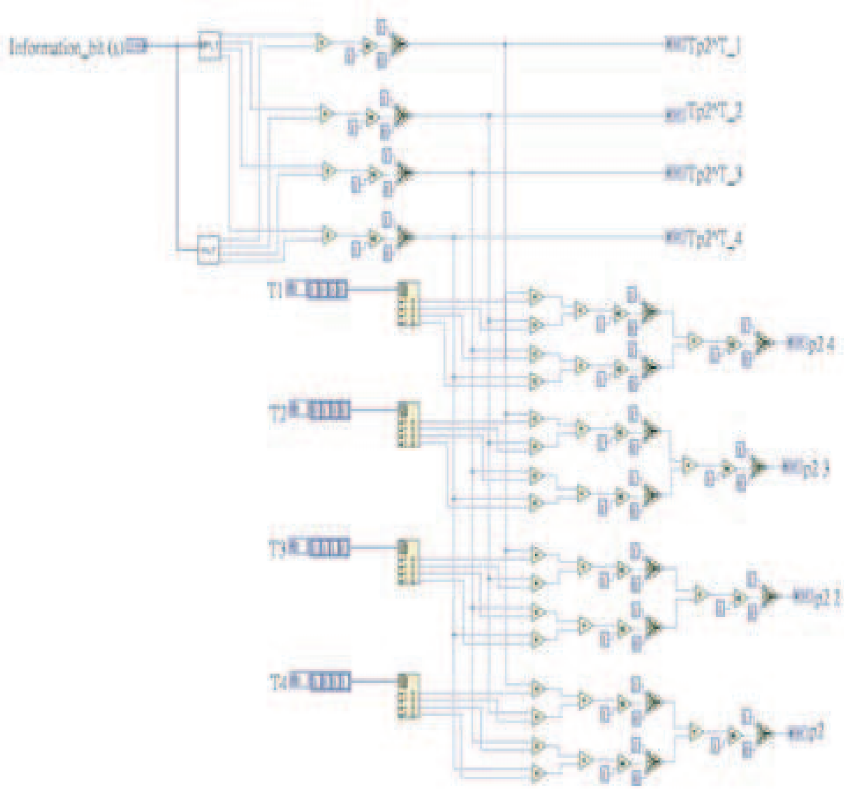

Figure 9: Redundant vector p_2^T circuit diagram.

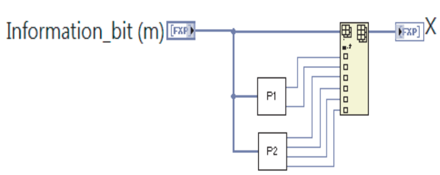

Figure 10: Approximate lower triangular LDPC encoding circuit diagram.

Element	number
Adders/Subtractors	172
Counters	6
Registers	668
Latches	3
Comparators	175
Multiplexers	2
Tristates	89
Xors	8

Figure 11: Circuit elements of LDPC encoder.

3.2. Circuit Elements of LDPC Encoder

There are eight circuit elements used in the weight (3, 6) approximate lower triangular regular parity check matrix, (as shown in Fig. 11): Add/Subtractors for adding and subtracting processes; Counters for counting process; Registers for saving bit information of Flip-Flop logical gates in processing; Latches for saving hard bit information of the digital circuit; Comparators including 2-bit equal, 4-bit greatequal, 4-bit less, 4-bit lessequal; 16-bit 6 to 1 multiplexers; Tristates for saving buffer information; and one-bit XOR.

3.3. Hardware Verification of the LDPC Encoding Circuit

The hardware verification of the LDPC encoding circuit can be realized by the operation of the equation $HX^T = 0$. The random generated codeword X is transposed and multiplied with the weight (3, 6) approximate lower triangular regular parity check matrix. It indicates that there are some errors exist, if HX^T is nonzero.

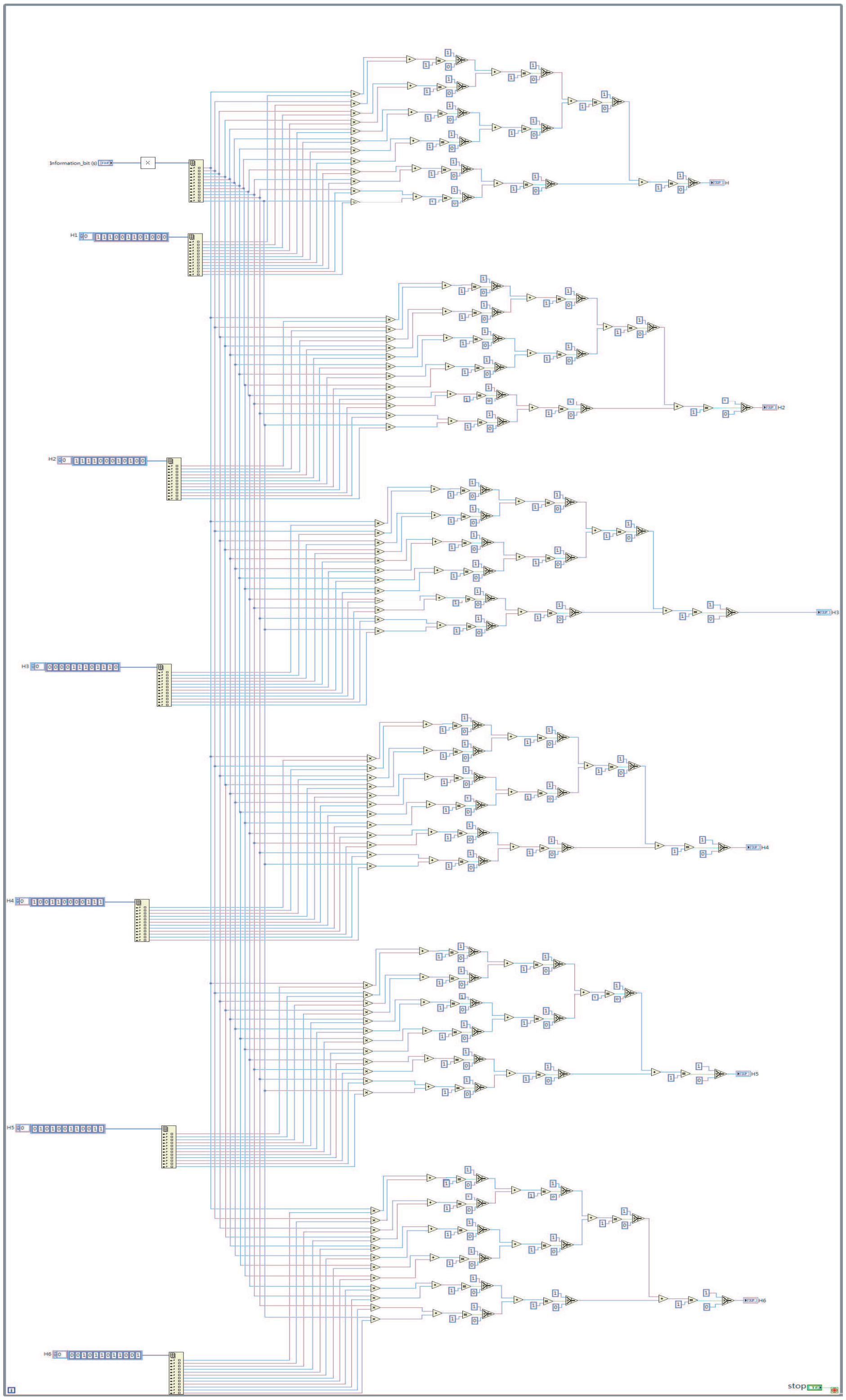

Figure 12: Approximate lower triangular LDPC encoding circuit diagram.

4. CONCLUSIONS

LabVIEW FPGA is a programming language that directly builds programming codes in hardware. In addition to saving complex detail to speed up design process, it can design all pulse periods by programming according to functional needs. On this SDR platform, we completed the approximate lower triangular LDPC encoding circuit and used the orthogonal characteristic of $HX^T = 0$ to verify the accuracy of encoding programs. LDPC is based on Message Passing Algorithm (MPA) [8] to decode. In the near future, we will use the programming decoding circuits of three commonly used LDPC decoding algorithms including Sum-of-Product Algorithm (SPA), Minimum-Sum Algorithm (MSA), Normalized Min-Sum Algorithm (NMSA) [9–11], with additional white Gaussian noise channel (AWGN Channel), BPSK Modulation [12] and decoding hardware verification as well as LDPC code error performance on 5641R FPGA card of NI SDR system will be conducted.

REFERENCES

1. SDR Forum website, http://www.sdrforum.org.
2. Shannon, C. E., "A mathematical theory of communication," *Bell Syst. Tech. J.*, 379–423 (Part1), 623–56 (Part2), Jul. 1948.
3. Gallager, R. G., "Low-density parity-check codes," *IRE Trans. Inform. Theroy*, 21–28, Jan. 1962.
4. Sklar, B., "Digital communications: Fundamentals and applications 2/E," 349–362, Taiwan Pearson Education Corporation, Sep. 2004.
5. MacKay, D. J. C., S. T. Wilson, and M. C. Davey, "Comparison of constructions of irregular Gallager codes," *IRE Trans. Inform. Theroy*, 220–229, Oct. 1999.
6. Richardson, T. J. and R. Urbanke, "Efficient encoding of low-density parity-check codes," *IEEE Trans. Inform. Theory*, Vol. 47, No. 2, 638–656, 2001.
7. Pei, Z., Z. Shi, and C. Wang, *Modern Coding Theory and Application*, 237–244, National Defence Industry Press, Beijing, Jan. 2007.
8. Kschischang, F. R. and B. J. Frey, "Iterative decodeing of compound codeds by probability propagation in graphical models," *IEEE Journal on Selected Areas in Communications*, Vol. 16, 219–230, Feb. 1998.
9. Kschischang, F. R., B. J. Frey, and H.-A. Loeliger, "Factor graphs and the sum-product algorithm," *IEEE Trans. Inform. Theory*, Vol. 47, 498–519, Feb. 2001.
10. Fossocier, M., M. Mihaljecvic, and H. Imai, "Reduced complexity iterative decoding of low-density parity check codes based on belief propagation," *IEEE Trans. on Commun.*, Vol. 47, No. 5, 673–680, May 1999.
11. Chen, J. and M. P. C. Fossorier, "Near-optimum universal belief propagation based decoding of low-density parity check codes," *IEEE Trans. Commun.*, Vol. 50, No. 3, 406–414, Mar. 2002.
12. Rappaport, T. S., *Wireless Communications: Principles and Practice,* 294–308, Prentice-Hall, Inc., 2002.

A Novel Function Tuner with Microstrip Circuit for Slot Patch Antenna

Chia-Ching Chu[1], **Lih-Shan Chen**[1], **Hsien-Chiao Teng**[3], **and Shen Cherng**[2]

[1]Department of Electronic Engineering, I-Shou University, Taiwan, R.O.C.
[2]Computer Science and information Engineering, Chengshiu University, Taiwan, R.O.C.
[3]Department of Electrical Engineering, ROC Military Academy, Taiwan, R.O.C.

Abstract— This paper presents a design of microstrip functional tuner for slot patch antenna. It consists of a SMA-connector and an adjustable microstrip circuit. The implemented antenna was excited through a T-shape feed line being coupled to the rectangular patch. The operation frequency is designed at 2.6 GHz. The connector is embedded to the rectangular patch being connected to the function tuner to control the impedance bandwidth of the proposed antenna. In this study, the impedance bandwidth of the proposed antenna can be simply controlled by adding resister on to the microstrip circuit. The impedance bandwidth of the proposed antenna without circuit loading was designed at 3.4%. If the circuit loading of $75\,\Omega$ was added, the impedance bandwidth of the proposed antenna would increase to 11.4%. If the circuit loading is changed to $50\,\Omega$ and $25\,\Omega$, the impedance bandwidth of the proposed antenna would be shifted to 14.3% and 20.8% respectively. The equivalent circuit simulated by ADS for our designed functional tuner is demonstrated. The calculated and experimental results confirmed that our proposed functional tuner embedded onto the implemented antenna has good performance.

1. INTRODUCTION

Microstrip antenna has been with advantages of low profile, low cost and easy integration to the microstrip circuits [1]. But, its major disadvantage is the low bandwidth [2]. Microstrip antenna with wide bandwidth has been used very often in wireless-LNA, Bluetooth and video-interface [3]. During earlier periods, the method of the modifying bandwidth was to create several resonance structures into one antenna [4]. However, the size of antenna should be increased. The previous designs for antenna's bandwidth included adding more layers to antenna [5], being changed dielectric constant of substrate [6, 7], modifying probe feed structure [8, 9] and being printed the slot to the radiator [10–12] etc.. Recently, microstrip antenna with the parasitic circuit increasing bandwidth has also been discussed [13]. The typical design for parasitic circuits included using of metal wire, metal plane [14] and adding slot to the ground [15] to increase the bandwidth of microstrip antenna as well as by adding the parasitic circuits for handheld products. In this study, we provided an effective design for the bandwidth of antenna by using of a microstrip functional tuner. The bandwidth of antenna can be improved to 10% at VSWR 2 : 1 by changing of the circuit loading. In addition, the equivalent circuit of microstrip antenna has been demonstrated through the simulation software ADS.

2. ANTENNA CONFIGURATION

In Figure 1(a), it is shown the geometry structure of the proposed antenna, which is implemented on the FR4 substrate ($\varepsilon_r = 4.4$) with the overall size of $69.5 \times 51 \times 1.6\,\text{mm}^3$. A slot $l_1 \times w_1$ and a rectangular plane $l_4 \times w_4$ being gap-coupled by S were printed on the ground. T-shape feed line consists of a microstrip line l_5 of $50\,\Omega$ impedance matching and a rectangular microstrip line $l_2 \times w_2$. The microstrip functional tuner was connected to the rectangular plane $l_3 \times w_3$ through a connector. The proposed antenna is excited through the single probe feed by a SMA connector to originate the signal and to couple with the rectangular plane $l_3 \times w_3$. The operation frequency was designed at 2.6 GHz. Simulation software Ansoft HFSS was used to optimize the parameters of the proposed antenna being listed in Table 1. In Figure 1(b), it is shown the microstrip functional tuner of the proposed antenna. The microstrip functional tuner in Figure 1 was simulated by using of Ansoft HFSS.

3. ANTENNA PERFORMANCES

The return loss and the voltage standing wave ratio (VSWR) for the proposed antenna are shown in Figures 2(a) and 2(b). The calculation results of bandwidth of the proposed antenna was demonstrated 3.4% at $R = 0\,\Omega$. The bandwidth of the proposed antenna can be improved to 11.4%

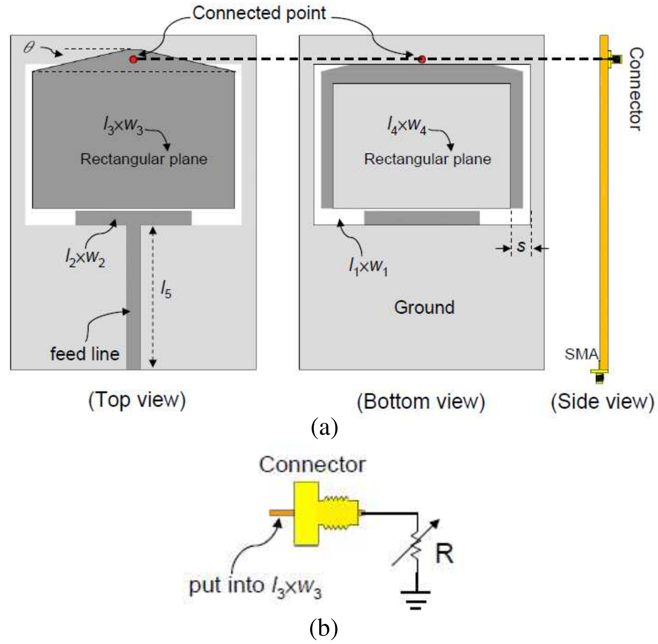

Figure 1: (a) Geometry of the proposed antenna, (b) simulated structure of microstrip functional tuner (by Ansoft HFSS).

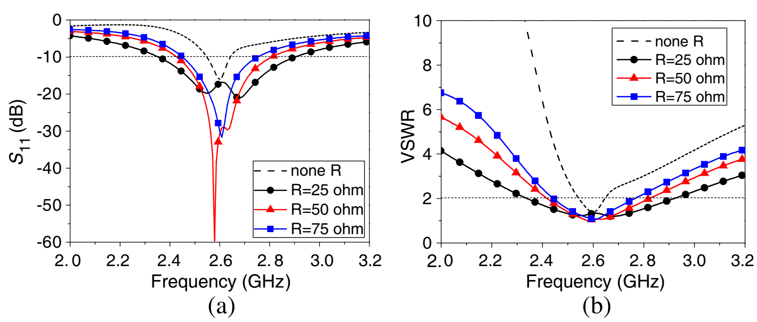

Figure 2: Simulation analysis of the proposed antenna. (a) Return loss, (b) VSWR.

Table 1: Parameters of the antenna structure.

Parameters	Size	Parameters	Size
$l_1 \times w_1$	$33.5 \times 45\,\mathrm{mm}^2$	$l_4 \times w_4$	$26 \times 37\,\mathrm{mm}^2$
$l_2 \times w_2$	$3 \times 24\,\mathrm{mm}^2$	l_5	$30\,\mathrm{mm}$
$l_3 \times w_3$	$28.5 \times 42\,\mathrm{mm}^2$	S, θ	$3.5\,\mathrm{mm}$, $13°$

Table 2: The bandwidths of the proposed antenna.

Resistors [Ω]	S_{11} [dB]	Bandwidths [%]
0	−16	3.4
25	−17	20.8
50	−30.36	14.3
75	−30.42	11.4

at $R = 75\,\Omega$. When the resistances were $50\,\Omega$ and $25\,\Omega$ respectively, the bandwidth of the proposed antenna can be adjusted to 14.3% as well as 20.8%.

The equivalent circuit of microstrip antenna was calculated by using of Smith Chart tool in the software ADS. In this study, it includes three parts to analyze the equivalent circuit. Part 1 is the equivalent circuit of proposed antenna without the functional tuner. Part 2 is the equivalent circuit of proposed antenna with the functional tuner. Part 3 is the calculated equivalent circuit.

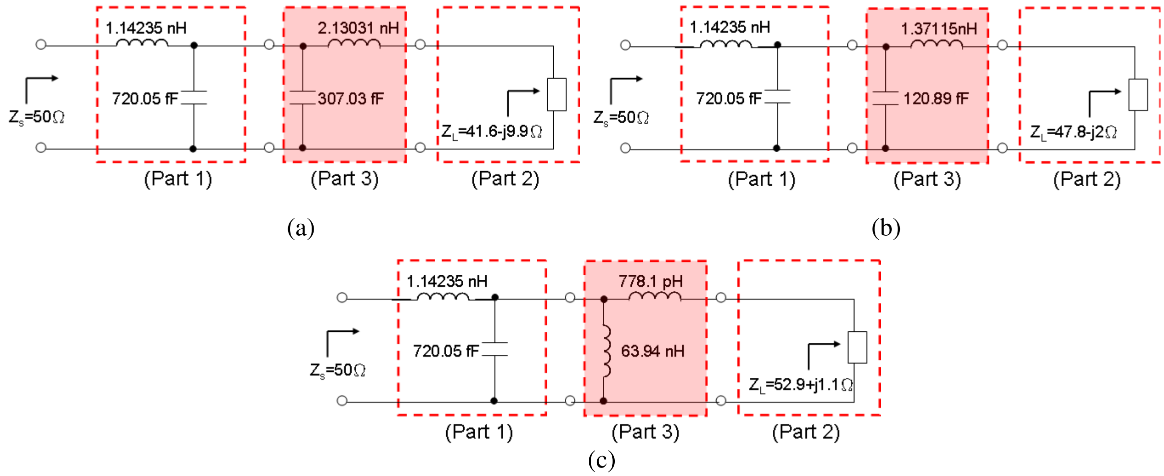

Figure 3: Equivalent circuits of the proposed antenna with circuit loading at (a) $R = 25\,\Omega$, (b) $R = 50\,\Omega$, (c) $R = 75\,\Omega$.

In Figures 3(a), 3(b) and 3(c), the equivalent circuits of the proposed antenna for adding functional tuner with different resistances are demonstrated. As in figures, when $R = 75\,\Omega$, the calculated equivalent circuit is the parallel circuit of two inductors. In contrary, when $R = 25\,\Omega$ and $R = 50\,\Omega$, the calculated equivalent circuit consists of a series inductor and a parallel capacitor. Therefore, the improved performance of the bandwidth at $R = 25\,\Omega$ is more better than $R = 75\,\Omega$ and $R = 50\,\Omega$.

4. CONCLUSION

This study is presented a novel slot patch antenna design and implication with the functional microstrip tuner by using of circuit loading to improve the bandwidth. The functional microstrip tuner can be analyzed as parasitic circuits. The bandwidth of the proposed antenna can be modified by adding of the functional microstrip tuner with the different circuit loadings. The calculated results confirmed that our proposed antenna has good performance.

REFERENCES

1. Türker, N., F. Güneş, and T. Yildirim "Artificial neural design of microstrip antennas," *Turk. J. Elec. Eng. & Comp. Sci.*, Vol. 14, No. 3, 2006.
2. Khodae, G. F., J. Nourinia, and C. Ghobadi, "A practical miniaturized U-slot patch antenna with enhanced bandwidth," *Progress In Electromagnetics Research B*, Vol. 3, 47–62, 2008.
3. Wang, S., H. W. Lai, K. K. So, K. B. Ng, Q. Xue, and G. Liao, "Wideband shorted patch antenna with a modified half U-slot," *IEEE Antennas and Wireless Propagation Letters*, Vol. 11, 689–692, 2012.
4. Abdelaziz, A. A., "Bandwidth enhansment of microstrip antenna," *Progress In Electromagnetics Research*, Vol. 63, 311–317, 2006.
5. Przesmycki, R., M. Bugaj, L. Nowosielski, and M. Wnuk, "Wideband multilayer microstrip antenna: Optimization of dielectric parameters on antenna bandwidth," *SBMO/IEEE MTT-S International Microwave and Optoelectronics Conference (IMOC)*, 217–220, Natal, Brazil, November 2011.
6. Zhang, L. X., Q. Zhang, and C. F. Hu, "The influence of dielectric constant on bandwidth of U-notch microstrip patch antenna," *IEEE International Conference on Ultra-Wideband (ICUWB)*, 1–4, Nanjing, China, September 2010.
7. Ahmed, O. M. H., A. R. Sebak, and T. A. Denidni, "Size reduction and bandwidth enhancement of a UWB hybrid dielectric resonator antenna for short-range wireless communications," *Progress In Electromagnetics Research Letters*, Vol. 19, 19–30, 2010.
8. Gujral, M., J. L.-W. Li, T. Yuan, and C.-W. Qiu, "Bandwidth improvement of microstrip antenna array using dummy EBG pattern on feedline," *Progress In Electromagnetics Research*, Vol. 127, 79–92, 2012.
9. Mitra, D., D. Das, and S. R. Bhadra Chaudhuri, "Bandwidth enhancement of microstrip line and CPW-FED asymmetrical slot antennas," *Progress In Electromagnetics Research Letters*, Vol. 32, 69–79, 2012.

10. Liu, X., "Bandwidth-expanded U-slot patch antenna with shorting wall," *International Symposium on Signals Systems and Electronics (ISSSE)*, 1–3, Nanjing, China, September 2010.
11. Kaewchan, B., W. Naktong, and A. Ruengwaree, "T-shape slot in rectangular slot antenna to enlarge bandwidth for broadband communication," *International Symposium on Antennas Propagation and EM Theory (ISAPE)*, 282–285, Guangzhou, China, December 2010.
12. Albooyeh, M., N. Kamjani, and M. Shobeyri, "A novel cross-slot geometry to improve impedance bandwidth of microstrip antennas," *Progress In Electromagnetics Research Letters*, Vol. 4, 63–72, 2008.
13. Ssorin, V., A. Artemenko, A. Sevastyanov, and R. Maslennikov, "Compact bandwidth-optimized two element MIMO antenna system for 2.5–2.7 GHz band," *Proceedings of the 5th European Conference on Antennas and Propagation*, 319–323, Rome, Italy, April 2011.
14. Jiang, X., S. Li, and G. J. Su, "Broadband planar antenna with parasitic radiator," *Electronics Letters*, Vol. 39, No. 23, 2003.
15. Feng, K. P., F. Y. Meng, and R. Z. Liu, "Coupled-fed monopole antenna with a parasitic open slot," *Proceedings of 2011 Cross Strait Quad-Regional Radio Science and Wireless Technology Conference (CSQRWC 2011)*, 523–526, Harbin, Heilongjiang, China, July 2011.

A Novel Design of Reconfigurable Annular Slot Active Patch Antenna

Yu-Ming Lee[1], **Shen Cherng**[2], **Hsien-Chiao Teng**[3], **and Shuming T. Wang**[1]

[1]Department of Electrical Engineering, I-Shou University, Taiwan, R.O.C.
[2]Computer Science and Information Engineering, Chengshiu University, Taiwan, R.O.C.
[3]Department of Electrical Engineering, ROC Military Academy, Taiwan, R.O.C.

Abstract— This paper presents a novel reconfigurable annular slot structure. The proposed antenna has a functional dual branch microstrip line components being coupled with annular slot to create circular polarized radiation. Two PIN diodes are embedded to the dual branch microstrip line and excited by $V_{dc} = 3\,\mathrm{V}$ and $I_{dc} = 150\,\mathrm{mA}$. Reconfigurable circular polarizations, including linear, right-handed and left-handed polarizations can be simply alternated by shifting the modes of pin-diode. Simulation and experimental results have shown the good impedance bandwidth for return loss and antenna gains in circularly polarized states.

1. INTRODUCTION

Reconfigurable patch antenna with multiple polarizations can optimize the system performance [1–3]. Offering an improved effectiveness in receiving the communication signal and having an exceptional ability of reducing multipath fading were also reported as the advantages for reconfigurable circular polarized states [4, 5]. Wilkinson power divider has been used very often in reconfigurable polarization antenna as tuners to modify the orthogonal radiation modes [6, 7]. The previous designs always would be studied in complicating DC circuit bias and probe feed efficiency [8]. In basic design, an annular slot antenna embedded with a single probe feed structure can always create circularly polarized states for instance, printing of the slot line at locations of 45° and 135° [9], adding of stub (open and short) and annular slot coupled with excite the orthogonal modes [1]. However, controlling the modes of PIN diode to adjust the surface current on radiator can be the alternative way to modify the polarization of the antenna [11]. Embedded the PIN diode into the patch antenna to reconfigure the circularly polarized states was reported before [12]. In this study, we present a novel design to modify circular polarization by using of dual branch microstrip line components being coupled with annular slot. The proposed antenna has two resonant frequencies which were excited by modifying the length of the branch microstrip line. For changing of the characteristic of polarization, two PIN diodes were embedded into the dual branch microstrip line components. The surface current on the radiator patch can thus be adjusted by changing of the operation modes of PIN diode. Moreover, the axial ratio can be adjusted by modifying the size of the notch of the annular slot.

2. ANTENNA CONFIGURATION

In Figure 1(a), it is shown the geometry structure of the proposed antenna, which is implemented on the FR4 substrate ($\varepsilon_r = 4.4$) with the overall size of $55 \times 55 \times 1.6\,\mathrm{mm}^3$. The circular patch with radius of r_1 is printed on the ground of the antenna and coupled the annular slot at radius r_2. The notch of the annular slot with the size of $l_3 \times w_3$ is also printed on the ground. The feed line l_7 was designed to be $50\,\Omega$ impendence matching and being connected to the left branch microstrip line components (l_4, l_2) as well as right branch microstrip line components (l_1, l_5) by using of two PIN diodes. DC bias transmission microstrips ($l_6 \times w_6$) were used to adjust the pin diodes. The proposed antenna is excited through the single probe feed by SMA connector to originate the signal and to couple with the circular patch as well as the annular slot. In order to be able to reconfigure the polarization, PIN diode 1 connects to the left branch components l_4. The PIN diode 2 connects to the right branch components l_5. The operation frequency was designed at 2.4 GHz with impendence bandwidth 20% at $-10\,\mathrm{dB}$ down being shown in Figure 4. Simulation software Ansoft HFSS was used to optimize the parameters of the proposed antenna being listed in Table 1. In Figure 1(b), it is shown the configurable polarizations of the proposed antenna. When the PIN diode 1 is short and PIN diode 2 is open, left hand circular polarization (LHCP) radiation is obtained. In contrary, when the PIN diode 1 is open and PIN diode 2 is short, right hand circular polarization (RHCP) radiation is thus obtained If the two PIN diodes are shorted at the same time,

Table 1: Parameters of the antenna structure.

Parameters	Dimensions	Parameters	Dimensions
$r_1,\ r_2$	12 mm, 15 mm	$l_3 \times w_3$	$2 \times 5\,\text{mm}^2$
$(l_1 = l_2,\ w_1)$	9 mm, 2 mm	$l_6 \times w_6$	$4 \times 0.5\,\text{mm}^2$
$(l_4 = l_5,\ l_7)$	35 mm, 15 mm	w_2	3 mm

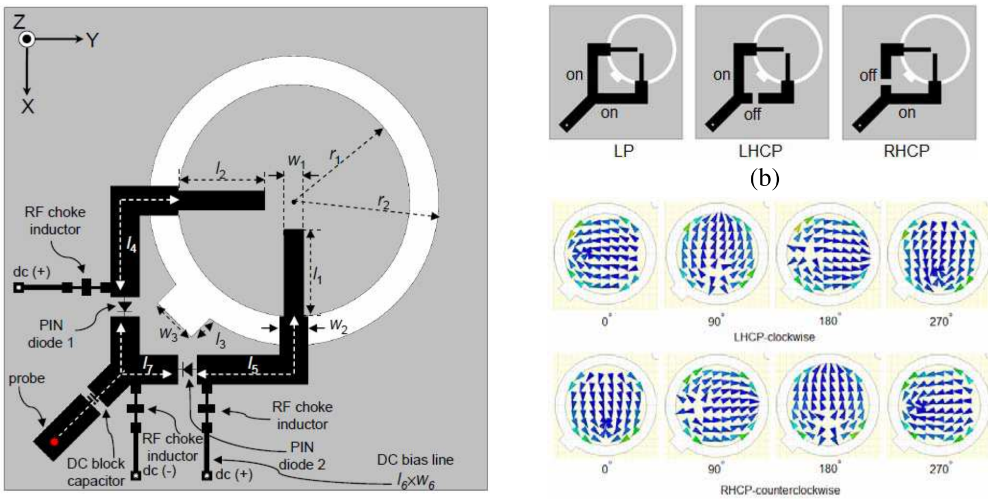

(a) (b) (c)

Figure 1: (a) Geometry of the proposed antenna. (b) Configurable polarizations. (c) Simulated surface currents (by Ansoft HFSS) on the radiator of the proposed antenna.

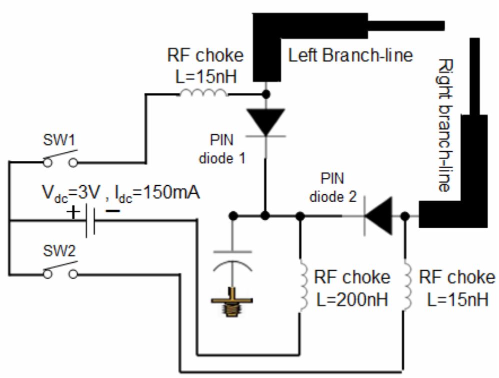

Figure 2: DC bias circuit of the switch.

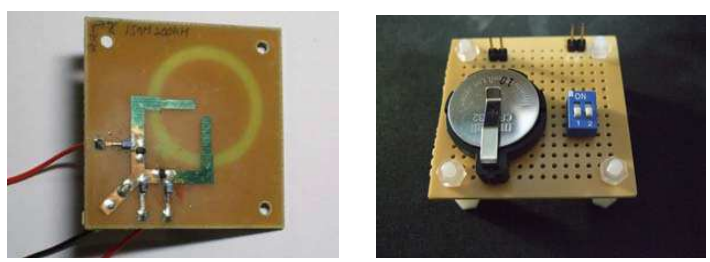

(a) (b)

Figure 3: (a) Prototype of the proposed antenna. (b) Constructed bias switch.

linear polarization is obtained. The calculated current distributions of the proposed antenna are shown in Figure 1(c) to demonstrate the radiation characteristics of circular polarization. If the maximum currents are located at the phase angles of 0°, 90°, 180°, and 270°, the current is flow counterclockwise to produce RHCP radiation. In contrary, the current flows clockwise to produce LHCP radiation.

In Figure 2, it is shown the functional switcher bias circuit and the PIN-diodes with the type of BAR64-04W being used [13]. As in the figure, it consists of three inductors used as RF choke, where the capacitor cab be functioned as DC block to avoid the DC current getting into SMA. Meanwhile, two switches are set for controlling the action of PIN diodes. When the switch 1 is short, diode 1 is short and the antenna is operated as LHCP characterized antenna. In contrary, when the switch 2 is short, diode 2 is short and the antenna is functioned as RHCP characterized antenna. In our design, DC block includes a capacitor ($C = 100\,\text{pF}$) with the impendence of $Z_C = -j0.75\,\Omega$. RF choke includes three inductors, two of them are 15 nH for each and another one is 200 nH being functioned to avoid RF signals getting into DC bias terminal. In this study, the power source is designed as $V_{dc} = 3\,\mathrm{V}$ and $I_{dc} = 150\,\mathrm{mA}$. The R_f is designed $0.85\,\Omega$ to minimize the loss on the microstrip line.

3. MEASUREMENTS AND SIMULATIONS

In Figures 3(a) and 3(b), the complemented antenna and the PIN diodes being designed bias circuit are demonstrated. The return loss of the proposed antenna is shown in Figure 4. The measurements of bandwidths of the proposed antenna are demonstrated 27.9% at LHCP, 30.8% at RHCP and 10.2% at LP. The measurements of the axial ratio and the antenna gains are shown in Figure 5. For the LHCP mode, the measured CP operating bandwidth, referred to 3 dB axial ratio, is 7.1% (150 MHz) with respect to the center frequency 2.11 GHz. As regard of RHCP mode, the CP operating bandwidth is 6.6% (140 MHz) centered at 2.12 GHz. In addition, the antenna gains are measured 3.88 dBi at LHCP, 4.1 dBi at RHCP and 3.89 dBi at LP. Details of the simulation and measurements are listed in Table 2.

In Figures 6(a) and 6(b), radiation patterns for LHCP and RHCP operated at center frequency 2.11 GHz are presented. As in the figures, they all have good performance in the main beam of the Co-polarization. And the level of Cross-polarization is shown to be lower to -20 dB. In Figure 6(c), it is shown the measured radiation pattern for LP which also has good performance in the main beam of the Co-polarization.

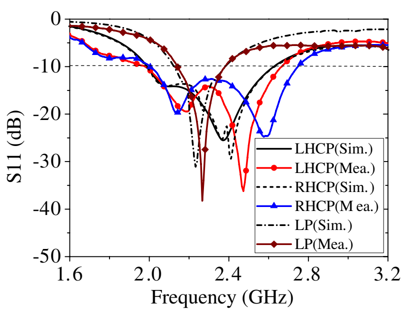

Figure 4: Simulated and measured return loss of the proposed antenna.

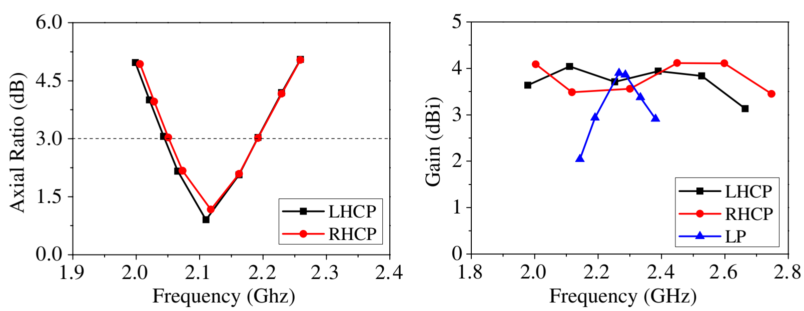

(a) (b)

Figure 5: Measured results of the proposed antenna. (a) Axial ratio. (b) Antenna gain.

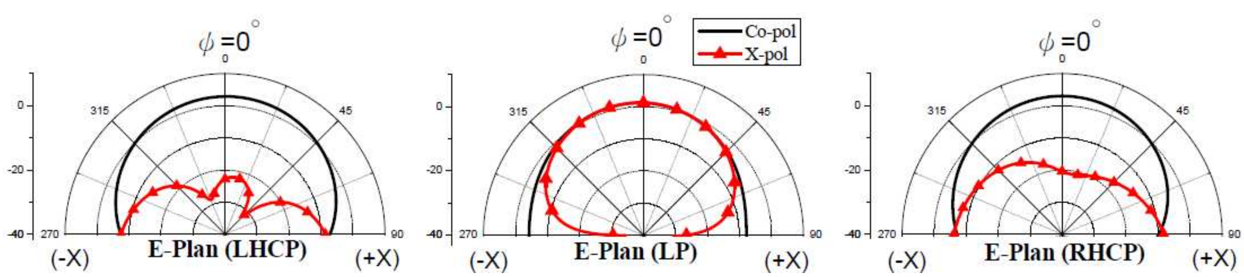

(a) (b) (c)

Figure 6: Measured radiation patterns of the proposed antenna. (a) LHCP state. (b) LP state. (c) RHCP state.

Table 2: Simulations and measurements of proposed antenna.

Polarization	Diode1	Diode2	S_{11} [dB]		Bandwidths [%]		3 dB Axial Ratio Bandwidths [%]	Gain [dBi]
			Sim.	Mea.	Sim.	Mea.		
LHCP	ON	OFF	-24.1	-20.4	26.3	27.9	7.1	3.88
RHCP	OFF	ON	-28.9	-13.7	26.3	30.8	6.6	4.1
LP	ON	ON	-31.1	-38.2	11.2	10.2	N/A	3.89

4. CONCLUSION

This study is presented a novel annular slot active patch antenna design and implication of using single probe feed to reconfigure the polarization. By observing the influence of various parameters on the performance of the antenna, any design parameter significantly affects the characteristic of polarization radiation. The polarization can be reconfigured by PIN diodes switcher bias and two resonant modes were observed by modifying the length of the branch microstrip line. The simulated and measured results confirmed the proposed patch antenna has good performance in different polarization

REFERENCES

1. Chen, R.-H. and J.-S. Row, "Single-fed microstrip patch antenna with switchable polarization," *IEEE Trans. Antennas Propag.*, Vol. 56, No. 4, 922–926, Apr. 2008.
2. Roy, J. S. and M. Thomas, "Design of a circularly polarized microstrip antenna for WLAN," *Progress In Electromagnetics Research M*, Vol. 3, 79–90, 2008.
3. Lin, S.-Y., Y.-C. Lin, and J.-Y. Lee, "T-strip FED patch antenna with reconfigurable polarization," *Progress In Electromagnetics Research Letters*, Vol. 15, 163–173, 2010.
4. Sun, L., B.-H. Sun, J.-Y. Li, Y.-H. Huang, and Q.-Z. Liu, "Reconfigurable circularly polarized microstrip antenna without orthogonal feeding network," *Journal of Electromagnetic Waves and Applications*, Vol. 25, No. 10, 1352–1359, 2011.
5. Kang, W., K. H. Ko, and K. Kim, "A compact beam reconfigurable antenna for symmetric beam switching," *Progress In Electromagnetics Research*, Vol. 129, 1–16, 2012.
6. Mireles, E. and S. K. Sharma, "A broadband microstrip patch antenna fed through vias connected to a 3 dB quadrature branch line coupler for worldwide UHF RFID reader applications," *Proc. IEEE Antennas Propag. Int. Symp.*, 529–532, Jul. 3–8, 2011.
7. Tsai, C.-L., S.-M. Deng, J.-C. Cheng, C.-H. Lin, and K.-W. Liu, "A dual-port antenna for GPS and UWB operations," *Journal of Electromagnetic Waves and Applications*, Vol. 25, Nos. 2–3, 365–377, 2011.
8. Yoon, W.-S., J.-W. Baik, H.-S. Lee, S. Pyo, S.-M. Han, and Y.-S. Kim, "A reconfigurable circularly polarized microstrip antenna with a slotted ground plane," *IET Microw. Antennas Propag.*, Vol. 9, 1161–1164, 2010.
9. Fries, M. K. and R. Vahldieck, "A novel concept for slot coupled circularly polarized patch antenna," *Proc. IEEE Antennas Propag. Soc. Int. Symp.*, Vol. 3, 490–493, 2001.
10. Hsieh, W.-T., T.-H. Chang, and J.-F. Kiang, "Dual-band circularly polarized cavity-backed annular slot antenna for GPS receiver," *IEEE Trans. Antennas Propag.*, Vol. 60, No. 4, 2076–2080, Apr. 2012.
11. Monti, G., L. Corchia, and L. Tarricone, "Patch antenna with reconfigurable polarization," *Progress In Electromagnetics Research C*, Vol. 9, 13–23, 2009.
12. Ali, M. T., M. N. Md Tan, A. R. B. Tharek, M. R. B. Kamarudin, M. F. Jamlos, and R. Sauleau, "A novel reconfigurable planar antenna array (RPAA) with beam steering control," *Progress In Electromagnetics Research B*, Vol. 20, 125–146, 2010.
13. Data sheet of BAR64-04W PIN Diodes, Infineon Technologies.

A Surface-potential Based Compact Model of Gate Capacitance in GaN HEMTs

Jie Wang[1,2], **Lingling Sun**[1,2], **Jun Liu**[1], **and Mingzhu Zhou**[1]

[1]Key Laboratory of RF Circuits and Systems, Ministry of Education, Hangzhou Dianzi University, China
[2]Department of Electrical Engineering, Zhejiang University, China

Abstract— A new surface-potential based compact model of the gate capacitance C_{gg} in GaN HEMTs is presented. The 2-D Poisson equation in the GaN layer included the spontaneous and piezoelectric charge terms is solved to obtain an accurate and continuous physics-based analytic explicit calculation of the surface potential. The proposed surface potential provides the accurate descriptions of accumulation and transitional region, develops consistent and higher order differential current and charge equations. The resulted C_{gg} expressions are given explicitly in close form, which will highly improve the simulation continuity and accuracy.

1. INTRODUCTION

As GaN HEMT devices become more widely used in communication systems, interest has grown in techniques that will allow more accurate models to be produced for these devices, contributing to a shorter design cycle. However, transistor modeling follows transistor development with a certain delay [1]. There are few analytical models available in the literature for GaN HEMTs. At this stage, most researchers focus their work on developing the empirical models [2, 3] and the threshold-voltage based models [4–6]. The empirical models which usually use regional approximations are more difficult to characterize. The threshold-voltage-based models are generally relying more on the smoothing functions and parameters than on the physical approximate expressions. Existing GaN HEMTs models are generally valid only for operation above flat-band. It is desirable to have a simpler and analytically model that is valid in all regions of operation.

In our GaN HEMTs potential-based model for C_{gg}, we incorporate the spontaneous and piezoelectric polarization effects into the source equation of the surface-potential which is computed analytically. The potential-based model offers straightforward insight of the physical layer phenomena, gives continuous equation, and precisely describes the I-V and the C-V characteristics in the whole operation range. The model is physically based in the different working regions and formulated to give reasonable capacitance modeling which is completely smooth, has no discontinuities.

2. DEVICE STRUCTURE

The cross-section view of an $Al_{0.2}Ga_{0.8}N$/GaN HEMT discussed in this paper is shown in Fig. 1. The polarization difference between the two materials induces a positive charge at the $Al_{0.2}Ga_{0.8}N$ /GaN interface which is ten times larger than conventional III-V or II-VI semiconductor compounds. Electrons are attracted by this positive charge, and tend to accumulate at the interface, thus forming a conductive channel. The under-gate energy-band diagram for positive gate bias is shown in Fig. 2.

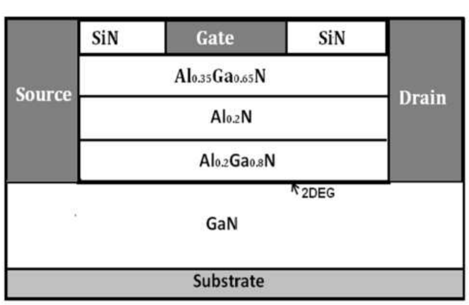

Figure 1: The structure of the $Al_{0.2}Ga_{0.8}N$/GaN HEMT.

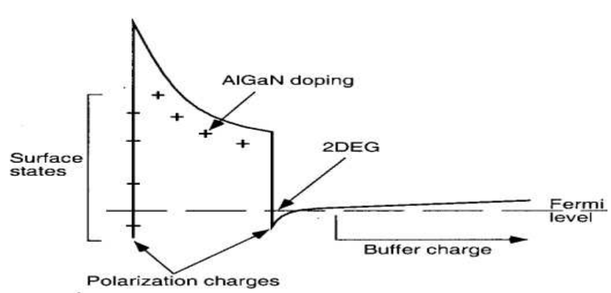

Figure 2: Schematic conduction band diagram for AlGaN/GaN HEMTs.

3. NEW MODEL DESCRIPTION

The surface potential ψ_s analysis of the GaN HEMTs, under the gradual channel approximation, gives (1), as the equation that must be solved for as a function of the voltage applied between the gate and the source V_{gs} and the flat band voltage V_{fs},

$$V_{gs}-V_{fs}-\psi_s(y)=\pm\gamma\sqrt{\begin{array}{l}-\psi_s(y)\cdot[(N_P/N_D^+)+1]+\phi_t\cdot\exp\{[(\psi_s(y)-2\phi_F(y)-V_{cs}(y)]/\phi_t\}\\+\phi_t\cdot\exp[-\psi_s(y)/\phi_t]-\phi_t\cdot\exp\{[(-2\phi_F(y)-V_{cs}(y))]/\phi_t\}-\phi_t\end{array}} \quad (1)$$

where the total polarization charge $N_P(N_P=\sigma/(q\cdot d_{ALGaN}))$ can't be neglect for the 2DEG density of GaN HEMT is much greater for the case. N_D^+ ionized donor density, the Fermi potential Φ_F, the thermal voltage Φ_t, the voltage applied between the channel and the source V_{cs}.

In the Equation (1), γ is the body factor, the positive sign before the square root term in Equation (1) is used for $V_{gs}-V_{fs}>0$ and the negative sign is used for $V_{gs}-V_{fs}<0$ (accumulation). The solution of Equation (1) was initiated [7] using different smoothing functions to connect asymptotic solutions of Equation (1) in neighbor region. We analytically compute the surface potential from accumulation to inversion regions without iterations.

The charge-voltage characteristics are one of the principal entities governing the performance and operation GaN HEMTs. The original work presented simplified formulation applicable when the surface potential satisfies $\psi_s>3\Phi_t$ excluding flat band condition and accumulation region essential in the formulation of the complete model. To remove the $\psi_s>3\Phi_t$ limitation, we modified the expression and present a more complete form.

For this purpose, we introduce the inversion q_i and bulk q_s charges per unit area. The bulk charge model included the accumulation region mobile hole charge in (2), the second term of the square root argument in (3). Three approximate formulations for q_s that are reasonable for ψ_s are

$$q_i=-(V_{gs}-V_{fs}-\psi_s)-q_s \quad (2)$$

where

$$q_s=-\gamma\sqrt{\psi_s-\phi_t\left(1-\exp\left(-\frac{\psi_s}{\phi_t}\right)\right)}\mathrm{sgn}(\psi_s) \quad (3)$$

$$\begin{aligned}q_s&=-\gamma\sqrt{\psi_s-\phi_t} && \text{for } \psi_s>3\Phi_t \quad (4)\\ q_s&=-\gamma\sqrt{\psi_s+\phi_t\left(\exp\left(-\frac{\psi_s}{\phi_t}\right)-1\right)} && \text{for } 0<\psi_s<3\Phi_t\\ q_s&=+\gamma\sqrt{\psi_s+\phi_t\left(\exp\left(-\frac{\psi_s}{\phi_t}\right)-1\right)} && \text{for } \psi_s<0\end{aligned}$$

The formulations (4) lead to closed form, analytic expressions for charges in the GaN HEMTs.

The ψ_m can be calculated from the accurate surface-potential which come from the following equations.

$$(V_{gs}-V_{fs}-\psi_s)^2=\gamma^2[\psi_s-\phi_t+\phi_t\Delta(\psi_s,\xi)] \quad (5)$$

where

$$\begin{aligned}\Delta(\psi_s,\xi)&=\exp\left(\frac{\psi_s-2\psi_f-\xi}{\phi_t}\right) && \psi_s>3\Phi_t\\ \Delta(\psi_s,\xi)&=\exp\left(\frac{\psi_s}{\phi_t}\right) && 0<\psi_s<3\Phi_t,\\ \Delta(\psi_s,\xi)&=\exp\left(\frac{-\psi_s}{\phi_t}\right) && \psi_s<0\\ \Delta(\psi_m,\xi_m)&=\frac{1}{2}[\Delta(\psi_{ss},\xi_s)+\Delta(\psi_{sd},\xi_d)]-\frac{(\psi_{sd}-\psi_{ss})^2}{4\gamma^2\phi_t} \quad (6)\end{aligned}$$

The physical meaning of the terminal charges

$$Q_G=WC_{ox}\int_0^L(V_{gs}-V_{fs}-\psi_s)dy \quad (7)$$

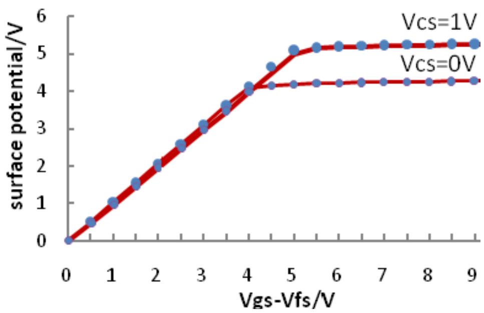

Figure 3: Surface potential computed from Pao Sah implicit model (dots) and our model (lines).

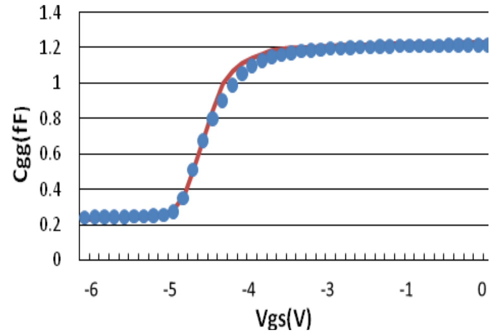

Figure 4: Bias dependence of C_{gg} where TCAD (dots) and our model (line) for $V_{ds} = 1\,\mathrm{V}$.

For a useful operating range the Schottky junction is reverse biased and the AlGaN layer is fully depleted. This makes the system a non-linear capacitor as only displacement current is expected. The displacement current is due to the variation in the 2DEG and the GaN layer charge with V_{gs}. But surface potential-based model can solve this problem for charge-current equation is continuous and differential.

The capacitances is

$$C_{ij} = \partial Q_i / \partial V_j \tag{8}$$

where i and j represent the drain, gate, source is labeled the different terminals.

4. MODEL VERIFICATION AND DKISCUSSION

The Fig. 3 shows a comparison between the ψ_S calculated with our model and the results obtained by the Pao Sah implicit model when $V_{cs} = 0\,\mathrm{V}$ and $1\,\mathrm{V}$, which show the feasibility of the surface potential-based compact core model.

A good agreement between our model and the TCAD data for the capacitance C_{gg} is shown in Fig. 4. It can be seen from Fig. 4, that from below but close to V_{fs} the C_{gg} rises sharply with V_{gs}. As V_{gs} is increased well above V_{fs} , the 2DEG charge density does not change much with V_{gs} and the C_{gg} reaches a constant value. When V_{gs} is below V_{fs}, the charge in the doped GaN layer becomes comparable to the 2DEG charge and it also contributes to the C_{gg}.

5. CONCLUSIONS

A physics-based gate-capacitance model for GaN HEMTs is presented. The GaN based device behaviors are excellent simulated in overall region and good match in the critical zones such as the accumulation and the transitional region. The model is in good agreement with TCAD data, which can be used in a physics-based compact model of GaN HEMTs.

ACKNOWLEDGMENT

This work was supported in part by the Major State Basic Research Development Program of China (973 Program) (No. 2010CB327403), Zhejiang Province Key Science and Technology Innovation Team (No. Gk110908002), and the National science foundation of china under Grant No. 61102027.

REFERENCES

1. Curtice, W. R., "Nonlinear modeling of compound semiconductor HEMTs state of the art," *2010 IEEE MTT-S International Microwave Symposium Digest (MTT)*, 1194–1197, 2011.
2. Leckey, J. G., "A scalable X-parameter model for GaAs and GaN FETs," *Microwave Integrated Circuits Conference (EuMIC)*, 13–16, 2011.
3. Agilent Technologies, ICCAP Software Documentation, Agilent Technologies Inc, Palo Alto, CA, 2009.
4. Cao, Y., X. Chen, and G. Wang, "Dynamic behavioral modeling of nonlinear microwave devices using real-time recurrent neural network," *IEEE Trans. Electron Devices*, Vol. 56, No. 5, 1020–1025, 2009.
5. Kumar, S. P., A. Agrawal, and R. Chaujar, "Threshold voltage model for small geometry AlGaN/GaN HEMTs based on analytical solution of 3-D Poisson's equation," *Microelec. J.*, Vol. 38, No. 2, 1013–1015, 2007.

6. Cheng, X., M. Li, et al., "Physics-based compact model for AlGaN/GaN MODFETs with close-formed *I-V* and *C-V* characteristics," *IEEE Trans. Electron Devices*, Vol. 56, No. 12, 2881–2887, 2009.
7. Gildenblat, G., X. Li, W. Wu, et al., "PSP: An advanced surface-potential-based MOSFET model for circuit simulation," *IEEE Trans. Electron Devices*, Vol. 53, No. 9, 1979–1993, 2006.

Electromagnetic Forces in the Curved Octonion Spaces

Zi-Hua Weng
School of Physics and Mechanical & Electrical Engineering
Xiamen University, Xiamen 361005, China

Abstract— J. C. Maxwell was the first to apply the quaternion and vectorial terminology to describe the electromagnetic theory. This method inspires the subsequent scholars to adopt the curved octonion space to study theories of electromagnetic and gravitational fields. In the curved octonion space, the octonion parallel transport and covariant derivation are defined from the concept of octonion orthogonality, and applied to depict simultaneously the physical features of electromagnetic and gravitational fields. The paper studies the field equation, linear momentum, angular momentum, energy-torque, power-force, and continuity equation etc. of electromagnetic and gravitational fields in the curved octonion space. The results reveal that the bending grade of curved octonion space will impact directly some force terms and other physical quantities in the electromagnetic and gravitational fields.

1. INTRODUCTION

In the classical electromagnetic theory, J. C. Maxwell [1] was the first to describe the physical feature of electromagnetic field with the quaternion [2]. In the theory of curved four-dimensional space-time, A. Einstein [3] adopted the tensor theory to depict the property of gravitational field in the curved four-dimensional space-time. The mixture of these two viewpoints arouses the subsequent scholars to introduce the curved quaternion and octonion spaces [4] to study the physics features of electromagnetic field [5] and gravitational field [6] in the curved spaces.

In the curved quaternion space, the scalar part of the power product of quaternion can be written as the space-time interval, and then be considered as the arc length of curved quaternion space further. Introducing the concepts of quaternion parallel transport and quaternion covariant derivation is able to depict the gravitational features in the curved quaternion space, including the gravitational strength, gravitational source, angular momentum, energy, and gravity etc..

Similarly in the curved octonion space [7], the scalar part of the power product of octonion is the space-time interval, and is the arc length of curved octonion space. Introducing the concepts of octonion parallel transport and octonion covariant derivation is able to depict simultaneously the physical features of gravitational and electromagnetic fields in the curved octonion space, including the gravitational strength, gravitational source, electromagnetic strength, electromagnetic source, angular momentum, energy, Lorentz force, Coulomb force, and gravity etc..

The results reveal that the connection coefficient and curvature of the curved octonion space have the influence on the Lorentz force, Coulomb force, and gravity etc., in the gravitational and electromagnetic fields to a certain extent. Contrarily measuring the forces in the strong gravitational and electromagnetic fields is able to determine the deviation amplitude of the curved octonion space relative to the flat octonion space.

2. CURVED QUATERNION SPACE

When the paper applies the differential geometry about the quaternion space to describe the feature of gravitational fields, two crucial factors should be considered mainly. The first point is that the arc length in the quaternion space is able to be written directly as the space-time interval in the physics. The second point is that the equations can be extended directly from the flat quaternion space to the curved quaternion space. According to the viewpoint, it is periphrastic that the scheme adopts the modular as the arc length in the quaternion space.

In the curved quaternion space, the quaternion radius vector is $\mathbb{R}_g(u^0, u^1, u^2, u^3)$, and the tangent frame quaternion is $\{\mathbf{e}_i\}$. The quaternion space-time interval is defined as

$$dR^2 = d\mathbb{R}_g \odot d\mathbb{R}_g = g_{ij} du^i du^j, \tag{1}$$

where the metric coefficient is $g_{ij} = \mathbf{e}_i \odot \mathbf{e}_j$. The tangent frame quaternion is $\mathbf{e}_j = \partial\mathbb{R}_g/\partial u^j$, with $\mathbf{e}_0$ being the scalar. $\odot$ denotes the scalar product of quaternions. $u^0 = ct$, and c is the speed of light, and t represents the time. $i,\ j,\ k,\ m = 0,\ 1,\ 2,\ 3.$

In the flat quaternion space, the quaternion product $\mathbb{G} \circ \mathbb{H}$ of two quaternions, $\mathbb{G}(g^i)$ and $\mathbb{H}(h^j)$, consists of the scalar part $\mathbb{G} \odot \mathbb{H}$ and the vector part $\mathbb{G} \otimes \mathbb{H}$. According to the definition of quaternion orthogonality, $\mathbb{G}$ and $\mathbb{H}$ are on an orthogonal state when $\mathbb{G} \odot \mathbb{H} = 0$. When the scalar part of each quaternion is equal to zero, the quaternions, $\mathbb{G}(g^i)$ and $\mathbb{H}(h^j)$, will be degenerated to the vectors $\mathbb{G}(g^1, g^2, g^3)$ and $\mathbb{H}(h^1, h^2, h^3)$ respectively, and then the quaternion orthogonality is degenerated to the vector orthogonality. $\circ$ denotes the quaternion multiplication.

In case the quaternion degenerates to the complex number, the quaternion orthogonality will degenerate to the 'orthogonality' of complex number. In the rectangular coordinate system, when the scalar part $\mathbb{G} \odot \mathbb{H}$ of the product $\mathbb{G} \circ \mathbb{H}$ of two complex numbers, $\mathbb{G}(g^0, g^1)$ and $\mathbb{H}(h^0, h^1)$, is equal to zero, these two complex numbers are on an 'orthogonal' state. However the angle between the radius vectors about $\mathbb{G}$ and $\mathbb{H}$ is not equal to $90°$ in the rectangular coordinate system. It should be in the oblique coordinates system to comprehend the 'orthogonality' of complex number.

In the planar oblique coordinate system OXY, the angle between the X-axis and Y-axis is α. The complex number $A(x, y)$ can be considered as the radius vector OA through the point of origin O. The angle between OA and the X-axis is θ. The length of OA is r, and its projection on the X-axis is x. The calculation result finds that $x/r = \sin(\alpha - \theta)/\sin\alpha$. Due to $0 \leq |x/r| \leq 1$, we can write that $x/r = \cos\beta$. Obviously when $x = 0$, there is $\sin(\alpha - \theta) = 0$ or $\cos\beta = 0$. This means that the radius vector OA superposes with the Y-axis, and its projection on the X-axis is zero. Therefore the radius vector OA is 'perpendicular' to the X-axis, with $\beta = 90°$. β is called as the intrinsic angle between OA and X-axis.

Similarly the complex numbers, $\mathbb{G}(g^0, g^1)$ and $\mathbb{H}(h^0, h^1)$, can be considered as the radius vectors OG and OH through the point of origin O respectively. And its inner product is written as, $\mathbb{G} \odot \mathbb{H} = |\mathbb{G}||\mathbb{H}|\cos\beta$, with β being the intrinsic angle between OG and OH. When the complex numbers, $\mathbb{G}$ and $\mathbb{H}$, are 'perpendicular' to each other, there is $\mathbb{G} \odot \mathbb{H} = 0$, or $g^0/g^1 = h^1/h^0 = k$, with k being the coefficient.

In the curved quaternion space, the quaternion quantity $\mathbb{A}_1$ in the tangent space $\mathbb{T}_1$ of one point $\mathbb{M}_1$ on the quaternion manifold can be disassembled in the tangent space $\mathbb{T}_2$ of the point $\mathbb{M}_2$ near $\mathbb{M}_1$. According to the definition of quaternion orthogonality, $\mathbb{A}_1$ can be separated into the projection component $\mathbb{A}_2$ in $\mathbb{T}_2$, and the orthogonal component $\mathbb{N}_2$ being perpendicular to $\mathbb{T}_2$. On the basis of the definition of quaternion parallel transport, $\mathbb{A}_2$ is parallel transported from $\mathbb{A}_1$.

For 1 rank contravariant tensor $Y^i(\mathbb{Q})$ of one point $\mathbb{Q}$ in the curved quaternion space, the component of the quaternion covariant derivation with respect to the coordinate u^k is,

$$\nabla_k Y^i = \partial Y^i / \partial u^k + \Gamma^i_{jk} Y^j, \tag{2}$$

where Γ^i_{jk} is the connection coefficient.

The connection coefficient can be expressed by the metric tensor,

$$\Gamma^i_{jk} = (1/2) g^{mi} \left(\partial g_{jm}/\partial u^k + \partial g_{mk}/\partial u^j - \partial g_{kj}/\partial u^m \right) , \tag{3}$$

where $g^{mi} = (g_{mi})^{-1}$.

3. FORCES IN THE GRAVITATIONAL FIELD

In the curved quaternion space, the gravitational potential $\mathbb{A}_g(a^0, a^1, a^2, a^3)$ is,

$$\mathbb{A}_g = \lozenge \circ \mathbb{X}_g = \lozenge \odot \mathbb{X}_g + \lozenge \otimes \mathbb{X}_g, \tag{4}$$

where $\lozenge x^i = \mathbf{e}^k \nabla_k x^i$, with $\mathbf{e}^j = g^{ij}\mathbf{e}_j$. The quaternion quantity $\mathbb{X}_g = x^j \mathbf{e}_j$. The scalar part $\lozenge \odot \mathbb{X}_g$ of $\mathbb{A}_g$ is $a^0 \mathbf{e}_0 = a$, while the vector part $\lozenge \otimes \mathbb{X}_g$ of $\mathbb{A}_g$ is $a^p \mathbf{e}_p = \mathbf{a}$. $p, q = 1, 2, 3$.

The gravitational strength $\mathbb{B}_g(k^0, k^1, k^2, k^3)$ is defined as,

$$\mathbb{B}_g = \lozenge \circ \mathbb{A}_g = \lozenge \odot \mathbb{A}_g + \lozenge \otimes \mathbb{A}_g, \tag{5}$$

where the scalar part of $\mathbb{B}_g$ is $\lozenge \odot \mathbb{A}_g = k^0 \mathbf{e}_0$, and the vector part of $\mathbb{B}_g$ is $\lozenge \otimes \mathbb{A}_g = k^p \mathbf{e}_p$. The gauge equation is chosen as, $k^0 = 0$, in the gravitational field. The vector part of the gravitational strength can be rewritten as, $k^p \mathbf{e}_p = \mathbf{g}/c + \mathbf{b}$. The first part, $\mathbf{g}/c = \nabla_0 \mathbf{a} + \nabla a$, is related with the acceleration, while the second part, $\mathbf{b} = \nabla \times \mathbf{a}$, is relevant to the angular velocity of rotation. $\nabla a = (\mathbf{e}^q \nabla_q) \circ (a^0 \mathbf{e}_0)$. $\nabla \times \mathbf{a} = (\mathbf{e}^q \nabla_q) \otimes (a^p \mathbf{e}_p)$. $\nabla_0 \mathbf{a} = \nabla_0 (a^p \mathbf{e}_p)$. $\nabla = \mathbf{e}^q \nabla_q$.

Table 1: Comparison of some characteristics in the flat and curved spaces.

Term	Euclidian space	Riemannian space	Quaternion space	Octonion space
tangent space	vector space	vector space	quaternion space	octonion space
orthogonality	vector	vector	quaternion	octonion
parallel transport	normal	Levi-Civita	quaternion	octonion
metric	scalar product of vectors	scalar product of vectors	scalar product of quaternions	scalar product of octonions
connection coefficient	Γ^i_{jk}	Γ^i_{jk}	Γ^i_{jk}	Γ^s_{rt}
covariant derivation	$\partial_k A^i$	$\nabla_k A^i$	$\nabla_k A^i$	$\nabla_t A^s$

The gravitational source $\mathbb{S}_g(s^0, s^1, s^2, s^3)$ is written as,

$$-\mu\mathbb{S} = -(\mu_g\mathbb{S}_g - \mathbb{B}^*_g \circ \mathbb{B}_g/c) = (\lozenge + \mathbb{B}_g/c)^* \circ \mathbb{B}_g, \tag{6}$$

or

$$-\mu_g\mathbb{S}_g = \lozenge^* \circ \mathbb{B}_g = \lozenge^* \odot \mathbb{B}_g + \lozenge^* \otimes \mathbb{B}_g, \tag{7}$$

where the scalar part of $\mathbb{S}_g$ is $-\lozenge^* \odot \mathbb{B}_g/\mu_g = s^0\mathbf{e}_0$, and the vector part is $-\lozenge^* \otimes \mathbb{B}_g/\mu_g = s^p\mathbf{e}_p$. μ and μ_g are the coefficients.

The quaternion angular momentum $\mathbb{L}_g(l^0, l^1, l^2, l^3)$ can be defined from the linear momentum,

$$\mathbb{L}_g = (\mathbb{R}_g + k_{rx}\mathbb{X}_g) \circ \mathbb{P}_g = (\mathbb{R}_g + k_{rx}\mathbb{X}_g) \odot \mathbb{P}_g + (\mathbb{R}_g + k_{rx}\mathbb{X}_g) \otimes \mathbb{P}_g \ , \tag{8}$$

where the linear momentum of field source is $\mathbb{P}_g = \mu\mathbb{S}/\mu_g$. The scalar part of $\mathbb{L}_g$ is $(\mathbb{R}_g + k_{rx}\mathbb{X}_g) \odot \mathbb{P}_g = l^0\mathbf{e}_0$, and the vector part of $\mathbb{L}_g$ is $(\mathbb{R}_g + k_{rx}\mathbb{X}_g) \otimes \mathbb{P}_g = l^p\mathbf{e}_p$. When there are several field sources, the accumulated angular momentum will become more complicated.

The quaternion energy-torque $\mathbb{W}_g(w^0, w^1, w^2, w^3)$ is defined as

$$\mathbb{W}_g = c(\lozenge + \mathbb{B}_g/c) \circ \mathbb{L}_g = c(\lozenge + \mathbb{B}_g/c) \odot \mathbb{L}_g + c(\lozenge + \mathbb{B}_g/c) \otimes \mathbb{L}_g, \tag{9}$$

where the scalar part of $\mathbb{W}_g$ is $c(\lozenge + \mathbb{B}_g/c) \odot \mathbb{L}_g = w^0\mathbf{e}_0$, and is relevant to the energy. The vector part of $\mathbb{W}_g$ is $c(\lozenge + \mathbb{B}_g/c) \otimes \mathbb{L}_g = w^p\mathbf{e}_p$, and is related with the torque.

The quaternion power-force $\mathbb{N}_g(n^0, n^1, n^2, n^3)$ is written as

$$\mathbb{N}_g = c(\lozenge + \mathbb{B}_g/c)^* \circ \mathbb{W}_g = c(\lozenge + \mathbb{B}_g/c)^* \odot \mathbb{W}_g + c(\lozenge + \mathbb{B}_g/c)^* \otimes \mathbb{W}_g, \tag{10}$$

where the scalar part of $\mathbb{N}_g$ is $c(\lozenge + \mathbb{B}_g/c)^* \odot \mathbb{W}_g = n^0\mathbf{e}_0$, and is relevant to the power as well as the mass continuity equation. The vector part of $\mathbb{N}_g$ is $c(\lozenge + \mathbb{B}_g/c)^* \otimes \mathbb{W}_g = n^p\mathbf{e}_p$, and is related with the force in the gravitational field.

In the curved quaternion space, the force in the gravitational field is,

$$\mathbf{f} = -\left(n^p\mathbf{e}_p\right)/(2c) \ , \tag{11}$$

where the force $\mathbf{f}$ includes the inertial force, gravity, gradient of energy, and extra force term due to the space bending etc.. The extra force term is dealt with the connection coefficient and curvature etc. of the curved quaternion space.

4. CURVED OCTONION SPACE

In the curved octonion space, the octonion radius vector is $\mathbb{R}(u^i, U^j) = \mathbb{R}_g(u^i) + k_{eg}\mathbb{R}_e(U^j)$. The octonion consists of the quaternion and the S-quaternion. In the quaternion space for the gravitational field, the quaternion radius vector is $\mathbb{R}_g(u^i)$, and the tangent frame quaternion is $\{\mathbf{e}_i\}$. In the S-quaternion space for the electromagnetic field, the S-quaternion radius vector is $\mathbb{R}_e(U^j)$, and the tangent frame S-quaternion is $\{\mathbf{E}_i\}$. The octonion radius vector can be written as $\mathbb{R} = u^s\mathbf{e}_s$, with $u^{j+4} = k_{eg}U^j$ and $\mathbf{e}_{j+4} = \mathbf{E}_j$. $r,\ s,\ t,\ u = 0,\ 1,\ 2,\ 3,\ 4,\ 5,\ 6,\ 7$.

The octonion space-time interval is defined as

$$dR^2 = d\mathbb{R} \odot d\mathbb{R} = g_{rs}du^r du^s \ , \tag{12}$$

where the metric coefficient is $g_{rs} = \mathbf{e}_r \odot \mathbf{e}_s$, the tangent frame octonion is $\mathbf{e}_r = \partial\mathbb{R}/\partial u^r$, with $\mathbf{e}_0$ being the scalar. $\odot$ denotes the scalar product of octonions. $u^0 = ct$, c is the speed of light, and t is the time.

The octonion product $\mathbb{G} \circ \mathbb{H}$ of two octonions, $\mathbb{G}(g^r)$ and $\mathbb{H}(h^s)$, consists of the scalar part $\mathbb{G} \odot \mathbb{H}$ and the vector part $\mathbb{G} \otimes \mathbb{H}$. According to the definition of octonion orthogonality, when $\mathbb{G} \odot \mathbb{H} = 0$, $\mathbb{G}$ and $\mathbb{H}$ are on an orthogonal state. $\circ$ denotes the octonion multiplication.

In the curved octonion space, the octonion quantity $\mathbb{A}_1$ in the tangent space $\mathbb{T}_1$ of one point $\mathbb{M}_1$ on the octonion manifold can be disassembled in the tangent space $\mathbb{T}_2$ of the point $\mathbb{M}_2$ near $\mathbb{M}_1$. According to the definition of octonion orthogonality, $\mathbb{A}_1$ can be separated into the projection part $\mathbb{A}_2$ in $\mathbb{T}_2$ of $\mathbb{M}_2$, and the orthogonal part $\mathbb{N}_2$ being perpendicular to $\mathbb{T}_2$. On the basis of the definition of octonion parallel transport, $\mathbb{A}_2$ is parallel transported from $\mathbb{A}_1$.

For 1 rank contravariant tensor $Y^s(\mathbb{Q})$ of one point $\mathbb{Q}$ in the curved octonion space, the component of the octonion covariant derivation with respect to the coordinate u^t is,

$$\nabla_t Y^s = \partial Y^s/\partial u^t + \Gamma^s_{rt} Y^r \ , \tag{13}$$

where $\Gamma^s_{rt} = (1/2)g^{us}\left(\partial g_{ru}/\partial u^t + \partial g_{ut}/\partial u^r - \partial g_{tr}/\partial u^u\right)$, and $g^{us} = (g_{us})^{-1}$.

5. FORCES IN THE ELECTROMAGNETIC FIELD

In the curved octonion space, the octonion field potential, $\mathbb{A} = \mathbb{A}_g + k_{eg}\mathbb{A}_e$, is defined as

$$\mathbb{A} = \lozenge \circ \mathbb{X} = \lozenge \odot \mathbb{X} + \lozenge \otimes \mathbb{X}, \tag{14}$$

where $\mathbb{A}_e(A^0, A^1, A^2, A^3)$ is the electromagnetic potential. $\lozenge X^p = \mathbf{e}^k \nabla_k X^p$. $\mathbb{X} = \mathbb{X}_g + k_{eg}\mathbb{X}_e$ is the octonion quantity. $\mathbb{X}_e = X^j \mathbf{E}_j$ is the S-quaternion quantity for the electromagnetic field. The 'scalar' part of $\mathbb{A}_e$ is $\lozenge \odot \mathbb{X}_e = A^0\mathbf{E}_0 = \mathbf{A}_q$, while the 'vector' part is $\lozenge \otimes \mathbb{X}_e = A^p\mathbf{E}_p = \mathbf{A}$.

The octonion field strength, $\mathbb{B} = \mathbb{B}_g + k_{eg}\mathbb{B}_e$, is written as,

$$\mathbb{B} = \lozenge \circ \mathbb{A} = \lozenge \odot \mathbb{A} + \lozenge \otimes \mathbb{A} \ , \tag{15}$$

where $\mathbb{B}_e(K^0, K^1, K^2, K^3)$ is the electromagnetic strength. The 'scalar' part of $\mathbb{B}_e$ is $\lozenge \odot \mathbb{A}_e = K^0\mathbf{E}_0$, while the 'vector' part of $\mathbb{B}_e$ is $\lozenge \otimes \mathbb{A}_e = K^p\mathbf{E}_p$. The gauge equation is chosen as, $K^0 = 0$, in the electromagnetic field. The 'vector' part of the electromagnetic strength can be rewritten as, $K^p\mathbf{E}_p = \mathbf{E}/v_0 + \mathbf{B}$. The first part, $\mathbf{E}/v_0 = \nabla_0\mathbf{A} + \nabla \circ \mathbf{A}_q$, is the electric field intensity, while the second part, $\mathbf{B} = \nabla \times \mathbf{A}$, is the magnetic flux density. $\nabla \circ \mathbf{A}_q = (\mathbf{e}^p\nabla_p) \circ (A^0\mathbf{E}_0)$. $\nabla \times \mathbf{A} = (\mathbf{e}^q\nabla_q) \otimes (A^p\mathbf{E}_p)$. $\nabla_0\mathbf{A} = \nabla_0(A^p\mathbf{E}_p)$.

The octonion field source, $\mu\mathbb{S} = \mu_g\mathbb{S}_g + k_{eg}\mu_e\mathbb{S}_e$, is defined as,

$$-\mu\mathbb{S} = -\left(\mu_g\mathbb{S}_g + k_{eg}\mu_e\mathbb{S}_e - \mathbb{B}^* \circ \mathbb{B}/v_0\right) = (\lozenge + \mathbb{B}/v_0)^* \circ \mathbb{B} \ , \tag{16}$$

or

$$\begin{aligned} -\mu_g\mathbb{S}_g &= \lozenge^* \circ \mathbb{B}_g = \lozenge^* \odot \mathbb{B}_g + \lozenge^* \otimes \mathbb{B}_g \ , \\ -\mu_e\mathbb{S}_e &= \lozenge^* \circ \mathbb{B}_e = \lozenge^* \odot \mathbb{B}_e + \lozenge^* \otimes \mathbb{B}_e \ , \end{aligned} \tag{17}$$

where $\mathbb{S}_e(S^0, S^1, S^2, S^3)$ is the electromagnetic source. $-\lozenge^* \odot \mathbb{B}_e/\mu_e = S^0\mathbf{E}_0$ is the 'scalar' part of $\mathbb{S}_e$, while $-\lozenge^* \otimes \mathbb{B}_e/\mu_e = S^p\mathbf{E}_p$ is the 'vector' part of $\mathbb{S}_e$. μ and μ_e are the coefficients.

The octonion angular momentum $\mathbb{L}_g(l^0, l^1, l^2, l^3, L^0, L^1, L^2, L^3)$ can be defined from the linear momentum $\mathbb{P}$,

$$\mathbb{L} = (\mathbb{R} + k_{rx}\mathbb{X}) \circ \mathbb{P} = (\mathbb{R} + k_{rx}\mathbb{X}) \odot \mathbb{P} + (\mathbb{R} + k_{rx}\mathbb{X}) \otimes \mathbb{P} \ , \tag{18}$$

where the linear momentum of field source is $\mathbb{P} = \mu\mathbb{S}/\mu_g$. The scalar part of $\mathbb{L}$ is $(\mathbb{R} + k_{rx}\mathbb{X}) \odot \mathbb{P} = l^0\mathbf{e}_0$, and the vector part of $\mathbb{L}$ is $(\mathbb{R} + k_{rx}\mathbb{X}) \otimes \mathbb{P} = l^p\mathbf{e}_p + L^0\mathbf{E}_0 + L^p\mathbf{E}_p$. For several field sources, the accumulated angular momentum will become more complicated.

The octonion energy-torque $\mathbb{W}(w^0, w^1, w^2, w^3, W^0, W^1, W^2, W^3)$ is defined as

$$\mathbb{W} = c(\lozenge + \mathbb{B}/c) \circ \mathbb{L} = c(\lozenge + \mathbb{B}/c) \odot \mathbb{L} + c(\lozenge + \mathbb{B}/c) \otimes \mathbb{L}, \tag{19}$$

where the scalar part of $\mathbb{W}$ is $c(\lozenge + \mathbb{B}/c) \odot \mathbb{L} = w^0\mathbf{e}_0$, and is relevant to the energy. The vector part of $\mathbb{W}$ is $c(\lozenge + \mathbb{B}/c) \otimes \mathbb{L} = w^p\mathbf{e}_p + W^0\mathbf{E}_0 + W^p\mathbf{E}_p$. The term $w^p\mathbf{e}_p$ is related with the torque.

The octonion power-force $\mathbb{N}_g(n^0, n^1, n^2, n^3, N^0, N^1, N^2, N^3)$ is written as

$$\mathbb{N} = c(\lozenge + \mathbb{B}/c)^* \circ \mathbb{W} = c(\lozenge + \mathbb{B}/c)^* \odot \mathbb{W} + c(\lozenge + \mathbb{B}/c)^* \otimes \mathbb{W}, \tag{20}$$

where the scalar part of $\mathbb{N}$ is $c(\lozenge + \mathbb{B}/c)^* \odot \mathbb{W} = n^0\mathbf{e}_0$, and is relevant to the power. The vector part of $\mathbb{N}$ is $c(\lozenge + \mathbb{B}/c)^* \otimes \mathbb{W} = n^p\mathbf{e}_p + N^0\mathbf{E}_0 + N^p\mathbf{E}_p$. The term $n^p\mathbf{e}_p$ is related with the force in the gravitational and electromagnetic fields. The scalar term $n^0\mathbf{e}_0$ and 'scalar' term $N^0\mathbf{E}_0$ are dealt with the mass continuity equation and current continuity equation respectively.

In the curved octonion space, the force in the gravitational and electromagnetic fields is,

$$\mathbf{f} = -\left(n^p\mathbf{e}_p\right)/(2c), \tag{21}$$

where the force $\mathbf{f}$ includes the inertial force, gravity, gradient of energy, Lorentz force, Coulomb force, and extra force term due to the space bending etc.. The extra force term is dealt with the connection coefficient and curvature etc. of curved octonion space.

6. CONCLUSIONS

In the curved quaternion space, by means of the definitions of the quaternion orthogonality, quaternion parallel transport, and quaternion covariant derivation, the paper deduces the gravitational potential, gravitational strength, linear momentum, angular momentum, power, torque, and force etc. in the gravitational fields. The force includes the inertial force, gravity, and extra force term caused by the quaternion space bending, and so on. The connection coefficient and curvature of the curved quaternion space will impact directly the extra force term.

In the curved octonion space, from the definitions of the octonion orthogonality, octonion parallel transport, and octonion covariant derivation, the paper derives the field potential, field strength, linear momentum, angular momentum, power, torque, and force etc. in the electromagnetic and gravitational fields. The force includes the inertial force, gravity, Lorentz force, and extra force term caused by the octonion space bending, and so on. And the connection coefficient and curvature of the curved S-quaternion space will impact directly the extra force term caused by the S-quaternion space bending.

It should be noted that the research for the forces in the curved octonion space has examined only some simple cases. Despite its preliminary characteristics, this study can clearly indicate that the force terms in the gravitational and electromagnetic fields will be influenced by the curved octonion space. Meanwhile the curved octonion space will result in the extra force terms in the electromagnetic and gravitational fields, in contrast to the flat octonion space.

ACKNOWLEDGMENT

This project was supported partially by the National Natural Science Foundation of China under grant number 60677039.

REFERENCES

1. Maxwell, J. C., *A Treatise on Electricity and Magnetism*, Dover Publications Inc., New York, 1954.
2. Hamilton, W. R., *Elements of Quaternions*, Longmans, Green & Co., London, 1866.
3. Einstein, A., *Relativity: The Special and the General Theory* (A Popular Exposition), 15th Edition, Translated by Robert W. Lawson, Crown Publishers, New York, 1961.
4. Cayley, A., *The Collected Mathematical Papers of Arthur Cayley*, The Cambridge University Press, Cambridge, 1889.
5. Tsagas, C. G., "Electromagnetic fields in curved spacetimes," *Classical and Quantum Gravity*, Vol. 22, No. 2, 393–407, 2005.
6. Beckwith, A., "Octonionic gravity formation, its connections to micro physics," *Open Journal of Microphysics*, Vol. 1, No. 1, 13–18, 2011.
7. Weng, Z.-H., "Electromagnetic and gravitational fields in the curved octonion spaces," *PIERS Proceedings*, 1372–1376, Moscow, Russia, Aug. 19–23, 2012.

Research of Improved Matching Doherty Solid State Power Amplifier

Zheng-Qin Li[1], **Wei-Wei Cheng**[2], **and Yuan-Yuan Wu**[3]

[1]Electronic Engineering Department, School of Information
City College of Wenzhou University, Wenzhou, Zhejiang 325025, China
[2]Institute of Microelectronics and Optoelectronics
Zhejiang University, Hangzhou, Zhejiang 310027, China
[3]College of Information Engineering, Guizhou Minzu University
Guiyang, Guizhou 550025, China

Abstract— This paper makes a detail analysis of the several important parameters of Doherty solid state power amplifier, which focus on the gain flatness, efficiency, power additional efficiency, matching impedance and so on. Then it proposed a method to optimize the matching technology to improve the linearity to balance the amplifiers, and the linearity increases by 5% with the general gain flatness.

1. INTRODUCTION

The power amplifier is an important component of the communication system to send part, in order to adapt to high-volume commercial application based on power amplifier of base station [1, 2], it raises the following requirements: high reliability, which is often the key point of the system; high efficiency, which often occupies the large proportion of the power consumption of the base station; linearity, and the more and more linear power amplifier is in order to avoid distortion of the base station; low cost, and the cost of power amplifier often accounts for a significant proportion of the base station costs; small size, generally occupies a larger portion of the system [3–5].

Because of the abnormal tension of wireless bandwidth, and the new technologies require that much more data is transferred within a very narrow band, it is necessary to adopt the complex modulation scheme, therefore, high demands on the linearity of the power amplifier module must be satisfied. In the most modern modulation techniques such as GSM, WCDMA, TD-SCDMA, the use of non-constant modulus modulation raises rapidly [6]. And the difference between peak value and average value is large. For the sake of meeting the requirements of linearity, it often uses some power back-off method to achieve the enhancement of linearity. With the rollback of the power amplifier, efficiency will be greatly reduced. And the relation between high linearity and high efficiency of the RF power amplifier is conflicting. Furthermore, these two indicators are the focus of the most attention in the RF power amplifier [7]. In fact, because of the important position of RF power amplifiers in base station equipment field, which results in that RF power amplifier becomes a hot industry, extensive research and attention.

2. ANALYSIS OF THE PARAMETERS OF RF POWER AMPLIFIER

The operating bandwidth of the amplifier means of the operating frequency range of the power amplifier to meet the indicators. The actual operating frequency range of the amplifier may be greater than the bandwidth of the defined work [8]. According to their working band width, there are narrow band high frequency power amplifiers and broad band high frequency power amplifier. Output circuit of narrow band high frequency power amplifiers typically is characterized as a frequency-selective filtering, so it is also called a tuned power amplifier or the resonant power amplifier. While the output circuit of broadband high frequency power amplifier output circuit is characterized as transmission line transformer or other broadband matching circuit, so it is also called non-tuned power amplifier.

The gain of the power amplifier is representative of the amplification capability of the amplifier to the input signal, and its expression is,

$$G = 10 \log \frac{\text{output power } (W)}{\text{input power } (W)} \, (\text{dB}) \tag{1}$$

And the power amplifier gain flatness is generally expressed with G, which defines the amount of the change of output amplitude in the amplified signal with the work frequency. It is represented by the difference between the maximum value and minimum value in the operating frequency range (in dB units), which is that the peak — peak value of the output amplitude which changes following the frequency,

$$\Delta G(\text{dB}) = G_{\max\text{output}} - G_{\max\text{output}} \tag{2}$$

Efficiency of power amplifier refers to the efficiency of the DC power transferring into RF power by amplifier. There are two representations in the form: the drain efficiency η and power additional efficiency PAE. And the drain efficiency η is defined as the ratio of the output of the RF power and the DC power consumption. While power additional efficiency is defined as the output RF power minus the input RF power, and then divided by the DC power consumption.

$$\eta = \frac{\text{radio frequency output power}}{\text{consumption of DC power}} \times 100\% \tag{3}$$

$$\text{PAE} = \frac{\text{output power }(W) - \text{input power }(W)}{\text{consumption of DC power }(W)} \times 100\% \tag{4}$$

In fact, power additional efficiency can better reflect the power conversion capacity of the power amplifier. See the Figure 1 about conduction angle.

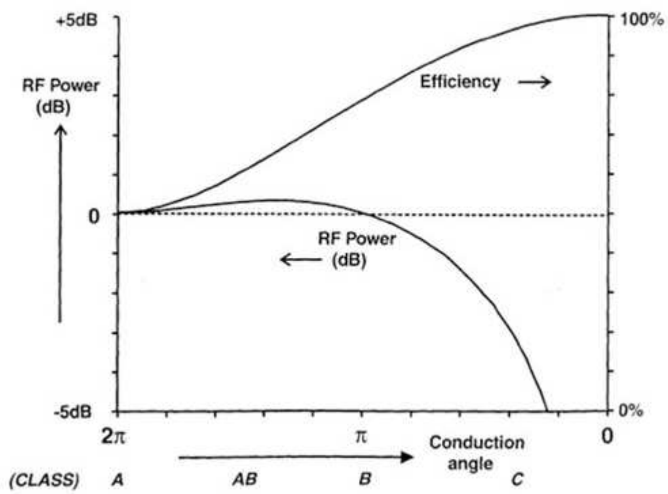

Figure 1: Conduction angle VS RF power.

3. MATCHING OF RF POWER AMPLIFIER IMPEDANCE

Doherty amplifier structure: bridge input splitters or 90 degrees (power distribution into two channels), two amplifier at different bias state (main amplifier and the peak amplifier), delay line, and two 90-degree impedance transformation lines, splitters and the bridge compose in accordance with a certain proportion of the input power distribution. The difference is the phase difference of 90 degrees produced by the bridge.

Concerned of the main amplifier matching to $50\,\Omega$ ohm, the quarter wavelength of the main amplifier output impedance conversion lines, is matched to the characteristic impedance of this transmission line is $R = 50\,\Omega$. When designing output combiner circuit, because of the final output of the Doherty amplifier needs to be matched to the $50\,\Omega$ system, it is required conversion lines at the output end of the impedance, that the length of it is a quarter wavelength, the impedance $R = 35\,\Omega$. See the Figure 2.

Peak amplifier bias affects the peak amplifier output power. In general, for the LDMOS amplifier, if it reduces the bias in the Class C amplifier, the conduction angle becomes low, while the output power is reduced. For the Doherty amplifier, as the same reason, the gate voltage of the peak amplifier is reduced, while the output power will be reduced. Similarly, because the gate voltage is reduced, it requires higher input power to open the peak power amplifier, which will affect the linearity of the amplifier. Before the open of the peak amplifier, the main amplifier's load continues to maintain high impedance, the nonlinearity of the main amplifier deteriorates, and the gate voltage of the peak amplifier deteriorates too, then the linearity of the main amplifier deteriorates.

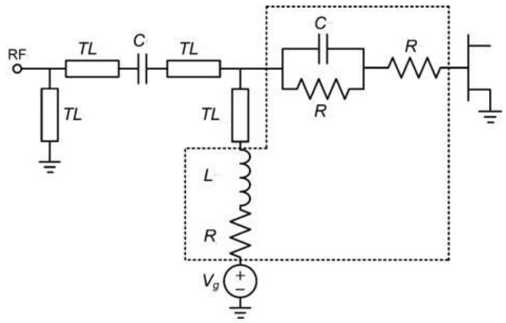

Figure 2: Matching structure of Doherty power amplifier to improve linearity.

4. IMPROVING LINEARITY OF RF POWER AMPLIFIER IMPEDANCE

This phenomenon can be observed in Figure 2. In the region that the input power is less than 32 dBm, the absolute value of IM3 increases with the increase of gate voltage of the peak amplifier, then the linearity increases too. After the peak amplifier open, because of the effect of the gain expansion of the peak power amplifier by the gate voltage of it, which offsets the third order intermodulation, and which is from the main power amplifier to improve the linearity, that it can be verified in Figure 3. In the region that the input power is more than 33 dBm, the decrease of gate voltage increases the absolute value of IM3, and then the linearity improves.

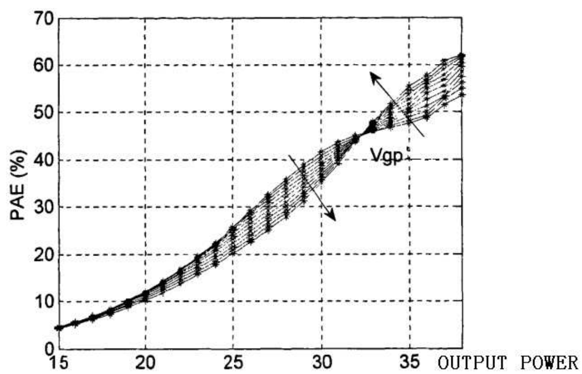

Figure 3: PAE vs. gate voltage of peak amplifier.

Similarly, the peak amplifier gate voltage affects the open of peak amplifier. When the gate voltage of the peak amplifier is low, the load impedance of main amplifier is high, the Doherty amplifier efficiency will be increased, but as the input power increases, the output power capacity of peak amplifier is lower than the output capability of high gate voltage. At this time, it will decrease the efficiency. As it can be seen in Figure 2, the direction shown by the arrow is the direction of increase of the gate voltage of the peak amplifier, when the input power is less than 32 dBm, Doherty amplifier efficiency decreases with the increase of the gate voltage of main amplifier; while the input power is greater than 32 dBm, Doherty amplifier efficiency decreases with the increase of the gate voltage of main amplifier.

5. CONCLUSION

This paper introduces several technologies to improve the linearity of radio frequency power amplifier with some important technical parameters, and give the method to optimize the matching technology to improve the linearity to balance the amplifiers, and the linearity increases by 5% with the general gain flatness.

ACKNOWLEDGMENT

The authors acknowledge support of the fund from the science research project of the department of education of Zhejiang province of China, the number is Y201223915.

REFERENCES

1. Bathich, K., A. Z. Markos, and G. Boeck, "Frequency response analysis and bandwidth extension of the Doherty amplifier," *IEEE Trans. Microwave Theory Tech.*, Vol. 59, No. 4, 934–944, Apr. 2011.
2. Jing, D., W. S. Chan, S. M. Li, and C. W. Li, "New linearization method using interstage second harmonic enhancement," *IEEE Microwave Guided Wave Lett.*, Vol. 8, 402–404, 1998.
3. Bathich, K. and G. Boeck, "Wideband harmonically-tuned GaN Doherty power amplifier," *Proc. 2012 IEEE MTT-S Int. Microwave Symp. Dig.*, 1–3, Jun. 2012.
4. Aitchison, C. S., M. Mbabele, M. R. Moazzam, D. Budimir, and F. Ali, "Improvement of third order intermodulation products of RF and microwave amplifiers by injection," *IEEE MTT Trans. Microwave Theory Tech.*, Vol. 49, 1148–1154, 2001.
5. Sun, G. and R. H. Jansen, "Broadband Doherty power amplifier via real frequency technique," *IEEE Trans. Microwave Theory Tech.*, Vol. 60, No. 1, 99–111, Jan. 2012.
6. Kusunoki, S., K. Kawakami, and T. Hatsugai, "Load-impedance and bias-network dependence of power amplifier with second harmonic injection," *IEEE Trans. Microwave Theory Tech.*, Vol. 52, 2169–2176, 2004.
7. Qureshi, J. H., N. Li, W. C. E. Neo, F. van Rijs, I. Blednov, and L. C. N. de Vreede, "A wide-band 20 W LMOS Doherty power amplifier," *Proc. 2010 IEEE MTT-S Int. Microwave Symp. Dig.*, 1504–1507, May 2010.
8. Males-Ilic, N., B. Milovanovic, and D. Budimir, "Improvement in 'second harmonics' linearization technique for multichannel amplifiers," *Microwave Opt. Technol. Lett.*, Vol. 38, 150–153, 2003.

Research of Doherty Solid State Power Amplifier with Improved Bias Matching

Ming-Hai Xu[1] **and Wei-Wei Cheng**[2]

[1]Electronic Engineering Department, School of Information
City College of Wenzhou University, Wenzhou, Zhejiang 325025, China
[2]Institute of Microelectronics and Optoelectronics
Zhejiang University, Hangzhou, Zhejiang 310027, China

Abstract— This paper makes a detail analysis of the several important ways to improve the efficiency of solid state radio frequency power amplifier, which focus on the power gain, efficiency, power additional efficiency, gate bias matching and so on. Then it proposed a method to optimize the bias technology to improve the linearity to balance the amplifiers, and the linearity increases by 6% with the general gain.

1. INTRODUCTION

Due to modern communications technology WCDMA, CDMA2000, OFDMA adopting high order modulation techniques, it is with high dynamic range and a large PAPR (Peak to average ratio) [1]. An envelope variation signal in order to meet the requirements of a certain linear and a certain communication rate, the amplifier often works in the linear region, thus resulting in low power amplifier efficiency [2]. Power amplifier to enhance the efficiency of the technology: the Kahn envelope separation and recovery technology, envelope tracking technology, LINC, Doherty techniques. Doherty technology compared with several other technologies, the way is relatively simple, the cost is relatively low. Doherty technology and digital pre-distortion technology are widely used in the base station amplifier [3].

2. MODERN HIGH-EFFICIENCY POWER AMPLIFIER TECHNOLOGY

It is the Kahn envelope of separation and recovery techniques. For the modern transmitter of wireless application, the application of the DSP digital processing techniques is easy to make envelope signal and phase modulated signal to be separated. Thus, phase-modulated signal with constant envelope adopts direct or secondary conversion scheme to make the signal convert to the RF frequency of the desired output. The direct conversion scheme includes direct modulation of the base band signal by the phase information to the RF carrier [4].

It is the envelope tracking (ET). The set of electrical grade (drain) of the power amplifier efficiency analysis by the following formula:

$$\eta=\frac{P_1}{P_0}=\frac{1}{2}\frac{I_1}{I_0}\frac{V}{V_{CC}} \tag{1}$$

Envelope tracking technology is very important to the amplifier working in wide dynamic range of the output power, and increasing the efficiency, and the so-called envelope tracking is to improve the DC power supply voltage according to the envelope of the RF signal [5].

It is the LINC technology. The signal component separator separates the input signal into two constant amplitude component of known and equal. As the two component amplitude is known and equal, the amplitude gain and phase shift of the non-linear power amplifier are known and equal, therefore, the two components of the nonlinear power amplifier, only need to be merged after the necessary phase shift correction, then the distortion-free signal can be obtained [6].

3. ANALYSIS OF THE WORK STATE OF RF POWER AMPLIFIER

Since the peak amplifier works in Class C bias region, while the main amplifier works in Class AB state, as well as the main amplifier load impedance is greater than 50 ohms, which is higher than the peak amplifier gain of the main amplifier. In order to study the distribution of input power Doherty amplifier, the main amplifier bias works in Class AB state, the gate voltage is 3.85 V, the peak power amplifier bias works in Class C region, the gate voltage is 3.0 V, the output impedance is of the standard two aliquots of synthetic design.

As shown in Figure 1.

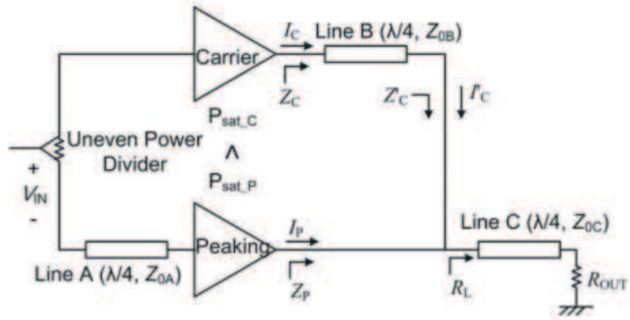

Figure 1: The schematic diagram of the designed DPA.

4. OPTIMIZING THE PEAK AMPLIFIER GATE BIAS TO IMPROVE THE EFFICIENCY OF RF POWER AMPLIFIER

The bias of peak power amplifier affects output power of peak amplifier. Generally, for the LDMOS amplifier, if bias voltage reduces, the conduction angle of amplifier working in C class region becomes low, the output power is reduced. As to Doherty amplifier, the same is true to reduce peak gate voltage of the amplifier resulting in reducing the output power. See the Figure 2 about analysis of the IM3 and IP3 of the Designed DPA under a certain work states.

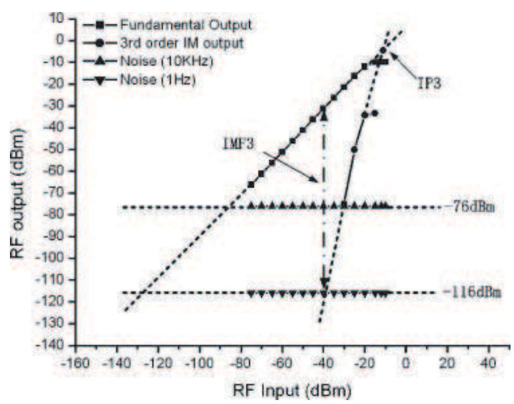

Figure 2: Analysis of the IM3 and IP3 of the designed DPA.

Similarly, because the gate voltage decreases, the need for higher input power is in order to open the peak amplifier, which will affect the linearity of power amplifier. Before the open of the peak amplifier, the main amplifier's load continues to maintain high impedance, and the nonlinear of main amplifier deteriorates, the gate voltage of peak amplifier reduces, and of the linearity of main amplifier deteriorates too.

Figure 3 shows the relation between current and conduction angle of RF power amplifier.

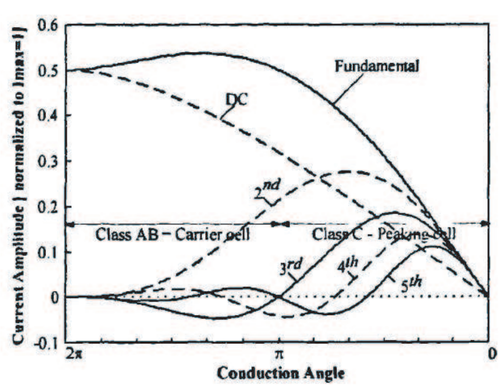

Figure 3: The relation between current and conduction angle of RF power amplifier.

5. CONCLUSION

This paper introduces several technologies to improve the efficiency of radio frequency power amplifier with some important technical ways, and give the method to optimize the bias matching technology to improve the efficiency to increase the current of the amplifiers, and the efficiency increases by 6% with the general gain.

ACKNOWLEDGMENT

The authors acknowledge support of the fund from the science research project of the department of education of Zhejiang Province of China, the number is Y201223915.

REFERENCES

1. Shin, B., J. Cha, J. Kim, Y. Y. Woo, J. Yi, and B. Kim, "Linear power amplifier based on 3-way Doherty amplifier with predistorter," *IEEE MTT-S International Microwave Symposium Digest*, 2027–2030, Fort Worth, TX, 2004.
2. Kang, D., D. Kim, Y. Cho, B. Park, J. Kim, and B. Kim, "Design of bandwidth-enhanced Doherty power amplifiers for handset applications," *IEEE Trans. Microw. Theory Tech.*, Vol. 59, No. 12, 3474–3483, Dec. 2011.
3. Saad, P., C. Fager, H. Cao, H. Zirath, and K. Andersson, "Design of a highly efficient 2–4-GHz octave bandwidth gan-hemt power amplifier," *IEEE Trans. Microw. Theory Tech.*, Vol. 58, No. 7, 1677–1685, Jul. 2010.
4. Braithwaite, R. N. and S. Carichner, "An improved Doherty amplifier using cascaded digital predistortion and digital gate voltage enhancement," *IEEE Trans. Microw. Theory Tech.*, Vol. 57, No. 12, 3118–3126, Dec. 2009.
5. Ogawa, T., T. Iwasaki, H. Maruyama, K. Horiguchy, M. Nakayama, Y. Ikeda, and H. Kurebayashi, "High efficiency feed-forward amplifier using RF predistortion linearizer and the modified Doherty amplifier," *IEEE MTT-S International Microwave Symposium Digest*, 537–540, Fort Worth, TX, 2004.
6. Dawson, D. E., "Closed-form solutions for the design of optimum matching networks," *IEEE Trans. Microw. Theory Tech.*, Vol. 57, No. 1, 121–129, Jan. 2009.

Analysis and Design of the Microstrip Matching for Doherty Amplifier

Ming-Hai Xu[1] **and Sheng-Yun Luo**[2]

[1]Electronic Engineering Department, School of Information
City College of Wenzhou University, Wenzhou, Zhejiang 325025, China
[2]Physical Electronics Lab, Department of Materials Science
Fudan University, Shanghai 200433, China

Abstract— This paper makes a detail analysis of the several important ways to improve the efficiency of RF power amplifier, and analyze the main structure and mechanism of Doherty amplifier, and proposes a microstrip matching way to improve the efficiency and linearity of radio frequency amplifier.

1. INTRODUCTION

The amplifier with Doherty structure can better solve the efficiency of power amplifier in the power back-off, combined with feed-forward and pre-distortion circuit, which can be to do a better balance between linearity and efficiency [1]. The basic principle of the Doherty circuit is that the average portion of the input signal and the peak portion is separately amplified, and then synthesized, so as to obtain high efficiency [2].

The Doherty amplifier includes two parts: a carrier amplifier and a peak amplifier. The linear region of their synthesis input-output characteristic becomes greatly more extended than in the linear region of the single amplifier, thus with ensuring the premise of the signal is in the linear region, it obtains a higher efficiency [3]. The Doherty technology needs to be with other linearization techniques, such as DPD (digital pre-distortion) technology, being used in conjunction with them [4]. When the Doherty technology and DPD technology are used together, then the efficiency is up to 25% or more [5].

2. TECHNOLOGIES TO IMPROVE THE EFFICIENCY OF RF POWER AMPLIFIER

KAHN technique as enveloping separation and recovery techniques is to amplify in the envelope signal and constant RF signal with the information contained respectively, and then synthesizing them to improve the efficiency [6]. See the Figure 1.

The ET (Envelope Tracking) technology is the method which is the use of amplifier power transistors operating in saturation when it's at its high efficiency situation to achieve high efficiency purposes [7].

The LINC technology stands for amplification using nonlinear component. Principle of LINC transmitter is very simple, and the DSP generates two signals which is of independent amplitude and phase modulation, and each signal is of quartered (IQ) format. the IQ modulator produces two separated phase-modulated signals respectively, added to the output power amplifiers of high efficiency. Then at the output end, the amplification of the FM signals are synthesized. Signals

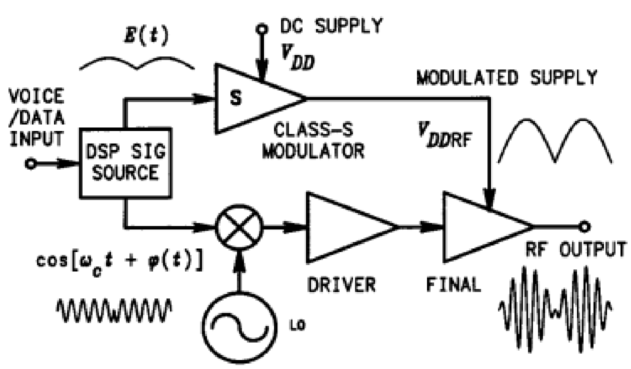

Figure 1: KAHN technique transmitter.

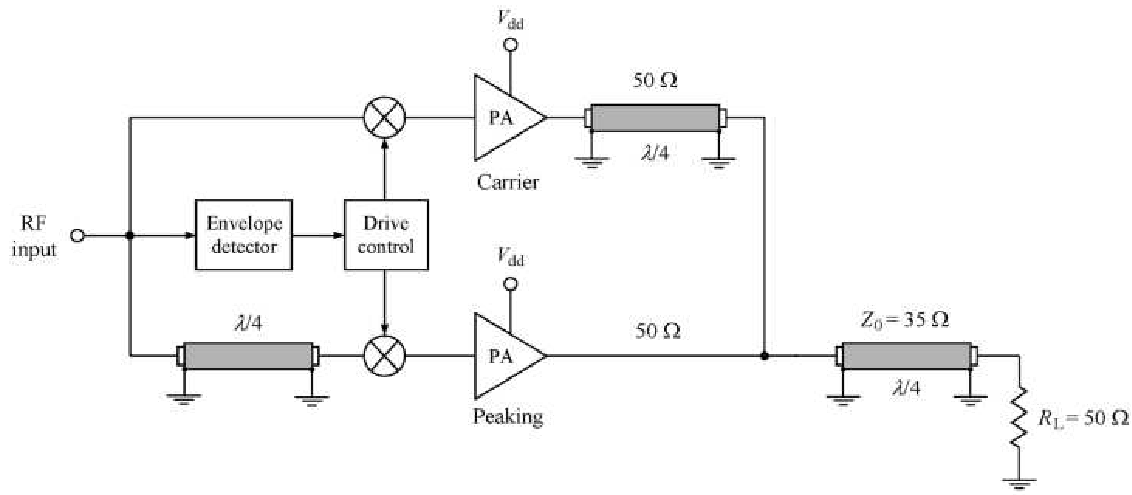

Figure 2: Doherty amplifier architecture with quarter-wave lines.

through the 180 degrees out phase are synthesized to cancel all undesirable distortion, and the both required signals are superimposed. Figure 2 shows the relation between current and conduction angle of RF power amplifier [8].

3. SELECTION OF LDMOS POWER AMPLIFIER

RF power LDMOS power amplifier with its high gain, excellent linearity, and low production costs, is widely used in wireless communication systems.

Compared with the RF power bipolar transistors in RF applications, it has a unique advantage. Its inductance, feedback capacitor and gate impedance are ultra-low, which allows LDMOS transistor can get 7 dB gain improvement applied in dual carrier devices; its power density is high, which includes less transistor package; its efficiency is superior, which reduces power consumption and costs; its source is connected to grounded directly, to enhance power gain and eliminates the demand of isolation from some substances; it optimizes the ultra-low thermal impedance, which can be reduced amplifier size, meet cooling requirements and improve reliability of production; in the GHz frequency bands, its power gain is high, which brings less design steps, easier and more cost-effective design, because of using low-cost, low-power driver transistor; its linearity is superior, which can make the signal pre-correction needs to a minimum demands.

4. ANALYSIS OF DOHERTY POWER AMPLIFIER

With best source impedance and load impedance matched to 50 ohm impedance transformation, Mix and match circuit topology is as microstrip line. Mixed microstrip matching circuit, usually adopts inductive elements with high impedance microstrip line; while capacitive elements are often adopted as lumped parameter tuning capacitors. The microstrip line is the basis of the microwave integrated circuit. It is used to connect the components in microwave integrated circuits. Microstrip

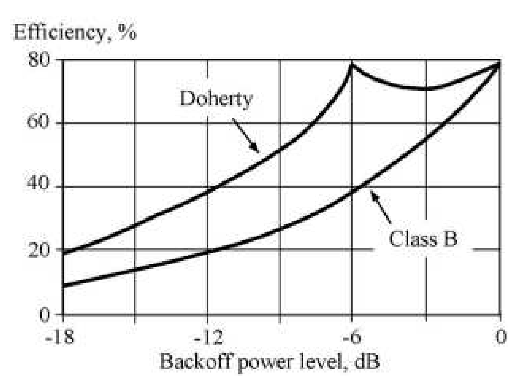

Figure 3: Efficiencies of Doherty amplifier.

line is composed as capacitance, inductance, resonant circuit, filters, impedance switch and power divider passive components. For power amplifiers, microstrip line is used to be the device input, output, and inter-stage matching circuits and power supply circuits, see the Figure 2.

When the power input, the main amplifier starts working, and amplifies the input signal, while the auxiliary amplifier does not work when input power is small, and the work will begin only when the main amplifier is close to saturation. There is a quarter-wavelength line at the output of the auxiliary amplifier, as a role of impedance transformation. At the input of the auxiliary amplifier, there is a quarter-wavelength line, which is used to compensate the output delay of the main amplifier. Two signal branches are combined, and the amplified signal is output via a microstrip line, see Figure 3.

5. CONCLUSION

This paper introduces several important technologies to improve the efficiency of RF power amplifier, and makes an analysis of the main structure and mechanism of Doherty amplifier, and then it proposes a microstrip matching way to improve the efficiency and linearity of radio frequency amplifier.

ACKNOWLEDGMENT

The authors acknowledge support of the fund from the science research project of the department of education of Zhejiang province of China, the number is Y201223915.

REFERENCES

1. Iwamoto, M., A. Williams, P.-F. Chen, A. G. Metzger, L. E. Larson, and P. M. Asbeck, "An extended Doherty amplifier with high efficiency over a wide power range," *IEEE Trans. Microw. Theory Tech.*, Vol. 49, No. 12, 2472–2479, Dec. 2001.
2. Males-Ilic, N., B. Milovanovic, and D. Budimir, "Effective linearization technique for amplifiers operating close to saturation," *Int. J. RF Microwave Comp. Eng.*, Vol. 17, 169–178, 2007.
3. Gustafsson, D., C. M. Andersson, and C. Fager, "A novel wideband and reconfigurable high average efficiency power amplifier," *Proc. 2012 IEEE MTT-S Int. Microwave Symp. Dig.*, 1–3, Jun. 2012.
4. Atanaskovic, A., N. Males-Ilic, and B. Milovanovic, "The suppression of intermodulation products in multichannel amplifiers close to saturation," *Proceedings of the 11th WSEAS International Multiconference CSCC*, 198–201, WSEAS Press 1, Agios Nikolaos, Crete Island, Greece, Jul. 23–28, 2007, http://www.wseas.com.
5. Cripps, S. C., *RF Power Amplifiers for Wireless Communications*, 2nd Edition, Artech House, Norwood, MA, 2006.
6. Chao, K. J., W. J. Kim, J. H. Kim, and S. P. Stapleton, "Linearity optimization of a high power Doherty amplifier based on post-distortion compensation," *IEEE Microwave Wireless Comp. Lett.*, Vol. 15, 748–750, 2005.
7. Staudinger, J., G. Bouisse, and J. Kinney, "High efficiency 450 W asymmetric three-device Doherty amplifier with digital feedback predistortion," *Proc. IEEE Radio Wireless Symp. (RWS)*, 116–119, Jan. 2010.
8. Cho, K. J., J. H. Kim, and S. P. Stapleton, "A highly efficient Doherty feedforward linear power amplifier for W-CDMA base-station applications," *IEEE Trans. Microw. Theory Tech.*, Vol. 53, 292–300, 2005.

A Novel Oscillator Based on Film Bulk Acoustic Resonator

Wei-Wei Cheng[1], **Shu-Rong Dong**[1], **and Sheng-Yun Luo**[2]

[1]Institute of Microelectronics and Optoelectronics
Zhejiang University, Hangzhou, Zhejiang 310027, China
[2]Physical Electronics Lab, Department of Materials Science
Fudan University, Shanghai 200433, China

Abstract— A novel low phase noise oscillator with film bulk acoustic resonator (FBAR) technology is presented. The longitudinal mode FBAR and shear mode FBAR are fabricated. The High Q FBAR also obtained from cutting AVAGO's FBAR produce. The Clapp oscillator based on FBAR at 1881 MHz is designed and fabricated on printed circuit board. The testing results show that the output power of this FBAR oscillator is -3.5 dBm.

1. INTRODUCTION

Film bulk acoustic resonator, as a new radio frequency (RF) MEMS technology, is being used as RF duplexer or filter [1, 2], voltage controlled oscillator (VCO) [3], and sensor oscillator for high mass sensitivity detection [4, 5]. Compared with other RF resonator, FBAR has good performances such as high operation frequency, very high Q factor, small negative temperature coefficient, middle-high power capacity, integrated process and very small size [6]. Considering the high Q factor of FBAR, using FBAR as a part of resonant network in oscillator is helpful to reduce noise. In this paper a novel oscillator with FBAR technology is proposed.

2. FBAR OSCILLATOR DESIGN AND FABRICATION

Al-ZnO-Au, as FBAR sandwich structure, is deposited on silicon wafer by RF reactive sputtering. The silicon wafer is back etched to form air bag reflector. The longitudinal mode FBAR, shown in Figure 1, and shear mode FBAR are fabricated.

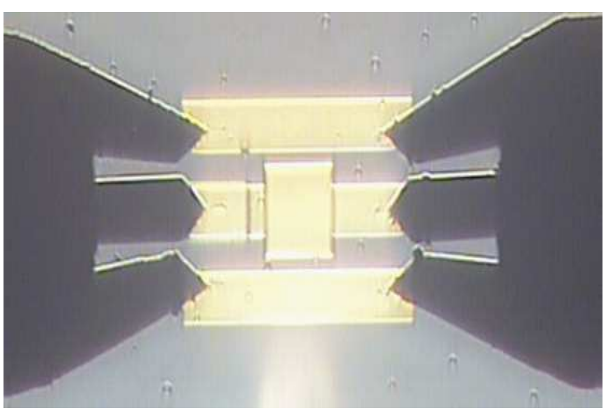

Figure 1: ZnO FBAR with air bag reflector.

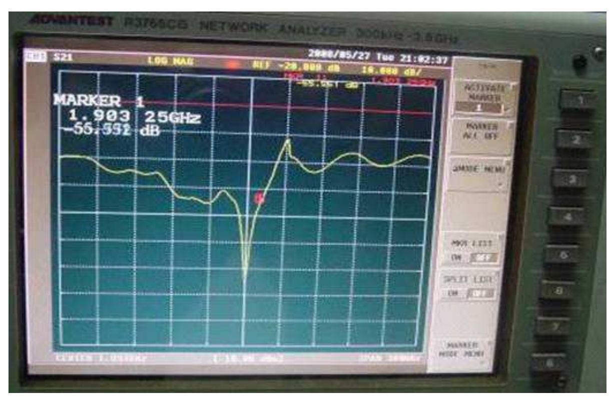

Figure 2: Resonant frequency curve of ZnO FBAR.

The FBAR resonant frequency curve is measured in Figure 2. Its Q factor is about 600.

3. FBAR OSCILLATOR

Figure 4(a) shows the Clapp oscillator circuit based on FBAR, which is modified from Colpitts oscillator [7, 8]. FBAR and C_6, C_7 compose the resonant network. This resonant network, bipolar transistor, C_1 and C_2 form the major part of Clapp oscillator. The capacitances constitute the necessary feedback required by oscillation. The resonant network determines the oscillating frequency and ensures the oscillation conditions. The resonant impedance is:

$$Z_{\text{resonant}} = j\left(L_{\text{FBAR}} - \frac{C_6 + C_7}{C_6 C_7 \omega}\right) \tag{1}$$

where C_7 is a varactor to adjust capacitor, whose capacitor value is controlled by the voltage of the adjusted resistor R_8, and LFBAR is the value of equivalent inductance of FBAR, namely Lm. And the resonant frequency of FBAR oscillator is given as

$$f_{\text{resonant}} = \frac{1}{2\pi\sqrt{L_{\text{FBAR}}\left(\frac{1}{C_1+C_2+C_3+C_4}\right)}} \tag{2}$$

As a matter of fact, the above Equations (1) and (2) are both only rough approximation because the actual FBAR is a complicated part with capacitances.

In practice, this oscillator can be temperature compensated by tuning C_1 with a varactor driven by a temperature-dependent voltage source, and the temperature stability of the FBAR oscillator is improved by almost an order of magnitude.

The FBAR oscillator circuit is implemented with discrete components on the radio frequency printed circuit board, see Figure 3.

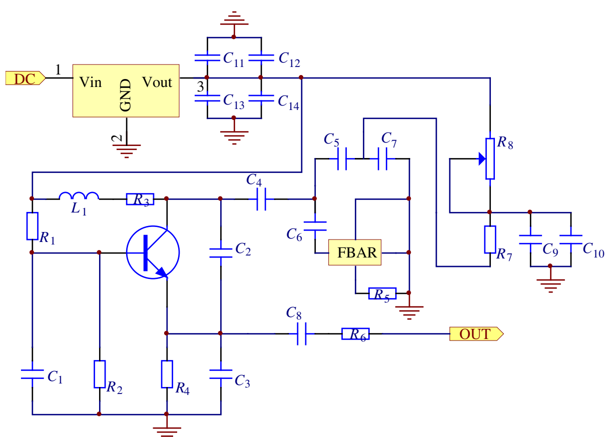

Figure 3: FBAR oscillator schematic.

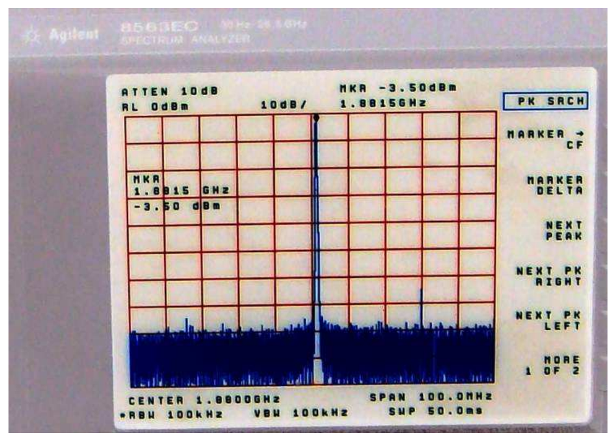

Figure 4: Test results of FBAR oscillator.

4. TEST RESULTS

The FBAR oscillator is measured by the spectrum analyzer is 8563EC of Agilent and results are shown in Figure 6. The output power of FBAR oscillator is −3.50 dBm in Figure 4.

5. CONCLUSION

This paper introduces a novel oscillator with film bulk acoustic resonator (FBAR) technology, the longitudinal mode FBAR and shear mode FBAR are fabricated. It proposes a Clapp oscillator based on FBAR at 1881 MHz, and the testing results show that the output power of this FBAR oscillator is −3.5 dBm.

ACKNOWLEDGMENT

This work is supported by a grant from the National Natural Science Foundation Key Program of China (No. 60936002).

REFERENCES

1. Mai, L., V. S. Pham, and G. Yoon, "High-quality 2.5 GHz ZnO-based FBAR devices for broadband WiMAX applications," *Electronics Letters*, Vol. 44, No. 5, 387–389, Feb. 2008.
2. Lee, J. and H. Kim, "Thin-film bulk acoustic resonator RF bandpass filter design technique using genetic algorithm," *Electronics Letters*, Vol. 39, No. 5, 444–445, Mar. 2003.
3. Pang, W., R. C. Ruby, R. Parker, P. W. Fisher, M. A. Unkrich, and J. D. Larson, "A temperature-stable film bulk acoustic wave oscillator," *IEEE Electron Device Letters*, Vol. 29, No. 4, 315–318, Apr. 2008.
4. Campanella, H., J. A. Plaza, J. Montserrat, A. Uranga, and J. Esteve, "High-frequency sensor technologies for inertial force detection based on thin-film bulk acoustic wave resonators (FBAR)," *Microelectronic Engineering*, Vol. 86, No. 4–6, 1254–1257, 2009.

5. Cheng, W. W., Y. Han, S. R. Dong, X. X. Han, S. H. Zhao, and H. J. Zhang, "Wireless tiny mass sensor system based on FBAR," *PIERS Proceedings*, 410–413, Moscow, Russia, Aug. 18–21, 2009.
6. Zhang, H. and E. S. Kim, "Micromachined acoustic resonant mass sensor," *Journal of Microelectromechanical Systems*, Vol. 14, No. 4, 699–706, Aug. 2005.
7. Jiang, T., S. Qiao, Z.-G. Shi, L. Peng, J. Huangfu, W.-Z. Cui, W. Ma, and L.-X. Ran, "Simulation and experimental evaluation of the radar signal performance of chaotic signals generated from a microwave Colpitts oscillator," *Progress In Electromagnetics Research*, Vol. 90, 15–30, 2009.
8. Shi, Z.-G., S. Qiao, K. S. Chen, W.-Z. Cui, W. Ma, T. Jiang, and L.-X. Ran, "Ambiguity functions of direct chaotic radar employing microwave chaotic Colpitts oscillator," *Progress In Electromagnetics Research*, Vol. 77, 1–14, 2007.

Analysis and Optimization of the Linearity and Efficiency for Doherty Amplifier

Zheng-Qin Li[1], **Wei-Wei Cheng**[2], **and Mei-Yi Xiang**[3]

[1]Electronic Engineering Department, School of Information
City College of Wenzhou University, Wenzhou, Zhejiang 325035, China
[2]Institute of Microelectronics and Optoelectronics
Zhejiang University, Hangzhou, Zhejiang 310027, China
[3]College of Information Science Technology
East China Normal University, Shanghai 200062, China

Abstract— This paper makes a detail analysis of the second-order product, the third order product, power back-off and 1 dB compression point, then makes adjustment for the matching to improve the linearity of amplifier, and proposes an optimization for the out power at $P_{1\,\mathrm{dB}}$ point to increase the efficiency.

1. INTRODUCTION

In the modern remote communication system, the power amplifier is very important to achieve high efficiency performance [1]. The work-point of Amplifier is near the compression point, which will lead to a dramatic increase in the signal spectral re-growth, which demands high linearity of the power amplifier [2]. Amplifier must operate in the linear region, therefore the power back-off becomes a common means of increasing the linearity [3].

2. ANALYSIS OF IP3 AND THE ADJUSTMENT OF AMPLIFIER

With power back-off, the efficiency of power amplifier will decline. Thus, with the meeting of the design requirements of power amplifier, high linearity and improving efficiency become the most important aspects of amplifier design [4].

Typically the second-order product and the third order product are the main components, which are near from the operating frequency band [5].

Only for measuring linearity of pass-band amplifier and bandwidth is less than an octave, it often makes the third order inter-modulation and the second order inter-modulation distortion to be equivalent, and only measuring the third-order inter-modulation. When measure the inter-modulation attenuation, it should measure all of the inter-modulation products in the measuring frequency band.

A useful metric of the third-order inter-modulation distortion is IP3, which is defined as: the output power of the frequencies $(2w_1 - w_2)$ or $(2w_2 - w_1)$, $P\,(2w_1 - w_2)$ or $P\,(2w_2 - w_1)$, in the frequency W_1, linear output power $P_o(w_1)$ outside the retreat of the intersection. See the Figure 1.

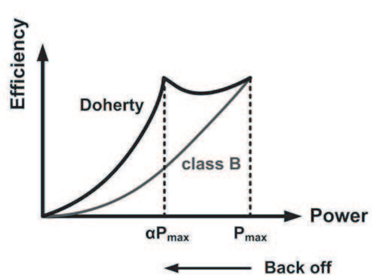

Figure 1: Efficiency Vs power back off.

When the non-linear of a system could be expressed by series expansion, the cut-off point is a very convenient method to estimate third-order inter-modulation distortion. IP3 is independent of the input power, which is solely caused by the nonlinearity of the system, therefore, it is a measure of the nonlinear. In this case:

$$\mathrm{IP3} = P_{1\,\mathrm{dB}} + 10.63\ (\mathrm{dBm}) \tag{1}$$

3. CHANGE OF THE MAIN AMPLIFIER AND AUXILIARY AMPLIFIER OF DOHERTY AMPLIFIER

The technology to enhance the efficiency of power amplifier includes the KAHN envelope separation and recovery technology, envelope tracking technology, LINC technology, Doherty technology [6]. Compared with several other technologies, Doherty technology has more advantages, such as simple realization mode, relatively low cost, the small impact of the linearity of the system being relative to other several ways [7]. Therefore, it has been widely used in modern wireless communication technology [8].

If the output power capacity of main amplifier and the auxiliary amplifier we chosen are different, the main amplifier power is small, the output power of the auxiliary power is large, and then it may be provided high efficiency of collector in a wider range of output power. This scheme has been applied in InGaP/GaAs HBT power amplifier, and successfully applied to the CDMA handset mobile.

It increases the efficiency of the power back, but also to meet the requirements of linearity. The ratio of the scale of HBT devices is 4 : 1. The, the areas of the main amplifier and the auxiliary amplifier are $3360\,\mu\text{m}^2$ and $840\,\mu\text{m}^2$ respectively. As a result, the power ratios between adjacent channel and alternate channel are -42 dBc and -54 dBc respectively. At the point of maximum output power of 25 dBm, the measured power added efficiency is 45%.

With 10 dB power back-off, added power efficiency remains high enough for 23%, whereas the traditional class AB power amplifier, for the same applications, power added efficiency is about four times lower. See the Figure 2.

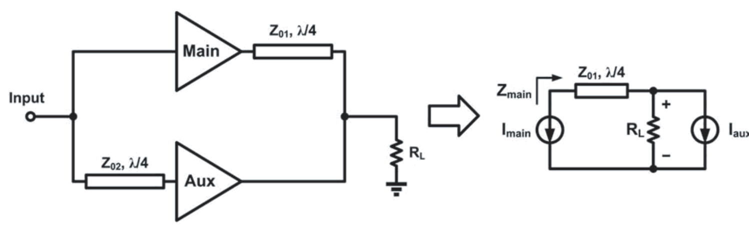

Figure 2: Equivalent circuit of Doherty amplifier.

4. 4 ANALYSIS OF $P_{1\,\mathrm{dB}}$ AND THE OPTIMIZATION OF AMPLIFIER

The corresponding gain in mind of 1 dB compression point is $G_{1\,\mathrm{dB}}$, and $G_{1\,\mathrm{dB}} = G_{0\text{–}1\,\mathrm{dB}}$, where G_0 is the small signal gain of the amplifier.

If the output power at compression point will be expressed in $P_{\mathrm{out},\,1\,\mathrm{dB}}$, then the corresponding input power $P_{\mathrm{in},\,1\,\mathrm{dB}}$ is

$$P_{\mathrm{out},1\,\mathrm{dB}}(\mathrm{dBm}) = G_{1\,\mathrm{dB}}(\mathrm{dB}) + P_{\mathrm{in},1\,\mathrm{dB}}(\mathrm{dBm}) = G_{0\,\mathrm{dB}}(\mathrm{dB}) - 1\,\mathrm{dB} + P_{\mathrm{in},1\,\mathrm{dB}}(\mathrm{dBm}) \tag{2}$$

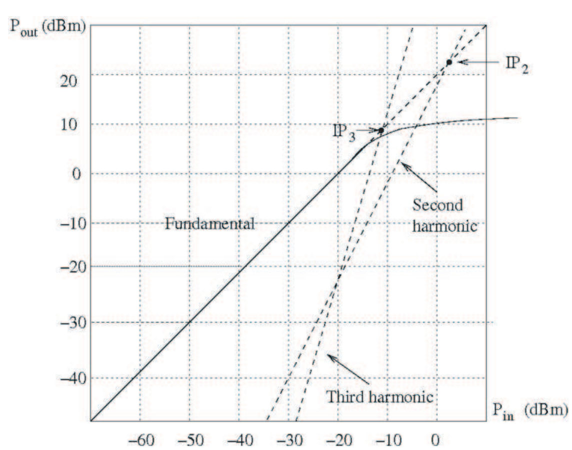

Figure 3: Inter-modulation products in the measuring frequency band.

See the Figure 3. When the input power is low, the output power and input power are proportional. However, when the input power exceeds a certain magnitude, the gain of amplifier starts to decline, the end result is that the output power is saturated. When the gain of the amplifier deviates from the constant, or is less than the small signal gain by 1 dB, then this point is a 1 dB compression point, and is used to measure the power capacity of the amplifier.

5. CONCLUSION

This paper introduces the second-order product, the third order product, power back-off and 1 dB compression point, and gives the result of adjustment for the matching to improve the linearity of amplifier, and proposes an optimization for the out power at $P_{1\,\mathrm{dB}}$ point to increase the efficiency.

ACKNOWLEDGMENT

The authors acknowledge support of the fund from the science research project of the department of education of Zhejiang Province of China, the number is Y201223915.

REFERENCES

1. Iwamoto, M., A. Williams, P.-F. Chen, A. G. Metzger, L. E. Larson, and P. M. Asbeck, "An extended Doherty amplifier with high efficiency over a wide power range," *IEEE Trans. Microw. Theory Tech.*, Vol. 49, No. 12, 2472–2479, Dec. 2001.
2. Males-Ilic, N., B. Milovanovic, and D. Budimir, "Effective linearization technique for amplifiers operating close to saturation," *Int. J. RF Microwave Comp. Eng.*, Vol. 17, 169–178, 2007.
3. Gustafsson, D., C. M. Andersson, and C. Fager, "A novel wideband and reconfigurable high average efficiency power amplifier," *Proc. 2012 IEEE MTT-S Int. Microwave Symp. Dig.*, 1–3, Jun. 2012.
4. Atanaskovic, A., N. Males-Ilic, and B. Milovanovic, "The suppression of intermodulation products in multichannel amplifiers close to saturation," *Proceedings of the 11th WSEAS International Multiconference CSCC*, 198–201, WSEAS Press 1, Agios Nikolaos, Crete Island, Greece, July 23–28, 2007, http://www.wseas.com.
5. Cripps, S. C., RF *Power Amplifiers for Wireless Communications*, 2nd Edition, Artech House, Norwood, MA, 2006.
6. Chao, K. J., W. J. Kim, J. H. Kim, and S. P. Stapleton, "Linearity optimization of a high power Doherty amplifier based on post-distortion compensation," *IEEE Microwave Wireless Comp. Lett.*, Vol. 15, 748–750, 2005.
7. Staudinger, J., G. Bouisse, and J. Kinney, "High efficiency 450 W asymmetric three-device Doherty amplifier with digital feedback predistortion," *Proc. IEEE Radio Wireless Symp. (RWS)*, 116–119, Jan. 2010.
8. Cho, K. J., J. H. Kim, and S. P. Stapleton, "A highly efficient Doherty feedforward linear power amplifier for W-CDMA base-station applications," *IEEE Trans Microwave Theory Tech.*, Vol. 53, 292–300, 2005.

Advances in the Theory of the Circular Waveguide with an Azimuthally Magnetized Ferrite Cylinder and a Dielectric Toroid

Mariana Nikolova Georgieva-Grosse[1] and Georgi Nikolov Georgiev[2]

[1]Consulting and Researcher in Physics and Computer Sciences
Meterstrasse 4, Gerlingen D-70839, Germany
[2]Faculty of Mathematics and Informatics
University of Veliko Tirnovo "St. St. Cyril and Methodius", Veliko Tirnovo BG-5000, Bulgaria

Abstract— Families of normalized in an appropriate way curves are presented, illustrating the phase behaviour of the circular waveguide, loaded with a symmetrically positioned latching ferrite cylinder of azimuthal magnetization, stuffed in a dielectric toroid, in contact with the structure wall which sustains normal TE_{0n} modes. The graphs are plotted, using numerical data, obtained by means of a recently developed reiterative procedure which employs the purely imaginary roots of the characteristic equation of configuration, derived in terms of complex Kummer confluent hypergeometric and real Bessel and Neumann functions. The work extends previous results for the geometry in question and constitutes a substantial contribution in building up its general theory.

1. INTRODUCTION

The analysis of the circular transmission lines, taking in a co-axial ferrite cylinder or toroid, magnetized azimuthally, under normal TE_{0n} modes excitation, faces serious mathematical difficulties [1–20]. They arise from the complexity of the interaction between the electromagnetic wave and the anisotropic medium, described by a permeability tensor of special form (from the complexity of the model adopted, see e.g., Refs. [1, 4, 7, 20]) and from the great number of parameters involved especially, if the geometry is multilayered [1–4, 7, 10–18]. The researchers in the field suggested different ways to overcome them. Worth noting here are the line of attack for solution of the propagation problem, suggested by D. M. Bolle and G. S. Heller [1], advanced by W. J. Ince and G. N. Tsandoulas [4], and by S. N. Samaddar [5] and summarized by A. J. Badel-Fuller [7], using new special functions, the ones, introduced by P. J. B. Clarricoats and A. D. Olver [2], employing the transverse network representation, by R. E. Eaves and D. M. Bolle [3], harnessing perturbation techniques, by Lindell [6], taking advantage of variational schemes, by M. R. Rawashdeh and N. I. Dib [11], applying the one-dimensional finite difference frequency domain method, and by G. N. Georgiev and M. N. Georgieva-Grosse [8–10, 12–20], profiting in their analysis by the confluent hypergeometric functions formalism or by that of the Coulomb wave functions, considered in a generalized sense. Thanks to this important features of some of the structures mentioned have been revealed [1–4, 6, 8–20]. The efforts in this direction, however, should go on.

This study aims at founding out new outcomes on the phase behaviour for the aforesaid sets of fields of a configuration of the class pointed out, whose inner area contains ferrite and the outer one — dielectric. They complement the recently published ones [8, 17] and permit to enrich the knowledge about its properties. The approach, proposed in the References cited, is accepted. To ease the investigation, the relative permittivities of both strata are assumed identical which diminishes the number of parameters, participating in the characteristic equation of the geometry. The discussion is restricted to the case when more than half of the cross-section of configuration is taken by ferrite. The results are depicted graphically in normalized form and are valid in all frequency bands for all imaginable values of the common relative permittivity of the loads. They are juxtaposed to the ones for a structure in which the places of the media are interchanged.

2. FORMULATION OF THE PROBLEM

The propagation of normal TE_{0n} modes is thrashed out in an infinitely long, perfectly conducting circular waveguide of radius r_0 which comprises an axial latching ferrite cylinder of radius r_1, magnetized along the azimuth to remanence by a thin central wire, whose thickness is neglected. The anisotropic load possesses a Polder permeability tensor of off-diagonal element $\alpha = \gamma M_r/\omega$, $(-1 < \alpha < 1)$, γ — gyromagnetic ratio, M_r — ferrite remanent magnetization, ω — angular frequency of the wave and a scalar permittivity $\varepsilon = \varepsilon_0\varepsilon_r$. The line's remainder is occupied by a dielectric toroid, having a scalar permittivity and permeability $\varepsilon^d = \varepsilon_0\varepsilon_d$ and $\mu^d = \mu_0\mu_d$, resp. It is accepted that $\varepsilon_r = \varepsilon_d$.

3. PHASE CURVES

Figures 1(a), (b), (c), and (d) portray the normalized phase curves $\bar{\beta}\,(\bar{r}_0)$ of the structure, corresponding to normal TE_{01} mode with solid and dashed lines for $\alpha_+ > 0$ and $\alpha_- < 0$, assuming the ferrite cylinder to waveguide radius ratio $\rho = 0.6$, 0.7, 0.8 and 0.9 as parameter, $[\bar{\beta} = \beta/\left(\beta_0\sqrt{\varepsilon_r}\right)$, $\bar{r}_0 = \beta_0 r_0\sqrt{\varepsilon_r}$, $\rho = \bar{r}_1/\bar{r}_0$, $\bar{r}_1 = \beta_0 r_1\sqrt{\varepsilon_r}$, $\beta_0 = \omega\sqrt{\varepsilon_0\mu_0}$, β-phase constant of the wave]. They are counted up, harnessing the scheme, elaborated initially for the circular waveguide, entirely filled with ferrite [1] and applied later on for the coaxial and for two-layered configurations in which the inner or outer area of the anisotropic medium is replaced by dielectric [10, 12–18]. In the second instance the calculations are performed through the numerical equivalents of the roots $\xi^{(c)}_{k,n}(\varepsilon_r, \varepsilon_d, \rho, \alpha)$ of the characteristics equation of the geometry, derived by complex Kummer confluent hypergeometric and real Bessel and Neumann functions in which $c = 3$, $n = 1$ [5, 7]. (The subscripts "+" and "−" relate to positive and negative magnetization.)

As for all structures from the family considered for all allowable values of $|\alpha|$ there are two phase curves $\bar{\beta}_+(\bar{r}_0)$ and $\bar{\beta}_-(\bar{r}_0)$, concurring to positive and negative ferrite magnetization $\alpha_+ > 0$ and $\alpha_- < 0$, resp. Similarly, the characteristics for both signs of α, originate in the cutoff frequency points $(\bar{r}_{0cr}, \bar{\beta}_{cr})$, $\bar{r}_{0cr\pm} = [\xi^{(c)}_{0,1}(\varepsilon_r, \varepsilon_d, \rho, \alpha_\pm)/2]/(1-\alpha^2_\pm)^{1/2}$, $\bar{\beta}_{cr\pm} = 0$, $(\bar{r}_{0cr+} \equiv \bar{r}_{0cr-})$ at the horizontal axes. In contrast to the circular and co-axial cases when the $\bar{\beta}_+(\bar{r}_0)$-lines are infinite beyond the frequency range above and the $\bar{\beta}_-(\bar{r}_0)$-ones only are restricted by En_{1-}-envelopes and like the configuration with a ferrite toroid, both kinds of characteristics are finite and end at the dotted En_{1+}- and En_{1-}-envelopes. (An exception makes the curve for $\alpha = 0$ solely which conforms to a waveguide with a dielectric filling.) This is due to the springing up of the $L_{3\pm}(c, \varepsilon_r, \varepsilon_d, \rho, \alpha_{en\pm}, n)$ numbers, linked with the roots $\xi^{(c)}_{k_\pm,n}(\varepsilon_r, \varepsilon_d, \rho, \alpha_\pm)$ of characteristic equation [5]. (Some values of these new quantities are listed in Table 3 of the same Reference.) The equations $\bar{\beta}_{en\pm} = \bar{\beta}_{en\pm}(\bar{r}_{0en\pm})$ of the En_{1+}- and En_{1-}-curves are written in parametric form as: $\bar{r}_{0en\pm} = L_{3\pm}(c, \varepsilon_r, \varepsilon_d, \rho, \alpha_{en\pm}, n)/[|\alpha_{en\pm}|(1-\alpha^2_{en\pm})^{1/2}]$, $\bar{\beta}_{en\pm} = (1-\alpha^2_{en\pm})^{1/2}$ [5]. The area of propagation is depicted by blue. Obviously, wave transmission may take place in bounded frequency band both for $\alpha_- < 0$ and $\alpha_+ > 0$. This behaviour resembles to the one of the structure with ferrite toroid [10, 12–16, 18] and differs from that of the ferrite waveguides at which in case $\alpha_+ > 0$ there is no upper border of the area in question [8, 9, 16, 19]. Evidently the phase behaviour

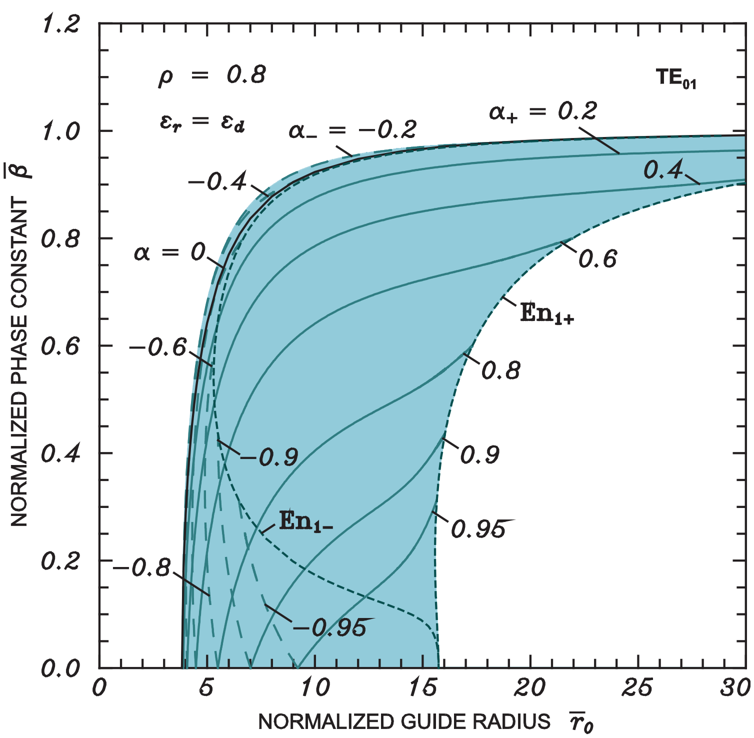

Figure 1: Phase curves $\bar{\beta}\,(\bar{r}_0)$ of the two-layered circular ferrite-dielectric waveguide for normal TE_{01} mode with α as parameter, assuming $\varepsilon_d = \varepsilon_r$ in case $\rho = 0.8$.

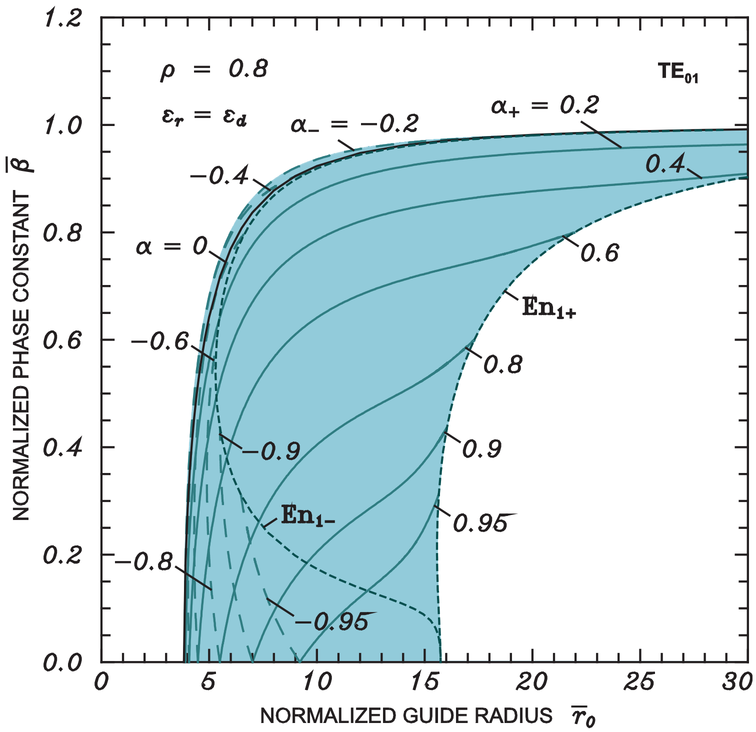

Figure 2: Phase curves $\bar{\beta}\,(\bar{r}_0)$ of the two-layered circular ferrite-dielectric waveguide for normal TE_{01} mode with α as parameter, assuming $\varepsilon_d = \varepsilon_r$ in case $\rho = 0.9$.

of the geometry is much more complicated in relation to that of the circular and coaxial ferrite waveguides [9, 16, 19, 20] and possesses similar features to the ones of the structure in which the places of the layers are interchanged [10, 12, 13, 15, 16].

The characteristics for $\alpha_+ > 0$ are situated completely to the right of the point in the phase diagram, corresponding to the cut-off frequency (to the critical guide radius). They are single-valued with respect to $\bar{r}_0$ and describe forward-wave propagation. Unlike them those for $\alpha_- < 0$ might lie entirely or partially to the left of the point mentioned. In the first case they might be single- or double-valued, conforming to backward or backward- and forward-wave propagation. In the second one their part below cut-off is double-valued, resp backward- and forward-wave propagation is observed. When the $\bar{\beta}_-\,(\bar{r}_0)$-curve is double-valued, there is one (inversion) point at which its direction is reversed. The cut-off itself is magnetically controlled. Above it the character of the $\bar{\beta}_-\,(\bar{r}_0)$-phase curve and of the corresponding wave is like provided $\alpha > 0$. If a part of the $\bar{\beta}_-\,(\bar{r}_0)$-characteristic lies to the right of cut-off, it is situated above the $\bar{\beta}_+\,(\bar{r}_0)$-one. Accordingly, for $\bar{r}_0$ larger than the critical radius, always it is fulfilled $\bar{\beta}_- > \bar{\beta}_+$ and the structure in this case may afford differential phase shift $\Delta\bar{\beta} = \bar{\beta}_- - \bar{\beta}_+$ $(\Delta\bar{\beta} > 0)$.

The change of ratio ρ influences substantially the phase pattern. Diminishing it from 1 to 0 leads to a shortening of the phase characteristics for both signs of α (of the bands in which propagation may take place). The envelopes are strongly deformed and the cut-off frequencies become smaller. This entails a shrinking of the area in which the structure produces phase shift (operates as digital phase shifter), as well. Besides, with the increase of ρ the envelopes are shifted towards the lower frequencies.

4. CONCLUSIONS

The replacement of the outer part of the circular ferrite waveguide of azimuthal magnetization, propagating normal TE_{0n} modes by a dielectric toroid complicates considerably its phase portrait. Envelope curves appear at which the phase characteristics for both signs of magnetization terminate. The dimensions of the area of wave propagation, of the frequency band in which differential phase shift is produced, as well its sign, are substantially influenced by the magnitude of dielectric insert.

ACKNOWLEDGMENT

We express our gratitude to our mother Trifonka Romanova Popnikolova and to our late father Nikola Georgiev Popnikolov for their self-denial and for their tremendous efforts to support all our undertakings.

REFERENCES

1. Bolle, D. M. and G. S. Heller, "Theoretical considerations on the use of circularly symmetric *TE* modes for digital ferrite phase shifters," *IEEE Trans. Microwave Theory Tech.*, Vol. 13, No. 4, 421–426, July 1965; Correction: *IEEE Trans. Microwave Theory Tech.*, Vol. 34, No. 4, 427, April 1986.
2. Clarricoats, P. J. B. and A. D. Olver, "Propagation in anisotropic radially stratified circular waveguides," *Electron. Lett.,* Vol. 2, 37–38, January 1966.
3. Eaves, R. E. and D. M. Bolle, "Perturbation theoretic calculations of differential phase shifts in ferrite-loaded circularly cylindrical waveguides in the TE_{01} mode," *Electron. Lett.,* Vol. 2, No. 7, 275–277, July 1966.
4. Ince, W. J. and G. N. Tsandoulas, "Modal inversion in circular waveguides. Part II. Application to latching nonreciprocal phasers," *IEEE Trans. Microwave Theory Tech.*, Vol. 19, No. 4, 393–400, April 1971.
5. Samaddar, S. N., "Special functions associated with azimuthally magnetized ferrite rod phase shifters," *J. Appl. Phys.*, Vol. 50, No. 1, 518–520, January 1979.
6. Lindell, I. V., "Variational methods for nonstandard eigenvalue problems in waveguide and resonator analysis," *IEEE Trans. Microwave Theory Tech.*, Vol. 30, No. 8, 1194–1204, August 1982.
7. Baden-Fuller, A. J., *Ferrites at Microwave Frequencies*, IEE Electromagnetic Waves Series 23, Peter Peregrinus, London, UK, 1987.
8. Georgiev, G. N. and M. N. Georgieva-Grosse, "Some new properties of the circular waveguides with azimuthally magnetized ferrite," *Proc. 25th ESA Antenna Worksh. Satell. Antenna Technol.*, 601–608, ESA/ESTEC, Noordwijk, The Netherlands, September 18–20, 2002.
9. Georgiev, G. N. and M. N. Georgieva-Grosse, "A new property of the complex Kummer function and its application to waveguide propagation," *IEEE Antennas Wireless Propagation Lett.*, Vol. 2, 306–309, December 2003.
10. Georgiev, G. N. and M. N. Georgieva-Grosse, "Propagation in an azimuthally magnetized circular ferrite-dielectric waveguide," *Proc. 3rd Europ. Conf. Antennas Propagat. EuCAP 2009*, 345–349, in CDROM, Berlin, Germany, March 23–27, 2009.
11. Rawashdeh, M. R. and N. I. Dib, "Full-wave analysis of azimuthally magnetized ferrite-loaded circular structures using the one-dimensional finite difference frequency domain method," *Int. J. RF and Microwave CAE*, Vol. 19, 397–404, May 2009.
12. Georgiev, G. N. and M. N. Georgieva-Grosse, "Phase behaviour of a two-layered circular ferrite-dielectric waveguide with azimuthal magnetization," *Progress In Electromagnetics Research Symposium Abstracts*, 742, Moscow, Russia, August 18–21, 2009; *PIERS Proceedings*, 1473–1477, Moscow, Russia, August 18–21, 2009.
13. Georgiev, G. N. and M. N. Georgieva-Grosse, "Effect of the dielectric filling on the phase behaviour of the circular waveguide with azimuthally magnetized ferrite toroid and dielectric cylinder," *Proc. Asia-Pacific Microwave Conf. APMC-2009*, 870–873, in CDROM, Singapore, December 7–10, 2009.
14. Georgiev, G. N. and M. N. Georgieva-Grosse, "The Tricomi theory of confluent hypergeometric functions and its application to waveguide propagation," *Proc. Radar Methods and Systems Worksh. RMSW-2010*, 250–254, Kiev, Ukraine, September 21–23, 2010, Invited Paper.
15. Georgieva-Grosse, M. N. and G. N. Georgiev, "Transmission properties of the circular waveguide, containing an azimuthally magnetized ferrite toroid and a dielectric cylinder," *Proc. 5th Europ. Conf. Antennas Propagat. EuCAP 2011*, 1870–1874, Rome, Italy, April 11–15, 2011.
16. Georgieva-Grosse, M. N. and G. N. Georgiev, "Transmission properties of the circular waveguide completely or partially filled with azimuthally magnetized ferrite: Review of recent results," *Proc. 1st IEEE-APS Topical Conf. Antennas Propagat. Wireless Commun. IEEE APWC'11*, 865–868, in CDROM, Turin, Italy, September 12–16, 2011, Invited Paper in the Special Session "Advances in wireless communications and their applications," organized by M. N. Georgieva-Grosse and G. N. Georgiev.

17. Georgiev, G. N. and M. N. Georgieva-Grosse, "Propagation in the circular waveguide, containing an azimuthally magnetized ferrite cylinder and a dielectric toroid," *Proc. 6th Europ. Conf. Antennas Propagat. EuCAP 2012*, 1141–1145, Prague, Czech Republic, March 26–30, 2012.
18. Georgiev, G. N. and M. N. Georgieva-Grosse, "On the confluent hypergeometric functions and their application: Basic elements of the Tricomi theory. Case of waveguide propagation," *Telecomm. Radioeng.*, Vol. 71, No. 3, 209–216, 2012.
19. Georgiev, G. N. and M. N. Georgieva-Grosse, "Advanced computational methods for analysis of the circular waveguide completely filled with azimuthally magnetized ferrite: Review of recent results," *Proc. Fourteenth Int. Conf. Electromagn. Adv. Applicat. ICEAA'12*, 62–65, in CDROM, Cape Town, South Africa, September 2–7, 2012, Invited Paper in the Special Session "Modern problems of mathematical and computational electromagnetics and their advanced applications," organized by M. N. Georgieva-Grosse and G. N. Georgiev.
20. Georgiev, G. N. and M. N. Georgieva-Grosse, "Circular waveguide, completely filled with azimuthally magnetized ferrite," *Wave Propagation*, Academy Publish, Cheyenne, Wyoming, USA, 2013, in print.
21. Tricomi, F. G., *Funzioni Ipergeometriche Confluenti*, Edizioni Cremonese, Rome, Italy, 1954.

Evaluation of Correlation Detector for Ship Detection with HF Radar

A. Gupta and T. Fickenscher
Helmut Schmidt University/University of the Federal Armed Forces Hamburg, Hamburg, Germany

Abstract— HF Surface Wave Radar (SWR) offers potential for cost effective long-range coastal ship traffic monitoring. Recently invented correlation detector observes the correlation of received power along the azimuth axis across neighbouring Range Doppler (RD) cells to detect the presence of a target. Using measured data successful detection of targets along the clutter edges and within first and second order sea clutter has already been demonstrated. Performance degradation of the detector due to the relative position of a target with respect to the centre of range and Doppler bin has been evaluated using a synthetic target of variable range, velocity and Radar Cross Section (RCS) and measured data from a coastal HF SWR. Evaluation of the detector in terms of probability of false alarm is also presented.

1. INTRODUCTION

The High Frequency Surface Wave Radar (HF SWR) has been proposed as a cost effective solution to the problem of long range littoral surveillance. HF SWR exploits low frequency (3–30 MHz) signals' ability to propagate well beyond the visible horizon due to the diffraction of the vertically polarized HF wave over conducting sea water. The nature of backscattered clutter signal of HF radar is significantly different from that of microwave radar. In a fully developed sea the waves having wavelength equal to half the radar wavelength correspond to a strong Bragg backscatter. At HF band the external noise — with sea clutter signal as its main contributor — is typically much higher than the internal receiver noise. The sea clutter backscatter is the main obstacle for ship detection as typical radial velocities of these targets result in a Doppler shifted signal that easily can be masked by the spectrum of the sea clutter signal. So far state of the art Constant False Alarm Rate (CFAR) detector does not make use of priory knowledge of sea clutter signal distribution along Doppler and azimuth axis [1]. The scheme uses a conventional CFAR detector with the thresholding scheme based on regression analysis of power spectrum values along range and Doppler axis hence is called Regression Thresholding Detector (RTD). The underlying assumption in RTD is that the clutter power is randomly distributed along the Doppler and azimuth axis. However, oceanographers have good understanding of the spectral nature of sea clutter in Doppler and azimuth domain. This a priori knowledge of sea clutter nature is not used in RTD which for example could be used to minimize the false alarm rate.

Recently a detector has been presented which can be used to localize the position of a target in range and Doppler domain [2, 3]. Known as correlation detector it is based on the assumption that due to spilling of target signal the azimuth variation of received power for a RD Vector Under Test (VUT) including a target will be more correlated across the adjacent RD cells as compared to a RD cell without a target. Though unlike CFAR detection scheme has been already used to successfully detect targets masked in a Bragg line [3] simulation results using a synthetic target and measured clutter signal uncovered a shortcoming of the current detector concept. The variation of power correlation along atimuth of in range neighbouring azimuth vectors as a function of actual target position within the range cell is as expected. There is a significant impact of target spilling on correlation of azimuth vectors which is vital for the detector concept. But it cannot be guaranteed that for any location of a target within a given range cell the correlation of signal power of the azimuth vector with its neighbouring azimuth vector will increase for all clutter scenarios. Depending on the clutter data and the actual position δR of the target with respect to the centre of the range cell some targets will be missed.

This paper provides a more detailed evaluation of the impact of the window length used for determinating the correlation of in range neighboring azimuth vectors. A synthetic target in the background of measured sea clutter signal is used to test the robustness of the detector. Section 2 of the paper briefly describes the detection algorithm. The evaluation scheme is presented in Section 3 alongside with the achieved results. Section 4 completes with a conclusion.

2. CORRELATION DETECTOR

Following from standard RD processing for Frequency Modulated Continuous Wave (FMCW) radar each received chirp is down mixed and undergoes Digital Fourier Transform (DFT) to separate various range components. Another DFT across all chirps within the coherent integration time along each range bin filters data into Doppler bins. Windowing functions are used for both range and Doppler transforms. The bearing of the signal is determined by a digital beamformer. The R_iD_j Vector Under Test (VUT, which is the azimuth vector for range cell R_i and Doppler cell D_j) contains b azimuth cells with corresponding scan angles ψ_k ($k = 1, \ldots, b$). The respective received signal power is stored in the vector $\mathbf{X}$ with elements x_k and the received signal power for the VUT of adjacent range bin $R_{i+1}D_j$ is saved in the vector $\mathbf{Y}$ with elements y_k, respectively (Fig. 1). A target in the VUT will impact the correlation between $\mathbf{X}$ and $\mathbf{Y}$ which is calculated by Pearson Product Moment Correlation Coefficient (PMCC) r. The distribution in both the vectors can be approximated by bivariate normal distribution so Fisher transform is applied on r to stabilize its variance, providing the correlation value z_{VUT} for the VUT. The threshold T is estimated adaptively by using all the range cells within a range window, *win* in the Doppler neighborhood of VUT as described in [2, 3]. The range window is defined in such a way that VUT always lie in the center of the window.

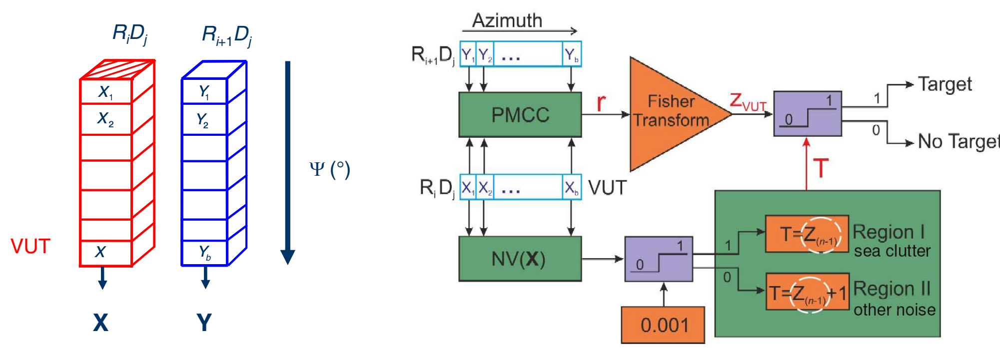

Figure 1: Block diagram of the proposed detector. The value of T changed adaptively for different RD cells.

3. EVALUATION

This paper uses the measurement results obtained by a coastal FMCW radar station (WERA) located at the North West German coast at Wangerooge [4]. Operating frequency was set to 12.27 MHz and transmitter power to 4 W. The 165 m long receiver array consists of 16 elements and transmitter was a flood light 4 element square antenna array. A single chirp used for each range transform was 0.26 s long with a bandwidth of 100 kHz resulting in a range resolution of $\Delta R = 1.5$ km. A set of 512 chirps was used for Doppler discrete Fourier transform (Doppler resolution $\Delta f = 0.015$ Hz).

Figure 2(a) shows the RD plot with look angle to boresight. The first order Bragg lines are visible around ± 0.7 Hz. Fig. 2(b) displays the values z_{VUT} and Fig. 2(c) the detection map corresponding to Fig. 2(a) including a linear trace of a synthetic target with Radar Cross Section RCS = 18.5 dBsm in range 30 km to 50 km with Doppler frequency -0.9315 Hz to -0.5258 Hz. Both graphs consider look angle $-30°, \ldots, +30°$. The synthetic target is clearly seen in both maps alongside with other targets as well as with very little signal originating from the first order Bragg lines. For the synthetic target placed at $\delta R/\Delta R = 40\%$ only a single drop out in the detection trace is observed when the target crosses the center of the Bragg line (Fig. 2(c)).

In a next step the probability of detection, P_{detect} of a target of given Radar Cross Section (RCS) is evaluated. Since the statistical properties of sea clutter are not fully understood it is not possible to derive P_{detect} theoretically. The shortcomings in Automatic Identification System (AIS) recordings and the lack of wide range of measured data sets also make the empirical estimation of P_{detect} by measurements difficult. This paper presents a solution to evaluate P_{detect} by implanting synthetic targets of various RCS in 100 collected data sets and make a statistical estimate. To calculate the value of P_{detect} for a given measurement data set first the RCS value of the synthetic target is fixed for example to 25 dBsm. In the next step this target is placed inside the measured data set at a range of 10 km, Doppler of -2.5 Hz and at boresight. Now the window length of the

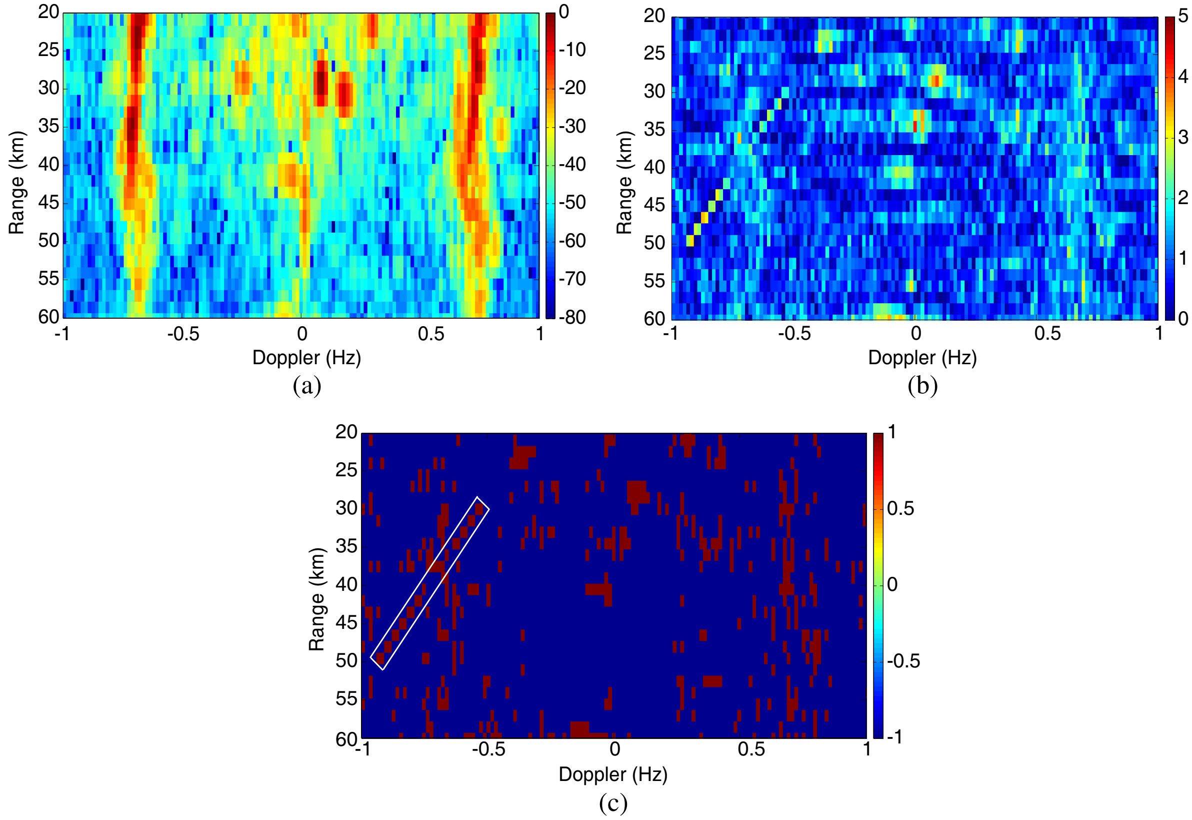

Figure 2: (a) Measured RD map for 16 element coastal HF SWR for look angle to boresight, first order Bragg peaks around $\pm 0.7\,\text{Hz}$, (b) corresponding z_{VUT} values and (c) detection map including a trace of synthetic targets (RCS $= 18.5\,\text{dBsm}$, $\delta R/\Delta R = 40\%$) for look angle $-30°, \ldots, +30°$.

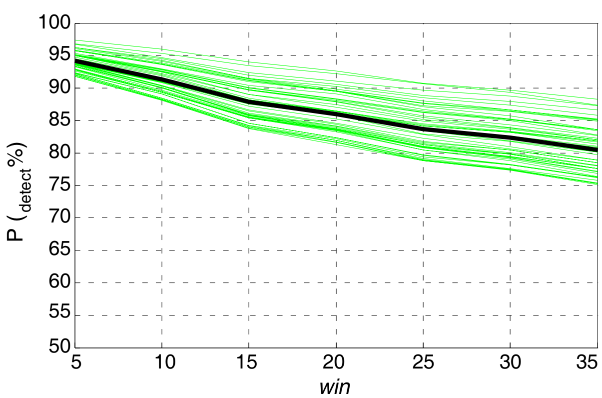

Figure 3: Probability of detection, P_{detect} versus window length, *win* for a target RCS of $25\,\text{dBsm}$ for various data sets. Wind speed $= 1.5\,\text{m/s}$. Black line represents the mean P_{detect}.

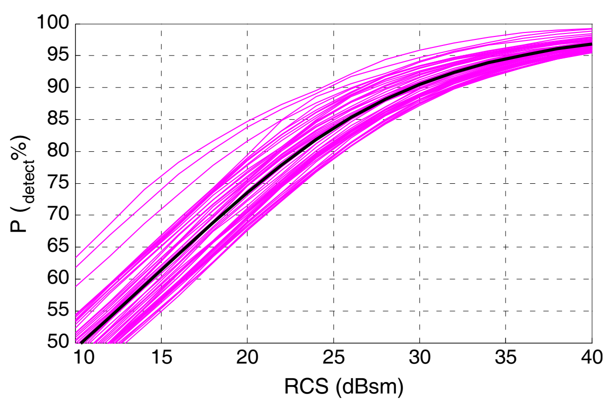

Figure 4: Probability of detection, P_{detect} versus target Radar Cross Section, RCS for window length of 25 for various data sets. Wind speed $= 1.5\,\text{m/s}$. Black line represents the mean P_{detect}.

correlation detector is set to a fixed value. The value of z_{VUT} for a target is minimum when it is in middle of the range cell hence to simulate the worst case scenario for P_{detect}.

4. CONCLUSIONS

Using a synthetic target in the background of measured sea clutter signal for various SCR scenarios is used to test the robustness of correlation detector. Though detection scheme has been already used to successfully detect targets masked in a Bragg line simulation results uncover a shortcoming of the current detector concept. The variation of correlation value z_{VUT} as a function of actual target position within the range cell is as expected. There is a significant impact of target spilling on correlation of azimuth vectors which is vital for the detector concept. But it cannot be guaranteed that within $0 < \delta R/\Delta R < 50\%$ a target will increase the correlation value z_{VUT} for all clutter scenarios. Depending on the actual position of the target within the range cell some targets will be missed. Further investigations are on its way in order to improve the detection scheme.

ACKNOWLEDGMENT

This work was supported by Wehrtechnische Dienststelle für Schiffe und Marinewaffen, Maritime Technologie und Forschung (WTD 71), Eckernförde, Germany. The authors would like to extend their warm gratitude to Helzel Messtechnik GmbH, Germany and Helmholtz-Zentrum Geesthacht, Germany for providing the measurement data.

REFERENCES

1. Dzyonkovskava, A. and H. Rohling, "Target detection with adaptive power regression thresholding for HF radar," *CIE International Conference on Radar*, 1–4, Shanghai, China, Oct. 2006.
2. Gupta, A. and T. Fickenscher, "Improved correlation detector for HF surface wave radar," *IEEE Radar Conference*, 212–216, Kansas City, USA, May 2011.
3. Fickenscher, T., A. Gupta, and P. Ludwig, "Performance evaluation of correlation detector for HF surface wave radar," *Asia-Pacific Microwave Conference, APMC 2012*, Kaohsiung, Taiwan, Dec. 2012.
4. Fickenscher, T., A. Gupta, M. Holters, J. O. Hinz, and U. Zölzer, "Recent advances in coastal surveillance by HFSWR in Germany," *Sensor Signal Processing for Defense (SSPD)*, London, United Kingdom, Sep. 2012.

A Planar PIM-generator for Antenna PIM Test Setup

Kohei Takada and Nobuhiro Kuga
Faculty of Engineering, Yokohama National University
Tokiwadai 79-5, Hodogaya-ku, Yokohama-shi 240-8501, Japan

Abstract— In this paper, a planar PIM-generator which uses steel wire as a PIM-source is proposed. By using a notched annular ring structure, high PIM is successfully obtained by a short steel wire. To examine dependency on the polarization of the proposed structure, radar cross section (RCS) is evaluated. From that result, it is confirmed that fluctuation in RCS is less than 1 dB. It is also presented that the proposed structure produces the PIM from −83 dBm to −107 dBm by rotating the mounting angle, and has good linearity for the input power when the proposed PIM-generator is placed 200 mm away from a printed dipole antenna in 2 GHz.

1. INTRODUCTION

Passive intermodulation (PIMs) is caused by non-linearity in passive circuits such as base-station antennas in mobile communication systems. Concerning antenna-PIM measurements, external PIM sources are always concerned in practical measurements because it has great influence on the reliabilities in the measurements [1]. To assess a measurement environment, the usage of a level-known PIM-generator is quite helpful. For that reason, the authors have proposed a concept of variable PIM generator using antenna [2–4] while fixed-level generators using connector have been used conventionally [5].

In the literature [6], the author used an external PIM-source using a diode. It utilized shunt wires for the diode to produce strong PIM, and its level was controlled by changing the mounting angle of the diode. As shown in our previous works diodes are useful to obtain strong intermodulation, however, their nonlinearity are too strong to omit the influence of the higher order PIM [7].

Therefore, a planar PIM-generator without diodes is considered in this paper. In the proposed model, thin steel wire is used as a PIM source. It will be shown by using a full-wave electromagnetic simulation that the PIM source is excited effectively by a shape of notched annular conductive ring. It is also shown that the produced PIM level can be controlled by rotating the relative angle to a tested antenna with small fluctuation of its radar cross section.

2. PLANAR PIM-GENERATOR

In this paper, 3 different models are examined as planar PIM-generators. The commonly used annular conductive ring has the outer and inner diameters of 70 mm and 30 mm, respectively, and a 4 mm-wide air-gap which is shorted by a 0.1 mm-tick steel wire. The difference of each model is the position and numbers of the shorting wire. In model A, the steel wire is placed only at the outer edge of the annular ring. In model B, the both ends of the air-gap are shorted by two steel wires. In model C, the center of the air-gap is also shorted by a steel wire as well as the both ends of the air-gap. Model 0 is an annular ring without air-gap, which is shown for a reference purpose.

The performance of the prepared planar PIM generators are examined by using a 2 GHz band PIM-tester. The frequencies of the input signals are $f_1 = 2.05$ GHz and $f_2 = 2.2$ GHz, and the one of the produced 3rd PIM is 1.9 GHz in this paper.

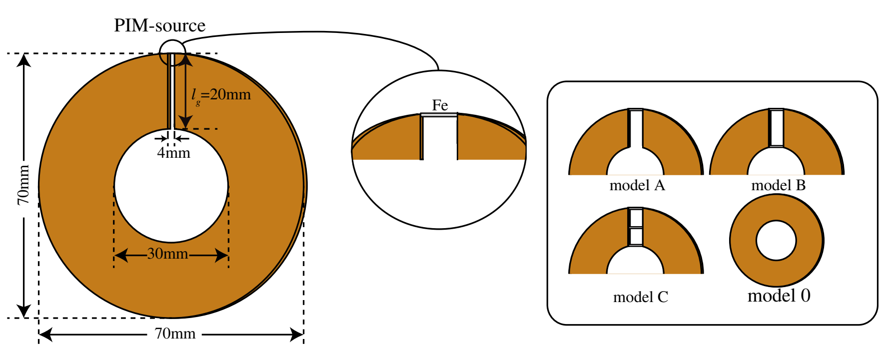

Figure 1: Configuration of a planar PIM generator.

A printed dipole antenna of which details were described in the literature [6] and a small anechoic chamber shown in Figure 2 are used as a test setup. The residual PIM level of the employed system is measured by experiments about -100 dBm for two-tone excitation using -43 dB carrier [6]. The PIM-generator is set on the transverse plane for the antenna. The position of the steel wire is expressed as the mounting angle ϕ_0 of the planar PIM-generator hereafter.

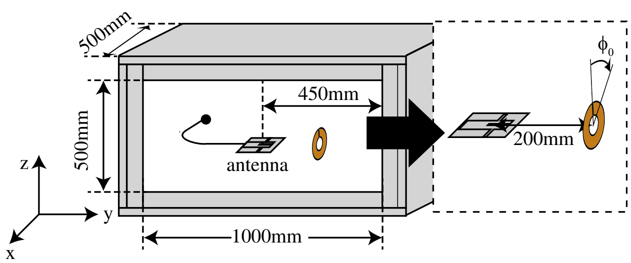

Figure 2: Antenna PIM test setup.

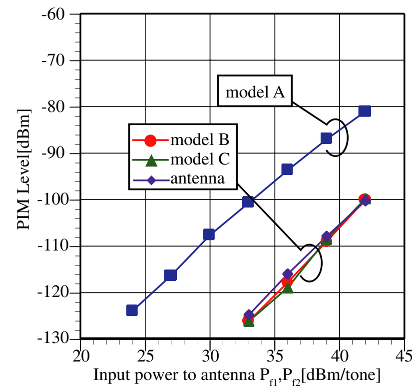

Figure 3: PIM level observed by the antenna as a function of input power to the antenna P_{f1}, P_{f2}.

Figure 3 shows PIM performance of each planar PIM-generator as a function of input power to the antenna, where $P_{f1} = P_{f2}$. The PIM generated from the antenna is also presented in the figure as a reference. The PIM generated from model B and C are too small to be observed by the antenna because the dimension of the employed annular ring is not optimized in this case. Contrary, model A generates much higher PIM with good linearity than other models. From the viewpoint of the strength of PIM production, it is concluded that model A is optimal as an external PIM source with known PIM generation.

The advantage of the annular ring structure is in its independency of the polarization. However in this paper, the air-gap incorporated into the ring has a possibility to degrade the independency. To evaluate the influence of the air-gap, the radar cross section (RCS) of each model is calculated using the full wave EM simulator. The result is shown as Figure 4, where their RCS are plotted as a function of the angle ϕ_0. It is natural that model-A has large fluctuation in RCS in comparison with model-B and C because of its structural asymmetry. As a consequence, it is confirmed that the fluctuation due to the air-gap is estimated as about 1 dB which will be caused at 1.9 GHz and 2.2 GHz. Although practical influence on PIM should be also examined, it is left as a future problem.

Figure 5 shows a simulated current distribution on the conductive ring of model A when it is excited by the Ex-polarized wave. According to the simulation, the current distribution is consistent for all the frequencies. The air-gap of which outer end is shorted by a steel wire can be considered

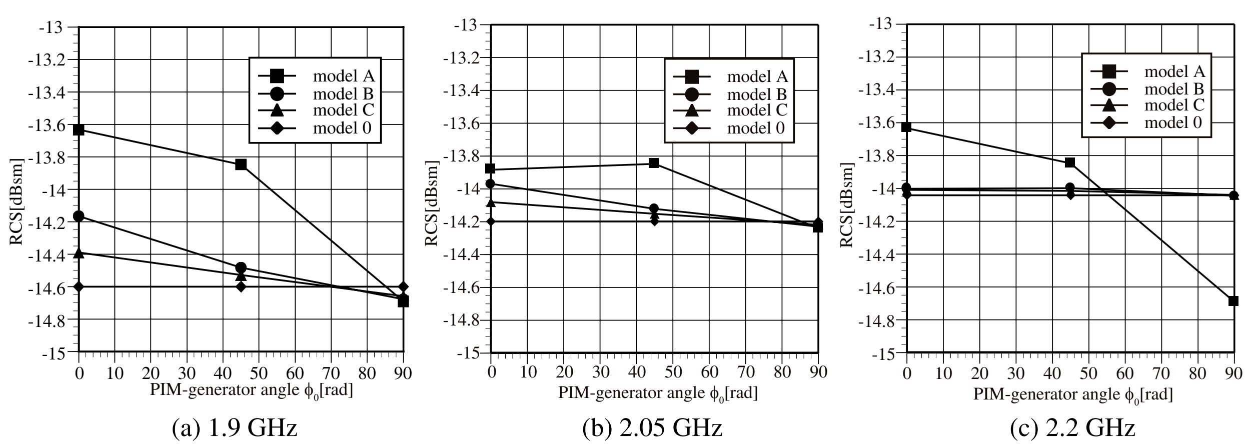

Figure 4: Radar cross-section as a function of PIM-generator angle ϕ_0.

as a notch of which open-end flare out to the inside the annular ring. As a consequence, the steel wire placed on the maximum current point in that notch produces strong PIM even though such a short steel wire is employed as a PIM source.

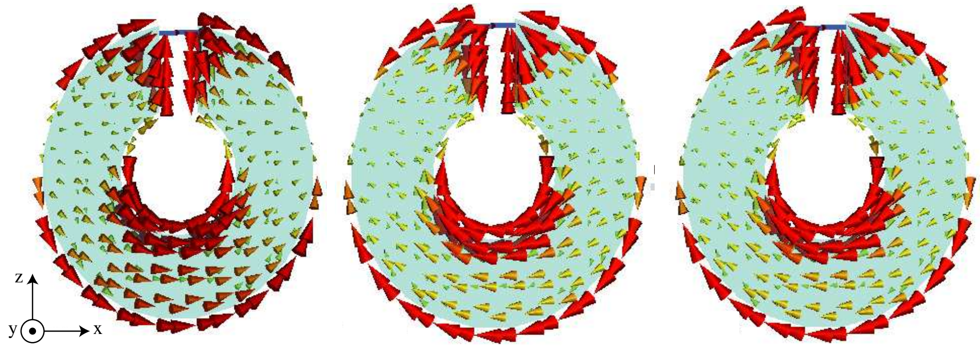

(a) 1.9 GHz (b) 2.05 GHz (c) 2.2 GHz

Figure 5: Current distribution on the annular conductive ring of the PIM-generator.

Figure 6(a) shows an observed PIM-level for model A as a function of the PIM-generator angle ϕ_0. As the angle ϕ_0 increases, the PIM-level decreases, and resultant PIM level is ranging from -83 dBm down to -107 dBm. The PIM takes the minimum at $\phi_0 = 70°$, which is lower than the residual noise of the antenna because of the cancelling of the PIMs from the PIM generator and the antenna. Figure 6(b) shows an observed PIM-level as a function of input power to the antenna when $\phi_0 = 0°$, $45°$, and $90°$, where the result of PIM-level generated from antenna is also shown as a reference. When ϕ_0 is smaller than $45°$, the result follows the 3 dB/dB line when $P_{f1} = P_{f2} \leq 30$ dBm and has decreased slope about 2 dB/dB for $P_{f1} = P_{f2} \geq 30$ dBm. When ϕ_0 is $90°$, the PIM due to the planar PIM source is not observed.

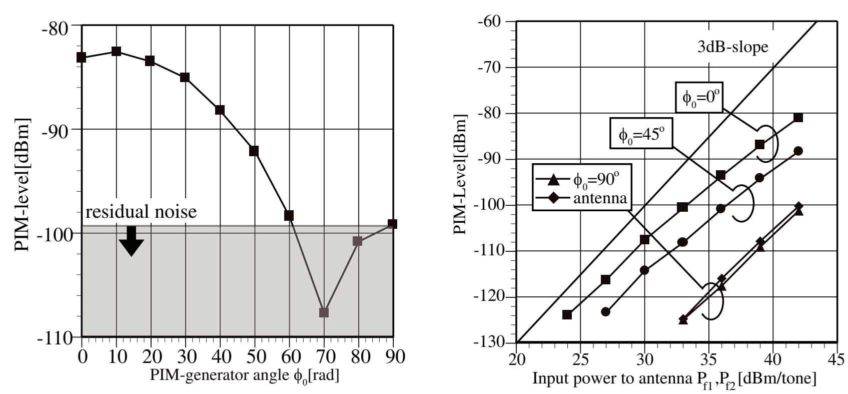

(a) (b)

Figure 6: Basic PIM-characteristics of planar PIM-generator. (a) Observed PIM-level as a function of angle of PIM-generator ϕ_0. (b) Observed PIM-level as a function of input power to the antenna P_{f1}, P_{f2}.

3. CONCLUSION

In this paper, the planar PIM-generator was proposed. It generated high PIM from steel by using the notched annular ring structure. The influence of the notch was evaluated by RCS, it was confirmed that the fluctuation of proposed model due to the air-gap was estimated as about 1 dB. In addition, it was confirmed that the proposed model produced PIM from -83 dBm to -107 dBm by rotating the mounting angle, and had good linearity for input power. As a future study, practical influence of RCS on PIM should be estimate.

ACKNOWLEDGMENT

We would like to thank Dr. Ihara with NTT Docomo for the support of experimental setup and fruitful discussion.

REFERENCES

1. Kim, J. T., L. K. Cho, M. Y. Jeong, and T .G. Choy, "Effects of external IM sources on antenna IM measurements," *ETRI Journal*, Vol. 24, No. 6, 435–442, Dec. 2002.
2. Irie, K. and N. Kuga, "Patch antenna with diode as passive intermodulation source," *IEICE Trans. Commun.*, Vol. J93-B, No. 9, 1170–1176, Sep. 2010 (in Japanese).
3. Irie, K., N. Kuga, and K. Cho, "PIM-linearity improvement by the size of a diode mounting hole," *IEICE Electronics Express*, Vol. 8, No. 14, 1198–1203, Jul. 2011.
4. Irie, K. and N. Kuga, "Elliptical disk monopole antenna with diode for PIM measurement facility assessment," *IEICE Trans. Commun.*, Vol. J94-B, No. 9, 1146–1152, Sep. 2011 (in Japanese).
5. Henrie, J., A. Christian, and W. J. Chappel, "Engineered passive nonlinearities for broadband passive intermodulation distortion mitigation," *IEEE Microw. Wirel. Compon. Lett.*, Vol. 19, No. 10, 614–616, Oct. 2009.
6. Takada, K., N. Kuga, and K. Cho, "An experimental consideration on the effect of antenna gain on the observed PIMs for an external PIM-source," *Proc. ISAP 2012*, 991–994, Japan, Nov. 2012.
7. Takada, K., D. Ishibashi, and N. Kuga, "Influence of the power-consumption at non-fundamental frequency on passive intermodulation generation," *Proc. ICSJ 2012*, 413–416, Japan, Dec. 2012.

Proposal of Technical Measures for a Partial Discharge Detection System Based on Real Measurement

P. Drexler, M. Čáp, R. Myška, P. Fiala, M. Steinbauer, and T. Kriz
Department of Theoretical and Experimental Electrical Engineering
Brno University of Technology, Czech Republic

Abstract— The article presents results of the measurement of partial discharge (PD) activity in power oil transformers. The method is based on measurement of electromagnetic waves in UHF spectrum produced by PD. The measurement of PD activity has been made on eight power transformers in the Dukovany nuclear power plant in the Czech Republic. The initial experimental measurement, which was under full working arrangements, has been accompanied by some issues. The recorded signals contained strong interference. It has been estimated, that the source of the interference is probably situated in the high voltage bushings, which feed the transformer from a turbo-generator. The interfering signal in form of electromagnetic waves has propagated through the air vicinity and it has coupled to the sensing heads. It has been found that the proper shielding is a crucial factor, while the PD signal level is far below the level of the interference. Further experiments have been conducted with an additional shielding and the interference level significantly decreased. The report on the results of the experimental measurement is given in the paper. There are shown waveform examples of the interfering signal. Further, the design of construction measure of the sensor casing, which allows to improve the shielding, is presented also. The functionality of proposed measure has been demonstrated in laboratory.

1. INTRODUCTION

The partial discharges (PD) are one of the problems in high-voltage technology field. In consequence of the activity of the PD in the power transformer the quality of its isolation properties declines, which can lead to breakdown or destruction of the transformer. The radiofrequency (RF) measurement method of PD is based on principles, which have been shown in recent publications [1, 2]. The PD sources electromagnetic RF radiation with spectral range from hundreds of MHz to units of GHz. The radiation might be detected and evaluated, which can point out the level of PD activity. Moreover, if a set of antennas will be used, it is possible to localize the radiation source [2]. This becomes possible, when we find a solution of equations set, which inputs are the time differences of pulse signal arrivals on antennas. The electromagnetic signal spreads out from the PD location and experiences multiple reflections before it reaches the antennas. It should be noted, that no quasi-stationary interference of multi-path propagating signal is observed. This is due to stochastic mechanism of PD RF signal generation. The PD signal behaves as noise and it doesn't form quasi-stationary standing waves [3]. The stochastic behavior of the PD signal is similar to others signals, which are produced in connection with electrical discharge activity or signals which are generated in devices with non-stationary oscillations [4].

In order to perform successful detection and localization of PD activity a unique diagnostic system has been built. The system is briefly described in Section 2.

2. PD DIAGNOSTIC SYSTEM OVERVIEW

The RF PD signal is detected by set of four sensing heads (Figure 1) that enter the transformer through its casing (Figure 1(b)). Each sensing head contains a conical antenna and a set of high-frequency components (limiter, filter, variable attenuator, amplifier), which adapt received signal. The signals from the sensing heads are acquired by four-channel digitizer at 2 GS/s. Acquired signals are evaluated by custom-made software in real time. This software also comprises a graphic user interface. The interface displays signal waveforms from each sensing head and a vector diagram, which indicates the time position of a partial discharge within a single period of voltage. However, the custom-made software and its base algorithms and methods are out of the scope of this paper and they will be described in another publication. The digitizer, together with another instrumentation (heads power supply, heads gain control), are enclosed in mobile shielding box (Figure 1(c)). An extensive attention has been paid to electromagnetic susceptibility of the system. The construction measures involved box door EMC gasket and EMC power supply filters [5]. A special EMC respecting two-stage feed-through allowing cables to enter the box has been designed.

(a) (b) (c)

Figure 1: PD diagnostic system: (a) antenna side head view; (b) transformer assembly; (c) the main unit.

Each sensing head is connected to the main unit via a pair of tri-axial cables. The tri-axial configuration has been chosen to improve electromagnetic immunity. One cable serves simultaneously to RF signal and head's DC supply power transmission. The second cable allows remote control of head's attenuator in order to set the head's gain. Since the two-cable connection makes the system installation more difficult, an autonomous head's power supply would be desirable. Then the RF signal and attenuator control may share one cable and the second cable would be spared. Accumulator supply and residual energy harvesting device [6] have been cogitated. However, the head power consumption is considerable, then the cable supply has been used.

3. FIELD MEASUREMENT FINDINGS

The experimental measurement of discharge activity has been made on eight power transformers in the Dukovany nuclear power plant in the Czech Republic under full working arrangements. Signals recorded within the initial measurement on transformer "01" contained strong interference. It has been estimated, that the source of the interference is probably situated in the high voltage bushings, which feed the transformer from a turbo-generator. In order to monitor the outer interference, the sensing head 4 has been placed on the footbridge, directly under the transformer's input bushings. Supposed source of interference has been confirmed, as shown in the left part of Figure 2. It contains a waveforms of signals from head 2, 3 and 4 (head 1 wasn't temporarily assembled). The signal level of head 4 is much stronger then the others. As supposed, signals 2 and 3 are attenuated due to complex propagation path through the transformer vessel. A vertical waveforms arrangement is shown in the right part of Figure 2. It shows that the signal of head 4 arrives to the antenna as first. Both confirm the interference source. Similar results have been obtained within the measurement on transformer "02"–"05". All of the transformers suffered from discharge activity in input bushings. Its radiation would unfortunately override possible PD activity RF signal.

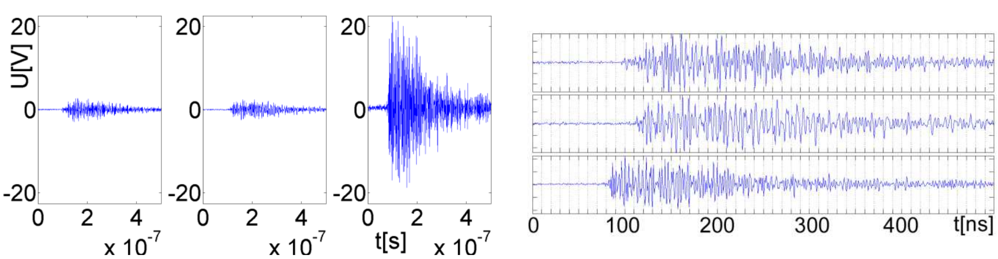

Figure 2: Waveforms record of head 2, 3 and 4 signals for transformer "01".

A different behavior has been identified in case of transformer "06". The signal from head 4, which was placed near the input bushings again, was significant weaker in compare to signal of other heads, as shown in left part of Figure 3. It is obvious, that the signal arrives to head 4 as latest, when the waveforms are set in vertical arrangement (Figure 3(b)). This excludes the transformers bushing as the source of interference. The explanation is, that the signal of distant source was acquired. At this point, the issue of signal coupling in to the channels 1, 2 and 3 occurs. Heads 1, 2 and 3 were inserted in to the vessel. The second conclusion is that the signal coupled in other channels through insufficient electromagnetic shielding of heads connections to the transformer vessel. The residual gap between the head shielding cover and vessel inlet performs as a secondary radiation element when exposed to outer RF signal. This secondary element radiates

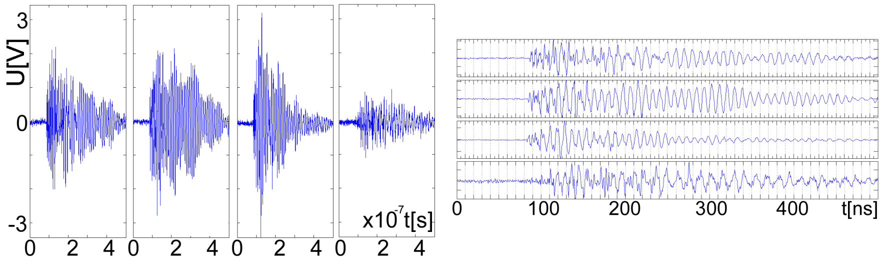

(a) (b)

Figure 3: Waveforms record of head 1, 2, 3 and 4 signals for transformer "06".

into the head cover.

Considering this, an experiment with additional head-to-vessel connection shielding was performed on-site. A special conductive fabric was used to fill up the gap, which shows the left and middle part of Figure 4. The result is shown in the right part of Figure 4. The first recorded waveform represents the signal of treated head; the second waveform represents the signal of untreated head. A huge difference in signal magnitudes is obvious. It has been found out, that the efficiency of additional shielding is 26 dB (in meaning of power attenuation).

(a) (b) (c)

Figure 4: (a), (b) Application of metallic fabric into the cover-inlet gap and (c) resulting signals ratio.

4. EFFICIENCY MEASUREMENT OF PROPOSED ADITIONAL SHIELDING

The findings of described experiments lead to requirement of head shielding improvement. The magnitude of interference is probably far more intensive than the PD signal magnitude and it would disable its detection. Designed shielding improvement utilizes elastic cooper gasket by Laird Technologies® (Figure 5(a)), which will be fixed in the head cover. Within the head installation, the gasket fills-up the gap and conductively connects the head cover to the vessel inlet. The efficiency of proposed measure has been verified in laboratory. A short metallic tube with end-cover has been used in order to simulate the transformer vessel inlet. The tube has been inserted in the head cover without and with the gasket (Figure 5(b)) subsequently. A short monopole receiving antenna has been installed in the head cover instead the head's circuitry (Figure 5(c)). Identical antenna has been used for EM signal radiation.

The distance of the antenna has been fixed and measurements of shielding efficiency at frequencies 1 GHz and 3 GHz have been performed. The transmitting antenna supply power was set

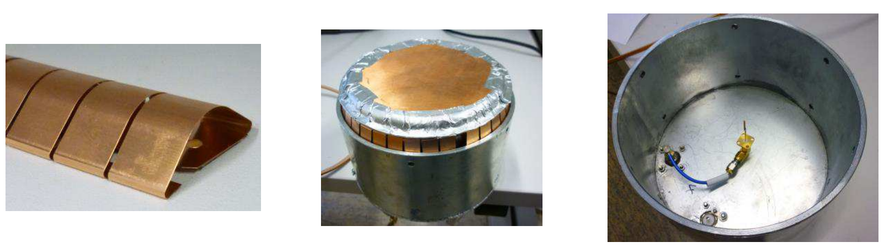

(a) (b) (c)

Figure 5: (a) Laird Technologies® gasket; (b) inlet-simulating covered tube inserted in the head cover with gasket; (c) short monopole receiving antenna inside the head cover.

to 17.08 dBm at 1 GHz. Measured power on the output of uncovered receiving antenna reached −43.1 dBm. When covered without the gasket, it decreased to −46 dBm. When covered with the gasket, it decreased to −91.2 dBm. Hence, the shielding efficiency is $-46 - (-91.2) = 45.2$ dB at 1 GHz. At 3 GHz, the supply power was set to 16.45 dBm. Uncovered antenna supplied −31 dBm; −33.8 dBm when covered without gasket and −80.5 dBm when covered with gasket. Hence, the shielding efficiency is $-33.8 - (-80.5) = 46.7$ dB at 3 GHz. Similar results have been obtained when the transmitting antenna and RF generator have been replaced with a high voltage generator [8] and a spark-gap in order to simulate the RF signal of discharge activity. However, description of this part of the experiment is out of scope of this paper.

5. CONCLUSIONS

Within the field PD activity measurement, outer interference susceptibility of detection system has been found out. Surrounding power plant systems have unexpectedly significant influence on detection abilities. Problematic part of the system is connection of detection heads with transformer vessel inlets, which allows penetration of the outer interference. On-site experiment has proved, that simple addition of conductive fabric may improve the shielding efficiency with factor of 26 dB. It has been proposed a construction measure utilizing cooper gasket. This approach has been verified by laboratory measurement. Resulting shielding efficiency improvement was better than 45 dB at frequencies 1 GHz and 3 GHz. The proposed measure will be verified by experimental field measurement. It might be expected, that the coupled outer interference will be sufficiently suppressed, which allows detection of possible weak real PD activity in transformer vessel. The results will be consequently published.

ACKNOWLEDGMENT

The research described in the paper was performed within the grant of Czech ministry of industry and trade No. FR-TI1/001 and it was also financially supported by project of the BUT Grant Agency FEKT-S-11-5.

REFERENCES

1. Fiala, P., T. Jirku, P. Drexler, and P. Dohnal, "Detection of partial discharge inside of HV transformer, modeling, sensors and measurement," *PIERS Proceedings*, 1013–1016, Cambridge, USA, Jul. 5–8, 2010.
2. Myška, R. and P. Drexler, "Simulation and verification of methods for partial discharge source localization," *PIERS Proceedings*, 704–708, Kuala Lumpur, Malaysia, Mar. 27–30, 2012.
3. Polivka, J., P. Fiala, and J. Machac, "Microwave noise field behaves like white light," *Progress In Electromagnetics Research*, Vol. 111, 311–330, 2011.
4. Fiala, P., "Pulse-powered virtual Cathode oscillator," *IEEE Trans. Dielectr. Electr. Insul.*, Vol. 18, No. 4, 1046–1053, 2011.
5. Szabo, Z., J. Sedlacek, and M. Hadinec, "Optimization method of EMI power filters and its measurement," *PIERS Proceedings*, 1085–1088, Hangzhou, China, Mar. 24–28, 2008.
6. Fiala, P. and P. Drexler, "Power supply sources based on resonant energy harvesting," *Microsystem Technologies-micro-and Nanosystems-information Storage and Processing Systems*, Vol. 18, Nos. 7–8, 1181–1192, 2012.
7. Szabo, Z. and P. Fiala, "Characterization and testing shielding fabrics," *PIERS Proceedings*, 1273–1276, Moscow, Russia, Aug. 18–21, 2009.
8. Marcon, P., P. Fiala, M. Steinbauer, and M. Cap, "Special high voltage function generator," *PIERS Proceedings*, 1000–1003, Suzhou, China, Sep. 12–16, 2011.

Analytical Model of Resonant Textile Dryer

Jan Vrba and Marika Pourová
Department of Electromagnetic Field, Czech Technical University in Prague
Technická 2, 166 27 Prague 6, Czech Republic

Abstract— In cooperation with Research Institute of Textile Machines Liberec we developed applicator for microwave drying of textile in manufacturing, which is working on the open resonator principle at working frequency 2.45 GHz. In this contribution, we would like to describe our new analytic model of microwave applicator for drying textile. The purpose of the present work is to investigate influence of distribution of the electric field strength on the dielectric properties of textile materials. We have numerical simulation and the analyses of the electric field strength in the plate of textile.

Our new model is created by several cells. Every cell has own magnetron which is source of electromagnetic energy. Magnetron is situated in the waveguide which is ended with funnel. All the cells are placed on one reflective plate.

1. INTRODUCTION

In this contribution, we would like to describe our new results dealing with microwave industrial applicators used for drying of textile materials. We have designed and evaluated two different types of these applicators: open-resonater-type and waveguide-type one. We would like to present theoretical models of the discussed applicators, results of numerical modeling and experimental evaluation as well. Protype of microwave drying machine working at frequency 2.45 GHz will be reported.

2. OPEN RESONATOR TYPE APPLICATOR

This type of applicator consists of many drying cells (17 in our prototype machine) — each of them is based on the idea of open resonator (i.e., Fabry-Perrot resonator), see Fig. 1. Each of these cells has its own magnetron placed in waveguide holder. Dryed textile material is in the middle plane between parallel conductive plates, distance between these plates is equal to $(3/2)\lambda$. In Fig. 1(b) there is a calculated 2D distribution of electric field strength. Plane of the textile material is in this 2D model given by an abscissa in the middle of the resonator — in the same plane there is an expected maximum of electric field strength.

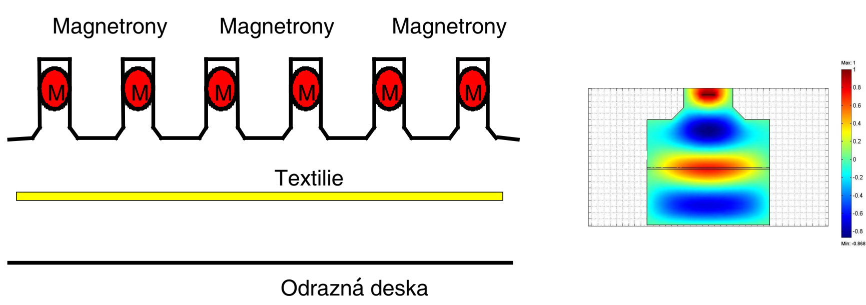

(a) (b)

Figure 1: (a) Schematics of 6 cells of open resonator type applicator for drying of textile materials. (b) E field strength 2D distribution in each one of that cells.

Optimization of the cells in longitudinal direction of drying machine is given by criteria to create maximum of electric field strength in the plane of dryed textile (E field vector parallel to the textile plane), see diagrams in Fig. 2. We can describe each one of that cells by a simple schematic sketch (a) and from it we can create oriented graph of this structure (b). Alternatively we can create diagram of EM waves inside this structure (c) and we will arrive to the resulting expression (d).

For our experiments we have built apparatus with a matrix of 6 cells in first raw, next 5 cells in the second raw and again 6 cells in the third raw — see apertures in the upper conductive plate in Fig. 3. Optimization of overall microwave dryer means to aproach to the best possible homogeneity

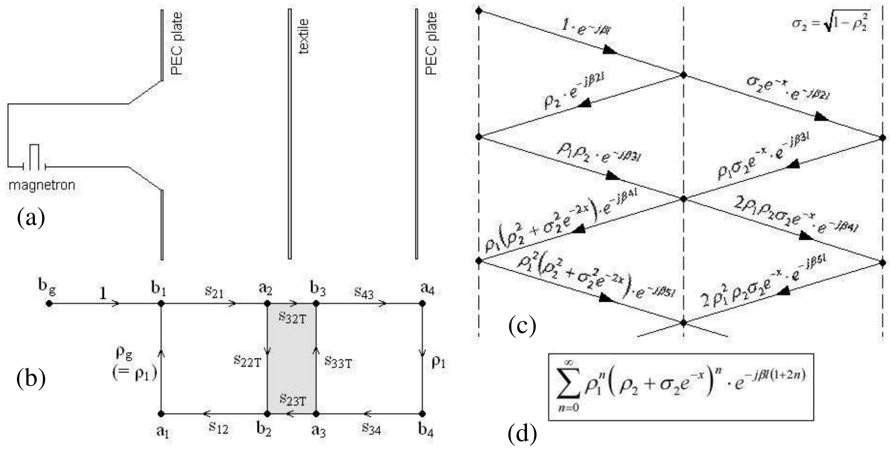

Figure 2: Tools for optimization of microwave dryer in longitudinal direction.

of absorbed microwave energy in the textile material. In the plane of textile material there is shown a calculated distribution of SAR (by aid of software product SEMCAD). Quite a good homogeneity of SAR can be observed and further improvement is obtained thanks to the movement of textile material through microwave drying machine.

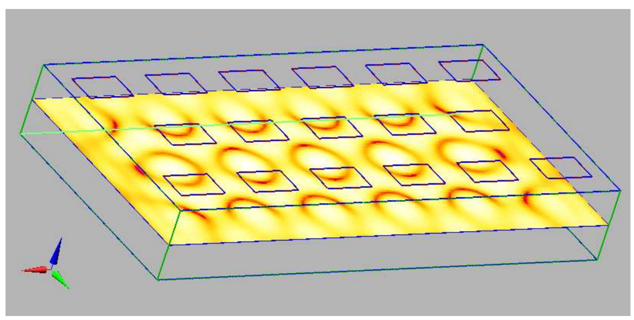

Figure 3: Microwave drying machine 3D schematics and SAR distribution in the plane of the wet textile material (6 cells in first raw, next 5 cells in the second raw and again 6 cells in the last third raw — calculated by SEMCAD).

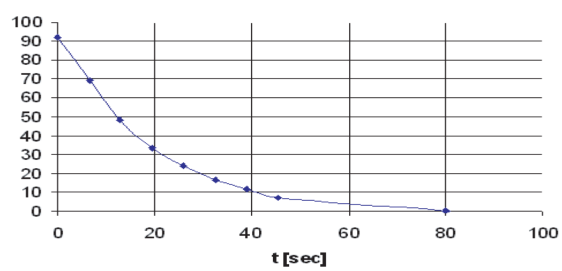

Figure 4: Typical drying characteristics of here described microwave drying systems (moisture in percents on vertical axis).

3. RESULTS

Next figure shows results of measurements of the moisture content in the dryed textile material with respect to time. We can observe, that microwave drying is very effective for moisture level above approximately 30%. Efficiency of microwave drying during our experiments was observed to be between 50 and 80% (it goes down when level of moisture inside dryed textile material is decreased during drying process).

Figure 5: Microwave part of the microwave drying machine.

4. PROTOTYPE OF MICROWAVE MACHINE FOR TEXTILE DRYING

Based on theoretical considerations a prototype of microwave drying machine has been built by Research Institute of Textile Machines and Technical University in Liberec. Following figure gives a look inside microwave part of the system. Waveguide horn apertures of several cells can be seen here (together with holes for draw of of the moisture).

5. CONCLUSIONS

As novel results of our work we would like to mention description and basic evaluation of two different microwave industrial applicators to be used for drying of textile materials: open-resonater-type and waveguide-type one. If this paper will be accepted for the program of EuMC 2005, we would like to present theoretical models of the discussed applicators, results of numerical modeling and experimental evaluation as well. Protype of microwave drying machine working at frequency 2.45 GHz will be reported in details.

ACKNOWLEDGMENT

This research is supported by the Czech Science Foundation by project P102/11/0649: "Research and measurements of signals generated by nanostructures".

REFERENCES

1. Vrba, J., *Applications of Microwave Techniques*, CTU Press, 2001.
2. Stejskal, M., J. Vrba, R. Klepl, and L. Oppl, "Microwave drier for fabrics," European Patent number EP1319914 A2, Jun. 18, 2003.
3. Vrba, J., "Microwave drying of textile materials," Series of Research Reports, 2001–2004.
4. Pourová, M., "Microwave drying of textile materials," Diploma Thesis, CTU, 2003.
5. Žák, O., "Waveguide applicator for drying of textile materials," Diploma Thesis, CTU, 2004.

Application of EM Field in Medicine

J. Vrba[1], L. Oppl[1], B. Vrbova[1], J. Vorlicek[1], J. Vrba, Jr.[2], and D. Vrba[2]

[1]Department of EM Field, Faculty of Electrical Engineering
Czech Technical University, Technická 2, Prague 16627, Czech Republic
[2]Department of Medical Devices, Faculty of Biomedical Engineering
Czech Technical University, Sítná st., Kladno, Czech Republic

Abstract— Medical applications of microwaves (i.e., using microwave energy and microwave technique and technology for therapeutical purposes) are a quite new and a very rapidly developing field. Microwave thermotherapy is being used in medicine for the cancer treatment and treatment of some other diseases since early eighties. In this contribution, we would like to offer general overview of present activities in the Czech Republic, i.e., clinical applications and results, technical aspects of thermo therapeutic equipment and last but not least, prospective diagnostics based on microwave principals ant technology and instrumentation.

1. INTRODUCTION

In this paper, we outline new trends in medical applications of microwaves, i.e., (microwave energy, microwave technique and technology used), microwave thermotherapy, both clinical and technical [1–6]. We can divide these new trends into two major groups:

- clinical trends,
- technical trends.

Our work is since 1981 focused on the design, optimization and tests of the microwave applicators for medical applications, above all for hyperthermia cancer and/or prostate treatment. This means to design a microwave structure capable:

- to transfer electromagnetic energy into the biological tissue,
- to get the best approximation of the area to be treated by the 3D distribution of SAR.

During last years we were interested in the local external applicators working at 434 MHz and 2450 MHz. These applicators were used for the treatment of more then 500 patients with superficial or subcutaneous tumors (up to the depth cca 4–6 cm). Now, following new trends in this field, we continue our research in the important directions of deep local and regional applicators.

2. CLINICAL RESULTS AND TRENDS

Applications of microwaves in medicine is a quite a new field of a high interest in the world (since early 80's). It is necessary to mention one of the most important trends in the research of medical applications of microwaves, i.e., the thermal effects of EM field (since early 80's a microwave thermotherapy is used for cancer treatment, for urology in BPH treatment and for some other

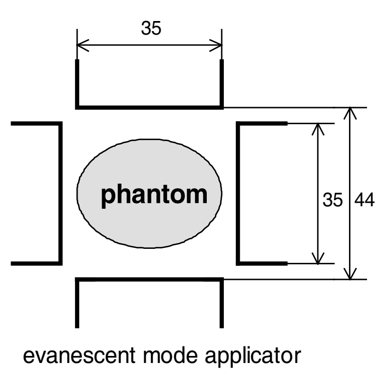

Figure 1: Set up of proposed regional applicator (4 evanescent mode applicators).

areas of medicine; it can be used also in combination with other complementary treatment methods, eventually).

E.g., in cancer treatment is thermotherapy usually used in the combination with some of other modalities used in the clinical oncology (e.g., radiotherapy, chemotherapy, immunotherapy or chirurgical treatment). It is used in USA, Japan and in many countries in Europe, including Czech Republic, from early 80s. Up to now local microwave hyperthermia for cancer treatment and thermotherapy of BPH are the most significant medical application of microwaves here. In Czech Republic we have treated more than 500 patients. Results of the treatment of one of our patients group is given the following table:

Table 1: Clinical results of cancer treatment by radiotherapy.

Complete response of the tumor	**52.4%**
Partial response of the tumor	**31.7%**
Without response	**15.9%**

Successful treatment thus has been indicated in the case of 84% of patients. This corresponds very well to the results published in EU and USA. Actual informations about microwave thermotherapy and its new developments is possible to get from "International Journal of Hyperthermia" issued by European Society for Hyperthermia Oncology (ESHO) together with North American Hyperthermia Society (NAHS) and Asian Society of Hyperthermia Oncology (ASHO). We receive this journal and we enable to other interested people to be informed.

3. TECHNICAL TRENDS

Most important technical fields of microwave thermotherapy development (covered also in our activities) can be specified as:

- Applicators: development and optimization of new applicators for more effective local, intracavitary and regional treatment.
- Treatment planning: mathematical and experimental modeling of the effective treatment.
- Noninvasive temperature measurement: research of the possibilities of new techniques (like NMR and US) for exact noninvasive measurements.
- Microwave medical diagnostics (Microwave Tomography).

4. DEEP LOCAL APPLICATORS

For the deep local thermotherapy treatment we are developing waveguide type applicators based on the principle of either dielectric filled waveguide or on the principle of evanescent modes (i.e., waveguides excited below its cut-off frequency) — which is our specific solution and original contribution to the theory of microwave hyperthermia applicators. Technology of evanescent mode applicators enable us to design applicators with as small aperture as necessary also for relatively low frequencies, e.g., from 10 to 100 MHz, needed for deep penetration into the biological tissue (i.e., up to 10 centimetres under the body surface).

5. NEW PRINCIPLES FOR THE REGIONAL APPLICATORS

Goal of this work is the development of the new applicators with higher treatment effects. Methodological approach for the solution of the problem will be theoretical and experimental study of the new types of regional applicators. Our aim is to improve the present theoretical model to optimize the temperature distribution in the treated area.

We can design the regional applicators on the basis of the analytical description of the excited electromagnetic field for the case of simplified homogeneous model of the treated biological tissue. For a more realistic case of the nonhomogeneous dielectric composition of the biological tissue the analytical calculation does not guarantee enough exact results. Therefore we would need to build the equipment for experimental tests of the applicators and we will study the possibilities of its numerical mathematical modeling.

6. CALCULATION AND MEASUREMENT OF THE TEMPERATURE DISTRIBUTION

In theoretical and experimental evaluation, the grade of homogeneity of the temperature distribution in the target area has been tested, see the Fig. 2. Our mathematical approach is based on idea of waveguide TM_{01} mode excited in the agar phantom under the given conditions (see the dashed lines). Measurement of SAR (full lines) has been done on agar phantom of the muscle tissue.

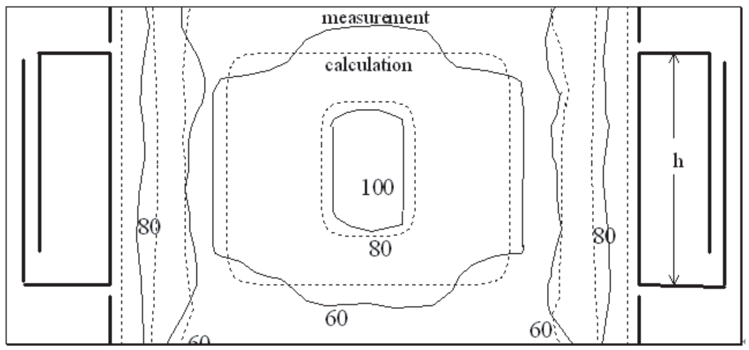

Figure 2: Normalized SAR distribution (both calculated and measured) in the heated agar phantom.

7. INTRACAVITARY APPLICATORS

These applicators are being used above all for prostate treatment in the case of BPH (Benign Prostate Hyperplasia). Of all the available minimal invasive treatment modalities, microwave is one of the most wide spread at present. Until now more than 1000 patients has been successfully treated here in Czech Republic.

The basic type of intracavitary applicator is a monopole applicator. The construction of this applicator is very simple, but calculated and measured "Specific Absorption Rate" ("SAR") distribution along the applicator is complicated. "SAR" can be measured either in water phantom or by infrared camera. During measurements of SAR along the applicator we have found, that typically there is not only a one main "SAR" maximum (first from the right side), but also a second and/or higher order maxims can be created, being produced by outside back wave propagating along the coaxial cable, see Fig. 3. To eliminate this second maximum and optimize the focusing of "SAR" in predetermined area of biological tissue needs to use the helical coil antenna structure, see Fig. 4. After coil radius and length optimization we have obtained very good results of "SAR" distribution.

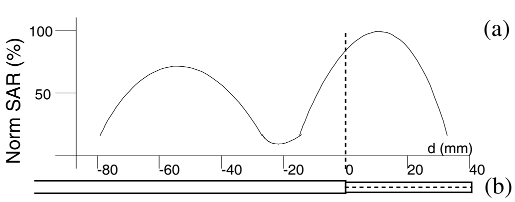

Figure 3: Monopole applicator.

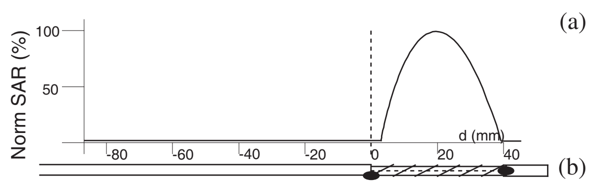

Figure 4: Helical coil applicator.

In Fig. 5, We can see a comparison of SAR resp. temperature distribution for three cases of intracavitay applicators: monopole, dipole and helical coil.

As in the previous case of external applicators we have studied the theoretical limits of intracavitary applicator heating depth. We have found the basic relation for determination of the limit of maximum heating depth for the case of "very long" intracavitary applicator. We suppose excitation of an ideal radial wave arround radiating applicator.

Very important is that there is a radial wave, not the plane wave, and that's why the penetration depth is smaller than penetratinon depth of plane wave. Some works published in this field give too optimistic results. Measurements discussed without theoretical analysis can give results influenced by thermal conductivity of mostly used agar phantom of muscle tissue. As the real heating depth is typically a few millimeters (in the best case up to cca 1 cm under the surface of the cavity), thermal conductivity of the phantom material can easily cause errors of several tenth of percents.

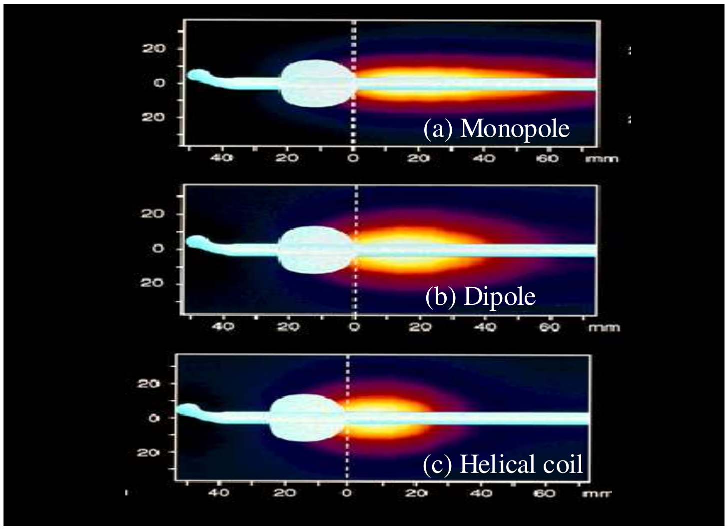

Figure 5: The heating pattern of different antennas: (a) the monopole, (b) the dipole, and (c) the helical coil.

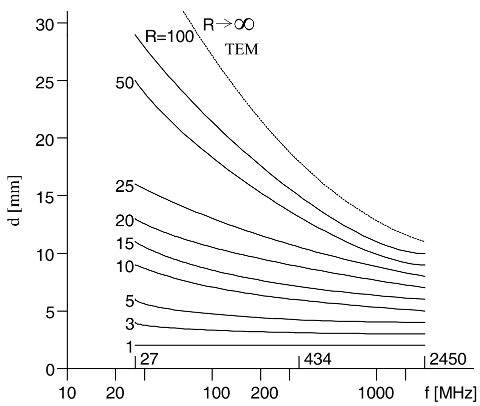

Figure 6: Effective depth of heating d with respect to frequency f [MHz] and radius R [mm].

8. CONCLUSIONS

As novel results of our work we could mention that the new type of microwave applicator for cancer treatment has been developed and evaluated. Evaluation procedures have shown, that this applicator is a very effective heating structure and excellent compatibility with NMR and US has been approved as well. Having approved this applicator in animal experiment, we are now working on development of its big version to be used in clinical praxis.

ACKNOWLEDGMENT

This research is supported by the Czech Science Foundation by project P102/11/0649: "Research and measurements of signals generated by nanostructures".

REFERENCES

1. Field, S. B. and C. Franconi, editors, "Physics and technology of hyperthermia," *NATO Seminar Proceedings*, Urbino, Italy, 1986.
2. Hand, J. and J. R. James, editors, *Physical Techniques in Clinical Hyperthermia*, Wiley, New York, 1986.
3. Vrba, J. and M. Lapeš, *Microwave Applicators for Medical Purposes*, CTU Press, 1996 (in Czech).
4. Vrba, J., C. Franconi, and M. Lapeš, "Theoretical limits for the penetration depth of the intracavitary applicators," *International Journal of Hyperthermia*, Vol. 12, No. 6, 737–742, 1996.
5. Franconi, C., J. Vrba, and F. Montecchia, "27 MHz hybrid evanescent-mode applicators with flexible heating field for deep and safe subcutaneous hyperthermia," *International Journal of Hyperthermia*, Vol. 9, No. 5, 655–674, 1993.
6. Vrba, J., C. Franconi, and F. Montecchia, "Evanescent-mode applicators for subcutaneous hyperthermia," *IEEE Trans. on Biomedical Engineering*, Vol. 40, No. 5, 397–407, May 1993.

Electromagnetic Applicators for Deep Local Treatment

D. Vrba and J. Vrba, Jr.
Department of Biomedical Technology, Faculty of Biomedical Engineering
Czech Technical University in Prague, Kladno, Czech Republic

Abstract— Paper deals with our new results in the field of applicators used for microwave regional thermotherapy, like, e.g., cancer treatment, physiotherapy, etc.. New types of applicators based on Metamaterial technology especially with zeroth order resonances will be introduced. The main aim of this work is to verify whether EM wave penetrating into the biological tissue can have good SAR homogeneity and depth of penetration approaching to theoretical limit.

1. INTRODUCTION

Several structures of metamaterial antennas were introduced in previous years. Antennas with sufficient radiation efficiency were presented in [1, 2]. Aim of this paper is to verify whether the metamaterial structure is possible to use for fabrication of the applicators for Hyperthermia Treatment. For this experiment antennas from [1, 2] will be used and further this structures will be modified with respect to required quality. Applicators have to be design with suitable shape of radiated electromagnetic wave. For local and deep local treatment electromagnetic plane wave can ensure:

- the best penetrating depth,
- the best homogeneity of SAR.

2. DESIGN OF THE APPLICATOR

For this experiment idea of applicators from [3–9] is used. Several changes were accomplished. The metamarerial antenna was inserted in the waveguide. Working frequency of such structure in the waveguide or outside the waveguide is the same $f = 434\,\mathrm{MHz}$ Working principle of this structure is the same as in [1, 2]. Thanks to excitation of zeroth order mode EM field in all the vertical parts (including feeding) of the antenna are in phase. As we can see further phenomenon of the Huygens principle arise. The radiated contribution from all vertical part is counted. Dimensions of the vertical part of the antenna were chosen to $\lambda/10$. Dimension of the unit cell can vary from 2–6 cm. According to this dimension it is necessary to adapt the dimensions of the interdigital capacitors.

3. ABSORBING OF EM POWER INTO THE TISSUE

To verify how these structures will radiate into the tissue several simulation of the real condition were done. Parameters of the muscle tissue are relative permittivity 57 and electrical conductivity 0.81 S/m. There is a water bolus placed between the aperture and tissue. SAR distribution is displayed in the pictures Figs. 2 and 3 in two planes. It can been seen that EM wave penetrating into the biological tissue had very good SAR homogeneity and depth of penetration approaching the theoretical limit.

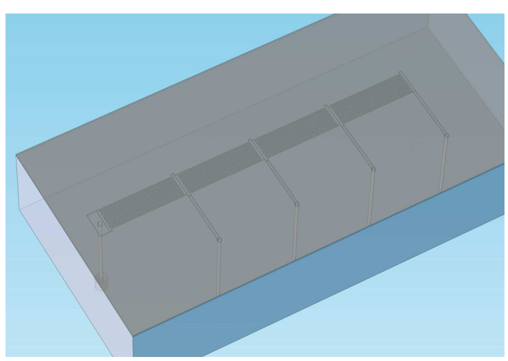

Figure 1: Design of the applicator consisted of four unit cell.

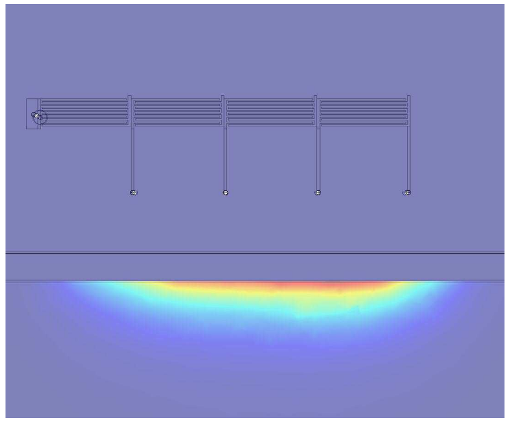

Figure 2: Top view of the applicator and the tissue.

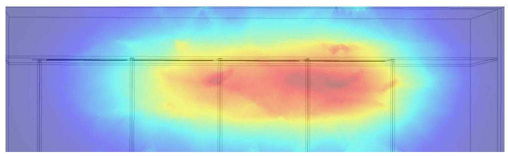

Figure 3: Radiated power from the aperture.

4. APPLICATOR REALIZED ON PRINTED CIRCUIT BOARD

In Fig. 4 there are another two structures with very good possibility to work as an applicator. The structure is designed on a micro-coplanar waveguide on substrate ($\varepsilon_r = 3.05$, $\tan\delta = 0.003$), the height of the substrate is $h_1 = 1.5\,\mathrm{mm}$, air bridges forming shunt inductors of height $h = 1.6\,\mathrm{cm}$ (shielded plane with substrate is not displayed here). Further description is in [1, 2].

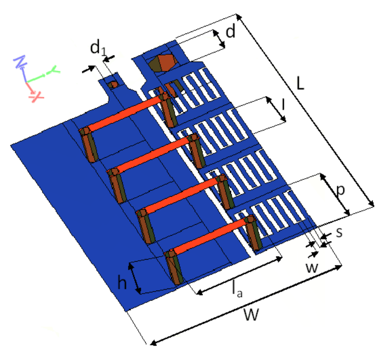

Figure 4: Co-planar type of applicator.

5. CONCLUSIONS

New MTM structures with capability of creating plane wave to be radiated into the biological tissue were introduced in this paper. It has been demonstrated here that EM wave penetrating into the biological tissue had very good SAR homogeneity and depth of penetration approaching theoretical limit. Our future plans will be to do an experiment of these structures and verify the promising simulations experimentally.

ACKNOWLEDGMENT

This research has been supported by the research program of Grant Agency of the Czech Republic, project 13-29857P Human Body Interactions with EM Field Radiated by Metamaterial Structures.

REFERENCES

1. Vrba, D. and M. Polívka, "Radiation efficiency improvement of zeroth-order resonator antenna," *Radioengineering*, Vol. 18, No. 1, 1–8, ISSN 1210-2512, 2009.
2. Polívka, M. and D. Vrba, "Shielded micro-coplanar CRLH TL zeroth-order resonator antenna: Critical performance evaluation," *Radioengineering*, Vol. 18, No. 4, 368–372, ISSN 1210-2512, 2009.
3. Franconi, C., J. Vrba, and F. Montecchia, "27 MHz hybrid evanescent-mode applicator," *Int. J. Hyperthermia*, Vol. 9, No. 5, 655–674, 1993.
4. Vrba, J., "Evanescent-mode applicators (EMA) for superficial and subcutaneous," *IEEE Transactions on Biomedical Engineering*, Vol. 40, No. 5, 397–407, ISSN 0018-9294, 1993.
5. Vrba, J., M. Lapeš, and L. Oppl, "Technical aspects of microwave thermotherapy," *Bioelectrochemistry and Bioenergetics*, Vol. 48, No. 10, 305–309, 1999.
6. Vrba, J., C. Franconi, and M. Lapeš, "Theoretical limits for the penetration depth of intracavitary applicators," *International Journal of Hyperthermia*, Vol. L2, No. 6, 737–742, ISSN 0265-6736, 1996.
7. Vrba, J., P. Togni, J. Vrba, Jr., and D. Vrba, "Theory of evanescent mode applicators," *PIERS Proceedings*, 767–770, Cambridge, USA, Jul. 2–6, 2008.
8. Togni, P., J. Vrba, and L. Vannucci, "Hyperthermia applicator for small superficial tumor treatment electromagnetics," *PIERS Proceedings*, 775–779, Cambridge, USA, Jul. 2–6, 2008.
9. Vrbová, B. and J. Vrba, "Microwave thermotherapy in cancer treatment: Evaluation of homogeneity of SAR Distribution," *Progress In Electromagnetics Research*, Vol. 129, 181–195. 2012.

EM Applicators: Apperture and Water Bolus Resonances

D. Vrba and J. Vrba, Jr.
Department of Biomedical Technology, Faculty of Biomedical Engineering
Czech Technical University in Prague, Kladno, Czech Republic

Abstract— This paper deals with our new results in the field of external applicators used for local microwave thermotherapy, like, e.g., cancer treatment, physiotherapy, etc.. We will focus here on a very special problem of aperture and water bolus resonances — a phenomenon, which can significantly deteriorate SAR and temperature distribution in the treated area and so significantly complicate the treatment of cancer patient. And to implement metamaterial technology.

1. INTRODUCTION

In our paper we describe specific aspects of external local applicators, usually working at 70, 434 and 2450 MHz [1–4]. These applicators were used here in Prague at Institute of Radiation Oncology for the treatment of more then 1000 cancer patients with superficial or subcutaneous tumours (up to the depth of approx. 6 cm).

We have studied waveguide applicators heating pattern for the aperture excitation at above and at under the cut-off frequency. It has helped us to get analytical approximations of the electromagnetic field distribution in the treated area of the biological tissue. In the Fig. 1, there is one of very important results — diagram showing the theoretical depth of heating d as a function of the used frequency f and of the aperture diameter D of the applicator. The most important results for the effective heating depth d can be characterised as follows:

- at high frequencies (above 1000 MHz) the depth of effective heating d is a function of frequency f,
- bellow 100 MHz d is the dominantly function of the diameter D of applicator aperture ($d = 0.386D$).

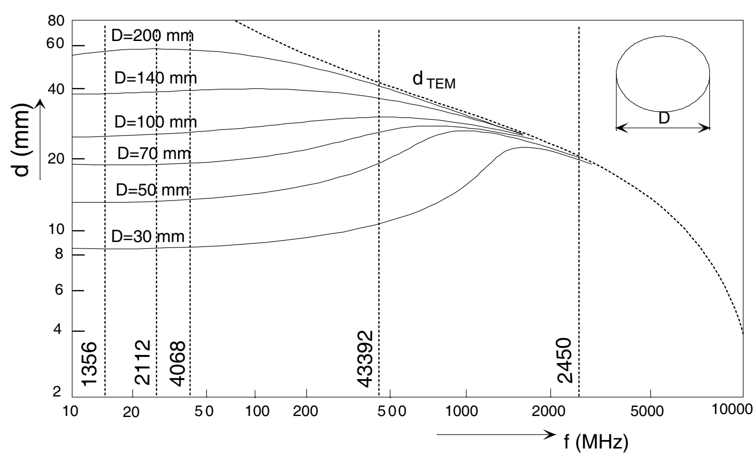

Figure 1: Effective depth of heating d for external applicator with respect to frequency f and diameter of aperture D.

Local microwave applicators can be either directly coupled to treated area, or they can be coupled through the so called water bolus (i.e., plastic sac).

2. RESONANCES IN THE APERTURE OF WAVEGUIDE APPLICATOR

In our contribution we would like to discuss what happens, when the frequency f of hyperthermia apparatus is either very different (much higher or lower) from the aperture resonance frequency f_r or very near (even equal) to the aperture resonance frequency f_r of the used waveguide applicator. This special case of our interest can happen when either the hyperthermia apparatus is tunable in broader frequency range or the aperture resonance frequency f_r of the applicator is changed by different dielectric parameters of various types of biological tissues.

There is a substantial difference between the two ways of the waveguide applicator excitation (i.e., above or under the aperture resonance frequency f_r) and in the propagation and "behaviour" of the EM field inside such applicator also. For the following discussion we have chosen the case of the rectangular applicator with a flange. But similar results is possible to obtain for other important cases like, e.g., rectangular applicators without flange or for the family of circular applicators.

In Fig. 2, a simple sketch of electric field strength line of the electromagnetic field irradiated from waveguide applicator is shown. It is the basis of our analysis of SAR distribution in front of the aperture of waveguide applicator, radiating into the heated biological tissue. Formulas describing the electric field distribution are given in the right side of this figure. Waveguide flange is in our approach considered as an electric wall; dashed line going into the biological tissue determines the magnetic wall of our model. The distance between these walls determines the aperture resonance frequency f_r of the applicator aperture. Of course, f_r is influenced by the tissue permittivity also.

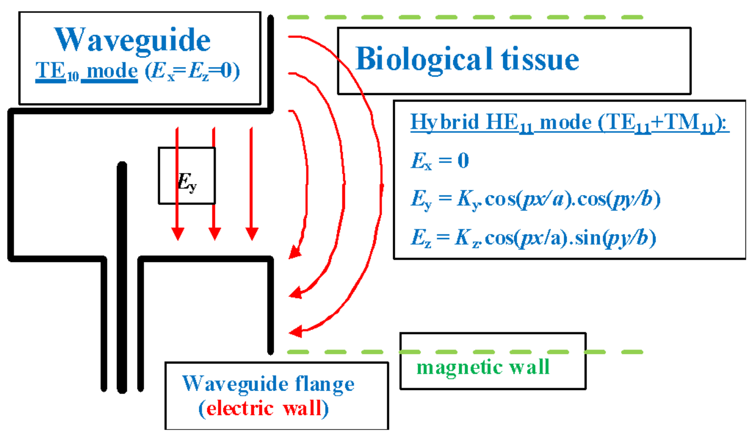

Figure 2: Schematics of the applicator radiating into the biological tissue.

Let us take into account the area of biological tissue surrounded by electric and magnetic walls. Then the hybrid waveguide mode HE_{11} (i.e., the lowest possible one) can be defined and excited in the biological tissue in front of applicator aperture and can be specified by the case $m = n = 1$. In fact, it is a linear superposition of the modes TE_{11} and TM_{11}. Higher order modes can be suppressed by the suitable construction of the applicator. Moreover these modes do not penetrate so deep in the tissue, therefore we need not to take them into account.

Waveguide flange is considered as an electric wall, dashed line going into the biological tissue determines the magnetic wall of our model. Let us take into account the area of biological tissue surrounded by electric and magnetic walls. Then the hybrid waveguide mode HE_{11} (i.e., the lowest possible one) can be defined and excited in the biological tissue in front of applicator aperture (it is a linear superposition of the modes TE_{11} and TM_{11}).

Series of the Figs. 3(a) to 3(e) show the change of the SAR in front of the applicator aperture as a function of working frequency f of the hyperthermia apparatus with respect to the f_r. There is big difference between f and f_r in the case shown in Fig. 3(a), instead both frequencies are very near each to other in the Fig. 3(e) (the difference between f and f_r is going down through the figure series). These results are important from theoretical point of view of the knowledge about the general properties of the waveguide applicators. And are very important also for the treatment — our results demonstrate very substantial changes of SAR distribution in the treated biological tissue. If f is going to f_r then so called hot spots complicating the treatment can arise.

- Higher order modes can be suppressed by the design of the applicator. Following 5 cases describe the change of the SAR in front of the applicator aperture as a function of working frequency f of the hyperthermia apparatus with respect to the f_c,
- if there is enough big difference between f and f_c, then homogeneous heating of the treated area can be expected — see Figs. 3(a), (b), (c), (d), (e),
- if the both frequencies are very near each to other (difference between f and f_c is going down), then overheating (hot-spots) out of the treated area can arise — see Figs. 3(d), (e).

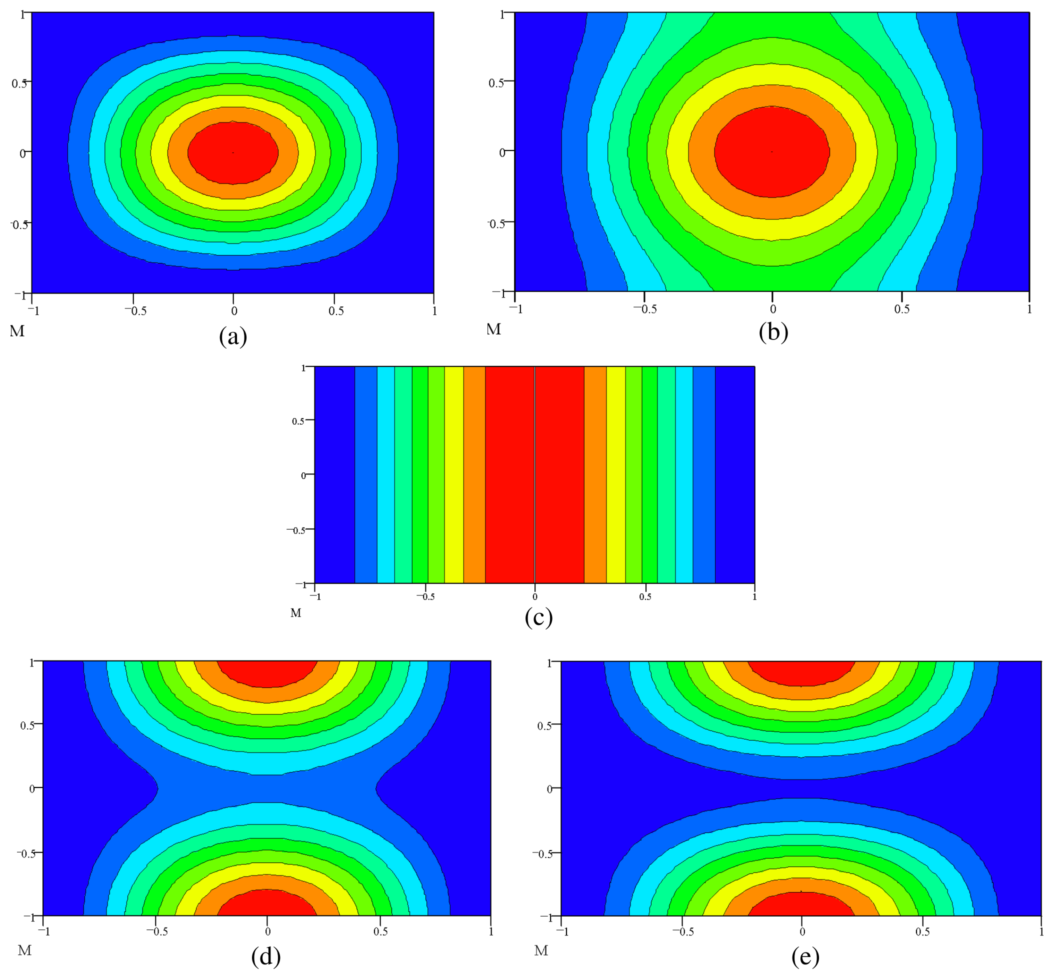

Figure 3: Calculated SAR in the waveguide aperture.

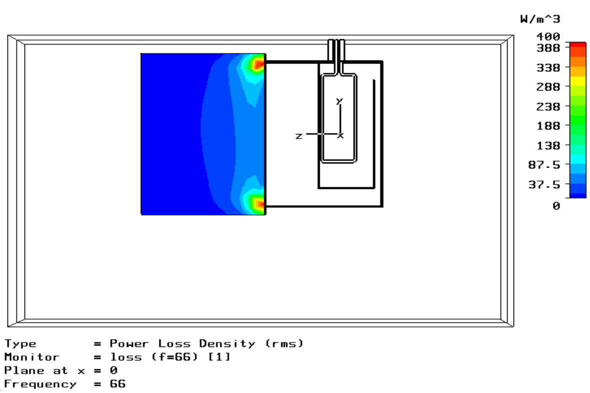

Figure 4: Numerical simulation of the applicator radiating into the biological tissue.

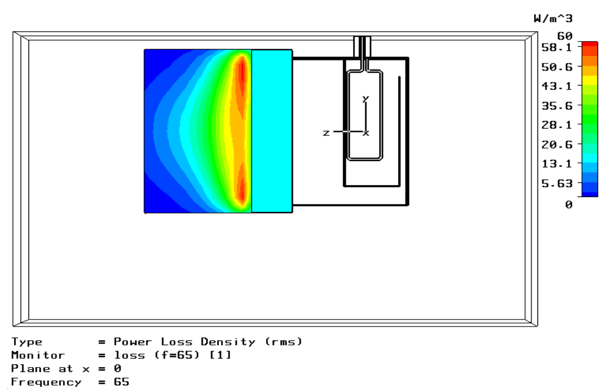

Figure 5: Numerical simulation of the applicator radiating into the biological tissue through the water bolus.

3. WATER BOLUS

Often waveguide applicator is not coupled directly to the biological tissue, but between its aperture and treated area so called water bolus is being placed — please compare Fig. 4 and Fig. 5.

There are several reasons to do this. Firstly if waveguide applicator could create so called hot spots (intensive overheating of certain part of the treated area as can be observed in Fig. 4) then water bolus can prevent patient from this problem, if water bolus will be used.

We have studied the influence of water bolus on SAR and temperature in the treated area. In

Fig. 5, we would like to give an example of SAR and temperature improvement obtained by aid water bolus in comparison to Fig. 5. In general, water bolus can often improve both SAR and temperature distributions in the treated area. But sometimes volume resonances can occur and in such case heating pattern in the area to be treated can deteriorate significantly. To prevent that, we need to study conditions of excitations of resonant modes inside water bolus and in the applicator aperture. Superposition of these mode can give very surprising EM field and temperature distribution in the treated area.

4. VOLUME RESONANCES IN THE WATER BOLUS

Further we will discuss possibilities of excitations of volume resonances in the water bolus. For simplicity we will work here only with electrical field strength components

$$\dot{E}(x,y,z)=\frac{E_0\exp\left(-ikz^*\right)}{\left[\left(z^*-a_0\right)\left(Z^*-b_0\right)\right]^{1/2}}\cdot\exp\left[\frac{-ikx^2}{2\left(z^*-a_0\right)}\right]\cdot\exp\left[\frac{-iky^2}{2\left(z^*-b_0\right)}\right] \tag{1}$$

From electromagnetic point of view water bolus can be considered to be a dielectric resonator with a series of the so called resonant modes and their resonant frequencies. Basic known equation for resonant frequencies of cavity resonator can be expressed as

$$f_{VO}^{mnl}=\frac{1}{2\sqrt{\varepsilon\mu}}\sqrt{\left(\frac{m}{a}\right)^2+\left(\frac{l}{b}\right)^2+\left(\frac{n}{d}\right)^2}=f_{op}. \tag{2}$$

In general we can distinguish volume resonances (in the case when n is different from 0) and aperture resonances (in the case when n is equal to 0).

Previous equation for resonant frequency of resonant modes is valid only for certain type of boundary conditions: metallic wall surrounding dielectric media. In our case situation is more complicated. In order to determine resonant modes and its resonant frequencies we have to take into account following transitions from the studied water bolus to:

- aperture of applicator,
- biological tissue,
- surrounding air.

To describe open wall resonators in microwave technology we often use a model of either so called electric wall or the so called magnetic wall. In both of these cases almost all incident electromagnetic power is being reflected back to water bolus, i.e., energy can be stored in the discussed water bolus and so it can behave like a resonating structure. Magnetic wall can be a good model for the case of the transitions between water bolus and surrounding air. And for the case of transitions between water bolus and aperture of applicator if this applicator is filled by air as well. Instead if we take into account either transition between water bolus and water filled applicator or transition between water bolus and biological tissue, then level of reflections is very low, as dielectric constant values are very near each to other in different parts of discussed system.

5. CONCLUSIONS

Microwave thermotherapy is successfully applied in clinics in the Czech Republic. Technical support is at present from the Czech Technical University in Prague. Our goal for the next technical development was to improve the theory of the local applicators design and optimisation, innovate the system for the applicator evaluation (mathematical modelling and measurements) and to implement metamaterial technology.

ACKNOWLEDGMENT

This research has been supported by the research program of Grant Agency of the Czech Republic, project 13-29857P Human Body Interactions with EM Field Radiated by Metamaterial Structures.

REFERENCES

1. Franconi, C., J. Vrba, and F. Montecchia, "27 MHz hybrid evanescent-mode applicator," *Int. J. Hyperthermia*, Vol. 9, No. 5, 655–674, 1993.

2. Vrba, J., "Evanescent-mode applicators (EMA) for superficial and subcutaneous," *IEEE Transactions on Biomedical Engineering*, Vol. 40, No. 5, 397–407, ISSN 0018-9294, 1993.
3. Vrba, J., M. Lapeš, and L. Oppl, "Technical aspects of microwave thermotherapy," *Bioelectrochemistry and Bioenergetics*, Vol. 48, No. 10, 305–309, 1999.
4. Vrba, J., C. Franconi, and M. Lapeš, "Theoretical limits for the penetration depth of intracavitary applicators," *International Journal of Hyperthermia*, Vol. L2, No. 6, 737–742, ISSN 0265-6736, 1996.
5. Vrba, J., P. Togni, J. Vrba, Jr., and D. Vrba, "Theory of evanescent mode applicators," *PIERS Proceedings*, 767–770, Cambridge, USA, Jul. 2–6, 2008.
6. Togni, P., J. Vrba, and L. Vannucci, "Hyperthermia applicator for small superficial tumor treatment electromagnetics," *PIERS Proceedings*, 775–779, Cambridge, USA, Jul. 2–6, 2008.
7. Vrbová, B. and J. Vrba, "Microwave thermotherapy in cancer treatment: Evaluation of homogeneity of SAR distribution," *Progress In Electromagnetics Research*, Vol. 129, 181–195, 2012.

Lens Applicator for EM Thermotherapy

D. Vrba and J. Vrba, Jr.
Department of Biomedical Technology, Faculty of Biomedical Engineering
Czech Technical University in Prague, Kladno, Czech Republic

Abstract— The paper deals with the introduction of microwave applicator with lens aperture operating at a frequency of 434 MHz. The applicator has a convergent effect of transmitted electromagnetic waves in lossy dielectrics the value of the relative permittivity close to the values of biological tissues. This study is the preparative phase for future development of a lens applicator based on metamaterial technology.

1. INTRODUCTION

The lens body is a geometric shape transparent to radio waves (Fig. 1). This means that transmit electromagnetic waves with a phase velocity v, is different from the phase velocity in air. We cannot therefore be regarded as a body with a refractive index n.

$$n = c/v \tag{1}$$

If the phase velocity is greater than the speed of light ($n < 1$), we can speak about accelerating lens. If the phase velocity is less than speed of light ($n > 1$), we can speak about retarding lens. As a result of differences in refractive index of the lens and the environment (e.g., air) the spherical or cylindrical wave is changing to a plane wave and vice versa.

2. ACCELARATING LENS

The theory of transmitting waves implies that the phase velocity of electromagnetic waves between two planar plates or in the waveguide is greater than the velocity of propagation in free space. This feature will be used in the implementation of lenses whose refractive index is smaller than one ($n < 1$). For illustration, we will consider the cylindrical face.

Metal lens is composed of a series of metal plates whose distance is always larger than half the wavelength and smaller than the wavelength calculated from the critical frequency waves in the waveguide. This should be ensured by guiding waves through the dominant mode. The incident electromagnetic wave whose electric field is parallel to the plates, to the input of the metal lenses, refraction occurs because the electromagnetic wave propagates between the plates faster than the phase velocity in free space. The system of parallel metal plate behaves as an environment with a refractive index

$$n = \frac{c}{v_f} = \sqrt{\left[1 - \left(\frac{\lambda}{2a}\right)^2\right]} \tag{2}$$

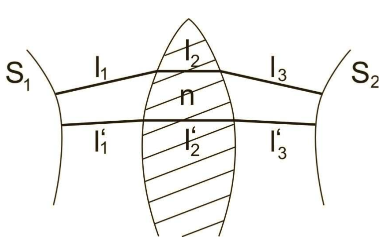

Figure 1: Schematic representation of lens function.

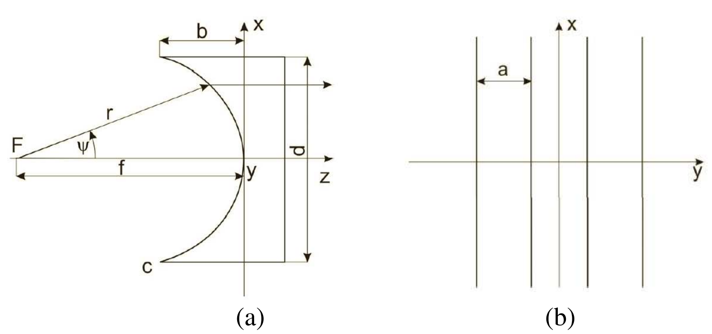

Figure 2: Acceleration lens in the XZ plane and XY plane.

where a is the distance between plates (see Fig. 2). To determine the focal length we can start from the equation:

$$f = \frac{n+1}{2}b + \frac{d^2}{8(1-n)b} \tag{3}$$

The profile of the metal lenses, the following relationship equation which corresponds to an ellipse, the primary radiator is positioned at the far focus.

$$r = \frac{f(1-n)}{1-n\cos\psi} \tag{4}$$

Theoretically, the distance between plates could be chosen between $\lambda/2 < a < \infty$. Refractive index would then be changed in the range of $0 < n < 1$. As we mentioned earlier, however, we require only the propagation of the dominant mode and therefore we choose $\lambda/2 < a < \lambda$. From $0 < n < 0.86$ for free space. Focal length is the place where the electromagnetic rays passing through the lens.

3. DESIGN OF THE APPLICATOR

Excitation of the applicator is realized by current probe. It is inserted into the waveguide so that the lines of force of the electric field were parallel with it. As shown in the Fig. 3, the probe is placed inside the waveguide at the point with coordinates $x = a/2$, where the electric field dominant mode TE_{10} has its maximum.

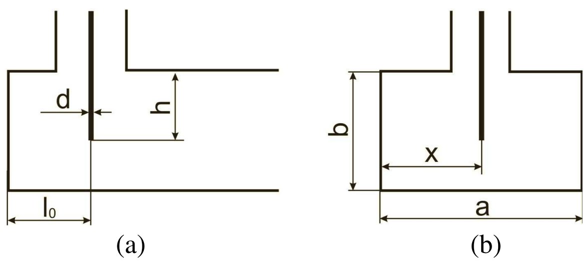

Figure 3: Dimensions of waveguide.

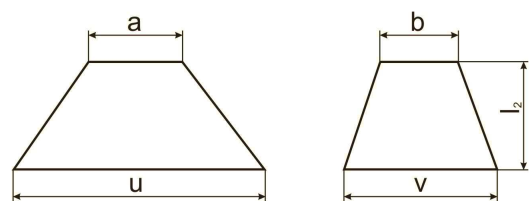

Figure 4: Waveguide horn.

Excitation probe is a source of electromagnetic field. Influence of the parameters of the transition has therefore its diameter and depth of insertion. For the construction of the excitation probe was used copper wire with a diameter $d = 2$ mm. Length insertion excitation probe was set to $\lambda/4$, i.e., $h = 25$ mm.

The waveguide is connected to the divergent part of the waveguide, the horn (Fig. 4). Used for a smooth transition of electromagnetic waves into a larger aperture, the electromagnetic lens. In this segment, thanks to its geometric shape there cannot be created higher order modes. Dimensions of the horn are designed with the dimensions of the lens aperture. It should also reduce the length of the applicator for better impedance matching (the shorter the applicator, the wider curve S_{11} — better adaptation). Length of the horn segment was determined according to previous mention theory to the value $L_2 = 40$ mm.

Proposal for lens aperture based on the idea of focusing not only in the plane of the magnetic field vector $\mathbf{H}$ but also in the plane of the electric field $\mathbf{E}$ [1, 2]. The Fig. 5 shows the location of the focusing counters in the XZ plane (plane of the magnetic field) and YZ (plane of electric field).

The distance d_i between the metal plates determines how fast electromagnetic wave will propagate within a given section. Because the applicator is excited by a frequency 434 MHz and it is important to excite only the dominant TE_{10} mode, the distance of metal plates is limited by the condition $\lambda/2 < d_i < \lambda$.

The propagation constant between two plates is given by equation:

$$k_i = \sqrt{\omega^2\mu\varepsilon - \left(\frac{\pi}{d_i}\right)^2}, \quad i = 1, 2, 3, \ldots, n \tag{5}$$

where ω is the angular frequency of electromagnetic waves, ε and μ are constants environment. To calculate the length of each partition using a simple relationship that is analogous to geometrical

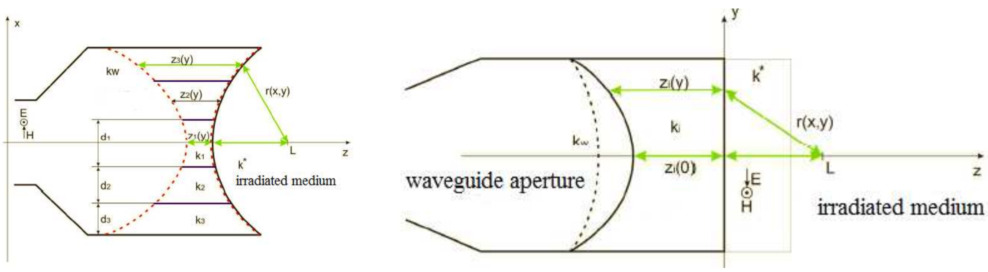

Figure 5: Metallic lens.

optics and is based on equality pathways of beams:

$$\mathrm{Re}(k_i)z_i(0) + \mathrm{Re}(k^*)r(x,0) = \mathrm{Re}(k_1)z_1(0) + \mathrm{Re}(k_w)(z_i(0) - z_1(0)) + \mathrm{Re}(k^*)L \qquad (6)$$

where k^* is the propagation constant in the irradiated medium k_w propagation constant across the aperture, and L is the distance between the focal point and the aperture of the applicator. We consider only the real part of the propagation constant. Other dimensions are shown in Fig. 5. Thus setting of the metal planes creates an electromagnetic lens that is shown in the picture (red line). If this condition is met, the electromagnetic waves passing through the aperture of the segments will be after the passage of focusing to a point in the plane of the magnetic field.

4. SIMULATION

At Fig. 6, we can see the simulation of applicator design according to previous theory. At Fig. 6(a), is aperture view including agar phantom. From Fig. 6(b), it is evident that thanks to superposition of the EM wave from different parts of applicator the penetration depth is twice deeper than in classical waveguide.

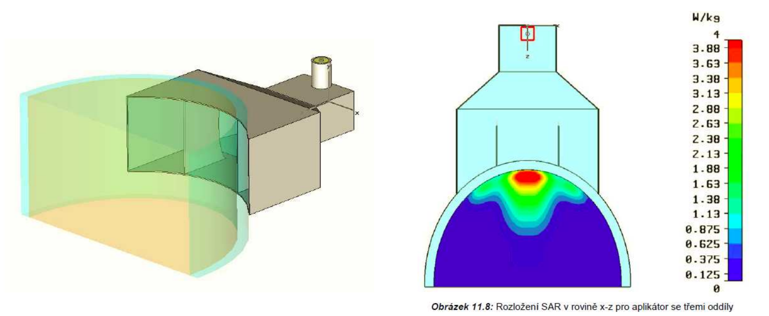

(a) (b)

Figure 6: Design of the applicator (a) from aperture view, (b) penetration depth of EM wave.

5. CONCLUSIONS

Microwave lens applicator operating at a frequency of 434 MHz was introduced in this paper. Its focusing effect was explained. The applicator has a convergent effect of transmitted electromagnetic waves in lossy dielectrics the value of the relative permittivity close to the values of biological tissues. This study is the preparative phase for future development of a lens applicator based on metamaterial technology.

ACKNOWLEDGMENT

This research has been supported by the research program of Grant Agency of the Czech Republic, project 13-29857P Human Body Interactions with EM Field Radiated by Metamaterial Structures.

REFERENCES

1. Yoshio, N. and W. Hiromi, "A direct-contact microwave lens applicator with a microcomputer-controlled heating system for local hyperthermia," *IEEE Transactions on Microwave Theory and Techniques*, Vol. 34, No. 5, IEEE Press, New York, 1986.

2. Yoshio, N. and K. Tohru, "An electric field converting applicator with heating patter controller for microwave hyperthermia," Vol. 34, No. 5, IEEE Press, New York, 1986.
3. Franconi, C., J. Vrba, and F. Montecchia, "27 MHz hybrid evanescent-mode applicator," *Int. J. Hyperthermia*, Vol. 9, No. 5, 655–674, 1993.
4. Vrba, J. and C. Franconi, "Evanescent-mode applicators for subcutaneous hyperthermia," *IEEE Trans. on BME*, Vol. 40, No. 5, 397–407, May 1993.
5. Vrba, J., "Evanescent-mode applicators (EMA) for superficial and subcutaneous," *IEEE Transactions on Biomedical Engineering*. Vol. 40, No. 5, 397–407, ISSN 0018-9294, 1993.
6. Vrba, J., M. Lapeš, and L. Oppl, "Technical aspects of microwave thermotherapy," *Bioelectrochemistry and Bioenergetics*, Vol. 48, No. 10, 305–309, 1999.
7. Vrba, J., C. Franconi, and M. Lapeš, "Theoretical limits for the penetration depth of intracavitary applicators," *International Journal of Hyperthermia*, Vol. L2, No. 6, 737–742, ISSN 0265-6736, 1996.

Compact LTCC-based Identification Reader Modules with Thermal Consideration for Ku-band Application

Yu Ye[1,2], **Liang Wu**[1], **Ling-Yun Li**[1], **Wei Wang**[1], **Shu-Na Wang**[1], **and Xiao-Wei Sun**[1]

[1]Key Laboratory of Terahertz Solid-State Technology
Shanghai Institute of Micro-system and Information Technology, Shanghai 200050, China
[2]University of Chinese Academy of Sciences, Beijing 100049, China

Abstract— A millimeter-wave identification readers for Ku-band short-range high data-rate backscattering communications is presented. The reader is composed of an oscillator, an amplifier, and a down converter based on GaAs pHEMT technology and integrated on a low temperature co-fired ceramic substrate. Power transmitted of the module is 7 dBm while the receiver 1 dB compression points are −5.5 dBm for Ku-band reader. The reader module achieves 4 GHz-wide IF bandwidth with miniaturized sizes of 15 mm × 11 mm for application.

1. INTRODUCTION

Recently, the mobile equipments with near-field communication (NFC) capability have already entered the market and got widespread development. However, the 424 kbit/s data rate at the 13.56 MHz band restricts the NFC technology applied within a distance of a few centimeters [1]. The application of NFC can be enlarged with high data rate and high operation frequency, while keeping the transponder inexpensive. Also this can be seen as a tendency of NFC [2]. An mm-wave identification (MMID) technology, has been introducing for the short range communication, where an active MMID reader with an inexpensive backscattering modulated transponder have been presented [3, 4]. There are several advantages when implemented MMID comparing with traditional RFID. The much wider bandwidth may offer much higher data rate in application such as mass memories wireless transferring in a few seconds. Furthermore, the directive antennas can be integrated for its small volume operating in mm-wave, which can provide the possibility of locating transponders in high-density sensor networks. What's more, the integrating technology can provide a smaller size in MMID than RFID, which makes the active reader more feasible to integrate on miniaturized terminations.

The multilayer low temperature co-fired ceramic (LTCC) technology has shown great potential due to its possibility to enable three-dimensional integration and interconnection. Passive components such as antennas, power dividers, and filters can be directly fabricated on LTCC [5]. Active components can be surface-mounted or buried to the LTCC substrate, where flip-chip and wire-bonding techniques have been implemented up to mm-wave range.

This paper presents an MMID reader that operating at Ku-band. The reader consists of GaAs monolithic micro-wave integrated circuits (MMICs) on a LTCC board. Oscillator, amplifier, and down converter have been realized in 0.15 µm pHEMT technology. The Ferro A6-M system LTCC is utilized for integration and package. The paper is organized as follow. Section 2 describes the architecture of the identification readers and in Section 3 three MMICs have been introduced. The LTCC assembling has been studied and an optimal packaging has been presented in Section 4. The experiment results are presented in Section 5. Finally, a conclusion is drawing in Section 6.

2. MMID READER ARCHITECTURE

MMID reader is very similar to a frequency-modulated continuous-wave (FMCW) radar. In FMCW radar, the local oscillator (LO) frequency is swept and the offset frequency arises from time delay of the reflection. However, in MMID, the LO is not swept, the offset frequency is introduced by the transponder, which modulates its reflection to carry information. Hence, in FMCW radars, a delicate phase-locked loop (PLL) architecture is needed to achieve better linearity of the frequency sweep [6], but this is not required in MMID readers, where the LO frequency is not swept.

In direct conversion architecture, assuming the signal incident to the reader Receiver (RX) is generated in a MMID transponder by backscattering modulation. Reference [3] can be utilized to calculate the modulated radar cross section for a transponder

$$\sigma_m = \frac{G_A^2 \lambda^2}{16\pi} \left|\Gamma_1 - \Gamma_2\right|^2 = \frac{G_A^2 \lambda^2}{4\pi} m \tag{1}$$

where G_A is transponder antenna gain and $m = |\Gamma_1 - \Gamma_2|^2/4$ is the modulation coefficient. Power incident to RX is

$$P_{rx} = P_{tx}\left[\frac{\lambda^2 G_{rx} G_{tx} \sigma_m}{(4\pi)^3 d^4} + L_{tx/rx}\right] \tag{2}$$

where P_{tx} is the transmit power, G_{rx} and G_{tx} represent the RX and transmitter (TX) antenna gain, respectively, d is the distance between the transponder and the reader, and $L_{tx/rx}$ is the isolation from the TX antenna port to RX antenna port. The signal-to-noise ratio (SNR) is given by

$$SNR = \frac{P_{tx}}{kT \cdot BW \cdot F} \frac{\lambda^2 G_{rx} G_{tx} \sigma_m}{(4\pi)^3 d^4} \tag{3}$$

where k is the Boltzmann constant, T is the absolute temperature, BW is the IF bandwidth, and F is the noise factor. As in our application, the specifications are set as $d = 5\text{–}15\,\text{cm}$, $G_{tx} = G_{rx} = G_A = 10\,\text{dB}$, $m = 1$, to achieve 2 GHz BW with a reasonable SNR in communication system, the transmitted power need to be more than 5 dBm.

As shown in Fig. 1, in 24 GHz application, the direct conversion architecture with a voltage-controlled oscillator (VCO) at 24 GHz is chosen for the MMID reader because it provides adequate sensitivity and output power. The oscillator output signal is divided by a power splitter to the TX output port and the LO port of the down converter. The complicated TX chain is not necessary for the VCO can provide enough power for the MMID reader, which greatly simplifies the system integration. The received signal is amplified using a low noise amplifier (LNA) and fed to the RF port of the down converter.

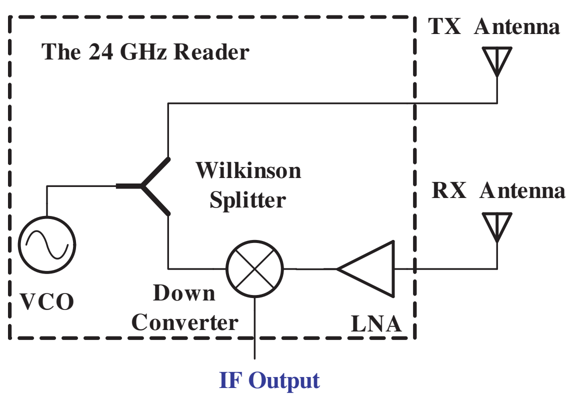

Figure 1: Block diagram of the 24 GHz MMID reader. The VCO, LNA, and down converter are implemented in GaAs pHEMT then integrated on LTCC.

3. MMIC DESIGN AND MEASURED PERFORMANCE

Three MMICs are fabricated using the commercial 0.15 µm GaAs pHEMT process at UMS for MMID reader application, which are featured in Fig. 2.

Figure 2: Photographs of the MMICs for 24 GHz MMID reader (from left to right): VCO, LNA and down converter.

3.1. VCO

A 24 GHz VCO has been designed for mm-wave signal generation, which is in Fig. 2. The circuit schematic of the VCO is based on the negative resistance concept using a common-source series feedback element to generate the negative resistance. Gate and drain biases of the transistor were chosen to achieve a good compromise between phase noise performance and optimum gm of the transistor. The feedback element that generates instability in the VCO consists of a short-end transmission line in parallel with an open-end transmission line. The resonance circuit on the gate side consists of a transmission line in series with a variable capacitance for frequency tuning. The variable capacitance is implemented by a common drain-source transistor whose capacitance is controlled by the gate voltage. A buffer amplifier is employed to further boost the output power. The performance of VCO is in Table 1.

Table 1: VCOs performance summary.

Parameter	VCO
Tuning Range	23.4–24.4 GHz
Output Power	12 dBm
Phase Noise	−85 dBc @ 1 MHz
DC Current	112 mA
DC Supply	3 V
Power Consumption	336 mW

3.2. Amplifier

As illustrated in Fig. 2, the low noise figure and high 1 dB compression point are the main design goals for 24 GHz LNA. Common-source cascaded architecture has been utilized. The gate width and bias current of the transistor in the last stage is determined by the output compression point, whereas the gate width and bias current of the first stage transistor is calculated to minimize noise figure and to satisfy the input matching condition. The small signal gain is 15 dB, with a noise figure of 3 dB. Other specifications are in Table 2.

Table 2: LNAs performance summary.

Parameter	LNA
Frequency Range	18–26 GHz
Small Signal Gain	15 dB
Input Return Loss	>10 dB
Output Return Loss	>5 dB
Noise Figure	3 dB
P_{in} 1 dB	−5 dBm
DC Current	60 mA
DC Supply	3 V
Power Consumption	180 mW

Table 3: Down converters performance summar.

Parameter	Down Conver
Frequency Range, RF	22 GHz–32 GHz
Frequency Range, IF	DC — 4 GHz
LO Input Power	8 dBm
Conversion Loss	11 dB
LO to RF Isolation	>20 dB
P_{in} 1 dB	10 dBm

3.3. Down Converter

The 24 GHz down converter has been realized with a pair of resistive transistors with a balanced architecture, which can provide a better local oscillator (LO) port to RF port isolation and enlarge the RF frequency range of down converter. The transistors are biased at −0.65 V to get an optimal conversion efficiency. The input 1 dB com-pression point is 11 dBm.

4. LTCC ASSEMBLING AND THERMAL VIA OPTIMIZATION

As shown in Fig. 3, the MMICs are mounted on the top metallized layer and wire-bonded to the LTCC, which is composed by 7 dielectric layers and 8 metallized layers. Each dielectric layer is about 100 μm thick after firing, while the metallized layer is about 5 μm thick. Trading off among performance, yield and cost, RF ground is chosen to be 3 dielectric layers under the top metallized layer.

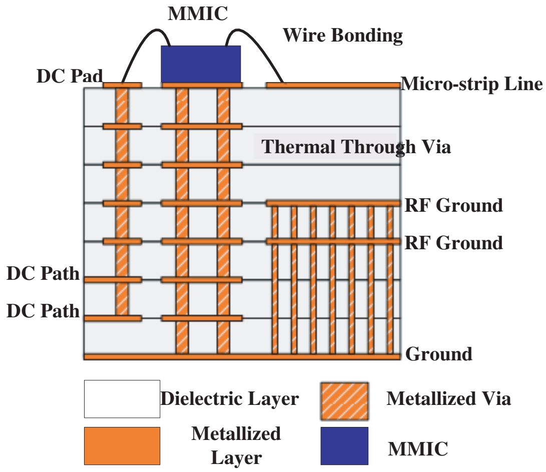

Figure 3: Configuration of layers in the LTCC assembling.

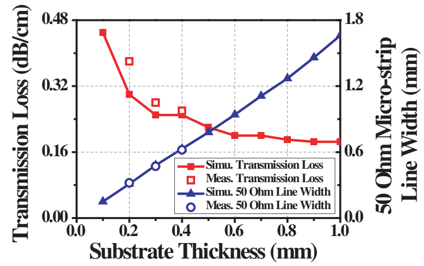

Figure 4: Measured and Simulated transmission loss and 50 Ohm line width.

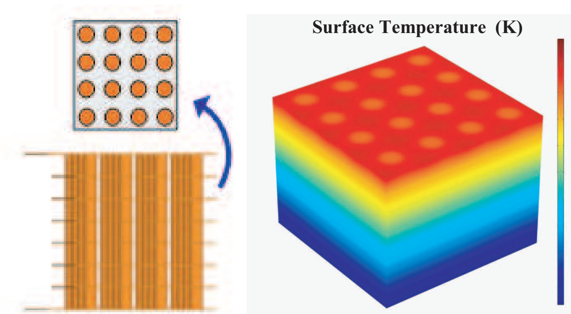

(a) (b)

Figure 5: Configurations of thermal via arrangement. (a) Sche-matic configuration. (b) Surface temperature distribution.

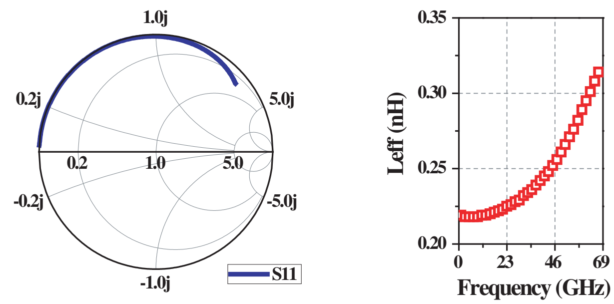

(a) (b)

Figure 6: The simulated results of thermal via arrangement. (a) Smith Chart of S_{11}. (b) Effective inductance.

As shown in Fig. 4, the transmission loss decreases with the substrate growing thicker but the decreasing gradually slows down when the substrate is thicker than 0.3 mm. Measured Results match well with simulations, which shows a 0.25 dB/cm transmission loss in 310 µm width 50 Ω micro-strip line upon a 0.3 mm LTCC substrate. Under the RF Ground there are two metallized layers for DC path while the bottom metallized layer as the virtual Ground.

The connections of MMIC backside and LTCC bottom ground are realized by thermal through vias, in which thermal and electromagnetic properties of such long through vias need to be considered carefully when implemented in mm-wave frequencies [7], because the performance of transistors is largely dependent with the operation temperature and other parasitic elements, especially for high power devices. To minimize the parasitic effects and maximize the cooling effects of the thermal through vias in LTCC board, the diameter and pitch of vias need to be optimized. The thermal through via arrangement we adopted is via-array with 100 µm diameter and 250 µm pitch. The schematic of the arrangement is featured in Fig. 5(a), which shows a 16-vias array per $1\,\text{mm} \times 1\,\text{mm}$. The COMSOL software has been implemented to simulate the thermal transferring effects.

Assuming a steady uniformed 0.5 W heat source is placed on a $1\,\text{mm} \times 1\,\text{mm}$ top metallized layer whereas the temperature of bottom metallized layer is fixed to 27°C. The thermal conductivities of ceramics and Ag alloy are 3 and 300 W/(mK), respectively. Fig. 5(b) shows that the top surface temperature distribution has only an about 2°C temperature deviation and the maximum temperature is 12°C higher than the room temperature. The simulated results depict a good thermal transferring consistency and a lower maximum surface temperature, for which can provide a more uniformed heat transferring platform in order to decrease the heat effects on MMICs.

The thermal through via imbeds inherently parasitic elements between MMIC transistors and the virtual ground. In simulation, the top surface of LTCC is connected to signals and the bottom is grounded, the frequency is up to 67 GHz. As described in Fig. 6, the simulated effective inductance of the thermal via arrangement is 0.22 nH. The Smith Chart of S_{11} shows the resonant frequency (f_{res}) is beyond 67 GHz, fitting for 24 GHz LTCC assembling.

5. EXPERIMENTAL RESULTS

The Ferro A6-M system was selected for this study due to its good high-frequency properties, which stay quite constant over a wide frequency range. Instead, the mm-wave performance of the LTCC modules is mainly affected by processing issues such as line width variations due to the printing steps or shrinkage during firing. Fig. 7 depicts the microphotograph of the LTCC modules in which the MMIC chips were wire-bonded on the surface. The fabricated micro-strip lines on LTCC for MMICs interconnections were designed properly to fit the charged impedance matching caused by the wire-bonding tech-nology, in which the length of the wire-bond is appro-ximately 150 µm. The losses of testing devices such as SMA connectors have been de-embedded from the results.

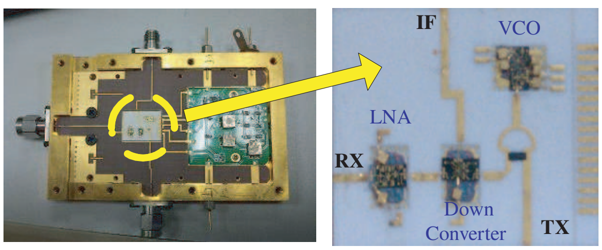

Figure 7: Photographs of fabricated and packaged reader module.

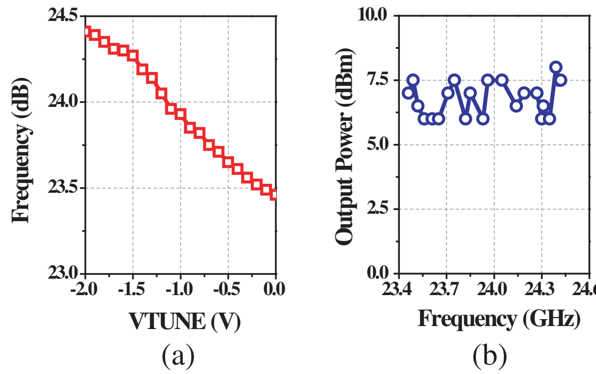

Figure 8: Measured transmitted frequency and power tuning curve of the reader. (a) Transmitted frequency vs. V_{TUNE}. (b) Transmitted power vs. tuning frequency.

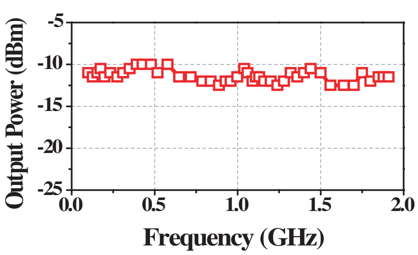

Figure 9: Measured IF output power with a −15 dBm frequency-tuned RF signal and a fixed 24 GHz LO signal.

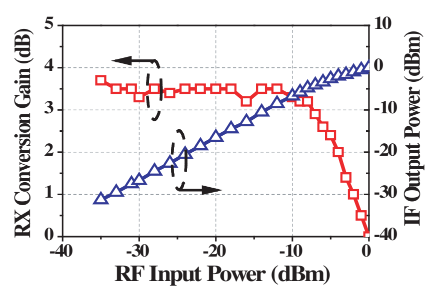

Figure 10: Measured RX conversion gain and IF output power with a power-tuned 24.4 GHz RF and a fixed 24 GHz LO signal.

Figure 8(a) illustrates the measured output frequency varied with tuned gate voltage of the VCO. The output signal has a linear tuning frequency range of about 1 GHz (from 23.4 GHz to 24.4 GHz). The output power is shown in Fig. 8(b), in which the average transmitted power is 7 dBm. The measured overall TX power is 2 dB less than estimated from component values only. However, the TX chain also includes several millimeters of transmission lines and wire bonds, as well as the splitter, which together can explain the additional attenuation.

The output IF power with a frequency-tuned −15 dBm input RF signal is shown in Fig. 9. The average IF output power (at down converter output) is around −11 dBm, while with a fixed 24 GHz LO frequency. When tuned the input RF frequency from 24.1 GHz to 25.9 GHz, the output IF signal has a low power variation, about ±1 dB around −11 dBm, which can provide a broad-band IF operation region with steady performance. The RX 1 dB compression point is −5.5 dBm, which is defined by the LNA input compression point, as featured in Fig. 10. The reader draws a total 160 mA (where VCO draws 100 mA, LNA draws 60 mA, respectively) from a 3 V DC supply.

The measured slight deviation of DC current between packaged and unpackaged MMICs can be explained as package parasitic effects or input/output mismatches. The reader totally has a DC power consumption of 480 mW and a 15 mm × 11 mm size.

6. CONCLUSION

This paper presents a Ku-band MMID reader. The reader consists of GaAs pHEMT Devices such as oscillator, amplifier, and down converter on Ferro A6-M system LTCC, where the assembling, especially the thermal via arrangement, has been studied and optimized. The characteristics of the whole system was measured and compared to the characteristics of the individual com-ponents. Good agreement in measured results are achieved. The transmit power is 7 dBm and the receiver input 1 dB compression point is −5.5 dBm while with a 4 GHz-wide IF band. The module size is only 15 mm × 11 mm.

REFERENCES

1. "NFC forum device requirements 1.0," NFC Forum Inc., Wakefield, MA, 2010, Available: http://www.nfc-forum.org/.
2. Pellerano, S., J. Alvarado, and Y. Palaskas, "A mm-wave power-harvesting RFID tag in 90 nm CMOS," *IEEE J. Solid-State Circuits*, Vol. 45, No. 8, 1627–1637, Aug. 2010.
3. Pursula, P., T. Vähä-HEikkilä, A. Müller, D. Neculoiu, G. Konstantinidis, A. Oja, and J. Tuovinen, "Millimeter wave identification — New radio system for low power, high data rate and short range," *IEEE Trans. Microw. Theory Tech.*, Vol. 56, No. 10, 2221–2228, Oct. 2008.
4. Pursula, P., T. Karttaavi, M. Kantanen, A. Lamminen, J. Holmberg, M. Lahdes, I. Marttila, M. Lahti, A. Luukanen, and T. Vähä-HEikkilä, "60-GHz millimeter-wave identification reader on 90-nm CMOS and LTCC," *IEEE Trans. Microw. Theory Tech.*, Vol. 59, No. 4, 1166–1173, Apr. 2011.
5. Lee, C.-H., A. Sutono, S. Han, K. Lim, S. Pinel, E. M. Tentzeris, and J. Laskar, "A compact LTCC-based Ku-band transmitter module," *IEEE Trans. Adv. Packag.*, Vol. 25, No. 3, 374–384, Aug. 2002.
6. Pohl, N., T. Jaeschke, and K. Aufinger, "An ultra-wideand 80 GHz FMCW radar system using a SiGe bipolar transceiver chip stabilized by a fractional-N PLL synthesizer," *IEEE Trans. Microw. Theory Tech.*, Vol. 60, No. 3, 757–765, Mar. 2012.
7. Sommer, J.-P., B. Mechel, and J. Jelonnek, "Thermally optimised millimeter wave package on an LTCC ceramic board," *IEEE Inter Society Conference on Thermal Phenomena*, 355–360, 2000.